

Measurement of the Permanent Electric Dipole Moment of the Neutron

C. Abel,¹ S. Afach,^{2,3} N. J. Ayres,^{1,3} C. A. Baker,⁴ G. Ban,⁵ G. Bison,² K. Bodek,⁶ V. Bondar,^{2,3,7} M. Burghoff,⁸ E. Chanel,⁹ Z. Chowdhuri,² P.-J. Chiu,^{2,3} B. Clement,¹⁰ C. B. Crawford,¹¹ M. Daum,² S. Emmenegger,³ L. Ferraris-Bouchez,¹⁰ M. Fertl,^{2,3,12} P. Flaux,⁵ B. Franke,^{2,3,d} A. Fratangelo,⁹ P. Geltenbort,¹³ K. Green,⁴ W. C. Griffith,¹ M. van der Grinten,⁴ Z. D. Grujić,^{14,15} P. G. Harris,¹ L. Hayen,^{7,e} W. Heil,¹² R. Henneck,² V. H elaine,^{2,5} N. Hild,^{2,3} Z. Hodge,⁹ M. Horras,^{2,3} P. Iaydjiev,^{4,n} S. N. Ivanov,^{4,o} M. Kasprzak,^{2,7,14} Y. Kermaidic,^{10,f} K. Kirch,^{2,3} A. Knecht,^{2,3} P. Knowles,¹⁴ H.-C. Koch,^{2,14,12} P. A. Koss,^{7,g} S. Komposch,^{2,3} A. Kozela,¹⁶ A. Kraft,^{2,12} J. Krempel,³ M. Kuźniak,^{2,6,h} B. Lauss,² T. Lefort,⁵ Y. Lemi ere,⁵ A. Leredde,¹⁰ P. Mohanmurthy,^{2,3} A. Mtchedlishvili,² M. Musgrave,^{1,i} O. Naviliat-Cuncic,⁵ D. Pais,^{2,3} F. M. Piegsa,⁹ E. Pierre,^{2,5,j} G. Pignol,^{10,a} C. Plonka-Spehr,¹⁷ P. N. Prashanth,⁷ G. Qu em ener,⁵ M. Rawlik,^{3,k} D. Rebreyend,¹⁰ I. Rien acker,^{2,3} D. Ries,^{2,3,17} S. Roccia,^{13,18,b} G. Rogel,^{5,1} D. Rozpedzik,⁶ A. Schnabel,⁸ P. Schmidt-Wellenburg,^{2,c} N. Severijns,⁷ D. Shiers,¹ R. Tavakoli Dinani,⁷ J. A. Thorne,^{1,9} R. Virost,¹⁰ J. Voigt,⁸ A. Weis,¹⁴ E. Wursten,^{7,m} G. Wyszynski,^{3,6} J. Zejma,⁶ J. Zenner,^{2,17} and G. Zsigmond²

¹Department of Physics and Astronomy, University of Sussex, Falmer, Brighton BN1 9QH, United Kingdom

²Paul Scherrer Institut, CH-5232 Villigen PSI, Switzerland

³ETH Z urich, Institute for Particle Physics and Astrophysics, CH-8093 Z urich, Switzerland

⁴STFC Rutherford Appleton Laboratory, Harwell, Didcot, Oxon OX11 0QX, United Kingdom

⁵LPC Caen, ENSICAEN, Universit e de Caen, CNRS/IN2P3, 14000 Caen, France

⁶Marian Smoluchowski Institute of Physics, Jagiellonian University, 30-348 Cracow, Poland

⁷Instituut voor Kern- en Stralingsfysica, University of Leuven, B-3001 Leuven, Belgium

⁸Physikalisch Technische Bundesanstalt, D-10587 Berlin, Germany

⁹Laboratory for High Energy Physics and Albert Einstein Center for Fundamental Physics, University of Bern, CH-3012 Bern, Switzerland

¹⁰Universit e Grenoble Alpes, CNRS, Grenoble INP, LPSC-IN2P3, 38026 Grenoble, France

¹¹University of Kentucky, 40506 Lexington, Kentucky, USA

¹²Institute of Physics, Johannes Gutenberg University Mainz, 55128 Mainz, Germany

¹³Institut Laue-Langevin, CS 20156 F-38042 Grenoble Cedex 9, France

¹⁴Physics Department, University of Fribourg, CH-1700 Fribourg, Switzerland

¹⁵Institute of Physics Belgrade, University of Belgrade, 11080 Belgrade, Serbia

¹⁶Henryk Niedwodniczanski Institute for Nuclear Physics, 31-342 Cracow, Poland

¹⁷Department of Chemistry - TRIGA site, Johannes Gutenberg University Mainz, 55128 Mainz, Germany

¹⁸CSNSM, Universit e Paris Sud, CNRS/IN2P3, F-91405 Orsay Campus, France



(Received 18 December 2019; accepted 3 February 2020; published 28 February 2020)

We present the result of an experiment to measure the electric dipole moment (EDM) of the neutron at the Paul Scherrer Institute using Ramsey's method of separated oscillating magnetic fields with ultracold neutrons. Our measurement stands in the long history of EDM experiments probing physics violating time-reversal invariance. The salient features of this experiment were the use of a ¹⁹⁹Hg comagnetometer and an array of optically pumped cesium vapor magnetometers to cancel and correct for magnetic-field changes. The statistical analysis was performed on blinded datasets by two separate groups, while the estimation of systematic effects profited from an unprecedented knowledge of the magnetic field. The measured value of the neutron EDM is $d_n = (0.0 \pm 1.1_{\text{stat}} \pm 0.2_{\text{sys}}) \times 10^{-26} e \cdot \text{cm}$.

DOI: 10.1103/PhysRevLett.124.081803

Published by the American Physical Society under the terms of the Creative Commons Attribution 4.0 International license. Further distribution of this work must maintain attribution to the author(s) and the published article's title, journal citation, and DOI. Funded by SCOAP³.

A nonzero permanent electric dipole moment $\vec{d} = 2d\vec{s}/\hbar$ for a nondegenerate particle with spin \vec{s} implies the violation of time-reversal symmetry. Invoking the CPT theorem [1,2] for quantum field theories, this also indicates the violation of the combined symmetry of charge conjugation and parity (CP). The standard model of particle physics (SM) contains two sources of CP violation: the phase of the Cabibbo-Kobayashi-Maskawa matrix,

resulting in the observed CP violation in K - and B -meson decays, and the $\bar{\theta}_{\text{QCD}}$ coefficient of the still-unobserved CP -violating term of the QCD Lagrangian [3]. Both are too small to account for the observed baryon asymmetry of the Universe [4], which requires CP violation as one of three essential ingredients [5]. Furthermore, many theories beyond the SM naturally have large CP -violating phases [6] that would result in an observable neutron EDM (nEDM). In combination with the limits from searches for the electron [7] and ^{199}Hg [8] EDM, the limit on the nEDM confirms and complements stringent constraints upon many theoretical models [9]. In particular, the nEDM alone stringently limits $\bar{\theta}_{\text{QCD}}$. This unnaturally small upper limit on $\bar{\theta}_{\text{QCD}}$ is known as the strong CP problem; it gave rise to searches for a Goldstone boson, the axion [10,11], which is also an attractive candidate to solve the dark matter mystery [12].

An overview of the spectrometer used for the measurement is shown in Fig. 1, while a detailed technical description of the apparatus (upgraded from that used for the previous best limit [13–15]) and of data taking may be found in Ref. [16]. A total of 54 068 individual measurement cycles, during 2015 and 2016, were used to determine the change in the Larmor precession frequency of the neutron:

$$f_n = \frac{1}{\pi\hbar} |\mu_n \vec{B}_0 + d_n \vec{E}|, \quad (1)$$

correlated with the change of polarity of the electric field $|\vec{E}| = 11$ kV/cm, where μ_n is the magnetic dipole moment and \vec{B}_0 a collinear magnetic field ($|\vec{B}_0| = 1036$ nT). For this purpose, we used Ramsey’s method of separate oscillating fields [17].

In each cycle, ultracold neutrons (UCNs) from the Paul Scherrer Institute’s UCN source [18,19] were polarized by

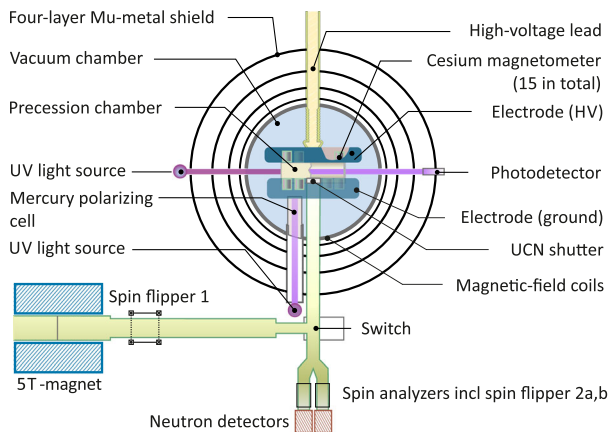


FIG. 1. Scheme of the spectrometer used to search for an nEDM. A nonzero signal manifests as a shift of the magnetic resonance frequency of polarized UCNs in a magnetic field B_0 when exposed to an electric field of strength E .

transmission through a 5 T superconducting solenoid; spin flipper 1 (SF1) then allowed the selection of the initial spin state (up or down). The switch directed the incoming neutrons to the cylindrical precession chamber situated 1.2 m above the beam line. The precession chamber (radius $R = 23.5$ cm, height $H = 12$ cm) was made of diamond-like-carbon-coated [20,21] aluminum electrodes and a deuterated-polystyrene-coated [22] insulator ring milled from bulk polystyrene. After 28 s, an equilibrium density of up to 2 UCN/cm³ inside the precession chamber was attained, and a UCN shutter in the bottom electrode was closed to confine the UCN for a total of 188 s. A small valve was opened for 2 s to release a sample of polarized ^{199}Hg vapor, that was used as a comagnetometer (HgM). A first low-frequency (LF) pulse of 2 s duration and frequency $|\mu_{\text{Hg}} B_0|/(\pi\hbar) \approx 7.8$ Hz tipped the ^{199}Hg spin by $\pi/2$. Ramsey’s technique was then applied to the neutrons, with an LF pulse (also of $t_{\text{LF}} = 2$ s duration) at a frequency of $|\mu_n B_0|/(\pi\hbar) \approx 30.2$ Hz tipping the UCN spins by $\pi/2$. After a period of $T = 180$ s of free precession, a second neutron LF pulse, in phase with the first, was applied. During data taking, the LF pulses were alternated between four frequencies in the steep regions of the central Ramsey fringe.

Immediately after the second neutron LF pulse, the UCN shutter in the bottom electrode was opened. The switch was also moved to the “empty” position connecting the precession chamber with the UCN detection system [23,24], which counted both spin states simultaneously in separate detectors. The state of the spin flippers (SF2a and SF2b) above each detector was alternated every fourth cycle, with one of them being off while the other was on, to average over detection, spin flipper, and spin analyzer efficiencies. For each cycle i , we recorded an asymmetry value between the number of spin-up ($N_{u,i}$) and spin-down neutrons ($N_{d,i}$): $A_i = (N_{u,i} - N_{d,i})/(N_{u,i} + N_{d,i})$. On average, $N_u + N_d = 11400$ neutrons were counted per cycle.

In addition, for each cycle we obtained a frequency $f_{\text{Hg},i}$ from the analysis of the mercury precession signal, as well as 15 frequencies $f_{\text{Cs},i}$ from cesium magnetometers (CsM) positioned above and below the chamber.

There are 22 base configurations of the magnetic field within the dataset. Each base configuration was defined by a full degaussing of the four-layer magnetic shield and an ensuing magnetic-field optimization using all CsM described in detail in Ref. [25]. This procedure was essential to maintain a high visibility, which was measured to be $\bar{\alpha} = 0.76$ on average. A base configuration was kept for a duration of up to a month, during which only the currents of two saddle coils on the vacuum tank, above and below the chamber, were changed to adjust the vertical gradient in a range of approximately ± 25 pT/cm [26]. Within a base configuration, all cycles with the same applied magnetic gradients were grouped in one sequence. The analyzed dataset consists of 99 sequences. The voltage

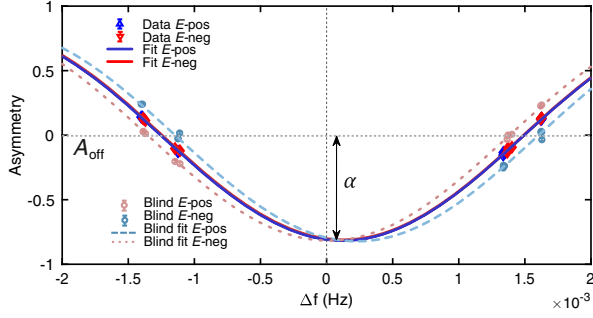


FIG. 2. Illustration of the fit to the Ramsey central fringe. Data without an electric field are omitted. The data scatter around the four working points. Faded data and lines are for the blinded case (illustration for a very large artificial EDM).

applied to the top electrode was changed periodically: eight cycles at zero volts followed by 48 cycles at ± 132 kV, with the pattern then being repeated under reversed polarity. During the analysis, sequences were split into subsequences having polarity patterns of $+ - - +$ or $- + + -$.

The analysis searched for shifts in the neutrons' Larmor precession frequency that were proportional to the applied electric field E_i . To determine the neutron frequency $f_{n,i}$ for each cycle from the measured asymmetry A_i , we fitted the Ramsey resonance

$$A_i = A_{\text{off}} \mp \alpha \cos\left(\frac{\pi \Delta f_i}{\Delta \nu} + \Phi\right) \quad (2)$$

to the data of each subsequence (see Fig. 2), with a negative (positive) sign for SF1 turned off (on). In Eq. (2), $\Delta \nu = (2T + 8t_{\text{LF}}/\pi)^{-1} = 2.7$ mHz is the resonance linewidth, Δf_i is the applied spin-flip frequency $f_{n,\text{LF}}$ corrected for magnetic-field changes [27], and A_{off} , α , and Φ , are free parameters: the offset, fringe visibility, and phase, respectively. Individual values of $f_{n,i}$ per cycle were extracted by keeping the fit parameters fixed and rearranging Eq. (2) for Δf_i .

The ratio of frequencies $\mathcal{R}_i = f_{n,i}/f_{\text{Hg},i}$ was then used to compensate for residual magnetic-field fluctuations and drifts as shown in Fig. 3. In what follows, the statistical analysis and the evaluation of systematic effects take into account all known effects affecting the ratio \mathcal{R}_i . These are summarized in the formula

$$\mathcal{R} = \left| \frac{\gamma_n}{\gamma_{\text{Hg}}} \right| \left(1 + \delta_{\text{EDM}} + \delta_{\text{EDM}}^{\text{false}} + \delta_{\text{quad}} + \delta_{\text{grav}} + \delta_{\mathcal{T}} + \delta_{\text{Earth}} + \delta_{\text{light}} + \delta_{\text{inc}} + \delta_{\text{other}} \right), \quad (3)$$

where the true EDM term is written

$$\delta_{\text{EDM}} = -\frac{2E}{\hbar|\gamma_n|B_0} (d_n + d_{n\leftarrow\text{Hg}}) \quad (4)$$

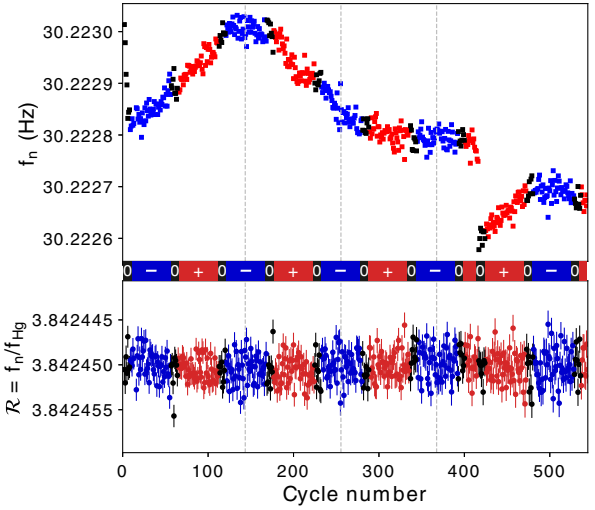


FIG. 3. A typical sequence of cycles. The upper plot shows the neutron frequency f_n as a function of the cycle number; the lower plot shows the frequency ratio \mathcal{R} . The colors correspond to the high-voltage polarity (blue, negative; red, positive; black, zero). The vertical lines separate the subsequences.

and neglecting the index i for the following. The ^{199}Hg EDM, measured to be $d_{\text{Hg}} = (-2.20 \pm 2.75_{\text{stat}} \pm 1.48_{\text{sys}}) \times 10^{-30}$ e.cm [8], induces a bias of the EDM term by $d_{n\leftarrow\text{Hg}} = |\gamma_n/\gamma_{\text{Hg}}|d_{\text{Hg}} = (-0.1 \pm 0.1) \times 10^{-28}$ e.cm, which we quote as a global systematic error.

Subsequent terms are undesirable effects that influence the neutron or mercury frequencies. We now discuss them individually.

The gravitational shift $\delta_{\text{grav}} = G_{\text{grav}}\langle z \rangle/B_0$ induced by the effective vertical magnetic-field gradient G_{grav} is due to the center of mass offset $\langle z \rangle = -0.39(3)$ cm of the UCNs in the chamber. We deduced $\langle z \rangle$ in an auxiliary analysis from an estimation of the slope $\partial\mathcal{R}/\partial G_{\text{grav}}$ by combining the CsM-array readings and offline magnetic-field maps. The static part of G_{grav} induces a shift of the mean value of \mathcal{R} in a sequence, whereas the fluctuating part induces a drift in \mathcal{R} within each subsequence. This gradient drift is compensated for at the cycle level using a combination of the HgM and the CsMs below the grounded bottom electrode. The CsMs mounted on the top electrode were not included in order to avoid any possible high-voltage susceptibility in their readings.

In each subsequence, we extract the EDM signal d_n^{meas} by fitting the \mathcal{R}_i values, compensated for the gradient drift, as a function of the time and electric field and allowing in addition for a linear time drift. This assumes perfect compensation of δ_{grav} and that δ_{EDM} is the only E -field-dependent term in Eq. (3). Deviations from this hypothesis are treated as systematic effects.

The dominant systematic effects arise from a shift linear in E due to the combination of the relativistic motional field $\vec{B}_m = \vec{E} \times \vec{v}/c^2$ [28] and the magnetic-field gradient:

$$\delta_{\text{EDM}}^{\text{false}} = -\frac{2E}{\hbar|\gamma_n|B_0}(d_n^{\text{net}} + d^{\text{false}}), \quad (5)$$

where d_n^{net} is the effect of a possible net motion of the UCNs (discussed later) and d^{false} is due to the random motion of the UCNs and ^{199}Hg atoms in a nonuniform magnetic field. The latter is largely dominated by the mercury and is written as [29,30]

$$d^{\text{false}} = \frac{\hbar}{8c^2}|\gamma_n\gamma_{\text{Hg}}|R^2(G_{\text{grav}} + \hat{G}), \quad (6)$$

where \hat{G} is the higher-order gradient term, which does not produce a gravitational shift. We used magnetic-field maps, measured offline, to extract a value of \hat{G} for each sequence and calculate a corrected EDM value $d_n^{\text{corr}} = d_n^{\text{meas}} - \hbar|\gamma_n\gamma_{\text{Hg}}|R^2\hat{G}/(8c^2)$. The main contribution in Eq. (6) depending on G_{grav} is then dealt with by the crossing-point analysis, shown in Fig. 4: d_n^{corr} is plotted as a function of $\mathcal{R}^{\text{corr}} = \mathcal{R}/(1 + \delta_T + \delta_{\text{Earth}})$, and we fit two lines with opposite slopes corresponding to the sequences with B_0 up and B_0 down. At the crossing point, we have $G_{\text{grav}} = 0$, and the main systematic effect is canceled. In the fit, the free parameters are the coordinates of the crossing

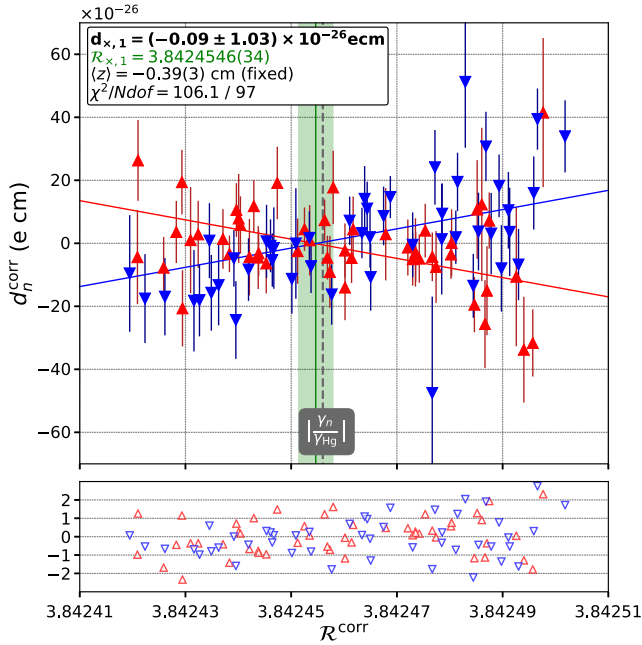


FIG. 4. Crossing point analysis: The corrected electric dipole moment d_n^{corr} is plotted vs $\mathcal{R}^{\text{corr}}$ (see the text for the exact definition of d_n^{corr} and $\mathcal{R}^{\text{corr}}$). Upward-pointing (red) and downward-pointing (blue) triangles represent sequences in which B_0 was pointing upward and downward, respectively. The fitted value of \mathcal{R}_x is represented by the green vertical band (1σ), and the vertical dashed line represents the ratio of gyromagnetic ratios calculated from the literature values of γ_n [31] and γ_{Hg} [32]. The lower panel shows the normalized fit residuals.

point \mathcal{R}_x and d_x ; the slope was fixed to the theoretical value $\partial d^{\text{false}}/\partial \mathcal{R} = \hbar\gamma_{\text{Hg}}^2 R^2 B_0/(8\langle z \rangle c^2)$. Because of the uncertainty on $\langle z \rangle = -0.39(3)$ cm, the slope has an error that propagates to become an additional error of 7×10^{-28} e.cm on d_x . As a check, we also considered the slope as a free parameter in the fit and found $\langle z \rangle = -0.35(6)$ cm, in agreement with the values found in Ref. [30].

In order to have $G_{\text{grav}} = 0$ at the crossing point, we had to correct \mathcal{R}_i for all shifts other than the gravitational shift: namely, the shift due to Earth's rotation δ_{Earth} and the shift due to transverse fields $\delta_T = \langle B_T^2 \rangle / (2B_0^2)$ [30]. The transverse shift for each sequence was calculated from the offline magnetic-field maps. The vertical corrections, related to \hat{G} , shifted the crossing point by $(69 \pm 10) \times 10^{-28}$ e.cm. The horizontal corrections, related to $\langle B_T^2 \rangle$, shifted the crossing point by $(0 \pm 5) \times 10^{-28}$ e.cm.

The corrections for the effect of the magnetic nonuniformities \hat{G} and $\langle B_T^2 \rangle$ are based on the mapping of the apparatus without a precession chamber, hence possibly missing the contribution of magnetic impurities in the precession chamber. All inner parts were scanned for magnetic dipoles before and after the data taking in the Berlin magnetically shielded room 2 at the Physikalisch Technische Bundesanstalt in Berlin. Initially, we verified that all parts showed no signals above the detection threshold 20 nAm^2 of the superconducting quantum interference device system; the second scan revealed a dozen dipoles with a maximum strength of 100 nAm^2 . The corresponding systematic error was evaluated to be 4×10^{-28} e.cm.

In addition to the false EDM due to the random motional field d^{false} , a net ordered motion of the UCN could generate a systematic effect $d_n^{\text{net}} = \eta\epsilon \cdot 6.7 \times 10^{-23}$ e.cm/(m/s), where η is the mean net velocity of the ordered motion orthogonal to E and B and ϵ is the misalignment angle between the electric and magnetic fields. Three possible sources of ordered motion were identified in the past [15]: a vertical motion due to microheating and initial transverse and rotational motions that are destroyed by collisions on the wall surfaces. Using the same trap geometry as in Ref. [15] and a softer initial UCN spectrum [33], we use the same value for ϵ and η . The error from heating was estimated to be 1×10^{-30} e.cm, while the error from rotational motion dominates: 2×10^{-28} e.cm.

The motional field also induces a shift quadratic in E of $\delta_{\text{quad}} = \gamma_{\text{Hg}}^2 R^2 E^2 / (4c^4)$ [34], where we consider only the (dominant) shift on the mercury frequency. We were able to exclude any possible polarity dependence of the E -field magnitude to a level of 10^{-4} and, therefore, state a conservative error of 0.1×10^{-28} e.cm for this effect.

Next, imperfect compensation of the δ_{grav} term by the CsMs can lead to a direct systematic effect in the case of a correlation between the E -field polarity and the magnetic-field uniformity. We evaluated the possible effect by

deactivating the gradient drift compensation in both analyses and found a mean difference of 7.5×10^{-28} e.cm; we quote the full shift as a systematic error. Leakage currents could be one source of such a correlation.

The term δ_{light} corresponds to a mercury frequency shift proportional to the power of the UV probe light [35]. We estimate that the largest shift of this type is at the level of 0.01 parts per million in our experiment. This can constitute a systematic effect if the power of the probe light is correlated with the polarity of the electric field, which we cannot exclude below the level of 0.14%. This results in a systematic error of 0.4×10^{-28} e.cm for mercury light shifts.

Ultracold neutrons co-precessing with polarized ^{199}Hg atoms are exposed to a pseudomagnetic field $\vec{B}^* = -4\pi\hbar n_{\text{Hg}} b_{\text{inc}} \vec{P} \sqrt{1/3} / (m\gamma_n)$ [36] due to a spin-dependent nuclear interaction quantified by the incoherent scattering length $b_{\text{inc}}(^{199}\text{Hg}) = \pm 15.5$ fm [37]. The mercury polarization \vec{P} could have a residual static component $P_{\parallel} = |P| \sin \zeta$ in the case of an imperfect $\pi/2$ pulse; this would generate a systematic effect if P_{\parallel} correlates with the electric-field polarity. We deduced ζ from the photomultiplier signal of the probe beam during the $\pi/2$ flip. The product $n_{\text{Hg}}|P|$ was estimated by comparing the ratio of precession amplitude to total light absorption in the ^{199}Hg -lamp readout and matching this to a laser measurement to calibrate for a pure $\lambda = 254.7$ nm light source. The systematic error induced by the term δ_{inc} was estimated to be 7×10^{-28} e.cm.

Table I lists the above-mentioned systematic effects. Additionally, the mercury pulse causes a small tilt of the neutron spin prior to the Ramsey procedure and is responsible for the shift δ_{pulse} . This shift is not correlated with the electric field; it behaves as an additional random error and was accounted for in the statistical analysis. Further effects

TABLE I. Summary of systematic effects in 10^{-28} e.cm. The first three effects are treated within the crossing-point fit and are included in d_{\times} . The additional effects below that are considered separately.

Effect	Shift	Error
Error on $\langle z \rangle$...	7
Higher-order gradients \hat{G}	69	10
Transverse field correction $\langle B_T^2 \rangle$	0	5
Hg EDM [8]	-0.1	0.1
Local dipole fields	...	4
$v \times E$ UCN net motion	...	2
Quadratic $v \times E$...	0.1
Uncompensated G drift	...	7.5
Mercury light shift	...	0.4
Inc. scattering ^{199}Hg	...	7
TOTAL	69	18

δ_{other} that were also studied and found to be negligible (smaller than 10^{-29} e.cm) include the effects of ac fields δ_{ac} induced by a ripple of the high-voltage supply; noise of the current supplies or Johnson-Nyquist noise generated by the electrodes; the movement of the electrodes correlated with an electric field; and a correlation of the orientation of the magnetic field with the electric field in combination with the rotation of Earth.

During data taking, a copy of the files with the neutron detector data was modified by moving a predefined randomly distributed number of neutrons from one UCN detector to the other (see Fig. 2). This injection of an artificial EDM signal into the data was applied twice, and two datasets with different artificial EDMs were distributed to two distinct analysis groups [38]. This double-blind procedure enforced the independence of the two analyses, in particular, for the data selection criteria. Once the two analyses had been completed using only double-blind datasets, it was confirmed that they gave consistent results when run on an identical blind dataset. Finally, both groups performed their analysis on the original never-blinded dataset. The results of the crossing-point fit are $d_{\times,1} = (-0.09 \pm 1.03) \times 10^{-26}$ e.cm, $\mathcal{R}_{\times,1} = 3.8424546(34)$ with $\chi^2/\text{dof} = 106/97$ and $d_{\times,2} = (0.15 \pm 1.07) \times 10^{-26}$ e.cm, $\mathcal{R}_{\times,2} = 3.8424538(35)$ with $\chi^2/\text{dof} = 105/97$.

The small difference between the two results can be explained by the different selection criteria, and we take as a final value the midpoint of the two. After adding the extra systematic effects quoted in the second part of Table I, the final result, separating the statistical and systematic errors, is

$$d_n = (0.0 \pm 1.1_{\text{stat}} \pm 0.2_{\text{sys}}) \times 10^{-26} \text{ e.cm.} \quad (7)$$

The result may be interpreted as an upper limit of $|d_n| < 1.8 \times 10^{-26}$ e.cm (90% C.L.). This has been achieved through an unprecedented understanding and control of systematic effects in the experiment. In particular, those related to magnetic-field nonuniformity were assessed with dedicated measurements that resulted in a significant correction, equivalent to 60% of the statistical uncertainty, that arose from higher-order magnetic-field gradients. Overall, the systematic error has been reduced by a factor of 5 compared to the previous best result [15].

We are profoundly grateful for the fundamental contributions to the field, in general, and to this project, in particular, of J.M. Pendlebury and to K.F. Smith and others also involved with the original development of the nEDM spectrometer with Hg comagnetometer. We acknowledge the excellent support provided by the PSI technical groups and by various services of the collaborating universities and research laboratories. In particular, we acknowledge with gratitude the long-term outstanding technical support by F. Burri and M. Meier. We thank

the UCN source operation group BSQ for their support. We acknowledge financial support from the Swiss National Science Foundation through Projects No. 117696, No. 137664, No. 144473, No. 157079, No. 172626, No. 126562, No. 169596 (all PSI), No. 181996 (Bern), No. 162574 (ETH), No. 172639 (ETH), and No. 140421 (Fribourg). University of Bern acknowledges the support via the European Research Council under the ERC Grant Agreement No. 715031-BEAM-EDM. Contributions of the Sussex group have been made possible via STFC Grants No. ST/M003426/1, No. ST/N504452/1, and No. ST/N000307/1. LPC Caen and LPSC Grenoble acknowledge the support of the French Agence Nationale de la Recherche (ANR) under Reference No. ANR-09-BLAN-0046 and the ERC Project No. 716651-NEDM. The Polish collaborators acknowledge support from the National Science Center, Poland, under Grants No. 2015/18/M/ST2/00056, No. 2016/23/D/ST2/00715, and No. 2018/30/M/ST2/00319. P. M. acknowledges State Secretariat for Education, Research and Innovation (SERI) Grant No. SERI-FCS 2015.0594. This work was also partly supported by the Fund for Scientific Research Flanders (FWO) and Project No. GOA/2010/10 of the KU Leuven. We acknowledge the support from the DFG (DE) specifically Projects No. BI 1424/2-1 and No. BI 1424/3-1. In addition, we are grateful for access granted to the computing grid PL-Grid infrastructure.

^aCorresponding author.
pignol@lpsc.in2p3.fr

^bCorresponding author.
roccia@ill.fr

^cCorresponding author.
philipp.schmidt-wellenburg@psi.ch

^dPresent address: TRIUMF, Vancouver, Canada.

^ePresent address: Department of Physics, North Carolina State University, Raleigh, North Carolina 27695, USA.

^fPresent address: Max-Planck-Institut für Kernphysik, Heidelberg, Germany.

^gPresent address: Fraunhofer-Institut für Physikalische Messtechnik IPM, 79110 Freiburg i. Breisgau, Germany.

^hPresent address: AstroCeNT, Nicolaus Copernicus Astronomical Center, Polish Academy of Sciences, Rektorska 4, Warsaw, Poland.

ⁱPresent address: MIT, Boston, USA.

^jPresent address: LPTMC, Sorbonne Université, Paris, France.

^kPresent address: Paul Scherrer Institut, CH-5232 Villigen PSI, Switzerland.

^lPresent address: CEA Saclay, Saclay, France.

^mPresent address: CERN, 1211 Genève, Switzerland.

ⁿOn leave from Institute of Nuclear Research and Nuclear Energy, Sofia, Bulgaria.

^oOn leave from Petersburg Nuclear Physics Institute, Russia.

[1] G. Luders, Dan. Mat. Fys. Medd. **28**, 1 (1954), <https://cds.cern.ch/record/1071765?ln=fr>.

- [2] W. Pauli, in *Niels Bohr and the Development of Physics* (Pergamon, New York, 1955), pp. 30–51.
- [3] G. t’Hooft, *Phys. Rev. Lett.* **37**, 8 (1976).
- [4] D. E. Morrissey and M. J. Ramsey-Musolf, *New J. Phys.* **14**, 125003 (2012).
- [5] A. D. Sakharov, *Sov. Phys. Uspekhi* **34**, 392 (1991).
- [6] J. Engel, M. J. Ramsey-Musolf, and U. van Kolck, *Prog. Part. Nucl. Phys.* **71**, 21 (2013).
- [7] V. Andreev *et al.* (ACME Collaboration), *Nature (London)* **562**, 355 (2018).
- [8] B. Graner, Y. Chen, E. G. Lindahl, and B. R. Heckel, *Phys. Rev. Lett.* **116**, 161601 (2016).
- [9] T. Chupp and M. Ramsey-Musolf, *Phys. Rev. C* **91**, 035502 (2015).
- [10] F. Wilczek, *Phys. Rev. Lett.* **40**, 279 (1978).
- [11] R. D. Peccei and H. R. Quinn, *Phys. Rev. Lett.* **38**, 1440 (1977).
- [12] J. de Swart, G. Bertone, and J. van Dongen, *Nat. Astron.* **1**, 0059 (2017).
- [13] C. A. Baker, D. D. Doyle, P. Geltenbort *et al.*, *Phys. Rev. Lett.* **97**, 131801 (2006).
- [14] C. Baker, Y. Chibane, M. Chouder *et al.*, *Nucl. Instrum. Methods Phys. Res., Sect. A* **736**, 184 (2014).
- [15] J. M. Pendlebury, S. Afach, N. J. Ayres *et al.*, *Phys. Rev. D* **92**, 092003 (2015).
- [16] C. Abel, N. J. Ayres, G. Ban *et al.*, *EPJ Web Conf.* **219**, 02001 (2019).
- [17] N. F. Ramsey, *Phys. Rev.* **78**, 695 (1950).
- [18] A. Anghel, F. Atchison, B. Blau *et al.*, *Nucl. Instrum. Methods Phys. Res., Sect. A* **611**, 272 (2009).
- [19] B. Lauss, *Phys. Procedia* **51**, 98 (2014).
- [20] F. Atchison, B. Blau, M. Daum *et al.*, *Phys. Lett. B* **642**, 24 (2006).
- [21] F. Atchison, B. Blau, M. Daum *et al.*, *Phys. Rev. C* **74**, 055501 (2006).
- [22] K. Bodek, M. Daum, R. Henneck *et al.*, *Nucl. Instrum. Methods Phys. Res., Sect. A* **597**, 222 (2008).
- [23] S. Afach, G. Ban, G. Bison *et al.*, *Eur. Phys. J. A* **51**, 143 (2015).
- [24] G. Ban, G. Bison, K. Bodek *et al.*, *Eur. Phys. J. A* **52**, 326 (2016).
- [25] C. Abel, S. Afach, N. J. Ayres *et al.*, [arXiv:1912.04631](https://arxiv.org/abs/1912.04631).
- [26] S. Afach, N. Ayres, C. A. Baker *et al.*, *Phys. Rev. D* **92**, 052008 (2015).
- [27] One analysis team has chosen to use $\Delta f_i = \langle f_{\text{Hg}} \rangle (f_{n,\text{LF}}/f_{\text{Hg},i})$ and $\Phi = \mathcal{R}\langle f_{\text{Hg}} \rangle (\Delta\nu/\pi)$, while the other team used $\Delta f = f_{\text{Hg},i} - \langle z \rangle g_z$ and the phase Φ .
- [28] J. M. Pendlebury, W. Heil, Y. Sobolev *et al.*, *Phys. Rev. A* **70**, 032102 (2004).
- [29] G. Pignol and S. Rocca, *Phys. Rev. A* **85**, 042105 (2012).
- [30] C. Abel, N. J. Ayres, T. Baker *et al.*, *Phys. Rev. A* **99**, 042112 (2019).
- [31] G. L. Greene, N. F. Ramsey, W. Mampe, J. M. Pendlebury, K. Smith, W. B. Dress, P. D. Miller, and P. Perrin, *Phys. Rev. D* **20**, 2139 (1979).
- [32] B. Cagnac, *Ann. Phys. (N.Y.)* **13**, 467 (1961).
- [33] G. Bison, B. Blau, M. Daum, L. Göttl, R. Henneck, K. Kirch, B. Lauss, D. Ries, P. Schmidt-Wellenburg, and G. Zsigmond, *Eur. Phys. J. A* **56**, 33 (2020).

- [34] G. Pignol, M. Guigue, A. Petukhov, and R. Golub, *Phys. Rev. A* **92**, 053407 (2015).
- [35] C. Cohen-Tannoudji, *Ann. Phys. (N.Y.)* **13**, 423 (1962).
- [36] A. Abragam and M. Goldman, *Nuclear Magnetism: Order and Disorder* (Oxford University Press, Oxford, 1982).
- [37] V. F. Sears, *Neutron News* **3**, 26 (1992).
- [38] N. J. Ayres, G. Ban, G. Bison *et al.*, [arXiv:1912.09244](https://arxiv.org/abs/1912.09244).

Analysis method for detecting topological defect dark matter with a global magnetometer network

Hector Masia-Roig^{a,*}, Joseph A. Smiga^{a,*}, Dmitry Budker^{a,b,c}, Vincent Dumont^b, Zoran Grujic^d, Dongok Kim^{e,f}, Derek F. Jackson Kimball^g, Victor Lebedev^d, Madeline Monroy^g, Szymon Pustelny^h, Theo Scholtes^{d,i,1}, Perrin C. Segura^j, Yannis K. Semertzidis^{e,f}, Yun Chang Shin^e, Jason E. Stalnaker^j, Ibrahim Sulai^k, Antoine Weis^d, Arne Wickenbrock^a

^aHelmholtz Institut Mainz, Johannes Gutenberg-Universität, 55099 Mainz, Germany

^bDepartment of Physics, University of California, Berkeley, CA 94720-7300, USA

^cNuclear Science Division, Lawrence Berkeley National Laboratory, Berkeley, CA 94720, USA

^dPhysics Department, University of Fribourg, Chemin du Musée 3, CH-1700 Fribourg, Switzerland

^eCenter for Axion and Precision Physics Research, IBS, Daejeon 34051, Republic of Korea

^fDepartment of Physics, KAIST, Daejeon 34141, Republic of Korea

^gDepartment of Physics, California State University — East Bay, Hayward, CA 94542-3084, USA

^hInstitute of Physics, Jagiellonian University, prof. Stanisława Lojasiewicza 11, 30-348, Kraków, Poland

ⁱLeibniz Institute of Photonic Technology, Albert-Einstein-Straße 9, D-07745 Jena, Germany

^jDepartment of Physics and Astronomy, Oberlin College, Oberlin, OH 44074, USA

^kDepartment of Physics & Astronomy, One Dent Drive, Bucknell University, Lewisburg, Pennsylvania 17837, USA

Abstract

The Global Network of Optical Magnetometers for Exotic physics searches (GNOME) is a network of time-synchronized, geographically separated, optically pumped atomic magnetometers that is being used to search for correlated transient signals heralding exotic physics. GNOME is sensitive to exotic couplings of atomic spins to certain classes of dark matter candidates, such as axions. This work presents a data analysis procedure to search for axion dark matter in the form of topological defects: specifically, walls separating domains of discrete degenerate vacua in the axion field. An axion domain wall crossing the Earth creates a distinctive signal pattern in the network that can be distinguished from random noise. The reliability of the analysis procedure and the sensitivity of the GNOME to domain-wall crossings are studied using simulated data.

1. Introduction

The compelling evidence for dark matter [1] has inspired various theories to explain its nature [2, 3]. Many of these theories propose new particles as dark matter candidates [2, 4], and various experiments have been designed to search for these particles [5, 6, 7, 8, 9]. A well-motivated class of plausible dark matter constituents are axions and axion-like particles [10, 11]. The canonical QCD axion was originally introduced to solve the strong-CP problem [12], and variants of this idea have surfaced, for example, in string theory [13] and in solutions to the hierarchy problem [14]. Hereafter, “axion” will refer to any axion-like particle and not only the canonical axion (which possesses particular constraints on the mass-coupling relationship).

Axions may form topological defects such as domain walls [15, 16] or composite objects such as axion stars due to self-interactions [17, 18, 19, 20]. In particular, axion domain walls form between spatial domains wherein the axion field is centered around discrete vacua — so the transition between these states must include field values that are not locally vacuum states. Axion domain walls are formed during a phase transition as the universe cools through expansion [21]. If the phase transition occurred after inflation, domain walls may continue to exist today; otherwise inflation would have pushed other domains outside of the observable universe. The domain walls may contain a substantial amount of energy, which may explain

*Corresponding author

Email addresses: hemasiar@uni-mainz.de (Hector Masia-Roig), jsmiga@uni-mainz.de (Joseph A. Smiga)

¹Current address is Leibniz Institute of Photonic Technology.

some component of dark matter [16] and possibly dark energy [22]. If the axion domain walls are a component of dark matter, it is reasonable to assume that they are virialized in the galaxy according to the standard halo model (SHM) with velocity dispersion of ≈ 290 km/s [23, 24, 25]. In this study, an analysis method is developed to search for axion domain walls using a global network of optical magnetometers, though the methods discussed in this paper could be applied to search for other objects such as axion stars.

The axion field can couple to ordinary matter in a variety of ways. For example, fermion spins may couple to the gradient of the axion field [21]. If fermionic matter crosses a region with an axion field gradient, such as a domain wall, it would experience a transient spin-dependent energy shift. This energy shift would appear as an effective magnetic field in atomic magnetometers which measure the energy-level splitting of different spin states.

To search for such transient spin-dependent effects, optical atomic magnetometers [26] were set up around the Earth to form the Global Network of Optical Magnetometers for Exotic physics searches (GNOME) [27, 28]. At the core of each GNOME magnetometer is a vapor cell containing a gas of spin-polarized atoms. The atomic vapor cells are mounted within multi-layer magnetic shields that isolate them from external magnetic perturbations while retaining sensitivity to exotic fields causing spin-dependent energy shifts [29]. Based on the experimental configuration, each magnetometer is sensitive to fields along a particular spatial axis and relatively insensitive to fields in the plane perpendicular to the sensitive axis. Each magnetometer has a characteristic bandwidth, typically ≈ 100 Hz. There are additional sensors (e.g., accelerometers, gyroscopes, unshielded magnetometers, laser diagnostics) to monitor data quality. Under typical operating conditions, individual GNOME magnetometers experience occasional periods of poor-quality data which are flagged by these additional sensors. Furthermore, there are down times during which the magnetometers are off and no data are collected. The position, alignments of sensitive axes, and average noise background of nine of the magnetometers are shown in Table 1. The noise background of each magnetometer is estimated by the average standard deviation of 30 min pre-processed data segments from December 2017. For further technical details on characteristics of the GNOME, see Ref. [27].

Table 1: Characteristics of the sensors used for the simulated data. This information is based on GNOME but may not fully reflect the real network. The positions, orientation of the sensitive axes, and noise are listed. The noise is the standard deviation of the Gaussian-distributed background used in the simulations.

Station	Location		Orientation		Noise (pT)
	Longitude	Latitude	Az	Alt	
Beijing	116.1868° E	40.2457° N	+251°	0°	10.4
Berkeley	122.2570° W	37.8723° N	0°	+90°	14.5
Daejeon	127.3987° E	36.3909° N	0°	+90°	116
Fribourg	7.1581° E	46.7930° N	+190°	0°	12.6
Hayward	122.0539° W	37.6564° N	0°	-90°	14.3
Hefei	117.2526° E	31.8429° N	+90°	0°	12.0
Krakow	19.9048° E	50.0289° N	+45°	0°	15.6
Lewisburg	76.8825° W	40.9557° N	0°	+90°	54.5
Mainz	8.2354° E	49.9915° N	0°	-90°	6.8

If the Earth encounters a domain wall, a distinctive signal pattern is imprinted in the network. Signals would appear at each station at particular times and with particular amplitudes. The pattern is determined by the relative velocity between the Earth and the domain wall as well as the orientation of the sensitive axes of the magnetometers. These distinctive signal patterns are used to distinguish potential domain-wall-crossing events from random noise. In the event of a discovery, signal characteristics can be used to extract information about the axion domain wall. For example, the physical thickness of the domain wall is inversely proportional to the axion mass [21].

This paper describes an analysis algorithm to search for signal patterns in the GNOME data that are consistent with domain-wall-crossing events and quantify their statistical significance. Additionally, a definition of network sensitivity is established that characterizes the properties of domain-wall signals observable by GNOME.

Before discussing the details of the analysis methods, a geometrical interpretation of the principles of the analysis procedure is introduced in Sec. 2. The analysis procedure follows several steps that are described in

detail in Sec. 3. The data are first binned and filtered to optimize the detection potential of the network. Then the processed data are analyzed to search for correlated signals matching the predicted pattern associated with the Earth crossing a domain wall. Each of the magnetometer’s data are time-shifted according to the expected delays. The most likely effective field vector associated with a potential domain wall is calculated at each time, accounting for the directional sensitivity of the sensors. Consistency between the expected and observed signals in the network is assessed to determine if the deviation between the observed and expected signal patterns can be explained by random noise. The statistical significance of a potential domain-wall-crossing event is assessed according to its signal-to-noise ratio. Thresholds used to evaluate both the consistency with a domain-wall signal pattern and the statistical significance of the event are determined by studying false-positive and false-negative rates [30]. This analysis procedure is shown to be sensitive to domain-wall-crossing events characterized by a particular range of parameters as discussed in Sec. 4. The analysis algorithm is tested with simulated data, as described in Sec. 5. Finally, concluding remarks are given in Sec. 6.

2. Geometrical picture

A geometric viewpoint of the measurements is used to describe the analysis procedure. The magnetometer network measures the signals $\{s_i\}$ from a domain-wall-crossing event in n magnetometers, where s_i corresponds to the amplitude measured at the i^{th} magnetometer. A single measurement in the network can be expressed as an n -dimensional vector \mathbf{s} . The measurements, \mathbf{s} , have a corresponding uncertainty that can be expressed in terms of the covariance matrix Σ_s . Since the magnetometers have uncorrelated noise, Σ_s is diagonal with entries corresponding to the respective variance in the magnetometer signals. For statistical considerations of significance, it helps to describe the measurements in terms of signal-to-noise ratios. The abstract vector space of all possible measurement vectors \mathbf{s} can be rescaled by the noise, so that a point $\mathbf{u} \mapsto \tilde{\mathbf{u}} \equiv \Sigma_s^{-1/2} \mathbf{u}$, where $\Sigma_s^{-1/2}$ is the matrix square-root² of Σ_s^{-1} . In the rescaled coordinates, each component of the vector $\tilde{\mathbf{s}}$ corresponds to the signal-to-noise ratio for some sensor.

The effective field associated with a domain-wall-crossing event can be described using a three-dimensional vector \mathbf{m} normal to the plane of the domain wall. This effective field vector will be referred to as the “ m -vector.” For GNOME, the m -vector describes an effective magnetic field value due to coupling between atomic spins and an axion field. The strength of the signal is proportional to the norm $\|\mathbf{m}\|$. Note that there is some ambiguity since \mathbf{m} can be either in the same or opposite direction to the relative velocity \mathbf{v} between the domain wall and the Earth. One can relate \mathbf{m} to the observed signal \mathbf{s} with the linear equation $D\mathbf{m} \approx \mathbf{s}$, where D is a $n \times 3$ matrix whose rows represent the sensitive direction of the magnetometers, adjusting for the interaction of an axion field with the particular atomic species used in each magnetometer [31]. Note that, in the event of a real domain-wall-crossing signal, equality will not quite hold due to measurement uncertainty. To distinguish the measured amplitudes \mathbf{s} from the expected observations from an m -vector \mathbf{m} , $\mu \equiv D\mathbf{m}$ is introduced. According to this linear equation,³ all possible domain-walls signals are contained in a three-dimensional subspace spanned by the columns of D . The points in this subspace can be expressed as either the three-dimensional vector \mathbf{m} or its corresponding point in the n -dimensional measurement space, $\mu = D\mathbf{m}$.

A key parameter used to test the consistency of an observed signal \mathbf{s} with that expected for a domain-wall crossing is the χ^2 . Given an expected domain wall effective field vector \mathbf{m}_0 , the χ^2 is defined as

$$\chi^2 = (\mathbf{s} - D\mathbf{m}_0)^T \Sigma_s^{-1} (\mathbf{s} - D\mathbf{m}_0) . \quad (1)$$

For the distance $\Delta\mathbf{s} \equiv \mathbf{s} - \mu_0$ (for $\mu_0 \equiv D\mathbf{m}_0$), $\chi^2 = \Delta\mathbf{s}^T \Sigma_s^{-1} \Delta\mathbf{s} = \|\Delta\tilde{\mathbf{s}}\|^2$. Thus, the χ^2 is the square of the distance from the set of measurements to the expected value in rescaled measurement space. Minimizing

²Specifically, $(\Sigma_s^{-1/2})^T \Sigma_s^{-1/2} = \Sigma_s^{-1}$. Existence of this matrix follows from the fact that the covariance matrix is positive definite. In this particular case, $\Sigma_s^{-1/2} = \text{diag}\{\sigma_i^{-1}\}$, where σ_i is the noise of the i^{th} magnetometer expressed as the standard deviation.

³It is possible to include non-linear effects, such as Earth’s rotation and non-linear responses in the sensors, but these will not be considered here, because they are expected to be negligible. For sensors on Earth with domain walls traveling at 3×10^5 m/s, the effects of the Earth’s rotation will attenuate a signal by about 0.3%.

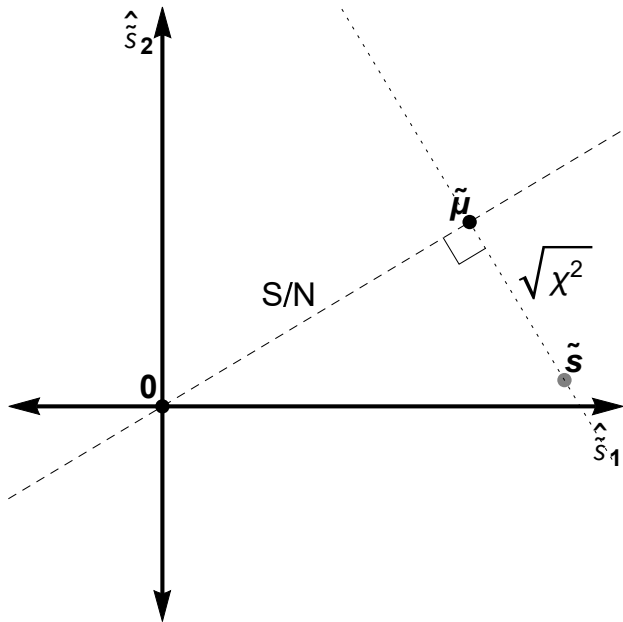


Figure 1: Geometric view of consistency check focusing on the plane in rescaled measurement space spanned by two sensors. A measured signal $\tilde{\mathbf{s}}$ shown with the expected amplitudes $\tilde{\boldsymbol{\mu}}$ defined by the physical parameters that would most-closely reproduce the measurement. The dashed line represents the subspace of possible domain wall measurements, while the dotted line represents the space of measurements that would yield the same expected amplitudes. The degree of statistical agreement between $\tilde{\mathbf{s}}$ and $\tilde{\boldsymbol{\mu}}$ scales with their distance $\sqrt{\chi^2}$. The signal-to-noise is given by the magnitude of $\tilde{\boldsymbol{\mu}}$.

the χ^2 is the same as finding the closest point between a measurement and a point $\tilde{\boldsymbol{\mu}}$ in the 3-dimensional subspace, which can be accomplished via a projection. A pictorial model simplified to have only two sensors and a one-dimensional subspace of possible measurements is shown in Fig. 1.

In the GNOME analysis procedure, the geometric picture provided in this section serves as a means of visualizing the data. In the rescaled measurement space, distances represent the degree of statistical agreement and measurements corresponding to domain-wall-crossing events exist in a three-dimensional linear subspace. Values \mathbf{s} in measurement space are constructed by sampling values from each magnetometer at some time accounting for expected delays. The delays are estimated by selecting a particular domain-wall-crossing velocity. As a result, a measurement \mathbf{s} can be generated for any given time and velocity, since each velocity results in a different set of delays. The direction of the velocity should be in agreement with the direction of the calculated \mathbf{m} .

3. Analysis procedure

The analysis procedure presented here is designed to search the GNOME data for domain-wall-crossing events. These events are modeled as a plane of finite thickness that travels through the Earth at a constant velocity. For a given plane orientation and speed,⁴ the signal pattern in the sensor network can be predicted. Assuming a linear coupling between the axion field gradient and fermion spins (i.e., of the form $J^\mu \partial_\mu a$ for J^μ related to the fermion spin and a being the axion field [21]), a transient pulse will appear in the measured magnetic field data as the domain wall crosses the Earth [21]. The transient pulse amplitude observed by an individual GNOME sensor is also affected by the specific axion-field coupling to that atomic species [31] and the angle between the axion-field gradient and the sensitive axis of the sensor [27].

The analysis procedure is composed of three steps designed to find domain-wall events. First, in the pre-processing stage, the raw data are filtered and a rolling average is applied in order to enhance the

⁴For an ideal plane, only the velocity perpendicular to the plane is observable. Thus, the velocity is entirely described by the speed and normal direction of the wall.

detection capabilities of the network. Second, in the velocity-scanning stage, the data from the individual magnetometers are time-shifted according to different domain-wall velocities. This ensures that the transient signals corresponding to a domain-wall crossing appear simultaneously in all magnetometers. Third, in the post-selection stage, each network measurement is characterized by three parameters: direction, magnitude, and consistency between the observed signal pattern and the expected signal for a domain-wall crossing. If an event passes a set of thresholds applied to these three parameters, it will be considered statistically significant (see Sec. 3.3.1). A basic flowchart of the procedure can be seen in Fig. 2.

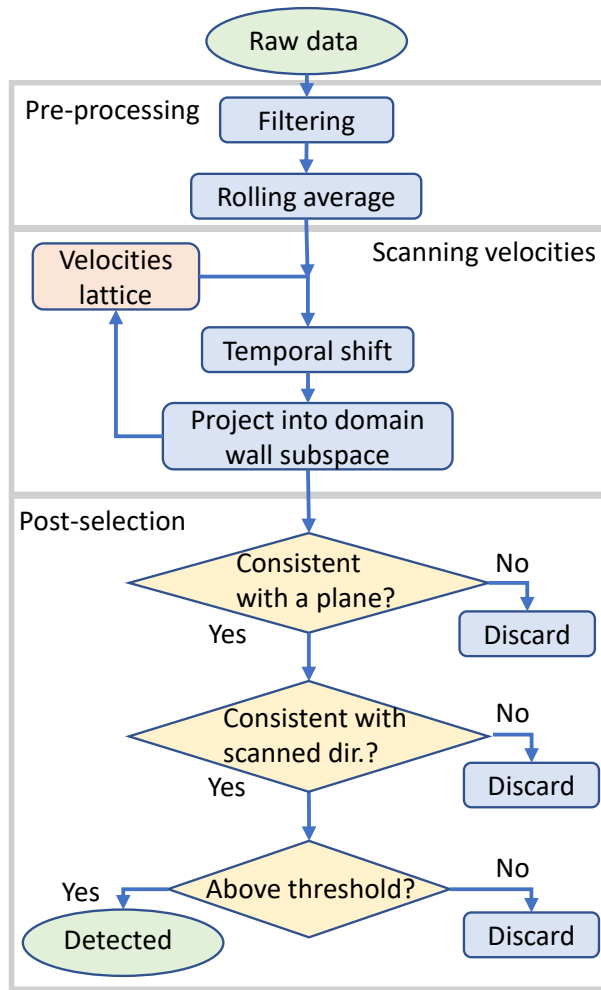


Figure 2: Flowchart describing the analysis algorithm used to detect domain-wall-crossing events in the GNOME data. After pre-processing, the data are aligned in time according to a velocity scanning grid (see Sec. 3.2). Comparing the measured and expected signals, different statistical parameters are extracted to quantify the agreement (see Sec. 3.3.1). Thresholds are applied to these statistical parameters to filter out plausible domain-wall-crossing signals (see Sec. 3.3.2).

3.1. Data pre-processing

In order to optimize for domain-wall search, the data are pre-processed through filtering and a rolling average is taken. Filters are used to remove long-term drifts as well as noisy frequency bands, e.g., the power-line frequency [27]. After filtering, we perform a rolling average of the data over time T_{avg} . Averaging the data enhances the signal-to-noise ratio for a certain signal duration and avoids complications arising from different magnetometers having different bandwidths. However, filtering and averaging data will also attenuate and modify the shape of the signal. A detailed analysis of the effects of filtering and averaging on the data is given in Appendix A.

The filters attenuate frequency bands containing known noise sources, however some non-Gaussian noise from unidentified sources may remain. Therefore, the noise is determined after the pre-processing steps. The uncertainty at a given time is estimated by the standard deviation of the data around that time. In order to minimize the effects of a signal in the estimation of the noise, outliers are removed from the calculation of the standard deviation.

3.2. Scanning over velocities

After the pre-processing stage, the data are time-shifted so that a domain-wall signal would appear at all magnetometers at the same time. This is possible because, for a given relative velocity between a domain wall and the Earth, the magnetometer signals appear in a predictable pattern.

The sensors in the network are located at different positions, $\{\mathbf{x}_i\}$ on the surface of the Earth. A domain wall with speed $\|\mathbf{v}\|$ in direction $\hat{\mathbf{v}}$ crossing the Earth is observed by different sensors at times $\{t_i\}$. The time difference from when a wall passes two locations can be expressed as

$$\Delta t_i = (\mathbf{x}_i - \mathbf{x}_0) \cdot \frac{\mathbf{v}}{\|\mathbf{v}\|^2},$$

where the sensor at \mathbf{x}_0 is used as a reference. The time at each data point is shifted according to Δt_i to align all the signals. The delays Δt_i are calculated in intervals of $T_{\text{avg}}/2$. Then, the corresponding points are extracted from the rolling averaged data. After this operation, an aligned set of measurements calculated with overlapping averaging windows is obtained. A graphical representation of the time shifting operation can be seen in Fig. 3.

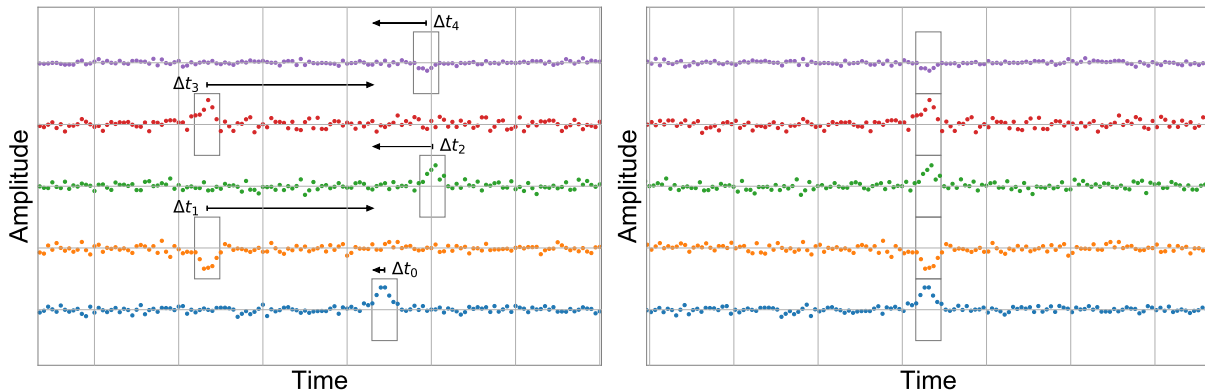


Figure 3: Simulated GNOME data featuring a domain wall signal before time-shifting (left) and after (right). The Δt_i for the different stations are determined by their geographical location and the velocity of the domain wall. The different amplitudes are determined by the orientation of the sensitive axes of the detectors relative to the domain wall velocity.

Earth-based sensors are in a noninertial (rotating) reference frame. For Earth's radius ($\approx 6.4 \times 10^6$ m), rotation period (1 day), and a domain-wall velocity of $v \approx 3 \times 10^5$ m/s, according to numerical estimates, the additional signal delay due to the Earth's rotation would be $\Delta t \lesssim 33$ ms. This effect is significant compared to the sensor bandwidth (expected to be ≈ 250 Hz) and should be corrected. To first order in time derivatives, each of the sensors moves at a constant velocity tangential to the Earth's surface, though only the component that is normal to the wall is observable. Including this correction,

$$\Delta t_i = \Delta \mathbf{x}_i \cdot \frac{\mathbf{v}}{\|\mathbf{v}\|^2 - \delta \mathbf{v}_i \cdot \mathbf{v}}, \quad (2)$$

where $\delta \mathbf{v}_i$ is the tangential velocity of the i^{th} sensor at the crossing time (when the wall crosses the center of the Earth). The first-order correction reduces the relative time error to $\Delta t \lesssim 0.05$ ms; well below the bandwidth of the GNOME magnetometers.

Assuming the Standard Halo Model (SHM), the distribution of domain wall velocities can be predicted. Within this model, the dark matter structures are virialized in the galaxy. This means that the domain-wall

velocity distribution is isotropic and quasi-Maxwellian⁵ with dispersion $\sigma_v \approx 290 \text{ km s}^{-1}$ and a cut-off above the galactic escape velocity of $v_{\text{esc}} \approx 550 \text{ km s}^{-1}$ [25]. The Earth moves through the dark matter halo with apparent velocity towards the Cygnus constellation. A range of speeds and relative angles with respect to the Earth movement are selected in the analysis so that 95% of the expected velocities are observable.

The scanning step size is estimated by considering two antipodal magnetometers. From Eq. (2) the changes in the delay time with respect to variation in the speed can be estimated. However, the delay is also dependent on the direction of the wall. In order to give an upper bound, the direction giving the largest variation of the delay is chosen. In addition, it is required that the maximum delay change must be smaller than half the bin size, $T_{\text{avg}}/2$, so the signal remains in the same bin. The speed range given by the SHM is scanned in steps of

$$\delta v \leq \frac{T_{\text{avg}} v^2}{4R_{\oplus}}, \quad (3)$$

where R_{\oplus} is the radius of the Earth. The same procedure can be followed to establish a scanning step for the angles. The step is given by

$$\delta\theta \leq \frac{T_{\text{avg}} v}{4R_{\oplus}}. \quad (4)$$

For a given speed, a lattice on the celestial hemisphere should have a point within every circle whose diameter spans an arc of $\delta\theta$. Note that the scanning step size is dependent on the speed.

To determine the lattice of directions, a set of points evenly distributed on the sphere are needed. One wants to guarantee that any circle whose radius on the sphere is given by $\delta\theta$ [Eq. (4)] contains at least one scanned direction. A roughly even distribution of points on the sphere is generated using the Fibonacci lattice method, with the number of points based on the step size (see, e.g., Ref. [32] for a description). Briefly, the Fibonacci lattice method is a means of generating a sequence of points that covers a surface. In this case, each sequential point has an azimuthal angle that increments by a factor of $2\pi\varphi$, where $\varphi \equiv \frac{1+\sqrt{5}}{2}$ is the golden ratio, while the polar angle is incremented such that the points are evenly distributed between the poles.

For each velocity, an abstract “measurement space” is constructed as described in Sec. 2. After adjusting for delays, the amplitudes measured at a given time belong to the same event. The events are represented as a vector in an n -dimensional space, where n is the number of magnetometers. However, measured events corresponding to a domain-wall crossing must lie in a 3-dimensional subspace of the measurement space parametrized by the m -vector. The application of the mathematical tools presented in Sec. 2 to the time-shifted data is discussed in the following sections.

3.3. Post-selection

After the measurements are temporally aligned according to the scanned velocities, their agreement with a domain-wall crossing is assessed by comparing the expected domain-wall signal pattern with the observed pattern. In the geometrical picture, the measured event is projected to the domain-wall subspace in coordinates scaled by the noise of the magnetometers, and the distance between the measurement and projected value quantifies the statistical agreement of the observation with an expected measurement; where the expected measurement is given by choosing physical parameters of the wall that most-closely reproduce the observed signal. Three parameters are relevant to determine if a set of measurements is statistically significant: the p -value measuring the statistical agreement between the measured signals \mathbf{s} and an expected domain-wall-crossing signal $\boldsymbol{\mu}$, the angle between the scanned velocity $\hat{\mathbf{v}}$ and observed wall orientation $\hat{\mathbf{m}}$, and the signal-to-noise ratio of $\|\mathbf{m}\|$.

3.3.1. Project into subspace

After time-shifting the data for a given velocity, one obtains a measurement \mathbf{s} at every time consisting of data from all active sensors. At each time, there is an expected domain-wall-crossing signal $\boldsymbol{\mu} \equiv D\mathbf{m}$ that is the closest point in the subspace of domain-wall signals to \mathbf{s} when using rescaled coordinates (as described in

⁵It is quasi-Maxwellian as opposed to Maxwellian due to the cut-off at the galactic escape velocity and the relative velocity of the Earth.

Sec. 2). The m -vector \mathbf{m} describes the effective field associated with the domain-wall-crossing event. Thus for every scanned velocity, a “most likely” m -vector is found for the \mathbf{s} at every time; i.e., the m -vector that would result in an expected signal that most closely reproduced the observed signal. In the next stages of the analysis it is determined whether \mathbf{s} is in statistical agreement with the “most likely” domain-wall-crossing event and cannot be explained by random noise.

One can assume that the amplitudes from the n sensors $\{s_i\}$ (for $i = 1, \dots, n$) obey a linear equation with signal attenuation caused by misalignment between the magnetometers’ sensitive directions $\{\hat{\mathbf{d}}_i\}$ and the effective magnetic field induced by the axion field:

$$D\mathbf{m} = \mathbf{s} \quad \text{for } D \equiv \begin{bmatrix} \hat{\mathbf{d}}_1^T \\ \hat{\mathbf{d}}_2^T \\ \vdots \\ \hat{\mathbf{d}}_n^T \end{bmatrix}, \quad \mathbf{s} \equiv \begin{bmatrix} s_1 \\ s_2 \\ \vdots \\ s_n \end{bmatrix}, \quad (5)$$

where \mathbf{m} is the three-dimensional m -vector whose norm represents the strength of the effective field and whose direction is normal to the domain wall. In general, the magnetometers are expected to experience different (though still linear) responses to an event due to different couplings of the axion field to different atomic species [31]. These effects can be included by multiplying the corresponding row in D by the appropriate response factor, though all magnetometers are assumed to have the same response here, for simplicity.

As discussed in Sec. 2, solving Eq. (5) as a least-squares minimization problem — given amplitudes \mathbf{s} and covariance Σ_s — is equivalent to performing a fit/projection of \mathbf{s} into the subspace spanned by the columns of D . The result is

$$\mathbf{m} = \Sigma_m D^T \Sigma_s^{-1} \mathbf{s} \quad \text{for } \Sigma_m = (D^T \Sigma_s^{-1} D)^{-1}. \quad (6)$$

Scanning velocities produces different values for \mathbf{s} at a given time, and therefore, different values for \mathbf{m} . A maximum on the norm of \mathbf{m} is expected when the scanned velocity corresponds to the domain-wall-crossing velocity present in the data, as can be seen in Fig. 4. The figure shows the signal magnitude observed at the time when the signal was inserted for different directions. The arcs originate when, for different directions, the signal occurs at the same delay time. The decrease in the signal magnitude is due to the effects of pre-processing the data.

An important statistical result from the fit is the χ^2 [Eq. (1)], which describes the deviation between a measurement and expected signal pattern. Assuming that the noise in the measurements are normally distributed, the χ^2 values are distributed according to the number of degrees of freedom ($\dim \mathbf{s} - \dim \mathbf{m} = n - 3$). The p -value is given by the integrated right tail of this distribution starting from the measured χ^2 . The p -value corresponds to the probability that the residual between the expected and measured values can be explained by deviations due to Gaussian noise.

3.3.2. Thresholds

For each time and scanned velocity, a signal vector \mathbf{s} and its corresponding m -vector and p -value are determined. Measurement vectors consistent with domain-wall crossings must be distinguished from signals originating from noise or systematic effects. This identification is accomplished by imposing thresholds on the p -value, the signal-to-noise ratio, and the direction of \mathbf{m} .

The agreement between the observed event and the domain-wall-crossing model is quantified by the p -value. This is related to the distance from the measured point \mathbf{s} to the subspace of domain walls, see Fig. 5. If the p -value is small, the candidate event can be rejected because the deviation from the expected signal pattern is too large to be explained by uncertainty in the measurement. For instance, if two sensors have the same sensitive direction, then it is unlikely that they would report significant amplitudes with opposite sign. The p -value is a powerful tool for rejecting spurious spikes in signals from individual magnetometers, as can be seen in Fig. 6. The magnitude reported could be large, however the p -value would be small because the other magnetometers would not feature a signal. The p -value threshold is chosen so that only 5% of real domain-wall events would be misidentified as noise. For Gaussian-distributed noise, this corresponds to a p -value threshold of 0.05, meaning that only events with greater p -values are processed further. However, if the noise is more complex, the p -value corresponding to 5% false-negatives has to be explicitly calculated, as shown in Sec. 5.1.

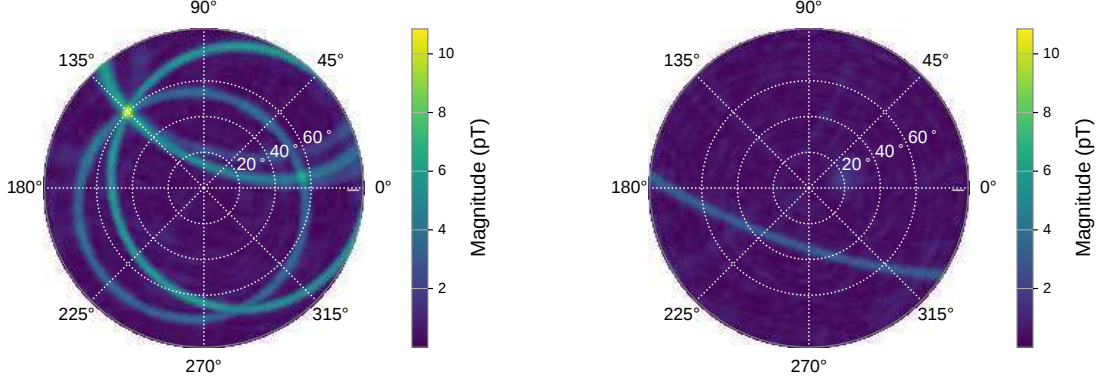


Figure 4: Illustration of the signal magnitude proportional to $\|\mathbf{m}\|$ found at different directions, \hat{v}_{scan} , across a single hemisphere. Left: a domain-wall-crossing event is inserted in the data with effective field magnitude corresponding to 20 pT and direction at polar angle 60° and azimuthal angle 135° . Note that the amplitude of the inserted signal is attenuated due to pre-processing. The bright arcs are likely a result of cases in which the different velocity does not change the delay time for some magnetometer(s). Right: the same domain-wall-crossing event is inserted but the time delays at each magnetometer are randomized. The simulation is performed using the magnetometers' characteristics from Table 1.

The data from each magnetometer are time-shifted according to a discrete set of velocities (see Sec. 3.2). However, the direction $\hat{\mathbf{m}}$ is reconstructed independent of the scanning velocity, \mathbf{v}_{scan} . Therefore, the agreement between the scanned and reconstructed directions must be checked. If the angular difference between \mathbf{v}_{scan} and \mathbf{m} is found to be larger than the angular lattice spacing, from Eq. (4), the event is rejected; it is inconsistent with a domain-wall crossing because the velocity $\hat{\mathbf{v}}$ is not parallel to the axion field gradient $\hat{\mathbf{m}}$.

After an event has passed the consistency checks, its significance has to be evaluated in terms of magnitude. The magnitude is given by the norm of the projection of \mathbf{s} to the domain-wall subspace,

$$\|\mathbf{m}\| \pm \frac{1}{\|\mathbf{m}\|} \sqrt{\mathbf{m}^T \Sigma_m \mathbf{m}}, \quad (7)$$

where Σ_m is the covariance matrix of the m -vector defined in Eq. (6). The quotient of the norm and its uncertainty is the signal-to-noise ratio. Events featuring a large signal-to-noise ratio are less likely to be produced by noise. Since the noise in the network is not purely Gaussian, the specific signal-to-noise ratio needed to claim a detection is fixed by studying the data. For this, a data set not containing any sought signal but featuring the typical noise characteristics of the network is analyzed. The rate of events found is studied with respect to their signal-to-noise ratio. Then the probability of finding an event above certain signal-to-noise threshold is assessed. This is called false-positive analysis and a case with simulated data is evaluated in Sec. 5. The thresholds are visualized in Fig. 5.

The rate of events found is expected to follow Poissonian statistics. Namely, the probability that one finds n_f events over an interval of duration \mathcal{T} , with an expected occurrence rate, r , is given by

$$P(n_f; r\mathcal{T}) = e^{-r\mathcal{T}} \frac{(r\mathcal{T})^{n_f}}{n_f!}. \quad (8)$$

For an interval T_{samp} of data, if n_f events are found, the upper-bound on the rate $r_0 \geq r$ at a confidence level C is given by solving

$$C = \int_0^{r_0 T_{samp}} P(n_f; x) dx. \quad (9)$$

From Eq. (8), the probability of finding more than zero events over the course of a \mathcal{T} -long run is then

$$P_{FP} \leq 1 - e^{-r_0 \mathcal{T}}. \quad (10)$$

To reach 5σ significance for detection, the maximum probability for finding more than zero events must be $P_{FP} < 5.7 \times 10^{-7}$, or 1 in 1.7 million, over the course of a data collection run. The signal-to-noise threshold

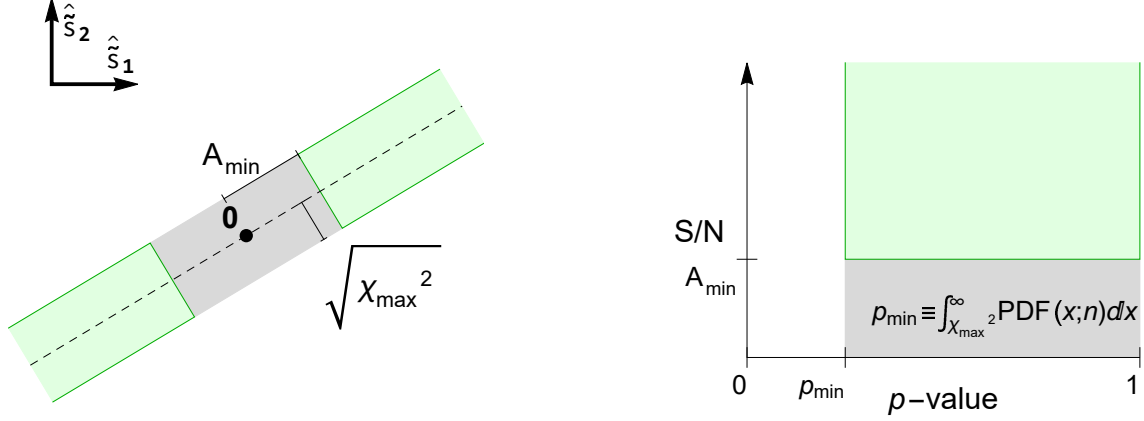


Figure 5: Geometric view of consistency check simplified in a lower dimension. The dashed line on the left image represents the 3-dimensional subspace of expected signals. A visualization of the thresholds where the green shaded region is accepted as a likely and significant signal. The signal-to-noise ratio threshold is A_{\min} while the χ^2 threshold is χ_{\max}^2 .

for detection is chosen so the rate of events found is smaller than 1 in 1.7 million. An example with simulated data is given in Sec. 5.

Note that if no domain-wall-crossing event is found above the detection threshold, no detection can be claimed. The event found with the maximum signal-to-noise ratio defines the detection threshold of the network for the measured time interval.

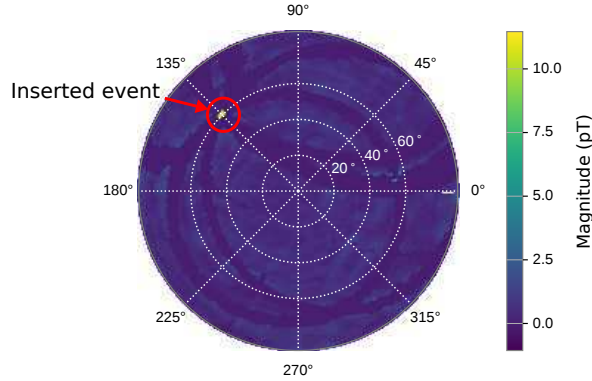


Figure 6: Illustration of the signal magnitude found at different velocities, \hat{v}_{scan} , across a single hemisphere. The speed is kept constant. The same data as Fig. 4 is used, however the requirement of a p -value greater than 0.05 is imposed. The high-magnitude points are now reduced to a point corresponding to the direction where the domain wall was injected.

4. Network sensitivity

In order to define the detection capabilities of GNOME, a notion of sensitivity must be established. Defining the matrix D and m -vector \mathbf{m} as in Eq. (5), one can define a function \mathcal{A} that takes the effective field vector \mathbf{m} , noise Σ_s , and D and returns a collective signal-to-noise ratio.

The output of this function is compared to some threshold α for finding a domain-wall-crossing event. For example, if $\mathcal{A}(\mathbf{m}, \Sigma_s, D) \geq \alpha$ for the event, then a signal is found, otherwise it is missed. Thus, the exact definition of \mathcal{A} is based on the analysis method. For the analysis described here, one finds signals by searching for instances in which the norm of the m -vector exceeds some multiple of its uncertainty. According

to Eq. (7), one finds

$$\mathcal{A}(\mathbf{m}, \Sigma_s, D) = \frac{m}{\sqrt{\hat{\mathbf{m}}^T (D^T \Sigma_s^{-1} D)^{-1} \hat{\mathbf{m}}}} .$$

Observe that when \mathbf{m} is an eigenvector of $D^T \Sigma_s^{-1} D$, then $\mathcal{A}(\mathbf{m}, \Sigma_s, D) = \|\Sigma_s^{-1/2} D \hat{\mathbf{m}}\| \equiv \mathcal{A}'(\Sigma_s^{-1/2} D \hat{\mathbf{m}})$.

The sensitivity of the system can be defined as the minimum signal needed to guarantee that the signal-to-noise is at least α . The sensitivity in the direction $\hat{\mathbf{m}}$ is obtained by solving $\mathcal{A}(\beta_\alpha \hat{\mathbf{m}}, \Sigma_s, D) = \alpha$ for β_α :

$$\beta_\alpha(\hat{\mathbf{m}}) \equiv \frac{\alpha}{\mathcal{A}(\hat{\mathbf{m}}, \Sigma_s, D)} = \alpha \sqrt{\hat{\mathbf{m}}^T (D^T \Sigma_s^{-1} D)^{-1} \hat{\mathbf{m}}} , \quad (11)$$

since \mathcal{A} is absolutely scalable — i.e., $\mathcal{A}(\beta \hat{\mathbf{m}}) = |\beta| \mathcal{A}(\hat{\mathbf{m}})$. Thus, if $\beta_\alpha(\hat{\mathbf{m}})$ is large, then a large magnitude is needed to induce a measurable signal in the direction $\hat{\mathbf{m}}$. The signal-to-noise threshold will be α , so a stricter, higher threshold results in a proportionally worse sensitivity.

An example of the network sensitivity is plotted in Fig. 7 in geocentric coordinates for $\alpha = 1$. The configuration of the sensors is described in Table 1. A clear pattern can be observed where the network is more sensitive to certain directions. An ideal configuration would show an homogeneous sensitivity in all directions. Nevertheless, the network features a fairly uniform sensitivity, only varying by a factor of two between the best and worse direction.

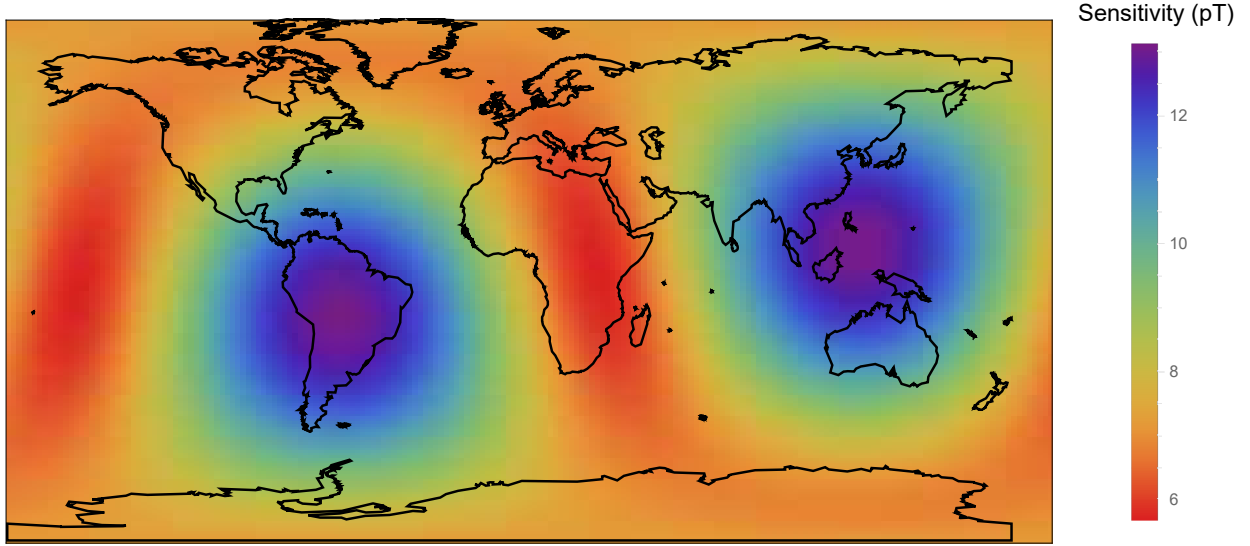


Figure 7: Directional sensitivity of the network according to the configuration used to generate simulated data (see Table 1). The color overlaid on the map of the Earth is $\beta_1(\hat{\mathbf{m}})$ from Eq. (11), where the position on the map corresponds to the first contact point of a domain wall on the Earth’s surface.

To reduce $\beta_\alpha(\hat{\mathbf{m}})$ to a single number, one could assume a distribution of signals based on some model (e.g., the SHM) and take the weighted average of the sensitivity over the signal distribution. Alternatively, one could achieve a sensitivity bound by considering the worst-case scenario in which β_α is maximized. In this case, this is accomplished by finding the smallest eigenvalue of $D^T \Sigma^{-1} D$. Denote λ_{\min} as the smallest eigenvalue and $\hat{\mathbf{x}}_{\min}$ as the corresponding eigenvector. Then the sensitivity in the worst direction is α/λ_{\min} for the worst direction $\hat{\mathbf{x}}_{\min}$. Note that the optimal orientation for adding an additional sensor to the network would be $\hat{\mathbf{x}}_{\min}$ in any location. Additionally, filtering and binning will alter the sensitivity of the network to particular signal shapes (e.g., for signals with different widths). These effects are discussed in Appendix A.

5. Testing analysis methods

The previous sections present the analysis algorithm and the relevant statistical parameters to identify domain-wall crossings in the GNOME data. In this section, this analysis algorithm is tested with simulated

data. The reliability of the algorithm is assessed based on the false-negatives and false-positive rates. False negatives occur when a domain-wall crossing is present but the algorithm fails to identify it, while false positives occur when noise is wrongly identified as a domain-wall crossing.

5.1. False-negative analysis

The proposed algorithm has to be able to identify signals which match the characteristics of a domain-wall-crossing event occurring at any time in the data. The expected directions and speeds of crossings are described by a probability distribution based on the SHM (see Sec. 3.2). Though the magnitude of \mathbf{m} and the duration of the domain-wall crossing can take any values, the range of observable values is limited by the sensitivity of the sensor network (see Sec. 4).

Twenty-minute-long simulated data segments with 512 Hz sampling rate are constructed with Gaussian-distributed noise according to Table 1. A Lorentzian-shaped pulse is added into the data of each magnetometer according to the model of a domain-wall-crossing event for a given velocity. The timing and amplitudes of the pulses are calculated based on Eq. (2) and Eq. (5). The crossing time is defined to be the moment the domain wall crosses the center of the Earth; this fixes the relative delays.

For the false-negative analysis, the crossing time and domain wall direction $\hat{\mathbf{v}}$ are randomized while the speed is kept constant. An effective field magnitude corresponding to 20 pT is chosen so that the signal amplitudes are clearly visible in the averaged data. A rolling average of the data is taken with averaging time of $T_{\text{avg}} = 1$ s, and a high-pass filter with a cut-off frequency of 1/300 Hz is applied to the data. Moreover, notch filters are applied corresponding to the electric network frequency for each station to include the effects of filtering on the signal.

The p -value represents the likelihood that deviations between the amplitudes measured at each sensor and the expected amplitudes corresponding to the most likely domain-wall-crossing event (as defined in Sec. 3.3.1) can be explained by the characteristic noise of the sensors. A relevant check of the analysis algorithm is the distribution of the false negatives with respect to the p -value. Domain-wall signals inserted in Gaussian-distributed noise should exhibit a flat distribution with respect to the p -value. This can be seen in blue in Fig. 8, where the cumulative probability of finding an event is proportional to the p -value, confirming the expected behavior.

In contrast, if pulses with random amplitudes are inserted into Gaussian-distributed noise, the p -value is generally close to zero; which can be seen in the red line in Fig. 8. The line is obtained by inserting pulses with timings consistent with a domain-wall crossing but having random amplitudes. This demonstrates how the p -value threshold provides a method to distinguish signal patterns matching domain-wall-crossing events from spurious non-Gaussian noise (such as random “spikes” in the magnetometer data).

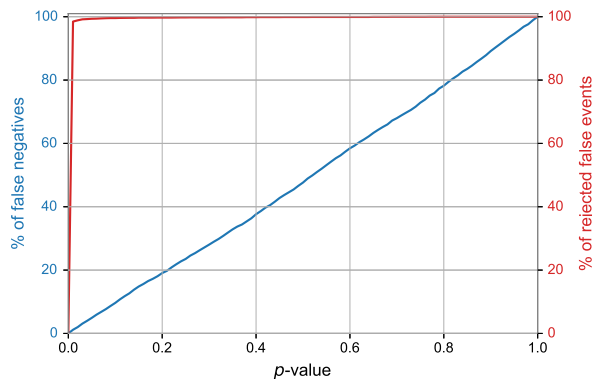


Figure 8: Blue line: the percent of false-negative signals as a function of p -value. This line was determined by simulating domain-wall signals on Gaussian-distributed noise (as per Table. 1). Red line: percent of true-negative signals as a function of p -value. The true-negative signals were generated similar to the true-positive signals, except with amplitude measurements inconsistent with a domain-wall signal.

5.2. False-positive analysis

In order to quantify whether a measured signal pattern is sufficiently unlikely to occur due to random noise, it is necessary to study the noise characteristics of the network. The first two stages of the post-selection process are to identify events whose p -values are above the designated threshold p_{\min} and to identify events for which the direction of \mathbf{m} matches that of \mathbf{v}_{scan} within the angular lattice spacing. Inevitably, some events arising from noise may pass the thresholds on p -value and directional consistency between \mathbf{m} and \mathbf{v} , so a third threshold characterizing the signal-to-noise of a measurement is introduced. A 5σ significance for an observed domain-wall-crossing event is imposed in order to claim discovery of a domain-wall crossing. This means a probability of about 1 in 1.7 million of being produced by noise over the course of the measurement campaign, \mathcal{T} .

The number of events above a certain signal-to-noise threshold is expected to follow Poissonian statistics. For a given period of time and number of events detected, a bound with 90% confidence level can be given as rate of false-positives per year. This bound on the false positive rate can be determined by solving Eq. (9) for r_0 , where n_f is determined by simulating T_{samp} -long data. For events appearing very seldom in the period of time analyzed, the bound is inaccurate because there are not enough events to accurately estimate the underlying rate. This effect is visible when demanding high signal-to-noise ratio events. However, if one would continue adding data, the rates are expected to continue an exponential trend.

In order to test the exclusion power of the post selection steps, simulated data with Gaussian-distributed noise and random Lorentzian spikes are studied. The data are simulated in 20 min segments. Spikes are inserted randomly with a probability of 10% at each magnetometer with at most one spike per simulated segment. The amplitude takes random values between -20 pT and +20 pT, and the width is fixed to 0.5 s. The standard deviation of the background noise is extracted from Table 1.

The spikes produce large signal-to-noise events which are shown by the black dotted line in Fig. 9. However, because the spikes are unrelated to domain walls, the p -value of a spike event is likely to be close to zero. Therefore, a significant amount of high signal-to-noise events can be easily rejected by the p -value threshold, as shown by the blue dotted line in Fig. 9. The rate of detected events per year is further decreased with the angle threshold as the green dotted line shows. After the post-selection procedure, the rate of false positives is reduced by about four orders of magnitude at a signal-to-noise ratio of 10. For reference, the solid red line indicates the rate of false positives measured with only Gaussian noise background (according to Table 1) and no spikes. As expected, it decays exponentially with the signal-to-noise ratio threshold.

For the 1.3 years of simulated data, the most stringent bound on the rate achievable is about 1.8 events per year. However, to determine the threshold for detection, that is, the signal-to-noise ratio resulting in a 5σ significance for detection for a measuring time of 1 month, a bound of less than $r_0 = 6.9 \times 10^{-6} \text{ yr}^{-1}$ is required. To ensure this significance, one would need to create about 4 million times more data than is being analyzed from a measuring campaign. This is computationally impractical, so the false positive rate as a function of the thresholds must be extrapolated to establish the appropriate signal-to-noise ratio threshold. The red solid line in Fig. 9 is extrapolated with an exponential decay shown by the orange solid line. The 5σ significance level is reached for a signal-to-noise ratio of 9.3 when measuring for 1 month.

A network configuration offers several benefits for detecting domain-wall-crossing events and other transient signals associated with beyond-standard-model physics. Since the same event is detected multiple times, a network of sensors offers greater statistical sensitivity compared to only one sensor. Furthermore, the global distribution of the magnetometers along with the GPS-disciplined timing enables accurate characterization of domain-wall-crossing event dynamics. Finally, the combination of the time-domain signal pattern and the pattern of signal amplitudes in the network enables efficient rejection of false-positive events. The rejection of spurious events improve the number of magnetometers taking part in the network.

The identification of plausible events is mainly based on solving Eq. (5), a system of linear equations with $n - 3 = 6$ degrees of freedom for $n = 9$ magnetometers. When more than four magnetometers are active, the analysis is able to veto events that do not match the expected pattern as described in Sec. 3.3.2.

To test the effects of adding/removing sensors, data were simulated in 1000 samples of 20 min segments. A randomly selected subset of magnetometers is used to simulate the performance of a network with 7 and 5 magnetometers in each sample. Thus the effect of choosing a particular set of magnetometers is averaged out. Apart from the number of magnetometers used, the parameters of the simulation are the same as in Fig. 9. The results are shown in Fig. 10. The left plot demonstrates the reduction in the rate of false-positive events with additional sensors for background data with random spikes injected (dashed lines). A network

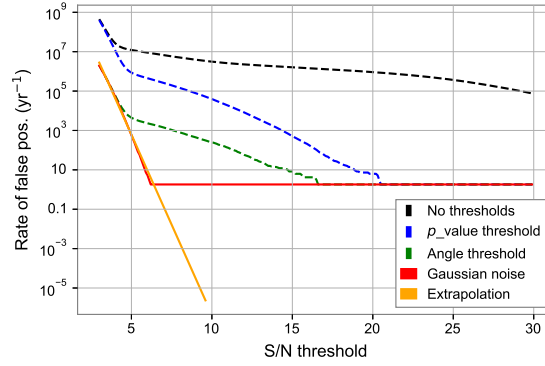


Figure 9: The false-positive analysis for the different stages of the post-selection. The rates are reported as upper-bounds at 90 % confidence. The data are composed of Gaussian noise with spurious Lorentzian spikes. The amplitude of the spikes take random values between -20 pT and $+20$ pT. The black line accounts for all the events, the blue line introduces the p -value threshold, the green includes the angle selection. In addition, the orange line shown the extrapolation to 5σ significance of detection.

of 9 sensors reduces the rate of false-positive events by more than an order of magnitude at a signal-to-noise threshold of 15 as compared to a network of 5 magnetometers. The solid lines show the bound on the false-positives rate for pure, Gaussian-distributed noise. No significant change in the rate of false-positive events on Gaussian-distributed noise is observed with different network sizes because the p -value behavior is independent of the number of sensors (or degrees of freedom) in this case. However, there is an improvement on the sensitivity with additional sensors. The right plot in Fig. 10 shows the β_1 sensitivity in the least-sensitive direction, as defined in Eq. (11). Every combination of the nine magnetometers is used to generate the box-and-whisker plots for different sizes of the subsets.

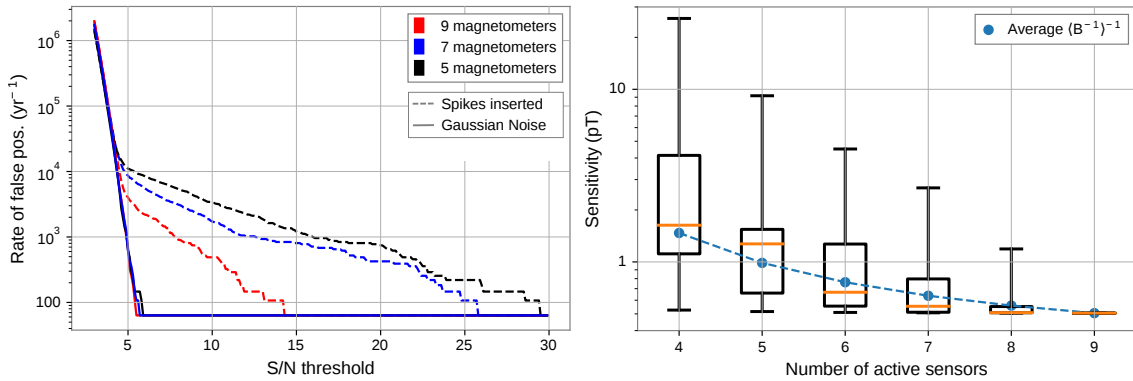


Figure 10: Left: False-positive analysis with different network sizes. The analysis is performed with Gaussian-distributed noise (solid lines) and Gaussian-distributed noise with spurious spikes injected randomly (dashed lines). Right: sensitivity of the GNOME network when containing different amount of magnetometers active. The box-and-whisker plots are constructed by considering all subsets of the nine magnetometers. The regions of the box-and-whisker indicate 25 % of the combinations with the boxes marking the upper- and lower-quartiles separated by the median (orange line).

5.3. Sensitivity

The detector network and analysis method determine a class of detectable signals. In particular, the noise of the individual magnetometers, the filters used, and the averaging time determine the duration and magnitude of the detectable signals. The sensitivity is discussed in Sec. 4 with the effects of averaging (binning) and filtering are discussed in Appendix A. For the network characteristics described in Table 1, an averaging time of 1 s, $1/300$ Hz high-pass filters, and notch filters corresponding to the power line frequencies,

the sensitivity to domain-wall signals (assumed to have a Lorentzian shape in the time-domain) is shown by the gray line in Fig. 11.

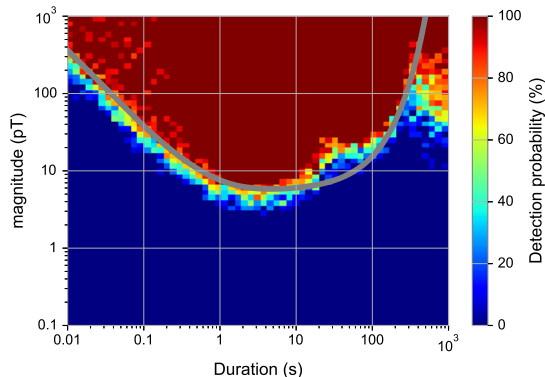


Figure 11: The probability of detection for the algorithm in terms of the magnitude and duration of a domain-wall-crossing signal. This plot is generated with 1 s averaging and a 1/300 Hz high-pass filter. The gray line represents the theoretical limit of detection at 9.3 signal-to-noise ratio.

The ability of the analysis algorithm to observe signals with different durations and magnitudes is studied in 40000 segments of 20 minutes (summarized in Fig. 11). Each of the segments contains a domain-wall signal at random amplitude, duration, direction, and crossing time. The signal is inserted on a Gaussian-distributed noise background defined from the noise characteristics shown in Table 1.

The signal-to-noise limit for accepting the signal is fixed to 9.3, to achieve the false-positive rate needed to reach 5σ significance for detection of for one month of measurement time (as per Sec. 5.2). If any event is found above the detection limit in the segment, it is marked as a detection. The parameter space is clearly split in two regions: in the lower part the algorithm is unable to identify events, while in the upper part, the events are reliably detected. These two regions are split by the theoretical sensitivity limit. The decrease on the sensitivity for small durations is due to the effects of averaging the data, while the decrease for long signals is due to the high-pass filtering of the data. The deviation from the theoretical line at large signal durations is likely due to poor noise-estimations since the signal spans a time comparable to the segment length. For short signal duration, small errors in aligning the signals through time-shifting leads to significant deviations from the expected amplitude. This results in poor statistical agreement; i.e., a small p -value.

The sensitivity plot is expressed in terms of signal characteristics. However, one is often interested in sensitivity to domain walls in terms of physical parameters. The exact conversion between the signal characteristics and physical parameters depends on the phenomenology being considered. Roughly speaking, the duration of a wall signal is determined by the axion mass (which scales inversely with physical width) and velocity, while the magnitude of the signal is related to the coupling strength. Furthermore, the likelihood that no domain wall was observed because they are rarer than the experiment duration must be considered. These issues will be explored in future publications.

6. Conclusions

In this work, an analysis algorithm to search for signals in the GNOME data associated with domain-wall crossings was described. The analysis algorithm is designed to look for peaks reproducing the expected timing and amplitude pattern of a domain-wall crossing. The signal pattern is specific to the configuration of GNOME, depending on the geographical location, the alignment of the sensitive axes and the noise characteristics of the magnetometers. The analysis algorithm is demonstrated to effectively discriminate between real domain-wall crossings and noise. The false-positive and false-negative rates for simulated data are analyzed, and a method to evaluate the overall sensitivity of the GNOME network was described.

The analysis algorithm presented in this work will be applied to the data of the GNOME collaboration. The main challenge with real data is the complexity of the noise characteristics. In order to assess the detection signal-to-noise threshold, the same data being analyzed must be used to estimate the noise. The

event rate background will be calculated sampling the data at random times. A real domain-wall signal would not be visible but the noise characteristics would remain. On this incoherent data, the signal-to-noise ratio required for a 5σ significance detection over the duration of the measurement campaign can be determined. If no events are found above this threshold, the strongest event detection will define the region of exclusion. This will move the gray curve in Fig. 11 down and include a larger region of signal characteristics.

Acknowledgements

We are sincerely grateful to Chris Pankow and Josh Smith for early contributions to the data analysis strategy and Andrei Derevianko, Ben Roberts, Conner Dailey, and Maxim Pospelov for valuable advice and insights. We are also thankful to all the members of the GNOME collaboration for useful discussions at many stages of development of the analysis procedure, especially H. Guo, T. W. Kornack, W. Li, S. Nix, M. Padniuk, X. Peng, and D. Sheng.

This work was supported by the U.S. National Science Foundation under grants PHY-1707875 and PHY-1707803, the Swiss National Science Foundation under grant No. 200021 172686, the European Research Council under the European Union's Horizon 2020 Research and Innovative Program under Grant agreement No. 695405, the Cluster of Excellence PRISMA+, the National Science Centre, Poland within the OPUS program (Project No. 2015/19/B/ST2/02129), and IBS-R017-D1-2019-a00 of the Republic of Korea.

References

- [1] P. Gorenstein, W. Tucker, Astronomical Signatures of Dark Matter, *Advances in High Energy Physics* 2014 (2014) 1–10. doi:10.1155/2014/878203.
URL <http://www.hindawi.com/journals/ahp/2014/878203/>
- [2] J. L. Feng, Dark Matter Candidates from Particle Physics and Methods of Detection, *Annual Review of Astronomy and Astrophysics* 48 (1) (2010) 495–545. doi:10.1146/annurev-astro-082708-101659.
URL <http://www.annualreviews.org/doi/10.1146/annurev-astro-082708-101659>
- [3] L. Bergström, Dark matter candidates, *New Journal of Physics* 11 (2009). doi:10.1088/1367-2630/11/10/105006.
- [4] G. Bertone, D. Hooper, J. Silk, Particle dark matter: evidence, candidates and constraints, *Physics Reports* 405 (5) (2005) 279–390. doi:10.1016/j.physrep.2004.08.031.
URL <http://www.sciencedirect.com/science/article/pii/S0370157304003515>
- [5] S. Moriyama, Dark matter searches, *AIP Conference Proceedings* 981 (2008) 80–83. doi:10.1063/1.2899007.
- [6] M. S. Safronova, D. Budker, D. DeMille, D. F. J. Kimball, A. Derevianko, C. W. Clark, Search for new physics with atoms and molecules, *Reviews of Modern Physics* 90 (2) (Jun. 2018). doi:10.1103/RevModPhys.90.025008.
URL <https://link.aps.org/doi/10.1103/RevModPhys.90.025008>
- [7] T. Marrodan Undagoitia, L. Rauch, Dark matter direct-detection experiments, *ArXiv e-prints* (2015). doi:10.1088/0954-3899/43/1/013001.
- [8] P. W. Graham, I. G. Irastorza, S. K. Lamoreaux, A. Lindner, K. A. van Bibber, Experimental Searches for the Axion and Axion-Like Particles, *Annual Review of Nuclear and Particle Science* 65 (1) (2015) 485–514. doi:10.1146/annurev-nucl-102014-022120.
URL <http://www.annualreviews.org/doi/10.1146/annurev-nucl-102014-022120>
- [9] Y. V. Stadnik, V. V. Flambaum, Searching for Dark Matter and Variation of Fundamental Constants with Laser and Maser Interferometry, *Physical Review Letters* 114 (16) (Apr. 2015). doi:10.1103/PhysRevLett.114.161301.
URL <https://link.aps.org/doi/10.1103/PhysRevLett.114.161301>

- [10] L. D. Duffy, K. v. Bibber, Axions as dark matter particles, *New Journal of Physics* 11 (10) (2009) 105008. doi:10.1088/1367-2630/11/10/105008.
URL <https://doi.org/10.1088/1367-2630/11/10/105008>
- [11] A. Ringwald, Axions and axion-like particles (2014). arXiv:1407.0546.
- [12] R. D. Peccei, H. R. Quinn, CP Conservation in the Presence of Pseudoparticles, *Physical Review Letters* 38 (25) (1977) 1440–1443. doi:10.1103/PhysRevLett.38.1440.
URL <https://link.aps.org/doi/10.1103/PhysRevLett.38.1440>
- [13] A. Arvanitaki, S. Dimopoulos, S. Dubovsky, N. Kaloper, J. March-Russell, String axiverse, *Phys. Rev. D* 81 (2010) 123530. doi:10.1103/PhysRevD.81.123530.
URL <https://link.aps.org/doi/10.1103/PhysRevD.81.123530>
- [14] P. W. Graham, D. E. Kaplan, S. Rajendran, Cosmological Relaxation of the Electroweak Scale, *Physical Review Letters* 115 (22) (Nov. 2015). doi:10.1103/PhysRevLett.115.221801.
URL <https://link.aps.org/doi/10.1103/PhysRevLett.115.221801>
- [15] P. Sikivie, Axions, Domain Walls, and the Early Universe, *Physical Review Letters* 48 (17) (1982) 1156–1159. doi:10.1103/PhysRevLett.48.1156.
URL <https://link.aps.org/doi/10.1103/PhysRevLett.48.1156>
- [16] M. Kawasaki, K. Saikawa, T. Sekiguchi, Axion dark matter from topological defects, *Physical Review D - Particles, Fields, Gravitation and Cosmology* 91 (6) (2015) 1–32. doi:10.1103/PhysRevD.91.065014.
- [17] S. Coleman, Q-balls, *Nuclear Physics B* 262 (2) (1985) 263–283. doi:10.1016/0550-3213(85)90286-X.
URL <http://linkinghub.elsevier.com/retrieve/pii/055032138590286X>
- [18] A. Kusenko, P. J. Steinhardt, Q-Ball Candidates for Self-Interacting Dark Matter, *Physical Review Letters* 87 (14) (Sep. 2001). doi:10.1103/PhysRevLett.87.141301.
URL <https://link.aps.org/doi/10.1103/PhysRevLett.87.141301>
- [19] D. F. Jackson Kimball, D. Budker, J. Eby, M. Pospelov, S. Pustelny, T. Scholtes, Y. V. Stadnik, A. Weis, A. Wickenbrock, Searching for axion stars and Q-balls with a terrestrial magnetometer network, *Phys. Rev. D* 97 (2018) 043002. doi:10.1103/PhysRevD.97.043002.
URL <https://link.aps.org/doi/10.1103/PhysRevD.97.043002>
- [20] A. Banerjee, D. Budker, J. Eby, H. Kim, G. Perez, Relaxion stars and their detection via atomic physics (2019). arXiv:1902.08212.
- [21] M. Pospelov, S. Pustelny, M. P. Ledbetter, D. F. J. Kimball, W. Gawlik, D. Budker, Detecting Domain Walls of Axionlike Models Using Terrestrial Experiments, *Phys. Rev. Lett.* 110 (2) (2013) 021803. doi:10.1103/PhysRevLett.110.021803.
URL <https://link.aps.org/doi/10.1103/PhysRevLett.110.021803>
- [22] A. Friedland, H. Murayama, M. Perelstein, Domain walls as dark energy, *Phys. Rev. D* 67 (4) (2003) 043519. doi:10.1103/PhysRevD.67.043519.
URL <http://link.aps.org/doi/10.1103/PhysRevD.67.043519>
- [23] K. Freese, M. Lisanti, C. Savage, *Colloquium* : Annual modulation of dark matter, *Reviews of Modern Physics* 85 (4) (2013) 1561–1581. doi:10.1103/RevModPhys.85.1561.
URL <https://link.aps.org/doi/10.1103/RevModPhys.85.1561>
- [24] A. Derevianko, M. Pospelov, Hunting for topological dark matter with atomic clocks, *Nature Physics* 10 (12) (2014) 933–936. doi:10.1038/nphys3137.
URL <http://www.nature.com/articles/nphys3137>
- [25] B. M. Roberts, G. Blewitt, C. Dailey, M. Murphy, M. Pospelov, A. Rollings, J. Sherman, W. Williams, A. Derevianko, Search for domain wall dark matter with atomic clocks on board global positioning system satellites, *Nature Communications* 8 (1) (Dec. 2017). doi:10.1038/s41467-017-01440-4.
URL <http://www.nature.com/articles/s41467-017-01440-4>

- [26] D. Budker, M. Romalis, Optical magnetometry, *Nature Physics* 3 (4) (2007) 227–234. doi:10.1038/nphys566.
- [27] S. Afach, D. Budker, G. DeCamp, V. Dumont, Z. Grujić, H. Guo, D. Jackson-Kimball, T. Kornack, V. Lebedev, W. Li, H. Masia-Roig, S. Nix, M. Padniuk, C. Palm, C. Pankow, A. Penafior, X. Peng, S. Pustelny, T. Scholtes, J. Smiga, J. Stalnaker, A. Weis, A. Wickenbrock, D. Wurm, Characterization of the global network of optical magnetometers to search for exotic physics (GNOME), *Physics of the Dark Universe* 22 (2018) 162–180. doi:10.1016/j.dark.2018.10.002. URL <https://linkinghub.elsevier.com/retrieve/pii/S2212686418301031>
- [28] S. Pustelny, D. F. Jackson Kimball, C. Pankow, M. P. Ledbetter, P. Wlodarczyk, P. Wcislo, M. Pospelov, J. R. Smith, J. Read, W. Gawlik, D. Budker, The Global Network of Optical Magnetometers for Exotic physics (GNOME): A novel scheme to search for physics beyond the Standard Model: The Global Network of Optical Magnetometers for Exotic physics (GNOME), *Annalen der Physik* 525 (8-9) (2013) 659–670. doi:10.1002/andp.201300061. URL <http://doi.wiley.com/10.1002/andp.201300061>
- [29] D. F. J. Kimball, J. Dudley, Y. Li, S. Thulasi, S. Pustelny, D. Budker, M. Zolotorev, Magnetic shielding and exotic spin-dependent interactions, *Phys. Rev. D* 94 (8) (2016) 082005. doi:10.1103/PhysRevD.94.082005.
- [30] G. Panelli, B. M. Roberts, A. Derevianko, Applying the matched-filter technique to the search for dark matter transients with networks of quantum sensors (2019). arXiv:1908.03320.
- [31] D. F. J. Kimball, Nuclear spin content and constraints on exotic spin-dependent couplings, *New Journal of Physics* 17 (7) (2015) 073008. doi:10.1088/1367-2630/17/7/073008. URL <https://doi.org/10.1088/1367-2630/17/7/073008>
- [32] R. Swinbank, R. James Purser, Fibonacci grids: A novel approach to global modelling, *Quarterly Journal of the Royal Meteorological Society* 132 (619) (2006) 1769–1793. doi:10.1256/qj.05.227. URL <http://doi.wiley.com/10.1256/qj.05.227>
- [33] B. P. Lathi, *Signal processing and linear systems*, Berkeley Cambridge Press, Carmichael, Calif, 1998.

Appendix A. Filtering/binning effects

Filtering and binning will affect both the signal and noise of a signal. The exact nature of these effects will be dependent on the specific characteristics of the signal and noise. Some relevant examples of signals and reasonable approximations of noises will be considered in this appendix. Specialized filters can be used to optimize dark matter searches [30], however this appendix will focus on the application of general frequency filters. Further reading related to this appendix can be found in standard textbooks on signal processing, e.g., Ref. [33].

The effects on noise and signal will be calculated in slightly different ways. In particular, the effects on noise will be calculated with discrete points, while the effects on the signal will be calculated in the continuous limit to simplify the calculation. For these calculations, it helps to define the discrete Fourier transform

$$(\mathcal{F}_D f)[k] \equiv \sum_{n=0}^{N-1} f[n] e^{-\frac{2\pi n k}{N} i} \quad \text{and} \quad (\mathcal{F}_D^{-1} \tilde{f})[n] = \frac{1}{N} \sum_{k=0}^{N-1} \tilde{f}[k] e^{+\frac{2\pi n k}{N} i}, \quad (\text{A.1})$$

where f is a set of data with N points and \tilde{f} is the Fourier transform. Similarly, the continuous Fourier transform is

$$\{\mathcal{F}_C f\}(\omega) \equiv \int_{-\infty}^{\infty} dt f(t) e^{-i\omega t} \quad \text{and} \quad \{\mathcal{F}_C^{-1} \tilde{f}\}(t) = \frac{1}{2\pi} \int_{-\infty}^{\infty} d\omega \tilde{f}(\omega) e^{+i\omega t}. \quad (\text{A.2})$$

Note that the discrete Fourier transform is given in terms of frequencies (in units of $r/2N$ where r is the sampling rate) and the continuous transform is given in terms of *angular* frequency, where $\omega \sim 2\pi k$.

Appendix A.1. Effects on noise

For simplicity, the noise in the sensors will be assumed to be Gaussian distributed. Later, additional approximations will be applied to make the effects easier to calculate. A general frequency filter $\tilde{g}[k]$ will affect the signal according to

$$f_{\text{filt}}[n] = (\mathcal{F}_D^{-1}(\tilde{g} \cdot \mathcal{F}_D f)) [n] . \quad (\text{A.3})$$

The filter satisfies $\tilde{g}[k] = \tilde{g}^*[N - k]$ so that $f_{\text{filt}} \in \mathbb{R}$. Note, also, that a circular boundary is assumed for simplicity, so $\tilde{g}[k] = \tilde{g}[N + k]$.

Filtering is a linear operation with a Jacobian matrix given by

$$\begin{aligned} J_{\text{filt}}[n, m] &\equiv \frac{\partial f_{\text{filt}}[n]}{\partial f[m]} = \frac{1}{N} \sum_{k=0}^{N-1} \tilde{g}[k] e^{-\frac{2\pi i}{N}(m-n)} \\ &= \frac{1}{N} \times \begin{cases} 2 \sum_{k=1}^{\frac{N+1}{2}-1} \text{Re} \left(\tilde{g}[k] e^{-\frac{2\pi i}{N}(m-n)} \right) + \tilde{g}[0] & N \text{ odd} \\ 2 \sum_{k=1}^{\frac{N}{2}-1} \text{Re} \left(\tilde{g}[k] e^{-\frac{2\pi i}{N}(m-n)} \right) + \tilde{g}[0] + (-1)^{m-n} \tilde{g}[N/2] & N \text{ even} \end{cases} , \quad (\text{A.4}) \end{aligned}$$

where $\tilde{g}[k] \in \mathbb{R}$ in the second line which will not shift the signal after filtering. One can show that the Jacobian is a real, circulant (i.e., elements given by the difference between the column and row number), and symmetric matrix.

For example, consider a simple band-pass filter,

$$\tilde{g}[k] = \begin{cases} 1 & k_0 \leq k < k_1 \text{ or } N - k_1 < k \leq N - k_0 \\ 0 & \text{else} \end{cases} .$$

One obtains the Jacobian

$$\begin{aligned} J_{\text{filt}}[n, m] &= \frac{1}{N} \times \left[\begin{cases} \frac{\sin(\frac{2\pi}{N}(m-n)(\min\{\lceil \frac{N}{2} \rceil, k_1\} - \frac{1}{2})) - \sin(\frac{2\pi}{N}(m-n)(\max\{k_0, 1\} - \frac{1}{2}))}{\sin(\frac{\pi}{N}(m-n))} & m \neq n \\ 2(\min\{\lceil \frac{N}{2} \rceil, k_1\} - \max\{k_0, 1\}) & m = n \end{cases} \right] \\ &\quad + \tilde{g}[0] + \begin{cases} (-1)^{m-n} \tilde{g}[\frac{N}{2}] & N \text{ even} \\ 0 & \text{else} \end{cases} \Big] . \end{aligned}$$

Likewise, averaging over M points in left-justified bins yields the Jacobian,

$$J_{\text{avg}}[n, m] = \begin{cases} \frac{1}{M} & 0 \leq m - n < M \\ 0 & \text{else} \end{cases} .$$

This is a rolling average, which can be extended by assuming circular boundary conditions on the indices, $n \sim n + N$. The rolling average is equivalent to applying the frequency filter

$$\tilde{g}_{\text{avg}}[k] = \frac{\sin \frac{M\pi}{N} k}{M \sin \frac{\pi}{N} k} e^{-i \frac{\pi}{N} k (M-1)} .$$

Observe that the phase is a result of the bins being left-justified and can be removed by using center-justified bins. According to the convolution theorem, the frequency filters can be combined via a product into a single filter.

If the initial covariance of the data is Σ , then the covariance in the filtered data is $(\Sigma_{\text{filt}})[n, m] = \sum_{j,k=0}^{N-1} J_{\text{filt}}[j, n] \Sigma[j, k] J_{\text{filt}}[k, m]$. Assuming that the errors are constant and uncorrelated ($\Sigma[m, n] = \sigma^2 \delta_{mn}$), then the resulting covariance is also circulant. This means that the covariance between two points only depends on the distance between those two points. The variance $\bar{\sigma}^2 = \sigma^2 \sum_{j=0}^{N-1} J_{\text{filt}}[j, 0]^2$ is of particular interest. Observe that since J_{filt} is symmetric and circulant, $J_{\text{filt}}[j, 0]^2 = J_{\text{filt}}[j, 0] J_{\text{filt}}[0, j] = J_{\text{filt}}[j, 0] J_{\text{filt}}[-j, 0]$. Thus,

$$\bar{\sigma}^2 = \frac{\sigma^2}{N} \sum_{k=0}^{N-1} |\tilde{g}[k]|^2 , \quad (\text{A.5})$$

equivalent to attenuating the variance by the inner product of the filter, up to a factor of N .

Appendix A.2. Effects on the signal

The effects of the filters on the signal is determined in the continuum limit. The frequency filter $\tilde{g}(\omega)$ on a signal $f(t)$ is given by

$$f_{\text{filt}}(t) = \{\mathcal{F}_C^{-1}\{\tilde{g} \cdot \mathcal{F}_C f\}\}(t) , \quad (\text{A.6})$$

where $g(-\omega) = g^*(\omega)$ similar to the discrete case. Expanding this equation,

$$f_{\text{filt}}(t) = \frac{1}{\pi} \int_0^\infty d\omega \operatorname{Re} (\tilde{g}(\omega) \{\mathcal{F}_C f\}(\omega) e^{i\omega t}) ,$$

where $\{\mathcal{F}_C f\}(-\omega) = \{\mathcal{F}_C f\}^*(\omega)$ since $f \in \mathbb{R}$.

For this study, it is useful to consider the case where the signal is Lorentzian,

$$f(t) = \frac{A}{1 + \left(\frac{t}{\frac{1}{2}\Gamma}\right)^2} , \text{ so } \{\mathcal{F}_C f\}(\omega) = \pi A \frac{\Gamma}{2} e^{-\frac{\Gamma}{2}|\omega|} . \quad (\text{A.7})$$

Also, a rolling average with binning time T_{avg} is accomplished with the frequency filter,

$$\tilde{g}_{\text{avg}}(\omega) = \frac{2}{\omega T_{\text{avg}}} \sin\left(\frac{\omega T_{\text{avg}}}{2}\right) .$$

Likewise, a simple high-pass filter is given by $\tilde{g}_{\text{hp}}(\omega) = \Theta(|\omega| - \omega_L)$.

First, consider applying both a rolling average and a high-pass filter. The resulting signal will be

$$f_{\text{filt}}(t) = \frac{A\Gamma}{2T_{\text{avg}}} \operatorname{Im} \left[\int_1^\infty \frac{d\nu}{\nu} e^{-\omega_L \left(\frac{\Gamma}{2} - i\frac{T_{\text{avg}}}{2} - i t\right)\nu} + \int_1^\infty \frac{d\nu}{\nu} e^{-\omega_L \left(\frac{\Gamma}{2} + i\frac{T_{\text{avg}}}{2} - i t\right)\nu} \right] .$$

If a frequency filter is applied without averaging,

$$f_{\text{filt}}(t) = \frac{A\Gamma}{2} \frac{\frac{\Gamma}{2} \cos(\omega_L t) - t \sin(\omega_L t)}{t^2 + (\Gamma/2)^2} .$$

Finally, consider averaging without a high-pass filter:

$$f_{\text{filt}}(t) = \frac{A\Gamma}{2T_{\text{avg}}} \left[\arctan\left(\frac{t + T_{\text{avg}}/2}{\Gamma/2}\right) - \arctan\left(\frac{t - T_{\text{avg}}/2}{\Gamma/2}\right) \right] .$$

When determining by how much the signal is changed, a point is sampled from f_{filt} . Optimistically, this will be the maximum, $f_{\text{filt}}(0)$. However, in practice, the data are binned meaning that instead of simply using the rolling average, only one point per bin width is used. This means that in the worst case, the maximum observed value is generally⁶ $f_{\text{filt}}(T_{\text{avg}}/2)$. If, for example, two sets of bins offset by half a bin width is used, this worst-case-scenario improves to $f_{\text{filt}}(T_{\text{avg}}/4)$.

⁶Strong filters can cause oscillatory effects in the signal. This means that the largest observed value may not be around the peak, depending on the signal width. For simplicity, signals with widths beyond which this effect occurs can be considered unobservable.

Optically Pumped Cs Magnetometers Enabling a High-Sensitivity Search for the Neutron Electric Dipole Moment

C. Abel,¹ S. Afach,^{2,3} N. J. Ayres,^{1,3} G. Ban,⁴ G. Bison,^{2,*} K. Bodek,⁵ V. Bondar,^{2,3,6} E. Chanel,⁷ P.-J. Chiu,^{2,3} C. B. Crawford,⁸ Z. Chowdhuri,² M. Daum,² S. Emmenegger,³ L. Ferraris-Bouchez,⁹ M. Fertl,^{2,3,10} B. Franke,^{2,3,†} W. C. Griffith,¹ Z. D. Grujić,^{11,12} L. Hayen,⁶ V. H elaine,^{2,4} N. Hild,^{2,3} M. Kasprzak,^{2,6,11,‡} Y. Kermaidic,^{9,§} K. Kirch,^{2,3} P. Knowles,^{11,¶} H.-C. Koch,^{2,10,11} S. Komposch,^{2,3} P. A. Koss,⁶ A. Kozela,¹³ J. Krempel,³ B. Lauss,² T. Lefort,⁴ Y. Lemi ere,⁴ A. Leredde,⁹ A. Mtchedlishvili,² P. Mohanmurthy,^{2,3} M. Musgrave,^{1,**} O. Naviliat-Cuncic,⁴ D. Pais,^{2,3} A. Pazgalev,¹⁴ F. M. Piegsa,⁷ E. Pierre,^{2,4} G. Pignol,⁹ P. N. Prashanth,^{2,6} G. Qu em ener,⁴ M. Rawlik,³ D. Rebreyend,⁹ D. Ries,¹⁵ S. Roccia,^{16,17} D. Rozpedzik,⁵ P. Schmidt-Wellenburg,² A. Schnabel,¹⁸ N. Severijs,⁶ R. Tavakoli Dinani,⁶ J. Thorne,^{1,7} A. Weis,¹¹ E. Wursten,^{6,††} G. Wyszynski,^{3,5} J. Zejma,⁵ and G. Zsigmond²

¹*Department of Physics and Astronomy, University of Sussex, BN1 9QH Brighton, England, United Kingdom*

²*Paul Scherrer Institute, 5232 Villigen, Switzerland*

³*Eidgen ossische Technische Hochschule Z urich, Institute for Particle Physics and Astrophysics, 8093 Z urich, Switzerland*

⁴*Normandie Universit e, ENSICAEN, UNICAEN,*

Centre National de la Recherche Scientifique IN2P3, LPC Caen, Caen, France

⁵*Marian Smoluchowski Institute of Physics, Jagiellonian University, 30-348 Cracow, Poland*

⁶*Instituut voor Kern- en Stralingsfysica, Katholieke Universiteit Leuven, 3001 Leuven, Belgium*

⁷*Laboratory for High Energy Physics, Albert Einstein Center for Fundamental Physics, University of Bern, 3012 Bern, Switzerland*

⁸*University of Kentucky, Lexington, Kentucky 40506, USA*

⁹*Universit e Grenoble Alpes, Centre National de la Recherche Scientifique, Grenoble INP, LPSC-IN2P3, Grenoble, France*

¹⁰*Institute of Physics, Johannes Gutenberg University Mainz, 55128 Mainz, Germany*

¹¹*Physics Department, University of Fribourg, 1700 Fribourg, Switzerland*

¹²*Institute of Physics Belgrade, University of Belgrade, 11080 Belgrade, Serbia*

¹³*Henryk Niewodniczanski Institute of Nuclear Physics, Polish Academy of Sciences, 31-342 Cracow, Poland*

¹⁴*Ioffe Physical Technical Institute, 194021 Saint Petersburg, Russia*

¹⁵*Institut f ur Kernchemie, Johannes Gutenberg University Mainz, 55128 Mainz, Germany*

¹⁶*CSNSM, Universit e Paris Sud, Centre National de la Recherche Scientifique IN2P3, Universit e Paris Saclay, Orsay, France*

¹⁷*Institut Laue-Langevin, 38042 Grenoble, France*

¹⁸*Physikalisch Technische Bundesanstalt, D-10587 Berlin, Germany*

(Dated: April 29, 2020)

An array of sixteen laser-pumped scalar Cs magnetometers was part of the neutron electric dipole moment (nEDM) experiment taking data at the Paul Scherrer Institute in 2015 and 2016. It was deployed to measure the gradients of the experiment’s magnetic field and to monitor their temporal evolution. The originality of the array lies in its compact design, in which a single near-infrared diode laser drives all magnetometers that are located in a high-vacuum chamber, with a selection of the sensors mounted on a high-voltage electrode. We describe details of the Cs sensors’ construction and modes of operation, emphasizing the accuracy and sensitivity of the magnetic field readout. We present two applications of the magnetometer array directly beneficial to the nEDM experiment: (i) the implementation of a strategy to correct for the drift of the vertical magnetic field gradient and (ii) a procedure to homogenize the magnetic field. The first reduces the uncertainty of the new nEDM result. The second enables transverse neutron spin relaxation times exceeding 1500 s, improving the statistical sensitivity of the nEDM experiment by about 35% and effectively increasing the rate of nEDM data taking by a factor of 1.8.

I. INTRODUCTION

The experimental search for a permanent electric dipole moment of the neutron (nEDM) has been an important topic of fundamental research since the early 1950s [1, 2]. Since then, the experimental sensitivity has been improved by more than six orders of magnitude. The largest leap in sensitivity was due to the development of sources of ultracold neutrons (UCN) [3, 4] permitting the storage of neutrons within a material “bottle” for hundreds of seconds [5]. This, in turn, created the requirement to keep experimental conditions, especially the

* corresponding author: georg.bison@psi.ch

† present address: TRIUMF, Vancouver, Canada

‡ corresponding author: malgorzata.kasprzak@psi.ch

§ present address: Max Planck Institut f ur Kernphysik, Heidelberg, Germany

¶ present address: LogrusData, Toronto, Ontario, Canada

** present address: Massachusetts Institute of Technology, Cambridge, MA, USA

†† corresponding author: elise.wursten@cern.ch; present address: CERN, Geneva, Switzerland

magnetic field, stable over similar time spans, which resulted in the development of magnetometers placed close to [6] or within [7] the storage bottle. The experimental method applied to search for an nEDM with ultra-cold neutrons is based on a precise determination of the neutron spin precession frequency in static homogeneous parallel/antiparallel magnetic and electric fields by the Ramsey technique of (time-)separated oscillatory fields [8]. The statistical and systematic uncertainties of this method are strongly dependent on the (non)uniformity of the magnetic field \mathbf{B} in which the neutrons precess.

This article is the second episode in a trilogy of papers that comprehensively treat the uncertainties in nEDM searches that originate from the inhomogeneity of the magnetic field. The first episode [9] gives a general introduction to the subject, defines the way we characterize gradients, and derives the relevant criteria for nEDM experiments. In the second episode, this paper, we discuss the general approach to measure and compensate magnetic field gradients using an array of magnetometers. We describe in detail the specific implementation of this approach used in the 2015 and 2016 data runs of the nEDM experiment at the Paul Scherrer Institute (PSI). The general concept and aspects of the implementation are applicable to other experiments where magnetic field homogeneity is a concern. The third part will present the offline characterization of the magnetic field uniformity in the apparatus with an automated field-mapping device.

The nEDM apparatus at PSI is an upgraded version of the Sussex–RAL–ILL apparatus [10] that is equipped with two high-sensitivity systems for monitoring magnetic field changes, namely a ^{199}Hg co-magnetometer [7, 10] and an array of sixteen laser-pumped Cs magnetometers [11, 12]. The PSI-nEDM experiment [13] was the first that used simultaneously a co-magnetometer and an array of external magnetometers during data taking. The Hg co-magnetometer employs an ensemble of spin-polarized ^{199}Hg atoms which occupy the same storage volume as the UCN, and whose spin precession frequency is used to correct for drifts of the magnetic field in every Ramsey cycle. The array of Cs magnetometers located above and below the storage chamber measures the spatial distribution of the magnetic field, allowing for control of the field homogeneity and extraction of the gradients across the neutron storage chamber. The focus of this article is the implementation and application of the Cs magnetometer array. In Section II we describe the principle of the PSI-nEDM measurement with emphasis on the required magnetic field sensitivity and resolution of the magnetic field gradient. Section III provides a technical description of the Cs magnetometer array, including the design of the Cs magnetometers, their modes of operation and their performance in terms of magnetic field sensitivity and accuracy. Section IV details the applications of the Cs magnetometer array in the nEDM experiment. A description of how to extract magnetic field gradients from the array field measurements is provided in Section

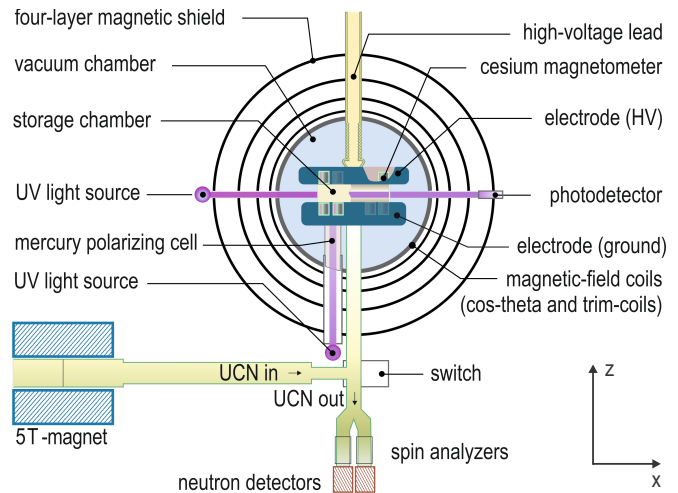


FIG. 1. Scheme of the nEDM apparatus. The magnetic and electric fields in the storage chamber are oriented vertically, each either parallel or anti-parallel to z .

IV A and Section IV B presents the procedure used to optimize the magnetic field.

II. THE nEDM EXPERIMENT AT PSI

Figure 1 shows the general scheme of the PSI-nEDM experiment [14], further called the ‘nEDM experiment’. The cylindrical neutron storage chamber, which also contains the ^{199}Hg co-magnetometer, consists of a polystyrene ring coated with deuterated polystyrene [15] and aluminum end caps coated with diamond-like carbon [16]. The latter serve as high-voltage and ground electrodes, which can generate a vertical electric field of up to 15 kV/cm in the chamber. The height of the cylinder (i.e., the distance between the electrodes) is 120 mm, and the radius is 235 mm. The Cs magnetometers that measure the magnetic field gradients are mounted on the high-voltage and ground electrodes. The storage chamber is located inside an aluminum vacuum chamber, onto which a cos-theta coil is wound. The vacuum tank also supports a set of 30 trim-coils and the B_1 coils used to generate magnetic resonance pulses for the neutrons and the Hg atoms. The cos-theta coil produces a vertical, static magnetic field of $\approx 1 \mu\text{T}$, while the set of trim-coils are used to homogenize the field and to apply specific field gradients when necessary. The vacuum chamber is surrounded by a passive four-layer μ -metal shield. The whole setup is enclosed in an air-conditioned, temperature-stabilized wooden hut. Three pairs of large ($\approx 8\text{m} \times 6\text{m}$) rectangular coils are mounted outside the hut and dynamically compensate the outer ambient field [17]. The system attenuates fluctuations in the ambient field by factor of 5-50 in a bandwidth from DC to 0.5 Hz which compensates the drop of passive shielding factor at small frequencies.

The operation of the apparatus during data taking

with UCN was recently reviewed in [18]. The effect of a finite nEDM d_n when the neutron is exposed to both an electric field \mathbf{E} and a magnetic field \mathbf{B} is an electric-field-dependent shift of the neutron spin precession frequency f_n . Statistical uncertainties in the determination of that frequency by Ramsey's method [8] propagate to the sensitivity of the nEDM measurement

$$\sigma(d_n) = \frac{\hbar}{2\alpha T E \sqrt{N} \sqrt{N_{\text{cycles}}}}, \quad (1)$$

where α is the contrast of the Ramsey fringe, T is the precession time, E the electric field strength, N the number of detected neutrons in one Ramsey cycle, and N_{cycles} the number of such cycles. In real measurements the statistical sensitivity is typically 10% worse due to imperfections and data cuts. Details of this procedure are given in [19]. The contrast α is determined by the transverse neutron spin depolarization time, and can be significantly improved by homogenizing the longitudinal (vertical) component of the magnetic field, as discussed in Section IV B.

The statistical sensitivity of the Sussex–RAL–ILL experiment [20, 21], which led to the former best value for d_n [22], was $\sigma_{\text{day}}(d_n) \approx 2 \times 10^{-25} e \cdot \text{cm}$ per day ($N_{\text{cycles}} = 400$). In the nEDM experiment at PSI [13] this value was improved by increasing α (see Section IV B 4), E , and neutron counting statistics and was on average $\sigma_{\text{day}}(d_n) \approx 1.1 \times 10^{-25} e \cdot \text{cm}$ per day ($N_{\text{cycles}} = 288$).

In order to keep the systematic uncertainty related to the control of the magnetic field and its gradients below the statistical sensitivity in Eq. (1), the resolution of the magnetic field measurement, $\sigma(B)$, in one Ramsey cycle should be:

$$\sigma(B) \ll \frac{E \sqrt{2N_{\text{cycles}}} \sigma_{\text{day}}(d_n)}{\mu_n}, \quad (2)$$

which gives $\sigma(B) \ll 0.5$ pT for the PSI-nEDM experiment. This resolution is provided by the ^{199}Hg comagnetometer, whose spin precession frequency f_{Hg} is used to monitor and correct for changes of the magnetic field from one Ramsey cycle to the next [10]. Mercury, and specifically its isotope ^{199}Hg , was chosen because in its ground state it has no electronic contribution to the atomic spin. The atomic spin, which can be optically pumped and probed, is thus a pure nuclear spin with coherence times of up to hundreds of seconds. This permits to monitor the magnetic field during a Ramsey cycle with a coherent spin precession signal achieving a sensitivity that is on average better than 80 fT. Using the comagnetometer signal as magnetic reference reduces the uncertainty of the neutron precession frequency due to magnetic field fluctuations to a few % of the total uncertainty.

All ^{199}Hg atoms are in the gas phase as the vapor pressure is much below the saturation pressure at room temperature. The atoms thus move with typical thermal velocities and sample the volume uniformly. The ultracold

neutrons, however, are noticeably affected by gravity because of their much lower velocity and thus preferentially inhabit the lower portion of the storage chamber. As a consequence, the ratio $\mathcal{R} = f_n/f_{\text{Hg}}$ is affected by any vertical magnetic field gradient $\frac{\partial B_z}{\partial z}$ across the storage chamber. Adopting the notation of [9],

$$\mathcal{R} = \frac{f_n}{f_{\text{Hg}}} = \frac{\gamma_n}{\gamma_{\text{Hg}}} \left(1 + \frac{G_{\text{grav}} \langle z \rangle}{B_0} + \delta_{\text{other}} \right), \quad (3)$$

where γ_n and γ_{Hg} are the gyromagnetic ratios of the neutron and ^{199}Hg atom respectively, G_{grav} is a combination of the relevant vertical gradients (see Section IV A), $\langle z \rangle$ is the vertical displacement of the center of mass of the neutrons with respect to the center of the storage chamber, $B_0 = \langle B_z \rangle_{\text{Hg}}$ is the magnetic field averaged over the precession volume as measured by the ^{199}Hg co-magnetometer and δ_{other} encompasses all other effects that change the \mathcal{R} -ratio, such as, e.g., the motional false EDM [23] and the rotation of the Earth [24]. The positive z -direction is defined upwards with respect to gravity so that a negative value is expected for the average displacement $\langle z \rangle$ of the neutrons. The required resolution of the gradient measurements $\sigma(G_{\text{grav}})$ for one Ramsey cycle can be estimated in a similar way as $\sigma(B)$ leading to

$$\sigma(G_{\text{grav}}) \ll \frac{\sigma(B)}{|\langle z \rangle|} \simeq 1.3 \text{ pT/cm}, \quad (4)$$

using $\langle z \rangle = -0.38(3)$ cm as determined in [9].

The temporal evolution of the magnetic field gradients was monitored with the array of sixteen Cs magnetometers installed close to the precession chamber. This allowed corrections to be made for gradient drifts (Section IV A) and the homogenization of the magnetic field using the variometer principle [25] (Sections III C and IV B). The latter resulted in larger values for the contrast α leading to a 35% increase in statistical sensitivity.

III. THE CS MAGNETOMETER ARRAY

This section describes the design, implementation and modes of operation of the Cs sensors installed above and below the precession chamber for monitoring magnetic field gradients. The design decisions were guided by the requirement to minimize any potential interference between the Cs sensors and the neutron EDM measurement. We chose to operate the sensors at room temperature since temperature gradients can lead to electrical currents that disturb the magnetic field in the experiment. Using Cs as the sensor medium combines two advantages in this situation: (i) Cs has the highest vapor pressure of all stable alkali metals and (ii) it has only one stable isotope, ^{133}Cs , with a large hyperfine splitting which suppresses interference from neighboring transitions. The sensors were operated in the M_x -mode [12, 26, 27] which features a stable steady state due to

the continuous magnetic resonance driven by an oscillating magnetic field. This weak field was suppressed by aluminum shielding cans and did not interfere with the neutron EDM measurement due to the large difference in resonance frequency (3.5 kHz for Cs vs. 30 Hz for the neutrons).

Similar sensor arrays have previously been used to measure the magnetic field generated by the human heart [28, 29]. For those biomagnetic measurements the performance of the array is limited by statistical uncertainties in the individual sensors. The sensors presented here are related to the ones used in [28] but have been optimized for stability and accuracy since statistical uncertainties are not the limiting factor for the large integration times relevant in nEDM measurements.

A. Design and implementation

The magnetometer array consists of sixteen Cs sensors that are made of nonmagnetic materials and are vacuum-compatible. The compact design allows their mounting close to the storage chamber. The sixteen magnetometers are arranged in a three-layer gradiometer configuration with sensors located both above and below the storage chamber. Seven sensors are installed on the high-voltage electrode, the centers of these sensors being 127.9 mm above the center plane of the neutron storage chamber. Nine sensors are installed below the ground electrode. They are arranged on two levels: 6 sensors are mounted on the aluminum plate directly below the ground electrode (128.5 mm below the center of the storage chamber), while three more sensors are positioned in a plane located 75 mm lower, as shown in Fig. 2. All sensors are placed with a position accuracy of about 0.5 mm.

1. Principle of the Cs magnetometer

The main components of a Cs magnetometer are shown in Fig. 3. The actual field-sensing element of each sensor is an evacuated glass cell, with an inner diameter of ~ 28 mm, whose inner wall is coated by a thin layer of paraffin [31]. The Cs density in the cell is determined by the saturated vapor pressure of a metallic droplet of ^{133}Cs at room temperature. The droplet is contained in a sidearm connected to the main cell volume by a capillary. The cesium atoms are spin-polarized by optical pumping using circularly polarized laser light whose frequency is resonant with the $F_g=4 \rightarrow F_e=3$ hyperfine component of the D_1 transition. The laser beam traverses the cell at an angle of 45° with respect to the magnetic field \mathbf{B} . The light from a frequency-stabilized laser is delivered to the sensor by a $400 \mu\text{m}$ multimode fiber. Before entering the cell, the light is collimated by a lens and circularly polarized by a linear polarizer and a quarter-wave plate (Fig. 3). The laser beam serves both to polarize the Cs atoms and to read out the precessing atomic spin polar-

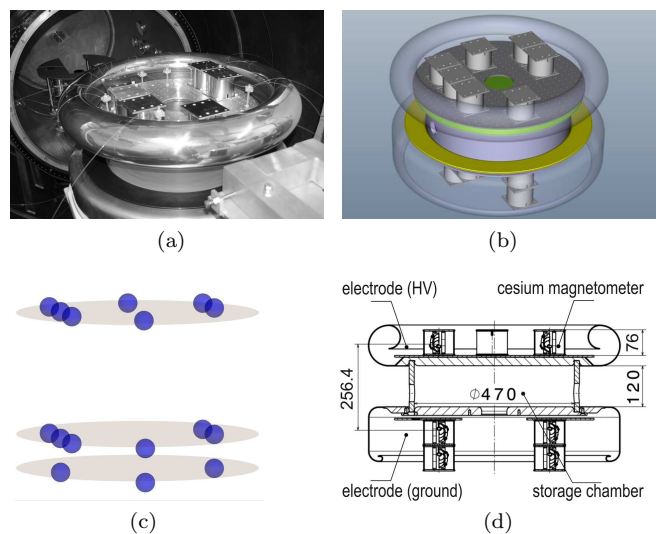


FIG. 2. Positions of the 16 Cs magnetometers in the nEDM experiment. Each sensor is enclosed in an aluminum cylinder which suppresses the interaction of its RF-field with the neighboring Cs sensors. (a) Storage chamber removed from the vacuum chamber (in the background) with 6 HV-compatible Cs magnetometers installed on an aluminum plate fixed to the HV electrode with corona ring. (b) Schematic view of the neutron storage chamber, the electrodes and the Cs magnetometers. (c) The blue spheres indicate the positions of the Cs sensors, they are arranged in three layers above and below the storage chamber. (d) Central vertical cut through (b) with dimensions in mm. The vertical distance of the Cs sensors from the center of the storage chamber is +127.9 mm, -128.5 mm, or -203.5 mm, the 13 closest magnetometers thus being a factor of 2.8 closer to the center of the precession chamber in comparison to the ^{87}Rb magnetometers in the earlier Sussex-RAL-ILL experiment [30].

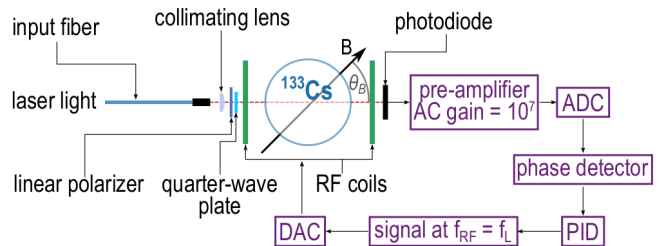


FIG. 3. Schematic of the Cs magnetometers' main components and electronics as described in the text.

ization (optically detected magnetic resonance). When exposed to the magnetic field \mathbf{B} , the magnetic moment associated with the spin polarization precesses at the Larmor frequency

$$f_L = \frac{\gamma_4}{2\pi} \|\mathbf{B}\|, \quad (5)$$

where $\gamma_4 \simeq 2\pi \times 3.50 \text{ Hz/nT}$ is the gyromagnetic ratio of the $F=4$ hyperfine level of the cesium ground state. The spin precession can be either continuously driven by an

oscillating magnetic field \mathbf{B}_1 or initiated by a magnetic resonance (\mathbf{B}_1) pulse (see Sec. III B 3). In both cases the \mathbf{B}_1 field is generated by a Helmholtz-like pair of coils surrounding the Cs cell. The coils were optimized to provide a homogeneous magnetic field over the volume of the Cs cell and are historically named RF-coils, a convention we adopt here despite the low oscillation frequency of 3.5 kHz. The precession of Cs atoms imposes an oscillation on the transmission of the laser light, which is detected on the photodiode.

All 16 magnetometers were operated with light delivered by a single high-stability diode laser (Toptica, DL pro 100) that was mounted in a dedicated housing in the temperature-stabilized room of the nEDM experiment. The laser frequency was actively locked to the $F_g=4 \rightarrow F_e=3$ hyperfine component of the Cs D_1 ($6S_{1/2} \rightarrow 6P_{1/2}$) transition at ~ 895 nm using Doppler-free saturation absorption spectroscopy (Toptica, CoSy), which allowed us to keep the laser continuously in frequency lock for weeks.

The beam from this laser was divided into multiple beams by a splitter system which was directly attached to the main vacuum chamber of the nEDM apparatus. The original beam was carried by a single 400 μm multimode fiber to a beam homogenizer (SUSS MicroOptics) producing a flat-topped intensity profile of quadratic cross section. The homogenized beam was then imaged onto a bundle of 36 fibers with 400 μm core diameter whose flat-polished input ends are arranged into a square brass-epoxy holder with an aperture of $3 \times 3 \text{ mm}^2$. Five of these fibers, including the four located at the corners of the bundle were used for monitoring purposes outside of the vacuum chamber. The remaining 31 fibers (~ 4.5 m long) were brought into the vacuum chamber, each with its own individual vacuum feedthrough. In order to achieve stable transmission efficiencies, the fibers ran uninterrupted through modified Swagelok feedthroughs which provided the vacuum sealing. Each fiber was terminated by a ferrule made of carbon-reinforced plastic that was inserted into the machined receptacle in the Cs sensor. On average, each output fiber carried $\sim 1.4\%$ of the input fiber's power.

2. HV-compatible sensor modules

The magnetometers mounted on the HV-electrode had to be fully opto-coupled. The light transmitted by the cell was not detected by a photodiode mounted next to the cell, but rather coupled into a 3 m long 800 μm diameter multimode fiber carrying the light to a photodiode mounted on the grounded vacuum tank. Tefzel[®] (dielectric constant 2.6) was selected as a fiber coating in order to allow good electrical isolation of the sensor. The RF signal driving the magnetic resonance was transmitted to the sensor by light generated by an IR LED (Lite-On Technology, model HSDL 4230) coupled to a 5 m long 800 μm multimode fiber. The plastic of the LED's casing

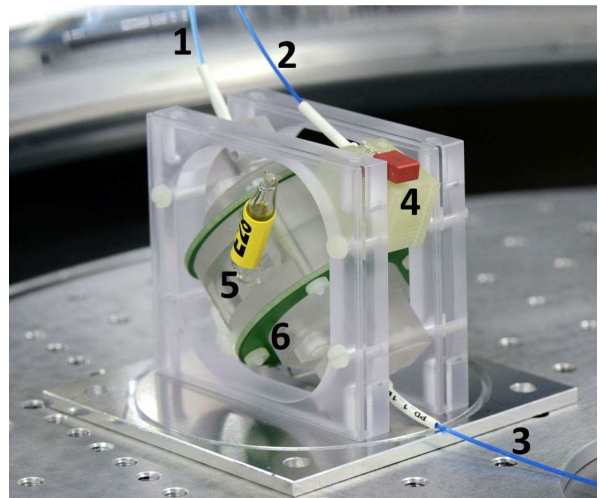


FIG. 4. HV-compatible magnetometer. The three fibers connected to the sensor provide the laser light (1), the RF signal (2), and collect the transmitted light (3). The Cs cell (of which only the sidearm, 5, is visible) is placed in a polycarbonate housing and surrounded by the RF coils printed on the (green) PCB boards (6). The photodiode and the capacitor forming the opto-coupler that drives the RF coils are mounted on a plastic holder (4).

was partly removed (down to a distance of ~ 1 – 2 mm from the semiconductor die) and polished to optimize coupling into the fiber. The light power had a constant and a sinusoidally modulated component which were converted to a current using a Si photodiode (Hamamatsu, model S6775-01) mounted near the sensor. The photo current was sufficient to drive the RF-coils after it passed through a non-magnetic 470 nF capacitor (WIMA 0.47 63/40) to suppress the DC component. All sensors were operated with RF-field amplitudes approximately equal to the linewidth converted to magnetic field units, < 4 nT.

B. Phase-feedback mode of operation

1. Description

The magnetometer is operated in the M_x configuration [12, 26, 27] in which the precession of the Cs atoms' magnetization around \mathbf{B} is continuously driven by a weak oscillating magnetic field $\mathbf{B}_{\text{RF}}(t) = \mathbf{B}_1 \sin(2\pi f_{\text{RF}}t)$. The \mathbf{B}_1 field is parallel to the wave vector of the laser beam, $\mathbf{B}_1 \parallel \mathbf{k}$, in order to avoid heading errors. In this geometry, the shape and center of the magnetic resonance do not depend on the orientation of \mathbf{B} with respect to \mathbf{k} [27, 32].

The light absorption by the Cs vapor depends on the projection of the atoms' magnetization onto \mathbf{k} . The continuous magnetic resonance leads to a steady state magnetization which precesses at the driving frequency f_{RF} and thus the transmitted light power has a component

$\delta P(t)$ modulated at that frequency

$$\delta P(t) = P_R \sin(2\pi f_{\text{RF}} t + \phi). \quad (6)$$

Here P_R is the modulation amplitude which depends on the light power, the degree of polarization, and the atomic absorption cross section. The phase ϕ is the phase difference with respect to the driving field \mathbf{B}_{RF} . It has a characteristic resonant behavior [27]

$$\phi_E = \phi - \phi_0 = -\arctan\left(\frac{f_{\text{RF}} - f_L}{\Gamma/2\pi}\right). \quad (7)$$

Here $\Gamma = 1/T_1 = 1/T_2$ is the Cs spin relaxation rate, which is assumed to be isotropic. In absence of any additional phase shifts in the electronic circuits, the reference phase ϕ_0 has the values of $\pm\pi/2$ depending on the direction of the magnetic field to be measured. The representation of the phase in Eq. (7) is chosen such that the variable ϕ_E has a zero-crossing in the center of the resonance at $f_{\text{RF}} = f_L = \gamma_4 B/2\pi$. Close to that point ϕ_E is proportional to the difference between the driving frequency and the Larmor frequency. Its slope with respect to a change of the magnetic field magnitude can thus be expressed as

$$\left.\frac{d\phi_E}{dB}\right|_{f_{\text{RF}}=f_L} = -\left.\frac{d}{dB} \arctan\left(\frac{f_{\text{RF}} - \gamma_4 B/2\pi}{\Gamma/2\pi}\right)\right|_{f_{\text{RF}}=f_L} = \frac{\gamma_4}{\Gamma}. \quad (8)$$

The phase ϕ_E is determined by a digital signal processing (DSP) system that generates the driving frequency f_{RF} via a digital-to-analog converter and samples the photocurrent of the photodiode via an analog-to-digital converter. For this, the photocurrent which is proportional to the light power transmitted through the Cs cell is converted to a voltage by a transimpedance amplifier, prior to digitization. The sampled voltage signal is then demodulated by a two-phase lock-in algorithm [27] that determines the amplitude of the oscillation and its phase. The reference phase ϕ_0 can be programmed via the digital interface of the DSP system which is also used to periodically read out the determined amplitude and phase values.

Figure 5 shows a measurement of ϕ as a function of f_{RF} . Such scans are used to determine the reference phase ϕ_0 which is necessary to compute the shifted phase ϕ_E . Phase shifts in the electronic circuits that are used in the generation of f_{RF} and the sampling of the photocurrent can cause changes in the reference phase ϕ_0 . The distinctive arctan line shape shown in Fig. 5 permits the determination of ϕ_0 independently of external references. This procedure thus constitutes an internal calibration and is performed periodically.

In normal operation f_{RF} is not scanned. It is rather controlled by a servo algorithm that uses ϕ_E as its error signal. If ϕ_0 was correctly determined, keeping $\phi_E = 0$ is equivalent to ensuring that $f_{\text{RF}} = f_L$. As a consequence,

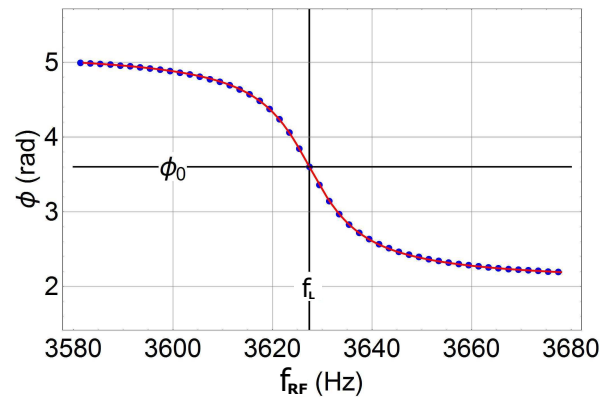


FIG. 5. Typical calibration curve of a Cs sensor shown with the fit using Eq. (7). The resulting fit parameters are: $\phi_0=3.6032(8)$ rad, $f_L=3619.980(8)$ Hz, and $\Gamma/2\pi=5.358(7)$ Hz.

f_{RF} , which is digitally synthesized in the DSP system, becomes a measure for the magnetic field which is periodically sampled directly in the DSP system. This mode of operation using a feedback loop is similar to standard phase-locked-loop schemes. Here, however, a frequency offset does not result in a linearly changing error signal. Thus, in contrast to standard phase-locked loop systems, the error signal ϕ_E must not only be kept constant but also equal to zero in order to match f_{RF} and f_L . This means that an offset $\Delta\phi_E$ in the determination of ϕ_E translates to an offset in the measured magnetic field according to Eq. (8)

$$\Delta B = \left(\frac{d\phi_E}{dB}\right)^{-1} \Delta\phi_E = \frac{\Gamma}{\gamma_4} \Delta\phi_E. \quad (9)$$

2. Magnetometric sensitivity

The statistical uncertainty of the magnetic field measurement can be computed according to the propagation of noise from the sampled photocurrent I^{PD} . The phase noise spectral density is given by

$$\rho(\phi) = \frac{\rho(I^{\text{PD}})}{I_{\text{RF}}^{\text{PD}}}, \quad (10)$$

where $I_{\text{RF}}^{\text{PD}}$ is the amplitude of the oscillation in the photocurrent at the applied RF frequency. Using Eq. (9) we find

$$\rho(B) = \frac{\Gamma\rho(\phi)}{\gamma_4} = \frac{\Gamma}{\gamma_4} \frac{\rho(I^{\text{PD}})}{I_{\text{RF}}^{\text{PD}}}. \quad (11)$$

In the shot noise limit, $\rho(I^{\text{PD}}) = \sqrt{2e I_{\text{DC}}^{\text{PD}}}$ with $I_{\text{DC}}^{\text{PD}}$ the DC component of the photocurrent, the magnetometric sensitivity for all sensors used was better than $\rho(B) = 50 \text{ fT}/\sqrt{\text{Hz}}$ after the light power and B_{RF} amplitude were individually optimized for each sensor. The

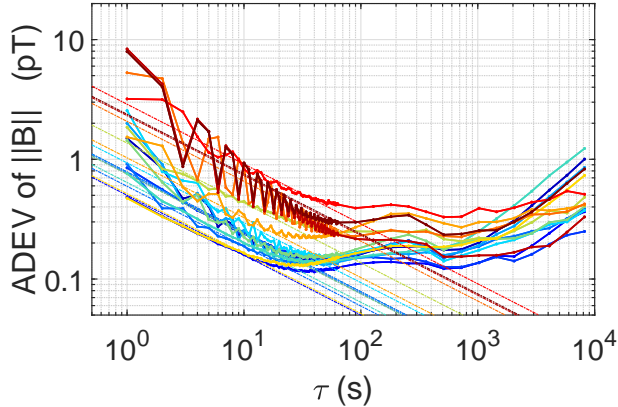


FIG. 6. Allan deviations of the magnetic field magnitude measured by 15 of the Cs magnetometers. The straight lines indicate the $\tau^{-1/2}$ behavior of pure white noise. The oscillations that are visible for some sensors are caused by the RF field of a neighboring sensor, as explained in the text.

shot noise limit was used as the figure of merit for this optimization since it can be computed independently of the external magnetic noise which depended significantly on the changing experimental environment. During nEDM measurements the typical statistical sensitivity of the Cs magnetometers was $\rho(B) = 750 \text{ fT}/\sqrt{\text{Hz}}$. The increase in statistical noise was due to the Johnson noise generated by the aluminum shielding cans (thickness 2 mm) that had to be installed around each sensor to suppress interference from the B_{RF} fields of neighboring sensors. Even with the cans installed, a small amount of beating was observed due to the remaining interference. This is the reason why some magnetometers show a pronounced structure in the Allan deviations shown in Fig. 6. The resulting average sensitivity (including the beating effect) ranges from 0.75 to $8 \text{ pT}/\sqrt{\text{Hz}}$.

3. Accuracy

One can distinguish two types of effects that influence the accuracy of the Cs magnetometer. The first relates to inaccuracies in determining the Larmor precession frequency f_L . The second category includes all effects that change f_L itself, modifying the relation between the Larmor precession frequency and the magnetic field as given by Eq. (5).

Below follows a short discussion of both types, concluding with recommendations on how to keep the offsets as stable as possible, allowing for high relative accuracy of the magnetic field reading.

As the extraction of the Larmor precession frequency relies heavily on the reference phase ϕ_0 , any drift of ϕ_0 without recalibration will worsen the accuracy of the sensor. Such drifts can occur due to temperature-related effects in the electronics or when, for example, the laser

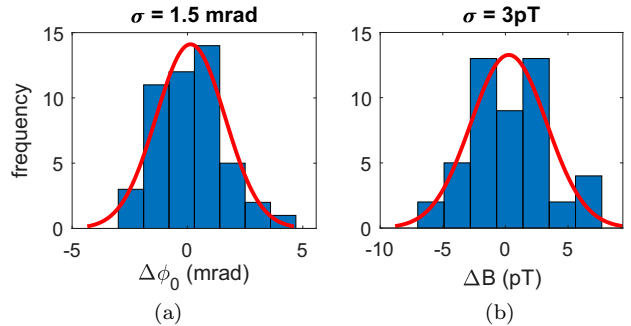


FIG. 7. (a) Histogram of the difference in extracted reference phase ϕ_0 between two consecutive calibrations. The typical time between the two calibrations is 1 to 4 days. (b) The corresponding offset in the magnetic field reading, as calculated by Eq. (9). The distributions in (a) and (b) are not identical, as the width Γ in the conversion factor depends on the light intensity, which varies from sensor to sensor. Over days of data taking the values for Γ were typically stable to better than 5%. During the whole two year-data taking period, all sensors had values of $\Gamma/2\pi$ between 4 Hz and 17 Hz.

intensity changes [33] and thus the capacitance of the photodiode. In order to quantify such drifts in the nEDM Cs magnetometer array, we have performed calibrations before and after each nEDM run, typically 1 to 4 days apart. Figure 7(a) shows a histogram of the extracted phase change $\Delta\phi_0 = \phi_{0,\text{after}} - \phi_{0,\text{before}}$ for one of the sixteen sensors. The typical change of reference phase is on the order of 1 to 2 mrad. An uncorrected drift $\Delta\phi_0$ of the on-resonance phase during phase-feedback operation results in an offset in the magnetic field measurement according to Eq. (9). Figure 7(b) shows the results of converting the phase differences in Fig. 7(a) to offsets in the magnetic field reading. The standard deviation of the magnetic field reading offset depends on the sensor properties and ranges from 1 to maximum 7 pT. This is of the same order of magnitude as the inherent uncertainty provided by the calibration procedure itself, which is about 1 pT.

Regarding the second category of inaccuracies, there are several effects that modify the Larmor precession frequency, or to be more precise, the energy separation of adjacent Zeeman sublevels of the $F=4$ ground state of the ^{133}Cs atoms. The resonance frequency that is measured by the Cs magnetometer in phase-feedback mode is a weighted average of the energy differences between the m and $m+1$ magnetic sublevels. In a system without laser interaction, the energy levels are the eigenvalues of the Cs ground state Hamiltonian containing the hyperfine interaction $A\mathbf{J} \cdot \mathbf{I}$ between the electronic spin \mathbf{J} and the nuclear spin \mathbf{I} , and the interaction of the magnetic moment with the applied magnetic field $\mu \cdot \mathbf{B}$. Applying perturbation theory to first order in $\mu B/A$ (for μB small compared to the scale given by the hyperfine structure constant A) then yields the linear Zeeman level splitting. The exact solution for this $J = 1/2$ system is given

by the Breit-Rabi equation [34]. For a magnetic field of $1\ \mu\text{T}$, the nonlinear terms in the Zeeman effect result in a maximum deviation equivalent to $3\ \text{pT}$ for neighboring magnetic sublevels, giving an upper limit on the inaccuracy due to nonlinear Breit-Rabi splitting.

A second effect of this category has to do with the use of a nonrotating driving field $\mathbf{B}_{\text{RF}} = \mathbf{B}_1 \sin(2\pi f_{\text{RF}} t)$. The nonrotating field produces a Bloch-Siegert shift [35, 36], which shifts the resonance by

$$\frac{(B_1 \sin \theta_B)^2}{16B_0} = \frac{B_1^2}{32B_0} \approx 0.5\ \text{pT}, \quad (12)$$

as the RF field of $4\ \text{nT}$ makes an angle of $\theta_B = \pi/4$ with the main B_0 field of $1\ \mu\text{T}$.

Another interaction that modifies the energy of the magnetic sublevels is the AC Stark shift induced by the coherent laser light, otherwise known as the virtual light shift [37]. It entails an interaction $\mathbf{d} \cdot \mathbf{E}$ between the electric dipole moment operator \mathbf{d} of the Cs atoms and the oscillating electric field \mathbf{E} of the laser light. Apart from modifying the hyperfine splitting and the common energy of all levels, it also produces a linear splitting and a quadratic splitting of the magnetic sublevels. The former is called a vector light shift, the latter a tensor light shift. The vector light shift can be interpreted as an effective magnetic field that is oriented along the direction of the laser beam for σ^+ light. As the laser light propagates at an angle of 45° with respect to \mathbf{B} , this effective magnetic field will add or subtract to the magnitude of the main magnetic field, depending on the direction of \mathbf{B} . Both the vector and the tensor light shift in the $F_g=4$ ground state depend linearly on the intensity of the light and have a dispersive line shape relative to the laser detuning around each hyperfine transition. Although the dispersive function vanishes when the laser frequency is resonant with the respective transition $F_g=4 \rightarrow F_e=3$, the light shift itself does not, as the dispersive function of the neighboring transition $F_g=4 \rightarrow F_e=4$ is quite broad and nonzero at that laser frequency. In order to determine the size of this effect in the nEDM experiment, dedicated measurements were done by changing the intensity of the light in a controlled way and scanning the detuning of the laser around the $F_g=4 \rightarrow F_e=3$ transition. To avoid the inaccuracy issues of the first type, the magnetometers were run in the free spin precession (FSP) mode [38, 39]. They could be operated in FSP mode without changing the sensor hardware or the laser power. The waveform of the signal driving the RF-coils was changed to a burst which alternates between RF-pulses and periods of zero RF amplitude. During the periods without RF field the ensemble spin precesses freely while the constant laser interaction pumps it slowly to an equilibrium state parallel to \mathbf{B} . The RF-pulses were tuned to flip the accumulated spin polarization by approximately 90° to the plane perpendicular to \mathbf{B} . During the next free precession period of about $50\ \text{ms}$ the laser, which is oriented at 45° with respect to \mathbf{B} , probes the spin component parallel to \mathbf{k} , which contains both the precessing signal of

the spin component perpendicular to \mathbf{B} and the growing spin polarization created along \mathbf{B} due to optical pumping. The advantage of operating the magnetometer in the FSP mode is that one directly detects the Larmor spin precession frequency f_L of the Cs atoms. These FSP studies [40] have shown that the sensors display shifts ranging from $\pm 10\ \text{pT}$ to $\pm 50\ \text{pT}$ at their typical light intensities, which are correlated to the light intensity, depend on the laser detuning and indeed change sign as the magnetic field is reversed. The FSP mode of operation was only used to test the Cs magnetometers since the pulse repetition frequency is close to the Larmor frequency of the ^{199}Hg atoms. Oscillating magnetic fields with frequency components close to the resonance frequency can cause changes in the Larmor precession of the ^{199}Hg atoms via the Ramsey-Bloch-Siegert shift which was not acceptable during nEDM data taking. Recent implementations of the FSP mode avoid interference via the RF field by using all-optical designs [38].

A fourth effect that modifies the Hamiltonian of the atom-light system is due to spin-exchange collisions between the ^{133}Cs atoms [41, 42]. The frequency shift operator contains a term proportional to $\mathbf{S} \cdot \langle \mathbf{S} \rangle$, where \mathbf{S} is the electron spin of the Cs atoms. This effect scales with the number density of the alkali atoms [43] and is therefore exponentially dependent on temperature. The exact implications for our magnetometer are not yet fully understood theoretically, but preliminary measurements comparing the precession frequency in different parts of the FSP signal (and thus at different directions of $\langle \mathbf{S} \rangle$) seem to indicate that the effect is smaller than $30\ \text{pT}$ for all sixteen sensors [40].

An overview of the effects discussed above is given in Table I. Combining the values of the different effects, the absolute accuracy of the sensors adds up to be in a range from 45 to $90\ \text{pT}$. For the purpose of measuring drifts of the vertical magnetic field gradient G_{grav} , the absolute accuracy of the magnetometers is not crucial, but it is important that the relative reading offsets of all sensors remain stable in time. It is therefore recommended to keep the light intensity sufficiently stable to avoid drifts in the reference phase and to keep the light shift in check. Additionally, large changes in temperature should be avoided, both for the stability of the electronics and the spin exchange effect. The achieved stability in the nEDM experiment was significantly better than the requirements for time scales up to $10\,000\ \text{s}$ as discussed in section IV A.

C. Variometer method

The array of Cs magnetometers can be used to obtain the vector components of the magnetic field by applying the variometer principle [25]. The implementation of this method will be explained in Section III C 1, its sensitivity and accuracy will be discussed in Sections III C 2 and III C 3 respectively.

TABLE I. Overview of effects that relate to inaccuracies in determining the Larmor precession frequency f_L (line 1), or that change f_L itself (lines 2 to 5) thereby modifying the relation between the Larmor precession frequency and the magnetic field as given in Eq. (5).

Effect	size (pT)
Reference phase drifts	1 to 7
Quadratic Zeeman splitting	3
Bloch-Siegert shift	0.5
Vector light shift	10 to 50
Spin exchange	<30

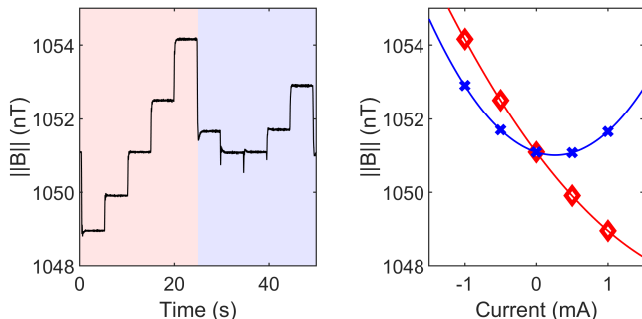


FIG. 8. On the left: the response of one of the Cs magnetometers to a current pattern of 1, 0.5, 0, -0.5 and -1 mA in steps of 5 s, first applied to a coil in the x -direction (0–25 s indicated in red), then to a coil in the y -direction (25–50 s indicated in blue). The main field of 1.051 μ T is maintained along the z -direction. A current of 1 mA corresponds to an applied field of about 50 nT. On the right: the corresponding parabolic behavior of the magnitude as a function of the applied current to a coil in the x -direction (red diamonds) and a coil in the y -direction (blue crosses).

1. Working principle

The variometer method consists of applying a well known magnetic field \mathbf{B}_T transverse to the main magnetic field of 1 μ T. Using the Cs magnetometers in phase-feedback mode to measure the magnitude of the total magnetic field, the additional transverse magnetic field changes the magnitude to:

$$\|\mathbf{B}_0 + \mathbf{B}_T I\|^2 = \|\mathbf{B}_0\|^2 + 2\mathbf{B}_0 \cdot \mathbf{B}_T I + \|\mathbf{B}_T\|^2 I^2, \quad (13)$$

where \mathbf{B}_0 represents the main magnetic field, I the current applied to the transverse coil, and \mathbf{B}_T the field produced by this transverse coil at the position of the Cs magnetometer when applying one unit of current. Probing the field magnitude with a set of different currents, one can extract $\|\mathbf{B}_0\|$, $\|\mathbf{B}_T\|$ and $\mathbf{B}_0 \cdot \mathbf{B}_T$ from the quadratic behavior of $\|\mathbf{B}_0 + \mathbf{B}_T I\|^2$ as a function of the current. The scalar product $\mathbf{B}_0 \cdot \mathbf{B}_T$ contains the angle between the applied transverse magnetic field and the main field \mathbf{B}_0 . Projecting on two known transverse magnetic field directions, one can reconstruct the direction of \mathbf{B}_0 .

An example of the readout of a Cs sensor during the application of the variometer method is shown in Fig. 8. Here, a sequence of five equally spaced currents is applied for five seconds each, first to a coil in the x -direction, then to a coil in the y -direction, whereas the main magnetic field is maintained in the z -direction. The currents are applied with an Agilent 33500B function generator, using a resistor of 10 k Ω in series with the transverse coils to convert the voltage generated by the function generator to a proportional current. In order to avoid magnetization of the μ -metal shield, the maximal current I is chosen such that the transverse field is about a factor of 20 smaller than the main magnetic field of 1 μ T. This results in a change of the magnetic field magnitude by typically 5 nT. As the Cs magnetometer is run in the phase-feedback mode, the reaction of the sensor to this sudden change of the magnetic field is not instantaneous, but has a time constant of a few 100 ms, depending on the parameters of the stabilizing PID algorithm. Consequently, the ramping parts of the signal have to be cut when averaging the magnitude over one current setting, effectively increasing the measurement uncertainty calculated in Section III C 2.

In order to extract the vector components of the main magnetic field, knowledge of the direction of the applied transverse field is crucial. The coils that are used to generate \mathbf{B}_T are normally used for applying the UCN and ^{199}Hg $\pi/2$ spin-flip pulses in the nEDM experiment. The magnetic fields produced by these coils were measured in 2014 with a nonmagnetic mapping device (the topic of the third episode in this trilogy) consisting of a three-axis fluxgate magnetometer mounted on a trolley. The trolley could move along a horizontal arm, which itself could rotate along a vertical axis and move up and down along the same vertical axis. Scanning the volume in discrete steps, the magnetic field map can be reconstructed from the corresponding fluxgate readings [44]. The resulting accuracy of these field maps at the specific Cs magnetometer positions is about 1 nT on each magnetic field component for a 50 nT total field produced by the coil.

This 2% inaccuracy of the field maps translates into a similar inaccuracy of all three vector components of \mathbf{B}_0 if the extraction is based purely on the two transverse projections. For this reason, we additionally include the fact that the magnetic field is predominantly homogeneous and assume that the B_{0z} component of the main field is closely approximated by the field magnitude $B_{0z} = \pm\|\mathbf{B}_0\|$ (true at the tens-of-pT level), with the sign being determined by the set B_0 direction. Using this approximation, one can extract B_{0x} and B_{0y} by solving the following set of equations:

$$\begin{bmatrix} \mathbf{B}_0 \cdot \mathbf{B}_1 - B_0 B_{1z} \\ \mathbf{B}_0 \cdot \mathbf{B}_2 - B_0 B_{2z} \end{bmatrix} = \begin{bmatrix} B_{1x} & B_{1y} \\ B_{2x} & B_{2y} \end{bmatrix} \begin{bmatrix} B_{0x} \\ B_{0y} \end{bmatrix}, \quad (14)$$

where \mathbf{B}_1 and \mathbf{B}_2 are the two applied transverse fields. To take into account slight differences in applied currents during the maps and the variometer measurement, the

\mathbf{B}_1 and \mathbf{B}_2 maps are scaled using the $\|\mathbf{B}_T\|^2$ parameter from the quadratic fit in Eq. (13). Matrix inversion of Eq. (14) yields

$$B_{0x} = \frac{B_{2y}(\mathbf{B}_0 \cdot \mathbf{B}_1 - B_0 B_{1z}) - B_{1y}(\mathbf{B}_0 \cdot \mathbf{B}_2 - B_0 B_{2z})}{B_{1x} B_{2y} - B_{2x} B_{1y}} \approx \frac{\mathbf{B}_0 \cdot \mathbf{B}_1 - B_0 B_{1z}}{B_{1x}} \quad (15)$$

and

$$B_{0y} = \frac{B_{1x}(\mathbf{B}_0 \cdot \mathbf{B}_2 - B_0 B_{2z}) - B_{2x}(\mathbf{B}_0 \cdot \mathbf{B}_1 - B_0 B_{1z})}{B_{1x} B_{2y} - B_{2x} B_{1y}}, \approx \frac{\mathbf{B}_0 \cdot \mathbf{B}_2 - B_0 B_{2z}}{B_{2x}} \quad (16)$$

where the second lines are obtained by assuming that B_{1y} and B_{2x} are negligible (meaning \mathbf{B}_1 is oriented predominantly along x and \mathbf{B}_2 predominantly along y). It is worth noting here that the statistical uncertainties on B_{0x} and B_{0y} originate from the terms proportional to the scalar products, whereas the accuracy is determined by the terms proportional to $B_0 B_{1z}$ and $B_0 B_{2z}$.

2. Magnetometric sensitivity

Based on the second line of Eqs. (15) and (16), the statistical uncertainty of the variometer method is determined by

$$\sigma(B_{0j}) = \frac{\sigma(\mathbf{B}_0 \cdot \mathbf{B}_T) - \sigma(B_0) B_{Tz}}{B_{Tj}}, \quad (17)$$

with j indicating the direction of the transverse coil producing \mathbf{B}_T . The components of \mathbf{B}_T do not introduce a statistical uncertainty, as they are fixed by the magnetic field maps. The precision with which the scalar product between \mathbf{B}_0 and \mathbf{B}_T can be determined depends on the amplitude and the duration of the currents applied to the transverse coils. Let us consider the case of a sequence of n steps of equal duration t_s with applied currents I_i , assuming an anti-symmetric sequence of currents: $\sum_i I_i = 0$. The uncertainty on the square of the magnetic field magnitude during one step is then given by $\sigma(B^2) = 2B\sigma(B) = 2B\rho(B)/\sqrt{2t_s}$, with $\rho(B)$ the noise density of the magnitude (Eq. (11)). Using weighted linear least squares fitting, the uncertainty on the coefficient of the linear term in Eq. (13) is given by

$$\sigma(2\mathbf{B}_0 \cdot \mathbf{B}_T) = \frac{\sigma(B^2)}{\sqrt{\sum_{i=1}^n I_i^2}} = \frac{2B\rho(B)}{\sqrt{2t_s} \sqrt{\sum_{i=1}^n I_i^2}}. \quad (18)$$

As B_{Tz} is typically not larger than a few nT, the uncertainty on the scalar product $\sigma(\mathbf{B}_0 \cdot \mathbf{B}_T)$ is about a factor

of 1000 larger than $\sigma(B_0)B_{Tz}$, hence one can neglect the second term in Eq. (17). The uncertainty during one measurement cycle is then

$$\sigma(B_{0j}) = \frac{B}{B_{Tj}} \frac{\rho(B)}{\sqrt{2t_s}} \frac{1}{\sqrt{\sum_{i=1}^n I_i^2}}. \quad (19)$$

Taking into account that two transverse projections are needed, the duration of one full variometer measurement cycle is $2n t_s$, hence giving the following noise density:

$$\rho(B_{0j}) = \sigma(B_{0j})\sqrt{4n t_s} = \rho(B) \frac{B}{B_{Tj}} \frac{\sqrt{2n}}{\sqrt{\sum_{i=1}^n I_i^2}}. \quad (20)$$

It is clear that in order to get the best sensitivity, one has to use the smallest number of steps $n = 3$ (I , 0 and $-I$) per transverse field direction at the highest possible current I . A typical variometer measurement cycle for the nEDM experiment then consists of applying a sequence of 3 steps of 6 s per transverse direction with a maximum applied transverse field of 50 nT. Such a measurement typically results in an uncertainty of about 10 pT, which is about a factor of 3 larger than expected from the calculated noise density. The reason is that, at this level of precision, the stability of the current source is a limiting factor. The uncertainty on the squared magnitude of the field should thus be modified to

$$\sigma(B^2) = \sqrt{\left(2B\sigma(B)\right)^2 + \left(\sigma(I) \frac{\partial B^2}{\partial I}\right)^2}, \quad (21)$$

such that the μA precision of the current source can be taken into account.

3. Stability and accuracy

The accuracy of the variometer method is determined by the accuracy of the field maps of \mathbf{B}_1 and \mathbf{B}_2 at the positions of the Cs sensors. These maps typically have an inaccuracy of 1 nT in all three components. Particularly the inaccuracy of the z -component propagates into a systematic error in B_{0x} and B_{0y} through the terms $B_0 B_{1z}/B_{1x}$ and $B_0 B_{2z}/B_{2x}$ of Eqs. (15) and (16) respectively. Using typical values of 1 μT for B_{0z} and 50 nT for B_{1x} and B_{2y} , the estimated accuracy is 20 nT for B_{0x} and B_{0y} . However, B_{0z} can be determined much more accurately as it is well approximated by the (directly-measured) magnitude $\|\mathbf{B}_0\|$.

If the transverse components remain smaller than 10 nT, as is typically the case in the nEDM experiment, the error made with this approximation is less than 100 pT.

Luckily, the inaccuracy due to the $B_{0z} B_{Tz}/B_{Tj}$ term is canceled when comparing two variometer measurements

of similar main magnetic fields. Assuming the main magnetic field direction is not changed too much, the difference between two magnetic fields can be determined with a relative accuracy of a few percent, since the main contribution of B_{0z} to the 20 nT cancels out when taking a difference. This of course does not hold when inverting the magnetic field direction. As shown in Section IV, these relative measurements are very useful for characterizing drifts of the main magnetic field and provide access to higher order magnetic field gradients that are inaccessible with the regular phase-feedback mode.

IV. APPLICATIONS OF THE MAGNETOMETER ARRAY

The Cs magnetometer array can be used for a variety of applications. The remainder of this paper will focus on two important ones directly beneficial to the nEDM experiment: (i) the implementation of a strategy to correct for the drift of the vertical magnetic field gradient and (ii) a procedure to optimize the homogeneity of the magnetic field. Section IV A describes how to extract the magnetic field gradients from the magnetometer array when vector or scalar magnetic field information is collected. This procedure is then applied to the data taken during the nEDM experiment to characterize the typical gradient drifts and to estimate the accuracy of the gradient extraction that is solely based on the magnitude readings. Section IV B outlines the optimization procedure that significantly improved the sensitivity of our nEDM experiment during the 2015 and 2016 data taking campaigns.

A. Spatial field distribution and gradient extraction

In order to extract the relevant magnetic field gradients, we model the spatial field distribution using a multipole expansion. The multipoles were chosen such that the relevant gradients can be described by a small number of expansion coefficients. Specifically, we use the multipole expansion as presented in [9], where the magnetic field at position \mathbf{r} is expanded in the form:

$$\mathbf{B}(\mathbf{r}) = \sum_{l,m} G_{l,m} \begin{bmatrix} \Pi_{x,l,m}(\mathbf{r}) \\ \Pi_{y,l,m}(\mathbf{r}) \\ \Pi_{z,l,m}(\mathbf{r}) \end{bmatrix}, \quad (22)$$

with the $\Pi_{l,m}$ harmonic polynomials of degree l in the Cartesian coordinates x , y and z , and $G_{l,m}$ the corresponding gradient coefficients. Each degree l has $2l + 3$ polynomials, with m ranging from $-(l + 1)$ to $l + 1$. The origin of the coordinate system is chosen at the center of the cylindrical precession chamber, as this significantly simplifies averaging over the chamber volume. The harmonic polynomials up to third order are listed in Table II of [9].

The gradient G_{grav} (introduced in Eq. (3)), relevant for the nEDM experiment, is a specific combination of the harmonic coefficients [9]:

$$G_{\text{grav}} = G_{1,0} + G_{3,0} \left(\frac{3H^2}{20} - \frac{3R^2}{4} \right), \quad (23)$$

where H is the height and R the radius of the cylindrical storage chamber. Evaluating this expression with the dimensions of the nEDM precession chamber, the vertical gradient is given by $G_{\text{grav}} = G_{1,0} - G_{3,0}(393 \text{ cm}^2)$.

1. Gradient extraction in the variometer mode

If the vector components of the magnetic field are known at positions \mathbf{r}_i , the gradients $G_{l,m}$ can be determined by solving the matrix equation

$$\begin{bmatrix} B_x \\ B_y \\ B_z \end{bmatrix} = \begin{bmatrix} \Pi_x \\ \Pi_y \\ \Pi_z \end{bmatrix} G, \quad (24)$$

where B_x is a column vector with elements B_x^i representing the x -component of the magnetic field measured at positions \mathbf{r}_i , Π_x is a matrix with elements $(\Pi_x)^{ij} = \Pi_{x,l_j,m_j}(\mathbf{r}_i)$, i.e., the harmonic polynomial defined by l_j and m_j evaluated at position \mathbf{r}_i , and G is a column vector containing the harmonic coefficients G_{l_j,m_j} . The expressions are similar for the y - and z -matrices. In the particular case of measurements with the variometer method there is, however, a significant difference between the uncertainty on B_z and the uncertainties on the transverse components B_x and B_y . Therefore, each line in the matrix equation is weighted with the inverse of the squared uncertainty of the corresponding magnetic field component value.

Since one of the HV-compatible magnetometers failed after an electrical discharge burned one of its optical fibers at an early stage of data taking, we only have 15 sensors available to fit the harmonic coefficients. This results in $3 \times 15 = 45$ equations, enabling us to comfortably fit up to third order (24 harmonics) while still having enough degrees of freedom for error estimation. This means that the harmonic coefficients necessary for the estimation of G_{grav} are easily accessible using the variometer method. However, since the method involves applying additional magnetic fields, it is not used during a typical nEDM measurement cycle as it would disturb the neutron EDM measurement.

2. Gradient extraction in the phase-feedback mode

Since in phase-feedback mode only the magnitude of the magnetic field is known at positions \mathbf{r}_i , we first have to make the following approximation:

$$\pm \|\mathbf{B}\| = B_z + \frac{B_x^2 + B_y^2}{2B_z} + \dots \approx B_z, \quad (25)$$

where the sign is determined by the main direction of \mathbf{B} , which is oriented along the z -axis. This approximation is valid in the nEDM experiment as the field maps have shown that the transverse components of the main 1 μT field are typically smaller than 10 nT. To extract the magnetic field gradients $G_{l,m}$, one has to solve the matrix equation $B_z = \Pi_z^S G^S$, with the matrices being defined as in Eq. (24), with the exception that the polynomials with $m_j = \pm(l_j + 1)$ are not included. The reason for this is that these modes are purely transverse and do not contribute to B_z , and are therefore not accessible via the magnitude. The superscript S (scalar) is added to make a clear distinction between gradients G determined from vector measurements and gradients G^S extracted from scalar measurements. Again, the uncertainty on the magnitude measurements can be used to assign weights to the equations.

As the nEDM experiment has sixteen Cs magnetometers, we typically limit the scalar harmonic expansion to second order (with 9 fit parameters), providing the following magnetic field description:

$$\begin{aligned} B_z(x, y, z) = & G_{0,0}^S + y G_{1,-1}^S + z G_{1,0}^S + x G_{1,1}^S \\ & + 2xy G_{2,-2}^S + 2yz G_{2,-1}^S \\ & + \left(z^2 - \frac{1}{2}(x^2 + y^2) \right) G_{2,0}^S \\ & + 2xz G_{2,1}^S + (x^2 - y^2) G_{2,2}^S. \end{aligned} \quad (26)$$

The cubic vertical gradient $G_{3,0}$ clearly cannot be determined using Eq. (26). However, the higher order terms do affect the extracted scalar gradients G^S . Assuming a multipole expansion $B_z = \Pi_z G$, the contribution of the higher order terms to the scalar fit parameters can be calculated explicitly:

$$G^S = \left((\Pi_z^S)^T W \Pi_z^S \right)^{-1} (\Pi_z^S)^T W \Pi_z G, \quad (27)$$

where W is a diagonal matrix containing the weight of each equation. Using the positions of the 15 Cs magnetometers that were operational during the 2015/2016 nEDM data taking and assuming equal weights for each magnetometer, the influence of the third order gradients on the vertical linear gradient $G_{1,0}^S = \sum a_{l,m} G_{l,m}$ is summarized in Table II. By comparing the prefactors in the definition of $G_{\text{grav}} = G_{1,0} - 393 \text{ cm}^2 G_{3,0}$ in Eq. (23) to the prefactors $a_{1,0}=1$ and $a_{3,0}=-288 \text{ cm}^2$, we can conclude that $G_{1,0}^S$ is a reasonable but slightly inaccurate estimator for G_{grav} . Adding weights W based on the typical uncertainties of each sensor changes the factors $a_{3,m}$ in Table II, but the prefactor for $G_{3,0}$ remains about 3/4 of the factor in G_{grav} .

3. Gradient extraction during nEDM data taking

In order to show that the Cs magnetometer array meets the requirements for gradient drift correction outlined at

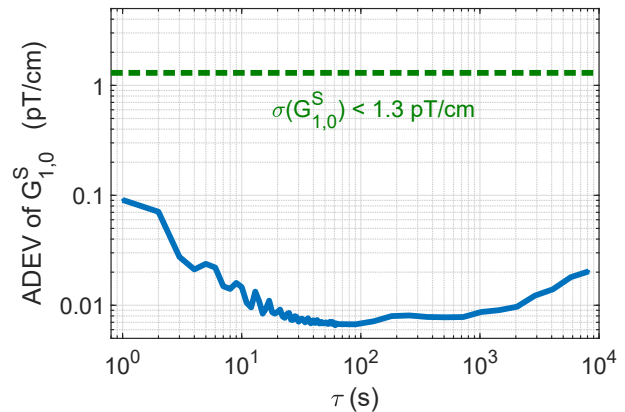


FIG. 9. The Allan deviation of the vertical gradient $G_{1,0}^S$ extracted from the data shown in Fig. 6 using the model in Eq. (26) is shown in blue. The achievable statistical uncertainty at the nEDM cycle duration of 180 s is 8 fT/cm, which is significantly below the upper limit indicated as a dashed green line. Statistical uncertainties in the magnetometers cause the rising slope towards small τ values. The result at 180 s is not limited by the slope but rather by the stability of the measurement system.

the end of Section II, we have to quantify the sensitivity and accuracy of the gradient extraction procedure based on the real magnetic field conditions in the nEDM experiment. To monitor the magnetic field during nEDM data taking, the typical measurement procedure regarding the Cs sensors consists of: (i) calibrations before and after each nEDM run to monitor the light intensity and the reference phase of the phase-feedback mode, (ii) followed by variometer measurements to monitor the higher order gradient drifts, and (iii) continuous measurements in the phase-feedback mode during the nEDM run. A run typically takes a few days, corresponding to about 500 Ramsey cycles which each take five minutes, while the electric field is reversed every 56 cycles.

In order to quantify the gradient drift sensitivity during a Ramsey cycle, we extract $G_{1,0}^S$ from the data used in Fig. 6 and calculate its Allan deviation (ADEV). The results are shown in Fig. 9. It is clear that the realized gradient sensitivity during the neutron storage time of 180 s is significantly better than the requirement of 1.3 pT/cm calculated in Section II. The ADEV slowly increases for longer integration times but remains far below the limit for all relevant time-scales.

Regarding the accuracy of the gradient drift measurement, there are two effects that play a role. On the one hand there are sensor-related drifts that translate into an artificial gradient drift, on the other hand there are drifts of $G_{1,0}^S$ induced by changes in the higher order magnetic field gradients. To estimate the former, we compare the calibrations before and after each nEDM run, to characterize the latter, we use the variometer measurements.

As discussed in Section III B 3, the typical change in reference phase between calibration pairs before and af-

TABLE II. Overview of the harmonic coefficients contributing to the fit parameter $G_{1,0}^S = \sum a_{l,m} G_{l,m}$ up to degree 3. For each harmonic coefficient $G_{l,m}$, the weighing factor $a_{l,m}$ and the standard deviation of the gradient drift $\sigma(\Delta G_{l,m})$ during a typical nEDM run are given. Taking into account the correlations between the different contributions, an estimation of the standard deviations of the drift of $G_{1,0}^S$ and its accuracy $G_{1,0}^S - G_{\text{grav}}$ are given in the last two lines. In the last line, the error estimation is scaled with $\sqrt{\chi^2/\nu}$ of the variometer fit to take into account the map-related inaccuracies of the method.

$G_{l,m}$	$a_{l,m}$ (cm ⁻¹)	$\sigma(\Delta G_{l,m})$ (pT/cm ^l)
$G_{1,0}$	1	1.71
$G_{3,-3}$	-135	0.0009
$G_{3,-2}$	344	0.0006
$G_{3,-1}$	22	0.0015
$G_{3,0}$	-288	0.0023
$G_{3,1}$	-23	0.0010
$G_{3,2}$	466	0.0010
$G_{3,3}$	1	0.0017
$G_{1,0}^S$		1.4–1.7
$G_{1,0}^S - G_{\text{grav}}$		< 0.7

ter an nEDM run results in reading offsets corresponding to a few pT. Using the magnetic field gradient model of Section IV A 2, these offsets produce a change of the fit-parameter $G_{1,0}^S$ with a standard deviation of 0.1 pT/cm in the time span of a few days. Similarly, the light intensity changes slightly over the course of an nEDM run, modifying the light shift in each sensor, resulting in an artificial gradient drift with standard deviation of 0.03 pT/cm. Since the light intensity typically decreases over time and the direction of the laser beams is opposite for the sensors above and below the storage chamber, the average change is about -0.01 pT/cm.

Comparing the variometer measurements before and after each nEDM run, we can extract the total change of each gradient $\Delta G_{l,m}$ during the run. The distribution of $\Delta G_{l,m}$ is Gaussian, with the standard deviation of the terms relevant to $G_{1,0}^S$ summarized in Table II. Taking into account the correlation between the drifts of $G_{1,0}$ and $G_{3,0}$, and using Eq. (23), the standard deviation of ΔG_{grav} is 1.4 pT/cm. Using the magnitude of the same data, the extracted drift of $G_{1,0}^S$ is in agreement with the drift of G_{grav} within the error bars of the parameters, which are typically 0.7 pT/cm for G_{grav} due to the inaccuracy of the variometer mode including map-related inaccuracies. This gives an upper limit on the relative accuracy of $G_{1,0}^S$: the accuracy is at least a factor of 2 better than the standard deviation of the drift on the timescale of an nEDM run. It follows that the dominant uncertainty on the extracted gradients is not due to the accuracy of the individual sensors, but rather due to the ‘aliasing effect’ of the higher order modes which are not included in the fit.

B. Homogenization of the magnetic field

The homogeneity of the magnetic field influences both the statistical precision of the nEDM experiment and its systematic effects. To improve the former without exacerbating the latter, we have developed a procedure for optimizing the magnetic field in the precession chamber. The principles behind this optimization strategy are explained in Section IV B 1. The implementation of the routine is described in Section IV B 2, followed by a discussion of the tuning of the algorithm in Section IV B 3. Finally, the resulting improvement in sensitivity is presented in Section IV B 4.

1. Principles behind the optimization

Improving the statistical sensitivity and minimizing the systematic effects impose different requirements on the magnetic field optimization. The magnetic-field-related contribution to the statistical precision of the nEDM measurement is captured in the parameter α of Eq. (1), which is the visibility or contrast of the Ramsey resonance. This parameter is predominantly defined by the neutrons’ transverse spin relaxation time T_2 via $\alpha(T) = \alpha_0 \exp(-T/T_2)$ where α_0 is the polarization at the start of the Ramsey procedure and T the precession time of the neutrons. The transverse relaxation time results from a combination of three types of neutron depolarization in the storage chamber, as discussed in [9]. The first mechanism is depolarization due to wall collisions, which is an effect that does not depend on the magnetic field. The second is gravitationally enhanced depolarization [45, 46], which is caused by the extremely low kinetic energy of the ultracold neutrons. Different energy groups of neutrons have a different average height in the chamber, so in the presence of a vertical gradient of the field’s main component their precession frequencies differ slightly. This causes a dephasing of the different energy groups, which results in a lower polarization at the end of the Ramsey procedure. To reduce this effect, it is crucial to minimize specifically the vertical gradient $\partial B_z/\partial z$. The third mechanism is intrinsic depolarization, which refers to the depolarization within each given energy group. Even though the neutrons have the same energy, their trajectories through the chamber differ, resulting in dephasing if the magnetic field is not homogeneous over the chamber volume. Such local changes in Larmor frequency are caused by all gradients of the main field component B_z while gradients of the transverse components B_x and B_y play a negligible role.

Conversely, the magnetic-field-related systematic effects that are not dealt with in the extension of the *crossing point analysis* of [9], involve the quantities $\langle B_{\text{T}}^2 \rangle$ and $G_{3,0}$. The first is defined as

$$\langle B_{\text{T}}^2 \rangle = \left\langle (B_x - \langle B_x \rangle)^2 + (B_y - \langle B_y \rangle)^2 \right\rangle \quad (28)$$

and stands for the square of the transverse magnetic field components averaged over the storage volume. It is a second order combination of the harmonic expansion coefficients $G_{l,m}$:

$$\langle B_T^2 \rangle = \sum a_{ij} G_{l_i, m_i} G_{l_j, m_j}. \quad (29)$$

The coefficients a_{ij} are given in Appendix B of [9]. The smaller the gradients of the transverse magnetic field components, the smaller this systematic effect.

The quantity $G_{3,0}$ is the cubic vertical gradient of B_z with a characteristic z -dependance $\mathbf{B}(x=0, y=0, z) \propto (0, 0, z^3)$. The systematic uncertainties related to $G_{3,0}$ can thus be suppressed by ensuring the homogeneity of B_z .

In summary, optimizing the homogeneity of the longitudinal field component B_z helps to suppress certain systematic uncertainties and is crucial to maintain long T_2 times and thus a high statistical sensitivity. Optimizing the homogeneity of the transverse field components B_x and B_y is equally important since a different systematic effect is related to those components.

2. Implementation

Firstly, the homogeneity of the longitudinal magnetic field component B_z can be directly accessed by the Cs magnetometer array. However, since the sensors are not perfectly accurate and require offline corrections, B_z was only available up to an accuracy of about 45 to 90 pT during online data taking (Table I). Therefore, the goal of the optimization routine is to reduce the spread of the Cs magnetometer readings to this level. Secondly, the transverse components are accessible with the variometer method, but the accuracy is not sufficient to keep $\langle B_T^2 \rangle$ below the goal of 2 nT^2 , which would correspond to a systematic effect at the level of a few $10^{-27} e \cdot \text{cm}$. For this reason, offline field maps, that were recorded before the period of nEDM data taking, are used to provide an estimate of $\langle B_T^2 \rangle$. The final correction of this systematic effect will be performed with more accurate values extracted from a more recent mapping campaign (the analysis of which will be included in the third part of the trilogy).

Combining the online information of the Cs sensors with the offline magnetic field maps, we developed a routine to optimize the currents I_{coil} applied to a set of 30 trim-coils wound around the vacuum tank. The magnetic field produced by each coil when applying one unit of current was characterized both online and offline, providing $\mathbf{B}_{\text{coil}}^{\text{CsM}}$ measured by the Cs magnetometer (CsM) in the variometer mode, and the harmonic expansion coefficients $G_{\text{coil}}^{\text{map}}$ as extracted from the magnetic field maps. After measuring the main magnetic field $\mathbf{B}_0^{\text{CsM}}$ on-line with the Cs magnetometer array, the optimal currents are calculated by minimizing the sum of the following

three terms:

$$S = S_{\text{Long}} + T_{\text{Trans}} S_{\text{Trans}} + T_{\text{Reg}} S_{\text{Reg}}, \quad (30)$$

where $S_{\text{Long}}(I_{\text{coil}})$ quantifies the homogeneity of the longitudinal component, $S_{\text{Trans}}(I_{\text{coil}})$ evaluates the systematic effect due to the transverse components and $S_{\text{Reg}}(I_{\text{coil}})$ is added as a regularization term since there are more parameters than constraints ($30 > 16+1$). The factors T_{Trans} and T_{Reg} are tuning parameters and assign a weight to the respective sums relative to S_{Long} .

The explicit expression for S_{Long} as a function of the currents I_{coil} is given by

$$S_{\text{Long}} = \sum_{\text{CsM}} \left(B_{0,z}^{\text{CsM}} + \sum_{\text{coil}} I_{\text{coil}} B_{\text{coil},z}^{\text{CsM}} - B_{\text{goal}} \right)^2, \quad (31)$$

where $B_{0,z}^{\text{CsM}}$ and $B_{\text{coil},z}^{\text{CsM}}$ are the z -components measured by the Cs magnetometer of the main magnetic field and the field produced by the coil when applying one unit of current respectively. B_{goal} is the goal value for the Cs sensor magnitude readings. Typically, the sensors are all assigned the same goal value to improve the homogeneity, but other configurations are possible.

The transverse requirements are taken into account by the following sum

$$S_{\text{Trans}} = \langle (B_T^{\text{map}})^2 \rangle = \sum_{i,j} a_{ij} G_{l_i, m_i}^{\text{map}} G_{l_j, m_j}^{\text{map}}, \quad (32)$$

where $G_{l_i, m_i}^{\text{map}} = G_{0, l_i, m_i}^{\text{map}} + \sum_{\text{coil}} I_{\text{coil}} G_{\text{coil}, l_i, m_i}^{\text{map}}$ is the harmonic coefficient G_{l_i, m_i} of the total magnetic field that would be produced if the currents I_{coil} would be applied to the coils as determined from the field maps. The coefficients a_{ij} are defined in [9].

The regularization term is given by

$$S_{\text{Reg}} = \sum_{\text{coil}} \left(I_{\text{coil}} \max_{\text{CsM}} (\|\mathbf{B}_{\text{coil}}^{\text{CsM}}\|) \right)^2, \quad (33)$$

where $\max_{\text{CsM}} (\|\mathbf{B}_{\text{coil}}^{\text{CsM}}\|)$ is the maximum magnitude measured by the Cs magnetometers when one unit of current is applied to the coil. This term makes sure that the magnetic field produced per coil is not too large, avoiding a loss in sensitivity due to local inhomogeneities created by the coils themselves.

In order to minimize Eq. (30), we solve the set of equations $\partial S / \partial I_{\text{coil}} = 0$. Since the terms in S are at most of order 2 in I_{coil} , $\partial S / \partial I_{\text{coil}}$ is of order 1 and can be solved efficiently using matrix inversion.

3. Optimizing the tuning parameters

The success of the algorithm is determined by the choice of the tuning parameters T_{Trans} and T_{Reg} . To determine the optimal values, we start off with an estimate of the optimal size of each sum in Eq. (30). Given

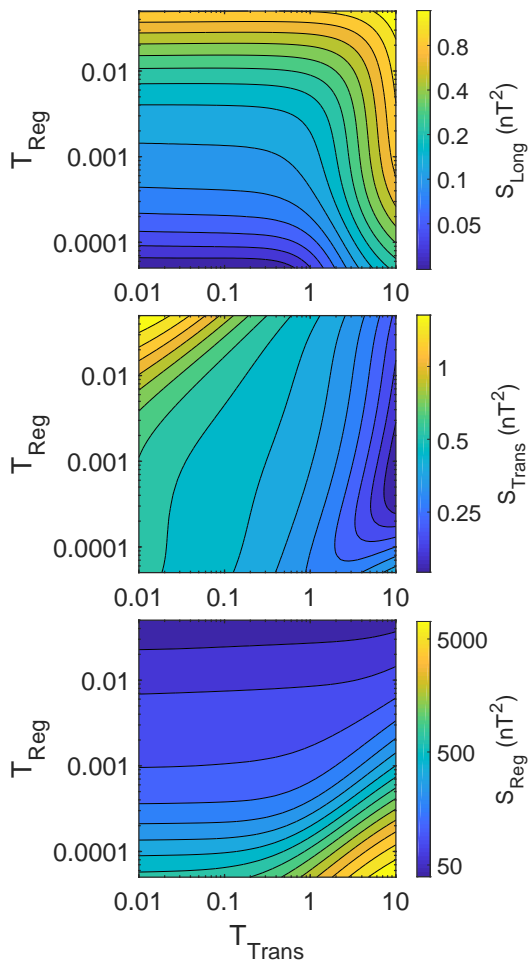


FIG. 10. The behavior of S_{Long} (top), S_{Trans} (middle) and S_{Reg} (bottom) evaluated at the optimal trim-coil currents as a function of the tuning parameters T_{Trans} and T_{Reg} . All scales (including the color scale) are logarithmic.

the on-line accuracy of the Cs magnetometers, we estimate the final standard deviation of $(B_z^{\text{CsM}} - B_{\text{goal}})$ at 100 pT, resulting in a longitudinal term S_{Long} of $(0.1 \text{ nT})^2 \times 16 = 0.16 \text{ nT}^2$. The value of $\langle B_T^2 \rangle$ should be as small as possible, but since the maps provide only a rough estimate, we set the goal value for S_{Trans} at 0.5 nT^2 . To avoid producing local inhomogeneities due to strong currents in the trim-coils, the tuning is started with a trial value of 2 nT produced per coil on average, resulting in a regularization term S_{Reg} of $(2 \text{ nT})^2 \times 30 = 120 \text{ nT}^2$. Comparing the size of each sum, first guesses for the tuning parameters are $T_{\text{Trans}} = S_{\text{Long}}/S_{\text{Trans}} = 0.32$ and $T_{\text{Reg}} = S_{\text{Long}}/S_{\text{Reg}} = 0.0013$.

Figure 10 shows the minimized values of each sum S_i in Eq. (30) in function of the tuning parameters, with the ranges centered around our initial guesses. The terms are calculated using a typical magnetic field which is measured on-line 30 minutes after degaussing the μ -metal shield, as is the typical procedure during nEDM data taking. As is clearly visible in the two uppermost plots

of Fig. 10, the tuning parameter T_{Trans} (horizontal axis) determines the relative importance of the longitudinal spread (top) versus the transverse homogeneity (middle). For values of T_{Trans} smaller than 1.0, the longitudinal spread is almost solely determined by the regularization parameter T_{Reg} . The smaller T_{Reg} , the larger the applied currents (bottom), and the smaller the predicted spread of B_z . For T_{Trans} larger than 1, the value of $\langle (B_T^{\text{map}})^2 \rangle$ is significantly reduced at the cost of a worse B_z homogeneity and much larger currents. The behavior at large T_{Trans} and small T_{Reg} (bottom right corner of each plot) suggests that it is nearly impossible to have both a small spread in on-line B_z^{CsM} -component and a small $\langle B_T^2 \rangle$ predicted from the maps, even if the restriction on the applied currents is relaxed. This indicates that the estimation of $\langle B_T^2 \rangle$ from the maps is only reliable down to the 0.3 nT^2 level. As the exact size of S_{Trans} is not crucial, T_{Trans} is typically fixed at a value smaller than 1.0 leading to $\langle (B_T^{\text{map}})^2 \rangle$ values smaller than the limit of 2 nT^2 .

The optimal choice for T_{Reg} is not so straightforward. It depends on the initial homogeneity of the magnetic field, as a larger inhomogeneity implies a larger amount of current necessary to compensate. Moreover, as the applied currents become larger, the uncertainty on the measurement of $B_{\text{coil},z}^{\text{CsM}}$ will make the estimation of the longitudinal spread inaccurate and thus reduce the predictive power for the value of α . On top of that, making the magnetic field magnitude the same at all sensor positions does not mean that the field in the storage chamber itself is homogeneous, especially when the applied trim-coil currents are large. For this reason, we typically selected a scan range of 0.0002 to 0.0020 for T_{Reg} and picked out the best setting by measuring the resulting α on-line.

4. Results

Different iterations of the optimization procedure were used during the nEDM data taking period of 2015 and 2016. For each chosen current setting during data taking, the value of $\langle B_T^2 \rangle$ was smaller than 2 nT^2 . The corresponding Ramsey visibilities are shown in Fig. 11. The effect of gravitational depolarization is clearly visible as α decreases when the vertical gradient $\Delta G_{1,0}^S$ moves away from zero. From dedicated measurements at different storage times, we know that the initial polarization α_0 in our storage bottle is 0.86. The α values of 0.76-0.81 at zero gradient then correspond to transverse neutron relaxation times between 1450 s and 3000 s.

The improvement of the neutron spin relaxation time T_2 and the corresponding increase of Ramsey contrast α is summarized in Table III, comparing data from 2014 without CsM based homogenization with data from 2015 and 2016. The transverse relaxation time has more than doubled with the new homogenization procedure, resulting in an increase of α by about 35% and an equal im-

TABLE III. Comparison of the transverse neutron spin relaxation time T_2 and the Ramsey contrast α at zero vertical gradient before and after the field homogenization was introduced in 2015. The polarization α_0 at the start of the Ramsey procedure is 0.86 in both datasets. In 2014 the α values were significantly different for the two B_0 field orientations.

Year	B_0 direction	T_2 (s)	α
2014	up	760	0.64
	down	439	0.52
2015 & 2016	up	1620-3000	0.77-0.81
	down	1450-3000	0.76-0.81

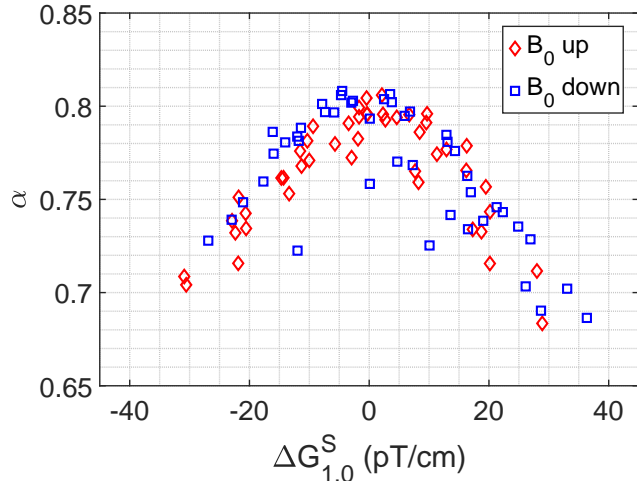


FIG. 11. The Ramsey contrast or visibility α measured during the nEDM data taking period of 2015 and 2016 as a function of the vertical gradient. The ‘zero’ gradient is defined per magnetic field base configuration (or equivalently per set of measurements that are based on the same homogenization result) as the gradient at which the visibility-parabola reaches its highest point. For nonzero vertical gradient, gravitational depolarization reduces the contrast of the Ramsey curve. Note that both B_0 up and B_0 down reach similar visibilities.

provement of the nEDM sensitivity. In order to realize the same improvement with neutron statistics, the total number of detected neutrons would have to be increased by a factor of 1.8 due to the \sqrt{N} scaling (see Eq. (1)). This is a significant improvement for an experiment that is scheduled to take data for several years.

V. SUMMARY

We have discussed the design, implementation and performance of the Cs magnetometer array installed at the PSI-nEDM experiment. The compact optical magnetometers are vacuum and HV compatible and are placed on the electrodes above and below the UCN storage chamber, providing on-line gradient information. The sensors are driven by a single diode laser, using beam

multiplexing to bring the light to the individual sensors in the vacuum chamber of the experiment. We have explained the phase-feedback mode of sensor operation in the M_x configuration and demonstrated an intrinsic magnetometer sensitivity which is below $50 \text{ fT}/\sqrt{\text{Hz}}$ in the shot noise limit. The final magnetometer noise in the nEDM experiment was significantly larger than the shot noise limit but it did not limit the extraction of important field parameters at the relevant integration time of 180 s. At such large integration times the performance is rather limited by system stability which we could demonstrate to be significantly better than required (see Fig. 9). We have discussed various systematic effects that influence the reading of the magnetometer and estimated an on-line accuracy of 45 to 90 pT. Using a set of two transverse coils, we can run the magnetometers in variometer mode, providing vector information of the local magnetic field.

A model was presented to describe the spatial field distribution, and the precision and accuracy of gradient extraction during nEDM data taking was discussed. Further, a magnetic field homogenization procedure, which more than doubled the transverse spin relaxation time of the neutrons, while at the same time keeping magnetic-field-related systematic effects under control, was presented. This resulted in an improvement of 35% of the statistical sensitivity of the nEDM experiment which reduced the time to reach a given statistical sensitivity by a factor of 1.8.

The presented techniques are useful in general for the measurement and control of magnetic field uniformity. We will use an upgraded version of the magnetometer array, based on all-optical sensors [38], in our new neutron EDM experiment (n2EDM). The new sensors use free spin precession in contrast to the driven spin precession in a M_x magnetometer. This leads to improved stability and accuracy, necessary to fulfill the requirements of our next-generation experiment.

VI. ACKNOWLEDGEMENTS

We would like to thank the mechanical workshop at the University of Fribourg for manufacturing the construction elements of Cs sensors, C. Macchione for the preparation of the paraffin-coated Cs cells and M. Meier and F. Burri for their support during the installation of the Cs magnetometer array and measurements at PSI.

The LPC Caen and the LPSC acknowledge the support of the French Agence Nationale de la Recherche (ANR) under Reference No. ANR-09-BLAN-0046. P.M. likes to acknowledge support from SNSF-FCS Grant No. 2015.0594 (ETHZ). E.W. acknowledges the fellowship of the Fund for Scientific Research Flanders (FWO). This research was partly financed by the Fund for Scientific Research, Flanders; Grant No. GOA/2010/10 of KU Leuven; the Swiss National Science Foundation projects 126562 (PSI), 140421 (UNIFR), 144473 (PSI), 149211 (ETH), 162574 (ETH), 172626 (PSI), 172639

(ETH), and 181996 (Bern), the Deutsche Forschungsgemeinschaft projects BI 1424/2-1 and /3-1, and Grants No. ST/K001329/1, No. ST/M003426/1, and No. ST/L006472/1 from the Science and Technology Facilities Council (STFC) of the United Kingdom. The orig-

inal nEDM apparatus without the Cs magnetometer array was funded by grants from the PPARC (now STFC) of the United Kingdom. Our Polish partners wish to acknowledge support from the National Science Centre, Poland, under Grants No. UMO-2015/18/M/ST2/00056 and UMO-2016/23/D/ST2/00715.

-
- [1] E. M. Purcell and N. F. Ramsey, *Phys. Rev.* **78**, 807 (1950).
- [2] J. H. Smith, E. M. Purcell, and N. F. Ramsey, *Phys. Rev.* **108**, 120 (1957).
- [3] G. Bison, M. Daum, K. Kirch, B. Lauss, D. Ries, P. Schmidt-Wellenburg, G. Zsigmond, T. Brenner, P. Geltenbort, T. Jenke, O. Zimmer, M. Beck, W. Heil, J. Kahlenberg, J. P. Karch, K. Ross, K. Eberhardt, C. Geppert, S. Karpuk, and N. Trautmann, *Phys. Rev. C* **95** (2016), 10.1103/PhysRevC.95.045503.
- [4] R. Golub, D. Richardson, and S. Lamoreaux, *Ultra-cold neutrons* (CRC Press, 1991).
- [5] J. Pendlebury, K. Smith, R. Golub, J. Byrne, T. McComb, T. Sumner, S. Burnett, A. Taylor, B. Heckel, N. Ramsey, K. Green, J. Morse, A. Kilvington, C. Baker, S. Clark, W. Mampe, P. Ageron, and P. Miranda, *Phys. Lett. B* **136**, 327 (1984).
- [6] K. Smith, N. Crampin, J. Pendlebury, D. Richardson, D. Shiers, K. Green, A. Kilvington, J. Moir, H. Prosper, D. Thompson, N. Ramsey, B. Heckel, S. Lamoreaux, P. Ageron, W. Mampe, and A. Steyerl, *Phys. Lett. B* **234**, 191 (1990).
- [7] K. Green, P. G. Harris, P. Iaydjiev, D. J. R. May, J. M. Pendlebury, K. F. Smith, M. van der Grinten, P. Geltenbort, and S. Ivanov, *Nucl. Inst. Meth. A* **404**, 381 (1998).
- [8] N. F. Ramsey, *Phys. Rev.* **78**, 695 (1950).
- [9] C. Abel, N. J. Ayres, T. Baker, G. Ban, G. Bison, K. Bodek, V. Bondar, C. B. Crawford, P.-J. Chiu, E. Chanel, Z. Chowdhuri, M. Daum, B. Dechenaux, S. Emmenegger, L. Ferraris-Bouchez, P. Flaux, P. Geltenbort, K. Green, W. C. Griffith, M. van der Grinten, P. G. Harris, R. Henneck, N. Hild, P. Iaydjiev, S. N. Ivanov, M. Kasprzak, Y. Kermaidic, K. Kirch, H.-C. Koch, S. Komposch, P. A. Koss, A. Kozela, J. Krempel, B. Lauss, T. Lefort, Y. Lemièrre, A. Leredde, P. Mohanmurthy, D. Pais, F. M. Piegsa, G. Pignol, G. Quéméner, M. Rawlik, D. Rebreyend, D. Ries, S. Roccia, D. Rozpedzik, P. Schmidt-Wellenburg, A. Schnabel, N. Severijns, R. Viro, A. Weis, E. Wursten, G. Wyszynski, J. Zejma, and G. Zsigmond, *Phys. Rev. A* **99**, 042112 (2019).
- [10] C. Baker, Y. Chibane, M. Chouder, P. Geltenbort, K. Green, P. Harris, B. Heckel, P. Iaydjiev, S. Ivanov, I. Kilvington, S. Lamoreaux, D. May, J. Pendlebury, J. Richardson, D. Shiers, K. Smith, and M. Van Der Grinten, *Nucl. Inst. Meth. A* **736**, 184 (2014).
- [11] A. Weis and R. Wynands, *Optics and Lasers in Engineering* **43**, 387 (2005).
- [12] S. Groeger, G. Bison, J. Schenker, R. Wynands, and A. Weis, *Eur. Phys. J. D* **38**, 239 (2006).
- [13] C. Abel, S. Afach, N. J. Ayres, C. A. Baker, G. Ban, G. Bison, K. Bodek, V. Bondar, M. Burghoff, E. Chanel, Z. Chowdhuri, P.-J. Chiu, B. Clement, C. B. Crawford, M. Daum, S. Emmenegger, L. Ferraris-Bouchez, M. Fertl, P. Flaux, B. Franke, A. Fratangelo, P. Geltenbort, K. Green, W. C. Griffith, M. van der Grinten, Z. D. Grujić, P. G. Harris, L. Hayen, W. Heil, R. Henneck, V. Hélaine, N. Hild, Z. Hodge, M. Horras, P. Iaydjiev, S. N. Ivanov, M. Kasprzak, Y. Kermaidic, K. Kirch, A. Knecht, P. Knowles, H.-C. Koch, P. A. Koss, S. Komposch, A. Kozela, A. Kraft, J. Krempel, M. Kuźniak, B. Lauss, T. Lefort, Y. Lemièrre, A. Leredde, P. Mohanmurthy, A. Mtchedlishvili, M. Musgrave, O. Naviliat-Cuncic, D. Pais, F. M. Piegsa, E. Pierre, G. Pignol, C. Plonka-Spehr, P. N. Prashanth, G. Quéméner, M. Rawlik, D. Rebreyend, I. Rienäcker, D. Ries, S. Roccia, G. Rogel, D. Rozpedzik, A. Schnabel, P. Schmidt-Wellenburg, N. Severijns, D. Shiers, R. Tavakoli Dinani, J. A. Thorne, R. Viro, J. Voigt, A. Weis, E. Wursten, G. Wyszynski, J. Zejma, J. Zenner, and G. Zsigmond, *Phys. Rev. Lett.* **124**, 081803 (2020).
- [14] C. Baker, G. Ban, K. Bodek, M. Burghoff, Z. Chowdhuri, M. Daum, M. Fertl, B. Franke, P. Geltenbort, K. Green, M. Van Der Grinten, E. Gutmiedl, P. Harris, R. Henneck, P. Iaydjiev, S. Ivanov, N. Khomutov, M. Kasprzak, K. Kirch, S. Kistryn, S. Knappe-Grüneberg, A. Knecht, P. Knowles, A. Kozela, B. Lauss, T. Lefort, Y. Lemièrre, O. Naviliat-Cuncic, J. Pendlebury, E. Pierre, F. Piegsa, G. Pignol, G. Quéméner, S. Roccia, P. Schmidt-Wellenburg, D. Shiers, K. Smith, A. Schnabel, L. Trahms, A. Weis, J. Zejma, J. Zenner, and G. Zsigmond, *Phys. Proc.* **17**, 159 (2011).
- [15] K. Bodek, M. Daum, R. Henneck, S. Heule, M. Kasprzak, K. Kirch, A. Knecht, M. Kuzniak, B. Lauss, M. Meier, G. Petzoldt, and M. Schneider, *Nucl. Inst. Meth. A* **597**, 222 (2008).
- [16] F. Atchison, T. Brys, M. Daum, P. Fierlinger, A. Foelsch-Schmitz, M. Gupta, R. Henneck, S. Heule, M. Kasprzak, K. Kirch, R. Kötz, M. Kuzniak, T. Lippert, C.-F. Meyer, F. Nolting, A. Pichlmaier, D. Schneider, B. Schultrich, P. Siemroth, and U. Straumann, *Diamond and Related Materials* **16**, 334 (2007).
- [17] S. Afach, G. Bison, K. Bodek, F. Burri, Z. Chowdhuri, M. Daum, M. Fertl, B. Franke, Z. Grujić, V. Helaine, R. Henneck, M. Kasprzak, K. Kirch, H.-C. Koch, A. Kozela, J. Krempel, B. Lauss, T. Lefort, Y. Lemièrre, and G. Zsigmond, *J. Appl. Phys.* **116** (2014), 10.1063/1.4894158.
- [18] C. Abel, N. J. Ayres, G. Ban, G. Bison, K. Bodek, V. Bondar, E. Chanel, P. J. Chiu, M. Daum, S. Emmenegger, L. Ferraris-Bouchez, P. Flaux, W. C. G. P. G. Harris, N. Hild, Y. Kermaidic, K. Kirch, P. A. Koss, J. Krempel, B. Lauss, T. Lefort, Y. Lemièrre, A. Leredde, P. Mohanmurthy, M. Musgrave, O. Naviliat-Cuncic, D. Pais, F. M. Piegsa, G. Pignol, M. Rawlik, D. Re-

- breyend, D. Ries, S. Roccia, D. Rozpedzik, P. Schmidt-Wellenburg, A. Schnabel, N. Severijns, J. Thorne, R. Viro, J. Voigt, A. Weis, E. Wursten, J. Zejma, and G. Zsigmond, EPJ Web of Conf. **219**, 02001 (2019).
- [19] P. G. Harris, ArXiv e-prints (2007), arXiv:0709.3100 [hep-ex].
- [20] P. Harris, C. Baker, K. Green, P. Iaydjiev, S. Ivanov, D. May, J. Pendlebury, D. Shiers, K. Smith, M. Grinten, and P. Geltenbort, Phys. Rev. Lett. **82**, 904 (1999).
- [21] C. A. Baker, D. D. Doyle, P. Geltenbort, K. Green, M. G. D. van der Grinten, P. G. Harris, P. Iaydjiev, S. N. Ivanov, D. J. R. May, J. M. Pendlebury, J. D. Richardson, D. Shiers, and K. F. Smith, Phys. Rev. Lett. **97**, 131801 (2006).
- [22] J. M. Pendlebury, S. Afach, N. J. Ayres, C. A. Baker, G. Ban, G. Bison, K. Bodek, M. Burghoff, P. Geltenbort, K. Green, W. C. Griffith, M. van der Grinten, Z. D. Grujić, P. G. Harris, V. Helaine, P. Iaydjiev, S. N. Ivanov, M. Kasprzak, Y. Kermaidic, K. Kirch, H. C. Koch, S. Komposch, A. Kozela, J. Krempel, B. Lauss, T. Lefort, Y. Lemièrre, D. J. R. May, M. Musgrave, O. Naviliat-Cuncic, F. M. Piegsa, G. Pignol, P. N. Prashanth, G. Quemener, M. Rawlik, D. Rebreyend, J. D. Richardson, D. Ries, S. Roccia, D. Rozpedzik, A. Schnabel, P. Schmidt-Wellenburg, N. Severijns, D. Shiers, J. A. Thorne, A. Weis, O. J. Winston, E. Wursten, J. Zejma, and G. Zsigmond, Phys. Rev. D **92**, 092003 (2015).
- [23] S. Afach, C. A. Baker, G. Ban, G. Bison, K. Bodek, Z. Chowdhuri, M. Daum, M. Fertl, B. Franke, P. Geltenbort, K. Green, M. G. D. van der Grinten, Z. Grujić, P. G. Harris, W. Heil, V. Helaine, R. Henneck, M. Horras, P. Iaydjiev, S. N. Ivanov, M. Kasprzak, Y. Kermaidic, K. Kirch, P. Knowles, H. C. Koch, S. Komposch, A. Kozela, J. Krempel, B. Lauss, T. Lefort, Y. Lemièrre, A. Mtchedlishvili, O. Naviliat-Cuncic, J. M. Pendlebury, F. M. Piegsa, G. Pignol, P. N. Prashanth, G. Quémèner, D. Rebreyend, D. Ries, S. Roccia, P. Schmidt-Wellenburg, N. Severijns, A. Weis, E. Wursten, G. Wyszynski, J. Zejma, J. Zenner, and G. Zsigmond, Eur. Phys. J. D **69**, 225 (2015).
- [24] S. Lamoreaux and R. Golub, Physical review letters **98**, 149101 (2007).
- [25] A. K. Vershovskii, M. V. Balabas, A. É. Ivanov, V. N. Kulyasov, A. S. Pazgalev, and E. B. Aleksandrov, Technical Physics **51**, 112 (2006).
- [26] E. B. Alexandrov and A. K. Vershovskiy, “ M_x and M_z magnetometers,” in *Optical Magnetometry*, edited by D. Budker and D. F. Jackson Kimball (Cambridge University Press, 2013) pp. 60–84.
- [27] A. Weis, G. Bison, and Z. D. Grujić, “Magnetic resonance based atomic magnetometers,” in *High Sensitivity Magnetometers*, edited by A. Grosz, M. J. Haji-Sheikh, and S. C. Mukhopadhyay (Springer International Publishing, Cham, 2017) pp. 361–424.
- [28] G. Bison, N. Castagna, A. Hofer, P. Knowles, J.-L. Schenker, M. Kasprzak, H. Saudan, and A. Weis, Appl. Phys. Lett. **95**, 173701 (2009).
- [29] G. Lembke, S. N. Erné, H. Nowak, B. Menhorn, A. Pasquarelli, and G. Bison, Biomed. Opt. Express **5**, 876 (2014).
- [30] J. Pendlebury, Nuclear Physics A **546**, 359 (1992).
- [31] N. Castagna, G. Bison, G. Di Domenico, A. Hofer, P. Knowles, C. Macchione, H. Saudan, and A. Weis, Appl. Phys. B **96**, 763 (2009).
- [32] S. Colombo, V. Dolgovskiy, T. Scholtes, Z. Grujić, V. Lebedev, and A. Weis, Appl. Phys. B **123**, 35 (2017).
- [33] J. R. Piller, *Accurate optical magnetometry based on precessing spin-aligned atoms*, Master’s thesis, Fribourg University, Fribourg Switzerland (2016).
- [34] G. Breit and I. I. Rabi, Phys. Rev. **38**, 2082 (1931).
- [35] F. Bloch and A. Siegert, Phys. Rev. **57**, 522 (1940).
- [36] J. Sudyka, S. Pustelny, and G. Wojciech, New J. Phys **21**, 023024 (2019).
- [37] W. Happer and B. S. Mathur, Phys. Rev. **163**, 12 (1967).
- [38] Z. Grujić, P. Koss, G. Bison, and A. Weis, Eur. Phys. J. D **69**, 135 (2015).
- [39] S. Afach, G. Ban, G. Bison, K. Bodek, Z. Chowdhuri, Z. D. Grujić, L. Hayen, V. Hélaine, M. Kasprzak, K. Kirch, P. Knowles, H.-C. Koch, S. Komposch, A. Kozela, J. Krempel, B. Lauss, T. Lefort, Y. Lemièrre, A. Mtchedlishvili, O. Naviliat-Cuncic, F. M. Piegsa, P. N. Prashanth, G. Quémèner, M. Rawlik, D. Ries, S. Roccia, D. Rozpedzik, P. Schmidt-Wellenburg, N. Severijns, A. Weis, E. Wursten, G. Wyszynski, J. Zejma, and G. Zsigmond, Opt. Express **23**, 22108 (2015).
- [40] E. Wursten, *A new precise measurement of the neutron electric dipole moment*, Ph.D. thesis, University of Leuven, Belgium (2020).
- [41] F. Grossetête, J. Phys. France **29**, 456 (1968).
- [42] Y. Shi, T. Scholtes, Z. D. Grujić, V. Lebedev, V. Dolgovskiy, and A. Weis, Phys. Rev. A **97**, 013419 (2018).
- [43] S. Appelt, A. B.-A. Baranga, C. J. Erickson, M. V. Romalis, A. R. Young, and W. Happer, Phys. Rev. A **58**, 1412 (1998).
- [44] G. Wyszynski, *Development of magnetic field control systems in the $nEDM$ experiment*, Ph.D. thesis, Jagiellonian University, Cracow, Poland (2015).
- [45] P. G. Harris, J. M. Pendlebury, and N. E. Devenish, Physical Review D **89** (2014), 10.1103/physrevd.89.016011.
- [46] S. Afach, N. J. Ayres, C. A. Baker, G. Ban, G. Bison, K. Bodek, M. Fertl, B. Franke, P. Geltenbort, K. Green, W. C. Griffith, M. van der Grinten, Z. D. Grujić, P. G. Harris, W. Heil, V. Helaine, P. Iaydjiev, S. N. Ivanov, M. Kasprzak, Y. Kermaidic, K. Kirch, H. C. Koch, S. Komposch, A. Kozela, J. Krempel, B. Lauss, T. Lefort, Y. Lemièrre, M. Musgrave, O. Naviliat-Cuncic, J. M. Pendlebury, F. M. Piegsa, G. Pignol, C. Plonka-Spehr, P. N. Prashanth, G. Quemener, M. Rawlik, D. Rebreyend, D. Ries, S. Roccia, D. Rozpedzik, P. Schmidt-Wellenburg, N. Severijns, D. Shiers, J. A. Thorne, A. Weis, E. Wursten, J. Zejma, J. Zenner, and G. Zsigmond, Phys. Rev. D **92**, 052008 (2015).



A search for neutron to mirror-neutron oscillations using the nEDM apparatus at PSI



nEDM Collaboration at PSI

C. Abel^a, N.J. Ayres^b, G. Ban^c, G. Bison^d, K. Bodek^e, V. Bondar^b, E. Chanel^f, P.-J. Chiu^{b,d}, C. Crawford^g, M. Daum^d, R.T. Dinani^h, S. Emmenegger^b, P. Flaux^c, L. Ferraris-Bouchezⁱ, W.C. Griffith^a, Z.D. Grujić^{j,1}, N. Hild^{b,d}, K. Kirch^{b,d}, H.-C. Koch^d, P.A. Koss^h, A. Kozela^k, J. Krempel^b, B. Lauss^d, T. Lefort^c, A. Lereddeⁱ, P. Mohanmurthy^{b,d,*}, O. Naviliat-Cuncic^c, D. Pais^{b,d}, F.M. Piegsa^f, G. Pignolⁱ, M. Rawlik^{b,d}, D. Rebreyendⁱ, I. Rienäcker^{b,d}, D. Ries^l, S. Rocca^{i,m}, D. Rozpedzik^e, P. Schmidt-Wellenburg^d, N. Severijns^h, J. Thorne^f, A. Weis^j, E. Wursten^{h,3}, J. Zejma^e, G. Zsigmond^{d,*}

^a Department of Physics and Astronomy, University of Sussex, Falmer, Brighton BN1 9QH, United Kingdom

^b Institute for Particle Physics and Astrophysics, ETH Zürich, 8093 Zürich, Switzerland

^c Normandie Université, ENSICAEN, UNICAEN, CNRS/IN2P3, LPC Caen, 14000 Caen, France

^d Paul Scherrer Institut, 5232 Villigen PSI, Switzerland

^e Marian Smoluchowski Institute of Physics, Jagiellonian University, 30-348 Kraków, Poland

^f Laboratory for High Energy Physics and Albert Einstein Center for Fundamental Physics, University of Bern, 3012 Bern, Switzerland

^g University of Kentucky, Lexington, KY 40508, United States of America

^h Institute for Nuclear and Radiation Physics, KU Leuven, 3001 Heverlee, Belgium

ⁱ Laboratoire de Physique Subatomique et de Cosmologie, Université Grenoble Alpes, CNRS/IN2P3, Grenoble, France

^j University of Fribourg, 1700 Fribourg, Switzerland

^k Henryk Niedwodniczański Institute of Nuclear Physics, 31-342 Kraków, Poland

^l Department of Chemistry - TRIGA site, Johannes Gutenberg University Mainz, 55128 Mainz, Germany

^m Institut Laue-Langevin, CS 20156, F-38042 Grenoble Cedex 9, France

ARTICLE INFO

Article history:

Received 22 September 2020

Received in revised form 18 November 2020

Accepted 23 November 2020

Available online 3 December 2020

Editor: M. Doser

Keywords:

Properties of neutrons

Ultracold neutrons

Nuclear matter

Mirror matter

Dark matter

Particle symmetries

ABSTRACT

It has been proposed that there could be a mirror copy of the standard model particles, restoring the parity symmetry in the weak interaction on the global level. Oscillations between a neutral standard model particle, such as the neutron, and its mirror counterpart could potentially answer various standing issues in physics today. Astrophysical studies and terrestrial experiments led by ultracold neutron storage measurements have investigated neutron to mirror-neutron oscillations and imposed constraints on the theoretical parameters. Recently, further analysis of these ultracold neutron storage experiments has yielded statistically significant anomalous signals that may be interpreted as neutron to mirror-neutron oscillations, assuming nonzero mirror magnetic fields. The neutron electric dipole moment collaboration performed a dedicated search at the Paul Scherrer Institute and found no evidence of neutron to mirror-neutron oscillations. Thereby, the following new lower limits on the oscillation time were obtained: $\tau_{nm'} > 352$ s at $B' = 0$ (95% C.L.), $\tau_{nm'} > 6$ s for $0.4 \mu\text{T} < B' < 25.7 \mu\text{T}$ (95% C.L.), and $\tau_{nm'} / \sqrt{\cos\beta} > 9$ s for $5.0 \mu\text{T} < B' < 25.4 \mu\text{T}$ (95% C.L.), where β is the fixed angle between the applied magnetic field and the local mirror magnetic field, which is assumed to be bound to the Earth. These new constraints are the best measured so far around $B' \sim 10 \mu\text{T}$ and $B' \sim 20 \mu\text{T}$.

© 2020 The Authors. Published by Elsevier B.V. This is an open access article under the CC BY license (<http://creativecommons.org/licenses/by/4.0/>). Funded by SCOAP³.

* Corresponding authors. Address for correspondence for author G. Zsigmond: Paul Scherrer Institut, 5232 Villigen PSI, Switzerland.

E-mail addresses: geza.zsigmond@psi.ch (G. Zsigmond), prajwal.thyagarthi.mohanmurthy@alumni.ethz.ch (P. Mohanmurthy).

¹ Present address: Institute of Physics, University of Belgrade, 11080 Belgrade, Serbia.

² Present address: University of Chicago, 5801 S Ellis Ave, Chicago, IL 60637, USA.

³ Present address: CERN, 1211 Genève, Switzerland.

1. Introduction

Lee and Yang noted, in their landmark paper [1], that parity symmetry in the weak interaction could be restored with the introduction of a parity conjugated copy of the same weakly interacting particles. It was shown by Kobzarev, Okun and Pomernichuk [2] that ordinary particles would not interact with their *mirror* counterparts, as they called them, via the strong, weak and electromagnetic interactions. Mirror particles would have their own interactions of the identical types *i.e.* also implying the existence of mirror photons and mirror electromagnetic fields. Foot and Volkas [3,4] detailed the aforementioned idea that by the introduction of mirror matter (hereafter denoted by SM' in analogy to SM particles), parity and time reversal symmetries could be restored in the electroweak interactions, and thus in a global sense as well.

Several works considered that mixing of SM and SM' particles could provide answers to a number of outstanding issues in physics today. Mirror matter could provide a viable dark matter candidate [5–10] (for direct detection possibilities see [11–14]). Mixings between neutrinos and mirror neutrinos [15–18] due to new feeble interactions could make mirror neutrinos to natural candidates for sterile neutrino species. Furthermore, interactions of SM and SM' particles with baryon/lepton number and CP violation could open co-baryogenesis channels, thereby helping to explain the baryon dark matter fractions in the universe [19,20]. A mechanism to relax the Greisen-Zatsepin-Kuzmin (GZK) limit on the maximum energy of cosmic rays through neutron to mirror-neutron oscillations was also proposed [21,22]. A comprehensive review of mirror matter physics and cosmology can be found in Refs. [12,23–26].

Mechanisms creating mirror magnetic fields (B') on the Earth, in the solar system or Galaxy are discussed in section 4. of Ref. [27]. This suggests the possibility of B' -s bound to Earth of the order of 100 μT which could be tested in neutron experiments.

Berezhiani and Bento [28] pointed out that the characteristic time for neutron to mirror-neutron ($n - n'$) oscillation, $\tau_{nn'}$, can be of the order of a few seconds, *i.e.* small compared to the lifetime of the neutron. In Ref. [27], Berezhiani showed that, as long as neutrons and their mirror counterparts have the same mass, decay widths and gravitational potential, application of a magnetic field equal to the mirror magnetic field in the same place can induce a degeneracy between the $|n\rangle$ and $|n'\rangle$ states. This enhances the oscillation probability resonantly as described by the non-relativistic Hamiltonian:

$$\mathcal{H} = \begin{pmatrix} -\mu_n \mathbf{B} \cdot \boldsymbol{\sigma} & \epsilon_{nn'} \\ \epsilon_{nn'} & -\mu_{n'} \mathbf{B}' \cdot \boldsymbol{\sigma} \end{pmatrix}, \quad (1)$$

where $\mu_n = -60.3 \text{ neV/T}$ is the magnetic moment of the neutron, $\epsilon_{nn'} = \hbar \tau_{nn'}^{-1}$ is the mass mixing term yielding a characteristic time for the $n - n'$ oscillation, $\tau_{nn'}$, and $\mathbf{B}^{(\prime)}$ is the (mirror) magnetic field vector. Equation (1) employs the 2×2 Pauli matrices, $\boldsymbol{\sigma} = (\sigma_x, \sigma_y, \sigma_z)$. The probability of $|n\rangle$ oscillating into its mirror counterpart, $|n'\rangle$, can be written as [27,29]:

$$P_{BB'}^{nn'}(t) = \frac{\sin^2[(\omega - \omega')t]}{2\tau_{nn'}^2(\omega - \omega')^2} + \frac{\sin^2[(\omega + \omega')t]}{2\tau_{nn'}^2(\omega + \omega')^2} + \left(\frac{\sin^2[(\omega - \omega')t]}{2\tau_{nn'}^2(\omega - \omega')^2} - \frac{\sin^2[(\omega + \omega')t]}{2\tau_{nn'}^2(\omega + \omega')^2} \right) \cos \beta \quad (2)$$

where, $\omega^{(\prime)} = |\mu_n B^{(\prime)}|/2 = 45.81 (\mu\text{T} \cdot \text{s})^{-1} B^{(\prime)}$ is a convenient notation for the angular frequency in the oscillating terms above, and t is the time which we know the neutrons spent in the pure normal state, $|n\rangle$. We assume a fixed angle, β , between \mathbf{B} and \mathbf{B}' , and

an approximate rotational symmetry around the Earth's axis for the mirror magnetic field, subject to experimental testing.

Neutron to mirror-neutron oscillation would manifest itself as an additional loss channel in ultracold neutron (UCN) storage experiments [30], since if a UCN oscillates into its mirror counterpart, it would escape the storage chamber. Far away from the resonance, when for UCNs $|\omega - \omega'|t \gg 1$, Eq. (2) can be averaged over time and reduced to [27]:

$$P_{BB'}^{nn'} = P_{0B'}^{nn'} \frac{1 + \eta^2 + 2\eta \cos \beta}{(1 - \eta^2)^2}, \quad (3)$$

where $\eta = \omega/\omega'$, and

$$P_{0B'}^{nn'} = 1/(2\tau_{nn'}^2 \omega'^2) \quad (4)$$

is the $n - n'$ oscillation probability in the absence of a magnetic field ($B = 0$) valid for $\omega't \gg 1$. The time t is reset to zero at each wall reflection since a successful reflection confirms the neutron being a SM particle. Using the mean time between two consecutive wall-collisions $\langle t_f \rangle$, the average number of free flight segments during a storage time t_s can be approximated as $m_s = t_s/\langle t_f \rangle$. For $P_{BB'}^{nn'}$, we consider the average over the free flight time t_f . The attenuation in the number of UCNs due to this loss channel is then $\exp(-m_s P_{BB'}^{nn'})$. Close to the resonance, Eq. (3) has to be complemented as explained in detail in Ref. [29] to cancel out the singularity at $\omega = \omega'$.

Berezhiani [27] pointed out that in order to set constraints on $\tau_{nn'}$ as a function of the mirror magnetic field it is convenient to work with the observables 'ratio' (E_B) and 'asymmetry' (A_B), respectively, defined as:

$$E_B^{(t_s)} + 1 = \frac{2n_0^{(t_s)}}{n_B^{(t_s)} + n_{-B}^{(t_s)}} = \frac{2e^{-(m_s P_{0B'}^{nn'})}}{e^{-(m_s P_{BB'}^{nn'})} + e^{-(m_s P_{-BB'}^{nn'})}}, \quad (5)$$

$$A_B^{(t_s)} = \frac{n_B^{(t_s)} - n_{-B}^{(t_s)}}{n_B^{(t_s)} + n_{-B}^{(t_s)}} = \frac{e^{-(m_s P_{BB'}^{nn'})} - e^{-(m_s P_{-BB'}^{nn'})}}{e^{-(m_s P_{BB'}^{nn'})} + e^{-(m_s P_{-BB'}^{nn'})}}, \quad (6)$$

where the $n_{\{0,B,-B\}}^{(t_s)}$ are the number of neutrons counted after storage for time t_s . The indices B and $-B$ in the above equations refer to the direction of the applied magnetic field along the vertical axis at the location of the UCN storage chamber. The attenuation in UCN counts due to losses at wall collisions and β -decay, and the detection efficiency are independent from the applied field B and thus will cancel out from the count ratios.

When we assume the mirror magnetic field to be zero ($B' = 0$), the relationships between the $n - n'$ oscillation time, $\tau_{nn'}^{(B'=0)}$, and the ratio observable in Eq. (5) becomes independent of the applied magnetic field. Considering the limits $\omega(t_f) \ll 1$ (no field applied) and $\omega(t_f) \gg 1$ (field applied) with $P_{BB'}^{nn'} \ll 1$, as in Refs. [30,31], yields:

$$\tau_{nn'}^{2, B'=0} \simeq \underbrace{-t_s \frac{\langle t_f^2 \rangle}{\langle t_f \rangle} \frac{1}{E_B}}_{-1/\Delta_0}. \quad (7)$$

Since probability and $\tau_{nn'}^2$ (see Eq. (4)) are positive quantities, Δ_0 is only physical for negative values (*e.g.* in the limit of $B \approx 0$, $B' \approx 0$, $E_B^{(t_s)} \approx -m_s P_{BB'}^{nn'}$). The rightmost terms in Eqs. (5)–(6) were defined in the context of a disappearance experiment, thus the number of SM neutrons can only decrease.

Including the case when the mirror magnetic field is non-zero, the ratio and asymmetry observables in Eqs. (5) and (6), respectively, are linked to the $n - n'$ oscillation time through Eq. (3) as follows [27]:

$$\tau_{nn'}^2 \stackrel{B' \neq 0}{\simeq} \frac{t_s}{\underbrace{\langle t_f \rangle}_{1/\Delta_B} E_B} \cdot \frac{\eta^2 (3 - \eta^2)}{\underbrace{2\omega'^2 (1 - \eta^2)^2}_{f_{E_B}(\eta)}}, \quad (8)$$

$$\frac{\tau_{nn'}^2}{\cos \beta} \stackrel{B' \neq 0}{\simeq} \frac{t_s}{\underbrace{\langle t_f \rangle}_{-1/D_B} A_B} \cdot \frac{\eta^3}{\underbrace{\omega'^2 (1 - \eta^2)^2}_{f_{A_B}(\eta)}}, \quad (9)$$

where $f_{\{E_B, A_B\}}(\eta)$ are scaling functions. The conditions $P_{BB'}^{nn'} \ll 1$ and $\omega' \langle t_f \rangle \gg 1$ have to be fulfilled. Δ_0 , Δ_B and D_B will be used and discussed in subsection 3.2. The null-hypothesis is that there are no $n - n'$ oscillations, and consequently the measured value of E_B and A_B , in Eqs. (5) and (6), respectively, would be consistent with zero. Deviations from the null-hypothesis are referred to as signals.

The first series of experiments with UCNs used the ratio observable under the assumption of $B' = 0$. They set the constraints of $\tau_{nn'} > 103$ s (95% C.L.) [31] and later $\tau_{nn'} > 414$ s (90% C.L.) [32]. Reference [32] has since updated their constraint to $\tau_{nn'} > 448$ s (90% C.L.) [33]. Reference [34] relaxed the conditions to $B' \neq 0$, while still using the ratio observable, and set a constraint of $\tau_{nn'} > 12$ s for $0.4 \mu\text{T} < B' < 12.5 \mu\text{T}$ (95% C.L.). In Ref. [29], Berezhiani et al. further analyzed the above experiments and indicated statistically significant signal-like anomalies for $n - n'$ oscillation in the asymmetry observable when $B' \neq 0$. The experiment presented here was designed to check the potential signals in Ref. [29], and provide sufficient sensitivity to exclude them if not real. A recent update by Berezhiani et al. [35,36] shows a persistence of the anomalous signals. Reference [35] also sets constraints of $\tau_{nn'} > 17$ s for $8 \mu\text{T} < B' < 17 \mu\text{T}$ (at 95% C.L.) and $\tau_{nn'}/\sqrt{\cos \beta} > 27$ s for $6 \mu\text{T} < B' < 25 \mu\text{T}$ (at 95% C.L.). The three statistically significant signals identified in the asymmetry (unfortunately deviating from those in Ref. [29]) are: a 3σ signal from the data in Ref. [31], a 5.2σ signal from data in Refs. [32,33], and a 2.5σ signal from the B2 data series in Ref. [35]. Testing the above anomalies in the asymmetry observable of $n - n'$ oscillation was the primary motivation for this measurement at the Paul Scherrer Institute (PSI) by the neutron electric dipole moment (nEDM) collaboration.

2. Experiment setup and data collection

For this experiment, the PSI collaboration made use of its repurposed nEDM apparatus described in Refs. [37–39] hosted at the PSI ultracold neutron source [40]. A UCN guide switch directed the neutrons coming from the beamport to a 21 liter cylindrical storage chamber. The storage chamber was made of a polystyrene insulator ring coated with deuterated polystyrene, sandwiched between two aluminum plates (the electrodes for the nEDM search) coated with diamond-like carbon [41–43]. The storage chamber was enclosed in a vacuum tank on which a coil system was found that generated the vertical magnetic field, B (called B_0 in the nEDM experiment). It was surrounded by a four-layer μ -metal shield which was housed inside an active magnetic field compensation system [44]. In this $n - n'$ oscillation search no electric field was used. The storage chamber was connected via the switch to a neutron detection system [45,46].

In this experiment we used unpolarized neutrons in order to maximize statistics. Data was collected in a series of runs and each run consisted of many cycles. The neutron storage time, t_s^* , during

each cycle was fixed per run, but the magnetic field was changed from cycle to cycle in a specific pattern. In the beginning of a cycle, the UCNs from the source were allowed to fill the storage chamber after passing through the appropriately configured switch. The UCN shutter at the bottom of the storage chamber was then shut. After a period of storage, the shutter of the storage chamber was opened and the neutrons were counted. We will refer to this part of the cycle as the emptying phase.

In order to compensate for fluctuations of the UCN source output [47] the detector counts at the end of a cycle had to be normalized using a monitor. The neutrons still emerging from the source during the storage phase were directly guided to the UCN detectors, serving as monitor counts. The monitor counts were of the order of a million; the emptying counts, after the storage, was of the order of a few tens of thousands. Thus, the uncertainty on the ratio of emptying and monitor counts is mostly dependent on the uncertainty coming from the emptying counts. Special care was taken to demonstrate that this ratio was stable enough for the $n - n'$ oscillation search as explained in Ref. [48]. Henceforth, we will denote the emptying counts corrected using the monitor counts as $n_{\{0, B, -B\}}^{(t_s)}$.

The data was taken with storage times, t_s^* , set to 180 s and 380 s. The selected longer storage time is the result of an optimization for the best sensitivity to $n - n'$ oscillation [48], while the shorter one allowed for a direct comparison to previous measurements. In order to account for the total time the neutrons spent in the magnetic field region, we also need to consider the average time of filling and emptying the chamber. During the filling of the chamber, the UCN density builds up until it reaches equilibrium. This is characterized by an exponential time constant. The chamber is filled and emptied through the same opening and same vertical guide. Consequently, for the energy spectrum of the UCNs detected at the end of storage, the filling time constant is approximately equal to the emptying time constant. We added twice the emptying time constant of the UCNs to the storage time set in the control system: $t_s = t_s^* + 2\tau_{\text{emp}}(t_s^*)$, where τ_{emp} is the filling (or emptying) time constant.

The magnetic field applied was calibrated using the ^{199}Hg comagnetometer [49] of the nEDM apparatus and a nanoampere meter to measure the current supplied to the B coil. Along with the $B = 0$ reference case, magnetic fields of $(10.20 \pm 0.02) \mu\text{T}$ and $(20.39 \pm 0.04) \mu\text{T}$ were used in these measurements, optimal to address the aforementioned anomalous signals of Ref. [29]. The errors given here are larger than the inhomogeneity of the field. The requirement for precision on the magnetic field is elaborated on in Ref. [48]. Patterns of 16 settings of the magnetic field, $[0, B, 0, -B, 0, -B, 0, B, 0, -B, 0, B, 0, B, 0, -B]$, were applied by changing the magnetic field after every *four* cycles. Such patterns can compensate for drifts in the magnetic field [50]. One full pattern consists of 64 cycles. We collected over 8000 cycles of data.

3. Data analysis and results

Apart from the data collected in the experiment, the analysis needs the distribution of the flight time between consecutive collisions, t_f , as an input. This input was provided by MC simulations fitted to measured data. Further, the data analysis focused on the two observables, the ratio and the asymmetry. The null result was interpreted by setting constraints on the $n - n'$ oscillation parameters.

3.1. Calculation of the free flight time distributions

We remind that Eqs. (7), (8), and (9) use the mean time, $\langle t_f \rangle^{(t_s)}$ between consecutive wall collisions. Below we summarize

the steps of our method. For calculation details we refer the reader to section 3.6 in Ref. [51].

To obtain $\langle t_f \rangle^{(t_s)}$ for each time of storage, t_s , the free flight time of UCNs had to be averaged first over the path through the chamber for each energy bin separately, and then over a given energy spectrum. The path history of UCNs in a storage chamber yielded a broad t_f distribution. Neutrons bouncing at the corners of the storage chamber, or slower neutrons bouncing due to gravity along the bottom surface of the chamber, will contribute to small values of t_f . Neutrons traversing the longest paths in the storage chamber will contribute to larger values of t_f (depending also on the magnitude of the velocity). While the geometry of the storage chamber determines the path length distribution as a function of energy very well, the uncertainty on $\langle t_f \rangle^{(t_s)}$ is dominated by the uncertainty of the less well-known energy spectrum.

The energy spectrum and the associated uncertainties were extracted using an analytical model for the storage curve as detailed in section 3.1.3 of Ref. [52] along with simulation tests. This model involves the energy dependent bounce rate $\nu(E)$ and the loss probability per bounce $\mu(E)$ [53] (their product giving the loss rate) via the decay function:

$$n(E, t_s) = n(E, 0) \exp(-t_s \nu(E) \mu(E)), \quad (10)$$

where $E = E_b - m_n g h$ denotes the kinetic energy at the average height of collision, h , and at the bottom of the chamber $E(h = 0) = E_b$. The energy spectrum at the bottom of the chamber and at the beginning of the storage phase ($t_s = 0$), was parameterized with a peak function of the form:

$$P(E_b) = P_0 \frac{E_b^\rho}{1 + \exp(\frac{E_b - E_p}{w})}, \quad (11)$$

where P_0 is a scaling constant, ρ is the exponent of the leading edge of the distribution, E_p is an upper cut-off value for the energy, and w is a smearing parameter for the cut-off. A similar sigmoidal definition was used in Ref. [54].

Equation (10) was integrated with the spectral weighting, Eq. (11), using the above definition $E_b = E + m_n g h$:

$$n(t_s) = \int n(E_b, t_s) P(E_b) dE_b. \quad (12)$$

We used this function to fit the storage curve, $n_{meas}(t_s)$, measured for this purpose at 15 different storage times [51]. The analytical model distinguished between the average loss rates, $\nu(E)\mu(E)$ at the top, bottom, and side surfaces, adding these together. Concerning the side wall, Eq. (5) in Ref. [55] for the average height of UCNs in a cylindrical chamber was employed. The fit to the measured storage curve was performed by randomly sampling the parameters $\{P_0, \rho, E_p, w\}$, and the wall loss parameter $\eta' = W/V$, which is the ratio of the imaginary and real parts of the optical potential of the coating material [53]. The Fisher statistical test [56] was used to obtain the confidence regions in the parameter space.

For every set of $\{P_0, \rho, E_p, w\}$, a center of mass offset of UCNs *w.r.t.* the center of the chamber, $\langle z \rangle$, was calculated [51]. A further constraint on the $\{P_0, \rho, E_p, w\}$ parameters was imposed by using the measurement of $\langle z \rangle$ in the nEDM experiment [39]. The nEDM search requires polarized neutrons, whereas this $n - n'$ oscillation search used unpolarized neutrons. The center of mass offset was simulated with both polarized and unpolarized neutrons from the beamline. The difference was within the error of the calculations.

The energy spectra associated with each set of parameters $\{P_0, \rho, E_p, w\}$ were next translated to distributions of $t_f^{(t_s)}$ by the means of ray-tracing using the MCUCN code [52]. The profiles turned out to be normal distributions. We noticed that the central

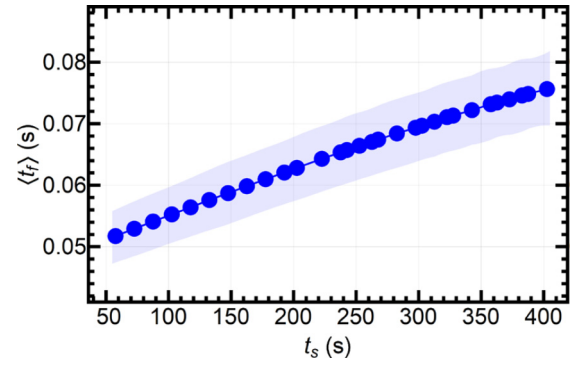


Fig. 1. Simulated dependence of $\langle t_f \rangle^{(t_s)}$ *w.r.t.* the storage time. The data points represent the central value of the $\langle t_f \rangle^{(t_s)}$ distribution and the shaded region shows the 95% C.L. contours of the width of the $\langle t_f \rangle^{(t_s)}$ distribution.

values of the $\langle t_f \rangle^{(t_s)}$ distributions and the associated uncertainties vary appreciably with storage time, as visible in Fig. 1. This was taken into account in the analysis. The largest contributor to the width of the $\langle t_f \rangle^{(t_s)}$ distribution is the uncertainty on the energy spectrum parameters. The uncertainty contribution from path averaging is much smaller, since, during the given storage times, the UCNs can bounce off the walls diffusely, a large number of times, thus achieving mechanical equilibrium. Its uncertainty is only limited by the statistical accuracy of the MC simulations.

While the $n - n'$ oscillation time in non-zero mirror magnetic fields, from Eqs. (8)-(9) only requires $\langle t_f \rangle^{(t_s)}$, in zero mirror magnetic field, Eq. (7) requires $\langle t_f^2 \rangle / \langle t_f \rangle^{(t_s)}$, and the associated uncertainty. These were calculated in a similar way by MCUCN simulations.

As a byproduct of the energy spectrum calculations, we also obtained a constraint on the wall loss parameter of the precession chamber in the nEDM experiment. This value is effectively averaged (in proportion to the area) over the insulator ring and the electrode surfaces: $\eta' = (2.5 \pm 0.3) \times 10^{-4}$.

3.2. Constraints on the ratio and asymmetry observables

Each run is associated with a storage time, t_s , and a maximum magnetic field, B , that was applied in the aforementioned pattern. Within each run the emptying counts corrected by the monitor counts cycle by cycle, $n_{\{B,0,-B\}}^{(t_s)}$, were grouped according to the three field configurations of $\{B, 0, -B\}$. Within each group the mean values and the standard errors on the mean were calculated. From these, the values $\langle E_B^{(t_s)} \rangle$ and $\langle A_B^{(t_s)} \rangle$ were obtained using Eqs. (5) and (6). The errors on the mean values, $\langle n_{\{B,0,-B\}}^{(t_s)} \rangle$, were propagated to obtain the errors on $\langle E_B^{(t_s)} \rangle$ and $\langle A_B^{(t_s)} \rangle$.

The terms, Δ_0 , Δ_B , and D_B , in Eqs. (7), (8), and (9), respectively, allowed us to combine the various runs as in Refs. [27,29,35], each with corresponding values of t_s and $\langle t_f \rangle^{(t_s)}$, which are shown for each run in Fig. 2 (Top), (Center), and (Bottom), respectively. The weighted averages and the corresponding errors for the various settings are:

$$\langle \Delta_0 \rangle = (3.0 \pm 5.0) \times 10^{-6} \text{ s}^{-2}, \quad (13)$$

$$\left\langle \underbrace{\langle E_{B \sim 10 \mu\text{T}} \rangle \frac{\langle t_f \rangle^{(t_s)}}{t_s}}_{\Delta_{B \sim 10 \mu\text{T}}} \right\rangle = (2.5 \pm 5.9) \times 10^{-8}, \quad (14)$$

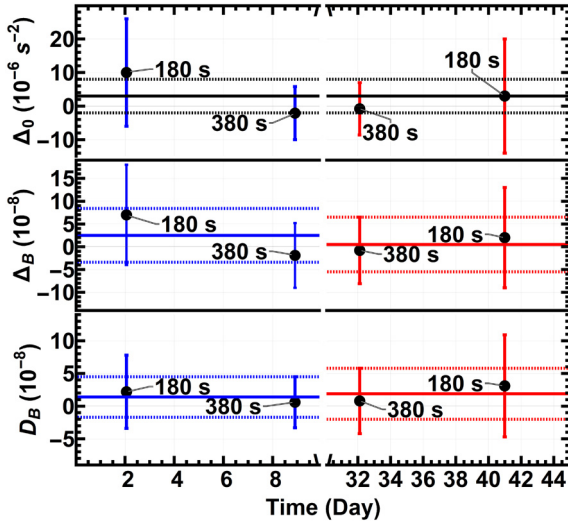


Fig. 2. Values of Δ_0 (Top), Δ_B (Center), and D_B (Bottom), from Eqs. (7), (8), and (9), respectively, plotted for each run as a function of the mean time at which the data for the run was collected. The data points associated with blue error bars show those runs involving a magnetic field of $B \sim 10 \mu\text{T}$, while the data points associated with red error bars show the runs involving a magnetic field of $B \sim 20 \mu\text{T}$. The solid lines of the same color represent the weighted mean of the data points, and the dashed lines represent the standard errors, as listed in Eqs. (13)–(17).

Table 1

Uncertainty contributions to $\langle\Delta_0\rangle$, $\langle\Delta_B\rangle$, and $\langle D_B\rangle$ separately from emptying counts (N_{emp}), monitor counts (N_{mon}), mean free flight time ($\langle t_f \rangle$, including also $\langle t_f^2 \rangle$), and effective storage time (t_s).

Errors for	From	N_{emp}	N_{mon}	$\langle t_f \rangle$	t_s
$\langle\Delta_0\rangle$ (10^{-6}s^{-2})		4.74	1.41	0.06	0.002
$\langle\Delta_{B\sim 10 \mu\text{T}}\rangle$ (10^{-8})		5.51	1.54	0.07	0.002
$\langle\Delta_{B\sim 20 \mu\text{T}}\rangle$ (10^{-8})		5.80	1.80	0.03	0.002
$\langle D_{B\sim 10 \mu\text{T}}\rangle$ (10^{-8})		2.92	0.85	0.02	0.002
$\langle D_{B\sim 20 \mu\text{T}}\rangle$ (10^{-8})		3.76	1.13	0.03	0.002

$$\left\langle \frac{E_{B\sim 20 \mu\text{T}}(t_f)^{t_s}}{t_s} \right\rangle_{\Delta_{B\sim 20 \mu\text{T}}} = (0.5 \pm 6.0) \times 10^{-8}, \quad (15)$$

$$\left\langle \frac{A_{B\sim 10 \mu\text{T}}(t_f)^{t_s}}{t_s} \right\rangle_{D_{B\sim 10 \mu\text{T}}} = (1.4 \pm 3.1) \times 10^{-8}, \quad (16)$$

$$\left\langle \frac{A_{B\sim 20 \mu\text{T}}(t_f)^{t_s}}{t_s} \right\rangle_{D_{B\sim 20 \mu\text{T}}} = (1.9 \pm 3.9) \times 10^{-8}. \quad (17)$$

The uncertainty associated with the values of $\langle\Delta_0\rangle$, $\langle\Delta_B\rangle$, and $\langle D_B\rangle$ in Fig. 2, comes from propagating the uncertainty on the values of $\langle E_B^{(t_s)} \rangle$, $\langle A_B^{(t_s)} \rangle$, t_s and $\langle t_f \rangle^{(t_s)}$, according to Eqs. (7), (8), and (9). We emphasize here that in the calculation of the distribution parameters of Δ_0 , Δ_B , and D_B we used both positive and negative values, contrary to subsection 3.3 where these quantities are sampled either in negative or positive intervals, wherever the oscillation probability is positive.

In order to give an estimate on the uncertainty contributions to $\langle\Delta_0\rangle$, $\langle\Delta_B\rangle$, and $\langle D_B\rangle$ separately from the emptying counts, monitor counts, $\langle t_f \rangle^{(t_s)}$, and t_s (via τ_{emp}), we calculated the error propagation from the definitions in Eqs. (7), (8) and (9). The different uncertainty contributions are compared in Table 1.

We did not observe any statistically significant deviations of $\langle E_B^{(t_s)} \rangle$ or $\langle A_B^{(t_s)} \rangle$ from zero, and consequently the weighted means in Eqs. (13)–(17) are consistent with zero. Therefore, we only present constraints on the $n - n'$ oscillation time parameter $\tau_{nn'}$.

3.3. Constraints on the $n - n'$ oscillation time and mirror magnetic field

By applying the constraints in Eqs. (13)–(17), we can construct exclusion diagrams in the parameter space of $n - n'$ oscillations. From Eq. (7) we see that the $n - n'$ oscillation time under the assumption of $B' = 0$ is given by the function $\tau_{nn'} = 1/\sqrt{-\langle\Delta_0\rangle}$. Therefore, we numerically sampled Δ_0 in the negative range of the normal distribution, to avoid imaginary numbers and negative probability, according to the parameters in Eq. (13), and obtained the following constraint:

$$\tau_{nn'}^{B'=0} > 352 \text{ s (95\% C.L.)}. \quad (18)$$

In case of the ratio observable, Eq. (8), since the sign of the function $f_{E_B}(\eta)$ changes at $B'\sqrt{3} = B$, we subsequently extracted the lower limit of $\tau_{nn'}^{B'\neq 0, E_B} / \sqrt{|f_{E_B}(\eta)|} = 1/\sqrt{\langle\Delta_B\rangle}$ using both the distributions of $\langle\Delta_B\rangle$ and $-\langle\Delta_B\rangle$, in their appropriate ranges, to avoid imaginary numbers for the oscillation time, $\tau_{nn'}^{B'\neq 0, E_B}$. Similar to the case where we assumed $B' = 0$, the weighted averages in Eqs. (14)–(15) were numerically sampled to obtain the following constraints, at 95% C.L.:

$$\frac{\tau_{nn'}^{B'\neq 0, E_B}}{\sqrt{|f_{E_B}(\eta)|}} > 3145 \text{ (} B \sim 10 \mu\text{T, } B'\sqrt{3} < B \text{)}, \quad (19)$$

$$> 2948 \text{ (} B \sim 20 \mu\text{T, } B'\sqrt{3} < B \text{)}, \quad (20)$$

$$> 2954 \text{ (} B \sim 10 \mu\text{T, } B'\sqrt{3} > B \text{)}, \quad (21)$$

$$> 2914 \text{ (} B \sim 20 \mu\text{T, } B'\sqrt{3} > B \text{)}. \quad (22)$$

The values of lower limits shown in Eqs. (19)–(22) were scaled by $f_{E_B}(\eta)$ in Eq. (8), to generate a constraint plot in the parameter space defined by $\tau_{nn'}$ and B' . In this way two separate constraint curves were generated corresponding to $B \sim \{10, 20\} \mu\text{T}$. A lower envelope of the constraints obtained separately from the two curves is shown as our final constraint from the ratio analysis in Fig. 3 (Top).

In the case of the asymmetry observable, Eq. (9), the function $f_{A_B}(\eta)$ does not change its sign. The lower limit of $\tau_{nn'}^{B'\neq 0, A_B} / (\sqrt{|f_{A_B}(\eta)|} \cdot \sqrt{\cos\beta}) = 1/\sqrt{-\langle D_B\rangle}$ was obtained in a similar fashion to the above cases, from Eqs. (16)–(17), also at 95% C.L.:

$$\frac{\tau_{nn'}^{B'\neq 0, A_B}}{\sqrt{|f_{A_B}(\eta)|} \cdot \sqrt{\cos\beta}} > 4363 \text{ (} B \sim 10 \mu\text{T} \text{)}, \quad (23)$$

$$> 3912 \text{ (} B \sim 20 \mu\text{T} \text{)}. \quad (24)$$

Our final constraint in the parameter space defined by $(\tau_{nn'}/\sqrt{\cos\beta})$ and B' from the asymmetry analysis is presented in Fig. 3 (Bottom) using the lower limits shown in Eqs. (23)–(24) and scaling by $f_{A_B}(\eta)$.

In Fig. 3, we also plotted the results from previous searches, including the signal-like anomalies listed in the caption. In case of a signal, in addition to the lower limit, a finite upper limit can be defined, making the confidence region a band along the B' axis.

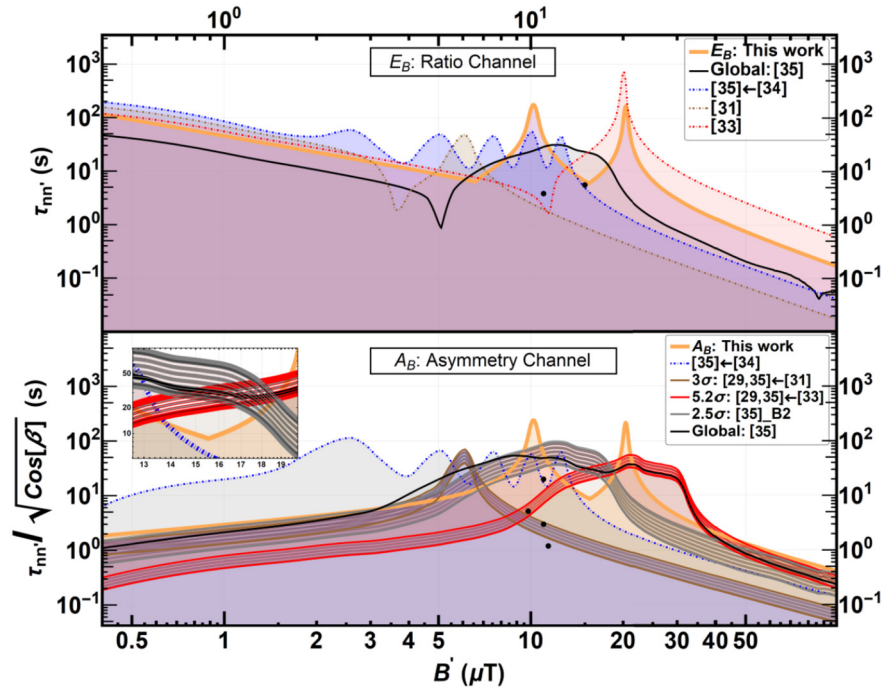


Fig. 3. Lower limits on the $n - n'$ oscillation time, $\tau_{nn'}$ at 95% C.L., using the ratio and asymmetry observables, while assuming $B' \neq 0$. Top (bottom) panel shows the ratio (asymmetry) analysis, where the solid orange curve represents the lower limit on $\tau_{nn'}^{B' \neq 0}$ ($\tau_{nn'}^{B' \neq 0} / \sqrt{\cos \beta}$). (Top): The dot-dashed blue curve represents the lower limit imposed using data in Ref. [34] by Ref. [35]. The black curve represents the global constraint calculated by Ref. [35] which imposes a weighted lower limit using data from Refs. [31,33,34] and the B2 series in Ref. [35]. The dot-dashed brown curve, represents the constraint from Ref. [31]. The dot-dashed red curve represents the constraint from Ref. [33]. The black dots indicate the solution consistent with the statistically significant signals as reported in Ref. [27]. (Bottom): The black curve is the global constraint calculated in Ref. [35]. The dot-dashed blue curve represents the lower limit imposed using data in Ref. [34] by Ref. [35]. The three striped regions are the signals (95% C.L.): (i) the red striped region, is the signal region calculated in Refs. [29,35] from the 5.2σ anomaly in Refs. [33]; (ii) the brown striped region is the signal calculated in Refs. [29,35] from the 3σ anomaly in Ref. [31]; and (iii) the gray striped region is the signal from the 2.5σ anomaly observed in the B2 series of Ref. [35]. The black dots indicate the solution consistent with the statistically significant signals as reported in Ref. [29]. The inset shows an enlarged portion of the bottom plot between the ranges of $12.8 \mu\text{T} < B' < 20 \mu\text{T}$.

4. Discussion

The constraints from this work shown in Fig. 3 (Top) and (Bottom) can be summarized as the following limits, respectively, at 95% C.L.:

$$\tau_{nn'}^{B' \neq 0, E_B} > 6 \text{ s}, \quad 0.36 \mu\text{T} < B' < 25.66 \mu\text{T}, \quad (25)$$

$$\frac{\tau_{nn'}^{B' \neq 0, A_B}}{\sqrt{\cos \beta}} > 9 \text{ s}, \quad 5.04 \mu\text{T} < B' < 25.39 \mu\text{T}. \quad (26)$$

The condition of $\omega' \langle t_f \rangle^{(t_s)} \gg 1$, under which Eqs. (8) and (9) are valid approximations, along with the value of $\langle t_f(t_s^* = 180 \text{ s}) \rangle = (0.0628 \pm 0.0027) \text{ s}$ from Fig. 1, gives the lower bound of validity $B' > 0.36 \mu\text{T}$ (at 95% C.L.), on the horizontal axis of the plots in Fig. 3. The upper bound on the horizontal axis for the region of interest in Fig. 3, $B' < 100 \mu\text{T}$, comes from constraints on UCN losses in the Earth's magnetic field [27,35].

According to Eqs. (8) and (9), the sensitivity to $n - n'$ oscillation has a singularity around $|B' - B| \sim 0$, and was thus truncated in height according to Eq. (6) in Ref. [35]. This behavior is responsible for the peaking of the solid curve in both plots in Fig. 3 at $B' = 10.20 \mu\text{T}$ and $B' = 20.39 \mu\text{T}$.

As in Ref. [27], in this analysis, we considered that the mirror magnetic field B' , and thus also β are constant at the site of the experiment. While all the previous constraints on the $n - n'$ oscillation time come from experiments performed at the Institute Laue-Langevin (ILL) [27,29,31–35] in Grenoble, France, our experiment was conducted at PSI in Villigen, Switzerland. A difference in B' w.r.t. the vertical between the geographic locations of PSI and ILL introduces an additional uncertainty when comparing exclusion

plots from measurements at PSI and ILL, respectively. The comparison to results from ILL is valid under the natural assumption that a mirror magnetic field created within the Earth [27] displays approximate rotational symmetry, similar to the Earth's magnetic field. That is, its components change only on the level of 5% between ILL and PSI [57], which would introduce a negligible offset on the horizontal axis of Fig. 3. In case the mirror magnetic field does not follow the Earth's rotation for various possible reasons, i.e. due to a galactic mirror field, the observables would undergo a sidereal modulation, an effect which was investigated in Ref. [51].

In the ratio analysis, our constraint shown as a solid orange curve in Fig. 3 (Top) is the best known constraint in the region $B' = 10 \mu\text{T}$. In the asymmetry analysis, our constraint shown as a solid orange curve in Fig. 3 (Bottom) excludes all signal spots (see black dots) reported in Ref. [29], for which our experiment was initially optimized.

It is important, however, to note that the three signal bands in the asymmetry analysis from Refs. [29,33,35] do not all overlap simultaneously, and thus exclude each other. Our analysis excludes three of the five regions where at least two of the signal bands overlap. Our result is also the best constraint at high mirror magnetic fields, $B' > 37 \mu\text{T}$ in the asymmetry channel, along with being the best constraint around the mirror magnetic fields of $B' \sim 10 \mu\text{T}$ and $B' \sim 20 \mu\text{T}$. However, in the region of $4 \mu\text{T} < B' < 37 \mu\text{T}$, our constraints do not exclude the signal bands of Ref. [35] which could be a focus of future efforts. The data for this experiment was collected in the summer of 2017. Even though our experiment was aimed at testing the signal-like anomalies indicated in Ref. [29] (2012), it excludes significant portions of the 2018 update of the signal-like anomalous regions in Ref. [35].

Declaration of competing interest

The authors declare that they have no known competing financial interests or personal relationships that could have appeared to influence the work reported in this paper.

Acknowledgements

We especially thank Z. Berezhiani for many valuable suggestions. The authors greatly acknowledge the exceptional support provided by Michael Meier, Fritz Burri and the BSQ group at PSI. The LPC and LPSC groups were supported by ANR (FR) grant # ANR-14-CE33-0007-02. The University of Sussex (UK) group was supported by STFC grants #ST/N504452/1, ST/M003426/1, and ST/N000307/1, and by their School of Mathematical and Physical Sciences. The PSI group was supported by the Swiss SNSF grants # 200020-137664, # 200021-117696, # 200020-144473, # 200021-126562, # 200020-163413 and # 200021-157079. ETHZ was supported by SNSF grant # 200020-172639. The University of Fribourg group was supported by SNSF grant # 200020-140421. The University of Bern group was supported by the grants SNSF # 181996 and ERC (EU) # 715031-BEAM-EDM. The Jagiellonian University group was supported by the Polish National Science Center grant # 2015/18/M/ST2/00056, # 2016/23/D/ST2/00715 and # 2018/30/M/ST2/00319. For the KU Leuven group, this work is also partly supported by Project GOA/2010/10 and Fund for Scientific Research in Flanders (FWO). One of the authors, P.M., would like to acknowledge support from the SERI-FCS (CH) award # 2015.0594 and Sigma Xi (USA) grants # G2017100190747806 and # G2019100190747806. We would like to acknowledge the grid computing resource provided by PL-GRID [58].

References

- [1] T.D. Lee, C.-N. Yang, *Phys. Rev.* 104 (1956) 254–258, <https://doi.org/10.1103/PhysRev.104.254>.
- [2] I.Yu. Kobzarev, L.B. Okun, I.Ya. Pomeranchuk, *Sov. J. Nucl. Phys.* 3 (1966) 837, <https://inspirehep.net/record/1351288>.
- [3] R. Foot, H. Lew, R.R. Volkas, *Phys. Lett. B* 272 (1991) 67–70, [https://doi.org/10.1016/0370-2693\(91\)91013-L](https://doi.org/10.1016/0370-2693(91)91013-L).
- [4] R. Foot, H. Lew, R.R. Volkas, *Mod. Phys. Lett. A* 07 (1992) 2567–2574, <https://doi.org/10.1142/S0217732392004031>.
- [5] M.Y. Khlopov, et al., *Sov. Astron.* 35 (1991) 21.
- [6] H.M. Hodges, *Phys. Rev. D* 47 (1993) 456–459, <https://doi.org/10.1103/PhysRevD.47.456>.
- [7] Z.G. Berezhiani, A.D. Dolgov, R.N. Mohapatra, *Phys. Lett. B* 375 (1996) 26, [https://doi.org/10.1016/0370-2693\(96\)00219-5](https://doi.org/10.1016/0370-2693(96)00219-5).
- [8] Z. Berezhiani, D. Comelli, F.L. Villante, *Phys. Lett. B* 503 (2001) 362–375, [https://doi.org/10.1016/S0370-2693\(01\)00217-9](https://doi.org/10.1016/S0370-2693(01)00217-9), arXiv:hep-ph/0008105.
- [9] Z. Berezhiani, et al., *Int. J. Mod. Phys. D* 14 (2005) 107, <https://doi.org/10.1142/S0218271805005165>.
- [10] Z. Berezhiani, et al., *Astropart. Phys.* 24 (2006) 495, <https://doi.org/10.1016/j.astropartphys.2005.10.002>.
- [11] R. Foot, *Phys. Rev. D* 86 (2012) 023524, <https://doi.org/10.1103/PhysRevD.86.023524>, arXiv:1203.2387.
- [12] R. Foot, *Int. J. Mod. Phys. A* 29 (2014) 1430013, <https://doi.org/10.1142/S0217751X14300130>, arXiv:1401.3965.
- [13] A. Addazi, et al., *Eur. Phys. J. C* 75 (2015) 400, <https://doi.org/10.1140/epjc/s10052-015-3634-z>.
- [14] R. Cerulli, et al., *Eur. Phys. J. C* 77 (2017) 83, <https://doi.org/10.1140/epjc/s10052-017-4658-3>.
- [15] E.K. Akhmedov, Z.G. Berezhiani, G. Senjanovic, *Phys. Rev. Lett.* 69 (1992) 3013–3016, <https://doi.org/10.1103/PhysRevLett.69.3013>, arXiv:hep-ph/9205230.
- [16] Z. Berezhiani, R.N. Mohapatra, *Phys. Rev. D* 52 (1995) 6607, <https://doi.org/10.1103/PhysRevD.52.6607>, arXiv:hep-ph/9505385.
- [17] Z.K. Silagadze, *Phys. At. Nucl.* 60 (1997) 272, arXiv:hep-ph/9503481.
- [18] V. Berezhinsky, M. Narayan, F. Vissani, *Nucl. Phys. B* 658 (2003) 254–280, [https://doi.org/10.1016/S0550-3213\(03\)00191-3](https://doi.org/10.1016/S0550-3213(03)00191-3), arXiv:hep-ph/0210204.
- [19] L. Bento, Z. Berezhiani, *Phys. Rev. Lett.* 87 (2001) 231304, <https://doi.org/10.1103/PhysRevLett.87.231304>, arXiv:hep-ph/0107281.
- [20] L. Bento, Z. Berezhiani, *Fortschr. Phys.* 50 (2002) 489, <https://doi.org/10.1002/9783527610853.ch8>.
- [21] Z. Berezhiani, L. Bento, *Phys. Lett. B* 635 (2006) 253–259, <https://doi.org/10.1016/j.physletb.2006.03.008>, arXiv:hep-ph/0602227.
- [22] Z. Berezhiani, A. Gazizov, *Eur. Phys. J. C* 72 (2012) 2111, <https://doi.org/10.1140/epjc/s10052-012-2111-1>, arXiv:1109.3725.
- [23] Z. Berezhiani, *Int. J. Mod. Phys. A* 19 (2004) 3775–3806, <https://doi.org/10.1142/S0217751X04020075>, arXiv:hep-ph/0312335.
- [24] Z. Berezhiani, in: M. Shifman, et al. (Eds.), *From Fields to Strings: Circumnavigating Theoretical Physics*, vol. 3, World Scientific, 2005, pp. 2147–2195, arXiv:hep-ph/0508233.
- [25] Z. Berezhiani, *Eur. Phys. J. Spec. Top.* 163 (2008) 271–289, <https://doi.org/10.1140/epjst/e2008-00824-6>.
- [26] Z. Berezhiani, *Int. J. Mod. Phys. A* 33 (2018) 1844034, <https://doi.org/10.1142/S0217751X18440347>.
- [27] Z. Berezhiani, *Eur. Phys. J. C* 64 (2009) 421, <https://doi.org/10.1140/epjc/s10052-009-1165-1>, arXiv:0804.2088.
- [28] Z. Berezhiani, L. Bento, *Phys. Rev. Lett.* 96 (2006) 081801, <https://doi.org/10.1103/PhysRevLett.96.081801>, arXiv:hep-ph/0507031.
- [29] Z. Berezhiani, F. Nesti, *Eur. Phys. J. C* 72 (2012) 1974, <https://doi.org/10.1140/epjc/s10052-012-1974-5>, arXiv:1203.1035.
- [30] Y.N. Pokotilovskii, *Phys. Lett. B* 639 (2006) 214, <https://doi.org/10.1016/j.physletb.2006.06.005>.
- [31] G. Ban, et al., *Phys. Rev. Lett.* 99 (2007) 161603, <https://doi.org/10.1103/PhysRevLett.99.161603>, arXiv:0705.2336.
- [32] A.P. Serebrov, et al., *Phys. Lett. B* 663 (2008) 181–185, <https://doi.org/10.1016/j.physletb.2008.04.014>, arXiv:0706.3600.
- [33] A.P. Serebrov, et al., *Nucl. Instrum. Methods Phys. Res. A* 611 (2008) 137–140, <https://doi.org/10.1016/j.nima.2009.07.041>, arXiv:0809.4902.
- [34] I. Altarev, et al., *Phys. Rev. D* 80 (2009) 032003, <https://doi.org/10.1103/PhysRevD.80.032003>, arXiv:0905.4208.
- [35] Z. Berezhiani, et al., *Eur. Phys. J. C* 78 (2018) 717, <https://doi.org/10.1140/epjc/s10052-018-6189-y>, arXiv:1712.05761.
- [36] R. Biondi, *Int. J. Mod. Phys. A* 33 (2018) 1850143, <https://doi.org/10.1142/S0217751X18501439>.
- [37] C.A. Baker, et al., *Nucl. Instrum. Methods Phys. Res. A* 736 (2014) 184–203, <https://doi.org/10.1016/j.nima.2013.10.005>.
- [38] C. Abel, et al., *EPJ Web Conf.* 219 (2019) 02001, <https://doi.org/10.1051/epjconf/201921902001>, arXiv:1811.04012.
- [39] C. Abel, et al., *Phys. Rev. Lett.* 124 (2020) 081803, <https://doi.org/10.1103/PhysRevLett.124.081803>, arXiv:2001.11966.
- [40] G. Bison, et al., *Eur. Phys. J. A* 56 (2020) 33, <https://doi.org/10.1140/epja/s10050-020-00027-w>.
- [41] F. Atchison, et al., *Nucl. Instrum. Methods Phys. Res. B* 260 (2007) 647–656, <https://doi.org/10.1016/j.nimb.2007.04.253>.
- [42] F. Atchison, et al., *Phys. Lett. B* 625 (2005) 19–25, <https://doi.org/10.1016/j.physletb.2005.08.066>.
- [43] F. Atchison, et al., *Phys. Rev. C* 74 (2006) 055501, <https://doi.org/10.1103/PhysRevC.74.055501>.
- [44] S. Afach, et al., *J. Appl. Phys.* 116 (2014) 084510, <https://doi.org/10.1063/1.4894158>, arXiv:1408.6752.
- [45] S. Afach, et al., *Eur. Phys. J. A* 51 (2015) 143, <https://doi.org/10.1140/epja/i2015-15143-7>, arXiv:1502.06876.
- [46] G. Ban, et al., *Eur. Phys. J. A* 52 (2016) 326, <https://doi.org/10.1140/epja/i2016-16326-4>, arXiv:1606.07432.
- [47] A. Anghel, et al., *Eur. Phys. J. A* 54 (2018) 148, <https://doi.org/10.1140/epja/i2018-12594-2>, arXiv:1804.08616.
- [48] C. Abel, et al., *EPJ Web Conf.* 219 (2019) 07001, <https://doi.org/10.1051/epjconf/201921907001>, arXiv:1811.01906.
- [49] P.G. Harris, et al., *Phys. Rev. Lett.* 82 (1999) 904, <https://doi.org/10.1103/PhysRevLett.82.904>.
- [50] E. Swanson, H. Schlamminger, *Meas. Sci. Technol.* 21 (2010) 115104, <https://doi.org/10.1088/0957-0233/21/11/115104>.
- [51] P. Mohanmurthy, A search for neutron to mirror-neutron oscillations, PhD Thesis (ETH Zurich 2019) <https://doi.org/10.3929/ethz-b-000417951>.
- [52] G. Zsigmond, *Nucl. Instrum. Methods Phys. Res. A* 881 (2018) 16–26, <https://doi.org/10.1016/j.nima.2017.10.065>, arXiv:1709.05974.
- [53] R. Golub, D. Richardson, S.K. Lamoreaux, *Ultra-Cold Neutrons*, CRC Press, 1991.
- [54] S. Afach, et al., *Phys. Rev. Lett.* 115 (2015) 162502, <https://doi.org/10.1103/PhysRevLett.115.162502>.
- [55] P.G. Harris, J.M. Pendlebury, N.E. Devenish, *Phys. Rev. D* 89 (2014) 016011, <https://doi.org/10.1103/PhysRevD.89.016011>.
- [56] Particle Data Group, et al., Review of particle physics, *Phys. Rev. D* 98 (3) (2018) 030001, <https://doi.org/10.1103/PhysRevD.98.030001>.
- [57] NOAA national centers for environmental information, <https://www.ngdc.noaa.gov/geomag/calculators/magcalc.shtml>.
- [58] PL-Grid, www.plgrid.pl/en.



Data blinding for the nEDM experiment at PSI

N. J. Ayres^{1,2}, G. Ban³, G. Bison⁴, K. Bodek⁵, V. Bondar^{1,4,6}, E. Chanel⁷, P.-J. Chiu^{1,4}, C. B. Crawford⁸, M. Daum⁴, S. Emmenegger¹, L. Ferraris-Bouchez⁹, P. Flaux³, Z. Grujić^{10,15}, P. G. Harris², N. Hild^{1,4}, J. Hommet³, M. Kasprzak^{4,6,10}, Y. Kermaidic⁹, K. Kirch^{1,4}, S. Komposch^{1,4}, A. Kozela¹¹, J. Krempel^{1,a}, B. Lauss⁴, T. Lefort³, Y. Lemièrre³, A. Leredde⁹, P. Mohanmurthy^{1,4}, A. Mtchedlishvili⁴, O. Naviliat-Cuncic³, D. Pais^{1,4}, F. M. Piegsa⁷, G. Pignol⁹, M. Rawlik¹, D. Rebreyend⁹, I. Rienäcker^{1,4}, D. Ries¹², S. Rocca^{9,13}, D. Rozpedzik⁵, P. Schmidt-Wellenburg⁴, A. Schnabel¹⁴, R. Viot⁹, A. Weis¹⁰, E. Wursten^{6,16}, J. Zejma⁵, G. Zsigmond⁴

- ¹ Institute for Particle Physics and Astrophysics, ETH Zürich, Zürich, Switzerland
² Department of Physics and Astronomy, University of Sussex, Falmer, Brighton, UK
³ Normandie Université, ENSICAEN, UNICAEN, CNRS/IN2P3, LPC Caen, Caen, France
⁴ Paul Scherrer Institute, Villigen, Switzerland
⁵ M. Smoluchowski Institute of Physics, Jagiellonian University in Krakow, Kraków, Poland
⁶ Instituut voor Kern- en Stralingsfysica, Katholieke Universiteit Leuven, Leuven, Belgium
⁷ University of Bern, Albert Einstein Center for Fundamental Physics, Laboratory for High Energy Physics, Bern, Switzerland
⁸ Department of Physics and Astronomy, University of Kentucky, Lexington, USA
⁹ Univ. Grenoble Alpes, CNRS, Grenoble INP, LPSC-IN2P3, Grenoble, France
¹⁰ Physics Department, University of Fribourg, Fribourg, Switzerland
¹¹ H. Niewodniczanski Institute of Nuclear Physics, Polish Academy of Sciences, Kraków, Poland
¹² Department of Chemistry - TRIGA site, Johannes Gutenberg University Mainz, Mainz, Germany
¹³ Institut Laue-Langevin, Grenoble, France
¹⁴ Physikalisches Technische Bundesanstalt, Berlin, Germany
¹⁵ Present address: Institute of Physics Belgrade, Belgrade, Serbia
¹⁶ Present address: CERN, Geneva, Switzerland

Received: 15 October 2020 / Accepted: 4 April 2021 / Published online: 28 April 2021
© The Author(s) 2021, corrected publication 2021
Communicated by Klaus Blaum

Abstract Psychological bias towards, or away from, prior measurements or theory predictions is an intrinsic threat to any data analysis. While various methods can be used to try to avoid such a bias, *e.g.* actively avoiding looking at the result, only data blinding is a traceable and trustworthy method that can circumvent the bias and convince a public audience that there is not even an accidental psychological bias. Data blinding is nowadays a standard practice in particle physics, but it is particularly difficult for experiments searching for the neutron electric dipole moment (nEDM), as several cross measurements, in particular of the magnetic field, create a self-consistent network into which it is hard to inject a false signal. We present an algorithm that modifies the data without influencing the experiment. Results of an automated analysis of the data are used to change the recorded spin state of a few neutrons within each measurement cycle. The flexible algorithm may be applied twice (or more) to the data, thus providing the option of sequentially applying various blinding offsets for separate analysis steps with

independent teams. The subtle manner in which the data are modified allows one subsequently to adjust the algorithm and to produce a re-blinded data set without revealing the initial blinding offset. The method was designed for the 2015/2016 measurement campaign of the nEDM experiment at the Paul Scherrer Institute. However, it can be re-used with minor modification for the follow-up experiment n2EDM, and may be suitable for comparable projects elsewhere.

1 Introduction

The electric dipole moment (EDM) of the neutron is a fundamental observable in particle physics that may directly relate to the observed dominance of matter over antimatter in the Universe. It has been sought experimentally for almost seven decades, with ever-improving sensitivity, but to date all results have been compatible with zero [1–5]. Many theories beyond the Standard Model naturally predict non-zero values that are close to current experimental sensitivities [6–8]. Thus, depending upon their outlook, scientists analysing

^ae-mail: Jochen.Krempel@phys.ethz.ch (corresponding author)

the data from EDM experiments may be biased unintentionally towards a result that favours their own expectations of either seeing, or not seeing, a statistically significant signal. Data blinding removes this psychological bias and, if applied properly, does not introduce any other bias. In experimental particle physics blinding has been used quite commonly for many years [9], but it has not previously been applied to any neutron EDM measurement.

In general, at least two different types of blinding can be distinguished:

1. Data corresponding to a region of interest is withheld from the analysis team, or, correspondingly, “fake” events can be added to obscure the signal. This is often the case in discovery experiments. See, *e.g.* (not the latest but representative) searches for rare decays [10], dark matter [11] or gravitational waves [12].
2. For precision experiments the observable of interest can be scaled by an unknown factor [13], or in some cases, an unknown offset can be added to the observable [14].

The latter is applicable to EDM experiments, and it is the approach that we have adopted for the nEDM experiment at the Paul Scherrer Institute (PSI) [15]. In deciding to modify the observable, one can choose to do so either by changing an aspect of the experiment itself, or by modifying the data *post hoc*. The latter has the advantage that it does not change or corrupt the experiment, and a hidden set of original data can be stored securely. Thus, if the blinding were to affect the data quality in any unforeseen way, *e.g.* by reducing the sensitivity or by introducing a new bias, the original data can still be used in the knowledge that the final result is unaffected by any systematic effects that may have been introduced through blinding. It should be mentioned that the data blinding described in this publication targets solely the psychological bias during data analysis. Any other potential bias of the measurement must be addressed by other means.

2 Experimental overview

In nEDM experiments the observable of interest is the dependence of the neutrons’ Larmor precession frequency upon an applied static electric field [15]. In most experiments to date the frequency measurement has been based on Ramsey’s technique of separated oscillatory fields [16]. In the experiment at PSI, polarized ultracold neutrons (UCN) were stored in a cylindrical vessel within a stable and highly uniform magnetic field parallel to the axis of the storage vessel. The two Ramsey spin-flip pulses, in phase with one another and each capable of inducing a $\pi/2$ spin rotation, were applied via a transverse rotating magnetic field. Between the two pulses, the neutron spins precessed freely. If the spin-flip frequency

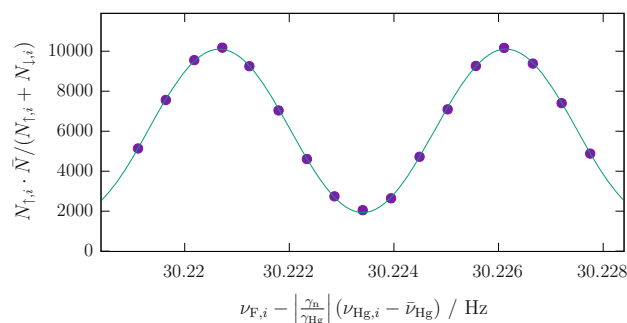


Fig. 1 Measured neutron counts plotted versus spin-flip frequency. Both quantities are corrected for fluctuations, as indicated in the axis labels. A sinusoidal curve with offset is fitted to the data points. $\bar{\nu}_{Hg}$ is the average reading of the mercury co-magnetometer. Both averages used in this plot are calculated from the measurements shown in this graph

was perfectly in resonance with the Larmor frequency of the neutrons, the neutrons would undergo a π spin-flip by the end of the procedure. If not, the accumulated phase difference – a highly sensitive measure of the difference between the Larmor and reference frequencies – would result in a partial spin-flip. Following this procedure, the neutrons were counted in a spin-sensitive detector. By repeating such measurements while scanning the reference frequency, and plotting the final neutron spin state versus that frequency, a Ramsey fringe pattern emerges as shown in Fig. 1. For a non-zero EDM value the pattern will shift horizontally when the electric field direction is reversed, which is done periodically.

An adiabatic fast-passage spin-flipper, referred to as SF1, was present at the entrance to the apparatus. When activated, it inverted the initial neutron spin orientation. This was used to investigate the influence of systematic effects. Regular changes of the magnetic field orientation and a variation of the magnetic field gradient serve the same purpose.

The 2015/16 data-taking campaign at PSI [15] employed a UCN storage volume of 22 litres, and the (highly uniform) magnetic field had a magnitude of approximately $1\mu\text{T}$. At the heart of each single measurement, known as a “cycle”, were the two $\pi/2$ spin-flip pulses; these had a frequency of $\nu_{F,i} \approx 30\text{Hz}$ and were applied for a duration of $t = 2\text{s}$ each. They were separated by a free precession period of $T = 180\text{s}$. Subsequent to this the neutrons were released from the storage volume and were counted in a spin-sensitive detector, yielding up to 20000 UCN per cycle.

The detector contained two separate branches, each consisting of a controllable adiabatic fast-passage spin-flipper, a magnetized spin-analysing foil, and a set of nine ${}^6\text{Li}$ based neutron detectors that were read out via photomultiplier tubes (PMTs) [17, 18]. This dual readout enabled the simultaneous measurement both of spin-up and of spin-down neutrons. Every time the current in one of the PMTs exceeded a certain

threshold, the recording of an “event” was triggered. Typically these events were caused by single neutrons, but some were due to incident photons. The timestamp, integrated charge and detector channel of every event were recorded in the data files. A set of consecutive cycles carried out with a stable magnetic field configuration, but with variation of the applied electric field, was called a “run”. During a run, lasting for up to several days and typically consisting of several hundred cycles, the configuration of the spin-flippers in the detector branches was reversed every four cycles, and the entrance spin-flipper status (the spin orientation of the neutrons entering the storage volume) was changed every 112 cycles. Within a run, eight cycles with no electric field were followed by 48 cycles with high voltage of a given polarity. Thus, both electric field polarities were applied between each change of the entrance spin-flipper state.

2.1 Formal description

The $\pi/2$ Ramsey spin-flip pulses of frequency $\nu_{F,i}$ that are applied in a particular cycle i cause a change in the relative proportions of spin-up and spin-down neutrons detected, with the position on the curve of Fig. 1 being determined by the phase

$$\phi_i = \frac{(\nu_{F,i} - \nu_L)}{\Delta\nu} \pi. \tag{1}$$

Here ν_L is the Larmor frequency, and the fringe width $\Delta\nu$ is

$$\Delta\nu = \frac{1}{2(T + 4t/\pi)}, \tag{2}$$

where T is the free-precession time and t the duration of each spin-flip pulse.

The true numbers of neutrons of each spin state, $N'_{\uparrow,i}$ and $N'_{\downarrow,i}$, within the storage volume just before they are guided to their respective detectors are

$$N'_{\uparrow,i} = \frac{N'_i}{2} (1 - \alpha' \cos \phi_i) \tag{3}$$

$$N'_{\downarrow,i} = \frac{N'_i}{2} (1 + \alpha' \cos \phi_i), \tag{4}$$

where N'_i is the total number of neutrons in the chamber after the precession and α' describes the true visibility after the precession; note that α' has a negative sign when SF1 is enabled.

The neutrons then fall through a polarisation analyser with spin selectivities p_A and p_B to reach the detectors that operate with efficiencies ϵ_A and ϵ_B . Thus, the numbers of neutrons measured are

$$N_{\uparrow,i} = (N'_{\uparrow,i} p_A + N'_{\downarrow,i} (1 - p_A)) \epsilon_A \tag{5}$$

$$N_{\downarrow,i} = (N'_{\downarrow,i} p_B + N'_{\uparrow,i} (1 - p_B)) \epsilon_B. \tag{6}$$

In this model the efficiency of the spin-flippers is neglected since it is very close to unity.

“Spin up” (\uparrow) refers to neutrons with the spin polarisation antiparallel to the magnetic field B_0 , and therefore with the magnetic moment parallel to the field. They are also known as “high field seekers”. When SF1 is off, this is the state in which they enter the bottle and is thus their state before the Ramsey sequence is applied.

A fit of Eqs. (1)–(6) to the data of all cycles of a run yields ν_L and α' , while T , t and all $\nu_{F,i}$ are known parameters. The steepest part of the slope, *i.e.* where $\phi_i \approx \pm 90^\circ$, is most sensitive to variations of the Larmor frequency. Thus the spin-flip frequencies were configured to operate sequentially at four distinct frequencies, the so-called working points (corresponding to the horizontal positions of the arrows in Fig. 2). These were detuned from the steepest point by about 5% of the fringe width in order to have some sensitivity also to further experimental parameters such as the visibility (effectively, the amplitude of the sinusoidal curve) and, in a more detailed analysis described in Sect. 3.2.2, the asymmetry of the detector efficiency.

In the presence of an nEDM d and an applied electric field \mathbf{E} collinear to the magnetic field \mathbf{B} , the resonant frequency ν_L shifts by

$$\delta\nu = 2 d \mathbf{E} \cdot \frac{\mathbf{B}}{B} / h, \tag{7}$$

where h is Planck’s constant. Note that the \mathbf{B}/B term is required only to obtain the appropriate sign.

Any change of the amplitude of the ambient magnetic field causes a corresponding change of the Larmor frequency. A mercury co-magnetometer was used to compensate for magnetic-field fluctuations by using the ratio of the measured frequencies $\mathcal{R} = \nu_n/\nu_{Hg}$ [19]. Correspondingly, Eq. (1) is altered as shown in Eq. (12). However, although the (thermal) mercury atoms populate the storage cell rather uniformly, the UCN have such low kinetic energies that under the influence of Earth’s gravitational field their mean vertical position lies a few mm below that of the mercury. Any vertical gradient of the magnetic field therefore results in a different average value of the magnetic field for the two species. This in turn leads to a small shift in the mercury-corrected neutron Larmor frequency. For a given vertical gradient, this shift is in opposite directions for the two different orientations (up vs. down) of the main magnetic field. Furthermore, there is a systematic effect leading to a significant false EDM arising from a conjunction of the vertical magnetic-field gradient and the relativistic motional magnetic field seen by the mercury atoms (in particular) as they move through the electric field [20]. It was therefore necessary to interpolate the measured nEDM results to zero vertical magnetic-field gradient. Since there was no absolute gradiometer, small magnetic-field gra-

dients were applied using trim coils in order to determine the situation at zero gradient from the intersection of the two curves arising from the two magnetic-field directions [15,20,21]. It is important to state that a blinding nEDM offset does not interfere with the interpolation of the curves.

3 Data blinding

3.1 Blinding concept

Any offset-based blinding method for an nEDM experiment must shift the measured Larmor frequency proportionally to the electric field, ideally while leaving all other observables unaltered. The following blinding procedures – each of which would have served to mimic an EDM within the usual analysis strategies – were briefly considered by our collaboration:

- Apply a modified spin-flip frequency with respect to the recorded value during the experiment. However, this would modify the experiment in an insidious manner as the change in actual physical conditions applied would be correlated to the electric field changes. This could therefore potentially introduce systematic effects, and, additionally, it would be irreversible. One would therefore have no possibility to investigate (or remove) it *a posteriori*.
- Register a shifted spin-flip frequency with respect to the one actually applied. This was not practicable in our case because of the finite resolution with which the frequency could be set. Furthermore, since this frequency was calculated from the mercury co-magnetometer reading of the previous cycle, this method would have required subtle alterations to all magnetometer readings in order to avoid the possibility of the shift being revealed through simple comparison. In our case this would have meant consistently adjusting a total of 16 magnetometer readings (one mercury and 15 caesium) [15,22] – a daunting task.

Although it does not apply to the current measurement it is also worth noting that these techniques could not be used in double-cell nEDM experiments, since common Ramsey spin-flip pulses would be applied to the entire assembly but the required shifts in each of the two cells would be in opposite directions.

There are various other observables that could have been modified but which would not have given exactly the same appearance as an EDM signal, and it would thus have been fairly trivial to identify them as fake signals. Note that manipulating the value of the electric field cannot be used to introduce a blinding offset.

The remaining variable that can usefully be modified is the number of neutrons counted in each spin state. The primary difficulty in this case is that, since the size of the required shift itself depends upon the number of neutrons counted, a partial but automatic preliminary analysis of the data must first be carried out. Furthermore, in order to deliver blinded data to the analysis teams as early as possible this preliminary analysis must be undertaken in real time in a manner that is fully defined before starting the actual data-taking campaign. Ultimately all of this proved to be manageable, and the approach was therefore adopted for the nEDM experiment. Its implementation will be described in detail in the following sections.

3.2 Algorithm

The blinding algorithm operates in a stepwise manner. First the necessary parameters are extracted from a full run (Sect. 3.2.2). Then the position of each cycle on the Ramsey curve, the so-called working point, is determined (Sect. 3.2.3), before the number of neutrons in each cycle can be modified (Sect. 3.2.4).

3.2.1 Calculation of the number of neutrons to be transferred

In order to generate an \mathbf{E} -field dependent frequency shift a small number of spin-up neutrons have to be reclassified as spin down, or *vice versa*, as illustrated in Fig. 2.

We follow Eqs. (1), (5), (6) and (7) as well as the first-order Taylor expansion $\delta N = \left(\frac{d}{d\phi} N\right) \left(\frac{d}{d\nu_L} \phi\right) \delta\nu$ to find the number of neutrons that need to change state:

$$\begin{aligned} \delta N_{\uparrow;i} &= \epsilon_A \frac{N'_i}{2} \alpha' (2p_A - 1) (\sin \phi_i) \left(\frac{d}{d\nu_L} \phi\right) \delta\nu & (8) \\ &= -\epsilon_A \frac{N'_i}{2} \alpha' (2p_A - 1) (\sin \phi_i) \frac{\pi}{\Delta\nu} \frac{2 d \mathbf{E} \cdot \mathbf{B} / B}{h}; & (9) \end{aligned}$$

$$\delta N_{\downarrow;i} = +\epsilon_B \frac{N'_i}{2} \alpha' (2p_B - 1) (\sin \phi_i) \frac{\pi}{\Delta\nu} \frac{2 d \mathbf{E} \cdot \mathbf{B} / B}{h}. \quad (10)$$

Note that \mathbf{E} and \mathbf{B} have to be parallel or antiparallel, and that the sign of α' can be negative depending upon the state of SF1.

It is convenient to introduce the total number of measured counts per cycle $N_i = \frac{\epsilon_A + \epsilon_B}{2} N'_i$ and its average over a run $\bar{N} = \langle N_i \rangle$. In light of the performance of the detectors [17, 23]) (see also Sect. 3.8.2), it is useful to note that, to a good approximation, $\epsilon_A = \epsilon_B$. Furthermore, since the data show that $(2p_A - 1) / (2p_B - 1) - 1 \approx 0.15\%$ the performance of the spin analysers can be assumed to be equal for the two spin states, *i.e.* $p_A = p_B$. Thus the measured visibility

becomes $\alpha = \alpha'(2p_A - 1)$, again with the usual caveat that it is negative when SF1 is enabled. Therefore,

$$\delta N_{\uparrow,\downarrow;i} = \mp N_i \frac{\pi \alpha d \mathbf{E} \cdot \mathbf{B}/B}{\Delta \nu} \frac{1}{h} \sin \phi_i. \tag{11}$$

The implications of removing the assumptions $\epsilon_A = \epsilon_B$ and $p_A = p_B$ will be discussed below.

Typical values for the nEDM experiment are $N_i = 15,000$, $|\sin \phi| = 0.99$, $\alpha = 0.75$, $T = 180\text{s}$, $t = 2\text{s}$, and $E = 11\text{kV/cm}$. Thus an EDM offset of $1.0 \times 10^{-25} \text{ e cm}$ would require a shift of about 3.39 neutrons in each cycle. Bearing in mind that the neutron has a negative magnetic moment, if \mathbf{B} and \mathbf{E} are parallel a positive nEDM would *reduce* the precession frequency. This would shift the Ramsey curves towards smaller frequencies, meaning that neutrons measured at a working point above the resonant frequency would shift from the spin-down detector arm to the spin-up. Neutrons that are measured at a working point below the resonant frequency would correspondingly shift from the spin-down to the spin-up detector arm. Figure 2 illustrates this reclassification and the resulting shift.

Obviously, it is impossible to shift a non-integer number of neutrons in a single cycle. One could simply round the number, but this would effectively cause a granularity of $\sim 3 \times 10^{-26} \text{ e cm}$ in the available blinding offsets. However, one can add to δN a small random number with a normal distribution, and round the sum to the nearest integer number. The choice of the width of this normal distribution had to strike a balance between two competing factors: On the one hand, a small width does not sufficiently smooth the granularity. On the other hand, a large width adds noise to the neutron counts and thus to the blinded nEDM value. A suitable compromise was found that used a standard deviation of 2 counts. In this case the granularity is sufficiently suppressed so that the result differs from a flat distribution by less than 10^{-7} . An improved method will be suggested in Sect. 6.

As mentioned above, this algorithm assumes the same \bar{N} and α for each of the two spin states. If this were not to be the case, a direct transfer of neutrons from one spin state to the other would not be appropriate. Instead, one would have to analyse and treat the two states separately, and neutrons would have to be added to or deleted from the spin-up and spin-down arrays as required. While this would be trivial if the neutron data were to consist merely of a simple sum of counts per cycle, it is a substantial effort for a more detailed data format such as ours, which lists charge and time per event.

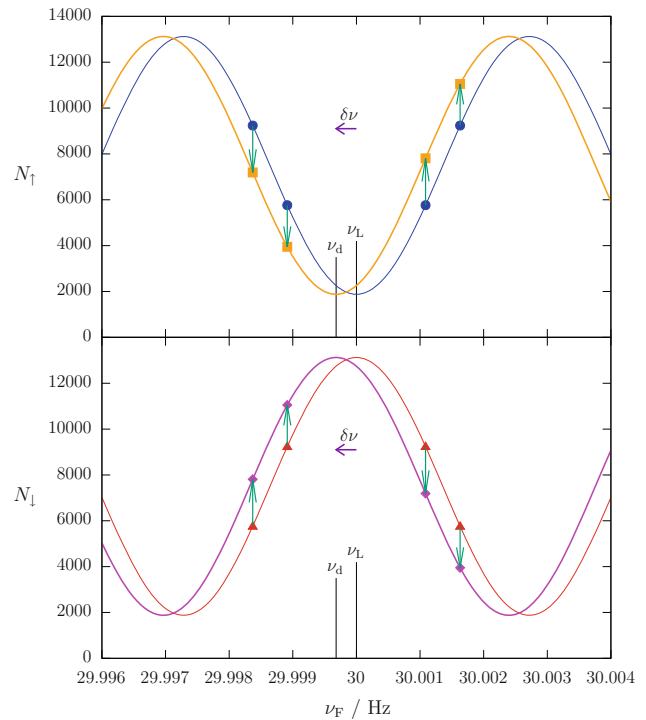


Fig. 2 Simulated neutron counts plotted versus applied spin-flip frequency ν_F . The transfer of a small number of neutrons (green arrows) from their initially recorded state, e.g. counts N_{\uparrow} (blue circles), corresponding to the original Larmor frequency ν_L , to the other spin state creates the blinded data points (orange squares). If this is done systematically and proportionally to the electric field, one can extract from the resulting dashed orange line a different Larmor frequency $\nu_d = \nu_L + \delta\nu$. The frequency shift by $\delta\nu$ (violet arrow) represents a false EDM signal d given by Eq. (7). For the detector arm counting the opposite spin state, e.g. N_{\downarrow} , the corresponding shift leads from the solid red to the dotted magenta curve. This yields the same false EDM signal. In the case where SF1 is active, all points and lines must be mirrored in a horizontal line at $N = 7500$. For clarity the strongly exaggerated values $|\sin \phi| = 0.951$ and $d = 3 \times 10^{-23} \text{ e cm}$ have been used here

3.2.2 Determination of α and detector asymmetry

As is evident from Eq. (11), before the data can be blinded one has to determine α and ν_L . While α is sufficiently constant throughout an entire run, ν_L might change from cycle to cycle and must be corrected with the field values recorded by the mercury co-magnetometer. We therefore refer to it as $\nu_{L,i}$ and write

$$\nu_{L,i} = \left| \frac{\gamma_n}{\gamma_{\text{Hg}}} \right| \nu_{\text{Hg},i} - \frac{\Phi}{\pi} \Delta \nu, \tag{12}$$

where γ_n and γ_{Hg} are the gyromagnetic ratios of the neutron and mercury respectively, $\nu_{\text{Hg},i}$ is the frequency obtained from the mercury co-magnetometer, and the phase Φ accommodates any difference in the average magnetic field sampled by the two species. The ratio of gyromagnetic ratios was measured in a previous experiment [24]. For the blinding

algorithm, a fixed value of

$$\left| \frac{\gamma_n}{\gamma_{\text{Hg}}} \right| = 3.8424574$$

was used. As magnetic field gradients were not changed during a run, Φ kept the same value throughout all cycles of the run.

Equations (5) and (6) can be rewritten as

$$\frac{N_{\uparrow,i} - N_{\downarrow,i}}{N_{\uparrow,i} + N_{\downarrow,i}} = \frac{\epsilon_A - \epsilon_B - \alpha' (\epsilon_A(2p_A - 1) + \epsilon_B(2p_B - 1)) \cos \phi_i}{\epsilon_A + \epsilon_B + \alpha' (-\epsilon_A(2p_A - 1) + \epsilon_B(2p_B - 1)) \cos \phi_i} \tag{13}$$

$$\approx \frac{\epsilon_A - \epsilon_B}{\epsilon_A + \epsilon_B} - \alpha \cos \phi_i, \tag{14}$$

where use is made of the approximations, justified by data, $p_A \approx p_B$ and $\epsilon_A \approx \epsilon_B$. The latter also implies that $\epsilon_A - \epsilon_B \ll \epsilon_A + \epsilon_B$.

We define $A_m = \frac{\epsilon_A - \epsilon_B}{\epsilon_A + \epsilon_B}$, which is the detector asymmetry originating from the slightly different efficiencies of the two detector arms counting the two spin states. Equations (12) and (1) are used to rewrite Eq. (14) as

$$\frac{N_{\uparrow,i} - N_{\downarrow,i}}{N_{\uparrow,i} + N_{\downarrow,i}} = f \left(\nu_{F,i} - \left| \frac{\gamma_n}{\gamma_{\text{Hg}}} \right| \nu_{\text{Hg},i} \right), \tag{15}$$

where we have defined the function

$$f(x) = A_m - \alpha \cos \left(\frac{\pi}{\Delta\nu} x + \Phi \right). \tag{16}$$

The independent variable x is beneficial for the fit algorithm, since it can be calculated from the observables for each cycle. It represents the difference between the applied spin-flip frequency and the neutron resonance frequency. The parameter estimation of A_m , α and Φ is carried out by fitting the data of a full run to Eq. 15. Every four cycles the spin-flipper states of both detector arms were inverted by activating and deactivating spin-flipper coils that are mounted inside the detector arms [17,18,23]. This results in a “normal” and an “inverted” configuration, with asymmetries A_N and A_I respectively. Both values are almost constant throughout a run. They were retained as fit parameters in order to accommodate long-term changes. Consequently the data contain two collated subsets, and the fit had to be conducted as a simultaneous fit within which α and Φ were common parameters while A_N and A_I applied only to the respective partial data sets.

3.2.3 Determination of the Ramsey phase ϕ_i

After having carried out the fit on the full run, Eq. (11) was used to calculate the number of neutrons to be transferred for each cycle. However, it was still necessary to determine ϕ_i . This could be done either via Eq. (14),

$$\cos \phi_i = \frac{1}{\alpha} \left(\frac{N_{\uparrow,i} - N_{\downarrow,i}}{N_{\uparrow,i} + N_{\downarrow,i}} - A_m \right), \tag{17}$$

or via Eq. (1),

$$\phi_i = \frac{\nu_{F,i} - \left| \frac{\gamma_n}{\gamma_{\text{Hg}}} \right| \nu_{\text{Hg},i}}{\Delta\nu} \pi + \Phi. \tag{18}$$

The first variant was implemented here, as it is more robust in instances where in a single cycle the co-magnetometer provides a reading with a large uncertainty which would potentially lead to a wrong blinding of that cycle. Note that this variant also uses Eq. (18) to determine the sign of ϕ_i .

3.2.4 Transferring neutrons

The data files are an event-driven list where each entry consists of a time stamp, the integrated charge recorded at the time, and the identification number of the photomultiplier tube that observed the event [18]. If the integrated charge exceeds a certain threshold then the event is classified as a neutron detection. Each of the two detector arms, one per spin state, contains a set of nine PMTs, which are sequentially numbered from 0 to 17 with 0–8 in the first arm and 9–17 in the second. In order to reclassify the spin of a neutron it is therefore sufficient to take the PMT number of that event, add 9 and carry out a modulo 18 operation. A neutron that is to be transferred is chosen by randomly selecting an event from the list counted in the correct detector arm, and then checking whether it is suitable to be moved simply and cleanly across: the requirement is that there must be a minimum separation in time between the event in question and the previous and subsequent events. We apply this condition to both the source and the recipient channel. The reason is to avoid the transfer of events for which the charge is split between neighbouring PMTs, or where the baseline correction algorithm has or would have to modify the charge [25]. If the event is not suitable, another randomly chosen event is tested until an appropriate one is found. The charge threshold for the neutron identification was investigated before the measurement campaign. Since the analysis teams could in principle have found and used a slightly different value, the blinding used a 60% higher threshold. We had carefully estimated that the change was small enough for the total number of events occurring between the two charge values to be suf-

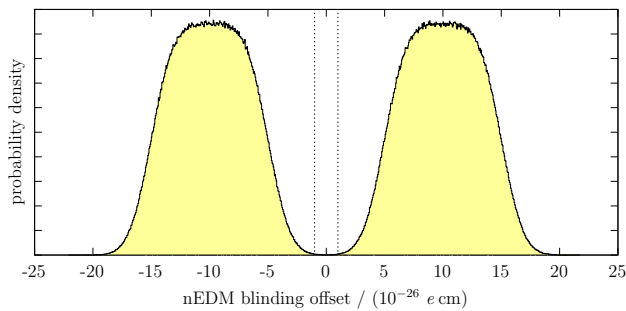


Fig. 3 Probability density function for the choice of the blinding offset created with 10^6 samples. The dashed vertical lines indicate the $\pm 1\sigma$ sensitivity of the data accumulated in 2015 and 2016 assuming a mean value of zero. For psychological reasons, the probability that an offset in this range is selected is kept very small but non-zero (integrated probability $\approx 2 \times 10^{-4}$)

ficiently low to yield a statistical uncertainty that would be too large to make a useful prediction of the blinding offset.

3.3 Choice of the blinding offset

Obviously, the value of the blinding offset must be kept secret from the analysis teams. In order to avoid providing any indirect psychological bias as to its value, it is necessary to choose it randomly from a distribution that allows a wide range of such values. It is convenient for its modulus to be larger than the known upper limit of the nEDM, since this allows a “sanity check” of having a sign that can be confirmed for consistency prior to publication of results (see Sect. 5).

At the same time, it should be sufficiently small to guarantee that the working points are not shifted away from the steep slope of the Ramsey pattern so that the sensitivity is maintained and the Taylor expansion used in Eqs. (8)–(10) remains valid. Any error in the calculation of the number of neutrons that are shifted by the blinding process will add noise to the EDM signal, and will therefore make it more difficult to look for effects and correlations that might indicate possible systematic effects such as the motional-field effect described above.

For the nEDM experiment, four Heaviside step functions were combined to define a range of $\pm 15 \times 10^{-26}$ e cm while excluding a modulus smaller than 5×10^{-26} e cm. This function was then blurred with a Gaussian of width $\pm 1.5 \times 10^{-26}$ e cm to ensure that even a large analysis result could not lead to a bias, while at the same time retaining the high likelihood of having a reasonably small offset.

The extremely unlikely possibility that a value from the tail of the Gaussian that extends beyond $\pm 1 \times 10^{-24}$ e cm might have been chosen was also explicitly excluded in order to ensure that the working points remained within the linear region of the original Ramsey fringe. One could argue that this latter step represents a small psychological bias, but –

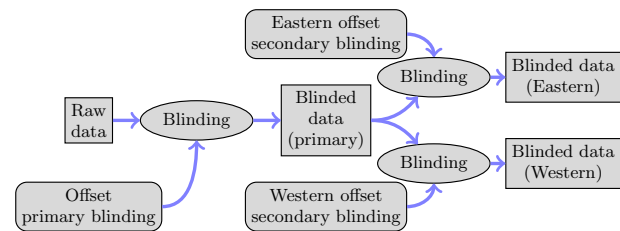


Fig. 4 Illustration of primary and secondary blinding. Each analysis group has access only to their respective blinded data set, “Eastern” or “Western”

notwithstanding the previously existing world limit – a one-day measurement without blinding leads to the certain conclusion that the true nEDM value must be smaller. Finally, a modulus of $< 1 \times 10^{-28}$ e cm was also excluded for technical reasons, since when communicating between different programs a value of exactly zero was used for cycles that should not be blinded at all, *e.g.* those with no applied electric field. Figure 3 shows the probability distribution of the blinding offset.

3.4 Secondary blinding and reblinding

The nEDM collaboration decided before data taking began to have the analysis carried out by two independent teams, referred to as Eastern and Western (loosely reflecting the geographic distributions of the involved institutions). In order to allow them to communicate without introducing a bias in case of any discrepancy over the mean value of the nEDM, it was decided that in addition to the first-stage “primary” blinding the same algorithm would be used to apply a separate “secondary” blinding that was distinct for each group, *i.e.* with a different additional offset. Figure 4 illustrates this process.

During the early days of data taking some concern was expressed that the automatic fitting algorithm might not work properly in all cases, or that some important properties of the data might be hidden as a result of the blinding, or that some other similarly unexpected events might make it necessary to significantly change the blinding algorithm. In order to provide a consistent data set in any of those cases, it would be necessary to run a modified blinding program again from scratch on the raw data. However, since the first set of blinded data would by then already be available to the analysis teams, it would be trivial for them to compare two versions of the same data file, and by leaving out all mismatching events they would have an unblinded data set with a statistical significance close to the original data set. In order to avoid such a scenario it was ensured that the pseudo-random number generator delivered reproducible numbers, and that the neutrons to be transferred were selected reproducibly. Thus, if *e.g.* one version of the blinding algorithm were to shift seven neutrons

and the other eight within a given cycle, the two resulting files would only differ by one neutron for that cycle. Therefore, a reblinding using the same or similar offset and a slightly modified algorithm could be carried out without danger of inadvertent unblinding. It should be noted that reblinding with an offset of opposite sign would immediately reveal both offsets.

In addition to transferring the neutrons between spin states, the blinding algorithm also marks each blinded data file with the date of blinding and the version number of the blinding code in order to ensure that those otherwise very similar files remain clearly distinguishable.

Ultimately, this reblinding feature was not used since no large discrepancies occurred within the data analysis.

3.5 Pseudo-random number generator (PRNG)

In principle, the random numbers used should meet the same strict requirements as those for strong cryptography regarding the prediction of numbers, the correlation between them and the uniformity of their distribution. However, the quantity of random numbers required was very small – typically a dozen per cycle for about 50,000 cycles, where each cycle gets a new seed. Therefore, a prediction attack to reveal the blinding offset would be extremely unlikely to succeed even if the random number generator were not to be of the highest quality. In contrast, the quality of the generator is important in terms of non-correlation and uniformity in order to avoid the danger of introducing noise or a systematic bias to the blinded data. The standard PRNG of many computer languages, the linear congruential generator, may therefore not be suitable. Furthermore, for the reblinding it is absolutely essential that the same algorithm should remain available for a significant number of years. Thus, any libraries that might be anticipated to vary either over time or between different computers were avoided, and the decision was made to use WELL1024a [26]. The Box-Muller transform [27] was used to convert uniformly distributed to normally distributed random numbers where necessary.

The random seed for each cycle must be reproducible over a time period of years, and it needs to remain secret after blinding. The data format used, which, as noted above, is an event list of particle detection per channel, includes a periodic counter of accumulated events in every channel. This led to the choice of using a 1024 bit checksum over the last 130kByte of the unblinded file. If the data files were not to include such a counter, the blinded data file would be very similar to the unblinded one and the seed would not be secret. In such cases an alternative approach would be to use the noise in the detector for the seed creation, *e.g.* from gamma events. For the secondary blinding, the original unblinded data were used for the seed calculation. This would help if a

reblinding at both primary and secondary level were ever to become necessary.

3.6 Online blinding

In order to calculate the phase of the actual working point ϕ_i the blinding process requires knowledge of Φ and α . This information is available only after a full run has been recorded, since it arises from the overall Ramsey fit. Consequently, no blinded data are available before the end of each run. However, it is absolutely necessary to have some live data available for quality checks of the ongoing measurement. An intuitive thought would be to publish a rounded version of the neutron counts in order to disguise the blinding offset. In fact, in order to make this disguise effective the rounding must be so coarse that the number obtained would be useless as a quality check. As a solution to this problem, an online blinding mechanism was devised. For this purpose, an additional blinding offset was created randomly for each run. The range for these random numbers, which were drawn from a uniform probability distribution, was $\pm 1 \times 10^{-23}$ e cm and thus was about a hundred times larger than the range of the regular blinding offset. The list of online blinding offsets used was stored in a location with restricted access, and has not been used for any other purpose than debugging the program. The online blinding algorithm does not provide a Φ parameter; this means that it assumes a zero magnetic-field gradient for the calculation of the number of neutrons to be shifted. Furthermore, it assumed perfectly symmetric detector efficiencies and uses \bar{N} instead of N_i . In all other aspects the algorithm was identical to that used for the regular blinding. The frequency shift introduced through the online blinding was of the same order of magnitude as those arising from changes in the magnetic field gradients, either intentionally introduced by the trim coils or by external fluctuations. With the online blinding system in place it was possible to make neutron counts available to the user immediately after each cycle, with adequate data quality to allow standard online checks to be carried out. However, these data obviously could not be used meaningfully for any further analysis.

It was important that cycles without electric field were not blinded at all, since they were used by the DAQ to choose the working points so as to have symmetric neutron count rates even in the presence of magnetic field gradients.

3.7 Technical details

The supervisory control and data acquisition systems of the experiment were partly modular, with all processes and file handling concerning neutron counting being hosted on a dedicated computer running Linux. Time was synchronised between all computers, and control communication was done via Ethernet (TCP/IP). Thus, with simple user permissions

provided by the file system it was possible to restrict access to the binary code of the blinding program, which contained the blinding offset, as well as to the raw data files. It was particularly beneficial that the computer could be started with a common unprivileged account. The DAQ program and thus the blinding process were given different permissions via the setuid bit. Consequently, the blinding process had access to the secret blinding offset and could write data files that standard users could not read.

A typical run of several days generated about a dozen gigabytes of data. With files of this size, the blinding process took several minutes. It was obviously desirable to have immediate feedback about the blinding and any potential problems, but in principle this would have meant blocking the DAQ system for significant periods of time. The blinding process was therefore split into two parts. The first part selected the data and carried out the fit of α , which was reported to the main DAQ and thus to the user. This could be completed within a second. The process would then fork itself, on the one hand quitting to make the system available for the following run, while on the other hand simultaneously carrying out the intensive work of transferring neutron data between the two detector arms.

During data taking the blinding program was supposed to run autonomously and without intervention. This meant that it had to handle some irregular conditions:

- Data that did not contain EDM information must not be blinded; they were instead revealed immediately. These were typically runs without applied high voltage, or runs with cycles that did not have two spin-flips. Such measurements occurred fairly frequently in order to characterise the UCN source [28,29], the detector, or the background.
- The fitting process ignored single cycles with a low neutron count rate. A lower threshold of 1000 counts was chosen, since such a low count rate would not be used for nEDM analysis.
- Cycles with an unphysically high count rate were not blinded, since these could effectively disclose the blinding offset. An upper threshold of 50,000 neutrons per cycle was chosen; this was a factor of ten greater than the actual numbers observed during commissioning, and nearly a factor of three greater than the genuine maximum observed.
- Blinding was only automatically applied if the quality of the Ramsey fit was sufficiently good. The threshold here was $\chi_{\text{red.}}^2 < 3$.

In case of doubt the blinding process neither blinded nor revealed data, but rather made a request via E-mail for human intervention.

3.7.1 Manual interventions

Great care was taken during the design of the blinding algorithm to minimize the need for human intervention during data taking. This required automatic handling of unusual circumstances with respect to data quality or malfunctions of parts of the apparatus. Inevitably, due to the complexity of the experiment, some manual interventions during data taking were necessary. In these circumstances the data were assessed by the blinding coordinator in order to either reject bad cycles and to apply the blinding on the remaining cycles of the run, or to divide a run into pieces between magnetic field jumps and to apply the blinding process separately on these parts. Between 13 September 2015 and 21 December 2016 inclusive, 1072 runs with neutron data were recorded. Of these, 113 runs were automatically blinded and 14 runs needed manual blinding. All of these contained information on the EDM. The remaining 945 runs were usually much shorter and were used for calibration, setup, and systemic studies of the apparatus, often undertaken when no neutrons were available. Of this set, 925 runs were revealed promptly, while 20 runs needed manual revealing. Notably, not a single run ($< 1\%$) was blinded or revealed automatically where not intended, while more than 96% were treated automatically, and therefore were not subject to any delay.

3.7.2 Secrecy

While no malign intent is assumed, there are a number of scenarios under which the blinding offset – a single simple number – could inadvertently be revealed if the raw data were not adequately protected:

- During the data analysis process there may be a temptation to carry out a test that would be simpler to run on the unblinded raw data.
- Obtaining access to “forbidden” data will always of itself be tempting to some, merely as a challenge or puzzle that they wish to demonstrate they can solve.
- Others may seek the “codebreaking” challenge of attempting to decrypt data or of applying statistical attacks on them.

With this in mind, the blinding offset was stored using asymmetric encryption with the public part of an RSA-key pair directly after it had been created. The blinding offset together with some metadata only amounts to 192 bits; thus, a simple asymmetric encryption is possible. The private key to decrypt the blinding offset was injected into the executable of the blinding program at compile time. Access to the executable program is restricted by file system permissions. The original private key was stored with password RSA encryption using OpenSSL and was thus only available to the blind-

ing coordinator. Access to data files was restricted by file system permissions.

These cryptographic and organisational measures were deemed reasonable in order to prevent accidental unblinding of the data. They were easy to implement and did not have any impact on permitted workflows. Although fairly robust, they are certainly not sufficient to protect against either physical theft of hard drives or manipulation of software with malicious intent. Any further protection would require the restriction of physical access to the DAQ computer or its boot process. Encryption of the operation system via a Trusted Platform Module chip is nowadays available and would suffice for this task. However, this could potentially have had an impact on the maintainability of the system, especially in case of hardware problems. The existing hurdles were therefore considered to be sufficiently high.

3.8 Effects of noise and asymmetry

The blinding algorithm manipulates the data, including with the use of random numbers and fit results. This procedure naturally introduces some noise. In this section we discuss the level of this noise and the resulting consequences.

3.8.1 Noise from fractional neutron numbers

In Sect. 3.2.1 we described how a random number (normal distribution with $\sigma = 2$) is added to the fractional number of neutrons to be transferred before rounding to an integer value. Solving Eq. (11) for d allows one to calculate how much noise is added to the final nEDM result due to this additional random process. Using the average number of neutrons per cycle $\bar{N} = 11,400$, the average visibility $|\bar{\alpha}| = 0.75$, and the applied electric field $E = 11$ kV/cm, the additional noise amounts to 7.7×10^{-26} e cm per cycle. The additional statistical uncertainty for the mean of all 54068 cycles is 3.3×10^{-28} e cm, which is about 3% of the uncertainty due to counting statistics.

3.8.2 Noise from detector asymmetry

In Sect. 3.2.2 we described the determination of α and A_m through fitting. These quantities each have their own statistical uncertainty. The mean of the fit value of the visibility $|\alpha|$ was 0.75, and the mean of its uncertainty was 0.003. The mean values of the detector asymmetry were $A_N = 0.032$ and $A_I = -0.036$ in 2015, both with a standard deviation of 0.002. In 2016 the mean was $|A_m| = 0.004$ with a standard deviation of 0.001. The mean of the individual uncertainties within each run was always below 0.001. Thus in 2015 there was a significant asymmetry. The number of neutrons to be transferred is calculated from these numbers via Eqs. (17) and (11). At our working points the result of

$\sin(\arccos(x))$ lies between 0.98 and 0.99 for any x . Thus no matter how large the fluctuations of A_m may have been, the resulting noise on δN is less than 1% and is therefore also negligible, being significantly smaller than the noise arising from the integer rounding described in Sect. 3.8.1.

3.8.3 Noise from visibility

The parameter α enters directly in Eq. (11), but as the observed relative uncertainty $\frac{0.003}{0.74} = 0.004$ is also very small, the contribution to the noise is once again negligible.

3.8.4 Noise from neutron number per cycle

The final parameter in Eq. (11) is the measured quantity N_i . Despite being a noisy observable, it does not contribute to any noise in the blinding since it represents the exact value of the number of neutrons for this particular cycle.

3.8.5 Verification on test data

The very earliest data, a set of 24 runs obtained prior to 13 September 2015, were taken with an early implementation of the blinding process. In order to test the blinding process with real data, this subset of the data was made available to the analysis teams both with and without a blinding offset of $d^* = +1.951 \times 10^{-25}$ e cm. (Note that the blinded sample was not used in the analysis presented in Ref. [5].) These runs each have an irreducible statistical sensitivity that ranges from 0.9×10^{-25} e cm to 2.4×10^{-25} e cm, accumulating to a total of 3.2×10^{-26} e cm. The data were analysed twice. The first time – with what was then still a fairly rudimentary data analysis – was in September 2015, just prior to the decision to continue with the full implementation of the blinding. The second occurrence used an almost final analysis. Both tests showed that the blinding algorithm increased the uncertainty by 2×10^{-28} e cm, corresponding to 0.5% of the statistical sensitivity of the data set. The blinding offset predicted by the analysis matched the applied offset to within 0.2×10^{-26} e cm, which was a tenth of the uncertainty of the analysis. This comparison was carried out before removal of the secondary blinding of the full data set in order to provide a metric to assist in judging the relative quality of the analyses. After unblinding, this test was repeated with the full data set as described in the next section.

4 Unblinding

Each data analysis team worked on a doubly (primary + secondary) blinded data set, and ultimately extracted their own estimator for the blinded nEDM value and its uncertainty. Once the collaboration was convinced that these analyses

were complete, a comparison based on appropriate parameters and distributions was undertaken. One comparator was, for example, the nEDM uncertainty. Moreover, after grouping the data in sequences (sets of cycles for which the magnetic field, in particular, did not change – and thus, normally one or several successive runs) it was possible to check, sequence by sequence, the difference between the extracted nEDM and its mean value (averaged over all sequences). This difference was useful to check that the two analysis results showed the same correlations with respect to external parameters. In particular, the measured neutron EDM is shifted from the true value of the neutron EDM by a systematic effect that is linear in the vertical gradient, and the analyses are designed to correct for this correlation [30].

The decision to proceed to the first unblinding step, which consisted of removing the secondary blinding offsets, was taken based on the agreement of all comparators.

After this first unblinding it was possible to cross-check the two analyses with respect to the secondary blinding offset, the results of which are shown in Table 1.

This allowed a direct comparison of the (singly blinded) nEDM values obtained by the two teams. If any discrepancy had been found, a longer and detailed comparison would have had to have been carried out at this point. Should this have become necessary, possible approaches that were discussed included (a) running both analysis codes on a common subset of data and converging parameters and code, *i.e.* cut criteria and methods, until the results matched, and (b) producing new sets of secondary blinded data, although this would have been of limited use since by then both analysis teams would implicitly know their offsets, and (c) producing an alternative blinded data set directly from the original raw data with a new unknown random offset.

Since the two analysis teams were in agreement, it was possible (once it had finally been confirmed that all known systematic effects had been evaluated) to proceed directly to the removal of the primary blinding. The offset was therefore revealed and subtracted, to yield a true nEDM estimator. In addition, the same analysis codes together with the same settings, *e.g.* for cuts, were applied to the original, non-blinded data set, which had been kept hidden up until that point. The result of the direct analysis of this non-blinded data set was of course expected to match with that emerging from the analysis of the blinded set minus the applied blinding offset. From theoretical estimation, as well as from the experience with the early data taken without blinding, agreement between these two approaches had been expected to be at the level of 10^{-27} e cm. In the posterior comparison, as shown in Table 1, this was confirmed perfectly. Fig. 5 shows a comparison between the injected blinding offset and the one predicted by the analysis from the Western team. The non-zero width of the peaks indicates that the blinding algorithm does indeed, as expected from Sect. 3.8.1,

inject some noise into the individual sequences or cycles. The widths of the Gaussians fitted to the distribution were $0.31(5) \times 10^{-26}$ e cm and $0.41(4) \times 10^{-26}$ e cm for secondary and primary blinding, respectively. The sequences consisted of 514 cycles on average. Thus, the observed widths are compatible with the expected uncertainty of the mean due to the noise of 0.34×10^{-26} e cm.

The agreement of the difference ‘analysis of blinded data’ minus ‘analysis of non-blinded data’ with the blinded offset is outstanding.

5 Costs and benefits

As discussed in Ref. [31], blinding does not in general come without cost. For the method presented here, the costs were primarily the manpower required for design, implementation and study of the technique. A small amount of statistical noise was introduced into the blinded data, but this tiny contribution was only present in the blinded data sets; it left the final analysis unaffected. Ultimately, the method described here did not suffer from the various costs that have typically been present for other blinding techniques – for example, all analysis channels were immediately available and no signals or features, other than the true nEDM itself, were hidden. It is notable that the blinding even permitted the analysis of a periodically changing nEDM [32] without revealing the unblinded result of the static signal.

Most importantly, the blinding provided a very substantial benefit to the nEDM analysis, and not only in that it eliminated the effects of an unconscious bias. Since in past measurements the true nEDM results have always been indistinguishable from zero they were sign insensitive, and as such also insensitive to potential sign errors in the analysis. However, in this case the false signal in the blinded data had a value significantly away from zero, and thus included a clearly identifiable sign. This sign showed up in the various analysis channels, *e.g.* with its dependence upon magnetic-field gradients, and as such at one point it actually revealed a mistake in an early version of our data analysis when the code was tested with a known nEDM offset.

6 Possible improvements

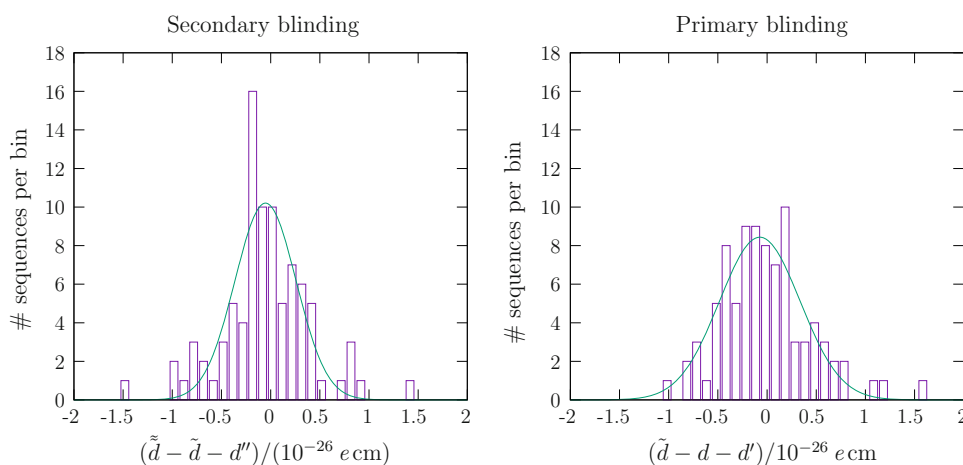
In order to handle the non-integer number of neutrons to be transferred in each single cycle, a normally distributed random number of width 2 was used as described in Sect. 3.2.1. Future implementations will use a rectangular probability density function of width 1. This will provide perfect linearity and will reduce the introduced noise by a factor of two, down to the intrinsic minimum.

Table 1 Estimators of the neutron EDM and their statistical uncertainties derived by the two analysis teams, in units of $\times 10^{-26}$ e cm

nEDM estimator	Western		Eastern	
	Value	χ^2/N_{dof}	Value	χ^2/N_{dof}
Doubly blinded \tilde{d}	15.39 ± 1.07	90.7/86	3.80 ± 1.11	91.2/86
Singly blinded \tilde{d}	5.97 ± 1.07	93.0/86	6.15 ± 1.11	93.2/86
Non-blinded d	-0.02 ± 1.07	92.5/86	0.16 ± 1.11	92.4/86
$\tilde{d} - \tilde{d}$	9.43		-2.35	
Input offset d''	9.48		-2.33	
Difference $\tilde{d} - \tilde{d} - d''$	-0.05		-0.02	
$\tilde{d} - d$	5.99		5.99	
Input offset d'	6.02		6.02	
Difference $\tilde{d} - d - d'$	-0.03		-0.03	

\tilde{d} is the estimator of the doubly blinded data, while \tilde{d} is the estimator of the singly blinded data. The input offset d'' is the value of the secondary blinding offset, which was de-encrypted during the first, relative, unblinding on 23 October 2019. The input offset d' is the value of the primary blinding offset, which was de-encrypted during the second unblinding on 28 November 2019. All analysis results in this table arise only from data taken after 13 September 2015; data prior to this were not blinded with the same offsets and thus cannot be compared. Consequently, the value d listed here differs slightly from the final result [5]. The observed span of χ^2 values of 1.8 corresponds to a change of uncertainty of 1×10^{-28} e cm. The fluctuation in this range – even to smaller values – is within statistical expectation

Fig. 5 Difference between results of the analysed blinded and unblinded data sets and the corresponding offsets, shown separately for each of the two blinding steps. The bin width is 10^{-27} e cm. Both peaks are centred well within 10^{-27} e cm. Only results from the Western analysis using data taken after 13 September 2015 are shown; the Eastern analysis yields similar results



7 Summary and conclusion

For the first time, a blinding technique has been developed for and applied to a neutron EDM measurement. The true EDM value is hidden by an offset, while other variables of interest are unaffected. The algorithm presented modifies only a copy of the recorded data, and saves the original data in a hidden location. Secondary blinding and the possibility of re-blinding are innovations that further reduce risks that are often associated with blinding. The artificial increase in noise in the blinded data sets as a result of this process has been shown to be negligibly small, and disappears automatically in the final result.

Acknowledgements We gratefully acknowledge financial support from the Swiss National Science Foundation through project grants 149211, 162574 and 172639 for the ETHZ group, grant 181996 for the Bern group and grants 117696, 144473, 137664, 163413, 169596, and 171626 for the PSI group. This work was funded in part by the United Kingdom Science and Technology Facilities Council (STFC) through grants ST/N000307/1 and ST/M503836/1, as well as by the School of Mathematical and Physical Sciences at the University of Sussex. One of the authors (P. M.) would like to acknowledge support from the Swiss State Secretariat for Education, Research and Innovation (SERI) - Federal Commission for Scholarships (FCS) award #2015.0594. We likewise gratefully acknowledge financial support from the Polish National Science Center, through grants UMO-2015/18/M/ST2/00056, UMO-2016/23/D/ST2/00715 and UMO-2018/30/M/ST2/00319. We are most grateful for the excellent support provided by the PSI technical groups and by various services of the collaborating universities and research laboratories.

Funding Information Open Access funding provided by ETH Zurich.

Data Availability Statement This manuscript has associated data in a data repository. [Authors' comment: The experimental data will be published at a later point.]

Open Access This article is licensed under a Creative Commons Attribution 4.0 International License, which permits use, sharing, adaptation, distribution and reproduction in any medium or format, as long as you give appropriate credit to the original author(s) and the source, provide a link to the Creative Commons licence, and indicate if changes were made. The images or other third party material in this article are included in the article's Creative Commons licence, unless indicated otherwise in a credit line to the material. If material is not included in the article's Creative Commons licence and your intended use is not permitted by statutory regulation or exceeds the permitted use, you will need to obtain permission directly from the copyright holder. To view a copy of this licence, visit <http://creativecommons.org/licenses/by/4.0/>.

References

1. S.K. Lamoreaux, R. Golub, J. Phys. G **36**(10), 104002 (2009). <https://doi.org/10.1088/0954-3899/36/10/104002>
2. C.A. Baker et al., Phys. Rev. Lett. **97**, 131801 (2006). <https://doi.org/10.1103/PhysRevLett.97.131801>
3. J.M. Pendlebury et al., Phys. Rev. D **92**, 092003 (2015). <https://doi.org/10.1103/PhysRevD.92.092003>
4. A.P. Serebrov et al., Phys. At. Nucl. **78**, 1601–1605 (2015). <https://doi.org/10.1134/S1063778815130293>
5. C. Abel et al., Phys. Rev. Lett. **124**, 081803 (2020a). <https://doi.org/10.1103/PhysRevLett.124.081803>
6. J. Ellis, Nucl. Instrum. Methods Phys. Res. A **284**(1), 33–39 (1989). [https://doi.org/10.1016/0168-9002\(89\)90243-X](https://doi.org/10.1016/0168-9002(89)90243-X)
7. D.E. Morrissey, M.J. Ramsey-Musolf, New J. Phys. **14**, 125003 (2012). <https://doi.org/10.1088/1367-2630/14/12/125003>
8. J. Engel, M.J. Ramsey-Musolf, U. van Kolck, Prog. Part. Nucl. Phys. **71**, 21–74 (2013). <https://doi.org/10.1016/j.pnpnp.2013.03.003>
9. J.R. Klein, A. Roodman, Annu. Rev. Nucl. Part. S. **55**(1), 141–163 (2005). <https://doi.org/10.1146/annurev.nucl.55.090704.151521>
10. J. Adam et al., Phys. Rev. Lett. **107**, 171801 (2011). <https://doi.org/10.1103/PhysRevLett.107.171801>
11. E. Aprile et al., Phys. Rev. Lett. **109**, 181301 (2012). <https://doi.org/10.1103/PhysRevLett.109.181301>
12. J. Abadie et al., Phys. Rev. D **81**, 102001 (2010). <https://doi.org/10.1103/PhysRevD.81.102001>
13. D.B. Chitwood et al., Phys. Rev. Lett. **99**, 032001 (2007). <https://doi.org/10.1103/PhysRevLett.99.032001>
14. A. Vacheret, D. Lhuillier, Eur. Phys. J. A **24**(2), 151–154 (2005). <https://doi.org/10.1140/epjad/s2005-04-038-6>
15. C. Abel et al., EPJ Web Conf. **219**, 02001 (2019). <https://doi.org/10.1051/epjconf/201921902001>
16. N.F. Ramsey, Phys. Rev. **78**, 695–699 (1950). <https://doi.org/10.1103/PhysRev.78.695>
17. S. Afach et al., Eur. Phys. J. A **51**(11), 143 (2015a). <https://doi.org/10.1140/epja/i2015-15143-7>
18. G. Ban et al., Eur. Phys. J. A **52**, 326 (2016). <https://doi.org/10.1140/epja/i2016-16326-4>
19. C.A. Baker et al., Nucl. Instrum. Methods Phys. Res. A **736**, 184–203 (2014). <https://doi.org/10.1016/j.nima.2013.10.005>
20. J.M. Pendlebury et al., Phys. Rev. A **70**, 032102 (2004). <https://doi.org/10.1103/PhysRevA.70.032102>
21. S. Afach et al., Phys. Rev. D **92**, 052008 (2015b). <https://doi.org/10.1103/PhysRevD.92.052008>
22. C. Abel et al., Phys. Rev. A **101**, 053419 (2020b). <https://doi.org/10.1103/PhysRevA.101.053419>
23. V. Helaine. Thesis, Université de Caen, 2014. URL <https://tel.archives-ouvertes.fr/tel-01063399>
24. S. Afach et al., Phys. Lett. B **739**, 128–132 (2014). <https://doi.org/10.1016/j.physletb.2014.10.046>
25. LPC Caen. FASTER Fast Acquisition System for nuclEar Research, 2013. <http://faster.in2p3.fr/>
26. F. Panneton, P. L'Ecuyer, M. Matsumoto, ACM Trans. Math. Softw. **32**(1), 1–16 (2006). <https://doi.org/10.1145/1132973.1132974>
27. G.E.P. Box, M.E. Muller, Ann. Math. Statist. **29**(2), 610–611 (1958). <https://doi.org/10.1214/aoms/1177706645>
28. G. Bison et al., Eur. Phys. J. A **56**, 33 (2020). <https://doi.org/10.1140/epja/s10050-020-00027-w>
29. B. Lauss, Phys. Proc. **51**, 98–101 (2014). <https://doi.org/10.1016/j.phpro.2013.12.022>
30. N. J. Ayres, et al. *In preparation* (2021)
31. R. Golub. In S. J. Seestrom, editor, *Next Generation Experiments to Measure the Neutron Lifetime*, pages 97–102, (2014). https://doi.org/10.1142/9789814571678_0010
32. C. Abel et al., Phys. Rev. X **7**, 041034 (2017). <https://doi.org/10.1103/PhysRevX.7.041034>



The design of the n2EDM experiment

nEDM Collaboration

N. J. Ayres¹, G. Ban², L. Bienstman³, G. Bison⁴, K. Bodek⁵, V. Bondar^{1,a}, T. Bouillaud⁶, E. Chanel⁷, J. Chen², P.-J. Chiu^{1,4}, B. Clément⁶, C. B. Crawford⁸, M. Daum⁴, B. Dechenaux², C. B. Doorenbos^{1,4}, S. Emmenegger¹, L. Ferraris-Bouchez⁶, M. Ferti⁹, A. Fratangelo⁷, P. Flaux², D. Goupillière², W. C. Griffith¹⁰, Z. D. Grujic¹¹, P. G. Harris¹⁰, K. Kirch^{1,4}, P. A. Koss^{3,15}, J. Krempel¹, B. Lauss⁴, T. Lefort², Y. Lemièrè², A. Leredde⁶, M. Meier⁴, J. Menu⁶, D. A. Mullins⁷, O. Naviliat-Cuncic², D. Pais^{1,4}, F. M. Piegsa⁷, G. Pignol^{6,b}, G. Quémener², M. Rawlik^{1,14}, D. Rebreyend⁶, I. Rienäcker^{1,4}, D. Ries¹², S. Rocchia⁶, K. U. Ross¹², D. Rozpedzik⁵, W. Saenz², P. Schmidt-Wellenburg⁴, A. Schnabel¹³, N. Severijns³, B. Shen¹², T. Stapf⁴, K. Svirina⁶, R. Tavakoli Dinani³, S. Touati⁶, J. Thorne⁷, R. Virost⁶, J. Voigt¹³, E. Wursten³, N. Yazdandoost¹², J. Zejma⁵, G. Zsigmond⁴

¹ Institute for Particle Physics and Astrophysics, ETH Zürich, 8093 Zurich, Switzerland

² Normandie Univ, ENSICAEN, UNICAEN, CNRS/IN2P3, LPC Caen, 14000 Caen, France

³ Institute for Nuclear and Radiation Physics, KU Leuven, 3001 Leuven, Belgium

⁴ Paul Scherrer Institut (PSI), 5232 Villigen, Switzerland

⁵ Marian Smoluchowski Institute of Physics, Jagiellonian University, 30-348 Cracow, Poland

⁶ LPSC, Université Grenoble Alpes, CNRS/IN2P3, Grenoble, France

⁷ Albert Einstein Center for Fundamental Physics, University of Bern, 3012 Bern, Switzerland

⁸ University of Kentucky, Lexington, USA

⁹ Institute of Physics, Johannes Gutenberg University, 55128 Mainz, Germany

¹⁰ Department of Physics and Astronomy, University of Sussex, Falmer, Brighton BN1 9QH, UK

¹¹ Institute of Physics Belgrade, University of Belgrade, 11080 Belgrade, Serbia

¹² Department of Chemistry-TRIGA site, Johannes Gutenberg University, 55128 Mainz, Germany

¹³ Physikalisch Technische Bundesanstalt, Berlin, Germany

¹⁴ Present Address: Paul Scherrer Institut (PSI), 5232 Villigen, Switzerland

¹⁵ Present Address: Fraunhofer Institute for Physical Measurement Techniques, 79110 Freiburg, Germany

Received: 5 February 2021 / Accepted: 30 May 2021 / Published online: 12 June 2021

© The Author(s) 2021

Abstract We present the design of a next-generation experiment, n2EDM, currently under construction at the ultracold neutron source at the Paul Scherrer Institut (PSI) with the aim of carrying out a high-precision search for an electric dipole moment of the neutron. The project builds on experience gained with the previous apparatus operated at PSI until 2017, and is expected to deliver an order of magnitude better sensitivity with provision for further substantial improvements. An overview of the experimental method and setup is given, the sensitivity requirements for the apparatus are derived, and its technical design is described.

1 Introduction and motivation

Searches for permanent electric dipole moments (EDM) of fundamental particles and systems are among the most sensitive probes for CP violation beyond the Standard Model (SM) of particle physics; see e.g. [1, 2].

Although the CP-violating complex phase of the CKM matrix is close to maximal, the resulting SM values for EDMs are tiny, while theories and models beyond the SM (BSM) often predict sizeable CP violating effects that lie within the range of experimental sensitivities. Some of these models use specific CP violating mechanisms together with other features to explain the observed baryon asymmetry of the universe (BAU) [3], which is inexplicable by known sources of CP violation in the SM.

The scale of CP violation in the QCD sector of the SM is experimentally constrained to be vanishingly small, through the non-observation to date of any non-zero hadronic EDM. This lack of EDM signals in searches with the neutron [4] and

^ae-mail: bondarv@phys.ethz.ch

^be-mail: guillaume.pignol@lpsc.in2p3.fr

^{199}Hg atom [5] in particular results in what is known as the “strong CP problem” [6]. Theory offers possible explanations for the suppression of the observable CP violation in the strong sector, most elegantly by introducing axions [7,8]. Axions are also viable Dark Matter candidates [9], but aside from the unexpectedly small EDMs there has so far been no other observations made in support of their existence.

Obviously, nobody today can safely predict where BSM CP violation will first manifest itself in any experiment. If it were to show up in an EDM measurement, it is not clear in which system this would be; thus there is a broad search strategy presently being pursued in many laboratories around the world [10–13]. In particular, ongoing efforts target intrinsic particle EDMs, e.g. of leptons and quarks, as well as those occurring due to or being enhanced by interactions in nuclear, atomic and molecular systems. In the current situation any sign of an EDM would be a major scientific discovery. In case of a discovery in any of these systems, however, corresponding EDM measurements in other systems will be needed to clarify the underlying mechanism of CP violation. The neutron is experimentally the simplest of the accessible strongly interacting systems, and as such remains a prime search candidate. Searches for EDMs of the proton and light nuclei will also become increasingly important.

The most sensitive neutron EDM search delivered a result of $d_n = (0 \pm 1.1_{stat} \pm 0.2_{sys}) \times 10^{-26} e \text{ cm}$, which sets an upper limit of $|d_n| < 1.8 \times 10^{-26} e \text{ cm}$ (90% CL) [4]. This measurement was performed with the apparatus originally built by the RAL/Sussex/ILL collaboration [14], which went through continuous upgrades of almost all subsystems and was also moved to the source of ultracold neutrons (UCNs) [15–17] at the Paul Scherrer Institute (PSI). Arguably the most important of the upgrades were the addition of an array of atomic cesium magnetometers [18] and of a dual spin detection system [19].

With this last measurement, the RAL/Sussex/ILL nEDM apparatus at the PSI UCN source reached its limits with respect both to systematic effects and to statistical sensitivity. Any further increase in sensitivity requires a new apparatus optimally adapted to the UCN source as well as the replacement of numerous subsystems with more modern and higher-specification equipment.

There are a number of collaborations around the world [20–25] attempting to improve the current neutron EDM limit by at least one order of magnitude. The most ambitious competing project is based on a totally new concept of a cryogenic experiment in superfluid helium, where both the UCN statistics and the electric-field strength could be enhanced [20]. More traditionally, we propose to push and extend the powerful and proven concept of a room-temperature UCN experiment with two separate and complementary magnetometry systems. The n2EDM spectrometer, the subject of this paper, is a next-generation UCN apparatus based on the

unification of two concepts: the double-chamber setup pioneered by the Gatchina nEDM spectrometer [26], and the use of Hg co-magnetometry [27].

The n2EDM apparatus is designed to measure the neutron EDM with a sensitivity of $1 \times 10^{-27} e \text{ cm}$, with further possibility to go well into the $10^{-28} e \text{ cm}$ range. The improvement of the statistical sensitivity will arise from the large double-chamber volume as well as an optimized UCN transport arrangement between the source and the spectrometer. The control of systematic effects needs to shadow these improvements, implying better stability, uniformity and measurement of the main magnetic field. These will be achieved by a dedicated coil system and better magnetic shielding, as well as by substantially improved magnetometry.

2 The principle of the n2EDM experiment

In this section we present the overall concept of the n2EDM apparatus. The heart of the experiment is a large-volume double storage chamber placed in a new, large, magnetically shielded room. Stable and uniform magnetic-field conditions are of paramount importance for a successful measurement. The magnetic field will be generated by a main magnetic-field coil in conjunction with about 70 trim coils, each powered by highly stable power supplies. Monitoring of the magnetic field is provided by atomic mercury co-magnetometry as well as by a large array of optically-pumped Cs magnetometers.

2.1 The n2EDM concept

The measurement relies on a precise estimation of f_n – the precession frequency of polarized ultracold neutrons stored in a weak magnetic field B and a strong electric field E . The neutron EDM is obtained by comparing the precession frequencies in the anti-parallel ($\uparrow\downarrow$) and parallel ($\uparrow\uparrow$) configurations of the magnetic and electric fields:

$$d_n = \frac{\pi \hbar}{2|E|} (f_{n,\uparrow\downarrow} - f_{n,\uparrow\uparrow}). \quad (1)$$

The statistical sensitivity in the former nEDM experiment [4] was limited by ultracold neutron counting statistics, which depend on the intensity of the UCN source, the efficiency of the UCN transport system, and the size and quality of the storage chambers. Independent of possible improvements of the yield of the PSI UCN source, the guideline for the conceptual design of the new apparatus was to maximize the neutron counting statistics while keeping the systematic effects under control. This will be achieved with a large UCN storage volume and an optimized UCN transport system, placed in a well-controlled magnetic-field environment.

Fig. 1 Cut through the central part of the n2EDM apparatus. Two vertically stacked storage (Ramsey spin-precession) chambers, filled with polarized UCNs and Hg atoms, are embedded in the same vertical magnetic field \mathbf{B} , but with opposite electric-field directions \mathbf{E}

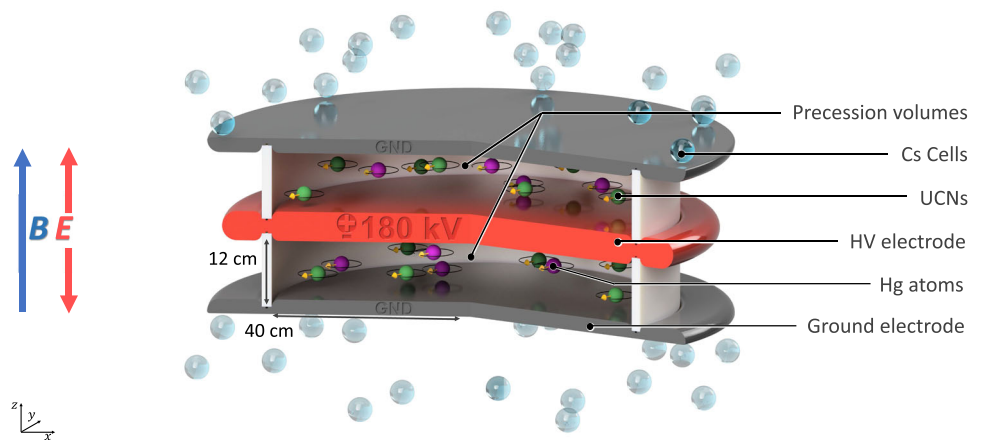


Figure 1 shows the basic concept of the n2EDM experiment. The design of the apparatus is based on two key features: (i) two cylindrical storage (Ramsey spin-precession) chambers, one stacked above the other; (ii) a combination of mercury and cesium magnetometry. The storage volumes are separated by the shared high-voltage electrode, and are each confined at the opposite end by a ground electrode and radially by an insulating ring. In addition to doubling the storage volume, the twin-chamber arrangement also permits simultaneous measurement of the neutron precession frequencies for both electric-field directions. Below we give short overviews of the core systems of the n2EDM apparatus, which will be presented in more detail in Sect. 5.

Precession chambers

- Each of the two precession chambers has internal diameter $D = 80$ cm and height $H = 12$ cm. The choice of the dimensions is explained in Sects. 3.1 and 5.1.1.
- As noted above the upper and lower chambers are separated by the common high-voltage (HV) electrode, which has a thickness of 6 cm. As in the previous experiment [4], the electrodes will be made of aluminum coated with diamond-like carbon and the insulator rings will be of polystyrene coated with deuterated polystyrene.
- The precession-chamber stack will be installed inside an aluminum vacuum vessel with an internal volume of approximately $1.6 \text{ m} \times 1.6 \text{ m} \times 1.2 \text{ m}$. This design allows for the optional installation of a double chamber with inner diameter of up to 100 cm, for a possible future upgrade of the experiment.

UCN polarization, transport and detection

- Neutrons arriving from the PSI UCN source are fully polarized using a 5 T superconducting magnet.
- Neutron guides made of coated glass tubes with ultralow surface roughness connect the precession chambers first to the UCN source and then to the detectors. This is achieved by different operational modes of the so-called UCN switch (see Sect. 5.1.3).

- Neutrons are counted by a spin-sensitive detection system based on fast gaseous detectors (see Sect. 5.1.4)

Magnetic shielding

To shield the experiment from external variations in the magnetic field, the sensitive part of the apparatus is installed inside a magnetic shield that has both passive and active components (see Sect. 5.2):

- The passive magnetic shield is provided by a large multi-layer cubic magnetically shielded room (MSR) with inner dimensions of $2.93 \text{ m} \times 2.93 \text{ m} \times 2.93 \text{ m}$.
- The active magnetic shield consists of eight actively-controlled coils placed around the MSR on a dedicated grid spanning a volume of about 1000 m^3 .

Magnetic-field generation

- A large coil will be installed inside the MSR (but outside the vacuum vessel) in order to produce a highly uniform vertical magnetic field B_0 throughout a large volume. The coil is designed to operate in the range $1 \mu\text{T} < B_0 < 15 \mu\text{T}$. In the short to medium term it is intended to work with $B_0 = 1 \mu\text{T}$, as was the case in the previous single-chamber experiment, but other options are being considered for the future.
- In addition to the main coil, an array of 56 independent trim coils is used to achieve the required level of magnetic-field uniformity.
- A further seven “gradient coils” will produce specific field gradients that play an important role in the measurement procedure.
- RF coils will be installed inside the vacuum tank to generate the oscillating-field pulses applied in the Ramsey measurement cycles.

Magnetometry

- Within each of the storage chambers the volume-averaged magnetic field will be measured using polarized ^{199}Hg atoms injected into the volume at the beginning of the

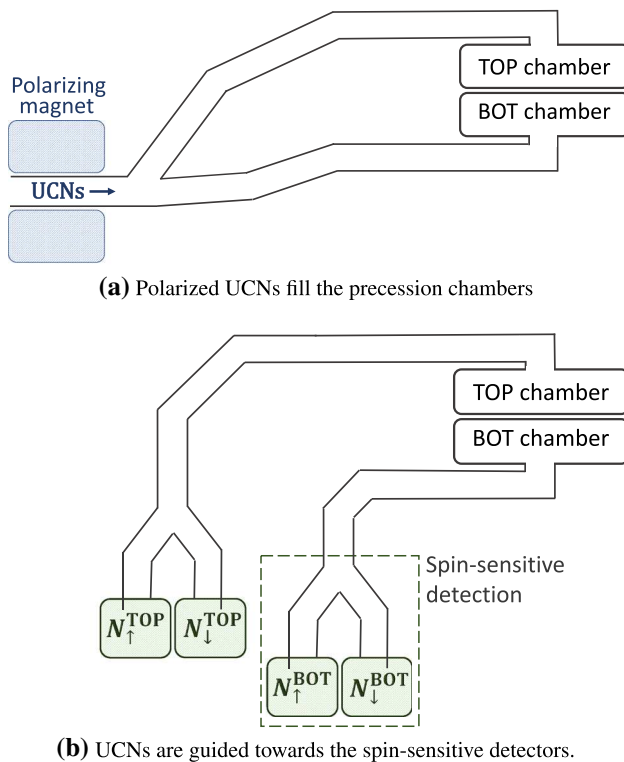


Fig. 2 Schematic view (not to scale) of the UCNs' path **a** while filling the precession chambers, and **b** following the Ramsey cycle, when transporting UCNs towards the spin-sensitive detectors for counting

cycle. The free-precession signal is observed using a UV light beam that traverses the chamber. Throughout the period prior to each measurement cycle the mercury gas is continuously polarized by optical pumping within a smaller adjacent volume separated from the main chamber by a shutter.

- An array of 114 Cs magnetometers will measure the field at a number of positions surrounding the chambers. This will provide instantaneous measurements of the magnetic-field uniformity.
- An automated magnetic-field mapper will be used offline for B-field cartography of all of the coils as well as for the correction and control of high-order gradients.

2.2 Measurement procedure

In the data taking mode, the full PSI proton beam will be kicked to the UCN source for 8 s every five minutes, producing a burst of ultracold neutrons. These UCNs are guided to the apparatus through the UCN transport system (see Fig. 2a). Along the way they are polarized (to almost 100% polarization level) by passage through the 5 T superconducting magnet.

Once the precession chambers have been filled with polarized UCNs, the UCN shutters close the chambers and the

neutrons are thereby stored. Ramsey's method of separated rotating fields is then performed:

1. A first horizontal rotating field is applied for $t_{\text{RF}} = 2$ s at a frequency $f_{\text{RF}} \approx |\gamma_n|/2\pi B_0 \approx 30$ Hz (for $B_0 \approx 1$ μ T). The amplitude of the field is chosen such that the neutron spins are tipped by $\pi/2$ into the (horizontal) plane perpendicular to the main magnetic field B_0 .
2. The neutron spins precess freely in the horizontal plane for a duration of $T = 180$ s (referred to as the "precession time"; see Sect. 3.3) at a frequency f_n which in principle will be slightly different in the two chambers.
3. A second rotating field, in phase with the first, is then applied for another 2 s. The vertical projection of the neutron spins (in units of $\hbar/2$) after the whole procedure is

$$A(f_{\text{RF}}) = -\alpha \cos \left[\pi \frac{f_{\text{RF}} - f_n}{\Delta\nu} \right], \quad (2)$$

where α (also referred to as the *visibility* of the resonance) is the final polarization of the ultracold neutrons, f_n is the neutron Larmor precession frequency to be measured, and

$$\Delta\nu = \frac{1}{2T + 8t_{\text{RF}}/\pi} \quad (3)$$

is the half-width of the resonance. The quantity A is called the *asymmetry*. Since f_n is likely to have a different value in each of the two chambers, the asymmetry in the top chamber A^{TOP} will not be identical to the asymmetry in the bottom chamber A^{BOT} . Notice however that the applied frequency f_{RF} is common to the two chambers.

4. The ultracold neutrons are released from the precession chambers by opening the UCN shutters, and are then guided to the spin analyzers (see Fig. 2b). Each chamber is connected to a dedicated spin-sensitive detector. These devices simultaneously and independently count the number of neutrons in each of the two spin states. These spin analyzers therefore provide, for each cycle, a measurement of the asymmetries for the top and bottom chambers:

$$A^{\text{TOP}} = \frac{N_{\uparrow}^{\text{TOP}} - N_{\downarrow}^{\text{TOP}}}{N_{\uparrow}^{\text{TOP}} + N_{\downarrow}^{\text{TOP}}} \quad \text{and} \quad A^{\text{BOT}} = \frac{N_{\uparrow}^{\text{BOT}} - N_{\downarrow}^{\text{BOT}}}{N_{\uparrow}^{\text{BOT}} + N_{\downarrow}^{\text{BOT}}}, \quad (4)$$

where $N_{\uparrow/\downarrow}^{\text{TOP/BOT}}$ are the numbers of neutrons from the top or bottom chamber, with spin parallel (\uparrow) or antiparallel (\downarrow) to the magnetic field.

Figure 3 shows an example of a measurement performed with the (single-chamber) nEDM apparatus scanning the

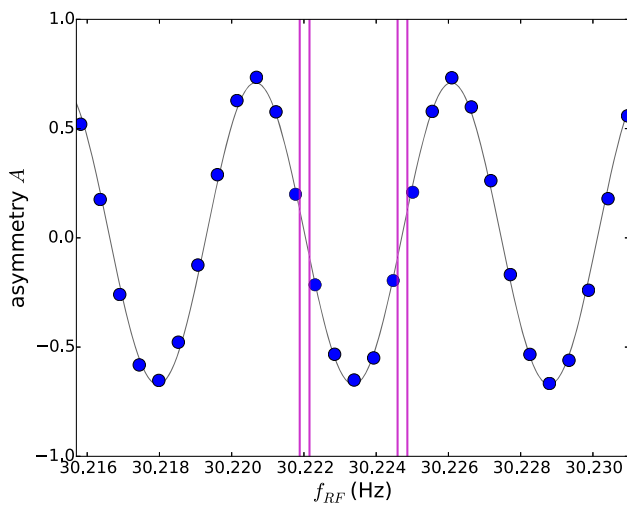


Fig. 3 The asymmetry $A = (N_{\uparrow} - N_{\downarrow}) / (N_{\uparrow} + N_{\downarrow})$ as a function of the applied frequency f_{RF} . The points represent experimental data where each point is a measurement cycle with a precession time of $T = 180$ s performed with the nEDM apparatus in September 2017 with the standard value of the magnetic field $B_0 = 1036.3$ nT corresponding to a Larmor precession frequency of 30.2235 Hz. The error bars are smaller than the size of the points. The line is the fit to the data using the function from Eq. 2. The vertical bars show the position of the four “working points” used in the nEDM data-taking in order to maximize the sensitivity

Ramsey resonance. If the parameter α is known, each cycle provides a measurement of f_n by inverting Eq. (2).

The statistical error arising from Poisson counting statistics for one measurement cycle is

$$\sigma(f_n) = \frac{\Delta\nu}{\pi\alpha\sqrt{N_{\uparrow} + N_{\downarrow}}} \left(1 - \frac{A^2}{\alpha^2}\right)^{-\frac{1}{2}}. \tag{5}$$

The maximal sensitivity is obtained for cycles measured at $A = 0$ where the slope of the resonance curve is highest. In fact, in nEDM data production mode the applied frequency f_{RF} is set sequentially to four “working points” indicated by the vertical bars in Fig. 3. Specifically, we set $f_{RF} = f_{n,0} \pm (1 \pm 0.1) \times \Delta\nu/2$, where we calculate $f_{n,0}$ from a measurement of the magnetic field performed in the previous cycle. Hence the four working points follow any possible magnetic-field drifts.

Magnetic-field drifts induce shifts of the resonance curve that are in practice much smaller than the width of the resonance $\Delta\nu$, but which nonetheless might be larger than the precision $\sigma(f_n)$ of the measurement; this will be discussed below. The slight departure of the working points from the two optimal points $f_{n,0} \pm \Delta\nu/2$ enable the extraction of the visibility α (as well as a small vertical offset of the resonance due to the imperfections of the spin analyzer system) by combining the data of many cycles of a run. This comes at the price of a sensitivity reduction of 2% in comparison to the optimal points.

With n2EDM, since the applied frequency is common to the two chambers it is important to ensure that the value of f_{RF} is set sufficiently close to the optimal points for the two chambers simultaneously. This is referred to as the *top-bottom resonance matching condition*. It imposes a requirement on the maximum permitted vertical gradient of the magnetic field. For n2EDM we require the shift between the resonance curves of the top and bottom chambers to be at most $0.2 \times \Delta\nu/2$ in order to limit the resulting sensitivity loss to values lower than 2%.

For a precession time of $T = 180$ s this corresponds to a maximum difference of 10 pT between the average field in the top and bottom chambers. With a separation between the centers of the two chambers of $H' = 18$ cm, the requirement on the vertical magnetic-field gradient is

$$\left| \frac{\partial B_z}{\partial z} \right| < 0.6 \text{ pT/cm}. \tag{6}$$

The measurement procedure described for one cycle is repeated continuously to form a sequence of data with many cycles.

Figure 4 shows an example of a sequence produced with the nEDM apparatus in 2016. For each cycle the neutron frequency f_n was extracted as explained above. The electric field polarity was alternated with a period of 112 cycles. As is evident from the figure, the neutron frequency is affected by the inevitable small drifts of the magnetic field. These drifts were compensated by the mercury co-magnetometer. At the beginning of a cycle, some mercury from the polarization cell is admitted to the precession chamber just after the UCN shutter is closed. A $\pi/2$ flip is then applied to the mercury spins, and they start to precess at a frequency of $f_{Hg} = \gamma_{Hg}/2\pi B_0 \approx 8$ Hz (for $B_0 \approx 1 \mu\text{T}$). The precession is recorded optically, by measuring the modulated transmission of a polarized horizontal UV beam. From the data one may then extract the mean precession frequency f_{Hg} of the mercury atoms sampling, to a very good approximation, *the same period of time and the same volume* as the precessing ultracold neutrons.

For each cycle we thus obtain simultaneous measurements both of the neutron frequency f_n and of the mercury frequency f_{Hg} . The neutron frequency includes contributions from both the magnetic and the electric dipole moments:

$$f_n = \left| \frac{\gamma_n}{2\pi} B_0 \right| \mp \frac{d_n}{\pi\hbar} |E|, \tag{7}$$

where the “-” sign refers to the parallel $\uparrow\uparrow$ configurations of the magnetic and electric fields and the “+” sign refers to the anti-parallel $\uparrow\downarrow$ configuration. The electric contribution, which is ultimately the goal of the search, is tiny: for $d_n = 10^{-26}$ e cm, $E = 15$ kV/cm and $B_0 = 1 \mu\text{T}$, the ratio between the electric and magnetic term is as small as 2×10^{-9} . The mercury precession frequency effectively

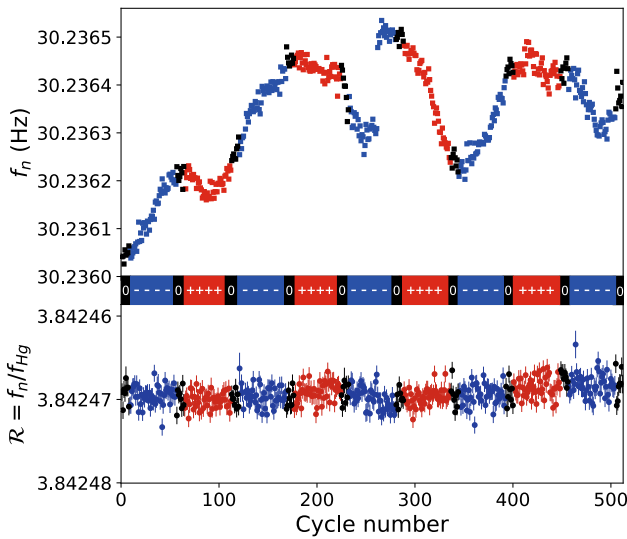


Fig. 4 A sequence of nEDM data produced in 2016; each point corresponds to a single measurement cycle. The upper plot shows the neutron frequency as a function of cycle number, whereas the lower plot shows the frequency ratio $\mathcal{R} = f_n/f_{Hg}$. The colors correspond to the high-voltage polarity (blue, negative; red, positive; black, zero)

has only a magnetic contribution: since the mercury EDM $d_{Hg} < 10^{-29} e \text{ cm}$ [5], the electrical term can be neglected. The frequency is then

$$f_{Hg} = \left| \frac{\gamma_{Hg}}{2\pi} B_0 \right|. \tag{8}$$

The ratio \mathcal{R} of neutron to mercury frequencies

$$\mathcal{R} \equiv \frac{f_n}{f_{Hg}} = \left| \frac{\gamma_n}{\gamma_{Hg}} \right| \mp \frac{|E|}{\pi \hbar f_{Hg}} d_n \tag{9}$$

is then free from the fluctuations of the magnetic field B_0 . This is illustrated in Fig. 4 where the ratio \mathcal{R} is plotted in the lower part. Notice that the co-magnetometer corrects for random drifts of the magnetic field that would spoil the statistical sensitivity *and also* for the B-field variations correlated with the electric field (due to leakage currents along the insulator for example) that would produce otherwise a direct systematic effect. In fact, Eq. (9) is an idealization. It is modified by several effects affecting either the neutron or mercury frequencies. For example, gradient drifts could induce shifts, as the one visible on the bottom panel of Fig. 4 after cycle 400. All known effects will be described in Sect. 4, where the associated systematic effects will be discussed.

Finally, with the single-chamber apparatus, the neutron EDM is calculated as follows:

$$d_n = \frac{\pi \hbar f_{Hg}}{2|E|} (\mathcal{R}_{\uparrow\downarrow} - \mathcal{R}_{\uparrow\uparrow}). \tag{10}$$

In n2EDM, both chambers host a mercury co-magnetometer, and each cycle will therefore provide the neutron and mercury Larmor precession frequencies in the two chambers

f_n^{TOP} , f_n^{BOT} , f_{Hg}^{TOP} and f_{Hg}^{BOT} . Therefore, we can form the two ratios

$$\mathcal{R}^{\text{TOP}} = f_n^{\text{TOP}}/f_{Hg}^{\text{TOP}}, \quad \mathcal{R}^{\text{BOT}} = f_n^{\text{BOT}}/f_{Hg}^{\text{BOT}}. \tag{11}$$

In principle, since the parallel and anti-parallel configurations of the fields are measured simultaneously in n2EDM, a measurement of d_n could be obtained without reversing the polarity of the electric field by calculating

$$d_n = \frac{\pi \hbar f_{Hg}}{2|E|} (\mathcal{R}_{\uparrow\downarrow}^{\text{TOP}} - \mathcal{R}_{\uparrow\uparrow}^{\text{BOT}}). \tag{12}$$

However, in order to compensate for shifts in \mathcal{R} arising from various effects described later in Sect. 4, the electric polarity of the central electrode will be reversed periodically as was done in the previous single-chamber nEDM experiment. The neutron EDM can then be calculated as follows:

$$d_n = \frac{\pi \hbar f_{Hg}}{4|E|} (\mathcal{R}_{\uparrow\downarrow}^{\text{TOP}} - \mathcal{R}_{\uparrow\uparrow}^{\text{TOP}} + \mathcal{R}_{\uparrow\downarrow}^{\text{BOT}} - \mathcal{R}_{\uparrow\uparrow}^{\text{BOT}}). \tag{13}$$

In the following section we will address the statistical and systematic errors of this measurement.

3 Projected statistical sensitivity

The statistical sensitivity of the measurement will be limited by the UCN counting statistics. By combining the expression for the statistical sensitivity $\sigma(f_n)$ of the neutron frequency at the optimal point $A = 0$ as given by Eq. (5) with Eq. (1), the following statistical sensitivity on the neutron EDM per cycle may be derived:

$$\sigma(d_n) = \frac{\hbar}{2\alpha ET\sqrt{N}}, \tag{14}$$

where α is the measured neutron polarization at the end of the Ramsey cycle, T is the neutron precession time, E is the magnitude of the electric field and N is the total number of neutrons counted from the two chambers.

Table 1 summarizes the expected values for each of those contributions. It is based on the demonstrated sensitivity of the nEDM apparatus, the average UCN source performance in 2016 and our Monte-Carlo simulation of the n2EDM UCN system. We will next discuss each of the parameters in Eq. (14).

3.1 UCN counts N

The prediction of the number of detected neutrons in the n2EDM apparatus is based on comprehensive Monte-Carlo simulations of the PSI UCN source, guides, and the experiment, treated as one system, performed with the MCUCN code [17,28].

As far as the UCN source and guides leading to the beamports were concerned, the relevant surface parameters of the

Table 1 Comparison between (i) the achieved performance of the nEDM apparatus during data taking at PSI in 2016, (ii) the nominal parameters for the n2EDM design (see Eq. (14) and text). In both cases coatings are made of diamond-like carbon (DLC) for the electrodes and deuterated polystyrene (dPS) for the insulator ring. The number of neutrons N is the total number of UCN counted (in the two chambers in case of n2EDM) after a precession time of $T = 180$ s. The error on the neutron frequency $\sigma(f_n)$ is given for one cycle and one chamber. Also shown are the d_n sensitivities in one day and the final accumulated sensitivities. The final sensitivity listed in the first column is that actually achieved in 2016; that of the second column represents the achievable sensitivity in n2EDM after an assumed 500 days of data taking, which could be achieved in four calendar years

	nEDM 2016	n2EDM
Chamber	DLC and dPS	DLC and dPS
Diameter D	47 cm	80 cm
N (per cycle)	15,000	121,000
T	180 s	180 s
E	11 kV/cm	15 kV/cm
α	0.75	0.8
$\sigma(f_n)$ per cycle	9.6 μ Hz	3.2 μ Hz
$\sigma(d_n)$ per day	11×10^{-26} e cm	2.6×10^{-26} e cm
$\sigma(d_n)$ (final)	9.5×10^{-27} e cm	1.1×10^{-27} e cm

neutron optics and the UCN flux were calibrated using dedicated test measurements of the achievable density at the West-1 beamport in 2016 [29,30]. The simulation parameters and values are listed in Table 4 of [17]. These are: optical (Fermi) potential, loss per bounce parameter, fraction of diffuse (Lambertian) reflections, and the attenuation constant of the windows. Separate values were considered for the following parts: the aluminum lid above the sD2 converter, the vertical NiMo coated guide above the sD2 vessel, the DLC coated storage vessel of the source, the NiMo coated neutron guides to the beamports, and the aluminum vacuum separation windows in the SC magnet and detectors.

For the n2EDM apparatus, the following parameters were used: For the NiMo coated guides, an optical potential of 220 neV as measured with cold-neutron reflectometry; a loss per bounce parameter of 3×10^{-4} as measured in [31] (with a 1σ error added); and an upper limit of 2% for fraction of Lambertian reflections (as benchmarked for NiMo on glass). The NiMo-coated aluminum guide inserts have a small surface fraction, and were assumed to be highly polished and thus not to increase the overall fraction of diffuse reflections above 2%. For the loss-per-bounce parameter of the precession chambers, we use a value of 2.8×10^{-4} , extracted from storage measurements with the single chamber [32] (with a 1σ error added). This was very close to the values reported in [33] for DLC (on aluminum foil at 300 K), and in [34] for dPS. We used optical potentials of 230 neV for DLC [17] and 165 neV for dPS, with the latter being the average of measured and theoretical values [34] (because of a large

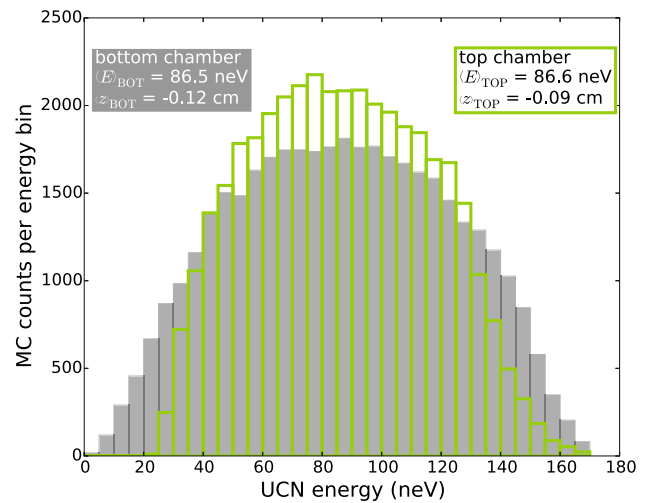


Fig. 5 Simulated energy spectra of the detected UCNs. The energy is the sum of the kinetic and the gravitational potential energy calculated at the floor levels of the respective chambers

measurement error). The diffuse reflection fraction for the electrodes was 2%, and a maximal roughness was assumed for the insulator ring (Lambertian reflections, corresponding to a diffuse reflection fraction of 100%).

The geometry of the parts of the n2EDM experiment dependent upon UCN optics, and in particular the height of the chambers above the beamline, was optimized in terms of UCN statistics. The optimal height is significantly lower than the height of the previous nEDM experiment. The simulated energy spectra of detected UCNs calculated at the bottom level of the chambers are shown in Fig. 5.

Due to the lower elevation of the chambers with respect to the beamline, the spectra of the stored UCNs are expected to be harder in comparison with the single chamber nEDM experiment. The absence of UCN at lower energies in case of the upper chamber is caused by filling from the top. The maximum attainable energy for the two spectra is determined mainly by the 165 neV optical potential of the insulator ring, and to a lesser extent by the difference in elevation.

The chosen design, with an 80 cm diameter double chamber of 12 cm individual heights, permits an increase of the total number of detected neutrons after 188 s storage time (i.e. 180 s precession time) from 15,000 in nEDM to 121,000 in n2EDM. The uncertainty of the calibration from MC counts to real UCN counts is $\pm 15\%$ [35]. This considerable gain in UCNs is the result of (i) a double chamber as compared to a single chamber, (ii) an increase of the volume of each individual chamber by a factor of three, (iii) an increase in the inner diameter of the UCN guides (6.6–13 cm), (iv) optimization of the vertical position of the precession chambers; the optimum was found to be 80 cm above the beamport. None of these estimates include any of the improvements in

the performance of the PSI UCN source that have taken place since 2017.

3.2 Electric field strength E

In the single-chamber nEDM apparatus the electric field was generated by charging the top electrode using a bipolar high-voltage supply of ± 200 kV. The top electrode was ramped regularly to ± 132 kV, while the bottom electrode was kept at ground potential. The maximum voltage was limited by the presence of many optical fibers in contact with both the charged electrode and the grounded vacuum tank. These fibers were used to operate six Cs magnetometers situated on the top electrode.

The same system, without the Cs magnetometers and the fibers, could sustain higher electric fields; tests were carried out up to 16.6 kV/cm.

In the n2EDM apparatus all Cs magnetometers will be mounted at ground potential, above and below the electrode stack. The electric field will not be limited by the presence of optical fibers close to the charged central electrode, and we expect to be able to operate the system at voltages of 200 kV or higher. However, a safe standard operation is anticipated at voltages of ± 180 kV, corresponding to an electric field of ± 15 kV/cm.

3.3 Precession time T

The choice of the precession time T results from balancing two dominant effects: increasing T reduces the width of the Ramsey resonance and tends to improve the sensitivity, but at the same time the number of surviving neutrons $N(T)$ decreases, and this decreases the sensitivity. Additionally, one has to take into account the fact that increasing T results in fewer measurement cycles per day. In detail, the daily sensitivity σ_{day} follows from the cycle sensitivity given by Eq. (14) and has the form

$$\sigma_{\text{day}} = \frac{\sigma(d_n)}{\sqrt{n_{\text{cyc}}}} = \frac{\hbar}{2\alpha E} \frac{1}{T\sqrt{N(T)}} \sqrt{\frac{T + T_{\text{dead}}}{24 \text{ h}}}, \quad (15)$$

where n_{cyc} is the number of cycles per day, the total length of a cycle being the sum of the precession time T and a dead time T_{dead} accounting for filling and emptying the chambers as well as ramping the electric field. In Eq. (15) we assume that the visibility α is not decreasing with time (i.e. we neglect UCN depolarization). This important point will be discussed later. The loss of neutrons in the chambers is encoded in the function $N(T)$; this is the main effect driving the choice of T .

In Fig. 6 we show a simulated storage curve, i.e. the number of neutrons counted after a storage duration t as a function of t . The storage duration $t = T + 8$ s within the EDM

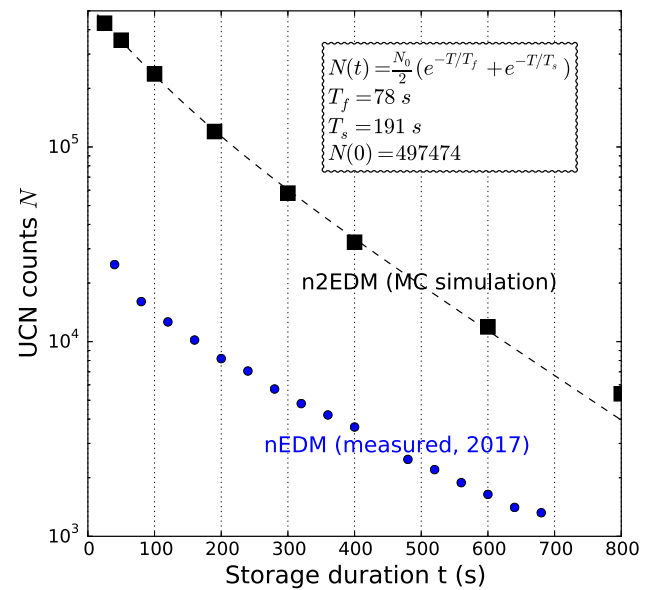


Fig. 6 Storage curve measured with nEDM in 2017 (blue points) and simulated storage curve in n2EDM (black squares). The n2EDM storage curve is plotted as a function of the storage time t . It is fitted with a double exponential model as a function of the precession time $T = t - 8$ s, where N_0 is the number of neutrons at zero precession time and T_f and T_s are the fast and slow time constants

cycles is a little longer than the precession time T in order to account for the additional time required to fill the mercury atoms, apply the mercury pulse (4s) and apply the two neutron pulses (4s).

As usual for UCN storage chambers at room temperature, the storage curve departs significantly from a pure exponential decay because the dominating losses originate from wall collisions rather than from beta decay ($\tau_n \approx 880$ s). Wall-collision rates and loss probability per collision are a function of neutron kinetic energy. This results in energy-dependent UCN loss rates and a clear departure from a simple exponential decay. We fit the storage curve with a double-exponential model assuming only two groups of neutrons equi-populated at $T = 0$.

In Fig. 7 we plot the projection of the daily sensitivity, Eq. (15), for the baseline design of n2EDM. For the sensitivity estimation we set $T = 180$ s (as in [4]).

3.4 Neutron polarisation α

In the perfect case of no depolarization during the precession period, the visibility of the Ramsey resonance would be as high as the initial polarization,¹ which was measured to be $\alpha_0 = 0.86$ in the single-chamber nEDM spectrometer.

¹ The term “initial polarization” is in fact the product of the polarization with the analyzing power of the detection system, and is limited by depolarization in the detection process.

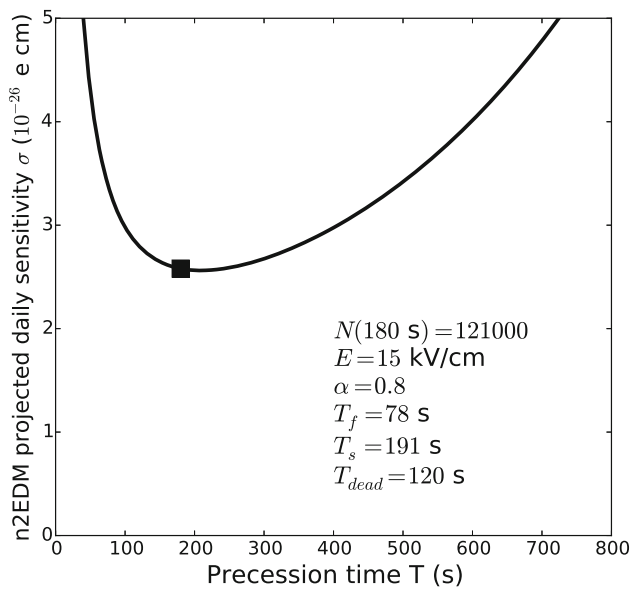


Fig. 7 Projected daily sensitivity with n2EDM as a function of the precession time T . The baseline parameter $T = 180$ s is indicated by the black square

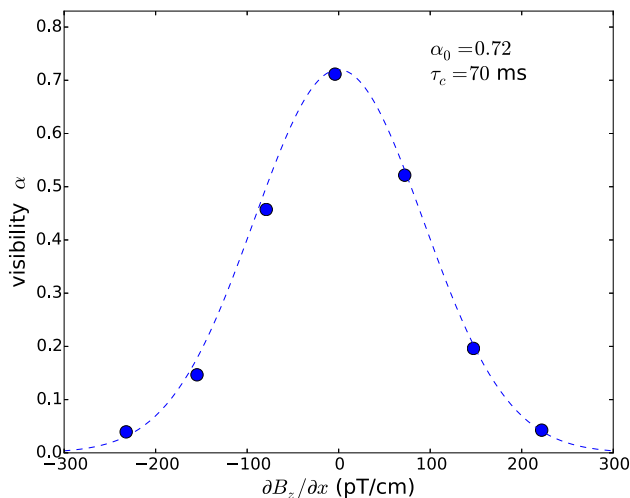


Fig. 8 Measurement of the visibility α after a precession time of $T = 180$ s as a function of an applied horizontal gradient $G_{1,1} = \partial B_z/\partial x$ performed with the nEDM apparatus in 2017. The dashed line corresponds to the exponential decay model $\alpha = \alpha_0 \exp(-T/T_{2,\text{mag}}(G_{1,1}))$, where $1/T_{2,\text{mag}}(G_{1,1})$ is given by Eq. (18) with $\tau_c = 70$ ms

In fact, the final polarization under measurement conditions ($T = 180$ s) was 0.75 on average.

The decay of polarization during storage $d\alpha/dt$ arises from three different contributions:

$$\frac{d\alpha}{dt} = -\frac{\alpha}{T_{\text{wall}}} + \dot{\alpha}_{\text{grav}} - \frac{\alpha}{T_{2,\text{mag}}} \tag{16}$$

We briefly discuss these effects, and we refer to Ref. [36] for a more complete treatment of this subject.

- The first contribution $-\alpha/T_{\text{wall}}$ is due to depolarization during wall collisions. The depolarization rate $1/T_{\text{wall}} = \nu\beta$ is given by the product of the wall collision rate ν , which is determined by the UCN spectrum, and the depolarization probability at each wall collision β , which is set by the surface properties of the chamber. This depolarization mechanism affects equally the transverse and the longitudinal polarization of the neutrons. Dedicated measurements performed with the nEDM apparatus in 2016 resulted in a determination of $T_{\text{wall}} \approx 4000$ s. In n2EDM we expect about the same values for β and ν . We anticipate that this process will reduce α from 0.86 to 0.83 after 180 s.
- A second contribution $\dot{\alpha}_{\text{grav}}$, called *gravitationally enhanced depolarization* [37,38], was identified in the nEDM single-chamber experiment. It is due to the vertical striation of UCN under gravity in combination with a vertical magnetic-field gradient. Neutrons with different kinetic energies have different mean heights \bar{z} due to gravity. Therefore, in the presence of a vertical field gradient, neutrons with different kinetic energies have different spin precession frequencies. This results in a relative dephasing, which in turn is visible as an effective depolarization quantified by the following expression:

$$\dot{\alpha}_{\text{grav}} = -\gamma_n^2 \left(\frac{\partial B_z}{\partial z} \right)^2 \text{Var}[\bar{z}] t. \tag{17}$$

The variance of the distribution of \bar{z} is a quantity that depends on the total height of the chamber H and on the energy spectrum of the stored UCNs. It was measured to be $\text{Var}[\bar{z}] \approx 0.2 \text{ cm}^2$ in the previous nEDM experiment and it is expected to be smaller in n2EDM: 0.07 cm^2 in the bottom chamber and 0.002 cm^2 in the top chamber, according to the simulated energy spectra. For datataking with the nEDM experiment, the vertical gradient was scanned in the range $-30 \text{ pT/cm} < \partial B_z/\partial z < 30 \text{ pT/cm}$ as part of the analysis strategy to correct for systematic effects. The cost of that is a decrease of the α parameter due to the gravitationally enhanced depolarization of about 0.05 on average. In n2EDM experiment the wide-range gradient scan is no longer necessary. The experiment will be operated in a much smaller range, $-0.6 \text{ pT/cm} < \partial B_z/\partial z < 0.6 \text{ pT/cm}$, in order to meet the top-bottom resonance matching condition discussed earlier. In this case the decrease in α will be negligible.

- The last contribution $-\alpha/T_{2,\text{mag}}$ corresponds to the *intrinsic depolarization*, i.e. the irreversible process of polarization decay within energy groups due to the random motion in a static but non-uniform field. Indeed, a neutron sees a longitudinal magnetic disturbance $b_z(t) = B_z(\mathbf{r}(t)) - \langle B_z \rangle$ as it moves randomly within the chamber with a trajectory $\mathbf{r}(t)$. Spin-relaxation theory [39] allows

calculation of the decay rate of the transverse polarization due to this disturbance, to second order in the perturbation, as:

$$\frac{1}{T_{2,\text{mag}}} = \gamma_n^2 \int_0^\infty \langle b_z(t)b_z(t+\tau) \rangle d\tau = \gamma_n^2 \langle b_z^2 \rangle \tau_c, \quad (18)$$

where τ_c is the correlation time, $\langle b_z(t)b_z(t+\tau) \rangle$ is the autocorrelation of the longitudinal disturbance and $\langle b_z^2 \rangle$ is the average of the quantity b_z^2 over all particles in the chamber, which in this case is the same as the volume average of $(B_z(r) - \langle B_z \rangle)^2$. In fact, Eq. (18) serves as a definition of the correlation time. It is important to notice that horizontal gradients $G_{1,1} = \partial B_z / \partial x$ (fields of the type $B_z = B_0 + G_{1,1}x$) are much more effective in this depolarization channel compared with vertical gradients $G_{1,0} = \partial B_z / \partial z$ (fields of the type $B_z = B_0 + G_{1,0}z$), due to the aspect ratio of the chambers (the height is significantly shorter than the diameter). Figure 8 shows a measurement of the visibility α as a function of an applied (artificially large) horizontal field gradient $G_{1,1} = \partial B_z / \partial x$ performed with the nEDM apparatus in 2017. In this case the mean squared inhomogeneity can be calculated to be

$$\langle b_z^2 \rangle = G_{1,1}^2 \langle x^2 \rangle = G_{1,1}^2 \frac{R^2}{4}, \quad (19)$$

where R is the radius of the chamber; $R = 23.5$ cm in the case of the previous single-chamber experiment. The measurement resulted in a determination of $\tau_c(\text{nEDM}) = 70$ ms. The correlation time scales as $\tau_c \propto R/v_h$, where $v_h = \langle \dot{x}^2 + \dot{y}^2 \rangle \approx 3$ m/s is the horizontal velocity of UCNs. However, the precise value is complicated to predict; it depends on the velocity spectrum of the stored neutrons, the degree of specularly of the collisions, and also on the shape of the non-uniform field. For an estimate of the UCN correlation time in the n2EDM, we simply extrapolate the value measured in the nEDM experiment by taking into account the increase in diameter of the chambers:

$$\tau_c(\text{n2EDM}) = \tau_c(\text{nEDM}) \times \frac{80 \text{ cm}}{47 \text{ cm}} = 120 \text{ ms}. \quad (20)$$

For a given field gradient, the depolarization decay rate (18) scales as the third power of the radius of the chamber, because τ_c is linear in R and $\langle b_z^2 \rangle$ is quadratic in R . This is a major challenge for the design of n2EDM because of the increased chamber radius; in fact, the intrinsic depolarization sets an important requirement for the generation of the magnetic field.

In order to reach a final visibility of $\alpha(180 \text{ s}) > 0.80$ in n2EDM, we require that the decrease of α due to the intrinsic depolarization to be not more than 2%. This corresponds to $T_{2,\text{mag}} > 9000$ s. Using Eqs. (18) and (20) we derive the corresponding requirement on the root mean square of the spatial variations of the field in the chamber:

$$\sigma(B_z) = \sqrt{\langle b_z^2 \rangle} < 170 \text{ pT}. \quad (21)$$

Notice that this requirement concerns the absolute value of the field, not the relative value $\sigma(B_z)/B_0$. It applies to the baseline choice $B_0 = 1 \mu\text{T}$ as well as for any other B_0 field.

3.5 Additional statistical fluctuations and final remarks

The expression Eq. (14) only takes into account the statistical error on the neutron frequency. In fact, when propagating the error in the \mathcal{R} ratio, the errors on both the neutron frequency and the mercury frequency contribute to the neutron EDM given by Eq. (13). Taking into account the mercury error, the total statistical error is increased by a factor

$$\sqrt{1 + \left(\frac{\sigma(f_{\text{Hg}})}{\sigma(f_n)} \mathcal{R} \right)^2}. \quad (22)$$

In addition, there are further sources of statistical fluctuations of the \mathcal{R} ratio, in particular the fluctuations of the magnetic-field gradient (due to the gravitational shift, see Sect. 4).

The goal for the mercury co-magnetometer design is to reduce the contribution from $\sigma(f_{\text{Hg}})$ to less than 2% of the total statistical error, which corresponds to $\sigma(f_{\text{Hg}}) < 0.05 \times \sigma(f_n) = 0.2 \mu\text{Hz}$ for one cycle of measurement in one chamber. In terms of magnetic-field sensitivity, this corresponds to 25 fT. In turn, the sensitivity goal of the co-magnetometer sets a goal for the temporal stability of the magnetic field during the expected 180 s spin-precession time. Indeed, the drift of the magnetic field during the precession time has an impact upon the mercury frequency extraction. In order to ensure that the accuracy of the co-magnetometer is not reduced by magnetic-field drifts, it should be of the same order as the magnetometer precision, i.e. $\sigma(B) \sim 25$ fT over 180 s.

Assuming the same UCN source performance that was provided in 2016 (see Table 1), we plan about 500 days of data taking, which can be accomplished within four years of operation. Therefore, after completion of the data taking, the total accumulated statistical sensitivity is expected to be at the level of $\sigma(d_n) = 1 \times 10^{-27} e \text{ cm}$. Further upgrades and UCN source improvements could allow the measurement to reach sensitivities well into the $10^{-28} e \text{ cm}$ range.

4 Frequency shifts and systematic effects

There are a number of known effects that shift the neutron and mercury frequencies from the ideal case given by Eqs. (7) and (8). These are all encapsulated in the following formula, which is valid for individual chambers:

$$\mathcal{R} = \frac{f_n}{f_{\text{Hg}}} = \left| \frac{\gamma_n}{\gamma_{\text{Hg}}} \right| (1 + \delta_{\text{elec}} + \delta_{\text{mag}} + \delta_{\text{other}}), \tag{23}$$

where the three terms δ_{elec} , δ_{mag} and δ_{other} are much smaller than one. The first contribution

$$\delta_{\text{elec}} = \delta_{\text{EDM}}^{\text{true}} + \delta_{\text{EDM}}^{\text{false}} + \delta_{\text{quad}} \tag{24}$$

corresponds to the electrical terms (i.e. they are absent in zero electric field). The second contribution

$$\delta_{\text{mag}} = \delta_{\text{grav}} + \delta_{\text{T}} \tag{25}$$

corresponds to the nonuniform magnetic terms (i.e. they are absent in a purely uniform magnetic field). The last contribution δ_{other} corresponds to all other effects.

The true EDM term $\delta_{\text{EDM}}^{\text{true}}$ is induced by the linear-in-electric field frequency shifts from the true neutron and mercury EDM:

$$\delta_{\text{EDM}}^{\text{true}} = \pm \frac{2}{\hbar |\gamma_n B_0|} |E| (d_n + d_{n \leftarrow \text{Hg}}), \tag{26}$$

where the + sign corresponds to the anti-parallel ($\uparrow\downarrow$ or $\downarrow\uparrow$) configurations, and the – sign corresponds to the parallel ($\uparrow\uparrow$ or $\downarrow\downarrow$) configurations. The contribution of the mercury EDM:

$$d_{n \leftarrow \text{Hg}} = \left| \frac{\gamma_n}{\gamma_{\text{Hg}}} \right| d_{\text{Hg}} = (0.8 \pm 1.2) \times 10^{-29} \text{ e cm}, \tag{27}$$

is negligible. Here we have used the most recent measurement by the Seattle group $d_{\text{Hg}} = (2.2 \pm 3.1) \times 10^{-30} \text{ e cm}$ [5].

All of the other δ shifts could generate two types of undesirable consequences. First, they could induce random fluctuations of the ratio \mathcal{R} which would increase the statistical error. Second, any correlation between the electric-field polarity and one of these terms will induce a direct systematic effect. Although the first type imposes requirements on the stability of environmental variables, in particular the magnetic-field gradients, it is possible to make these additional fluctuations negligible and we will not address them. Here we will concentrate on the latter effects which, following Eq. (13), correspond to a systematic effect of

$$\delta d_n = \frac{\pi \hbar f_{\text{Hg}}}{4|E|} \left(\delta_{\uparrow\downarrow}^{\text{TOP}} - \delta_{\uparrow\uparrow}^{\text{TOP}} + \delta_{\uparrow\downarrow}^{\text{BOT}} - \delta_{\uparrow\uparrow}^{\text{BOT}} \right), \tag{28}$$

when considering the two-chamber extraction of the neutron EDM.

Before we describe all of the δ terms in detail, we pause to explain the different conventions used here.

For the sign conventions, we define an angular frequency ω as an algebraic quantity the sign of which is determined with respect to the z axis pointing upwards, i.e. $\omega > 0$ corresponds to a rotation in the horizontal plane following the right hand rule. Note that, since $\gamma_n < 0$, the neutron angular frequency $\omega_n = \gamma_n B_0$ is negative when the magnetic field is pointing up. It is opposite for the mercury atoms because $\gamma_{\text{Hg}} > 0$. The quantity B_0 is likewise algebraic. It is positive when the field is pointing up and negative when the field is pointing down. The frequencies are defined as positive quantities, i.e. $f = |\omega|/2\pi$.

To describe the magnetic-field non-uniformities, we use the framework developed in [36] which defines a parametrization of a general field in the form of

$$\mathbf{B}(\mathbf{r}) = \sum_{l \geq 0} \sum_{m=-l}^l G_{l,m} \boldsymbol{\Pi}_{l,m}(\mathbf{r}), \tag{29}$$

where $G_{l,m}$ are the generalized gradients and the functions $\boldsymbol{\Pi}_{l,m}$, or *modes*, form a basis of harmonic functions constructed from the solid harmonics. The modes expressed in Cartesian coordinates are polynomials in x, y, z of degree l . Note that the center of the system of coordinates is in the middle of the two chambers. The $G_{l,m}$ gradients describe the field in the entire inner experiment where the two chambers are located.

In cylindrical coordinates ρ, ϕ, z the modes take the form of

$$\boldsymbol{\Pi}_{l,m}(\mathbf{r}) = \tilde{\boldsymbol{\Pi}}_{l,m}(\rho, z) \cdot \mathbf{y}_m(\phi) \tag{30}$$

with $\tilde{\boldsymbol{\Pi}}_{l,m}(\rho, z)$ being a polynomial function of ρ and z of degree l , and the azimuthal part is

$$\mathbf{y}_m(\phi) = \begin{cases} \cos(m\phi)\mathbf{e}_\rho + \sin(m\phi)\mathbf{e}_\phi + \cos(m\phi)\mathbf{e}_z & \text{if } m \geq 0, \\ \sin(m\phi)\mathbf{e}_\rho + \cos(m\phi)\mathbf{e}_\phi + \sin(m\phi)\mathbf{e}_z & \text{if } m < 0. \end{cases}$$

Explicit expressions for the relevant modes are specified in Table 2.

4.1 Gravitational shift and uncompensated gradient drift

The kinetic energy of ultracold neutrons is so low that their spatial distribution is significantly affected by gravity, and their center of mass lies a fraction of a centimeter below the geometric center of the chamber. In contrast, the mercury atoms form a gas at room temperature that fills the precession chamber nearly uniformly. This results in slightly different average magnetic fields being sampled by the neutrons and the atoms in the presence of a vertical magnetic-field gradient. This effect is called the gravitational shift δ_{grav} . In the framework of the harmonic decomposition of the field up to the second order, the volume average of the vertical

Table 2 Expressions for the relevant harmonic modes $\Pi_{l,m}$ in cylindrical coordinates

l	m	$\Pi_{l,m}$
0	-1	$\mathbf{e}_y = \sin \phi \mathbf{e}_\rho + \cos \phi \mathbf{e}_\phi$
0	0	\mathbf{e}_z
0	1	$\mathbf{e}_x = \cos \phi \mathbf{e}_\rho - \sin \phi \mathbf{e}_\phi$
1	-2	$\rho(\sin 2\phi \mathbf{e}_\rho + \cos 2\phi \mathbf{e}_\phi)$
1	-1	$z(\sin \phi \mathbf{e}_\rho + \cos \phi \mathbf{e}_\phi) + \rho \sin \phi \mathbf{e}_z$
1	0	$-\frac{1}{2}\rho \mathbf{e}_\rho + z \mathbf{e}_z$
1	1	$z(\cos \phi \mathbf{e}_\rho - \sin \phi \mathbf{e}_\phi) + \rho \cos \phi \mathbf{e}_z$
1	2	$\rho(\cos 2\phi \mathbf{e}_\rho - \sin 2\phi \mathbf{e}_\phi)$
2	0	$-\rho z \mathbf{e}_\rho + (z^2 - \frac{1}{2}\rho^2) \mathbf{e}_z$
3	0	$\frac{3}{8}\rho(-4z^2 + \rho^2) \mathbf{e}_\rho + (z^3 - \frac{3}{2}z\rho^2) \mathbf{e}_z$
4	0	$\frac{1}{2}\rho(-4z^3 + 3\rho^2 z) \mathbf{e}_\rho + (z^4 - 3z^2\rho^2 + \frac{3}{8}\rho^4) \mathbf{e}_z$
5	0	$\frac{5}{16}\rho(-8z^4 + 12\rho^2 z^2 - \rho^4) \mathbf{e}_\rho + (z^5 - 5z^3\rho^2 + \frac{15}{8}z\rho^4) \mathbf{e}_z$

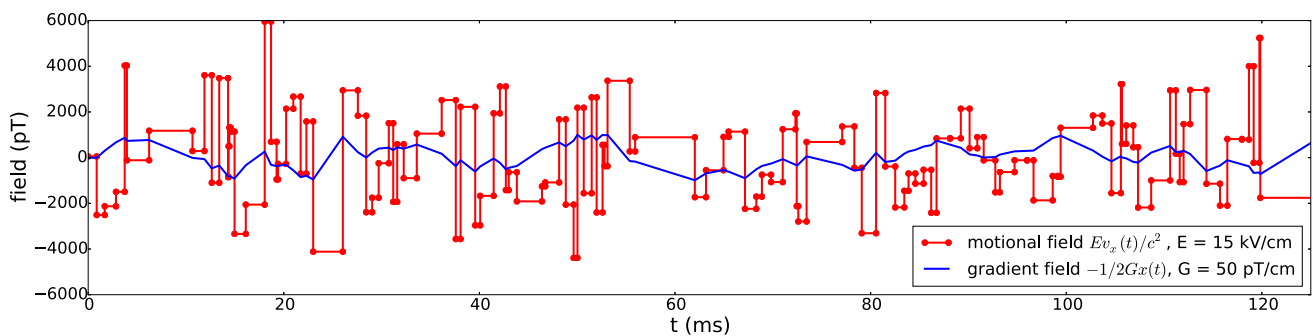


Fig. 9 Monte-Carlo simulation of the transverse field seen by a mercury atom in thermal ballistic motion inside one n2EDM precession chamber. Red lines with dots: motional field along y induced by the electric field. Blue line: non-uniform field along x in a (very large) gradient of $G_{1,0} = 50$ pT/cm

component is

$$\delta_{\text{grav}}^{\text{TOP}} = (G_{1,0} + H'G_{2,0}) \frac{\langle z \rangle_{\text{TOP}}}{B_0}, \tag{31}$$

$$\delta_{\text{grav}}^{\text{BOT}} = (G_{1,0} - H'G_{2,0}) \frac{\langle z \rangle_{\text{BOT}}}{B_0}, \tag{32}$$

where $\langle z \rangle_{\text{TOP}}$ and $\langle z \rangle_{\text{BOT}}$ are the center of mass offset between the neutron and mercury in the top and bottom chamber, and $H' = 18$ cm is the height difference between the centers of the top and bottom chambers.

The gravitational shift could induce an additional statistical error (due to an instability of the gradients $G_{1,0}$ or $G_{2,0}$) and a systematic effect (due to a direct correlation of the gradients with the electric-field polarity). For simplicity we will only discuss the effect of the linear gradient $G_{1,0}$, and will neglect the second order term $G_{2,0}$. In the nEDM single-chamber apparatus we measured a value of $\langle z \rangle = -0.39$ cm. For the n2EDM estimates we use the values calculated from the simulated energy spectra in Fig. 5, $\langle z \rangle_{\text{TOP}} = -0.09$ cm and $\langle z \rangle_{\text{BOT}} = -0.12$ cm.

A fluctuation of the gradient $G_{1,0}$ with a RMS value of $\sigma(G)$ induces a contribution to the fluctuation of \mathcal{R}_{TOP} –

\mathcal{R}_{BOT} of

$$\sigma(\mathcal{R}_{\text{TOP}} - \mathcal{R}_{\text{BOT}}) = \left| \frac{\gamma_n \langle z \rangle_{\text{TOP}} - \langle z \rangle_{\text{BOT}}}{\gamma_{\text{Hg}} B_0} \right| \sigma(G). \tag{33}$$

Notice that the effect of the linear gradient drift is reduced when using the double-chamber concept, as compared to the single chamber, because $\langle z \rangle_{\text{TOP}} \approx \langle z \rangle_{\text{BOT}}$. Still, the residual imperfect compensation of the gradient drifts could generate a direct systematic effect which is called the *uncompensated gradient drift*. The application of the electric field might itself generate a magnetic-field change which is correlated to the voltage of the central electrode V . Such an effect might be due to the leakage current from the high-voltage electrode to the ground electrodes. It could also be due to a magnetization of the shield by the charging currents during voltage ramps. In principle the mercury co-magnetometer cancels any field fluctuations, including those correlated with the electric field. However, the cancellation is not perfect due to the gravitational shift. The false EDM due to the correlated part of the gradient $\delta G(V)$ is

$$\delta d_n = \frac{\hbar \gamma_n}{4E} (\langle z \rangle_{\text{BOT}} - \langle z \rangle_{\text{TOP}}) \delta G(V). \tag{34}$$

The goal for n2EDM is to have this systematic effect under control at the level of $1 \times 10^{-28} e \text{ cm}$, corresponding to a control over the correlated part of the gradient at the level of $\delta G(V) \leq 1.5 \text{ fT/cm}$.

One possible strategy would be to perform dedicated tests to check for a possible G/V correlation, with frequent reversals of the electric polarity while measuring the magnetic-field gradient with the mercury co-magnetometers and the array of atomic cesium magnetometers. For definiteness we consider a series of 1000 polarity reversals, each one lasting about 5 min. The stability of the magnetic-field gradient $\sigma(G)[5 \text{ min}]$ will limit the resolution on the sought effect: $\delta G = \sigma(G)[5 \text{ min}]/\sqrt{1000}$. This sets a requirement on short time variations of the gradient to:

$$\sigma(G)[5 \text{ min}] < 50 \text{ fT/cm.} \tag{35}$$

4.2 Shift due to transverse fields

Residual transverse field components B_x and B_y are averaged differently by the neutrons and the mercury atoms. This produces a shift in \mathcal{R} denominated the transverse shift δ_T . When a particle (a neutron or a mercury atom) moves in a static but non-uniform field it effectively sees a fluctuating magnetic field $\mathbf{B}(\mathbf{r}(t))$, where $\mathbf{r}(t)$ is the random trajectory. In addition to the intrinsic depolarization process already discussed in the previous section, the fluctuation induces a shift of the Larmor precession frequency. In fact the shift is induced by the transverse component of the field, which can be described by the complex perturbation

$$b(t) := \mathbf{B}(\mathbf{r}(t)) \cdot (\mathbf{e}_x + i\mathbf{e}_y). \tag{36}$$

We will again make use of the autocorrelation function of the perturbation $\langle b^*(t)b(t + \tau) \rangle$, where the brackets $\langle \cdot \rangle$ denote the ensemble average over all of the particles in the chamber. Note that since the motion of the particles is stationary in the statistical sense, $\langle b^*(t)b(t + \tau) \rangle = \langle b^*(0)b(\tau) \rangle$ is independent of t . Spin-relaxation theory allows calculation of the angular-frequency shift at second order in the perturbation b :

$$\delta\omega = \frac{\gamma^2}{2} \int_0^\infty d\tau \text{Im} \left[e^{i\omega\tau} \langle b^*(0)b(\tau) \rangle \right]. \tag{37}$$

The timescale of the correlation function is set by the correlation time τ_c that we introduced in the previous section. Although Eq. (18) defines and Eq. (20) estimates the correlation time for the longitudinal field b_z and not that of the transverse field b , the quantity of concern here, the two are in general approximately equal. The autocorrelation function $\langle b^*(0)b(\tau) \rangle$ decays to zero at times large compared to τ_c .

Let us consider first the case of the neutrons. We have seen in the previous section that the anticipated value for the correlation time of stored UCNs in n2EDM is $\tau_c(\text{ucn}) \approx 120 \text{ ms}$ according to the estimation of Eq. (20). In a $B_0 =$

$1 \mu\text{T}$ field the neutron angular frequency is $\omega_n = \gamma_n B_0 = -183 \text{ s}^{-1}$. Thus, we have $|\omega_n \tau_c(\text{ucn})| = 22 \gg 1$; we say that the neutrons are in the *high-frequency regime*, sometimes also called the *adiabatic regime*. In this regime one can expand Eq. (37) in powers of $1/\omega$, and we find at the lowest order

$$\delta\omega_n = \frac{\gamma_n^2 \langle b^*(0)b(0) \rangle}{2 \omega_n}. \tag{38}$$

The ensemble average $\langle b^*(0)b(0) \rangle$ is simply the volume average of the quantity $b^*b = B_x^2 + B_y^2$. This result of Eq. (38) can be understood with an intuitive picture of quasi-static neutrons: at any given time, each neutron precesses at a frequency $|\gamma_n/2\pi||\mathbf{B}|$ set by the magnitude of the field at the position of the neutron. This picture is correct because the precession frequency is very fast: a neutron stays at the same place throughout several spin rotations. At second order in b we have $|\mathbf{B}| = |B_z| + \frac{B_x^2 + B_y^2}{2|B_z|}$. The ensemble of neutron spins precesses on average at a rate

$$f_n = \frac{|\gamma_n|}{2\pi} \langle |\mathbf{B}| \rangle = \frac{|\gamma_n|}{2\pi} \left(\langle B_z \rangle + \frac{\langle B_x^2 + B_y^2 \rangle}{2|B_z|} \right). \tag{39}$$

The second term of this expression is consistent with Eq. (38).

Now let us consider the case of the mercury atoms. They have a mean speed of 180 m/s, which is much faster than the neutrons. Therefore, the correlation time is much shorter: $\tau_c(\text{Hg}) \approx 5 \text{ ms}$. In a $B_0 = 1 \mu\text{T}$ field the mercury angular frequency is $\omega_{\text{Hg}} = \gamma_{\text{Hg}} B_0 = 48 \text{ s}^{-1}$. Thus, we have $\omega_{\text{Hg}} \tau_c(\text{Hg}) = 0.24 \ll 1$, and therefore the mercury atoms are in the *low-frequency regime*, sometimes also called the *non-adiabatic regime*. In this regime one can expand Eq. (37) in powers of ω to get the following order-of-magnitude estimate:

$$\delta\omega_{\text{Hg}} \sim \gamma_{\text{Hg}}^2 \omega_{\text{Hg}} \tau_c^2 \langle b^*b \rangle. \tag{40}$$

From this estimate one concludes that the relative frequency shift of mercury is much smaller than the relative frequency shift of the neutrons because

$$\frac{\delta\omega_{\text{Hg}}/\omega_{\text{Hg}}}{\delta\omega_n/\omega_n} \sim (\omega_{\text{Hg}} \tau_c(\text{Hg}))^2 \sim 0.06. \tag{41}$$

The mercury atoms are much less sensitive to the transverse field compared to the neutrons. Indeed, during one spin rotation period a mercury atom explores the entire chamber several times and therefore the transverse components of the field effectively average out. In the case of the magnetic-field design value of $B_0 = 1 \mu\text{T}$ we will work in the approximation of perfect averaging of the transverse magnetic-field components, and write

$$f_{\text{Hg}} = \frac{|\gamma_{\text{Hg}}|}{2\pi} \langle B_z \rangle \tag{42}$$

for the mercury frequency, i.e. effectively using a volume average of B_z , only. Equations (39) and (42) can then be

used to compute the shift δ_T . Note that in these expressions the ensemble average $\langle B_z \rangle$ is in principle different for the neutrons and the mercury atoms, but this difference is already accounted for by the gravitational shift. The expression of the transverse shift is therefore

$$\delta_T = \frac{\langle B_T^2 \rangle}{2B_0^2}, \quad (43)$$

where $B_T^2 = B_x^2 + B_y^2$. With transverse fields of the order of $\langle B_T^2 \rangle \approx (500 \text{ pT})^2$, the transverse shift would give $\delta_T \approx 0.1 \text{ ppm}$. Although this is a significant shift relative to the statistical precision of \mathcal{R} , it is not a critical concern in the double chamber design. This is because a direct systematic effect could arise only through a difference in the shift between the top and bottom chamber; correlated with the electric-field polarity, this is promoted to a direct systematic effect. This in turn is necessarily associated with a non-uniformity of the longitudinal component B_z .

4.3 Motional field: introduction

Let us now come to the important description of the frequency shift induced by the motional field. According to special relativity, particles moving with a velocity \mathbf{v} (in our case $|\mathbf{v}| \ll c$) in an electric field \mathbf{E} experience a “motional” magnetic field

$$\mathbf{B}_m = \mathbf{E} \times \mathbf{v}/c^2. \quad (44)$$

The effect of the motional field on stored particles was first considered by Lamoreaux [40] who discussed the associated frequency shift quadratic in the electric field. Then Pendlebury et al. [41] discovered that the motional field also leads to a linear-in-electric-field frequency shift in the presence of magnetic-field gradients. Since then this topic has been studied theoretically [42–49] and experimentally [36, 50].

This motional field affects both ultracold neutrons and mercury atoms when they are stored in the n2EDM chambers. Since the velocities of the particles are changing randomly in time, the motional field is in fact a magnetic noise transverse to \mathbf{E} . Let us estimate the magnitude of this noise in a vertical electric field $E = 15 \text{ kV/cm}$, i.e. the design value for n2EDM. For neutrons with RMS horizontal velocity $v_h \approx 3 \text{ m/s}$, we obtain magnetic fields of about 50 pT . For mercury atoms at room temperature, the RMS horizontal velocity is 157 m/s and the corresponding RMS motional magnetic field is 2.6 nT .

The motional field $\mathbf{B}_m(t)$ adds to the fluctuating field $\mathbf{B}(\mathbf{r}(t))$ originating from the random motion of the particle in the non-uniform magnetic field. Equation (36) can then be generalized, and the total fluctuating transverse field is described by the complex perturbation

$$b(t) = (\mathbf{B}_m(t) + \mathbf{B}(\mathbf{r}(t))) \cdot (\mathbf{e}_x + i\mathbf{e}_y) \quad (45)$$

$$= E/c^2(-\dot{y}(t) + i\dot{x}(t)) + \mathbf{B}(\mathbf{r}(t)) \cdot (\mathbf{e}_x + i\mathbf{e}_y). \quad (46)$$

Table 3 Goal for the control of systematic effects in the 2EDM design

Systematic effect	(10^{-28} e cm)
Uncompensated gradient drift	1
Quadratic $\mathbf{v} \times \mathbf{E}$	1
Co-magnetometer accuracy	1
Phantom mode of order 3	3
Phantom mode of order 5	3
Dipoles contamination	3
Total	6

In Fig. 9 a simulated random realization of the transverse field seen by a mercury atom is shown. As discussed before (at which time the motional field was neglected) any transverse magnetic perturbation generates a frequency shift given by Eq. (37). The total shift can be decomposed in powers of E as

$$\delta\omega = \delta\omega_{B^2} + \delta\omega_{BE} + \delta\omega_{E^2}. \quad (47)$$

The term linear in E is

$$\delta\omega_{BE} = \frac{\gamma^2 E}{c^2} \int_0^\infty d\tau \cos(\omega\tau) \langle B_x(0)\dot{x}(\tau) + B_y(0)\dot{y}(\tau) \rangle, \quad (48)$$

while the term quadratic in E is

$$\delta\omega_{E^2} = \left(\frac{\gamma E}{c^2} \right)^2 \int_0^\infty d\tau \sin(\omega\tau) \langle \dot{x}(0)\dot{x}(\tau) \rangle. \quad (49)$$

The constant term $\delta\omega_{B^2}$ was discussed previously; it corresponds to the transverse shift δ_T . Next we will discuss the effects of the other two terms.

4.4 Motional field: quadratic-in-E shift

Let us first specify the angular-frequency shift $\delta\omega_{E^2}$ for the neutrons, by taking the high-frequency limit of Eq. (49). For this purpose we expand the integral in powers of $1/\omega$ by integration by parts and retain the dominant term

$$\delta\omega_{E^2, n} = \left(\frac{\gamma_n E}{c^2} \right)^2 \frac{\langle \dot{x}^2 \rangle}{\omega_n}. \quad (50)$$

Second, we specify $\delta\omega_{E^2, \text{Hg}}$ for the mercury atoms, which are in the low-frequency limit if $B_0 = 1 \text{ } \mu\text{T}$. To calculate the low-frequency limit of Eq. (49) we first do an integration by parts to obtain

$$\delta\omega_{E^2} = - \left(\frac{\gamma E}{c^2} \right)^2 \omega \int_0^\infty d\tau \cos(\omega\tau) \langle \dot{x}(0)x(\tau) \rangle. \quad (51)$$

Then, by the stationarity property

$$\langle \dot{x}(0)x(\tau) \rangle = \langle \dot{x}(-\tau)x(0) \rangle = -\frac{d}{dt} \langle x(-\tau)x(0) \rangle$$

$$= -\frac{d}{dt} \langle x(0)x(\tau) \rangle = -\langle x(0)\dot{x}(\tau) \rangle, \tag{52}$$

we have

$$\delta\omega_{E^2} = \left(\frac{\gamma E}{c^2}\right)^2 \omega \int_0^\infty d\tau \cos(\omega\tau) \langle x(0)\dot{x}(\tau) \rangle. \tag{53}$$

Finally, we obtain the angular-frequency shift for the mercury atoms in the low-frequency limit by setting $\cos(\omega\tau) = 1$ in the above integral:

$$\delta\omega_{E^2, \text{Hg}} = -\left(\frac{\gamma_{\text{Hg}} E}{c^2}\right)^2 \omega_{\text{Hg}} \langle x^2 \rangle = -\left(\frac{\gamma_{\text{Hg}} E}{c^2}\right)^2 \omega_{\text{Hg}} \frac{R^2}{4}. \tag{54}$$

The combination of Eqs. (50) and (54) leads to the expression for the quadratic-in-electric-field shift:

$$\begin{aligned} \delta_{\text{quad}} &= \frac{\delta\mathcal{R}}{\mathcal{R}} = \frac{\delta\omega_{E^2, n}}{\omega_n} - \frac{\delta\omega_{E^2, \text{Hg}}}{\omega_{\text{Hg}}} \\ &= \left(\frac{v_h^2}{2B_0^2} + \frac{\gamma_{\text{Hg}}^2 R^2}{4}\right) \frac{E^2}{c^4}. \end{aligned} \tag{55}$$

With $v_h = 3$ m/s, $B_0 = 1 \mu\text{T}$, $R = 40$ cm, $E = 15$ kV/cm we have $\delta_{\text{quad}} = 2.7 \times 10^{-8}$. Notice that the term induced by the mercury atoms is about 20 times larger than the term induced by the neutrons.

If the strength of the electric field is not exactly the same in the top and bottom chambers, due to a slightly different height of the two chambers, the quadratic frequency shift generates a term $\mathcal{R}^{\text{TOP}} - \mathcal{R}^{\text{BOT}}$. This generates a systematic effect if we consider the Top/Bottom EDM channel defined as $d_{\text{TB}} = \frac{\pi\hbar f_{\text{Hg}}}{2|E|} (\mathcal{R}^{\text{TOP}} - \mathcal{R}^{\text{BOT}})$. An asymmetry of $\Delta E/E = 10^{-3}$ corresponds to $d_{\text{TB}} = 10^{-28}$ e cm.

Similarly, if the strength of the electric field is different in the positive and negative polarity, due to an imperfect polarity reversal of the HV source, the quadratic frequency shift generates a term $\mathcal{R}_+ - \mathcal{R}_-$. This generates a systematic effect if we consider the Plus/Minus EDM channel defined as $d_{+/-} = \frac{\pi\hbar f_{\text{Hg}}}{2|E|} (\mathcal{R}_+ - \mathcal{R}_-)$. An asymmetry of $\Delta E/E = 10^{-3}$ corresponds to $d_n^{+/-} = 10^{-28}$ e cm.

However, in the double-chamber concept, these two types of imperfections are compensated and do not generate a false EDM, as can be deduced from Eq. (13). Nonetheless, we give requirements for the uncompensated channels d_{TB} and $d_{+/-}$.

First, we set a requirement on the electric-field asymmetry. In order to limit the systematic effect due to the quadratic frequency shift in the d_{TB} channel to lower than 1×10^{-27} e cm, the electric-field strength must be the same in the top and bottom chamber with a precision better than 1% (i.e. $|\Delta E/E| < 10^{-2}$). Second, we set a requirement on the voltage reversal. In order to limit the systematic effect due to the quadratic frequency shift in the $d_{+/-}$ channel to lower than 1×10^{-28} e cm the absolute value of the voltage

applied to the central electrode must be the same in the positive and negative polarities with a precision better than 0.1% (i.e. $|\Delta V/V| < 10^{-3}$).

4.5 Motional field: false EDM

Now we will sketch the derivation of the high- and low-frequency limits of the frequency shift linear in electric field given by Eq. (48).

The high-frequency limit, which applies for ultracold neutrons, is obtained by using the following approximation:

$$\int_0^\infty d\tau \cos(\omega\tau) f(\tau) = -\frac{1}{\omega^2} \dot{f}(0), \tag{56}$$

which is valid if $f(\tau)$ and $\dot{f}(\tau)$ are smooth functions decaying to 0 for $\tau \rightarrow \infty$. We apply this scheme to the function

$$f(\tau) = \langle B_x(0)\dot{x}(\tau) \rangle = \langle B_x(-\tau)\dot{x}(0) \rangle. \tag{57}$$

We have

$$f'(\tau) = \frac{d}{d\tau} \langle B_x(-\tau)\dot{x}(0) \rangle = -\left\langle \frac{\partial B_x}{\partial x}(-\tau)\dot{x}(-\tau)\dot{x}(0) \right\rangle. \tag{58}$$

Therefore, at high frequency

$$\int_0^\infty d\tau \cos(\omega\tau) \langle B_x(0)\dot{x}(\tau) \rangle = \frac{1}{\omega^2} \left\langle \frac{\partial B_x}{\partial x} \right\rangle \langle \dot{x}^2 \rangle. \tag{59}$$

Doing the same with the function $\langle B_y(0)\dot{y}(\tau) \rangle$, and using Maxwell's equation $\frac{\partial B_x}{\partial x} + \frac{\partial B_y}{\partial y} = -\frac{\partial B_z}{\partial z}$, we find

$$\delta\omega_{BE} = -\frac{\gamma^2 E}{2c^2} \frac{1}{\omega^2} \left\langle \frac{\partial B_z}{\partial z} \right\rangle v_h^2 \quad (\text{high frequency limit}), \tag{60}$$

with $v_h^2 = \langle \dot{x}^2 \rangle + \langle \dot{y}^2 \rangle = 2\langle \dot{x}^2 \rangle$.

Now, the low-frequency limit, which applies to mercury atoms at low values of B_0 , is simply obtained by using the approximation $\cos(\omega\tau) = 1$ in the integral Eq. (48):

$$\delta\omega_{BE} = -\frac{\gamma^2 E}{c^2} \langle xB_x + yB_y \rangle \quad (\text{low frequency limit}). \tag{61}$$

With Eqs. (60) and (61), we can derive the corresponding shift in the \mathcal{R} ratio as

$$\delta_{\text{EDM}}^{\text{false}} = \pm \frac{2}{\hbar|\gamma_n B_0|} |E| \left(d_n^{\text{false}} + d_{n \leftarrow \text{Hg}}^{\text{false}} \right), \tag{62}$$

where the + sign corresponds to the anti-parallel ($\uparrow\downarrow$ or $\downarrow\uparrow$) configurations and the - sign corresponds to the parallel ($\uparrow\uparrow$ or $\downarrow\downarrow$) configurations. The formula for the false neutron EDM in the high-frequency limit is

$$d_n^{\text{false}} = -\frac{\hbar v_h^2}{4c^2 B_0^2} \left\langle \frac{\partial B_z}{\partial z} \right\rangle. \tag{63}$$

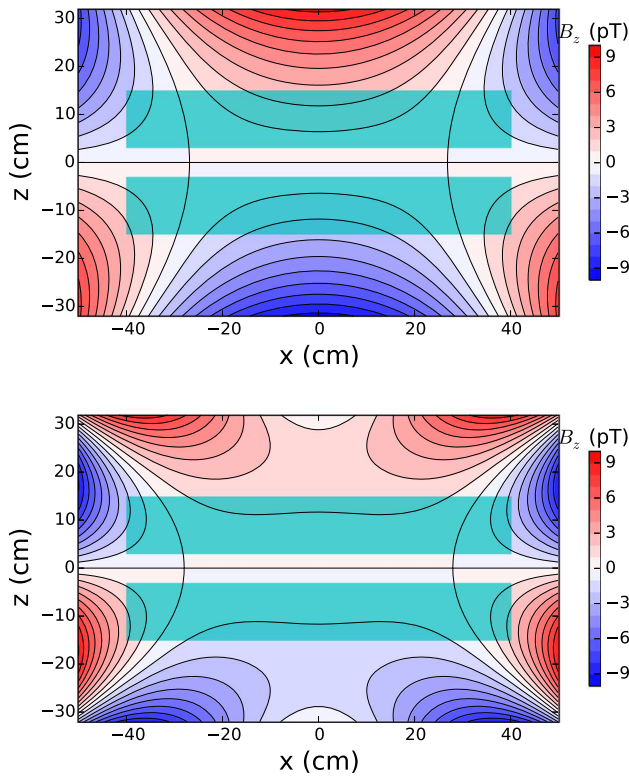


Fig. 10 Longitudinal component of the phantom modes. Top: phantom mode of order 3 $B_z = \hat{G}_3 \hat{I}_{z,3}$ with $\hat{G}_3 = 78$ fT/cm. Bottom: phantom mode of order 5 $B_z = \hat{G}_5 \hat{I}_{z,5}$ with $\hat{G}_5 = 78$ fT/cm. Both field configurations generate a false EDM of $d_{n \leftarrow \text{Hg}}^{\text{false}} = 1 \times 10^{-27}$ e cm. The light green rectangles represent the inner volume of the precession chambers

The false EDM transferred from the mercury in the low-frequency limit is

$$d_{n \leftarrow \text{Hg}}^{\text{false}} = -\frac{\hbar |\gamma_n \gamma_{\text{Hg}}|}{2c^2} \langle x B_x + y B_y \rangle. \tag{64}$$

4.6 False EDM in a uniform gradient

At this point it is important to note that the false EDM is really the combined effect of the motional field and the non-uniformities of the static B_0 field. An assumption of a simple uniform vertical gradient of the form

$$\mathbf{B} = B_0 \begin{pmatrix} 0 \\ 0 \\ 1 \end{pmatrix} + G_{1,0} \begin{pmatrix} -x/2 \\ -y/2 \\ z \end{pmatrix} \tag{65}$$

leads to

$$\left\langle \frac{\partial B_z}{\partial z} \right\rangle = G_{1,0} \tag{66}$$

and

$$\langle x B_x + y B_y \rangle = -G_{1,0} \frac{R^2}{4}. \tag{67}$$

In this situation, one can estimate the false EDM directly induced on the neutrons d_n^{false} and the one induced via the mercury $d_{n \leftarrow \text{Hg}}^{\text{false}}$:

$$d_n^{\text{false}} = -\frac{\hbar v_h^2}{4c^2 B_0^2} G_{1,0} \tag{68}$$

$$= -\frac{G_{1,0}}{1 \text{ pT/cm}} \times 1.65 \times 10^{-28} \text{ e cm}, \tag{69}$$

$$d_{n \leftarrow \text{Hg}}^{\text{false}} = \frac{\hbar |\gamma_n \gamma_{\text{Hg}}| R^2}{8c^2} G_{1,0} \tag{70}$$

$$= \frac{G_{1,0}}{1 \text{ pT/cm}} \times 1.28 \times 10^{-26} \text{ e cm}, \tag{71}$$

where $v_h = 3$ m/s, $B_0 = 1 \mu\text{T}$ and $R = 40$ cm. It should be noted that the mercury-induced false neutron EDM is much larger than the directly induced neutron motional false EDM.

Even if the residual field gradient inside the shield is reduced down to a fraction of a pT/cm, a systematic effect greater than 10^{-27} e cm could still be generated. The general strategy to cancel the effect is to split the data production into many runs with different gradient configurations within the allowed range ± 0.6 pT/cm. In this way we will measure the EDM as function of the gradient, extrapolating to zero gradient in the final step. In the nEDM experiment the gradient was inferred from the gravitational shift. However, the shift of the \mathcal{R} ratio correlates only imperfectly with the gradient, because of all the other frequency shifts. In n2EDM the gradient can be extracted in a more robust way thanks to the double-chamber design. We define the *Top/Bottom gradient* as

$$G_{\text{TB}} = \frac{\langle B_z \rangle_{\text{TOP}} - \langle B_z \rangle_{\text{BOT}}}{H'} \tag{72}$$

where $H' = 18$ cm is the distance between the geometrical centers of the two chambers. The G_{TB} will be accurately measured with the mercury co-magnetometers.

At this point one can identify two possible failures of the extrapolation method that would each produce a residual systematic effect.

- First, a systematic shift of the mercury precession frequency of the upper co-magnetometer relative to the lower co-magnetometer will result in a systematically wrong gradient. This is quoted as *co-magnetometer accuracy* in Table 3. The aim is to constrain that error to lower than 1×10^{-28} e cm. This sets a requirement on the accuracy of the magnetometers, which must be $\delta B_{\text{Hg}} < 100$ fT. Note that this requirement is less stringent than the requirement on the precision per cycle of 25 fT derived in section Sect. 3.5. All known sources of frequency shifts of the co-magnetometer are listed in the previous section (see also Sect. 5.4 for magnetometry).

- Second, and more importantly, the extrapolation procedure to $G_{TB} = 0$ fails if the field non-uniformities are more complicated than a uniform gradient $G_{1,0}$. It is useful to distinguish two types of non-uniformities: (i) Large-scale spatial B -modes of cubic and higher orders. These are generated by the imperfection of the mu-metal shield, for example due to the openings, and by imperfections of the B_0 coil. (ii) Magnetic dipole sources localized near the precession chambers, due to the contamination of the apparatus by small ferromagnetic impurities.

4.7 False EDM and phantom modes

To discuss more complicated field non-uniformities, we describe the field by the generalized gradients $G_{l,m}$ as defined in (29). With this formalism we can calculate the Top/Bottom gradient

$$G_{TB} = G_{1,0} - L_3^2 G_{3,0} + L_5^4 G_{5,0} + \dots \tag{73}$$

where L_l are geometric coefficients. Modes with $m \neq 0$ do not contribute to the Top/Bottom gradient because the chamber is symmetric by rotation around the magnetic-field axis. Modes with even values of l are also absent because the top chamber is the mirror image of the bottom chamber with respect to the plane $z = 0$. An explicit calculation for the cubic and fifth-order modes gives the geometric coefficients

$$L_3^2 = \frac{3}{4}R^2 - \frac{1}{4}(H^2 + H'^2) = (32.9 \text{ cm})^2, \tag{74}$$

$$L_5^4 = \frac{5}{8}R^4 - \frac{5}{8}R^2(H^2 + H'^2) + \frac{1}{48}(3H'^2 + H^2)(H^2 + 3H'^2) = (32.7 \text{ cm})^4. \tag{75}$$

There are axially symmetric field configurations, i.e. linear combinations of $m = 0$ modes, which are invisible in the double-chamber because they satisfy $G_{TB} = 0$. We call these field configurations *phantom modes*. We define the basis of phantom modes of odd degree as

$$\dot{\Pi}_3 = c_3 \left(\Pi_{1,0} + \frac{1}{L_3^2} \Pi_{3,0} \right), \tag{76}$$

$$\dot{\Pi}_5 = c_5 \left(\Pi_{1,0} - \frac{1}{L_5^4} \Pi_{5,0} \right), \tag{77}$$

and similarly for all odd modes

$$\dot{\Pi}_{2k+1} = c_{2k+1} \left(\Pi_{1,0} - \frac{(-1)^k}{L_{2k+1}^{2k}} \Pi_{2k+1,0} \right). \tag{78}$$

The normalization of the phantom modes of odd degree are chosen such that

$$\langle \rho \dot{\Pi}_\rho \rangle_{\text{TOP}} = \langle \rho \dot{\Pi}_\rho \rangle_{\text{BOT}} = -R^2/4. \tag{79}$$

In particular, for the phantom modes of degrees 3 and 5:

$$c_3 = \frac{4L_3^2}{R^2 + 2H'^2}, \tag{80}$$

$$c_5 = \frac{48L_5^4}{15R^4 + 10R^2(3H'^2 - H^2) - 4H'^2(3H'^2 + 5H^2)}. \tag{81}$$

The even modes $\Pi_{2,0}, \Pi_{4,0}$ are also phantom in the sense previously defined, but they do not produce a false EDM and will not be discussed further. The odd phantom modes are of particular interest because they generate a false EDM without generating a Top/Bottom gradient. Specifically, a field configuration of the type

$$\mathbf{B} = B_0 \mathbf{e}_z + G_{TB} \Pi_{1,0} + \dot{G}_3 \dot{\Pi}_3 + \dot{G}_5 \dot{\Pi}_5 + \dots \tag{82}$$

generates a false EDM through Eq. (64),

$$d_{n \leftarrow \text{Hg}}^{\text{false}} = \frac{\hbar |\gamma_n \gamma_{\text{Hg}}| R^2}{8c^2} \left(G_{TB} + \dot{G}_3 + \dot{G}_5 + \dots \right). \tag{83}$$

Obviously, the contribution proportional to G_{TB} will be removed by the extrapolation to $G_{TB} = 0$, but the contribution proportional to the phantom gradient, $\dot{G} = \dot{G}_3 + \dot{G}_5 + \dots$, will remain.

In Fig. 10 we show the B_z field configuration corresponding to the phantom modes of order 3 and order 5. Our strategy to control the phantom modes is to use a combination of online and offline measurements, the former being more adequate for the low-order modes and the latter more appropriate for the high-order modes.

The online measurement of the field will be provided by an array of cesium magnetometers, which will be able to extract the gradients $G_{l,m}$ up to order $l = 5$. In particular the array will provide, online, a measurement of $\dot{G}_3 = \frac{L_3^2}{c_3} G_{3,0}$ that will be used to correct for the corresponding systematic effect. As a guide to the design of the magnetometer array, we set the requirement that the error on the correction for the cubic phantom mode must be lower than $3 \times 10^{-28} e \text{ cm}$. This corresponds to an accuracy of $\delta \dot{G}_3 < 20 \text{ fT/cm}$.

The offline measurement will be performed by a mechanical mapping device. During the mapping the inner parts of the vacuum vessel, including the precession chambers, will be removed. This imposes a requirement on the reproducibility of the field configuration (it needs to be identical during the mapping and during the data-taking), and also a requirement on the accuracy of the magnetic-field mapper. As a design guide we set the requirement that the error on the correction for the fifth-order phantom mode $\dot{G}_5 = \frac{L_5^4}{c_5} G_{5,0}$ must be lower than $3 \times 10^{-28} e \text{ cm}$. This corresponds to an accuracy of $\delta \dot{G}_5 < 20 \text{ fT/cm}$. The requirements related to the control of the high-order gradients are summarized below in Tables 3 and 4. Note that the requirements on $\delta \dot{G}_3$ and $\delta \dot{G}_5$ concern the magnetic-field measurement and not the magnetic-field generation.

Table 4 Summary of the requirements for the magnetic-field measurement (B-meas), magnetic-field generation (B-gen) and electric-field generation (E-gen) for the n2EDM design

Related to statistical errors	
(B-gen) Top-Bottom resonance matching condition	$-0.6 \text{ pT/cm} < G_{1,0} < 0.6 \text{ pT/cm}$
(B-gen) Field uniformity in the chambers	$\sigma(B_z) < 170 \text{ pT}$
(B-gen) Field stability on minutes timescale	$< 25 \text{ fT}$
(B-meas) Precision Hg co-magnetometer, per cycle, per chamber	$< 25 \text{ fT}$
Related to systematical errors	
(B-gen) Gradient stability on the timescale of minutes	$\sigma(G)[5 \text{ min}] < 50 \text{ fT/cm}$
(B-meas) Accuracy mercury co-magnetometer per chamber	$< 100 \text{ fT}$
(B-meas) Accuracy on cubic mode (Cs magnetometers)	$\delta\dot{G}_3 < 20 \text{ fT/cm}$
(B-gen) Reproducibility of the order 5 mode	$\sigma(\dot{G}_5) < 20 \text{ fT/cm}$
(B-meas) Accuracy of the order 5 mode (field mapper)	$\delta\dot{G}_5 < 20 \text{ fT/cm}$
(B-gen) Dipoles close to the electrode	$< 20 \text{ pT at } 5 \text{ cm}$
(E-gen) Relative accuracy on E field magnitude	$< 10^{-3}$

4.8 False EDM and magnetic-dipole sources

Contamination of the inner parts of the apparatus by small ferromagnetic impurities generate a second important type of magnetic-field nonuniformity. Here we evaluate the induced systematic effect, and specify the tolerated level of contamination. A small magnetic impurity can be described as a magnetic dipole \mathbf{m} . Such a dipole located at distance \mathbf{r}_d is a source of a dipolar magnetic field of the form $\mathbf{B}_d(\mathbf{r}) = (\mu_0/4\pi)(3(\mathbf{m}\cdot\mathbf{u})\mathbf{u} - \mathbf{m})/|\mathbf{r} - \mathbf{r}_d|^3$, with $\mathbf{u} = (\mathbf{r} - \mathbf{r}_d)/|\mathbf{r} - \mathbf{r}_d|$ representing the unit vector pointing from the dipole position. This will induce a false EDM $d_{n\leftarrow\text{Hg}}^{\text{false}}$ given by Eq. (64). In addition, the dipole source will generate a Top/Bottom gradient G_{TB} measured by the mercury co-magnetometers, and will also affect the cubic phantom gradient $\dot{G}_{3,\text{meas}}$ extracted from the readings of the cesium magnetometers. However, the measured correction

$$d_{\text{meas}}^{\text{false}} = \frac{\hbar|\gamma_n\gamma_{\text{Hg}}|R^2}{8c^2} (G_{\text{TB}} + \dot{G}_{3,\text{meas}}) \quad (84)$$

will imperfectly estimate the actual false EDM given by Eq. (83), because $\dot{G}_{3,\text{meas}}$ will be shifted from the true value \dot{G}_3 and also because the higher-order gradients $\dot{G}_5, \dot{G}_7, \dots$ generated by the dipole are not corrected for.

A thorough numerical study of the influence of dipole strength and location was conducted, by considering a given dipole placed at different locations in the experimental volume outside the precession chambers and calculating the residual effect $d_{n\leftarrow\text{Hg}}^{\text{false}} - d_{\text{meas}}^{\text{false}}$. The value $\dot{G}_{3,\text{meas}}$ was calculated by considering the field produced by the dipole at the position of each magnetometer (see Sect. 5.4.3 for a description of the designed optimized positions of the magnetometers) and performing the harmonic fit to cubic order (up to $l = 3$). A sample of the results can be seen in Fig. 11, and

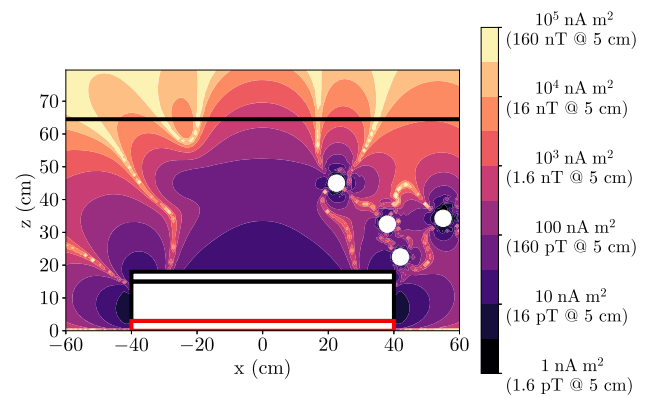


Fig. 11 Magnetic dipole strength values corresponding to a residual systematic effect of $d_{n\leftarrow\text{Hg}}^{\text{false}} - d_{\text{meas}}^{\text{false}} = 3 \times 10^{-29} e \text{ cm}$ (mean of top and bottom chambers), as a function of the position of the dipole in the $y = 0$ plane. The direction of the dipole m was chosen to be along the z -axis, which is the most sensitive direction. This cut ($y = 0$) intersects a unit of four magnetometers represented by the white circles. The top plate of the vacuum tank is represented by the horizontal black line at $z = 65 \text{ cm}$. The cross section of the electrodes are represented by the black and red-edged rectangles

corresponds to the top half of the $y = 0 \text{ cm}$ plane of the experiment. It shows the dipole strength $|\mathbf{m}|$ that produces a residual effect of $3 \times 10^{-29} e \text{ cm}$, the chosen maximum tolerated contribution for a single dipole. We allow for the presence of a maximum of 100 impurities with random and uncorrelated direction, such that the total systematic effect will be $\sqrt{100}$ times the contribution of one individual dipole, i.e. $3 \times 10^{-28} e \text{ cm}$ (see Table 3).

The regions of the apparatus that are most sensitive to the presence of magnetic contamination are the outside of the insulating rings and the immediate proximity of each magnetometer. At these locations the critical dipole strength, i.e.

the maximum tolerated dipole strength to meet the requirement for the contribution for individual dipole, was found to be 5 nA m^2 . This dipole strength corresponds to an iron dust particle of diameter $\approx 20 \text{ }\mu\text{m}$ magnetized to saturation. It would produce a field of approximately 1 pT at 10 cm distance. Other locations are less sensitive but must still be protected against magnetic contamination. In fact all components of the apparatus inside the magnetic shield must be magnetically scanned to exclude dipoles larger than specified. For example, the vacuum tank (represented as a horizontal black line at $z = 65 \text{ cm}$ in Fig. 11) must be carefully quality controlled such that dipoles larger than 500 nA m^2 are excluded.

4.9 The magic-field option to cancel the false EDM

We have argued that the significant gain in statistical sensitivity in n2EDM will be obtained by the use of a large double chamber. In the described design the diameter of the chambers will be 80 cm , while the vacuum vessel is designed to host a chamber as large as 100 cm for a future phase of the experiment. This is made possible by the very large magnetically shielded room, with inner dimensions of almost $3 \times 3 \times 3 \text{ m}^3$. The enlargement of the chambers, as compared to the 47 cm diameter single-chamber of the previous nEDM apparatus, comes at the price of an increase in the systematic effect due to the mercury motional false EDM. This can be clearly seen from Eq. (64). As discussed, controlling the effect induced by the phantom modes brings about a number of challenges: (i) the cesium magnetometers must reach the required accuracy to measure at least the cubic phantom mode online, (ii) the higher-order modes must be reproducible enough to be able to measure these modes offline, (iii) magnetic contamination must be kept at a very low level.

These challenges, and the associated risks for the measurement, prevail if the mercury co-magnetometer operates in the low field regime, as it is the case in the design with $B_0 = 1 \text{ }\mu\text{T}$. There is an alternative possibility that can considerably relax the constraints on the measurement of field nonuniformities. It consists of increasing the B_0 field to a value that cancels the mercury false EDM [51]. We recall that the false neutron EDM inherited from the mercury is

$$d_{n\leftarrow\text{Hg}}^{\text{false}} = \frac{\hbar|\gamma_n\gamma_{\text{Hg}}|}{2c^2} \int_0^\infty d\tau \cos(\omega\tau)\dot{C}(\tau), \tag{85}$$

where $C(\tau)$ is the correlation function

$$C(\tau) = \langle B_x(0)x(\tau) + B_y(0)y(\tau) \rangle \tag{86}$$

and $\omega = \gamma_{\text{Hg}}B_0$. The correlation function $C(\tau)$ can be calculated with a Monte Carlo simulation of the thermal motion of mercury atoms in the chamber.

In Fig. 12 we show the result for the false EDM as a function of the magnitude of the B_0 field. It is possible to

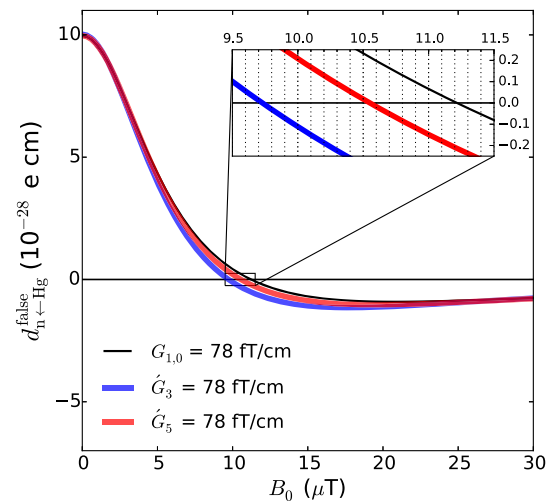


Fig. 12 False EDM due to a uniform field gradient (black), a 3-phantom mode (blue), a 5-phantom mode (red) as a function of the magnitude of the B_0 field for $R = 40 \text{ cm}$, $H = 12 \text{ cm}$, $H' = 18 \text{ cm}$

adjust the value of B_0 to cancel the systematic effect produced by a given mode. We define as “magic fields” the magnetic field values

$$B_{\text{magic},3} = 9.7 \text{ }\mu\text{T}, \quad B_{\text{magic},5} = 10.5 \text{ }\mu\text{T}, \tag{87}$$

which cancel the effect of the respective phantom modes. The magic fields for the different modes are very close. This makes the magic option attractive because it allows substantial reduction of the effect of several modes at the same time.

The magic-field upgrade option consists of setting the magnetic field to $B_0 = 10.5 \text{ }\mu\text{T}$. This will suppress the effect of the fifth order phantom mode completely and will also reduce the effect of the cubic phantom mode by a factor of 30. The magic field is a factor of ten higher than that of the baseline design, and it therefore increases the difficulty of producing a stable and uniform field by an order of magnitude. It should be noted that the requirements of the field uniformity and stability concern the absolute rather than relative values. The n2EDM apparatus is designed to allow operation of the apparatus at the magic field and slightly above, after first running in the baseline configuration.

4.10 Other frequency shifts

In addition to the electric and magnetic terms, there are a number of other known shifts of either the neutron or the mercury precession frequencies that correspondingly affect the \mathcal{R} ratio:

$$\delta_{\text{other}} = \delta_{\text{AC}} + \delta_{\text{Earth}} + \delta_{\text{light}} + \delta_{\text{pulse}} + \delta_{\text{psmag}}. \tag{88}$$

Below we discuss each individual contribution.

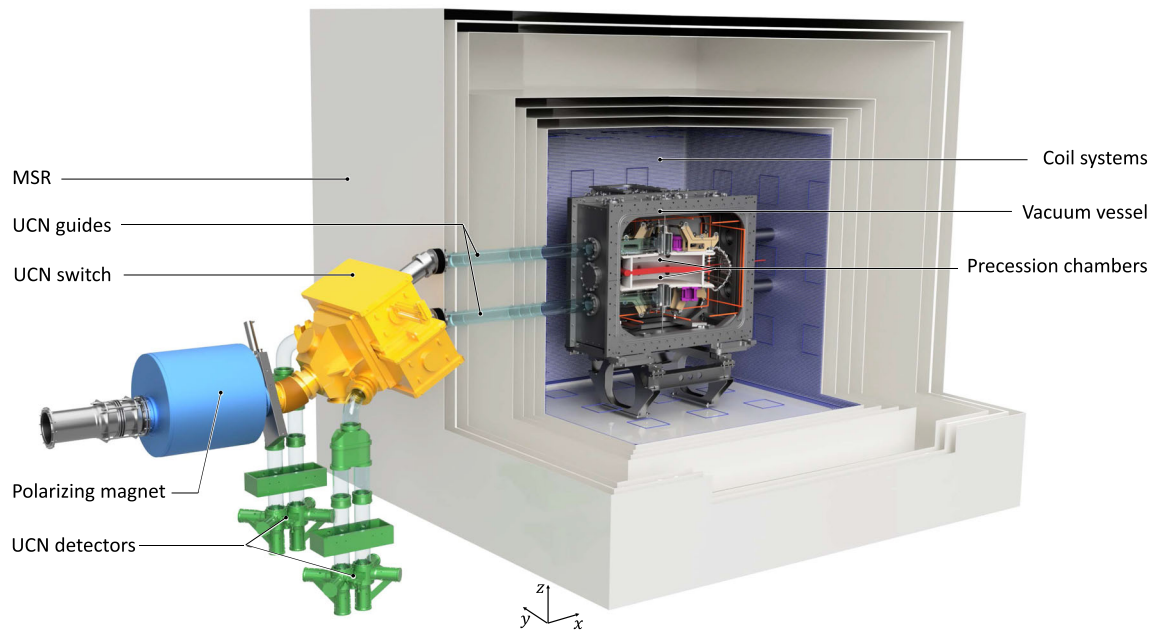


Fig. 13 The full model of the n2EDM setup, displaying the core components of the experiment

4.10.1 Effects of AC fields during the precession: δ_{AC}

Any transverse AC magnetic field during the precession generates a frequency shift for the neutrons and mercury atoms. In addition to the AC field seen by the particles moving in a static but non-uniform field (already taken into account by the term δ_T) as well as the fluctuating motional $\mathbf{E} \times \mathbf{v}/c^2$ field (already taken into account by the terms δ_{EDM}^{false} and δ_{Quad}), the other known possible source of AC fields are

- (i) ripples in the voltage generated by the HV source [14];
- (ii) the Johnson–Nyquist noise generated by the metallic parts, in particular by the electrodes [52]. These were found to be very small effects and will not be discussed in detail here.

4.10.2 The effect of Earth's rotation: δ_{Earth}

Since the precession frequencies of mercury and neutron spins are measured in the Earth's rotating frame, the frequencies are shifted from the pure Larmor frequency in the magnetic field [53]. One can derive the following expression for the associated shift of \mathcal{R} :

$$\delta_{Earth} = \mp \left(\frac{f_{Earth}}{f_n} + \frac{f_{Earth}}{f_{Hg}} \right) \cos \theta = \mp 1.4 \times 10^{-6}, \quad (89)$$

where $f_{Earth} = 11.6 \mu\text{Hz}$ is the Earth's rotation frequency, $f_n = 29.2 \text{Hz}$ and $f_{Hg} = 7.6 \text{Hz}$ are the neutron and mercury precession frequencies in a field of $B_0 = 1 \mu\text{T}$, and $\theta = 42^\circ$ is the angle between the direction of B_0 and the rotation axis of the Earth. In the previous formula the - sign

corresponds to B_0 pointing upwards and the + sign corresponds to B_0 pointing downwards. The shift is large enough to be resolved in principle with a single data cycle (although in fact measurements are needed with both directions of the B_0 , so two cycles are required), provided the other shifts are constant.

A direct systematic effect could arise in principle if electric-field reversals cause a tilt of the magnetic axis relative to the Earth's rotation axis. However, in the double-chamber design this direct systematic effect could arise only in the case of different tilts in the top and bottom chamber (see Eq. (28)). Such a magnetic tilt is necessarily associated with a gradient of the longitudinal field, and the requirement set on the control of the gradients in Eq. (35) guarantees that the direct systematic effect due to the Earth's rotation will be negligible.

4.10.3 The mercury light shift: δ_{light}

This term corresponds to a shift of the mercury precession frequency proportional to the intensity of the UV probe light. This small effect should be taken into account in the design of the mercury co-magnetometer (in particular, good monitoring of the light intensity must be foreseen) but does not impose stringent requirements on the magnetic field generation or magnetic field measurement.

4.10.4 The effect of the mercury pulse: δ_{pulse}

The mercury pulse is generated while the neutrons are already present in the chamber. Therefore, the neutron spins are

affected by the mercury pulse: they will be slightly tilted before the first neutron pulse is applied. In turn, this could shift the measured Ramsey resonance frequency. This effect must be taken into account when designing the generation of the mercury pulse. The frequency shift can be reduced by adjusting the duration, phase, and shape of the mercury pulse. Care will be taken to avoid indirect cross-talk with the high-voltage polarity. However, this effect does not impose stringent requirements on the magnetic field generation or magnetic field measurement.

4.10.5 The pseudomagnetic field generated by polarized mercury: δ_{psmag}

Due to the spin-dependent nuclear interaction between the neutron and the mercury-199 nucleus, quantified by the incoherent scattering length $b_i(^{199}\text{Hg}) = \pm 15.5 \text{ fm}$ [54], the UCNs precessing in the polarized mercury medium are exposed to a pseudo-magnetic field [55]

$$\mathbf{B}^* = -\frac{4\pi\hbar}{\sqrt{3}m_n\gamma_n}b_in_{\text{Hg}}\mathbf{P}, \quad (90)$$

where m_n is the neutron mass, n_{Hg} is the number density of atoms in the precession chamber and \mathbf{P} is the mercury polarization. The pseudo-magnetic field is much larger than the genuine magnetic dipolar field generated by the polarized mercury atoms. The mercury polarization normally precesses in the transverse plane, but it could have a residual static longitudinal component P_{\parallel} in the case of an imperfect $\pi/2$ pulse. In this case, a shift of the neutron frequency arises that corresponds to a relative shift of the \mathcal{R} ratio of

$$\delta_{\text{psmag}} = \pm \frac{2\hbar}{\sqrt{3}m_n f_n}n_{\text{Hg}}b_i P_{\parallel}. \quad (91)$$

This small effect will be taken into account in the design of the mercury magnetometer, in particular the control of the mercury pulse, but it does not impose stringent requirements on the magnetic field generation or magnetic field measurement.

4.11 Summary of the requirements

In summary, we have described the known sources of systematic effects and discussed how to address them in the n2EDM experiment. The apparatus is designed to keep the total systematic error below $6 \times 10^{-28} e \text{ cm}$. The error contributions are expected to be distributed according to the budget shown in Table 3. The dominant contributions to this budget originate from the mercury false EDM effect, which could be reduced by operating the apparatus at the magic value of the magnetic field in a future upgrade.

Through consideration of the statistical and systematic errors we have derived the basic requirements on the perfor-

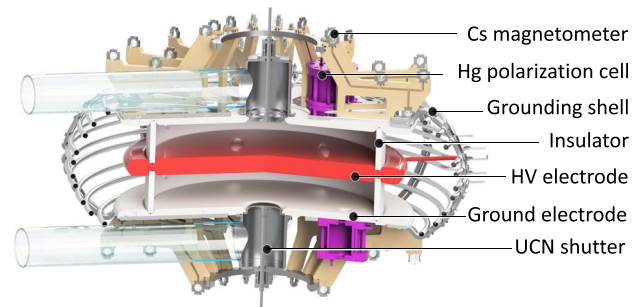


Fig. 14 Central part of the apparatus. Precession volumes are confined by HV and ground electrodes separated by insulator rings. The UCNs enter the chambers via UCN shutters

mance of the n2EDM apparatus. For convenience we reproduce in Table 4 the requirements specifically related to magnetic field generation and measurement. These requirements constitute the basis for the technical design of the core systems of the n2EDM apparatus, which are described in the next section.

5 The core systems of the n2EDM apparatus

In this section we give an overview of the n2EDM baseline design. Figure 13 shows the layout of the apparatus positioned in the experimental area south of the UCN source at PSI. We describe the core n2EDM systems responsible for UCN transport and storage, as well as those for the required magnetic field environment and its control.

5.1 UCN system

5.1.1 UCN precession chambers

The two UCN precession chambers lie at the heart of the experiment. They consist of three electrodes separated by two insulator rings, stacked vertically as shown in Fig. 14.

The precession chambers are cylindrical in shape, of height 12 cm and inner diameter of 80 cm, with a design that will allow an upgrade to 100 cm. The diameter is increased in comparison to the previous nEDM experiment in order to increase the number of stored neutrons, while the (unchanged) height results from a compromise between the electric field strength and the number of stored neutrons. The dimensions and shape are based on the experience with the previous apparatus and are scaled to the largest possible diameter, currently limited by raw material size and machining capacities.

The upper and lower chambers are separated by the central HV electrode, which is supplied with $\pm 180 \text{ kV}$. The insulator rings separating the electrodes have a wall thickness of 2 cm. The design of the electrodes is driven by minimizing UCN

losses, optimizing the storage behavior for polarized UCNs and polarized Hg atoms, and withstanding high electric fields (see Sect. 5.1.2).

The storage of UCNs requires surfaces to have a high neutron optical potential. We use diamond-like carbon (DLC) [56–61], with a measured optical potential $V_{\text{DLC}} \approx 230$ neV, as the electrode coating. For the insulator-ring coating it is planned to use deuterated polystyrene (dPS) [34], with $V_{\text{dPS}} \approx 160$ neV, or else a coating based on similar deuterated polymers.

The precession chamber stack will be placed inside the vacuum vessel, which is itself manufactured from aluminum with a usable internal volume of $1.6 \times 1.6 \times 1.2\text{m}^3$. The size of the magnetically sensitive area is significantly larger than in any previous or ongoing EDM experiment. This imposes serious challenges in order to ensure a stable and uniform magnetic field environment (see Sects. 5.2–5.4).

5.1.2 Electric field generation

The system of electrodes both confines the UCN precession volumes and provides the electric field in the n2EDM experiment. The central electrode will be connected via a feedthrough in the vacuum tank to the HV power supply, which will provide ± 180 kV. The two outer electrodes will be grounded. The optimisation of the electrode design is essential for achieving the highest electric field within the precession chamber, which increases the sensitivity to the neutron EDM. The optimisation process was performed with COMSOL [62], a finite element simulation software that allows one to build complex geometries of different materials and to simulate the resulting fields. The only requirement for the HV system is to provide a stable and uniform 15 kV/cm electric field, but there are several additional constraints on the design of electrodes.

- The Cs magnetometer arrays are mounted on the outer surfaces of the ground electrodes. The array has components that are sensitive to electric fields, and exposure must be minimized.
- Sharp edges can trigger field emission, limiting the maximum achievable electric field. In particular, the vacuum tank has a structured inside surface so the electric field should be close to zero there.
- The overall height of the entire precession chamber stack, including the components mounted on the outer surfaces – namely the UCN shutters, mercury polarization volumes and Cs magnetometer arrays – must fit in the available space. In total, this means an upper limit of 400 mm from the outer surface of one ground electrode to that of the other.

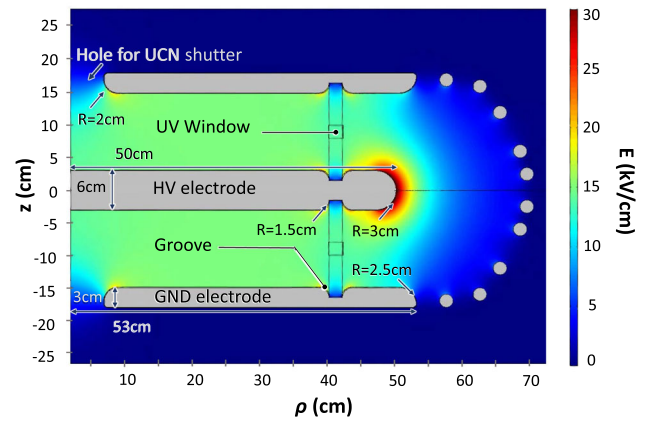


Fig. 15 COMSOL simulation of the n2EDM optimised geometry. The central (high voltage) electrode is at a potential of 180 kV. The simulation is symmetric on the top and bottom half of the figure

The maximum potential difference attained in the previous nEDM experiment was ± 200 kV. Using a COMSOL simulation with the nEDM geometry the maximum electric field at any point was found to be 30 kV/cm, which provided a limit for the highest acceptable field in the n2EDM design.

In Fig. 15 the optimized electrode geometry is illustrated. The different parameters of the geometry, listed in the legend, were varied independently of one another. Particular care was taken during the optimization process to control the electric field strength at the locations indicated by the arrows.

To meet the electric field goal, the thickness of the HV electrode was set to 6 cm to give a large enough radius on the electrode corona. The diameter of the HV electrode was found to be optimal at 100 cm to separate the influence of the electric field generated by the corona radius and the presence of the window needed for the UV light beam of the Hg magnetometer.

The thickness of the ground electrode was determined by the need for moderate radii around the UCN shutter hole (see Fig. 15), the groove for the insulator ring, and the corona, while still staying within the available space constraints. It was optimized to be 3 cm. The insulator ring groove depth is limited by the available material thickness to 1.5 cm.

A grounded cage of discrete aluminum rods surrounds the central electrodes and insulator in order to minimize the electric fields outside the region of the electrode stack. Several concepts were investigated: an assembly of rings, a fully enclosed shell, or a hybrid of the two designs. Performing COMSOL simulations of the various designs determined that they were all similar in terms of electric field containment. A fully enclosed shell, however, would have caused severe attenuation of the $\pi/2$ -flip Ramsey pulses, and therefore a hollow-ring open-cage design was chosen. This also minimises weight, simplifies the design and installation, and allows better vacuum performance. The simulations opti-

mised the shape and position of the rings while taking into account the need to allow the shell to be split into two halves for mechanical mounting and to have a large enough gap between each ring for effective vacuum pumping and penetration of the Ramsey-pulse fields.

5.1.3 UCN transport

The n2EDM apparatus is set up at Beamport South of the PSI UCN source. The position of the UCN chambers and the guiding of the UCNs from the UCN source to the chambers was optimized using the MCUCN code [28].

The UCNs first traverse the open beamport shutter, located just after the superconducting magnet (see Fig. 16). Then the UCN guide splits smoothly into two separate tubes, guiding the UCNs towards the two precession chambers through the UCN switch - a major component of the UCN transport system. The switch is located between the superconducting magnet and the MSR, and can operate in filling and counting configurations (see insert in Fig. 16). This is achieved by two movable UCN guides, one for each precession chamber. The UCNs first fill the precession chambers (filling configuration). The chambers are then closed by UCN plugs connected to two shutters: one on the top of the upper chamber, the other below the lower chamber. When emptying the precession chamber, the switch connects the same UCN guides used during filling to the spin-sensitive detection system (counting configuration). The third (test) mode of the switch permits the guiding of UCNs directly from the source to the detectors in order to monitor the UCN source performance.

The switch design was based on the common theme of maximizing the transmission efficiency. This resulted in stringent specifications such as the necessity to maintain the same total cross section for UCNs throughout their path in the apparatus, the optimization of the number of bends and the maximization of their radius of curvature, and the minimization of gaps between guides as far as reasonably possible with a target of 0.1 mm.

The UCN guides are made of glass tubes with an inside diameter of 130 mm and a NiMo coating with ultralow surface roughness [17]. The manufacturing of the UCN guides follows the process developed and successfully employed during the construction of the PSI UCN source [63]. The same process was used to produce the guides of the nEDM apparatus, where UCN transmissions above 97% per meter were achieved.

5.1.4 UCN spin-sensitive detection

At the end of the precession time, UCNs stored in the upper and lower precession chambers are released and directed towards two identical spin-sensitive counters. There, UCNs

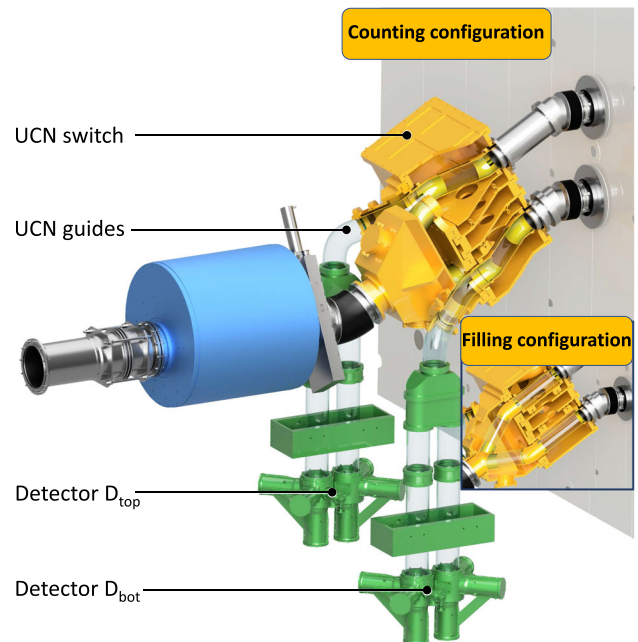


Fig. 16 Scheme of the beamline outside the MSR. The switch with movable UCN guides can operate in three modes: when UCNs are filling the precession chambers (filling configuration); when UCNs from the precession chambers are directed towards the two simultaneous spin-sensitive detectors (counting configuration); and a third (test) mode of the switch (not shown here) that permits guiding of UCNs directly from the source to the detectors in order to monitor the UCN source performance

are counted as a function of their spin state, behind distinct simultaneous spin analysers [64].

A UCN may be detected either in a spin-up state (spin parallel to the main magnetic field) or in a spin-down state (spin antiparallel to the main magnetic field). In order to detect simultaneously UCN of both spin states, a custom device consisting of two vertical arms, each arm being dedicated to the analysis of one spin state, has been designed and built. The first element of the device splits the UCN guide into two arms (see the Fig. 16 for the detailed geometry). Each arm consists of an adiabatic spin-flipper (ASF), an analyzing foil and a UCN counter (see Fig. 17). The adiabatic spin-flipper consists of a shielded RF coil installed upstream of the foil. Its operating principle is described in [65]. Spin-up UCNs are counted in the arm where the ASF is on, and spin-down UCNs in the arm where the ASF is off. The role of each arm is regularly reversed in order to minimize systematic effects. Ultracold neutrons entering the wrong arm with respect to their polarization (around 50% of the incoming UCNs) are reflected on the foil, and obtain a second chance to be detected in the correct arm. The internal shape of the unit is specifically designed to guide the reflected UCNs from one arm to the other and hence to improve the efficiency of the spin analysis.

The spin analysis itself is performed by transmission through (or reflection from) an iron foil magnetized to saturation ($B_{sat} \approx 2 T$) and located below the ASF. Ultracold neutrons are able to cross the foil if their kinetic energy associated with motion perpendicular to the foil (E_{\perp}) is larger than

$$U = V_{Fe} + \boldsymbol{\mu}_n \cdot \mathbf{B}_{sat} = V_{Fe} \pm |\mu_n| B_{sat}, \quad (92)$$

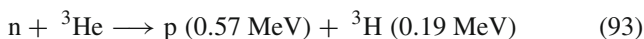
where V_{Fe} is the Fermi potential of iron, μ_n is the neutron magnetic moment, and B_{sat} the magnetic induction inside the iron layer. The \pm sign reflects the spin dependency of the magnetic interaction and stands for the spin-up and spin-down components, respectively.

Numerical estimates performed with the Fermi potential of the iron foil ($V_{Fe} = 210$ neV) and the magnetic potential energy ($\mu_n B_{sat} = 120$ neV) show that UCNs with energy $E_{\perp} < 90$ neV are reflected on the foil whatever their spin state while UCNs with $E_{\perp} > 330$ neV are transmitted through the foil. Between 90 neV and 330 neV the spin analysis (discrimination) is operational: spin-down UCNs are able to cross the foil while spin-up UCNs are reflected. Finally, the number of UCNs of a given spin state is counted with the counter installed below the foil.

It is important to emphasize that the height between the precession chambers and the spin analyzing foils is a critical parameter. The maximum kinetic energy of UCNs exiting the precession chambers is given by the Fermi potential of the insulator ring coating, $V_{DPS} = 165$ neV, as shown in Fig. 5. As a result, the height difference between the precession chambers and the spin analyzing foils should not exceed 165 cm in order to prevent UCN exceeding 330 neV - the maximum analyzable kinetic energy of the UCNs.

5.1.5 UCN counter

The UCN counter is a fast gaseous detector [66]. The neutron detection is based on scintillation occurring in a gas mixture of ^3He and CF_4 . Neutrons are captured by ^3He nuclei through the reaction



and the emitted proton and triton cause scintillation of the CF_4 molecules. The scintillation decay time is only about 10 ns [67], which provides a high count-rate capability up to a few 10^6 counts/s. The scintillation light is detected by three photomultiplier tubes working in coincidence. The partial ^3He gas pressure required to fully stop the UCN beam is low, between 10 and 20 mbar. The gas mixture is completed with CF_4 , and the detector is sealed. In order to reduce the probability of gamma interaction on CF_4 molecules as well as UCN upscattering, the partial CF_4 gas pressure is reduced to $P(\text{CF}_4) = 400$ mbar.

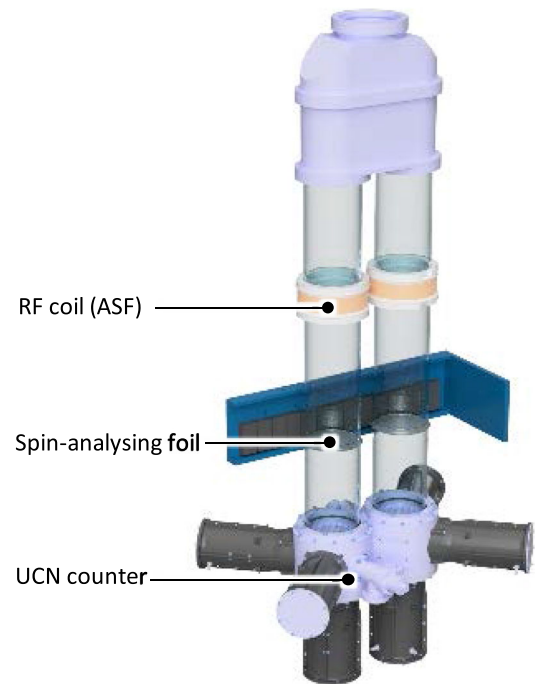


Fig. 17 Simultaneous spin analyzer. Each arm is equipped with an adiabatic spin-flipper (RF coil), a spin-analyzing foil and a UCN counter

5.2 Magnetic field shielding

A magnetically stable and uniform field is mandatory in order to exploit fully the statistical reach of the experiment. This is achieved by means of passive and active magnetic shielding, which are illustrated in Fig. 18.

Passive magnetic shielding is provided by a large cubic magnetically shielded room (MSR). Its performance in the low frequency range (< 5 Hz) is improved by the active magnetic shield (AMS), which consists of a system of actively controlled coils. The AMS is mounted on a grid around the MSR, and it compensates external magnetic field changes at the outermost mu-metal layer of the MSR.

5.2.1 Passive magnetic shield

The MSR, which was built in partnership with the company VAC,² provides the magnetic environment for the central part of the experiment. It suppresses external, quasi-static fields by roughly five orders of magnitude: a quasistatic shielding factor of better than 70,000 at 0.01 Hz was specified. After degaussing, the innermost central space was required to have a residual magnetic field smaller than 0.5 nT and a magnetic field gradient of less than 0.3 nT/m.

² VAC GmbH, Hanau, Germany (<https://www.vacuumschmelze.com>).

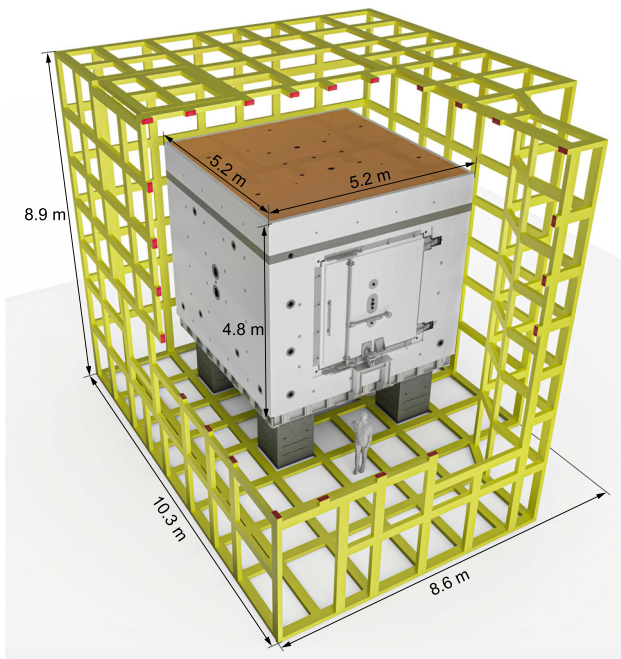


Fig. 18 Magnetic shielding. Passive shielding is provided by a large cubic magnetically shielded room (MSR). Active shielding consists of actively-controlled coils mounted on a grid around the MSR

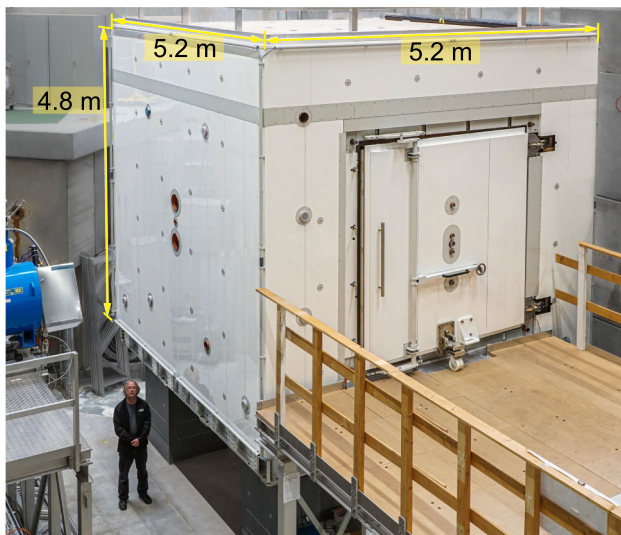


Fig. 19 Photo of the magnetically shielded room with indicated outer dimensions

The MSR design is based on the magnetic shielding requirements alongside the need to house the n2EDM apparatus in an optimal fashion. It incorporates six cubic layers of mu-metal and one additional layer of aluminum for radio-frequency shielding.

The MSR is composed of two cubic-shaped nested mu-metal rooms, referred to as “inner” and “outer”. The overall outer dimensions are given by a footprint of about

5.2 m × 5.2 m, as indicated in Fig. 19, and a height of 4.8 m. It has a total weight of about 50 tons.

The outer room has a two-layer mu-metal wall as well as an 8 mm thick aluminum layer that serves as an eddy-current shield. The inner room consists of a four-layer mu-metal shield, where the innermost layer is constructed from a specially selected high-permeability metal. It is a cube with inner dimensions of 293 cm on each axis. A small but accessible intermediate space between the inner and the outer rooms creates a useful and moderately magnetically shielded space close to the central apparatus. There, sensitive electronics for signal amplification, shaping and measurement may be located, e.g. pre-amplifiers for magnetometers, or precision-current sources. All parts of the inner cabin were tested for magnetic impurities at PTB’s BMSR-2 facility [68].

Each layer of the MSR is equipped with a separate set of degaussing coils. The ability to degauss each layer in this manner helps to provide uniform residual magnetic fields.

An air-conditioned thermal enclosure maintains the outer MSR at a temperature stable to 1 °C, and the innermost magnetically shielded room together with the apparatus has a temperature stability of better than 0.1 °C. This prevents thermal gradients across the MSR or temperature changes that would otherwise lead to magnetic-field changes through thermal expansion of materials and/or thermal currents.

The position of the MSR was chosen so as to allow for a straight path for UCNs from the source in order to minimize transport distance and losses.

5.2.2 Active magnetic shield

The n2EDM experiment is located in the vicinity of other facilities generating variable magnetic fields of similar strength to the Earth’s own field. Our experiment therefore experiences a magnetically noisy environment, subject to changes in the ambient magnetic field of up to tens of μT on timescales from minutes to hours. In order to realize the required magnetic field conditions in the inner part of n2EDM, shielding from external magnetic field changes is of key importance.

The stability of the magnetic field within the MSR is directly dependant on the stability of the field around the MSR. There are two complementary mechanisms for this. First, attenuation of external field fluctuations before they affect the MSR will improve the overall shielding factor multiplicatively. Second, avoiding changes in the magnetization of the outer passive shielding layers eliminates long-term drifts of the magnetic field inside the MSR.

In order to provide stable magnetic-field conditions around the MSR, the Active Magnetic Shielding (AMS) system was designed. It consists of a system of actively controlled coils.

Before the n2EDM construction, the magnetic field in the empty experimental area was mapped in 3D several times with different combinations of nearby superconducting magnets from other research installations switched on or off. It was found that the external field can be described with a precision of approximately $1 \mu\text{T}$ using a set of eight harmonic polynomials: three homogeneous components with five first-order gradients were able to match the reproducibility of the measurement. The measured field values were up to $50 \mu\text{T}$ in each spatial direction, and the gradients were up to $5 \mu\text{T/m}$ in each of the five linear components, thus specifying the required field strength for each component needed fully to compensate the large external field changes. The $1 \mu\text{T}$ field mapping accuracy was chosen as a target for the field-compensation accuracy.

The space available for the placement of coils is limited, being approximately 8 m in each dimension. A complex coil geometry is required to produce the desired compensating field. Additionally, coil elements cannot be placed at arbitrary locations due to conflicts with other parts of the apparatus as well as other practical considerations. An algorithm was developed to allow the design of geometry-confined coils that would produce arbitrary field configurations [69]. This allows the placing of current-carrying wires along a predetermined but not completely uniform grid that is mounted on the inside of the thermal shell around the MSR (see Fig. 18).

5.3 Magnetic field generation

Ramsey's method of oscillating fields requires polarized UCNs, a static B_0 field and two RF field pulses. The UCN polarization is achieved with a 5 T superconducting solenoid. The static field is mainly generated by a single large coil (the " B_0 coil") and its coupling to the innermost layer of the shield. An array of 56 independent correcting coils is used to tune the field to the required level of uniformity. Seven coils produce specific gradients that play an important role in the measurement procedure. Finally, the RF pulses of the Ramsey cycle are generated by RF coils installed inside the vacuum tank.

5.3.1 B_0 field generation

A B_0 field of $1 \mu\text{T}$ is produced by a vertical cubic solenoid complemented with two sets of seven horizontal loops symmetrically located on the top and the bottom. These end-cap loops help to suppress the field nonuniformities induced by the finite size of the magnet. The coil is fixed on a cubic support outside the vacuum tank, located at about 10 cm from the innermost mu-metal layer of the shield (Fig. 20). On one side, a large rotating door of size of $2 \text{ m} \times 2 \text{ m}$ allows access to the central part of the experiment.

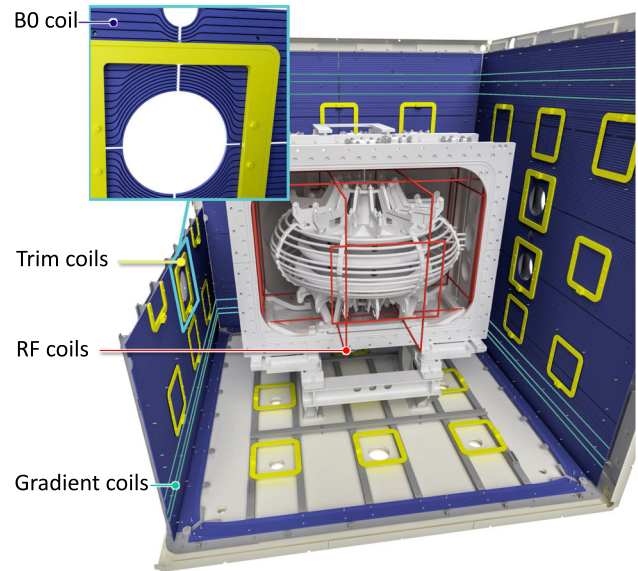


Fig. 20 The coil system inside the MSR (close to the innermost layer of the shield). For clarity, only the G10 coil is shown as an example of a gradient coil

The field produced by the B_0 coil and its coupling to the innermost layer of the shield was simulated with the COMSOL software package. For a current of 12 mA through the B_0 coil the magnitude of the field at the center is about $1 \mu\text{T}$, with approximately one third arising from the magnetization of the innermost mu-metal layer. The B_0 field is expected to increase a few percent after equilibration (degaussing within a non-zero surrounding and/or inner field). The field variations around the central value $B(\mathbf{0})$ have been estimated by computing $\Delta B(\mathbf{r}) = |\mathbf{B}(\mathbf{r}) - \mathbf{B}(\mathbf{0})|$. The variations, shown in Fig. 21, do not exceed 100 pT in a large volume that includes the precession chambers. The observed nonuniformities come from the openings that are present in the MSR walls as well as from a recess of the MSR door with respect to its surrounding wall.

From the simulated field maps it is also possible to estimate the field uniformity $\sigma(B_z)$ in the region of the precession chambers. The achieved uniformity, $\sigma(B_z) = 16 \text{ pT}$, is well below the requirement of 170 pT (see Sect. 3.4). The requirement is also fulfilled when the magnetic field is increased to the "magic" value of $10 \mu\text{T}$.

Such a high degree of uniformity is very sensitive to the reproducibility of the equilibration, and also to imperfections in the shielding material due to the construction from single sheets and the coupling of the B_0 field with the innermost shielding layer. Mechanical alignment is also critical; for instance, a vertical misalignment of one millimeter between the entire B_0 coil and the MSR triples the field nonuniformities as compared to the ideal symmetric case. While the B_0 coil will be installed with great care, unavoidable imperfections will remain. In order to suppress the induced

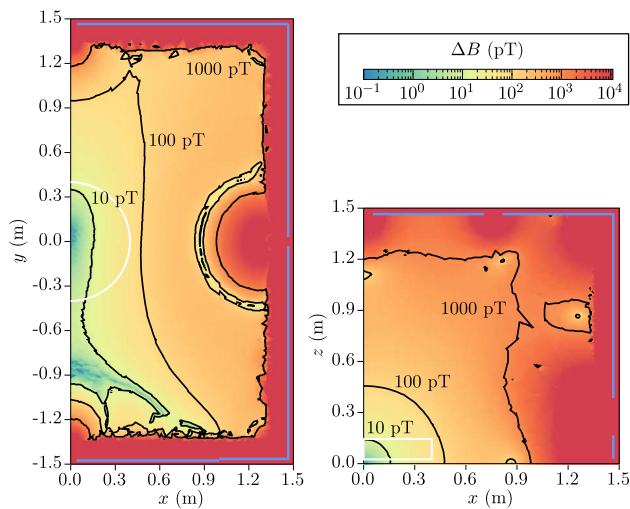


Fig. 21 COMSOL B-field simulation, showing field variations produced by the B_0 coil in the horizontal plane at $z = 0$ m (left) and the vertical plane $y = 0$ m (right). The rainbow scale corresponds to $\log_{10}(\Delta B)$. The contours of the precession chambers, which have a diameter of 80 cm, are shown in white, while the innermost layer of the MSR is shown in blue on the edges of the plots. The black bold contour lines highlight $\Delta B = 10, 100,$ and 1000 pT. The simulations are performed with the dimensions of the innermost layer of the MSR measured *in situ*. The μ_r values for the mu-metal material were communicated by the producer VAC² and are proprietary information

nonuniformities a set of 56 independent rectangular trim coils is used. They are fixed on the same cubic support as the B_0 coil, with nine or ten coils per side. These can produce all generic field gradients up to the 5th order.

With a B_0 field of $1 \mu\text{T}$, a stability of a few dozen fT on the timescale of a minute is required to achieve an efficient operation of the Hg co-magnetometer (see Sect. 5.4.1). The coil is therefore powered by an ultra-stable current source with a relative stability of a few $\times 10^{-8}$.

5.3.2 Generation of specific gradients

To control the magnetic-field gradient during data taking, as well as to study various systematic effects, seven additional field and gradient coils are mounted to the B_0 coil support.

A constant offset value for the three field components can be generated by three independent coils, with the underlying uniform B_z component being produced by the B_0 coil. The linear gradients of the B_z component, $\partial B_z/\partial x$, $\partial B_z/\partial y$, and $\partial B_z/\partial z$, can also be generated. Besides the optimisation of α (see Sect. 3.4), these are used to monitor and/or control *in situ* the positioning of every Cs magnetometer at the mm level (see Sect. 5.4.2). The field measured by each magnetometer probes their position in the three directions. The $\partial B_z/\partial z$ field is also used to perform the vertical tuning of the B_z component in order to fulfill the top/bottom matching condition (see

Sect. 3.4). The power supply of the $\partial_z B_z$ coil allows variation in the vertical linear gradient with a resolution of 0.01 pT/cm.

Finally, it is important to control the gradients responsible for the most significant systematic effect, the motional EDM. Therefore, in addition to the $\partial B_z/\partial z$ gradient, two other gradients that are of particular interest, $G_{2,0}$ and $G_{3,0}$, are produced by two additional independent coils.

5.3.3 RF field generation

Rotating fields perpendicular to the B_0 field are used at the beginning and end of the Ramsey cycles to flip the spins of the UCNs and of the Hg atoms into and out of the horizontal plane. These fields, of frequencies ~ 30 Hz and ~ 8 Hz respectively, are generated by the eight RF coils: four along the x axis and four along the y axis. The coils are located inside rather than outside the vacuum tank because of the pronounced damping that would be caused by the thick aluminum walls. Finite-Element Method simulations using ANSYS [70] were performed to study the impact of the electrodes and other conductive components close to the coils, and to optimize the setup. The simulated spatial homogeneity inside the precession chamber for the UCN pulse is $\sigma_{\text{RF}} < 120$ pT, well below the 170 pT upper limit requirement (see Eq. (21)).

5.3.4 UCN spin transport

The 5 T superconducting magnet (SCM) acts as an almost perfect polarizer ($P > 99\%$), producing an axial (horizontal) polarization. The transport of the UCN spin from the SCM to the precession chambers has two parts: outside the MSR, the SCM fringe field is sufficiently large to fulfil the adiabatic transport condition. At the MSR, the field is rotated from axial (horizontal) to transverse (vertical) and is adapted to the B_0 field strength between the shield entrance and the inner cabin of the MSR.

5.4 Magnetic field measurement

5.4.1 Magnetometry concept

Statistical and systematic uncertainties in a neutron EDM experiment depend on the homogeneity and the stability of the main magnetic field B_0 , in which the neutrons precess. The overall goal of the magnetometry systems in the n2EDM experiment is to ensure that all magnetic-field-related uncertainties are small compared to the fundamental statistical uncertainty given by the UCN counting. The two major magnetometry systems are the Hg co-magnetometer and an array of Cs magnetometers.

The magnetic-field information provided by the magnetometers of n2EDM is used in three sequential phases: before,

during, and after the actual measurement. In an initial phase, before the neutron measurements start, information about the magnetic field has to be acquired in order to provide a magnetic environment that allows for long neutron precession times. Magnetic-field inhomogeneities increase the neutron's depolarization rate and thus lead to a smaller visibility α , which in turn decreases the statistical sensitivity (see Eq. (5)). Since it is impossible to correct for a faster loss of neutron spin polarization after the measurement, the B_0 field must be sufficiently tuned for a high visibility α . We plan to use a magnetic-field mapper to study the distribution of the field inside the MSR in dedicated measurements once per year, usually during the accelerator shutdown period. We will also employ the array of Cs magnetometers (see Sect. 5.4.3) to fine-tune the field homogeneity during UCN data taking after each change of the magnetic-field polarity. This concept proved to be successful in our previous nEDM experiment and routinely provided neutron spin relaxation times of more than 1200 s [18].

During the data taking with neutrons, magnetic-field information is essential in order to keep the neutrons in a magnetic resonance condition. Ramsey's method provides a unique sensitivity to the Larmor precession frequency only if the final measurement of the neutron spin is on the steep slope of the interference pattern. In order to stay at these positions, it is necessary to correct for drifts of the magnetic field by adjusting the rf-pulse frequency or the relative phase between first and second pulse. In the previous experiment the field value measured in the previous Ramsey cycle using the Hg co-magnetometer (see Sect. 5.4.2) was used to compute the frequency of the Ramsey pulses. In n2EDM we will use the magnetic-field values deduced from the two Hg magnetometers to stabilize the working points. To achieve that, two parameters need to be controlled, for example the $\partial B_z/\partial z$ gradient and the frequency of the Ramsey pulses. We plan to keep the parameters that influence the working points static during a Ramsey cycle. They are chosen before the cycle starts based on the information from the previous Ramsey cycle. A dynamic compensation that uses information gained during the current cycle to update those parameters will only be considered if EDM sensitivity is lost in significant amounts due to drifting working points.

Last but not least, the entire time resolved, synchronously recorded information on the magnetic field will be used in the offline analysis to correct for the effect of magnetic-field fluctuations on the nEDM result. All magnetometer systems are involved in this process. The Hg co-magnetometer provides the primary magnetic reference measurement for the neutrons that helps us to distinguish changes in the neutron spin precession frequency due to magnetic-field changes or due to a possible EDM. A second magnetic reference is provided by the Cs magnetometers that surround the two neutron volumes. All magnetometers will be used to determine

magnetic-field gradients that cause systematic errors in the nEDM measurement.

5.4.2 Hg magnetometry

The n2EDM Hg magnetometry will follow the same operation principle as the original Hg co-magnetometer used in our previous experiment and introduced by the RAL/Sussex collaboration [27]. Atomic vapor of ^{199}Hg is polarized by optical pumping in a polarization cell placed on each of the ground electrodes of the precession chamber stack. The vapor in the polarization cell enters through a small valve into the precession chambers once they are filled with UCN. The application of a $\pi/2$ pulse starts the precession of the ^{199}Hg spins in the same volume as the neutrons. During the precession time, a photodetector records the power of a beam of resonant light traversing the chamber, which is modulated at the Larmor frequency by the interaction of the probe beam with precessing Hg atoms.

The sensitivity requirement per cycle of 25 fT (0.03 ppm at 1 μT) was already demonstrated for a 180 s precession time with our previous apparatus as part of our Hg R&D program [71]. This was made possible by replacing the Hg discharge-lamps used so far for the probe beam by a tunable UV laser. The analysis only uses data during two analysis windows at the beginning and the end of the signal. While the first window is always 20 s long the length of the second window (and correspondingly the amount of data used) can be varied. Figure 22 shows that statistical uncertainties are smaller than the required 25 fT for most combinations of Hg T_2 time and window length. Even stricter requirements, which might be necessary for a potential upgrade of n2EDM, can be fulfilled if the same performance as in our former experiment with T_2 times around 100 s can be achieved. Our experience shows clearly that long T_2 times of the Hg atoms can only be achieved if the precession chambers are periodically discharge cleaned.

5.4.3 Cs magnetometry

Cesium magnetometers were introduced to the nEDM experiments as auxiliary magnetometers in order to monitor the main magnetic field and its gradients. We plan to mount a set of such magnetometers in close vicinity to the neutron precession volume (see Fig. 14). The sensors of choice are optically pumped magnetometers (OPM) that detect the spin precession of Cs atoms and so gain an optical signal that is modulated at the Larmor frequency [72]. The basic sensor principle has been known for more than 50 years [73] and was initially studied using discharge lamps as light sources. Since affordable lasers for the required near-infrared wave-

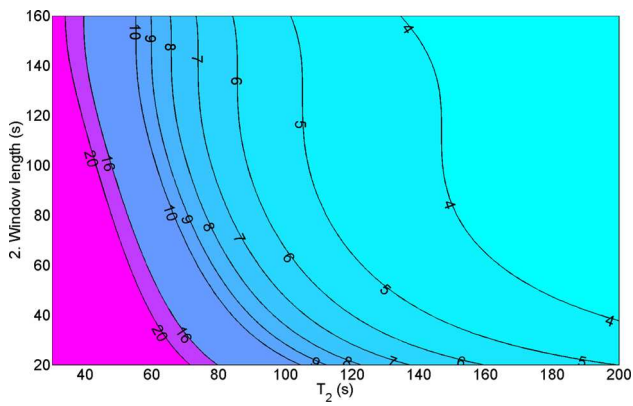


Fig. 22 Statistical magnetometer uncertainty based on a signal/noise measurement using laser light to polarize and probe the Hg atoms. The values are given in fT as a function of the Hg spin depolarization time (T_2) and the length of the signal windows used for the analysis

lengths have become available, this measurement principle has gained a renewed interest that has led to the development of many different OPM variants [74]. The OPMs in previous nEDM experiments [18, 75] used a mode of operation, called the M_x mode, that is sensitive to the magnitude of the magnetic field.

In past experiments [18] it was realized that the accuracy of the Cs sensors is the most critical factor limiting the usefulness of the measurements. Accurate sensor readings are necessary in order to extract information about the field gradients, which have to be known on an absolute scale. As a consequence our research and development efforts in Cs magnetometry has for several years focused on sensor stability and accuracy. We have developed highly stable vector magnetometers [76] and magnetically silent (all optical) magnetometers [77]. These designs are based on a pulsed approach that allows us to monitor the free-spin precession, in contrast to the M_x mode which is based on a continuously driven magnetic resonance. The free precession has significant advantages for the sensor accuracy, since it avoids a whole class of systematic effects. There is, however, a class of systematic errors related to the complex atomic spin structure that is present in all tested magnetometer schemes. The shift is significantly smaller if the magnetometer is operated with linearly polarized light, which creates and detects atomic spin alignment, in contrast to circularly polarized light, which interacts with atomic spin orientation. The offset is further suppressed if the light is propagating parallel to the magnetic field, since there is no first-order dependence on misalignment in this geometry. A prototype of a scalar magnetometer that combines the features mentioned above has been realized, showing a statistical uncertainty of $1 \text{ pT/Hz}^{1/2}$. This will be sufficient to meet the requirements of n2EDM.

In n2EDM we plan to mount an array of 114 Cs sensors above and below the two ground electrodes. The ability to

extract all relevant gradients from the measurements of the Cs sensors depends largely on the placement of the sensors. Such placement must minimise the effects of the uncertainty of their position and field readings, and is a non-trivial task. For this reason, a genetic algorithm was developed to output optimised coordinates of the CsM array. Its fitness function includes all $G_{l,0}$ gradients up to $l = 7$ weighted appropriately. These positions optimize the extraction of all gradient components responsible for systematic shifts in the neutron EDM and thus facilitate the correction of EDM results based on spatially resolved magnetic-field measurements. This optimized set of positions has the advantage that the correction is significantly less dependent on the accuracy of the Cs sensor readings and on the errors in their position. Figure 23 shows the remaining error in the most important gradient, $G_{3,0}$, after the correction with the Cs array as a function of placement accuracy. The light green area indicates the goal necessary for the projected initial performance of n2EDM. The curves show simulation results with an assumed magnetic measurement accuracy ranging from 0 pT (perfectly accurate) to 10 pT. Our goal is to achieve a geometrical placement accuracy of $\pm 0.5 \text{ mm}$, which leads to virtually no increase in extraction uncertainty of the gradient. Our goal for the magnetometric accuracy is 5 pT, which would give us a certain headroom for later upgrades of n2EDM. These goals, necessary for corrections to the neutron EDM measurements, are by far the most stringent requirements for the Cs magnetometer array. Requirements deduced from other types of measurements for which the CsM array will be used, like the homogenization of the magnetic field in order to avoid gradient-induced depolarization of neutrons, is thus automatically fulfilled if the simulated performance is achieved.

Since accuracy is so important, we plan to evaluate individually the accuracy of each Cs sensor in the array. For that purpose a calibration setup is currently being installed in the magnetic shield of the previous single-chamber spectrometer at PSI. The setup consists of a rotating platform that can accommodate up to seven Cs sensors and a reference magnetometer based on ^3He [78]. The setup permits the comparison of the reading of each of the Cs sensors and of the ^3He magnetometer to calibrate every Cs sensor that will be deployed.

5.4.4 Mapper

An automated magnetic-field mapper will be used for the coil system commissioning and its cartography as well as for offline control of high-order gradients and searches for magnetic contamination within the apparatus. These measurements require an empty vacuum vessel in which to install the mapper, and will be performed once per year during the accelerator shutdown period. Such a mapper apparatus has already been in use in the previous nEDM experiment. Although the

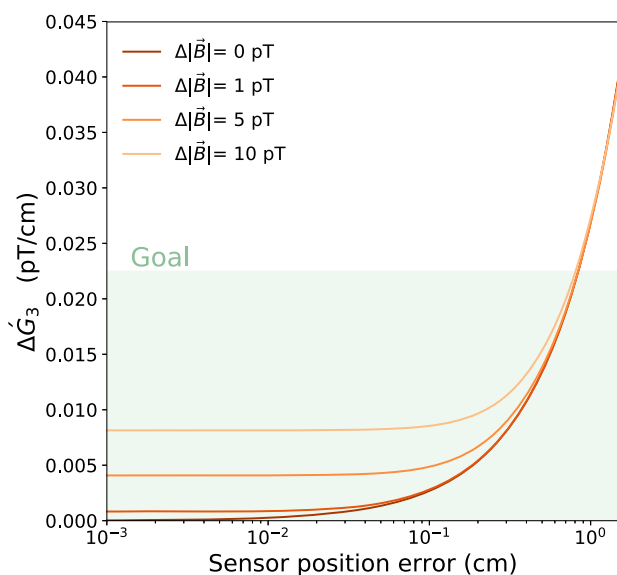


Fig. 23 Uncertainty of the calculation of the phantom gradient \hat{G}_3 . The different curves show simulations for different assumptions of Cs magnetometer accuracy

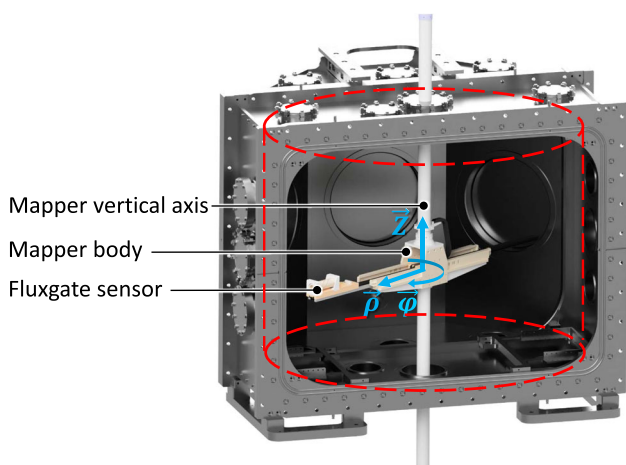


Fig. 24 Cutaway view of the mapper installed inside the vacuum vessel. The fluxgate can move along the ρ , φ , and z axes and can explore almost the entire volume of the vacuum vessel

design has evolved substantially over the years, the concept remains the same: a remote motion system allows movement of a magnetometer inside a large volume of interest.

The sensor, usually a three-axis low-noise fluxgate, will explore a cylinder of 80 cm diameter and 90 cm height, thus covering the majority of the vacuum vessel's inner volume (see Fig. 24).

The fluxgate can also be turned along the ρ axis in $\pi/2$ steps to determine the overall DC offset of each single fluxgate for absolute field measurements with < 200 pT accuracy. Every part of the robot mounted inside the MSR is made

of non-magnetic material (e.g. PEEK, POM and ceramics) and, in order to avoid Johnson noise, there are no metallic parts close to the magnetometer. The motorization block will be located outside, below the MSR, and is composed of three motors that are coupled to encoders for relative positioning of the magnetometer along the ρ , φ and z axes with a respective resolution of around 100 μm , 2 mrad and 5 μm . The absolute position of the mapper will be determined after each installation and before each dismantling using photogrammetry, with an accuracy on the order of 100 μm . The combination of the relative and absolute sensor position knowledge is well within the requirements needed to extract the fifth-order phantom mode \hat{G}_5 detailed in Sect. 4.

A typical map acquisition lasts a few hours for a few thousand measurement points, and therefore several magnetic field configurations can be measured in a single day. The complete analysis routine described in [79] will be used to extract the magnetic field gradients within a few seconds once the measurement sequence is complete.

Summary and conclusions

We presented details of the new n2EDM apparatus being developed and built by the international nEDM collaboration based at the ultracold neutron source at PSI, Switzerland, with a view to significantly improving the sensitivity of the ongoing search for an electric dipole moment of the neutron. The concept employed is based upon a room-temperature measurement of the spin-precession frequency of stored ultracold neutrons, using Ramsey's method of separated oscillatory fields in combination with an atomic mercury co-magnetometer. This principle lies behind the most successful measurement that has been made to date.

The concepts and requirements for the development of the new components, which are based on our experience with the previous apparatus, have been presented in detail. The expected increase in statistical sensitivity of a single Ramsey cycle for the chosen new design is stated. Advances in our understanding of systematic effects have been elaborated, and from these are derived the planned strategies to keep such effects under control.

The technical design of the core components is complete, and construction is ongoing. The various components developed by the collaborating institutions are gradually arriving at PSI for integration into the new apparatus. It has been demonstrated that a sensitivity of 1×10^{-27} e cm can be reached after 500 days of data taking. Possible future modifications are expected to lead to a sensitivity well within the 10^{-28} e cm range.

Acknowledgements We gratefully acknowledge the outstanding support from technicians, engineers and other professional services throughout the collaboration: B. Blau, K. Boutellier, B. Bougard, J. F. Cam, B. Carniol, M. Chala, A. Chatzimichailidis, M. Dill, P. Desrues, P. Erisman, A. Ersin, D. Etasse, R. Faure, C. Fourel, J. Fulachier, C. Fontbonne, C. Geraci, A. Gnädinger, U. Greuter, J. Hadobas, L. Holitzner, J. Hommet, M. Horisberger, S. Hauri, B. Jehle, R. Käch, G. Käslin, C. Kramer, K. Lojek, S. Major, M. Mähr, J. Marpaud, C. Martin, M. Marton, Y. Merrer, O. Morath, R. Nicolini, L. Noorda, F. Nourry, J. Odier, J. Oertli, C. Pain, J. Perronnel, M. Philippin, W. Pfister, S. Roni, S. Roudier, D. Reggiani, R. Schwarz, J.P. Scordilis, M. Stöckli, C. Strässle, V. Talanov, V. Teufel, C. Thomassé, C. VanDamme, C. Vescovi, A. Van Loon, R. Wagner, X. Wang, J. Welte. We are grateful for financial support from the the Swiss National Science Foundation through projects 200020-188700 (PSI), 200020-137664 (PSI), 200021-117696 (PSI), 200020-144473 (PSI), 200021-126562 (PSI), 200021-181996 (Bern), 200020-172639 (ETH), R'EQUIP under numbers 139140 and 177008 and FLARE 20FL21-186179. The support by Emil-Berthele-Fonds is acknowledged. The LPC Caen and the LPSC Grenoble acknowledge the support of the French Agence Nationale de la Recherche (ANR) under reference ANR-14-CE33-0007 and the ERC project 716651-NEDM. The Polish collaborators acknowledge support from the National Science Center, Poland, Grants no. 2015/18/M/ST2/00056, no. 2018/30/M/ST2/00319, no. 2016/23/D/ST2/00715 and no. 2020/37/B/ST2/02349. Support by the Cluster of Excellence "Precision Physics, Fundamental Interactions, and Structure of Matter" (PRISMA & EXC 2118/1) funded by the German Research Foundation (DFG) within the German Excellence Strategy (Project ID 39083149) is acknowledged. This work was partly supported by the Fund for Scientific Research Flanders (FWO) and Project GOA/2010/10 of the KU Leuven. The Core Facility "Metrology of Ultra-Low Magnetic Fields" at PTB was funded by Deutsche Forschungsgemeinschaft (DFG) through funding codes: DFG KO 5321/3-1 and TR408/11-1.

Data Availability Statement This manuscript has no associated data or the data will not be deposited. [Authors' comment: Data is available upon request from the Authors.]

Open Access This article is licensed under a Creative Commons Attribution 4.0 International License, which permits use, sharing, adaptation, distribution and reproduction in any medium or format, as long as you give appropriate credit to the original author(s) and the source, provide a link to the Creative Commons licence, and indicate if changes were made. The images or other third party material in this article are included in the article's Creative Commons licence, unless indicated otherwise in a credit line to the material. If material is not included in the article's Creative Commons licence and your intended use is not permitted by statutory regulation or exceeds the permitted use, you will need to obtain permission directly from the copyright holder. To view a copy of this licence, visit <http://creativecommons.org/licenses/by/4.0/>. Funded by SCOAP³.

References

- M. Pospelov, A. Ritz, *Ann. Phys.* **318**(1), 119 (2005). <http://www.sciencedirect.com/science/article/pii/S0003491605000539>
- J. Engel, M.J. Ramsey-Musolf, U. van Kolck, *Prog. Part. Nucl. Phys.* **71**, 21 (2013). <http://www.sciencedirect.com/science/article/pii/S0146641013000227>
- D.E. Morrissey, M.J. Ramsey-Musolf, *New J. Phys.* **14**(12), 125003 (2012). <https://doi.org/10.1088/1367-2630/14/12/125003>
- C. Abel et al., *Phys. Rev. Lett.* **124**(8), 081803 (2020). <https://doi.org/10.1103/PhysRevLett.124.081803>
- B. Graner et al., *Phys. Rev. Lett.* **116**(16), 161601 (2016). <https://doi.org/10.1103/PhysRevLett.116.161601>
- P. Sikivie, *Comptes Rendus Phys.* **13**(2), 176 (2012). <http://www.sciencedirect.com/science/article/pii/S1631070511002039>
- R.D. Peccei, H.R. Quinn, *Phys. Rev. Lett.* **38**(25), 1440 (1977). <https://doi.org/10.1103/PhysRevLett.38.1440>
- D.J. Marsh, *Phys. Rep.* **643**, 1 (2016). <http://www.sciencedirect.com/science/article/pii/S0370157316301557>
- P.W. Graham et al., *Annu. Rev. Nucl. Part. Sci.* **65**(1), 485 (2015). <https://doi.org/10.1146/annurev-nucl-102014-022120>
- K. Jungmann, *Annalen der Physik* **525**(8–9), 550 (2013). <https://doi.org/10.1002/andp.201300071>
- T. Chupp, M. Ramsey-Musolf, *Phys. Rev. C* **91**(3), 035502 (2015). <https://doi.org/10.1103/PhysRevC.91.035502>
- T.E. Chupp et al., *Rev. Mod. Phys.* **91**(1), 015001 (2019). <https://doi.org/10.1103/RevModPhys.91.015001>
- G. Pignol (2019). [arXiv:1912.07876](https://arxiv.org/abs/1912.07876)
- C. Baker et al., *Nucl. Instrum. Methods A* **736**, 184 (2014). <http://www.sciencedirect.com/science/article/pii/S0168900213013193>
- B. Lauss et al., *AIP Conf. Proc.* **1441**(1), 576 (2012). <https://doi.org/10.1063/1.3700622>
- B. Lauss, *Phys. Procedia* **51**, 98 (2014). <http://www.sciencedirect.com/science/article/pii/S1875389213007104>
- G. Bison et al., *Eur. Phys. J. A* **56**(2), 33 (2020). <https://doi.org/10.1140/epja/s10050-020-00027-w>
- C. Abel et al., *Phys. Rev. A* **101**(5), 053419 (2020). <https://doi.org/10.1103/PhysRevA.101.053419>
- S. Afach et al., *Eur. Phys. J. A* **51**, 143 (2015). <https://doi.org/10.1140/epja/i2015-15143-7>
- M. Ahmed et al., *J. Instrum.* **14**(11), 11017 (2019). <https://doi.org/10.1088/1748-0221/14/11/p11017>
- T.M. Ito et al., *Phys. Rev. C* **97**(1), 012501 (2018). <https://doi.org/10.1103/PhysRevC.97.012501>
- R. Picker, *J.P.S. Conf. Proc.* **13**, 010005 (2017). <https://doi.org/10.7566/JPSCP.13.010005>
- E. Chanel et al., in *Proceedings of the International Workshop on Particle Physics at Neutron Sources (PPNS)*, vol. 219 (2019), p. 02004. <https://doi.org/10.1051/epjconf/201921902004>
- D. Wurm et al., in *Proceedings of the International Workshop on Particle Physics at Neutron Sources (PPNS)*, vol. 219 (2019), p. 02006. <https://doi.org/10.1051/epjconf/201921902006>
- A. Serebrov, *POS (INPS2016)* **281**, 179 (2017). <https://doi.org/10.2323/1.281.0179>
- I.S. Altarev et al., *Nucl. Phys. A* **341**(2), 269 (1980). <http://adsabs.harvard.edu/abs/1980NuPhA.341..269A>
- K. Green et al., *Nucl. Instrum. Methods A* **404**(2–3), 381 (1998). <http://adsabs.harvard.edu/abs/1998NIMPA.404..381G>
- G. Zsigmond, *Nucl. Instrum. Methods A* **881**, 16 (2018). <http://www.sciencedirect.com/science/article/pii/S0168900217311476>
- D.A. Ries, The source for ultracold neutrons at the Paul Scherrer Institute—characterisation, optimisation, and international comparison. Ph.D. thesis, ETH Zurich, Zürich (2016). <https://doi.org/10.3929/ethz-a-010795050>
- G. Bison et al., *Phys. Rev. C* **95**(4), 045503 (2017). <https://doi.org/10.1103/PhysRevC.95.045503>
- V. Bondar et al., *Phys. Rev. C* **96**(3), 035205 (2017). <https://doi.org/10.1103/PhysRevC.96.035205>
- C. Abel et al., *Phys. Lett. B* **812**, 135993 (2021). <https://doi.org/10.1016/j.physletb.2020.135993>
- F. Atchison et al., *Phys. Lett. B* **625**, 19 (2005). <https://www.sciencedirect.com/science/article/abs/pii/S0370269305011846?via=ihub>
- K. Bodek et al., *Nucl. Instrum. Methods* **597**(2), 222 (2008). <http://www.sciencedirect.com/science/article/pii/S0168900208014381>

35. G. Bison et al., Experimental and simulation study of the energy dependent ultracold neutron transport at the PSI UCN source. *Eur. Phys. J. A* (2021) (in preparation)
36. C. Abel et al., *Phys. Rev. A* **99**(4), 042112 (2019). <https://doi.org/10.1103/PhysRevA.99.042112>
37. S. Afach et al., *Phys. Rev. D* **92**, 052008 (2015). <https://doi.org/10.1103/PhysRevD.92.052008>
38. S. Afach et al., *Phys. Rev. Lett.* **115**, 162502 (2015). <https://doi.org/10.1103/PhysRevLett.115.162502>
39. A.G. Redfield, *IBM J. Res. Dev.* **1**(1), 19 (1957). <https://ieeexplore.ieee.org/abstract/document/5392713>
40. S.K. Lamoreaux, *Phys. Rev. A* **53**(6), R3705 (1996). <https://doi.org/10.1103/PhysRevA.53.R3705>
41. J.M. Pendlebury et al., *Phys. Rev. A* **70**(3), 032102 (2004). <https://doi.org/10.1103/PhysRevA.70.032102>
42. S.K. Lamoreaux, R. Golub, *Phys. Rev. A* **71**(3) (2005). <https://doi.org/10.1103/PhysRevA.71.032104>, <https://link.aps.org/doi/10.1103/PhysRevA.71.032104>
43. A.L. Barabanov, R. Golub, S.K. Lamoreaux, *Phys. Rev. A* **74**(5), 052115 (2006). <https://doi.org/10.1103/PhysRevA.74.052115>
44. S.M. Clayton, J. Magn. Reson. **211**(1), 89 (2011). <http://www.sciencedirect.com/science/article/pii/S1090780711001418>
45. C. Swank, A. Petukhov, R. Golub, *Phys. Lett. A* **376**(34), 2319 (2012). <http://www.sciencedirect.com/science/article/pii/S0375960112006330>
46. G. Pignol, S. Rocchia, *Phys. Rev. A* **85**(4), 042105 (2012). <https://doi.org/10.1103/PhysRevA.85.042105>
47. G. Pignol et al., *Phys. Rev. A* **92**(5), 053407 (2015). <https://doi.org/10.1103/PhysRevA.92.053407>
48. R. Golub et al., *Phys. Rev. A* **92**(6), 062123 (2015). <https://doi.org/10.1103/PhysRevA.92.062123>
49. C.M. Swank, A.K. Petukhov, R. Golub, *Phys. Rev. A* **93**(6), 062703 (2016). <https://doi.org/10.1103/PhysRevA.93.062703>
50. S. Afach et al., *Eur. Phys. J. D* **69**(10), 225 (2015). <https://doi.org/10.1140/epjd/e2015-60207-4>
51. G. Pignol, *Phys. Lett. B* **793**, 440 (2019). <http://www.sciencedirect.com/science/article/pii/S0370269319303235>
52. C. Abel et al., Johnson–Nyquist noise effects in neutron electric-dipole-moment experiments. *Phys. Rev. A* (2021) (in preparation)
53. S.K. Lamoreaux, R. Golub, *Phys. Rev. Lett.* **98**(14), 149101 (2007). <https://doi.org/10.1103/PhysRevLett.98.149101>
54. P. Schofield, *Neutron News* **3**(3), 29 (1992). <https://ncnr.nist.gov/resources/n-lengths/elements/hg.html>
55. A. Abragam et al., *J. Phys. Lett.* **36**(11), 263 (1975). <https://hal.archives-ouvertes.fr/jpa-00231204>
56. M. van der Grinten et al., *Nucl. Instrum. Methods A* **423**(2), 421 (1999). <http://www.sciencedirect.com/science/article/pii/S0168900298013382>
57. F. Atchison et al., *Phys. Lett. B* **642**(1), 24 (2006). <http://www.sciencedirect.com/science/article/pii/S037026930601166X>
58. F. Atchison et al., *Phys. Rev. C* **74**(5), 055501 (2006). <https://doi.org/10.1103/PhysRevC.74.055501>
59. F. Atchison et al., *Phys. Rev. C* **76**(4), 044001 (2007). <https://doi.org/10.1103/PhysRevC.76.044001>
60. F. Atchison et al., *Diam. Relat. Mater.* **16**(2), 334 (2007). <http://www.sciencedirect.com/science/article/pii/S0925963506002160>
61. F. Atchison et al., *Nucl. Instrum. Methods A* **587**, 82 (2008). <https://www.dora.lib4ri.ch/psi/islandora/object/psi:18824>
62. COMSOL Multiphysics®, ver. 5.3. <http://www.comsol.com>
63. B. Blau et al., *Nucl. Instrum. Method A* **807**, 30 (2016). <http://www.sciencedirect.com/science/article/pii/S0168900215013091>
64. S. Afach et al., *Eur. Phys. J. A* **51**(11), 143 (2015). <https://doi.org/10.1140/epja/i2015-15143-7>
65. S. Grigoriev, A. Okorokov, V. Runov, *Nucl. Inst. Method A* **384**(2), 451 (1997). <http://www.sciencedirect.com/science/article/pii/S0168900296009199>
66. W. Saenz, A gaseous detector for ultracold neutrons in the n2edm project. Master's thesis, Université de Caen Normandie (2019). <http://hal.in2p3.fr/in2p3-02957354>
67. G. Lehaut et al., *Nucl. Instrum. Methods A* **797**, 57 (2015). <https://www.sciencedirect.com/science/article/abs/pii/S0168900215007093?via=ihub>
68. J. Bork et al., in *Proceedings of the 12th International Conference on Biomagnetism Biomag2000*, vol. 970 (2001)
69. M. Rawlik et al., *Am. J. Phys.* **86**(8), 602 (2018). <https://doi.org/10.1119/1.5042244>
70. ANSYS®. <http://www.ansys.com>
71. G. Ban et al., *Nucl. Instrum. Methods A* **896**, 129 (2018). <https://doi.org/10.1016/j.nima.2018.04.025>
72. E. Aleksandrov et al., *Tech. Phys. Lett.* **32**(7), 627 (2006). <https://doi.org/10.1134/S1063785006070236>
73. A.L. Bloom, *Appl. Opt.* **1**, 61 (1962). <https://doi.org/10.1364/AO.1.000061>
74. D. Budker, M. Romalis, *Nat. Phys.* **3**, 227 (2007). <https://doi.org/10.1038/nphys566>
75. A.P. Serebrov et al., *Phys. Rev. C* **92**(5), 055501 (2015). <https://doi.org/10.1103/PhysRevC.92.055501>
76. S. Afach et al., *Opt. Express* **23**(17), 22108 (2015). <http://www.opticsexpress.org/abstract.cfm?URI=oe-23-17-22108>
77. Z.D. Grujić et al., *Eur. Phys. J. D* **69**, 135 (2015). <https://doi.org/10.1140/epjd/e2015-50875-3>
78. H.C. Koch et al., *EPJ D* **69**, 202 (2015). <https://doi.org/10.1140/epjd/e2015-60018-7>
79. C. Abel et al., Mapping of the magnetic field to correct systematic effects in a neutron electric dipole moment experiment. *Phys. Rev. A* (2021) (in preparation)

Johnson-Nyquist Noise Effects in Neutron Electric-Dipole-Moment Experiments

N. J. Ayres,¹ G. Ban,² G. Bison,³ K. Bodek,⁴ V. Bondar,¹ P.-J. Chiu,^{1,3,*} B. Clement,⁵ C. B. Crawford,⁶ M. Daum,³ S. Emmenegger,¹ M. Fertl,⁷ A. Fratangelo,⁸ W. C. Griffith,⁹ Z. D. Grujić,¹⁰ P. G. Harris,⁹ K. Kirch,^{1,3} P. A. Koss,^{11,†} B. Lauss,³ T. Lefort,² P. Mohanmurthy,^{1,3,‡} O. Naviliat-Cuncic,² D. Pais,^{1,3} F. M. Piegsa,⁸ G. Pignol,⁵ D. Rebreyend,⁵ I. Rienäcker,^{1,3} D. Ries,¹² S. Rocchia,^{5,13} K. U. Ross,¹² D. Rozpedzik,⁴ P. Schmidt-Wellenburg,^{3,§} A. Schnabel,¹⁴ N. Severijns,¹¹ B. Shen,¹² R. Tavakoli Dinani,¹¹ J. A. Thorne,⁸ R. Virost,⁵ N. Yazdandoost,¹² J. Zejma,⁴ and G. Zsigmond³

¹*ETH Zürich, Institute for Particle Physics and Astrophysics, CH-8093 Zürich, Switzerland*

²*Normandie Université, ENSICAEN, UNICAEN, CNRS/IN2P3, LPC Caen, 14000 Caen, France*

³*Paul Scherrer Institut, CH-5232 Villigen PSI, Switzerland*

⁴*Marian Smoluchowski Institute of Physics, Jagiellonian University, 30-348 Cracow, Poland*

⁵*Université Grenoble Alpes, CNRS, Grenoble INP, LPSC-IN2P3, 38026 Grenoble, France*

⁶*Department of Physics and Astronomy, University of Kentucky, Lexington, Kentucky, 40506, USA*

⁷*Institute of Physics, Johannes Gutenberg University Mainz, 55128 Mainz, Germany*

⁸*Laboratory for High Energy Physics and Albert Einstein Center for Fundamental Physics, University of Bern, CH-3012 Bern, Switzerland*

⁹*Department of Physics and Astronomy, University of Sussex, Falmer, Brighton BN1 9QH, United Kingdom*

¹⁰*Institute of Physics Belgrade, University of Belgrade, 11080 Belgrade, Serbia*

¹¹*Instituut voor Kern- en Stralingsfysica, University of Leuven, B-3001 Leuven, Belgium*

¹²*Department of Chemistry - TRIGA site, Johannes Gutenberg University Mainz, 55128 Mainz, Germany*

¹³*Institut Laue-Langevin, CS 20156 F-38042 Grenoble Cedex 9, France*

¹⁴*Physikalisch-Technische Bundesanstalt, D-10587 Berlin, Germany*

Magnetic Johnson-Nyquist noise (JNN) originating from metal electrodes, used to create a static electric field in neutron electric-dipole-moment (nEDM) experiments, may limit the sensitivity of measurements. We present here the first dedicated study on JNN applied to a large-scale long-measurement-time experiment with the implementation of a co-magnetometry. In this study, we derive surface- and volume-averaged root-mean-square normal noise amplitudes at a certain frequency bandwidth for a cylindrical geometry. In addition, we model the source of noise as a finite number of current dipoles and demonstrate a method to simulate temporal and three-dimensional spatial dependencies of JNN. The calculations are applied to estimate the impact of JNN on measurements with the new apparatus, n2EDM, at the Paul Scherrer Institute. We demonstrate that the performances of the optically pumped ¹³³Cs magnetometers and ¹⁹⁹Hg co-magnetometers, which will be used in the apparatus, are not limited by JNN. Further, we find that in measurements deploying a co-magnetometer system, the impact of JNN is negligible for nEDM searches down to a sensitivity of $4 \times 10^{-28} e \cdot \text{cm}$ in a single measurement; therefore, the use of economically and mechanically favored solid aluminum electrodes is possible.

I. INTRODUCTION

The search for a permanent electric dipole moment of the neutron (nEDM) has been an important topic in fundamental physics research since the 1950s [1]. These experiments have been carried out by comparing the Larmor precession frequencies of neutron spins (f_n) under static uniform parallel and anti-parallel electric and magnetic fields, using the Ramsey technique of separated oscillating fields [2, 3]. For an accurate and precise measurement of f_n , controlling the stability and uniformity as well as reducing the noise of the magnetic field in the apparatus are of paramount importance. A potential source of magnetic-field disturbance is Johnson-Nyquist noise (JNN) [4, 5], originating from the thermal motion of electrons in metal components within the experimental apparatus.

Johnson-Nyquist noise was originally observed as a “random variation of potential between the ends of a conductor” [4]. The same underlying effect, random ther-

mal motion of charge carriers, also results in fluctuation of the electromagnetic field near a conductor. Magnetic JNN is relevant in various research domains, all related to measurements with highest precision. The first published numerical analysis of JNN came from the bio-magnetic measurements [6] using superconducting quantum interference devices (SQUIDs). Johnson-Nyquist noise often exceeds the intrinsic noise of modern high-sensitivity detectors such as SQUIDs [6–9] and high-density alkali atomic magnetometers [10]. More recently, it was observed that these magnetic-near-field fluctuations induce spin-flip processes, and in turn are a crucial element of decoherence in magnetic traps which limits the trapping lifetime of atoms [11–16]. In addition, relaxations of spin states in the presence of magnetic fluctuations were also studied in the context of magnetic resonance force microscopy and quantum computation [17]. In EDM measurements, following the requirement of sensitivity enhancement, potential constraints from JNN received extensive attentions in the last few decades [18–21]. Johnson-Nyquist noise from metal parts in high precision experiments impose a limit on the measurement sensitivity. Quantifying the impact of JNN in the design of the n2EDM experiment [22, 23] to search for an nEDM at the Paul Scherrer Institute (PSI) in Villigen, Switzerland, with the PSI ultracold-neutron (UCN) source [24, 25] motivates the presented research.

* Corresponding author: pin-jung.chiu@psi.ch

† Present address: Fraunhofer-Institut für Physikalische Messtechnik IPM, 79110 Freiburg i. Breisgau, Germany

‡ Present address: University of Chicago, 5801 S Ellis Ave, Chicago, IL 60637, USA.

§ Corresponding author: philipp.schmidt-wellenburg@psi.ch

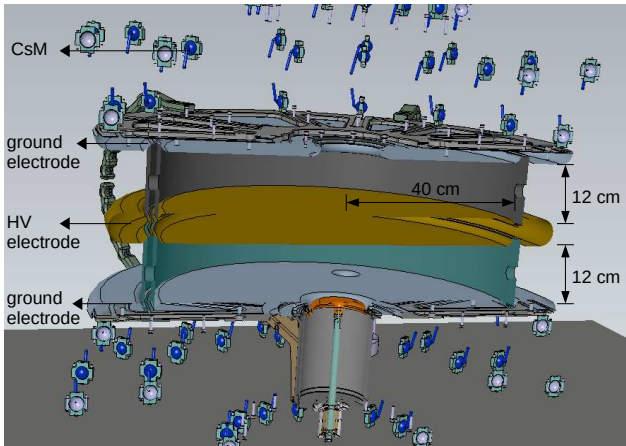


FIG. 1: Cross-sectional drawing of the central storage chambers of the n2EDM apparatus located inside the vacuum tank. Included are only components relevant to this study. For a better visibility, the support structure of the Cs magnetometers (CsM) and the top UCN shutter are omitted. The electrodes are separated by polystyrene insulating rings.

As in the past, the challenges in measuring nEDM, d_n , are the increase of the statistical sensitivity and the corresponding control of systematic effects. New sources of UCN worldwide [26, 27] improve the statistical sensitivity, $\sigma_{d_n} \propto N^{-1/2}$, by increasing the number of neutrons available after storage, N . Nevertheless, owing to systematic effects, e.g. random frequency shifts due to possible magnetic-field noise or drifts, the improvement in pure counting statistics might be compromised. This study investigates the impact of JNN on nEDM experiments, focusing especially on the n2EDM spectrometer [22, 23] currently under construction at the PSI.

The n2EDM apparatus features two cylindrical storage chambers, 12 cm in height and 40 cm in radius, stacked vertically. The two chambers share the central plane, an electrode to which a high voltage of up to 200 kV can be applied. The top and bottom of the cylinder pair are closed with grounded plates. Figure 1 shows a simplified drawing of the central storage chambers with the components relevant to this paper, whereas detailed descriptions and schematics of the experimental apparatus can be found in Figs. 1 and 2 of Ref. [22]. The three electrodes are made of aluminum plates, whose surfaces pointing towards the inside of the UCN storage chambers are coated with diamond-like carbon (DLC) [28, 29] in order to optimize the UCN reflection properties.

Thermal motion of charge carriers in the bulk aluminum results in magnetic JNN, which might affect the sensitivity of the magnetometers in its vicinity. In the following, we investigate the effects of JNN on the cesium magnetometers (CsM) [30, 31], glass bulbs filled with saturated ^{133}Cs vapor positioned around the precession chambers, the UCN and the mercury co-magnetometers (HgM), polarized ^{199}Hg atoms occupying the same volumes as the UCN in the chambers and read out by resonant light beams [32–34].

II. SPECTRUM OF MAGNETIC JOHNSON-NYQUIST NOISE

The relevant magnetic JNN spectrum was first analytically derived for research in biophysical applications [6, 8]. There it is shown that for an infinite-slab conductor of thickness a and conductivity σ at a temperature T , the normal component of the amplitude spectral density (ASD) found in a distance d to the conductor surface within a finite frequency interval Δf , with the z -axis defined to be perpendicular to the conductor surface, can be written as [6]

$$\begin{aligned} \mathcal{B}_z(d, f) &= \sqrt{B_z(d, f)^2 / \Delta f} \\ &= \mu_0 \sqrt{\frac{2\sigma k_B T}{\pi}} \left[\int_0^\infty R(\rho, a, \sigma, f) e^{-2\rho d} \rho d\rho \right]^{1/2}, \end{aligned} \quad (1)$$

where k_B is the Boltzmann constant, ρ is the radial component of the infinite conductor, and $B_z(d, f)$ is the magnetic-field amplitude normal to the surface at a given frequency f [35]. $R(\rho, a, \sigma, f)$ in Eq. (1) is a function of conductor properties, a and σ , at a given frequency f , with the original expression defined in Eq. (39) of Ref. [6]. For the horizontal components, due to symmetry and Maxwell's equations, one can infer that [6]

$$\mathcal{B}_x(d, f) = \mathcal{B}_y(d, f) = \frac{1}{\sqrt{2}} \mathcal{B}_z(d, f). \quad (2)$$

All three components of the noise spectrum depend on the normal distance between the point of interest and the surface of the infinite slab. Figure 2 shows the normal ASD of a 2.5-cm-thick aluminum infinite-slab conductor, $\sigma = 3.77 \times 10^7$ S/m, under 20 °C at various distances, using Eq. (1). The spectral line flattens at low frequencies towards a constant value equal to the root-mean-square (RMS) limit for $f \rightarrow 0$. With increasing frequency, the noise amplitude decreases due to self-damping of high-frequency noise within the conductor slab.

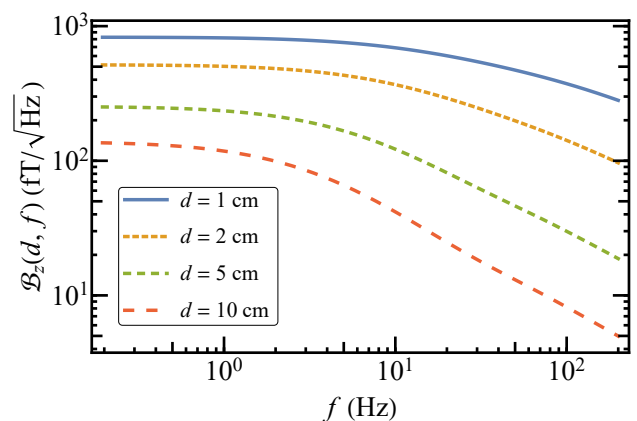


FIG. 2: Normal amplitude spectral density of a 2.5-cm-thick aluminum ($\sigma = 3.77 \times 10^7$ S/m) infinite-slab conductor at various distances under 20 °C.

To verify these noise spectra, measurements of the magnetic-field noise created by an aluminum sheet were carried out in the magnetically shielded room BMSR-2 at the Physikalisch-Technische Bundesanstalt (PTB), Berlin, Germany [36], using the 304-channel SQUID-vector-magnetometer system [37]. The system is based on

nineteen modules placed on a hexagonal grid with each comprising of sixteen SQUIDs placed at various vertical planes. A total of 304 SQUIDs each with a 7 mm effective pickup-coil diameter permit to calculate all three vector components of the magnetic field on three measurement planes. The noise of a sheet made of 99.5% aluminum with dimensions of $1.3 \text{ m} \times 1 \text{ m} \times 0.5 \text{ mm}$ was measured. In the first measurement, the sheet was placed to touch the flat bottom of the dewar cryostat, resulting in a minimal distance of 27.5 mm between sample and SQUIDs, due to the cold-warm distance of the dewar. Another measurement was carried out by adding a wood plate in between aluminum sheet and dewar to provide an additional 7.5 mm distance to the dewar bottom. In each measurement, seven SQUIDs at different heights from two central modules were used, with four measuring the vertical field component w.r.t. the probe and three measuring the horizontal field component.

Figures 3a and 3b are the combined results from the two measurements, with or without the wood plate, with the former showing the vertical field component and the latter displaying the horizontal component. The spectra are results from 300 s measurements averaged over 5 s samples. The background noise measured without aluminum sheet was subtracted. The increase in noise below $2 \text{ fT}/\sqrt{\text{Hz}}$ is due to the SQUID white noise. Mechanical vibrations influence the measurement between 5-25 Hz at the level of $10 \text{ fT}/\sqrt{\text{Hz}}$. Comparing between the measured spectra and the theoretical ASD calculated with Eqs. (1) and (2), with $\sigma = 3.77 \times 10^7 \text{ S/m}$ and $T = 22 \text{ }^\circ\text{C}$, discrepancies up to $\sim 15\%$ are found. The uncertainties on σ and T are not enough to explain the differences. Nenonen, Montonen and Katila [8] pointed out that correlation of JNN within pickup coils with finite surface areas should be taken into account if the pickup-coil diameter is larger than the measurement distance (see Sec. III B for details). In our measurements, the ratios between the pickup-coil diameter and the distances were all smaller than one third; thus, the correlation is considered negligible (see Fig. 4). Additionally, considering the dimensions of the aluminum sheet, the pick-up coils and the measurement separations, we can approximate the aluminum sheet as an infinite conductor.

Comparisons between theoretical calculations and noise measurements on copper [6] and aluminum [8] conductors using first-order gradiometers have been performed in bio-magnetic researches. It is reported in Ref. [6] that the agreement lies within uncertainties of $\pm 15\%$. Our measurements performed with a magnetometer confirm the theoretical spectrum in a non-differential manner to a fairly good level, and verify the relation between transverse and normal noise components (Eq. (2)). The reason for the small disagreement is still unclear; nonetheless, by using the theoretical ASD, we guarantee that the noise will not be underestimated.

For JNN studies in EDM experiments, a principle simplification can be made assuming that the frequency of the fluctuating field is low enough such that the eddy currents generated in the bulk material can be neglected. This is stated as the *static approximation* by Lamoreaux [18], which is valid when the thickness of the conductor is smaller than the skin depth

$$\lambda = \sqrt{\frac{1}{\pi\mu\sigma f}}, \quad (3)$$

where f is the fluctuation frequency. In the context of

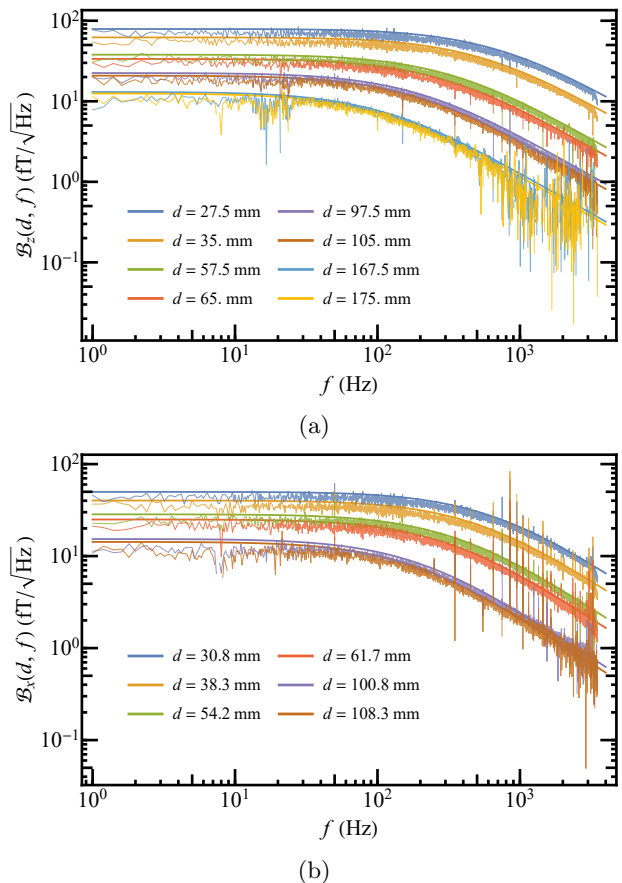


FIG. 3: (a) Vertical and (b) horizontal magnetic-field noise component of a 0.5-mm-thick aluminum sheet measured by the SQUID system at PTB w.r.t. the theoretical ASD at various distances. The spectra were averaged over 5 s samples from 300 s measurements. The ASD decreases with increasing distance.

EDM experiments, this corresponds to approximately the reciprocal of the spin-coherence time, T_2 . In the nEDM experiment, the free-spin-precession period for a single measurement will be $\Delta t \sim 200 \text{ s}$, approximately two times the spin-coherence time of mercury and a fraction of the spin-coherence time of neutrons. Hence, we assume $f^{-1} = \Delta t \sim 200 \text{ s} \approx T_{2, \text{Hg}}$ will be the free-spin-precession period for a single measurement. At 5 mHz, $\lambda \sim 116 \text{ cm}$, so the low-frequency assumption can be applied safely for conductors with a thickness of less than 10 cm.

III. MAGNETIC-FIELD FLUCTUATION OBSERVED BY FIELD-SENSING PARTICLES

During an nEDM-measurement cycle, ^{199}Hg atoms occupying the same volumes as UCN, are used as co-habiting magnetometers (HgM) [32–34]. As the HgM and the UCN measure the magnetic field simultaneously, the ratio of the two precession frequencies, f_n/f_{Hg} , is robust against magnetic-field changes. Nonetheless, the two spin species sample the magnetic field differently. The UCN sample the field adiabatically and have a negative center-of-mass offset whereas the ^{199}Hg atoms sample the field non-adiabatically [38]. For a nominal field of $B_0 = 1 \mu\text{T}$, we investigate the degree to which the effects of JNN can be controlled when taking the frequency ratio of two ensembles within one precession chamber.

A. Analytical derivation of spatial properties

In the first step to calculate the RMS magnetic-field noise sensed by the particles, it is useful to derive the spatial correlation of JNN at different locations within the volume. For this purpose we calculated the magnetic noise originating from thermal noise currents by dividing a volume conductor into infinitesimal cuboidal elements, $\Delta V = \Delta x \Delta y \Delta z$, similar to the seminal calculation in Refs. [6, 8]. There an *equivalent current dipole* for the volume element is defined, whose component $P_\alpha = I_\alpha \Delta \alpha$ ($\alpha = x, y, z$) in the direction α is the product of this short-circuit current and the finite size of the element. Following this concept, the source of thermal magnetic noise is represented by a great number of randomly oriented current dipoles on the surface of the conductor.

We consider an infinite conductor and assume its surface is an $x - y$ plane on the reference of the vertical coordinate $z = 0$. A current dipole element on an infinitesimal surface area ds located at $(\mathbf{x}, 0)$, where \mathbf{x} now denotes a two-dimensional vector on the $x - y$ plane, is written as $\mathbf{I}(\mathbf{x}) ds$, where the $z = 0$ component is omitted for simplicity. The magnetic field created by this dipole at a point (\mathbf{r}, z) can be calculated, according to the Biot-Savart law, as

$$d\mathbf{B} = \frac{\mu_0}{4\pi} \frac{\mathbf{I}(\mathbf{x}) ds \times \mathbf{k}}{d^2}, \quad (4)$$

where

$$\mathbf{k} = \frac{\mathbf{r} - \mathbf{x}}{d} + \frac{z}{d} \hat{e}_z \quad (5)$$

is the unit directional vector pointing from $(\mathbf{x}, 0)$ to (\mathbf{r}, z) , and

$$d = \sqrt{|\mathbf{r} - \mathbf{x}|^2 + z^2} \quad (6)$$

is the distance between the dipole and the observation point. Now, we obtain the normal component \hat{e}_z of the field

$$\begin{aligned} dB_z(\mathbf{r}, z) &= d\mathbf{B} \cdot \hat{e}_z \\ &= \frac{\mu_0}{4\pi} \left(\mathbf{I}(\mathbf{x}) ds \times \frac{\mathbf{r} - \mathbf{x}}{d^3} \right) \cdot \hat{e}_z \\ &= \frac{\mu_0}{4\pi} (\hat{e}_z \times \mathbf{I}(\mathbf{x}) ds) \cdot \frac{\mathbf{r} - \mathbf{x}}{d^3} \\ &= \frac{\mu_0}{4\pi} \mathbf{F}(\mathbf{r} - \mathbf{x}, z) \cdot \mathcal{I}(\mathbf{x}) ds, \end{aligned} \quad (7)$$

with

$$\mathbf{F}(\mathbf{x}, z) \equiv \frac{\mathbf{x}}{(|\mathbf{x}|^2 + z^2)^{3/2}} \quad (8)$$

and

$$\mathcal{I}(\mathbf{x}) \equiv \hat{e}_z \times \mathbf{I}(\mathbf{x}) \quad (9)$$

being the rotated current component transformed from the triple product.

1. Variance of a disk-averaged field

Consider a disk parallel to the conductor, which has a radius R and is located at a normal distance z above

the conductor. The average normal magnetic field over this disk generated by thermal noise in a finite element ds from the conductor can be written as

$$\begin{aligned} d\bar{B}_z(R, z) &\equiv \int_{S_R} \frac{d^2r}{\pi R^2} dB_z(\mathbf{r}, z) \\ &= \frac{\mu_0}{4\pi} \int_{S_R} \frac{d^2r}{\pi R^2} \mathbf{F}(\mathbf{r} - \mathbf{x}, z) \cdot \mathcal{I}(\mathbf{x}) ds \\ &= \frac{\mu_0}{4\pi} \mathcal{I}(\mathbf{x}) ds \cdot \bar{\mathbf{M}}(\mathbf{x}, R, z), \end{aligned} \quad (10)$$

where

$$\bar{\mathbf{M}}(\mathbf{x}, R, z) \equiv \int_{S_R} \frac{d^2r}{\pi R^2} \mathbf{F}(\mathbf{r} - \mathbf{x}, z) \quad (11)$$

is the average over the disk. For an infinite conductor, we integrate over all dipoles

$$\bar{B}_z(R, z) = \int d\bar{B}_z(R, z). \quad (12)$$

The variance of this surface average is then calculated as

$$\begin{aligned} \langle \bar{B}_z(R, z)^2 \rangle &= \left(\frac{\mu_0}{4\pi} \right)^2 \int ds \int ds' \\ &\langle (\mathcal{I}(\mathbf{x}) \cdot \bar{\mathbf{M}}(\mathbf{x}, R, z)) (\mathcal{I}(\mathbf{x}') \cdot \bar{\mathbf{M}}(\mathbf{x}', R, z)) \rangle. \end{aligned} \quad (13)$$

As shown in Eq. (1) in Ref. [6], based on Nyquist's theorem,

$$\langle \mathcal{I}(\mathbf{x}) \mathcal{I}(\mathbf{x}') \rangle = 4\sigma k_B T \Delta f a \delta(\mathbf{x} - \mathbf{x}'), \quad (14)$$

where the conductor properties are identical to those indicated in Eq. (1). With the change of variables and further derivations, the variance of the surface-averaged field can be expressed as

$$\begin{aligned} \langle \bar{B}_z(R, z)^2 \rangle &= \frac{C\pi}{2z^2} \mathcal{J} \left(\frac{R}{z} \right) \\ &= \langle B_z(\mathbf{r}, z)^2 \rangle \mathcal{J} \left(\frac{R}{z} \right) \\ &= \langle B_z(0, z)^2 \rangle \mathcal{J} \left(\frac{R}{z} \right), \end{aligned} \quad (15)$$

normalized to the variance of the single-point field at a random location of distance z , $\langle B(\mathbf{r}, z)^2 \rangle = \langle B(0, z)^2 \rangle$, with

$$C \equiv \left(\frac{\mu_0}{4\pi} \right)^2 4\sigma k_B T \Delta f a. \quad (16)$$

$\mathcal{J}(R/z)$ is an integration over three two-dimensional vectors calculated as

$$\begin{aligned} \mathcal{J}(\xi) &\equiv \frac{2}{\pi^3} \xi^4 \int_{S_1} d^2u \int_{S_1} d^2v \int d^2X \\ &\frac{\mathbf{u} - \mathbf{X}}{(\xi^2 |\mathbf{u} - \mathbf{X}|^2 + 1)^{3/2}} \cdot \frac{\mathbf{v} - \mathbf{X}}{(\xi^2 |\mathbf{v} - \mathbf{X}|^2 + 1)^{3/2}}. \end{aligned} \quad (17)$$

\mathbf{u} and \mathbf{v} are two observation points on the disk, where an integration over a unit circle S_1 is performed, and \mathbf{X} is a dipole on the conductor integrated from zero to infinity.

2. Variance of a cylinder-averaged field

In our case, we are interested in the average field observed within a cylinder of radius R and height H on the surface of the conductor,

$$d\bar{B}_z(R, H) \equiv \int_0^H \frac{dz}{H} \int_{S_R} \frac{d^2r}{\pi R^2} dB_z(\mathbf{r}, z). \quad (18)$$

Physically, direct contact between a dipole and an observation point will result in a divergent magnetic field; hence, we regularize the integration by starting from a small distance h ($h \ll H, R$) to the conductor surface

$$\begin{aligned} d\bar{B}_z(R, H) &\approx d\bar{B}_z(R, H, h) \\ &= \int_h^{h+H} \frac{dz}{H} \int_{S_R} \frac{d^2r}{\pi R^2} dB_z(\mathbf{r}, z) \\ &= \frac{\mu_0}{4\pi} \int_h^{h+H} \frac{dz}{H} \int_{S_R} \frac{d^2r}{\pi R^2} \mathbf{F}(\mathbf{r} - \mathbf{x}, z) \cdot \mathcal{I}(\mathbf{x}) d\mathbf{s} \\ &= \frac{\mu_0}{4\pi} \mathcal{I}(\mathbf{x}) d\mathbf{s} \cdot \bar{\mathbf{M}}(\mathbf{x}, R, H, h), \end{aligned} \quad (19)$$

with

$$\bar{\mathbf{M}}(\mathbf{x}, R, H, h) \equiv \int_{S_R} \frac{d^2r}{\pi R^2} \bar{\mathbf{F}}(\mathbf{r} - \mathbf{x}, H, h) \quad (20)$$

and

$$\bar{\mathbf{F}}(\mathbf{x}, H, h) \equiv \int_h^{h+H} \frac{dz}{H} \mathbf{F}(\mathbf{x}, z). \quad (21)$$

Similarly, the contributions of all dipoles are integrated over, $\bar{B}_z(R, H, h) = \int d\bar{B}_z(R, H, h)$, and the variance of the volume-averaged field can be carried out as

$$\langle \bar{B}_z(R, H, h)^2 \rangle = \frac{C}{\pi^2 R^2} \mathfrak{J} \left(\frac{H}{R}, \frac{h}{R} \right), \quad (22)$$

where

$$\begin{aligned} \mathfrak{J}(\eta, \zeta) &\equiv \frac{1}{\eta^2} \int_{S_1} d^2u \int_{S_1} d^2v \int d^2X \\ &\left\{ \frac{(\eta + \zeta)(\mathbf{u} - \mathbf{X})}{|\mathbf{u} - \mathbf{X}|^2 \left[|\mathbf{u} - \mathbf{X}|^2 + (\eta + \zeta)^2 \right]^{1/2}} - \frac{\zeta(\mathbf{u} - \mathbf{X})}{|\mathbf{u} - \mathbf{X}|^2 \left(|\mathbf{u} - \mathbf{X}|^2 + \zeta^2 \right)^{1/2}} \right\} \\ &\left\{ \frac{(\eta + \zeta)(\mathbf{v} - \mathbf{X})}{|\mathbf{v} - \mathbf{X}|^2 \left[|\mathbf{v} - \mathbf{X}|^2 + (\eta + \zeta)^2 \right]^{1/2}} - \frac{\zeta(\mathbf{v} - \mathbf{X})}{|\mathbf{v} - \mathbf{X}|^2 \left(|\mathbf{v} - \mathbf{X}|^2 + \zeta^2 \right)^{1/2}} \right\}. \end{aligned} \quad (23)$$

At the limit of $H \rightarrow 0$, the variance of the volume average reduces to the variance of the disk average at a distance h , which gives

$$\langle \bar{B}_z(R, H \rightarrow 0, h)^2 \rangle \approx \langle \bar{B}_z(R, h)^2 \rangle. \quad (24)$$

B. Analytical derivation computed with Monte Carlo integration

The variances of surface and volume averages are important for practical purposes. To calculate the corresponding results, integrals in Eqs. (17) and (23) were computed using the method of Monte Carlo integration [39].

As described in Ref. [8], SQUID detectors used to measure magnetic fields have pickup coils with finite surface areas within which the correlation of JNN should be taken into account. Nenonen *et al.* [8] calculated the magnetic noise observed by a single circular coil of diameter d parallel to a conducting slab at a distance z , $B_{n,z}^{\text{coil}}$, and plotted the ratio to the single-point spectral density, $B_{n,z}^{\text{coil}}/B_{n,z}$, as a function of d/z , shown in Fig. 4 of Ref. [8]. $B_{n,z}^{\text{coil}}$ and $B_{n,z}$ are the notations used in the original paper of Nenonen *et al.*, where n in the subscript stands for JNN. They are equivalent to $\bar{B}_z(R, z)$ and $B_z(\mathbf{r}, z)$ in our study, respectively. The ratio $B_{n,z}^{\text{coil}}/B_{n,z}$ is the same as $\mathfrak{J}(R/z)^{1/2}$ in Eq. (15). We computed this integral $\mathfrak{J}(R/z)$ and compared it to the calculation made by Nenonen *et al.* shown in Fig. 4. The black solid line in the graph is the result from Ref. [8]. The red dashed line is our result using the Monte Carlo integration, averaged over thirty random numerical solutions. The other colored points were calculated with a numerical finite-element method which will be explained in Secs. III C and III D. All methods agree with one another, and the remaining small deviations are inconsequential for our pragmatic intent.

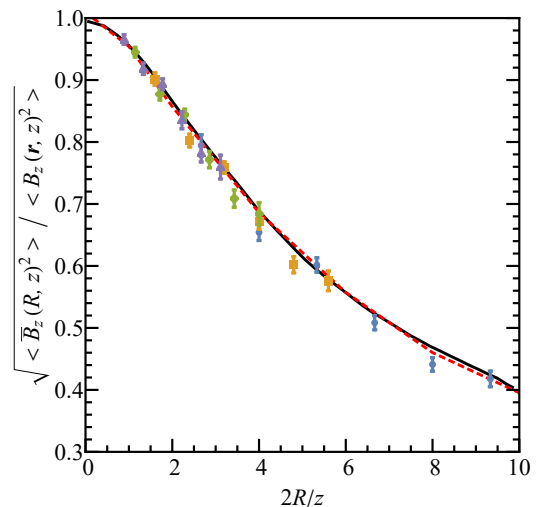


FIG. 4: Root-mean-square normal noise averaged over a finite area w.r.t. a random single point (\mathbf{r}, z) .

Comparison among results obtained with Monte Carlo integration based on analytical derivation (red dashed line), calculation shown in Ref. [8] (black solid line) and numerical finite-element method computed at various distances (colored points).

As described in Eq. (24), with reduction of cylinder height, the volume variance converges to the surface variance. Figure 5 displays both $\langle \bar{B}_z(R, H \rightarrow 0, h)^2 \rangle$ (red, square) and $\langle \bar{B}_z(R, h)^2 \rangle^{1/2}$ (blue, circular) for various chamber radii. Integrations were performed using ten to fifty random solutions in the Monte Carlo method for various radii, where the mean values are plotted with their standard errors shown as error bars. Filled

data points were computed with a regularization distance $h = 2.5$ mm, whereas open points were calculated with $h = 10$ μ m. Both methods agree with each other which confirms the validity of the convergence of the volume calculation to the surface solution in the limit of zero chamber height ($H \rightarrow 0$).

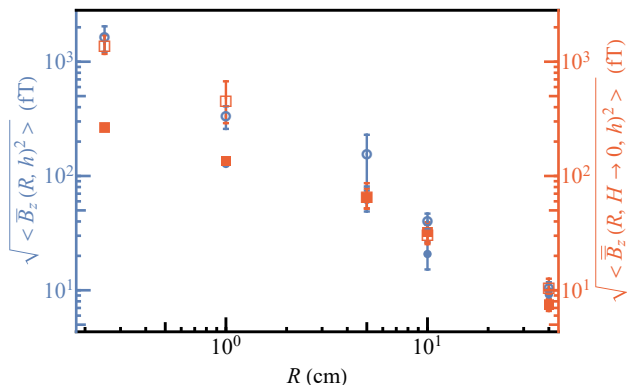


FIG. 5: Comparison of RMS normal noise amplitude at a frequency bandwidth $\Delta f = 1/(2 \times 200$ s) between surface average (blue, circular) and volume average with an infinitesimal cylinder height (red, square). Two regularization distances, $h = 2.5$ mm or 10 μ m, are shown as filled or open data points, respectively.

By integrating over a larger cylinder height, H , the volume-averaged JNN decreases as a result of averaging over uncorrelated noise at relatively larger distances. Results of $\langle \bar{B}_z(R, H, h)^2 \rangle^{1/2}$ with various H and R are displayed in Fig. 6. Again, filled and open points were computed with $h = 2.5$ mm and 10 μ m, respectively.

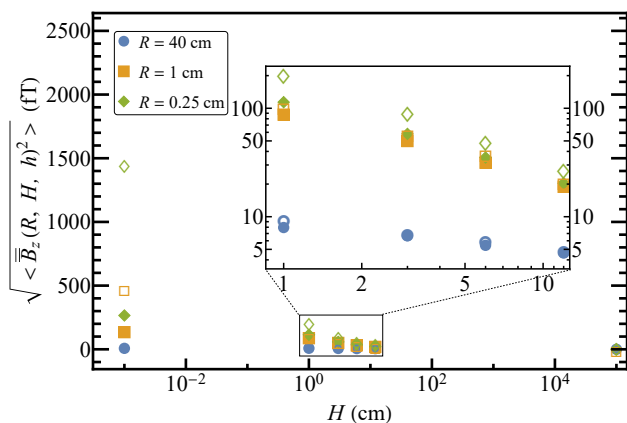


FIG. 6: Volume-averaged RMS normal noise amplitude at a frequency bandwidth $\Delta f = 1/(2 \times 200$ s) with various cylinder dimensions. Two regularization distances, $h = 2.5$ mm or 10 μ m, are shown as filled or open data points, respectively.

From Figs. 5 and 6, one can see that the larger the cylinder volume (R or H), the smaller the influence of the regularization distance, h .

C. Finite-element method with discrete dipoles

To estimate the JNN originating from the electrodes, instead of infinite slabs, conductors of finite size need to

be considered. Lee and Romalis [40] calculated magnetic noise from conducting objects of simple geometries. The JNN calculation for a thin circular planar conductor is shown in Tab. VI of Ref. [40], which accords with the geometry of the electrodes and was used in our study. To estimate an upper limit of the average-field difference observed by UCN and HgM in the presence of JNN, it is sufficient to apply the static approximation, where only a *white-noise* spectrum at the limit of $f \rightarrow 0$ should be considered, as shown in Fig. 2. The z component of the ASD measured at a normal distance d generated by a thin film of radius R , thickness a and conductivity σ at a temperature T is [40] [41]

$$\frac{1}{\sqrt{8\pi}} \frac{\mu_0 \sqrt{k_B T \sigma a}}{d} \frac{1}{1 + \frac{d^2}{R^2}} =: \mathcal{B}_z^{\text{thin}}(d, f \rightarrow 0). \quad (25)$$

However, for a calculation of the magnetic field sampled by particles within the chamber, the JNN spectrum shown above, Eq. (25), which depends only on the normal distance between the source of noise and the observation point need to be replaced with a time-dependent three-dimensional magnetic-noise source. For this reason, we used a supplementary method by considering a finite number of random magnetic dipoles on the surface of the conductors as noise sources.

Although the n2EDM apparatus consists of a double-chamber, to study the possible cancellation of field fluctuation deploying a co-magnetometer system, we considered only the field measurements taken place in one precession chamber. In general, only the contribution from the two electrodes defining top and bottom of the relevant chamber needs to be considered, as the effect from metal plates further away is exponentially suppressed. Random time series were generated for each discrete dipole on both electrodes. The superposition of all these time series and the applied field B_0 at discrete positions within the volume of the chamber permits to calculate the distinct magnetic field $\mathbf{B}(\mathbf{r}, t)$ for any time and locations.

Following the idea of equivalent current dipoles introduced initially in Refs. [6, 8] described in Sec. III A, we divided the surface of the electrodes into triangular areas. The motivation of using triangular grids instead of common quadrilateral meshing methods will be explained later. For each triangular element, three noise-current sources located at the center of the triangle and oriented along the three Cartesian coordinates representing the normal component of the three directions were created. For a sampling period of Δt , the magnetic field created by a number of n_{dip} dipoles and measured at position \mathbf{r} can be calculated by the discrete Biot-Savart law,

$$\mathbf{B}(\mathbf{r}, \Delta t) = \frac{\mu_0}{4\pi} \sum_{i=1}^{n_{\text{dip}}} \sum_{\alpha=x,y,z} \frac{I_{\alpha,i}(\Delta t) d\mathbf{l} \times (\mathbf{r} - \mathbf{r}'_i)}{|\mathbf{r} - \mathbf{r}'_i|^3}, \quad (26)$$

where \mathbf{r}'_i and $I_{\alpha,i}(\Delta t)$ are the position and current of an individual dipole in direction α , and the unit-length vector $d\mathbf{l}$ was defined to be the average side length of the triangles.

The white-noise ASD of the thermal current is [6, 8, 40]

$$\mathcal{I} = \sqrt{k_B T \sigma a}, \quad (27)$$

having a unit of $\text{A}/\sqrt{\text{Hz}}$. By using the power spectral density (PSD = ASD²), the variance of the dipole-current

time series can be calculated as

$$\begin{aligned}\sigma^2(I(\Delta t)) &= 2\mathcal{I}^2\Delta f_{\text{BW}} \\ &= 2k_{\text{B}}T\sigma a\Delta f_{\text{BW}},\end{aligned}\quad (28)$$

where Δf_{BW} is the bandwidth, corresponding to $1/(2\Delta t)$ with Δt being the average observation time. The current $I_{\alpha,i}(\Delta t)$ in Eq. (26) is a random current drawn from a Gaussian distribution with the defined variance, $\sigma^2(I(\Delta t))$.

The surface of the aluminum electrode was divided into approximately 1500 finite surface elements, whose average side length was about 28 mm. The electrode-division layout was optimized to provide a theoretically compatible noise spectrum and to be computationally efficient. A dipole with three time-averaged current components lies at the center of each surface element. The current components were randomly created from a Gaussian distribution with a defined variance using $\Delta t = 200$ s, which is the free-spin-precession period of one measurement. Figure 7 shows the time-domain magnetic-field distribution along a horizontal cut line, $x = -40 \dots 40$ cm within the diameter of the chamber, with one random current-dipole set, where (a)-(d) indicate field distributions at various distances from the electrode. The shorter the distance to the source, the larger the amplitude of the field. Note that also the fluctuation of the field is larger in close vicinity to the source. This validates the argument in the beginning of this section, that a normal-distance dependent JNN spectrum, Eq. (25), is inadequate for the purpose of calculating the impact of JNN on the sensitivity of field-sensing spin- $\frac{1}{2}$ particles, since the spatial correlation between adjacent observation points is not considered in the spectral-density formulation.

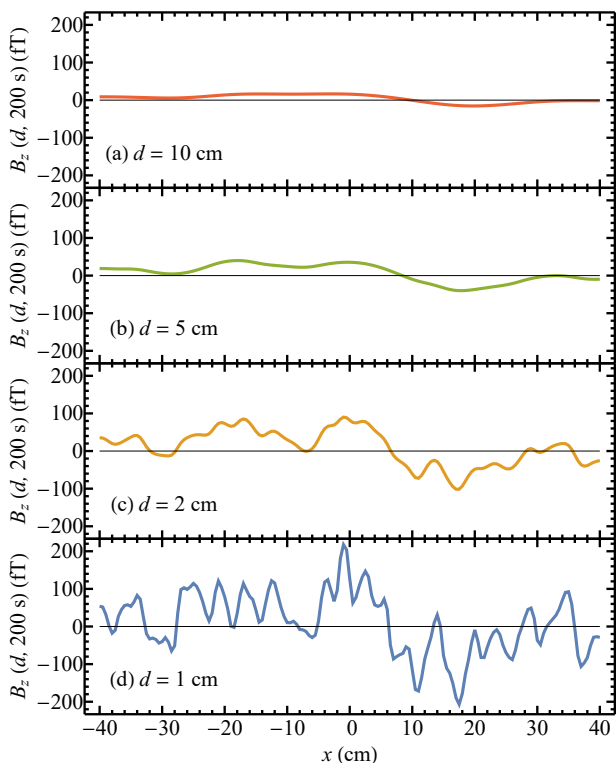


FIG. 7: Normal component of time-domain magnetic-field distribution along a horizontal cut line at various distances. This is an example created from one random current-dipole set.

This finite-element method was used to calculate the time-and-volume-averaged magnetic field observed by field-sensing particles within the chamber over one measurement, in the presence of JNN. Monte Carlo simulations matching experimental results [42] show that the whole volume of the chamber is sampled isotropically during one 200 s measurement in the case of a large number of particles; therefore, it is sufficient to divide the chamber into equally-sized finite volumes, and calculate the magnetic fields observed at the center of each of these rectangular cuboids. A good balance between numerical accuracy and computational efficiency was reached with a size of $10 \times 10 \times 5$ mm³ for these voxels. The reason for using a smaller vertical dimension was due to the fact that, according to the noise spectrum, JNN is normal-distance dependent; hence, a transverse separation between two observation points has fewer impacts than a vertical separation. This was confirmed by using voxels with a size of $5 \times 5 \times 5$ mm³ whose result was comparable to that calculated with a 10 mm transverse dimension. In addition, the volume that was divided has a six times larger diameter than height; to partition the chamber in both transverse and vertical directions into numbers of units with the same order of magnitude, we decided to use a voxel with a smaller vertical size. Voxels with a size of $10 \times 10 \times 2$ mm³ were also studied which gave a negligible difference. As a result, for a better computational efficiency, a voxel size of $10 \times 10 \times 5$ mm³ was selected as the optimal size for chamber partition and used for the results presented below.

The reason for using triangular meshes for the conductor is to avoid aligned patterns between the conductor grids and the voxels within the chamber volume. In a preliminary study, we found that an alignment between the two meshing patterns could result in artifacts that computed extremely large magnetic-field values due to minimum distances between the noise sources and the observation points. This should be avoided and was resolved by implementing different meshing geometries for the conductors and the chamber where alignments could be well reduced.

D. Comparison between the analytical derivation and the finite-element method

With the finite-element method, the magnetic noise averaged over a disk or a cylinder can be easily estimated. With the optimal voxel height of 5 mm, the n2EDM precession chamber was divided into 24 layers each consists of 5024 pieces. First, we calculated the average field over different numbers of adjacent voxels on the same layer, corresponding to radii ranging from 10...35 mm, w.r.t. a *central* piece, where 100 random central pieces were selected. Results from four different layers, with distances of 7.5...22.5 mm, are shown in distinct colors and shapes in Fig. 4. The error bar on each point is the standard deviation of these 100 randomly chosen central pieces. We confirmed that the surface-averaged magnetic-field noise computed with the finite-element method is in good agreement with both the analytical derivation and the calculation performed in Ref. [8]. Next, to calculate a cylinder average with the finite-element method compatible with the analytical description, we considered only half of the precession chamber and one electrode. The half-chamber volume average of normal mag-

netic field generated by magnetic dipoles on this electrode, $\langle B_z \rangle$, was computed and shown in Fig. 8. Each entry in the histogram is the result of one simulated cycle. For one finite-element calculation, i.e. one simulated cycle, approximately 1500 dipoles were created on the conductor using three random noise currents at a bandwidth of $\Delta f_{\text{BW}} = 1/(2 \times 200 \text{ s})$. A total of more than 3000 random configurations were generated to accumulate statistics. The standard deviation of these random solutions is $\sigma_{B_z} = (3.060 \pm 0.037) \text{ fT}$. The uncertainty is the standard error of σ_{B_z} estimated theoretically with $SE(\sigma_{B_z}) = \sigma_{B_z}/\sqrt{2S-2}$, where $S = 3450$ is the number of simulations. On the other hand, using the analytical formula of volume variance, Eq. (22), and replacing the infinite conductor with a finite conductor of $R = 40 \text{ cm}$, the standard deviation of the volume average with twenty random solutions for the Monte Carlo integration is

$$\left\langle \bar{B}_z(40 \text{ cm}, 6 \text{ cm}, 2.5 \text{ mm})^2 \right\rangle^{1/2} = 2.805 \pm 0.005 \text{ fT}, \quad (29)$$

where the error is the statistical error of the Monte Carlo sample. The results from the two methods agree within half a femtotesla. The small deviation is negligible for our purpose and confirms the use of voxels for volume-average calculation with the finite-element method.

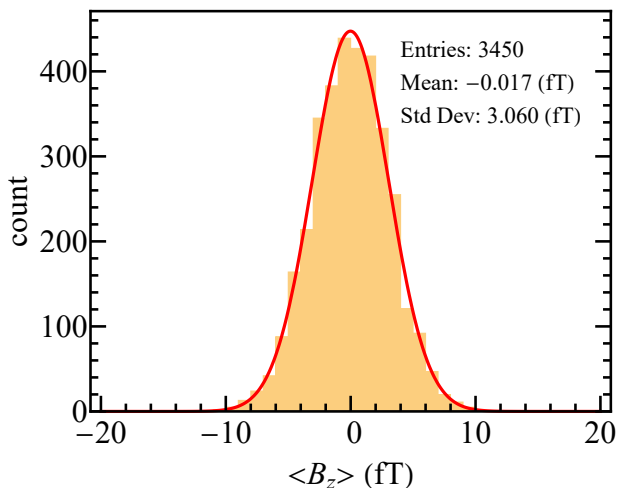


FIG. 8: Volume average of normal JNN component $\langle B_z \rangle$ over half of the n2EDM chamber calculated with the numerical finite-element method.

IV. EFFECTS ON THE n2EDM EXPERIMENT

A. Magnetic fields observed by UCN and HgM

Due to the difference in the velocity spectrum and the Larmor precession frequency, UCN and HgM sample the volume differently under a nominal $1 \mu\text{T}$ B_0 field. Much faster thermal ^{199}Hg atoms fall into the non-adiabatic regime. The spins precess under a vectorial volume average of the field; hence, the average magnetic field observed by ^{199}Hg atoms is calculated as

$$\begin{aligned} \langle B_{\text{Hg}} \rangle &= |\langle \mathbf{B} \rangle| \\ &= \sqrt{\langle B_x \rangle^2 + \langle B_y \rangle^2 + \langle B_0 + B_z \rangle^2}. \end{aligned} \quad (30)$$

By contrast, due to the much smaller velocity and larger precession frequency, UCN sample the volume in the adiabatic regime, such that their spins precess under the volume average of the modulus of the field. In addition, taking into account the negative center-of-mass offset $\langle z \rangle$ of the ensemble of UCN, the average field sampled by UCN is

$$\begin{aligned} \langle B_{\text{UCN}} \rangle &= \langle |\mathbf{B}| \rho_{\text{UCN}}(z) \rangle \\ &= \left\langle \sqrt{B_x^2 + B_y^2 + (B_0 + B_z)^2} \rho_{\text{UCN}}(z) \right\rangle, \end{aligned} \quad (31)$$

where

$$\rho_{\text{UCN}}(z) = \frac{1}{H} \left(1 + \frac{12 \langle z \rangle}{H^2} z \right) \quad (32)$$

is the normalized vertical UCN density function.

To estimate the time-and-volume average of the magnetic fields over one precession chamber sandwiched between two electrodes, the finite-element method was employed. Figure 9 shows the average magnetic fields observed by UCN and HgM over one simulated cycle, calculated with $\langle z \rangle = -4.1 \text{ mm}$ for Eq. (32). This offset value was obtained using a Monte Carlo simulation [42] and is in agreement with the offset obtained in Ref. [43]. Each entry in the histogram in Fig. 9 is the result of one $\Delta t = 200 \text{ s}$ time average simulated with approximately 1500 dipoles created on both electrodes. The average magnetic fields were computed with Eqs. (30) and (31). Histograms for UCN and ^{199}Hg atoms are shown in Figs. 9a and 9b, respectively. The standard deviation of these distributions, $\sigma(\langle B_{\text{UCN}} \rangle) = (3.781 \pm 0.046) \text{ fT} \approx \sigma(\langle B_{\text{Hg}} \rangle) = (3.777 \pm 0.046) \text{ fT}$, are comparable within the statistical error, confirming the naive hypothesis that they similarly sense the effects from JNN. In addition, this is an order of magnitude lower than the sensitivity requirement, 30 fT per measurement cycle, for the HgM in the n2EDM experiment [23], indicating that the performance of HgM will not be limited by JNN.

Next, we studied the influence of JNN on the ratio of precession frequencies of the two spin- $\frac{1}{2}$ ensembles by looking at the difference of the average magnetic fields (see Fig. 10). The standard deviation of the differences of average magnetic fields is $\sigma(\langle B_{\text{UCN}} \rangle - \langle B_{\text{Hg}} \rangle) \sim 0.1 \text{ fT}$. The sensitivity of an nEDM measurement depends on the uncertainty of the magnetic-field measurement. By using a mercury co-magnetometer, the effect from JNN is reduced to $\sigma_{\text{JNN}} \sim 0.1 \text{ fT}$ per measurement, and induces an uncertainty on the neutron EDM of

$$\sigma_{d_n} = \frac{\hbar}{2E} \gamma_n \sigma_{\text{JNN}} = 4 \times 10^{-28} \text{ e} \cdot \text{cm}, \quad (33)$$

assuming an electric field $E = 15 \text{ kV/cm}$ and $\gamma_n/2\pi = 29.16 \text{ MHz/T}$ is the gyro-magnetic ratio of the neutron. The experiment will consist of a total of M 200 s long measurement cycles to improve the statistical sensitivity. Note that the uncertainty on σ_{d_n} calculated for one cycle in Eq. (33) scales statistically with $M^{-1/2}$. Results shown in Figs. 9 and 10 had been crosschecked with another 2000 random configurations which showed similar results, confirming the negligibility of the statistical error arising from the sampling size.

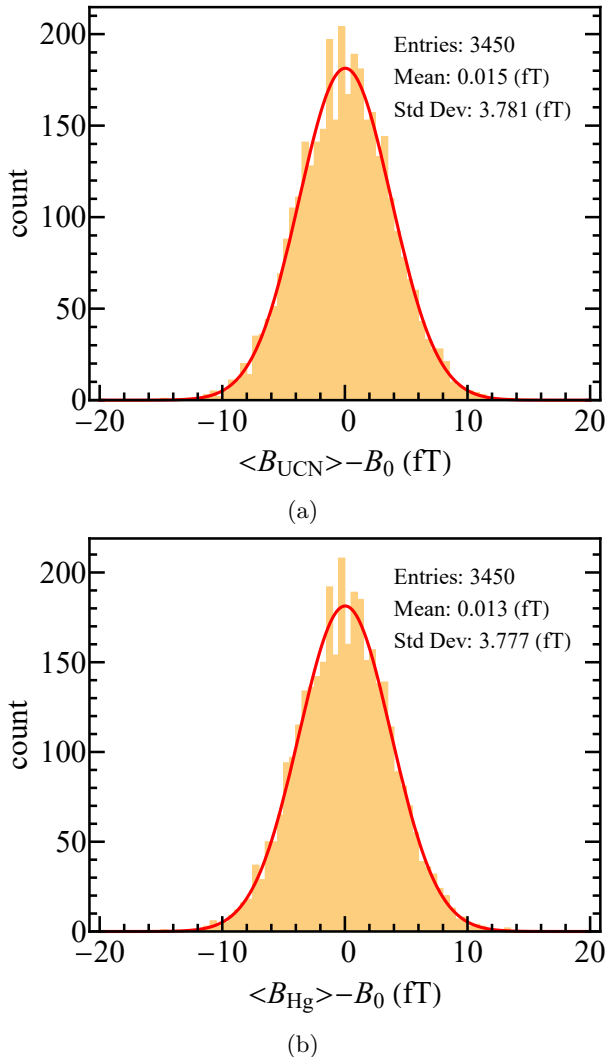


FIG. 9: Deviations of time-and-volume-averaged field to the nominal constant B_0 magnetic field sampled by (a) UCN and (b) ^{199}Hg atoms.

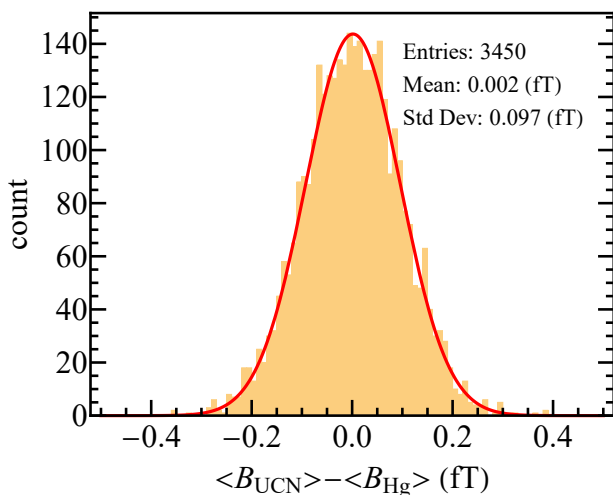


FIG. 10: Difference between the average fields sampled by UCN and mercury ensembles, $\langle B_{\text{UCN}} \rangle - \langle B_{\text{Hg}} \rangle$.

B. Magnetic field measured by CsM

The design of the n2EDM experiment [23] deploys more than 100 cesium magnetometers (CsM) being installed

above and below the precession-chamber stack in order to provide essential information about the homogeneity and stability of the magnetic field. They are arranged radially in groups of four on vertical modules. Each CsM contains a glass bulb filled with saturated vapor pressure of ^{133}Cs atoms. They are operated as Bell-Bloom type [44] magnetometers. Tensor-polarization (alignment) is created by amplitude-modulated linearly-polarized laser light that traverses the bulb, at a frequency roughly matched with the ^{133}Cs Larmor precession frequency, similar as in Refs. [45, 46]. Once the atomic vapor is spin aligned, the light intensity is reduced and kept constant. As the spin-polarized atoms precess under the influence of \mathbf{B} with a frequency proportional to the magnitude of the magnetic field, the intensity of transmitted light is periodically modulated by precessing atoms and detected by a photodiode.

Consider a CsM with a radius of 1.5 cm placed above the top-most electrode. Polarized ^{133}Cs atoms at different locations within the bulb are exposed to magnetic noise from the electrode which decreases with distance according to Eq. (1). The finite-element method introduced in Sec. III C was employed to calculate the average magnetic field measured by ^{133}Cs atoms in the presence of JNN. For a CsM bulb, the measurement time of the magnetic field is $\delta t = 70$ ms, which is roughly two times the spin-coherence time of ^{133}Cs atoms. The skin depth at 14 Hz is 2.2 cm which is outside of the thickness range in which the static approximation is valid. Nonetheless, the static approximation can be used to obtain an upper limit for the field fluctuation.

In this case, only the closest electrode which was relevant to a specific CsM was considered. Similarly, the noise source was represented by a number of dipoles lying on the surface of the electrode, each with three random noise currents at the bandwidth of $\Delta f_{\text{BW}} = 1/(2 \times 70 \text{ ms})$. The bulb was divided into about 14000 voxels of size 1 mm^3 , much smaller than the voxel size used for chamber division due to the orders of magnitude smaller volume. The ^{133}Cs atoms sense the field in the same way as the ^{199}Hg atoms in the precession chamber. Hence, the average magnetic field observed by a CsM was calculated by averaging over the fields in all voxels using Eq. (30). More than 3000 random dipole sets were simulated. The average magnetic fields from JNN for four CsM bulbs placed on one module with different distances to the electrode were simulated. The corresponding standard deviations of the time-and-volume-averaged fields at these positions are shown as orange points in Fig. 11 whose statistical errors are three orders of magnitude smaller.

In a perfectly spherical CsM bulb, the ^{133}Cs atoms are uniformly distributed over the volume. Due to the fast movement of ^{133}Cs atoms, the average magnetic field over the sphere is sampled homogeneously and its value is equal to the field measured at the center based on the mean-value theorem [47, 48], assuming all sources are outside the sphere. The RMS magnetic noise can be estimated by the noise observed at the center of the bulb within a time span δt . At a distance d measured to the center of the bulb, the RMS magnetic noise is

$$B_i^{\text{CsM}}(d, \delta t) = \left\{ \int_0^{\frac{1}{2\delta t}} \mathcal{B}_i(d, f)^2 df \right\}^{1/2}, \quad (34)$$

with i being x, y or z . In the presence of an applied $B_0 \parallel B_z$ field of about $1 \mu\text{T}$, the lateral components

$B_x, B_y \ll B_0$ of JNN are quadratically suppressed, hence negligible. For this reason, we only take the vertical component into account. The normal RMS magnetic noise estimated at the center of the CsM, $B_z^{\text{CsM}}(d, \delta t)$, as a function of distance, is also displayed in Fig 11.

In the figure, both methods deliver similar results with small differences which can be understood by the following explanations. Equation (34) is the frequency-bandwidth integrated RMS noise generated by an infinite slab, whereas the finite-element method took a finite size of the electrode and only the low-frequency noise was considered. Therefore, the results calculated from the finite-element method will in principle be larger due to the use of static approximation which is true for three of the cases. As for the result calculated at $d = 16.3$ cm, the finite-element method computed a smaller value. For this specific case, the CsM is placed at $R = 55$ cm, which is larger than the electrode radius; hence, the effect of noise from the electrode will be smaller compared to the theoretical calculation which used an infinite conductor. In general, this method provides a sufficiently precise estimation of the impact of JNN on the measurements by the CsM.

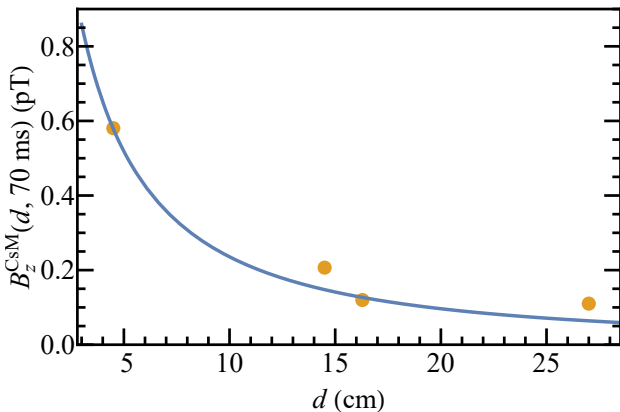


FIG. 11: Comparison between RMS normal noise amplitude integrated over 70 ms, calculated from the noise spectrum (blue line), and the average-field noise measured by a CsM estimated with the finite-element method (orange points). The statistical errors on the results calculated with the finite-element method are smaller than the marker size.

The sensitivity goal for n2EDM translates to a maximum RMS noise of 2.7 pT in 70 ms for the CsM [23]. The upper limits of the noise for CsM at various distances all lie below the sensitivity limit. In addition, for an nEDM-measurement cycle of $200 \text{ s} \gg 70 \text{ ms}$, the magnetic noise seen by a CsM will be averaged out to a much lower value; hence, we confirm that JNN from the electrodes is negligible for the design and placement of all CsM within the experiment.

V. CONCLUSION

This paper reports on a finite-element study of Johnson-Nyquist noise (JNN) originating from the bulk metal electrodes in the n2EDM experiment being constructed by the nEDM collaboration at PSI. In the first part, we revisited the theoretical noise spectra [6, 8], and compared them to the measurements on a thin aluminum

sheet using a superconducting quantum interference device (SQUID).

Next, we derived for a given frequency bandwidth expressions for the root-mean-square normal noise amplitudes of averages over a two-dimensional disk and a cylinder of finite volume. These are important in understanding the spatial correlation of JNN and are necessary for practical purposes. Numerical results from the analytical derivation were computed with the method of Monte Carlo integration and demonstrate good agreement with the calculation performed in the literature [8].

Using a discretization of the electrodes into a finite number of magnetic white-noise dipoles, we calculated temporal and spatial magnetic fields generated by JNN. By averaging these magnetic fields over time and volume, we obtained the mean magnetic field sensed by precessing ultracold neutrons (UCN) and mercury (^{199}Hg) atoms. The standard deviation of more than 3000 randomly produced configurations for UCN and mercury is approximately 3.8 fT, which we consider as small enough for next-generation neutron electric-dipole-moment (nEDM) searches. With the same method, we found that for the cesium (^{133}Cs) vapor magnetometers, the maximum RMS noise observed within a measurement time of 70 ms is approximately 0.6 pT, which lies below the sensitivity goal of 2.7 pT for n2EDM. Thus, we confirm that the precision of the cesium magnetometers will not be constrained by JNN from the aluminum electrodes.

Additionally, by computing the average-field difference observed by UCN and mercury, we found that the noise is sensed highly correlated and mostly cancels out by using a co-magnetometer to normalize the UCN measurements. That is, the impact of JNN is negligible for nEDM searches down to a sensitivity of $4 \times 10^{-28} e \cdot \text{cm}$ for a single 200 s measurement. Assuming a projected experiment of 500 days with ~ 280 cycles per day, this results in a factor of 374 smaller limit, which is sufficiently small for our planned nEDM search using a co-magnetometer concept.

VI. ACKNOWLEDGMENTS

We would like to thank A. Crivellin and M. Spira for helpful discussions. We are grateful for the technical support from P. Hömmen and R. Körber with the material measurements in BMSR-2, PTB, Berlin. The material measurements inside BMSR-2 were supported by the Core Facility “Metrology of Ultra-Low Magnetic Fields” at PTB funded by Deutsche Forschungsgemeinschaft (DFG) through funding codes: DFG KO 5321/3-1 and TR408/11-1. The swiss members acknowledge the financial support from the Swiss National Science Foundation through projects 157079, 163413, 169596, 188700 (all PSI), 181996 (Bern), 172639 (ETH), and FLARE20FL21-186179. This work has also been supported by the Cluster of Excellence “Precision Physics, Fundamental Interactions, and Structure of Matter” (PRISMA + EXC2118/1) funded by DFG within the German Excellence Strategy (Project ID 39083149) from Johannes Gutenberg University Mainz. This work is also supported by Sigma Xi grants # G2017100190747806 and # G2019100190747806, and by the award of the Swiss Government Excellence Scholarships (SERI-FCS) # 2015.0594. The group from Jagellonian University Cracow acknowl-

edges the support from National Science Centre, Poland, through grants No. 2018/30/M/ST2/00319, and

No. 2020/37/B/ST2/02349. The group from University of Leuven acknowledges supports from the Fund for Scientific Research Flanders (FWO).

-
- [1] J. H. Smith, E. M. Purcell, and N. F. Ramsey, *Phys. Rev.* **108**, 120 (1957).
- [2] N. F. Ramsey, *Phys. Rev.* **78**, 695 (1950).
- [3] E. M. Purcell and N. F. Ramsey, *Phys. Rev.* **78**, 807 (1950).
- [4] J. B. Johnson, *Phys. Rev.* **32**, 97 (1928).
- [5] H. Nyquist, *Phys. Rev.* **32**, 110 (1928).
- [6] T. Varpula and T. Poutanen, *J. Appl. Phys.* **55**, 4015 (1984).
- [7] J. R. Clem, *IEEE Trans. Magn.* **23**, 1093 (1987).
- [8] J. Nenonen, J. Montonen, and T. Katila, *Rev. Sci. Instrum.* **67**, 2397 (1996).
- [9] R. Körber, in *EMBEC & NBC 2017*, Vol. 65, edited by H. Eskola, O. Väisänen, J. Viik, and J. Hyttinen (Springer, Singapore, 2018) pp. 795–798.
- [10] J. C. Allred, R. N. Lyman, T. W. Kornack, and M. V. Romalis, *Phys. Rev. Lett.* **89**, 130801 (2002).
- [11] M. P. A. Jones, C. J. Vale, D. Sahagun, B. V. Hall, and E. A. Hinds, *Phys. Rev. Lett.* **91**, 080401 (2003).
- [12] D. M. Harber, J. M. McGuirk, J. M. Obrecht, and E. A. Cornell, *J. Low Temp. Phys.* **133**, 229 (2003).
- [13] Y.-J. Lin, I. Teper, C. Chin, and V. Vuletić, *Phys. Rev. Lett.* **92**, 050404 (2004).
- [14] P. K. Rekdal, S. Scheel, P. L. Knight, and E. A. Hinds, *Phys. Rev. A* **70**, 013811 (2004).
- [15] C. Henkel, *Eur. Phys. J. D* **35**, 59 (2005).
- [16] A. Emmert, A. Lupaşcu, G. Noguez, M. Brune, J.-M. Raimond, and S. Haroche, *Eur. Phys. J. D* **51**, 173 (2009).
- [17] J. A. Sidles, J. L. Garbini, W. M. Dougherty, and S.-H. Chao, *Proc. IEEE* **91**, 799 (2003).
- [18] S. K. Lamoreaux, *Phys. Rev. A* **60**, 1717 (1999).
- [19] C. T. Munger, Jr., *Phys. Rev. A* **72**, 012506 (2005).
- [20] J. M. Amini, C. T. Munger, Jr., and H. Gould, *Phys. Rev. A* **75**, 063416 (2007).
- [21] I. M. Rabey, J. A. Devlin, E. A. Hinds, and B. E. Sauer, *Rev. Sci. Instrum.* **87**, 115110 (2016).
- [22] C. Abel *et al.*, *EPJ Web Conf.* **219**, 02002 (2019).
- [23] N. J. Ayres *et al.*, *Eur. Phys. J. C* **81**, 512 (2021).
- [24] B. Lauss, *Phys. Proc.* **51**, 98 (2014).
- [25] G. Bison, B. Blau, M. Daum, L. Göttl, R. Henneck, K. Kirch, B. Lauss, D. Ries, P. Schmidt-Wellenburg, and G. Zsigmond, *Eur. Phys. J. A* **56**, 33 (2020).
- [26] G. Bison, M. Daum, K. Kirch, B. Lauss, D. Ries, P. Schmidt-Wellenburg, G. Zsigmond, T. Brenner, P. Geltenbort, T. Jenke, *et al.*, *Phys. Rev. C* **95**, 045503 (2017).
- [27] T. M. Ito *et al.*, *Phys. Rev. C* **97**, 012501(R) (2018).
- [28] F. Atchison *et al.*, *Phys. Lett. B* **625**, 19 (2005).
- [29] F. Atchison *et al.*, *Phys. Rev. C* **74**, 055501 (2006).
- [30] A. Weis and R. Wynands, *Opt. Lasers Eng.* **43**, 387 (2005).
- [31] S. Groeger, G. Bison, J.-L. Schenker, R. Wynands, and A. Weis, *Eur. Phys. J. D* **38**, 239 (2006).
- [32] K. Green, P. G. Harris, P. Iaydjiev, D. J. R. May, J. M. Pendlebury, K. F. Smith, M. van der Grinten, P. Geltenbort, and S. Ivanov, *Nucl. Instrum. Methods Phys. Res. A* **404**, 381 (1998).
- [33] C. A. Baker *et al.*, *Nucl. Instrum. Methods Phys. Res. A* **736**, 184 (2014).
- [34] G. Ban *et al.*, *Nucl. Instrum. Methods Phys. Res. A* **896**, 129 (2018).
- [35] Compare to Eq. (38) of Ref. [6], where variables z , distance, and t , thickness, were replaced with d and a in our paper to avoid confusion with other variables used in the remainder of the article.
- [36] J. Bork, H.-D. Hahlbohm, R. Klein, and A. Schnabel, in *Biomag2000, Proc. 12th Int. Conf. on Biomagnetism* (2001) pp. 970–973.
- [37] F. Thiel, A. Schnabel, S. Knappe-Grüneberg, M. Burghoff, D. Drung, F. Petsche, S. Bechstein, U. Steinhoff, W. Müller, D. Stollfuß, *et al.*, *Biomed. Technik* **50**, 169 (2005).
- [38] C. Abel *et al.*, *Phys. Rev. A* **99**, 042112 (2019).
- [39] R. E. Caflisch, *Acta Numerica* **7**, 1 (1998).
- [40] S.-K. Lee and M. V. Romalis, *J. Appl. Phys.* **103**, 084904 (2008).
- [41] Compare to the original expression shown in Ref. [40], where variables a , distance, t , thickness, and r , radius, were replaced with d , a and R in our paper to avoid confusion and keep consistency with other variables used in the remainder of the article.
- [42] G. Zsigmond, *Nucl. Instrum. Methods Phys. Res. A* **881**, 16 (2018).
- [43] C. Abel *et al.*, *Phys. Rev. Lett.* **124**, 081803 (2020).
- [44] W. E. Bell and A. L. Bloom, *Phys. Rev. Lett.* **6**, 280 (1961).
- [45] Z. D. Grujić, P. A. Koss, G. Bison, and A. Weis, *Eur. Phys. J. D* **69**, 135 (2015).
- [46] S. Afach *et al.*, *Opt. Express* **23**, 22108 (2015).
- [47] D. J. Griffiths, *Introduction to Electrodynamics*, 4th ed. (Cambridge University Press, 2017).
- [48] J. D. Jackson, *Classical Electrodynamics*, 3rd ed. (WILEY, 1998).



OPEN

Search for topological defect dark matter with a global network of optical magnetometers

Samer Afach^{1,2}, Ben C. Buchler³, Dmitry Budker^{1,2,4}, Conner Dailey^{5,26}, Andrei Derevianko⁵, Vincent Dumont⁶, Nataniel L. Figueroa^{1,2}, Ilja Gerhardt⁷, Zoran D. Grujić^{8,9}, Hong Guo¹⁰, Chuanpeng Hao¹¹, Paul S. Hamilton¹², Morgan Hedges³, Derek F. Jackson Kimball¹³, Dongok Kim^{14,15}, Sami Khamis¹², Thomas Kornack¹⁶, Victor Lebedev⁹, Zheng-Tian Lu¹⁷, Hector Masia-Roig^{1,2}✉, Madeline Monroy^{4,13}, Mikhail Padniuk¹⁸, Christopher A. Palm¹³, Sun Yool Park^{19,27}, Karun V. Paul³, Alexander Penafior¹³, Xiang Peng¹⁰, Maxim Pospelov^{20,21}, Rayshaun Preston¹³, Szymon Pustelny¹⁸, Theo Scholtes^{9,22}, Perrin C. Segura^{19,28}, Yannis K. Semertzidis^{14,15}, Dong Sheng¹¹, Yun Chang Shin¹⁴, Joseph A. Smiga^{1,2}✉, Jason E. Stalnaker¹⁹, Ibrahim Sulai²³, Dhruv Tandon¹⁹, Tao Wang²⁴, Antoine Weis⁹, Arne Wickenbrock^{1,2}, Tatum Wilson¹³, Teng Wu¹⁰, David Wurm²⁵, Wei Xiao¹⁰, Yucheng Yang¹⁰, Dongrui Yu¹⁰ and Jianwei Zhang¹⁰

Ultralight bosons such as axion-like particles are viable candidates for dark matter. They can form stable, macroscopic field configurations in the form of topological defects that could concentrate the dark matter density into many distinct, compact spatial regions that are small compared with the Galaxy but much larger than the Earth. Here we report the results of the search for transient signals from the domain walls of axion-like particles by using the global network of optical magnetometers for exotic (GNOME) physics searches. We search the data, consisting of correlated measurements from optical atomic magnetometers located in laboratories all over the world, for patterns of signals propagating through the network consistent with domain walls. The analysis of these data from a continuous month-long operation of GNOME finds no statistically significant signals, thus placing experimental constraints on such dark matter scenarios.

The nature of dark matter—an invisible substance comprising over 80% of the mass of the Universe^{1,2}—is one of the most profound mysteries of modern physics. Although evidence for the existence of dark matter comes from its gravitational interactions, unravelling its nature likely requires observing non-gravitational interactions between dark matter and ordinary matter³. One of the leading hypotheses is that dark matter consists of ultralight bosons such as axions⁴ or axion-like particles (ALPs)^{5–7}.

Axions and ALPs arise from spontaneous symmetry breaking at an unknown energy scale f_{SB} , which—along with their mass m_a —determines many of their physical properties.

ALPs can manifest as stable, macroscopic field configurations in the form of topological defects^{8–10} or composite objects bound together by self-interactions such as boson stars^{11,12}. Such ALP field configurations could concentrate the dark matter density into many distinct, compact spatial regions that are small compared

¹Helmholtz-Institut Mainz, GSI Helmholtzzentrum für Schwerionenforschung, Darmstadt, Germany. ²Johannes Gutenberg-Universität Mainz, Mainz, Germany. ³Centre for Quantum Computation and Communication Technology, Research School of Physics, The Australian National University, Acton, ACT, Australia. ⁴Department of Physics, University of California at Berkeley, Berkeley, CA, USA. ⁵Department of Physics, University of Nevada, Reno, NV, USA. ⁶Computational Research Division, Lawrence Berkeley National Laboratory, Berkeley, CA, USA. ⁷Institute for Quantum Science and Technology (IQST), 3rd Institute of Physics, and Max Planck Institute for Solid State Research, Stuttgart, Germany. ⁸Institute of Physics Belgrade, University of Belgrade, Belgrade, Serbia. ⁹Physics Department, University of Fribourg, Fribourg, Switzerland. ¹⁰State Key Laboratory of Advanced Optical Communication Systems and Networks, Department of Electronics, and Center for Quantum Information Technology, Peking University, Beijing, China. ¹¹Department of Precision Machinery and Precision Instrumentation, University of Science and Technology of China, Hefei, People's Republic of China. ¹²Department of Physics and Astronomy, University of California, Los Angeles, CA, USA. ¹³Department of Physics, California State University–East Bay, Hayward, CA, USA. ¹⁴Center for Axion and Precision Physics Research, IBS, Daejeon, Republic of Korea. ¹⁵Department of Physics, KAIST, Daejeon, Republic of Korea. ¹⁶Twinleaf LLC, Plainsboro, NJ, USA. ¹⁷Hefei National Laboratory for Physical Sciences at the Microscale, University of Science and Technology of China, Hefei, People's Republic of China. ¹⁸Institute of Physics, Jagiellonian University, Kraków, Poland. ¹⁹Department of Physics and Astronomy, Oberlin College, Oberlin, OH, USA. ²⁰School of Physics and Astronomy, University of Minnesota, Minneapolis, MN, USA. ²¹William I. Fine Theoretical Physics Institute, School of Physics and Astronomy, University of Minnesota, Minneapolis, MN, USA. ²²Leibniz Institute of Photonic Technology, Jena, Germany. ²³Department of Physics and Astronomy, Bucknell University, Lewisburg, PA, USA. ²⁴Department of Physics, Princeton University, Princeton, NJ, USA. ²⁵Technische Universität München, Garching, Germany. ²⁶Present address: Department of Physics and Astronomy, University of Waterloo, Waterloo, Canada. ²⁷Present address: JILA, NIST and Department of Physics, University of Colorado, Boulder, CO, USA. ²⁸Present address: Department of Physics, Harvard University, Cambridge, MA, USA. ✉e-mail: hemasiar@uni-mainz.de; jsmiga@uni-mainz.de

with the Galaxy but much larger than the Earth. In such scenarios, Earth-bound detectors would only be able to measure signals associated with dark matter interactions on occasions when the Earth passes through such a dark matter object. It turns out that there is a wide range of parameter space—consistent with observations—for which such dark matter objects can have the required size and abundance such that the characteristic time between encounters could be of the order of one year or less^{9,10,12}. This opens up the possibility of searches with terrestrial detectors. Here we present the results of such a search for ALP domain walls, a class of topological defects that can form between regions of space with different vacua of an ALP field^{8,9}. We note that although some models suggest that axion domain walls cannot survive to the present epoch^{13–15}, there do exist a number of ALP models demonstrating the theoretical possibility that ALP domain walls or composite dark matter objects with similar characteristics^{12,16,17} can survive to modern times^{18–20} and have the characteristics of cold dark matter^{9,10,21}.

Since ALPs can interact with atomic spins³, the passage of Earth through an ALP domain wall affects atomic spins similar to a transient magnetic-field pulse^{9,12}. Considering a linear coupling between the ALP field gradient $\nabla a(\mathbf{r}, t)$ and atomic spin \mathbf{S} , the interaction Hamiltonian can be written as

$$H_{\text{lin}} = -(\hbar c)^{3/2} \frac{\xi}{f_{\text{SB}}} \frac{\mathbf{S}}{\|\mathbf{S}\|} \cdot \nabla a(\mathbf{r}, t), \quad (1)$$

where \hbar is the reduced Planck's constant, c is the speed of light, \mathbf{r} is the position of spin, t is time, and $f_{\text{SB}}/\xi \equiv f_{\text{int}}$ is the coupling constant in units of energy described with respect to the symmetry-breaking scale f_{SB} (ref. 22); here ξ is unitless. In most theories, the coupling constants f_{int} describing the interaction between standard model fermions and the ALP field are proportional to f_{SB} ; however, f_{int} can differ between electrons, neutrons and protons by model-dependent factors that can be substantial^{3,5}.

Analogous to equation (1), the Zeeman Hamiltonian describing the interaction of magnetic field \mathbf{B} with atomic spin \mathbf{S} can be written as

$$H_Z = -\gamma \mathbf{S} \cdot \mathbf{B}, \quad (2)$$

where γ is the gyromagnetic ratio. Since equations (1) and (2) have the same structure, the gradient of the ALP field—even though it couples to the particle spin rather than the magnetic moment—can be treated as a ‘pseudo-magnetic field’ as it causes energy shifts of Zeeman sublevels. An important distinction between the ALP-spin interaction (equation (1)) and the Zeeman interaction (equation (2)) is that although γ tends to scale inversely with the fermion mass, no such scaling of the ALP-spin interaction is expected³.

The amplitude, direction and duration of the pseudo-magnetic-field pulse associated with the transit of the Earth through an ALP domain wall depends on many unknown parameters such as the energy density stored in the ALP field, coupling constant f_{int} , thickness of the domain wall, and relative velocity \mathbf{v} between Earth and the domain wall. The dynamical parameters, such as the velocities of dark matter objects, are expected to randomly vary from encounter to encounter. We assume that they are described by the standard halo model for virialized dark matter²³. Furthermore, the abundance of domain walls in the Galaxy is limited by physical constants, namely, m_a and f_{SB} , as these determine the energy contained in the wall, and the total energy of all the domain walls is constrained by estimates of the local dark matter density²⁴. The expected temporal form of the pseudo-magnetic-field pulse can depend on the theoretical model describing the ALP domain wall as well as particular details of the terrestrial encounter (such as the orientation of Earth). The relationships between these parameters and characteristics of the pseudo-magnetic-field pulses searched

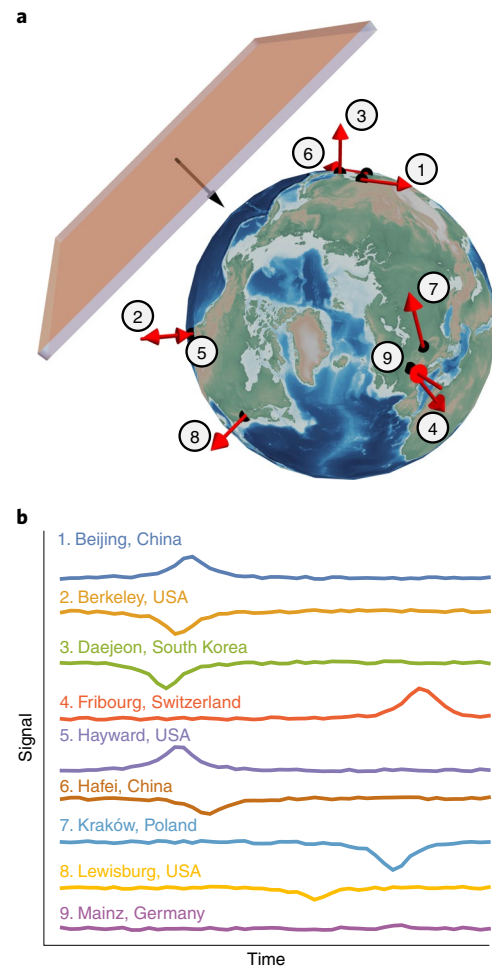


Fig. 1 | Visualization of an ALP domain-wall crossing. a, Image showing the Earth together with the position and sensitive axes of the GNOME magnetometers during Science Run 2. Position and sensitive axes are shown as red arrows. The crossing direction of the domain wall is represented as a black arrow (Extended Data Table 1). **b**, Simulation of the signals expected to be observed from a domain-wall crossing at the different magnetometers comprising the network.

for in our analysis are discussed in Supplementary Section II and other studies^{9,12,22}.

The global network of optical magnetometers for exotic (GNOME) physics searches is a worldwide network searching for correlated signals heralding beyond-the-standard-model physics that currently comprises more than a dozen optical atomic magnetometers, with stations (each with a magnetometer and supporting devices) in Europe, North America, Asia, the Middle East and Australia. A schematic of a domain-wall encounter with GNOME is shown in Fig. 1. The measurements from the magnetometers are recorded with custom data-acquisition systems²⁵; synchronized to the global positioning system (GPS) time; and uploaded to servers located in Mainz, Germany, and Daejeon, South Korea. Descriptions of the operational principles and characteristics of GNOME magnetometers are presented in Methods, Extended Data Table 1, and ref. 26.

The active field sensor at the heart of every GNOME magnetometer is an optically pumped and probed gas of alkali atoms. Magnetic fields are measured by variations in the Larmor spin precession of the optically polarized atoms. The vapour cells containing the alkali atoms are placed inside multilayer magnetic-shielding systems that

reduce background magnetic noise by orders of magnitude²⁷ despite retaining sensitivity to exotic spin couplings between ALP dark matter and atomic nuclei.

If the ALP field only couples to electron spins, interactions between the ALP field and magnetic shield will reduce the ALP-induced signal amplitudes in each magnetometer by roughly the magnetic shielding factors of 10^6 – 10^7 , as discussed in ref. ²⁸. Therefore, in the present work, we only consider interactions between ALP fields and atomic nuclei. Since all the GNOME magnetometers presently use atoms whose nuclei have a valence proton, the signal amplitudes measured by GNOME due to an ALP-spin interaction are proportional to the relative contribution of proton spin to nuclear spin (as discussed in Supplementary Section II and ref. ²⁹). This pattern of signal amplitudes (equation (1)) can be characterized by a pseudo-magnetic field B_j measured with sensor j :

$$B_j = \frac{\sigma_j \eta_j}{g_{E,j}} \mathcal{B}_p, \quad (3)$$

where

$$\mathcal{B}_p(\mathbf{r}, t) = (\hbar c)^{3/2} \frac{2\xi}{\mu_B f_{SB}} \nabla a(\mathbf{r}, t) \quad (4)$$

is the normalized pseudo-magnetic field describing the effect of the ALP domain wall on proton spins and μ_B is the Bohr magneton. The ratio between the Landé g -factor and the effective proton spin ($g_{E,j}/\sigma_j$) accounts for the specific proton-spin coupling in the respective sensor. This ratio depends on the atomic and nuclear structure in addition to details of the magnetometry scheme (Supplementary Section II). Since each GNOME magnetometer measures the projection of the field along a particular sensitive axis, the factor η_j is introduced to account for directional sensitivity. This factor, given by the cosine of the angle between \mathcal{B}_p and the sensitive axes, takes on values between +1 and –1.

In spite of the unknown properties of a particular terrestrial encounter with an ALP domain wall, GNOME measures a recognizable global pattern of the associated amplitudes of the pseudo-magnetic-field pulse described by equation (3), as illustrated in Fig. 1b. The associated pseudo-magnetic-field pulses would point along a common axis, have the same duration and exhibit a characteristic timing pattern. The data-analysis algorithm used in the present work to search for ALP domain walls is described in Methods and ref. ³⁰. The algorithm searches for a characteristic signal pattern across GNOME, having properties consistent with the passage of Earth through an ALP domain wall. Separate analyses to search for transient oscillatory signals associated with boson stars¹² and bursts of exotic low-mass fields from cataclysmic astrophysical events³¹ are presently underway.

Here we report the results of a dark matter search with GNOME: a search for transient couplings of atomic spins to macroscopic dark matter objects, thereby demonstrating the ability of GNOME to explore the parameter space previously unconstrained by direct laboratory experiments. Searches for macroscopic dark matter objects based on similar ideas were carried out using atomic clock networks^{10,23,32,33}, and there are a number of experimental proposals utilizing other sensor networks^{34–37}. All these networks are sensitive to bosonic dark matter with a scalar coupling to standard model particles³. GNOME is sensitive to a different class of dark matter: bosons with pseudo-scalar couplings to standard model particles. Pseudo-scalar bosonic dark matter generally produces no observable effects in clock networks³, but it does couple to atomic spins via the interaction described by equation (1). Thus, GNOME is sensitive to a distinct—so far, mostly unconstrained—class of interactions compared with other sensor networks.

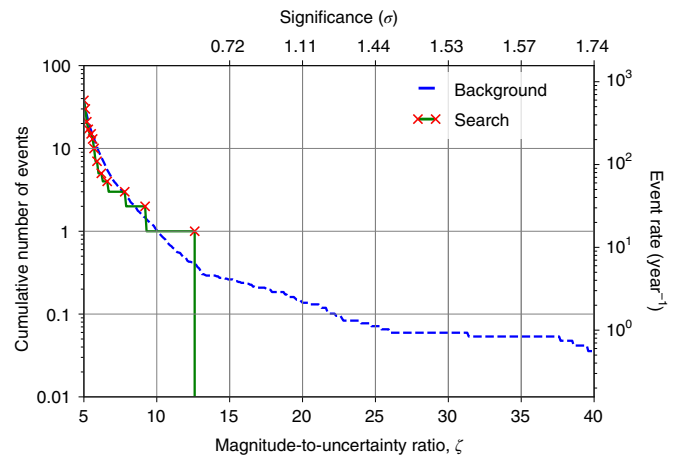


Fig. 2 | Significance of the search events. The blue dashed line represents the cumulative number of events expected from the background in the 23 days of data from Science Run 2. Here 10.7 years of time-shuffled data are used to evaluate the background. Such a duration is an arbitrary choice, but it is sufficiently long to characterize the background. The number of candidate events measured in the background data is re-scaled to the duration of Science Run 2. The solid green line represents the cumulative number of events measured in Science Run 2. The red crosses indicate the magnitude-to-uncertainty ratio at which new events are found in the search data. The upper axis indicates the statistical significance in units of Gaussian standard deviations of finding one event in the search data. The significance is given by the probability of detecting one or more background events at a magnitude-to-uncertainty ratio above that of the candidate event (equation (5)). The right axis shows the normalized number of events over a period of a year. The event with the greatest magnitude-to-uncertainty ratio is found at 12.6.

Search for ALP domain-wall signatures

There have been four GNOME science runs between 2017 and 2020, as discussed in Methods. Here we analyse the data from Science Run 2, which had comparatively good overall noise characteristics and consistent network operation (as shown in Extended Data Fig. 1). Nine magnetometers took part in Science Run 2 that spanned from 29 November 2017 to 22 December 2017. The characteristics of the magnetometers are summarized in Extended Data Table 1.

Before the data are searched for evidence of domain-wall signatures, they are preprocessed by applying a rolling average, high-pass filters, and notch filters to the raw data. The averaging process enhances the signal-to-noise ratio for certain pulse durations, avoids complications arising from different magnetometers having different bandwidths, and reduces the amount of data to be analysed. The high-pass and notch filters reduce the effects of long-term drifts and noisy frequency bands. We refer to the filtered and rolling-averaged dataset as the ‘search data.’

The search data are examined for the evidence of collective signal patterns corresponding to planes with uniform, non-zero thickness, crossing Earth at constant velocities. The imprinted pattern of amplitudes depends on the domain-wall-crossing velocity³⁰. We assume that the domain-wall-velocity probability density function follows the standard halo model for virialized dark matter. The signature of a domain wall crossing the magnetometer network depends on the component of the relative velocity between the domain wall and the Earth that is perpendicular to the domain-wall plane, v_{\perp} . A lattice of points in the velocity space is constructed such that the search algorithm covers 97.5% of the velocity probability density function. The algorithm scans over the velocity lattice and, for every velocity, the data from each magnetometer are appropriately

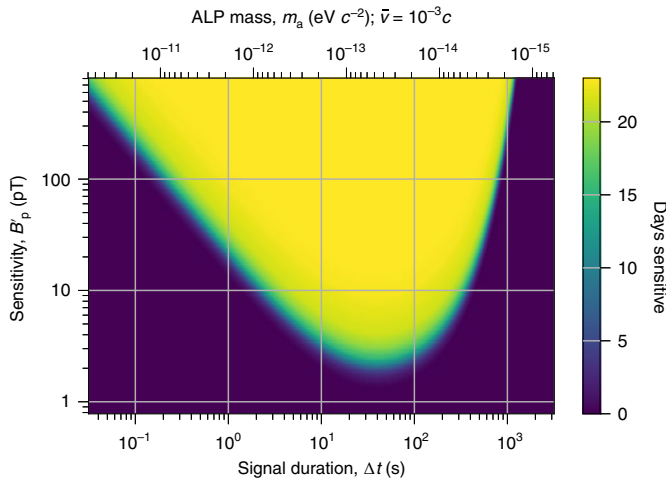


Fig. 3 | Sensitivity of the GNOME network to domain walls. Amount of time T , indicated in colour, for which GNOME had a normalized pseudo-magnetic-field-magnitude sensitivity above B'_p (that is, the domain wall would induce a magnitude-to-uncertainty ratio of at least one) for domain walls with a given duration Δt (defined as the FWHM of a Lorentzian signal) throughout Science Run 2. The upper axis shows the range of ALP masses to which GNOME is sensitive (equation (9)). The characteristic shape of the sensitive region is a result of the filtering and averaging of the raw data, as described in Methods. Averaging reduces the sensitivity of the search data to short pulse durations and high-pass filtering suppresses sensitivity to long Δt . The sensitivity of GNOME varies in time with changes in the number of active GNOME magnetometers recording data and their background noise. Only the worst-case direction is considered. The plot assumes the parameters of the analysis: 20 s averaging time, 1.67 mHz first-order zero-phase Butterworth filter, and 50 and 60 Hz zero-phase notch filters with a quality factor of 60.

time-shifted so that the signals in different magnetometers from a hypothetical domain-wall crossing with the given velocity occur at the same time. For each velocity and at each measurement time, the amplitudes measured by each magnetometer are fit to the ALP domain-wall-crossing model described in ref. ³⁰. As a result, estimations for signal magnitude and domain-wall direction, along with associated uncertainties, are obtained for each measurement time and all the lattice velocities. The magnitude-to-uncertainty ratio of an event is given by the ratio between the signal magnitude and its associated uncertainty.

The search algorithm uses two different tests to evaluate if a given event is likely to have been produced by an ALP domain-wall crossing: a domain-wall model test and a directional-consistency test³⁰. The domain-wall model test evaluates whether the event amplitudes measured by the GNOME magnetometers match the signal amplitudes predicted by the ALP domain-wall-crossing model, and is quantified by the P -value, as discussed in Methods and ref. ³⁰. The directional-consistency test checks the agreement between the direction of the scanned velocity and the estimated domain-wall direction, and is quantified by the angle between the two directions normalized by the angle between the adjacent lattice velocities. The thresholds on these tests are chosen to guarantee an overall detection efficiency $\epsilon \geq 95\%$ for the search algorithm, considering both incomplete velocity lattice coverage and detection probability (Extended Data Fig. 2).

The search data are analysed for domain-wall encounters using the algorithm presented in ref. ³⁰. The cumulative distribution of candidate events as a function of their magnitude-to-uncertainty ratio is shown as the solid green line in Fig. 2. The candidate event

in the search data with the largest magnitude-to-uncertainty ratio (namely, 12.6) had a significance of less than one sigma. Therefore, we find no evidence of an ALP domain-wall crossing during Science Run 2. Rare domain-wall-crossing events that produce signals below a magnitude-to-uncertainty ratio of 12.6 are indistinguishable from the background. Therefore, we base constraints on the ALP parameters on the absence of any detection above the ‘loudest event’ in a manner similar to that described, for example, in ref. ³⁸.

To evaluate the domain-wall characteristics excluded by this result, the observable domain-wall-crossing parameters above a magnitude-to-uncertainty ratio of 12.6 during Science Run 2 are determined. GNOME has non-uniform directional sensitivity³⁰; we conservatively estimate the network sensitivity assuming the domain wall comes from the least-sensitive direction. Figure 3 shows the active time $T(\Delta t, B'_p)$, that is, how long the network was sensitive to domain walls as a function of sensitivity of the pseudo-magnetic-field magnitude, B'_p , and pulse duration, Δt . A signal with pseudo-magnetic-field magnitude B_p produces a magnitude-to-uncertainty ratio of $\zeta = B_p/B'_p$. The active time, $T(\Delta t, B'_p)$, can be used to constrain the ALP domain-wall parameter space, as discussed in Supplementary Section II.

If one assumes a probability distribution for the number of domain-wall encounters, an upper bound on the rate R_C of such encounters can be calculated with confidence level C . We assume a Poisson probability distribution for the domain-wall crossings. Since the excess number of events in the search data compared with the background data was not statistically significant, the upper bound on the observable rate is given by the probability of measuring no events during the effective time³⁸. Note that since T depends on the parameters of the domain-wall crossing, our constraint on the observed rate depends on the ALP properties. We choose the confidence level to be $C = 90\%$.

Constraints on ALP domain walls

Analysis of the GNOME data did not find any statistically significant excess of events above the background during Science Run 2 that could point to the existence of ALP domain walls, as shown in Fig. 2. The expected rate of domain-wall encounters (r) depends on the ALP mass (m_a), domain-wall energy density in the Milky Way (ρ_{DW}), typical relative domain-wall speed (\bar{v}) and symmetry-breaking scale (f_{SB}). The region of parameter space to which GNOME is sensitive is defined by the ALP parameters expected to produce signals above the magnitude-to-uncertainty ratio of 12.6 with rates $r \geq R_{90\%}$ during Science Run 2 (Fig. 3). Based on the null result of our search, the sensitive region is interpreted as the excluded ALP parameter space.

The ALP parameters and the phenomenological parameters describing the ALP domain walls in our Galaxy, namely, thickness Δx , surface tension or energy per unit area σ_{DW} and the average separation L , can be related through the ALP domain-wall model described elsewhere^{9,22}. A full derivation of how the observable parameters are related to the ALP parameters is given in Supplementary Section II.

The coloured region in Fig. 4a describes the symmetry-breaking scales up to which GNOME was sensitive with 90% confidence. The parameter space is spanned by ALP mass, maximum symmetry-breaking scale, and ratio between the symmetry-breaking scale and coupling constant. The shape of the sensitive area shown in Fig. 4a is determined by the event with the largest magnitude-to-uncertainty ratio and the characteristics of preprocessing applied to the raw data.

Figure 4b shows the various cross sections for different ratios between the symmetry-breaking scale and the coupling constant, as indicated by the dashed lines in Fig. 4a. The upper bound of f_{SB} that can be observed by the network is shown in Fig. 4b for different values of $\xi \equiv f_{SB}/f_{int}$. Because $B_p \propto m_a$ (Supplementary equation (10) in Supplementary Section II), there is a sharp cutoff for low

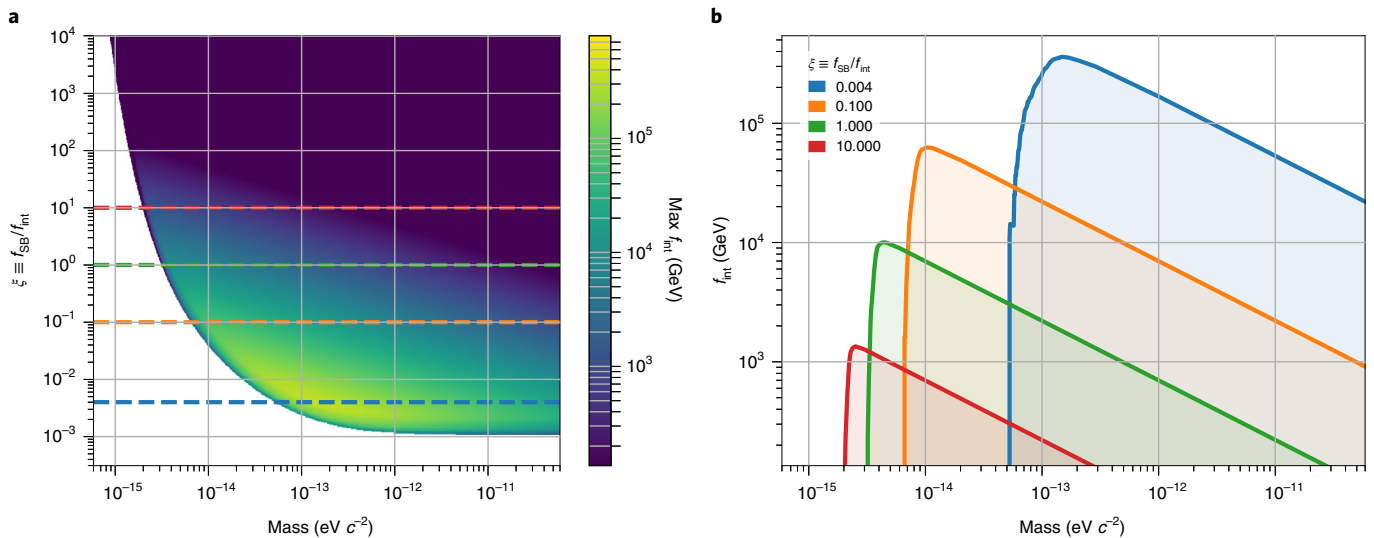


Fig. 4 | Bounds on the ALP parameter space. The bounds are drawn from the presented analysis of Science Run 2 with 90% confidence level. Relationship between the parameters from ALP theory and measured quantities is discussed in Supplementary Section II. **a**, In colour, upper bound on the interaction scale for axion–nucleon coupling, f_{int} , to which GNOME was sensitive as a function of m_a and the ratio between symmetry-breaking and interaction scales ($\xi \equiv f_{\text{SB}}/f_{\text{int}}$). The dashed horizontal lines highlight the cross-section used in **b** with the respective colour. **b**, Cross-sections of the excluded parameter volume in **a** for different ξ ratios. We note that the domain walls may not be the only form of dark matter; therefore, $\rho_{\text{DW}} < 0.4 \text{ GeV cm}^{-3}$. If the domain-wall energy density is substantially smaller, this would affect the bounds shown here.

ALP mass where the corresponding field magnitude falls below the network sensitivity. Even though \mathcal{B}_p increases for large m_a , the mean rate of domain-wall encounters decreases with increasing mass (equations (11) and (12)). Correspondingly, the upper limit for the symmetry-breaking scale f_{SB} is $\propto 1/\sqrt{m_a}$. Given that no events were found, the sensitive region of the ALP domain-wall parameter space during Science Run 2 can be excluded.

Our experiment explores the ALP parameter space up to $f_{\text{int}} \approx 4 \times 10^5 \text{ GeV}$ (Fig. 4). This goes beyond that excluded by previous direct laboratory experiments searching for ALP-mediated exotic pseudo-scalar interactions between protons that have shown that $f_{\text{int}} \gtrsim 300 \text{ GeV}$ over the ALP mass range probed by GNOME³⁹. Although astrophysical observations suggest that $f_{\text{int}} \gtrsim 2 \times 10^8 \text{ GeV}$, there are a variety of scenarios in which such astrophysical constraints can be evaded^{40,41}. The parameter space for f_{int} and m_a explored in this search is well outside the typical predictions for axions in quantum chromodynamics^{42,43}. However, for ALPs, a vast array of possibilities for the generation of ALP masses and couplings are opened by a variety of beyond-the-standard-model theories, meaning that the values of f_{int} and m_a explored in our search are theoretically possible^{44,45}.

Future work of the GNOME collaboration will focus on both upgrades to our experimental apparatus and new data-analysis strategies. One of our key goals is to improve the overall reliability and duration of continuous operation of GNOME magnetometers. The intermittent operation of some magnetometers due to technical difficulties during Science Runs 1–3 made it difficult to search for signals persisting for $\gtrsim 1 \text{ h}$. Additionally, magnetometers varied in their bandwidths and reliability, as well as stability of their calibration. These challenges were addressed in Science Run 4 through a variety of magnetometer upgrades and instituting daily worldwide test and calibration pulse sequences. However, GNOME suffered disruptions due to the COVID-19 pandemic. We plan to carry out Science Run 5 in 2021 to take full advantage of the improvements. Furthermore, by upgrading to noble-gas-based comagnetometers^{46,47} for future science runs (advanced GNOME), we expect to considerably improve the sensitivity to ALP domain

walls. Additionally, GNOME data can be searched for other signatures of physics beyond the standard model, such as boson stars¹², relaxation halos⁴⁸ and bursts of exotic low-mass fields from black-hole mergers³¹.

In terms of the data-analysis algorithm used to search for ALP domain walls, recent studies⁴⁹ have considered a possible back-action that the Earth may have on a domain wall when certain interactions are important, namely, up-to-quadratic coupling terms between a scalar field and fermions. In contrast to another study⁴⁹, the present work analyses a completely different interaction, namely, a linear coupling between a pseudo-scalar field and fermion spins, which produces no major back-action effect. Regardless, it would be worthwhile to consider interactions generating similar back-action effects of the Earth on domain walls and the ALP field in later analysis. Further, in future work, we aim to improve the efficiency of the scan over the velocity lattice. The number of points in the velocity lattice to reliably cover a fixed fraction (for example, 97.5%) of the ALP-velocity probability distribution grows as $(\Delta t)^{-3}$ (where Δt is given by equation (9)). This makes the algorithm computationally intensive. We are investigating a variety of analysis approaches, such as machine-learning-based algorithms, to address these issues.

Online content

Any methods, additional references, Nature Research reporting summaries, source data, extended data, supplementary information, acknowledgements, peer review information; details of author contributions and competing interests; and statements of data and code availability are available at <https://doi.org/10.1038/s41567-021-01393-y>.

Received: 9 March 2021; Accepted: 17 September 2021;
Published online: 7 December 2021

References

- Bertone, G., Hooper, D. & Silk, J. Particle dark matter: evidence, candidates and constraints. *Phys. Rep.* **405**, 279–390 (2005).
- Gorenstein, P. & Tucker, W. Astronomical signatures of dark matter. *Adv. High Energ. Phys.* **2014**, 878203 (2014).

3. Safronova, M. et al. Search for new physics with atoms and molecules. *Rev. Mod. Phys.* **90**, 025008 (2018).
4. Preskill, J., Wise, M. B. & Wilczek, F. Cosmology of the invisible axion. *Phys. Lett. B* **120**, 127–132 (1983).
5. Graham, P. W., Irastorza, I. G., Lamoreaux, S. K., Lindner, A. & van Bibber, K. A. Experimental searches for the axion and axion-like particles. *Annu. Rev. Nucl. Part. Sci.* **65**, 485–514 (2015).
6. Graham, P. W., Kaplan, D. E. & Rajendran, S. Cosmological relaxation of the electroweak scale. *Phys. Rev. Lett.* **115**, 221801 (2015).
7. Co, R. T., Hall, L. J. & Harigaya, K. Predictions for axion couplings from ALPogenesis. *J. High Energy Phys.* **2021**, 172 (2021).
8. Vilenkin, A. Cosmic strings and domain walls. *Phys. Rep.* **121**, 263–315 (1985).
9. Pospelov, M. et al. Detecting domain walls of axionlike models using terrestrial experiments. *Phys. Rev. Lett.* **110**, 021803 (2013).
10. Derevianko, A. & Pospelov, M. Hunting for topological dark matter with atomic clocks. *Nat. Phys.* **10**, 933–936 (2014).
11. Braaten, E., Mohapatra, A. & Zhang, H. Dense axion stars. *Phys. Rev. Lett.* **117**, 121801 (2016).
12. Jackson Kimball, D. et al. Searching for axion stars and Q-balls with a terrestrial magnetometer network. *Phys. Rev. D* **97**, 043002 (2018).
13. Sikivie, P. Axions, domain walls, and the early Universe. *Phys. Rev. Lett.* **48**, 1156–1159 (1982).
14. Press, W. H., Ryden, B. S. & Spergel, D. N. Dynamical evolution of domain walls in an expanding Universe. *Astrophys. J.* **347**, 590–604 (1989).
15. Buschmann, M., Foster, J. W. & Safdi, B. R. Early-Universe simulations of the cosmological axion. *Phys. Rev. Lett.* **124**, 161103 (2020).
16. Coleman, S. Q-balls. *Nucl. Phys. B* **262**, 263–283 (1985).
17. Kusenko, A. & Steinhardt, P. J. Q-ball candidates for self-interacting dark matter. *Phys. Rev. Lett.* **87**, 141301 (2001).
18. Bucher, M. & Spergel, D. Is the dark matter a solid? *Phys. Rev. D* **60**, 043505 (1999).
19. Avelino, P., Martins, C., Menezes, J., Menezes, R. & Oliveira, J. Dynamics of domain wall networks with junctions. *Phys. Rev. D* **78**, 103508 (2008).
20. Hiramatsu, T., Kawasaki, M., Saikawa, K. & Sekiguchi, T. Axion cosmology with long-lived domain walls. *J. Cosmol. Astropart. Phys.* **2013**, 001 (2013).
21. Baek, S., Ko, P. & Park, W.-I. Hidden sector monopole, vector dark matter and dark radiation with Higgs portal. *J. Cosmol. Astropart. Phys.* **2014**, 067 (2014).
22. Pustelny, S. et al. The global network of optical magnetometers for exotic physics (GNOME): a novel scheme to search for physics beyond the Standard Model. *Ann. Phys.* **525**, 659–670 (2013).
23. Roberts, B. M. et al. Search for domain wall dark matter with atomic clocks on board global positioning system satellites. *Nat. Commun.* **8**, 1195 (2017).
24. Bovy, J. & Tremaine, S. On the local dark matter density. *Astrophys. J.* **756**, 89 (2012).
25. Włodarczyk, P., Pustelny, S., Budker, D. & Lipiński, M. Multi-channel data acquisition system with absolute time synchronization. *Nucl. Instr. Meth. Phys. Res. A* **763**, 150–154 (2014).
26. Afach, S. et al. Characterization of the global network of optical magnetometers to search for exotic physics (GNOME). *Phys. Dark Universe* **22**, 162–180 (2018).
27. Yashchuk, V. V., Lee, S.-K. & Paperno, E. in *Optical Magnetometry* (eds Budker, D. & Kimball, D. F. J.) Ch. 2 (Cambridge Univ. Press, 2013).
28. Jackson Kimball, D. F. et al. Magnetic shielding and exotic spin-dependent interactions. *Phys. Rev. D* **94**, 082005 (2016).
29. Jackson Kimball, D. F. Nuclear spin content and constraints on exotic spin-dependent couplings. *New J. Phys.* **17**, 073008 (2015).
30. Masia-Roig, H. et al. Analysis method for detecting topological defect dark matter with a global magnetometer network. *Phys. Dark Universe* **28**, 100494 (2020).
31. Dailey, C. et al. Quantum sensor networks as exotic field telescopes for multi-messenger astronomy. *Nat. Astron.* **5**, 150–158 (2021).
32. Wcisło, P. et al. Experimental constraint on dark matter detection with optical atomic clocks. *Nat. Astron.* **1**, 0009 (2017).
33. Roberts, B. M. et al. Search for transient variations of the fine structure constant and dark matter using fiber-linked optical atomic clocks. *New J. Phys.* **22**, 093010 (2020).
34. Stadnik, Y. V. & Flambaum, V. V. Enhanced effects of variation of the fundamental constants in laser interferometers and application to dark-matter detection. *Phys. Rev. A* **93**, 063630 (2016).
35. Jacobs, D. M., Weltman, A. & Starkman, G. D. Resonant bar detector constraints on macro dark matter. *Phys. Rev. D* **91**, 115023 (2015).
36. Arvanitaki, A., Dimopoulos, S. & Van Tilburg, K. Sound of dark matter: searching for light scalars with resonant-mass detectors. *Phys. Rev. Lett.* **116**, 031102 (2016).
37. McNally, R. L. & Zelevinsky, T. Constraining domain wall dark matter with a network of superconducting gravimeters and LIGO. *Eur. Phys. J. D* **74**, 61 (2020).
38. Brady, P. R., Creighton, J. D. E. & Wiseman, A. G. Upper limits on gravitational-wave signals based on loudest events. *Class. Quantum Grav.* **21**, S1775–S1781 (2004).
39. Ramsey, N. F. The tensor force between two protons at long range. *Physica A* **96**, 285–289 (1979).
40. DeRocco, W., Graham, P. W. & Rajendran, S. Exploring the robustness of stellar cooling constraints on light particles. *Phys. Rev. D* **102**, 075015 (2020).
41. Bar, N., Blum, K. & D’Amico, G. Is there a supernova bound on axions? *Phys. Rev. D* **101**, 123025 (2020).
42. Shifman, M., Vainshtein, A. & Zakharov, V. Can confinement ensure natural CP invariance of strong interactions? *Nucl. Phys. B* **166**, 493–506 (1980).
43. Svrcek, P. & Witten, E. Axions in string theory. *J. High Energy Phys.* **2006**, 051 (2006).
44. Marsh, D. J. Axion cosmology. *Phys. Rep.* **643**, 1–79 (2016).
45. Irastorza, I. G. & Redondo, J. New experimental approaches in the search for axion-like particles. *Prog. Part. Nucl. Phys.* **102**, 89–159 (2018).
46. Kornack, T. W. & Romalis, M. V. Dynamics of two overlapping spin ensembles interacting by spin exchange. *Phys. Rev. Lett.* **89**, 253002 (2002).
47. Kornack, T. W., Ghosh, R. K. & Romalis, M. V. Nuclear spin gyroscope based on an atomic comagnetometer. *Phys. Rev. Lett.* **95**, 230801 (2005).
48. Banerjee, A., Budker, D., Eby, J., Kim, H. & Perez, G. Relaxion stars and their detection via atomic physics. *Commun. Phys.* **3**, 1 (2020).
49. Stadnik, Y. V. New bounds on macroscopic scalar-field topological defects from nontransient signatures due to environmental dependence and spatial variations of the fundamental constants. *Phys. Rev. D* **102**, 115016 (2020).

Publisher’s note Springer Nature remains neutral with regard to jurisdictional claims in published maps and institutional affiliations.



Open Access This article is licensed under a Creative Commons Attribution 4.0 International License, which permits use, sharing, adaptation, distribution and reproduction in any medium or format, as long as you give appropriate credit to the original author(s) and the source, provide a link to the Creative Commons license, and indicate if changes were made. The images or other third party material in this article are included in the article’s Creative Commons license, unless indicated otherwise in a credit line to the material. If material is not included in the article’s Creative Commons license and your intended use is not permitted by statutory regulation or exceeds the permitted use, you will need to obtain permission directly from the copyright holder. To view a copy of this license, visit <http://creativecommons.org/licenses/by/4.0/>.

© The Author(s) 2021

Methods

GNOME consists of over a dozen optical atomic magnetometers, each enclosed within a multilayer magnetic shield, distributed around the world²⁷. GNOME magnetometers are based on a variety of different atomic species, optical transitions and measurement techniques: some are frequency- or amplitude-modulated nonlinear magneto-optical rotation magnetometers^{50,51}, some are radio-frequency-driven optical magnetometers⁵⁰, whereas others are spin-exchange-relaxation-free magnetometers⁵². A detailed description and characterization of six GNOME magnetometers are given in ref. ²⁶. A summary of the properties of the GNOME magnetometers active during Science Run 2 is presented in Extended Data Table 1.

Each GNOME station is equipped with auxiliary sensors, including accelerometers, gyroscopes and unshielded magnetometers, to measure local perturbations that could mimic a dark matter signal. Suspicious data are flagged²⁶ and discarded during the analysis.

The number of active GNOME magnetometers during the four science runs and the combined network noise, as defined in ref. ³⁰, are shown as a function of time in Extended Data Fig. 1. Although Science Run 4 was carried out over a longer period of time than Science Run 2, it featured poorer noise characteristics and consistency of operation compared with Science Run 2. Since many GNOME stations underwent upgrades in 2018 and 2019, further characterization of the data from Science Run 4 is needed, and the results will be presented in future work. The number of active magnetometers during Science Runs 1 and 3 was often less than four, which is insufficient to characterize a domain-wall crossing. We thus present the analysis efforts on the data from Science Run 2.

Here we provide more details on the analysis procedure. The identification of events likely to be produced by ALP domain-wall crossings comprise three stages: preprocessing, velocity scanning and post-selection³⁰. First, in the preprocessing stage, a rolling average and filters are applied to the raw data from the GNOME magnetometer, which are originally recorded by the GPS-synchronized data-acquisition system at the rate of 512 samples per second (ref. ²⁵). The rolling average is characterized by a 20 s time constant. Noisy frequency bands are suppressed using a first-order Butterworth high-pass filter at 1.67 mHz together with notch filters corresponding to power-line frequencies of 50 or 60 Hz with a quality factor of 60. These filters are applied forward and backward to remove any phase effects. This limits the observable pulse properties to a frequency region to which all the magnetometers are sensitive. Additionally, it guarantees that the duration of the signal is the same for all the sensors. We note that these filter settings may be changed in future analyses.

The local standard deviation around each point in the magnetometer's data is determined using an iterative process. Outliers are discarded until the standard deviation of the data in the segment converges. The local standard deviation is calculated taking 100 down-sampled points around each data point.

Additionally, auxiliary measurements have shown that the calibration factors used by each magnetometer to convert raw data into magnetic-field units experience change over time due to, for example, changes in the environmental conditions. Upper limits on the errors in the calibration factor due to such drifts over the course of Science Run 2 have been evaluated, as listed in Extended Data Table 1. Calibration errors result in magnetic-field measurement errors proportional to magnetic field B_p . The uncertainty resulting from the calibration error is later used to determine the agreement with the domain-wall model, but not in the magnitude-to-uncertainty ratio estimate resulting from the model, since the calibration error affects the signal and noise in the same way.

Second, at the velocity-scanning stage, data from the individual magnetometers are time-shifted according to different relative velocities between Earth and the ALP domain walls. To sample 97.5% of the velocity probability distribution, a scan of the speeds from 53.7 to 770 km s⁻¹ with directions covering the full 4π solid angle is chosen; therefore, the domain walls can take any orientation with respect to the movement of Earth. Note that this distribution considers just the observable perpendicular component of the relative domain-wall velocity and neglects the orbital motion of the Earth around the Sun. For low relative velocities, both time between signals at different magnetometers and signal duration diverge. Therefore, the velocity range is determined by the chosen 97.5% coverage and the maximum relative speed of the domain walls travelling at the Galactic escape speed.

The corresponding time-shifted data along with their local standard deviation estimate are fetched from each magnetometer's rolling-average full-rate data at the rate of 0.1 samples per second. This reduces the amount of data to process, even though keeping the full timing resolution.

The step size used in the speed scan is chosen so that a single step in speed corresponds to time-shift differences of less than the down-sampled sampling period. For each speed, a lattice of directions covering the full 4π solid angle is constructed. The angular difference between adjacent directions is informed by the sampling rate and speed³⁰ such that, as for the speed scan, a single step in direction results in time-shift differences of less than the down-sampled sampling period. With the settings used, the velocity-scanning lattice consists of 1,661 points. This number scales with the cube of the down-sampled sampling rate.

After the time shift, the pulses produced by a domain-wall crossing simultaneously appear as if all the magnetometers were placed at the Earth's centre. This process results in a time-shifted dataset for each lattice velocity on which

χ^2 minimization is performed for each time point to estimate the domain-wall parameters. An ALP domain-wall-crossing direction and magnitude \mathcal{B}_p with the corresponding P -value quantifying the agreement is obtained. The P -value is evaluated as the probability of obtaining the given χ^2 value or higher from χ^2 minimization. The P -value is calculated using the quadrature sum of the standard deviation of the data and the uncertainty due to drifts in the calibration factors. All the data points in every time-shifted dataset are considered to be potential events, characterized by time, P -value, and direction and magnitude \mathcal{B}_p with their associated uncertainties. The magnitude-to-uncertainty ratio of an event ζ is the ratio between \mathcal{B}_p and its associated uncertainty.

Third, in the post-selection stage, two tests are carried out to check if a potential event is consistent with an ALP domain-wall crossing. The domain-wall model test evaluates if the observed signal amplitudes are consistent with the expected pattern of a domain-wall crossing from any possible direction. It is quantified by the aforementioned P -value. The directional-consistency test is based on the angular difference between the estimated domain-wall-crossing direction and the direction of velocity corresponding to the particular time-shifted dataset being analysed. In a real domain-wall-crossing event, these two directions should be aligned.

To evaluate the consistency of a potential event with a domain-wall crossing, we impose thresholds on the P -value and the angular difference normalized with respect to the angular spacing of the lattice of velocity points for that speed. The thresholds are chosen to guarantee a detection probability of 97.5% with the minimum possible false-positive probability. The false-positive analysis is performed on the background data. The true-positive analysis is performed on the test data consisting of background data with randomly inserted domain-wall signals as described below.

A single signal pattern may appear as multiple potential events in the analysis, whereas we are seeking to characterize a single underlying domain-wall-crossing event. For example, a signal consistent with a domain-wall crossing lasting for multiple sampling periods would appear as multiple potential events in a single time-shifted dataset. Furthermore, even if such a signal lasts only for a single sampling period, the corresponding potential events appear in different time-shifted datasets. Since it is assumed that domain-wall crossings rarely occur, such clusters of potential events are classified as a single 'event'. To reduce the double counting of these events, conditions are imposed. If potential events passing the thresholds occur at the same time in different time-shifted datasets or are contiguous in time, the potential event with the greatest magnitude-to-uncertainty ratio is classified as the corresponding single event.

To evaluate the detection probability of the search algorithm, a well-characterized dataset that includes domain-wall-crossing signals with known properties is required. For this purpose, we generate a background dataset by randomly time shuffling the search data so that the relative timing of measurements from different GNOME stations is shifted by amounts so large that no true-positive events could occur. By repeating the process of time shuffling, the length of background data can be made to far exceed the search data. This method is used to generate background data with noise characteristics closely reproducing those of the search data³³. A set of pseudo-magnetic-field pulses matching the expected amplitude and timing pattern produced by the passages of Earth through the ALP domain walls are inserted into the background data to create the test data.

The true-positive analysis studies the detection probability as a function of the thresholds. Multiple test datasets are created featuring domain-wall-signal patterns with random parameters by inserting Lorentzian-shaped pulses into the background data of the different GNOME magnetometers. The domain-crossing events have magnitudes of \mathcal{B}_p randomly selected between 0.1 and 10^4 pT and durations randomly selected between 0.01 and 10^3 s. The distributions of the these randomized parameters are chosen to be flat on a logarithmic scale. Additionally, the signals are inserted at random times with random directions. To simulate the effects of calibration error, the pulse amplitudes inserted in each magnetometer are weighted by a random factor whose range is given in Extended Data Table 1. The crossing velocity is also randomized within the range covered by the velocity lattice. For each inserted domain-wall-crossing event, the P -value, normalized angular difference and magnitude-to-uncertainty ratio are computed.

Extended Data Fig. 2a shows the detection probability as a function of the threshold on the lower limit of the P -value and the threshold on the upper limit of the normalized angular difference. We restrict the analysis in Extended Data Fig. 2a to events inserted with a magnitude-to-uncertainty ratio between 5 and 10. This enables a reliable determination of the true-positive detection probability without major contamination by false-positive events, since the background event probability above $\zeta = 5$ is below 0.01% in a 10 s sampling interval. Since the detection probability increases with the signal magnitude, we focus on the events below $\zeta = 10$. The detection probability is then the number of detected events divided by the number of inserted events. The black line marks the numerically evaluated boundary of the area, guaranteeing at least 97.5% detection. All points along this black line yield the desired detection probability; therefore, this particular choice is made to minimize the number of candidate events when applying the search algorithm to the background data. Here the values determined for the P -value threshold and directional-consistency threshold are 0.001 and 3.5, respectively (represented as the white dot in Extended Data Fig. 2a). Extended Data Fig. 2b shows that the detection probability is greater than 97.5% for events

featuring a magnitude-to-uncertainty ratio above 5 and guarantees $\epsilon \geq 95\%$. This results in an overall detection efficiency of $\epsilon \geq 95\%$ for the search algorithm, considering both incomplete velocity lattice coverage and detection probability.

Since the noise has a non-zero probability of mimicking the signal pattern expected from an ALP domain-wall crossing well enough to pass the P -value and directional-consistency tests, we perform a false-positive study on background data of length T_b . The analysis algorithm is applied to $T_b = 10.7$ years of time-shuffled data to establish the rate of events solely expected from the background. Because of the larger amount of background data analysed, lower rates and larger magnitude-to-uncertainty ratios are accessible compared with the search data. Based on the false-positive study, the probability of finding one or more events in the search data above ζ is²⁴

$$P(\geq 1 \text{ above } \zeta) = 1 - \exp\left(-\frac{T}{T_b} [1 + n_b(\zeta)]\right), \quad (5)$$

where $T = 23$ days is the duration of Science Run 2 and $n_b(\zeta)$ is the number of candidate events found in the background data above ζ . The significance is then defined as $S = -\sqrt{2} \operatorname{erf}^{-1} [1 - 2(1 - P)]$, where erf^{-1} is the inverse error function. The significance is given in units of the Gaussian standard deviation that corresponds to a one-sided probability of P .

After characterizing the background for Science Run 2, the search data are analysed. The results are represented as a solid green line in Fig. 2. For $\zeta > 6$, only a few events were found. The event with the largest magnitude-to-uncertainty ratio, ζ_{\max} , was measured at 12.6 followed by additional events at 6.2 and 5.6. From equation (5), the significance associated with finding one or more events produced by the background featuring at least ζ_{\max} is lower than one sigma. This null result defines the sensitivity of the search and is used to set constraints on the parameter space describing the ALP domain walls.

The observable rate of domain-wall crossings depends on how long GNOME was sensitive to different signal durations and magnitudes. For the evaluation of this effective time, the raw data of each magnetometer are divided into continuous segments between one and two hours depending on the availability of data. The preprocessing steps are applied to each segment. Then, the data are binned by taking the average in 20 s intervals. To estimate the noise in each magnetometer, the standard deviation in each binned segment is calculated to define the covariance matrix Σ . The domain-wall magnitude, crossing with the worse-case direction \mathbf{m} , needed to produce $\zeta = 1$ is calculated, as in ref.³⁰, for each bin.

$$\mathcal{B}'_p(\Delta t) = \sqrt{\mathbf{m}(D_{\Delta t}^T \Sigma^{-1} D_{\Delta t})^{-1} \mathbf{m}}, \quad (6)$$

The matrix $D_{\Delta t}$ contains the sensitivity axes of the magnetometers, factor σ_j/g , and effects of preprocessing as a function of signal duration (as described in ref.³⁰). Such preprocessing effects rely on a Lorentzian-shaped signal and give rise to the characteristic shape shown in Fig. 3. The effective time T is defined as the amount of time for which the network can measure a domain wall with duration Δt and magnitude \mathcal{B}'_p , producing $\zeta \geq 1$. Monte Carlo simulations analysing segments with inserted domain-wall encounters on the raw data show good agreement with the sensitivity estimation in equation (6).

Assuming that the domain-wall encounters follow Poisson statistics, a bound on the observable rate of events above ζ_{\max} with 90% confidence is set as³⁸

$$R_{90\%} = \frac{-\log(0.1)}{\epsilon T(\Delta t, \mathcal{B}'_p)}. \quad (7)$$

The domain-wall thickness is determined by the ALP mass, and is of the order of the ALP-reduced Compton wavelength λ_a (ref.²²):

$$\Delta x \approx 2\sqrt{2} \lambda_a = 2\sqrt{2} \frac{\hbar}{m_a c}. \quad (8)$$

The constant prefactor of $2\sqrt{2}$ is obtained by approximating the spatial profile of the field-gradient magnitude as a Lorentzian and defining the thickness as the full-width at half-maximum (FWHM). For a given relative-velocity component perpendicular to the domain wall v_{\perp} , the signal duration is

$$\Delta t = \frac{\Delta x}{v_{\perp}} \propto m_a^{-1}. \quad (9)$$

We assume that domain walls comprise the dominant component of dark matter. Thus, with the energy density $\rho_{\text{DW}} \approx 0.4 \text{ GeV cm}^{-3}$ in the Milky Way²⁴, the energy per unit area (surface tension) in a domain wall, σ_{DW} , determines the average separation between the domain walls, L . The surface tension σ_{DW} is related to the symmetry-breaking scale⁹ as

$$\sigma_{\text{DW}} = \frac{8}{\hbar^2} m_a f_{\text{SB}}^2. \quad (10)$$

The average domain-wall separation is then approximated by

$$L \approx \frac{\sigma_{\text{DW}}}{\rho_{\text{DW}}} = \frac{8}{\hbar^2} \frac{m_a f_{\text{SB}}^2}{\rho_{\text{DW}}}, \quad (11)$$

which results in the average domain-wall encounter rate of

$$r = \bar{v}/L \propto \left(m_a f_{\text{SB}}^2\right)^{-1}. \quad (12)$$

We assume the typical relative domain-wall speed to be equal to the Galactic rotation speed of Earth.

The ALP parameter space is constrained by imposing $r \geq R_{90\%}$. The experimental constraint on the coupling constant is written as follows (Supplementary equation (13) in Supplementary Section II).

$$f_{\text{int}} \leq \frac{\hbar}{\xi} \sqrt{\frac{\bar{v} \rho_{\text{DW}} \epsilon}{8 m_a \log(0.1)} T(\Delta t, \mathcal{B}'_p)} \quad (13)$$

The signal duration can be written in terms of the mass of the hypothetical ALP particle and the specific domain-wall-crossing speed, $\Delta t = \frac{2\sqrt{2}\hbar}{v m_a c}$. When calculating the constraints on f_{int} , we fix the domain-wall-crossing speed to the typical relative speed from the standard halo model, $\bar{v} = 300 \text{ km s}^{-1}$ (ref.²³). In contrast to the signal duration, the pseudo-magnetic-field signal depends on all the parameters of the ALPs, mass, and ratio between the coupling and symmetry-breaking constants, namely, $\mathcal{B}'_p = \frac{4m_a c^2 \xi}{\mu_B c}$. The data shown in Fig. 4 are obtained using equation (13) by taking $\zeta = 12.6$. The shape of the constrained space is given by the fact that T varies depending on the target m_a and ξ .

Data availability

Source data are provided with this paper. The datasets and analysis code used in the current study are available from the corresponding authors upon reasonable request. Also, see the collaboration website <https://budker.uni-mainz.de/gnome/> where all the available data are displayed.

Code availability

The code used in the current study is available from the corresponding authors upon reasonable request.

References

- Budker, D., Kimball, D., Yashchuk, V. & Zolotarev, M. Nonlinear magneto-optical rotation with frequency-modulated light. *Phys. Rev. A* **65**, 055403 (2002).
- Gawlik, W. et al. Nonlinear magneto-optical rotation with amplitude modulated light. *Appl. Phys. Lett.* **88**, 131108 (2006).
- Allred, J., Lyman, R., Kornack, T. & Romalis, M. V. High-sensitivity atomic magnetometer unaffected by spin-exchange relaxation. *Phys. Rev. Lett.* **89**, 130801 (2002).
- Abbott, B. P. et al. GW150914: first results from the search for binary black hole coalescence with advanced LIGO. *Phys. Rev. D* **93**, 122003 (2016).
- Usman, S. A. et al. The PyCBC search for gravitational waves from compact binary coalescence. *Class. Quantum Grav.* **33**, 215004 (2016).

Acknowledgements

We are grateful to C. Pankow, J. R. Smith, J. Read, M. Givon, R. Folman, W. Gawlik, K. Grimm, G. Łukasiewicz, P. Fierlinger, V. Schultze, T. Sander-Thömmes and H. Müller for insightful discussions. This work was supported by the U.S. National Science Foundation under grants PHY-1707875, PHY-1707803, PHY-1912465 and PHY-1806672; the Swiss National Science Foundation under grant no. 200021 172686; the German Research Foundation (DFG) under grant no. 439720477; the German Federal Ministry of Education and Research (BMBF) within the Quantumtechnologien program (FKZ 13N15064); the European Research Council under the European Union's Horizon 2020 research and innovation programme under grant agreement no. 695405; the Cluster of Excellence PRISMA+; DFG Reinhart Koselleck Project; Simons Foundation; a Fundamental Physics Innovation Award from the Gordon and Betty Moore Foundation; Heising-Simons Foundation; the National Science Centre of Poland within the OPUS program (project no. 2015/19/B/ST2/02129); USTC startup funding; the National Natural Science Foundation of China (grant nos. 62071012 and 61225003); the National Hi-Tech Research and Development (863) Program of China and IBS-R017-D1-2021-a00 of the Republic of Korea. We acknowledge funding provided by the Institute of Physics Belgrade through a grant by the Ministry of Education, Science and Technological Development of the Republic of Serbia.

Author contributions

All the authors have contributed to the publication, being responsible for the construction and operation of the different magnetometers, building the software infrastructure, assuring the quality of the data being taken, and establishing phenomenological motivation. The data-analysis procedure presented here was led by J.A.S. and H.M.-R.,

with collaboration from the other authors. D.F.J.K. coordinated collaboration between the different teams within GNOME. The manuscript was drafted by H.M.-R., J.A.S., A. Wickenbrock and D.F.J.K. It was subject to an internal collaboration-wide review process. All the authors reviewed and approved the final version of the manuscript.

Funding

Open access funding provided by GSI Helmholtzzentrum für Schwerionenforschung GmbH.

Competing interests

The authors declare no competing interests.

Additional information

Extended data is available for this paper at <https://doi.org/10.1038/s41567-021-01393-y>.

Supplementary information The online version contains supplementary material available at <https://doi.org/10.1038/s41567-021-01393-y>.

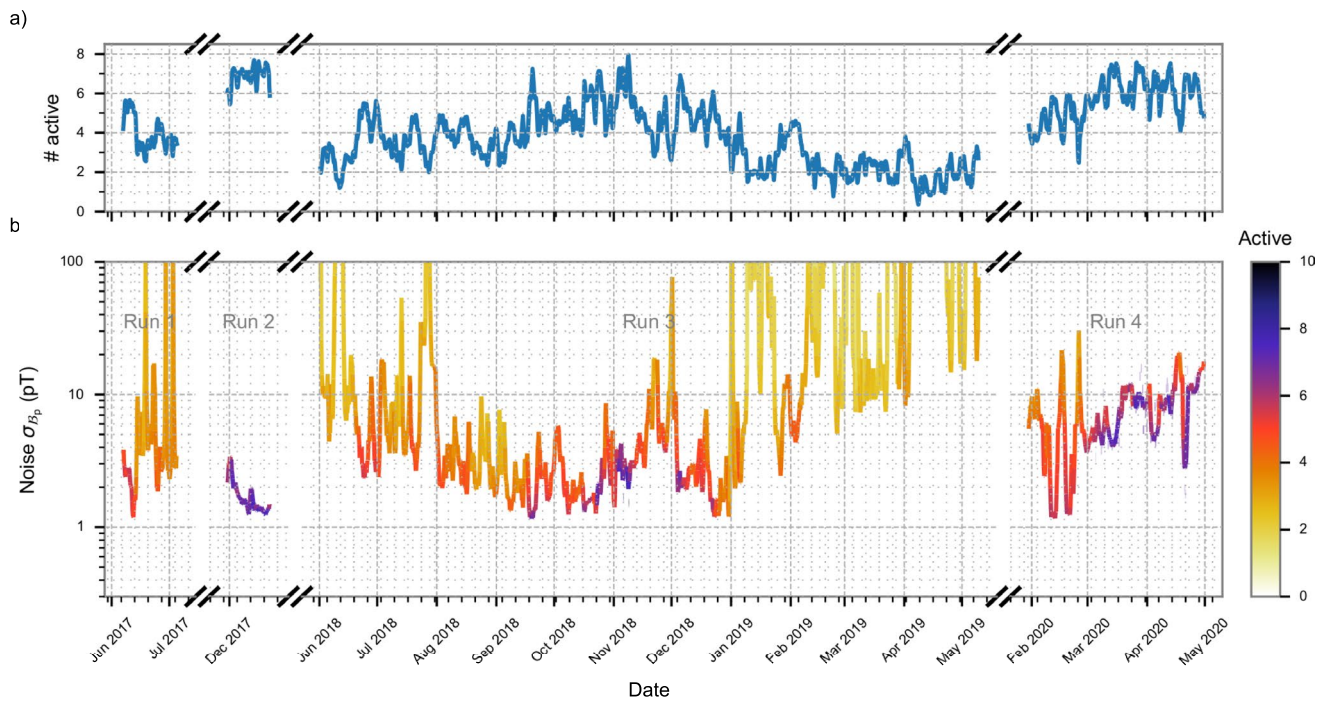
Correspondence and requests for materials should be addressed to Hector Masia-Roig or Joseph A. Smiga.

Peer review information *Nature Physics* thanks Timothy Chupp and the other, anonymous, reviewer(s) for their contribution to the peer review of this work.

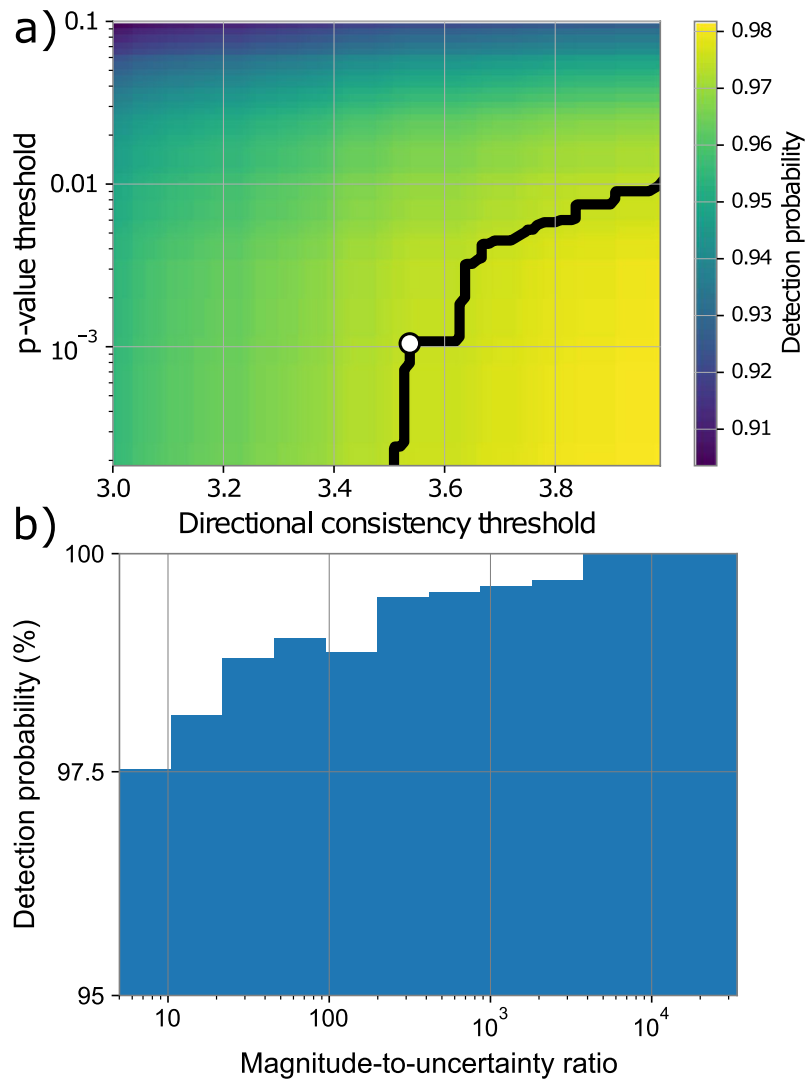
Reprints and permissions information is available at www.nature.com/reprints.

Extended Data Table 1 | Characteristics of the magnetometers active during Science Run 2. The station name, location in longitude and latitude, orientation of the sensitive axis, type of magnetometer (NMOR^{50,51}, rf-driven²⁶, or SERF⁵²), and probed transition are listed. The bandwidth indicates the measured -3 dB point of the magnetometers' frequency response to oscillating magnetic fields. The calibration error takes into account potential temporal variation of the magnetometers' calibration over the course of Science Run 2, and is estimated based on auxiliary measurements. The rightmost column lists the estimated ratio between the effective proton spin polarization and the Landé g-factor for the magnetometer, σ_p/g , which depends on the atomic species and the magnetometry scheme as described in Sec. II of the Supplementary Information. The σ_p/g value is used to relate the measured magnetic field to the signal expected from the interaction of an ALP field with proton spins. The indicated uncertainty describes the range of values from different theoretical calculations²⁹

Station	Location		Orientation		Type	Probed transition	Bandwidth	Cal. Error	σ_p/g
	Longitude	Latitude	Az	Alt					
Beijing	116.1868° E	40.2457° N	+251°	0°	NMOR	¹³³ Cs D2 F=4	115 Hz	20%	-0.39 ^{+0.19} _{-0.00}
Berkeley	122.2570° W	37.8723° N	0°	+90°	NMOR	¹³³ Cs D2 F=4	7 Hz	40%	-0.39 ^{+0.19} _{-0.00}
Daejeon	127.3987° E	36.3909° N	0°	+90°	NMOR	¹³³ Cs D2 F=4	10 Hz	20%	-0.39 ^{+0.19} _{-0.00}
Fribourg	7.1581° E	46.7930° N	+190°	0°	rf-driven	¹³³ Cs D1 F=4	94 Hz	5%	-0.39 ^{+0.19} _{-0.00}
Hayward	122.0539° W	37.6564° N	0°	-90°	NMOR	⁸⁵ Rb D2 F=3	37 Hz	5%	-0.36 ^{+0.05} _{-0.00}
Hefei	117.2526° E	31.8429° N	+90°	0°	SERF	⁸⁵ Rb & ⁸⁷ Rb D1	127 Hz	5%	-0.38 ^{+0.05} _{-0.00}
Krakow	19.9048° E	50.0289° N	+45°	0°	NMOR	⁸⁷ Rb D1 F=2	3 Hz	20%	0.50 ^{+0.00} _{-0.11}
Lewisburg	76.8825° W	40.9557° N	0°	+90°	SERF	⁸⁷ Rb D2	200 Hz	10%	0.70 ^{+0.00} _{-0.15}
Mainz	8.2354° E	49.9915° N	0°	-90°	NMOR	⁸⁷ Rb D2 F=2	99 Hz	2%	0.50 ^{+0.00} _{-0.11}

















Extended Data Fig. 1 | Summary of the GNOME performance during the four Science Runs from 2017 to 2020. The raw magnetometer data are averaged for 20 s and their standard deviation is calculated over a minimum of one and a maximum of two hours segments depending on the availability of continuous data segments. For each binned point, the combined network noise considering the worst case domain-wall crossing direction is evaluated as defined in Ref. ³⁰. (a) One-day rolling average of the number of active sensors. (b) Multi-colored solid line represents the one-day rolling average of the combined network noise and the multi-colored dashes show the noise of the individual sampled segments. The data are preprocessed with the same filters used for the analysis. The number of magnetometers active is indicated by the color of the line and dashes.



Extended Data Fig. 2 | Summary of the true-positive analysis results. (a) shows the probability of detecting a domain-wall-crossing event with randomized parameters (as discussed in the text) as a function of p-value and directional-consistency thresholds. The inserted events have a magnitude-to-uncertainty ratio between 5 and 10. The black line indicates the combination of parameters corresponding to a 97.5% detection probability. The white dot indicates the particular thresholds chosen for the analysis. (b) Shows the mean detection probability reached for different magnitude-to-uncertainty ratios for the chosen thresholds.

The very large n2EDM magnetically shielded room with an exceptional performance for fundamental physics measurements

N. J. Ayres; G. Ban; G. Bison ; K. Bodek; V. Bondar; T. Bouillaud; B. Clement ; E. Chanel; P.-J. Chiu; C. B. Crawford; M. Daum; C. B. Doorenbos; S. Emmenegger; A. Fratangelo ; M. Fertl ; W. C. Griffith ; Z. D. Grujic ; P. G. Harris ; K. Kirch; J. Krempel; B. Lauss ; T. Lefort; O. Naviliat-Cuncic ; D. Pais; F. M. Piegsa; G. Pignol; G. Rauscher; D. Rebreyend; I. Rienäcker; D. Ries; S. Roccia; D. Rozpedzik; W. Saenz-Arevalo; P. Schmidt-Wellenburg; A. Schnabel ; N. Severijns ; B. Shen; M. Staab; K. Svirina ; R. Tavakoli Dinani; J. Thorne; N. Yazdandoost ; J. Zejma ; G. Zsigmond; The nEDM Collaboration



Rev. Sci. Instrum. 93, 095105 (2022)
<https://doi.org/10.1063/5.0101391>



Articles You May Be Interested In

The nEDM experiment at the Paul Scherrer Institute, Switzerland

AIP Conference Proceedings (October 2013)

Degaussing procedure and performance enhancement by low-frequency shaking of a 3-layer magnetically shielded room

Rev. Sci. Instrum. (November 2023)

Publisher's Note: "The very large n2EDM magnetically shielded room with an exceptional performance for fundamental physics measurements" [*Rev. Sci. Instrum.* 93, 095105 (2022)]

Rev Sci Instrum (November 2022)

Challenge us.

What are your needs for periodic signal detection?


Zurich Instruments

Find out more



The very large n2EDM magnetically shielded room with an exceptional performance for fundamental physics measurements

Cite as: Rev. Sci. Instrum. 93, 095105 (2022); doi: 10.1063/5.0101391

Submitted: 31 May 2022 • Accepted: 19 August 2022 •

Published Online: 29 September 2022 • Publisher Error Corrected: 03 October 2022



View Online



Export Citation



CrossMark

N. J. Ayres,¹ G. Ban,² G. Bison,^{3,a)}  K. Bodek,⁴ V. Bondar,¹ T. Bouillaud,⁵ B. Clement,⁵ 
E. Chanel,^{6,b)} P.-J. Chiu,^{3,c)} C. B. Crawford,⁷ M. Daum,³ C. B. Doorenbos,^{3,c)} S. Emmenegger,¹
A. Fratangelo,⁶  M. Fertl,⁸  W. C. Griffith,⁹  Z. D. Grujic,¹⁰  P. G. Harris,⁹  K. Kirch,¹ J. Krempel,¹
B. Lauss,^{3,a)}  T. Lefort,² O. Naviliat-Cuncic,²  D. Pais,³ F. M. Piegsa,⁶ G. Pignol,⁵ G. Rauscher,¹¹
D. Rebreyend,⁵ I. Rienäcker,^{3,c)} D. Ries,¹² S. Rocchia,⁵ D. Rozpedzik,⁴ W. Saenz-Arevalo,²
P. Schmidt-Wellenburg,³ A. Schnabel,¹³  N. Severijns,¹⁴  B. Shen,¹² M. Staab,¹¹ K. Svirina,⁵ 
R. Tavakoli Dinani,¹⁴ J. Thorne,⁶ N. Yazdandoost,¹²  J. Zejma,⁴  and G. Zsigmond,³

The nEDM Collaboration

AFFILIATIONS

¹Institute for Particle Physics and Astrophysics, ETH Zürich, CH-8093 Zurich, Switzerland

²Normandie Université, ENSICAEN, UNICAEN, CNRS/IN2P3, LPC Caen, 14000 Caen, France

³Paul Scherrer Institut, CH-5232 Villigen PSI, Switzerland

⁴Marian Smoluchowski Institute of Physics, Jagiellonian University, 30-348 Cracow, Poland

⁵Université Grenoble Alpes, CNRS, Grenoble INP, LPSC-IN2P3, 38026 Grenoble, France

⁶Laboratory for High Energy Physics and Albert Einstein Center for Fundamental Physics, University of Bern, CH-3012 Bern, Switzerland

⁷Department of Physics and Astronomy, University of Kentucky, Lexington, Kentucky 40506, USA

⁸Institute of Physics, Johannes Gutenberg University, D-55128 Mainz, Germany

⁹Department of Physics and Astronomy, University of Sussex, Falmer, Brighton BN1 9QH, United Kingdom

¹⁰Institute of Physics, Photonics Center, University of Belgrade, 11080 Belgrade, Serbia

¹¹VAC-Vacuumschmelze, Grüner Weg 37, 63450 Hanau, Germany

¹²Department of Chemistry–TRIGA Site, Johannes Gutenberg University Mainz, D-55128 Mainz, Germany

¹³Physikalisch-Technische Bundesanstalt, Abbestr. 2-12, D-10587 Berlin, Germany

¹⁴Instituut voor Kern-en Stralingsfysica, University of Leuven, B-3001 Leuven, Belgium

^{a)} Authors to whom correspondence should be addressed: georg.bison@psi.ch and bernhard.lauss@psi.ch

^{b)} Current address: Institut-Langevin, Grenoble, France.

^{c)} Also at: ETH Zürich, Zurich, Switzerland.

ABSTRACT

We present the magnetically shielded room (MSR) for the n2EDM experiment at the Paul Scherrer Institute, which features an interior cubic volume with each side of length 2.92 m, thus providing an accessible space of 25 m³. The MSR has 87 openings of diameter up to 220 mm for operating the experimental apparatus inside and an intermediate space between the layers for housing sensitive signal processing electronics. The characterization measurements show a remanent magnetic field in the central 1 m³ below 100 pT and a field below 600 pT in the entire inner volume, up to 4 cm to the walls. The quasi-static shielding factor at 0.01 Hz measured with

a sinusoidal 2 μT peak-to-peak signal is about 100 000 in all three spatial directions and increases rapidly with frequency to reach 10^8 above 1 Hz.

© 2022 Author(s). All article content, except where otherwise noted, is licensed under a Creative Commons Attribution (CC BY) license (<http://creativecommons.org/licenses/by/4.0/>). <https://doi.org/10.1063/5.0101391>

I. INTRODUCTION

Magnetic shielding is used when the absolute magnetic field strength at a measurement site must be lower than the Earth's magnetic field or when Earth's or ambient magnetic field fluctuations would limit the measurement accuracy.

A commonly used parameter to describe the performance of shields is their shielding factor. It is defined as the ratio of the magnetic flux density \vec{B} measured at the center of the shield and the magnetic flux density without any shield at the same position.

There are two classes of magnetic shields at room temperature, viz., active and passive, which can be used either individually or in combination.

Passive magnetic shields are built from high-permeability materials with a high "conductivity" for magnetic fields. A shell of such material guides the external magnetic field around an inner volume, thus reducing the static magnetic field as well as the magnetic field variations in that volume.

The shielding effect of a passive shield of one layer is proportional to the layer thickness. For two separated layers, the shielding effect is the product of the shielding factors of the single shells if the distance in between is large enough.^{1,2} Using multiple shield layers hence reduces the amount of expensive high-permeability material required to achieve the same shielding factor, but it increases the volume of the shield walls.

The field guiding effect of high-permeability materials is the dominating shielding effect only for magnetic disturbances with frequencies below about 1 Hz. For these frequencies, the shielding factor approaches a constant value, the quasi-static shielding factor, measured here with an excitation field oscillating at a frequency of $f_{\text{ex}} = 0.01$ Hz. The rapid increase in shielding factor above 1 Hz is caused by the electrical conductivity of the shielding layer, and it can be further increased by an additional "eddy-current" layer. This is usually made of copper or copper-coated aluminum with a thickness of 5–12 mm.

For magnetic field disturbances above 1 kHz, the shielding factor is dominated by the radio-frequency (RF) shielding properties of the shield, which would be perfect for an electrically closed conducting surface, but in practice, it is limited by the size and design of the largest openings. If the openings are designed as electrically conducting pipes in the RF shield, the shielding effect can be maintained for larger frequencies if the length to diameter ratio is appropriately chosen. For most magnetic shields, the incorporated eddy-current shield is designed to simultaneously act as an RF shield.

A static active shield uses a constant current in an arrangement of coils to create a magnetic field that compensates for the surrounding field in the volume of interest. A dynamic active shield is a coil arrangement additionally equipped with one or more reference magnetic field sensors and a feedback control system that adjusts the current source driving the coils to compensate for the detected magnetic field variations, see, e.g., Refs. 3–6. The passive shield described

in this article will be finally surrounded by an active magnetic shielding installation to further enhance the shielding performance at frequencies below 5 Hz.

A common passive shielding material is permalloy, which is a nickel-iron alloy with nickel content above 75%. Various brand names with slightly different material compositions and properties exist. Their high permeability is achieved by a special annealing process in a reductive atmosphere at temperatures above ~ 1050 °C. Another relevant manufacturing factor is the necessary careful handling of the material after annealing. Any mechanical stress acting on the material, for example, during bending, reduces its permeability. Large shields have to be assembled from flat sheets and edge pieces bent before annealing.

The first magnetic shields large enough for human use, used to measure the magnetic field of the heart or brain, were built in the 1960s.^{7–10} Such large shields with two or more magnetic shielding layers and door access, called magnetically shielded rooms (MSRs), are nowadays commercially available from different companies.

Initially, the installation of large MSRs with more than two layers^{11–13} was driven by the need for precise measurements of biomagnetic fields in the human body. For many years, the MSR with the highest shielding factor was "BMSR-2" at the Physikalisch-Technische Bundesanstalt, Berlin, Germany, with originally seven, now eight, magnetic shielding layers, having a shielding factor of 75 000¹⁴ at 0.01 Hz, which was improved to 300 000 after a recent upgrade with an additional layer, which reduced the available shielded volume.¹⁵

Large multilayer shields were also pioneered in the field of fundamental physics measurements already in the 1980s, e.g., Refs. 16–20. One of the first large MSRs dedicated to physics experiments was built at the Oak Ridge National Laboratory,²¹ followed by one at the Technical University of Munich.^{22,23}

The MSR described in this work serves to shield the n2EDM apparatus, aimed at obtaining an improved measurement of the neutron electric dipole moment (nEDM).²⁴ The key requirement for n2EDM, besides a high shielding factor, is the ability to generate a very uniform magnetic field in the central 1 m³ volume of the MSR.²⁵ The MSR design has to meet those requirements while complying with mechanical boundary conditions, such as shield geometry, size, weight, number and size of openings, and accessibility. The factors that affect the field uniformity are the magnetization state of the shielding metal, the homogeneity of a desired field produced by an internal coil system necessary for the nEDM experiment, and disturbances caused by the openings. Since these effects drop off with distance, MSRs with a large inner volume facilitate achieving good magnetic field uniformity, while MSRs with a smaller inner volume make it easier to achieve large shielding factors.² The design presented here is a compromise between these two factors, which optimizes the overall performance of our experiment. In this study, we demonstrate that the realized design achieves both a high shielding factor and a low and homogeneous enough magnetic field, which

results from low disturbances of field uniformity due to the MSR's magnetization state.

II. DESIGN GUIDELINES

The MSR design was driven by the performance needed to reach the sensitivity goals of the n2EDM experiment and by the restrictions imposed by the apparatus to be installed inside the MSR.²⁴ Further constraints were set by the spatial dimensions of the installation area within the experimental hall.

The number and dimensions of the openings were determined by the components of the apparatus. Two very large openings with a diameter of 220 mm are required for the installation of the ultracold neutron guides. As a design principle, all openings are symmetrically mirrored on opposite MSR walls, which helps to suppress first-order gradients.

The doors must provide a minimum of $2 \times 2 \text{ m}^2$ access for the inner chamber to allow for equipment installation, the largest one being the vacuum tank.

The key specified design performance criteria were (1) a quasi-static magnetic shielding factor at 0.01 Hz of 70 000 and (2) a remanent magnetic field in the central 1 m^3 below 500 pT with a field gradient lower than 300 pT/m.

III. CONSTRUCTION OF THE MSR

The MSR was engineered, designed, and constructed by VAC, Germany,²⁶ in an iterative process with input from the nEDM collaboration. The high-permeability materials used in all shielding layers were produced via smelting from the original ores in the furnaces of the VAC Hanau facility.

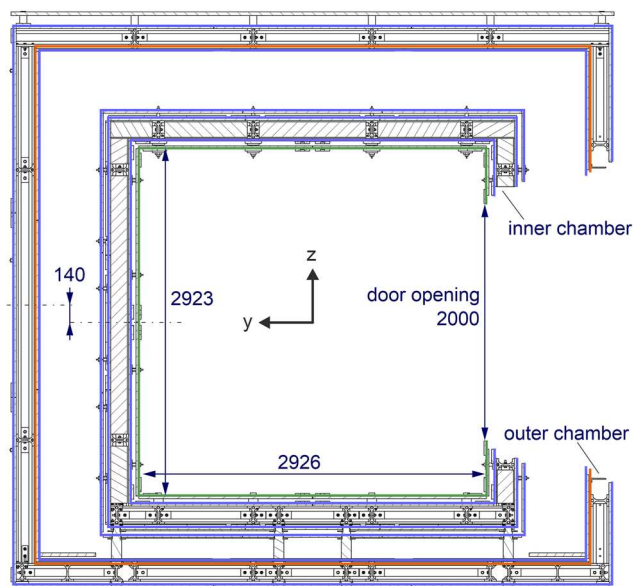


FIG. 1. Vertical cut showing the positioning and dimensions of the inner and outer chambers with shielding layers, with the MUMETALL[®] layers indicated in blue, ULTRAVAC[®] layer in green, and aluminum layer in red, as listed in Table I. All dimensions are in mm.

The MSR design consists of an outer and an inner chamber and an intermediate space as shown in Fig. 1. The inner chamber is centrally placed and separated from the outer chamber horizontally by a distance of $\sim 45 \text{ cm}$ in all directions from the outer wall, with a vertical offset of 14 cm toward the floor. The intermediate space between the chambers shown in Fig. 2 is RF shielded, and it is magnetically shielded with a quasi-static shielding factor of about 65. It is accessible to workers and can be used for housing additional experimental equipment as well as sensitive signal electronics that are too magnetic to be located next to the central n2EDM apparatus. The outer dimensions of the MSR are $5.2 \times 5.2 \text{ m}^2$ horizontally and 4.8 m vertically. The inner chamber is almost perfectly cubic with a side length of 2.92 m, thus featuring 25 m^3 of internal volume for the installation of the experimental apparatus.

The presence of several openings in all six walls of the MSR provides access to and allows the operation of the n2EDM apparatus on the inside. The two neutron guides require the largest openings, with 220 mm diameter, with their centers separated by 550 mm. The diagram in Fig. 2 illustrates this arrangement. Identical openings on opposite sides of the chamber will be used for two pumping lines. Furthermore, nine large openings are symmetrically placed on the roof and the floor (Fig. 3), which will be used for, e.g., laser paths, optical fibers, cables, and sensor tubing. A few openings are present only either in the inner or in the outer chamber. The total number of openings amounts to 87, planned with contingency:

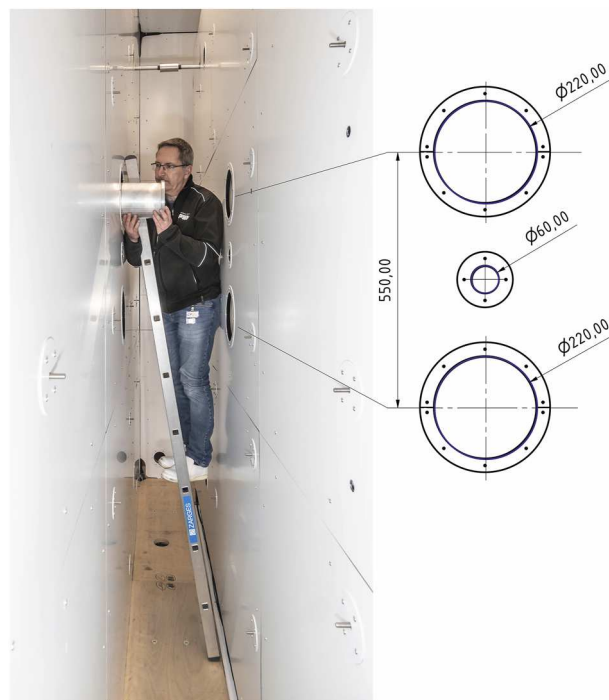


FIG. 2. Intermediate space between the inner and outer chamber. The image shows a test with a vacuum tube passing through one large opening. The diagram to the right depicts the dimensions and separation of the large openings in the center of the wall. All dimensions are in mm.

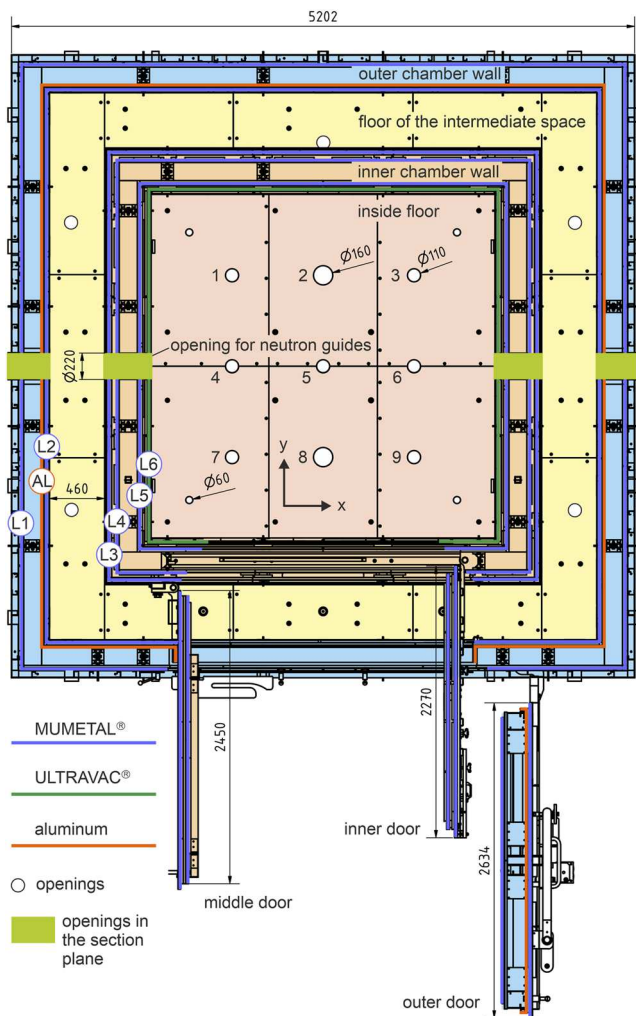


FIG. 3. Vertical section view onto the floor of the MSR. All dimensions are in mm. The layers are as given in Table I. There are two openings with an ID of 160 mm, seven openings with an ID of 110 mm, and four openings with an ID of 60 mm in the central region of the floor (roof). The pattern of openings in the floor is mirrored on the ceiling of the MSR. Some openings are numbered to allow the identification of measurement locations. Additional openings in the outside wall allow for external connections of the equipment that will be installed in the intermediate space.

- 4 with inner diameter (ID) = 220 mm,
- 4 with ID = 160 mm,
- 43 with ID = 110 mm (21 only in outer chamber),
- 2 with ID = 80 mm,
- 26 with ID = 60 mm (8 only in inner chamber), and
- 8 with ID = 55 mm.

Apart from the openings which are in one chamber only, all openings are coaxially passing through the inner and outer chamber walls. Figure 3 provides a sense of the arrangement of the openings in the floor of the MSR.

The assembled MSR, installed in the experimental area south of the ultracold neutron (UCN) source^{27,28} at the Paul Scherrer

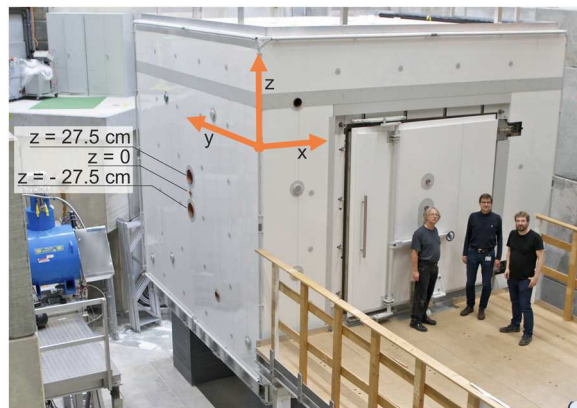


FIG. 4. The MSR installed in the area south of the PSI UCN source. The experiment's coordinate system is indicated. The openings used for the horizontal scans along the x axis (see Fig. 13) are labeled with their z-coordinates.

Institute (PSI), is shown in Fig. 4 from the side of the entrance door and in Fig. 5 from the rear. It is placed on an aluminum frame positioned on four 1364 mm high granite pillars with a 1 × 1 m² base, all placed on top of its own concrete foundation, vibrationally isolated from the surrounding concrete floor of the experimental hall.

The MSR consists of seven shielding layers (Table I), with one aluminum layer acting as eddy-current and RF shield. Of the six soft magnetic layers, the five outer ones are made of MUMETALL (Ni 77%, Cu 4.5%, Mo 3.3%, Fe balance), a soft magnetic NiFe alloy with a Z-shaped hysteresis curve²⁹ and correspondingly high maximum permeability. MUMETALL is a standard alloy used for magnetic shielding. However, the alloy ULTRAVAC 816 (Ni 81%, Mo 6%, Fe balance) employed for the innermost layer was applied here for the first time in MSRs. This novel NiFe alloy has a round-loop-shaped hysteresis curve due to its composition.²⁹ In



FIG. 5. View of the rear side of the MSR. Two of the tubes carrying the excitation coils used to measure the shielding factor are indicated. The openings used for the horizontal scans along the y axis (see Fig. 14) are labeled with their z-coordinates.

06 October 2024 15:46:55

TABLE I. Naming scheme and thicknesses of all shielding layers.

Chamber	Layer	Thickness (mm)	Material
Outer	L1	3.75	MUMETALL
Outer	Al	8.00	Aluminum
Outer	L2	3.75	MUMETALL
Inner	L3	6.75	MUMETALL
Inner	L4	6.75	MUMETALL
Inner	L5	4.5	MUMETALL
Inner	L6	6.0	ULTRAVAC

this alloy, remagnetization processes take place mainly via reversible domain wall motion. This material is characterized by high initial permeability even at saturation levels of magnetic field strength $H < 0.1$ A/m in the shielding layer and by a lower maximum permeability compared to MUMETALL. Due to its round-loop-shaped hysteresis curve, the remanence of ULTRAVAC 816 with a residual magnetic flux density $B_r = 0.2\text{--}0.3$ T is less than half that of MUMETALL ($B_r = 0.45\text{--}0.55$ T). This hysteresis shape allows for an optimal demagnetization of the innermost layer to achieve minimum residual fields. All the walls were manufactured using the VAC proprietary panel technique.

All the additional materials used in the MSR construction were previously checked for magnetic contamination with different specifications. The most stringent restrictions applied to materials in the inner chamber, allowing for a maximum 200 pT signal at 50 mm distance, when scanned in the BMSR-2 magnetic testing facility at PTB, Berlin.¹⁴ Expanded polystyrene placed between the individual layers served as thermal insulation.

Figure 6 shows a photograph of the open MSR with the doors visible on the sides. Information about the dimensions can be found in Fig. 3. All doors are larger than the door openings. The overlap is necessary to reduce the magnetic resistance for the field when passing from the wall to the door. On all the doors, dedicated aluminum plates allow the mechanical contact pressure to be increased. The opening and closing operations are fully manual and can be done in

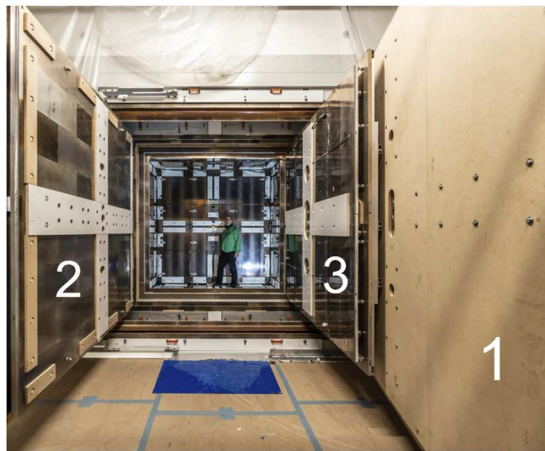


FIG. 6. View of the MSR with all three numbered doors open.

about 20 min. With a weight of 1500 kg, the outermost door needs to be supported by an additional wheel.

IV. SHIELDING FACTOR

The shielding factor was measured using excitation coils on the outer edges of all the outermost walls of the MSR (see Fig. 5). The coil constants K_{ex} of those coils were calibrated with an additional external coil system, which had been mounted on a large frame before the installation of the MSR. The distance of these coils to the later position of the MSR walls was ~ 1.5 m. The excitation coils produced a sinusoidal signal $B_{ex} = K_{ex} I_{ex} \sin(2\pi f_{ex} t)$ with $2 \mu\text{T}$ peak-to-peak amplitude at the MSR center position. A QuSpin[®] magnetometer³⁰ recorded the excitation signal inside the inner chamber. The sensor was installed in the center of the chamber, inside a small calibration coil that generated a sinusoidal reference signal $B_{ref} = K_{ref} I_{ref} \sin(2\pi f_{ref} t)$ with the reference frequency f_{ref} well separated from the excitation frequency f_{ex} . The coil constant K_{ref} of the reference coil was independently measured and was found to agree to better than 1% with the calculated value. During data collection, the magnetometer signal and the monitor signals for the two currents in the coils I_{ex} and I_{ref} were recorded by a multichannel analog-to-digital converter (ADC) synchronized with the function generator that supplied the f_{ex} and f_{ref} signals. The duration of the time series recorded by the ADC for each test frequency was programmed such that it contained an exact integer multiple of the oscillation periods of f_{ex} and f_{ref} . This simplified the data analysis since each oscillation signal was guaranteed to contribute only to a single frequency bin in the Fast Fourier Transformation (FFT) spectrum of the time series. This method minimizes the influence of external disturbances on the final result because any noise in frequency bins other than the ones centered at f_{ex} and f_{ref} is disregarded. The applied FFT algorithm extracted the root-mean-square amplitudes of the signals at the relevant frequencies. Those were the amplitude of the current in the excitation coil I_{ex}^{rms} , the amplitude of the current in the reference coil I_{ref}^{rms} , the magnetometer signal at the excitation frequency B_{ex}^{rms} , and the magnetometer signal at the reference frequency B_{ref}^{rms} . Comparing the measured reference signal to the expected amplitude gave us an in-place correction factor C_{cal} for the calibration of the magnetometer,

$$C_{cal} = \frac{B_{ref}^{rms}}{K_{ref} I_{ref}^{rms}}. \quad (1)$$

The shielding factor F_S is obtained in a similar way by comparing the measured amplitude at the excitation frequency to the value calculated from the coil constant and current,

$$F_S = \frac{K_{ex} I_{ex}^{rms}}{B_{ex}^{rms}} C_{cal} = \frac{K_{ex} I_{ex}^{rms}}{B_{ex}^{rms}} \frac{B_{ref}^{rms}}{K_{ref} I_{ref}^{rms}}. \quad (2)$$

The measurement method results are independent of the magnetometer calibration and dependent only on amplitude measurements and coil constants, which were independently cross-checked. The measurement was performed for the three spatial directions in almost the same way. Only the density of excitation frequencies f_{ex} was increased for the x and z directions in order to investigate the noise above 5 Hz.

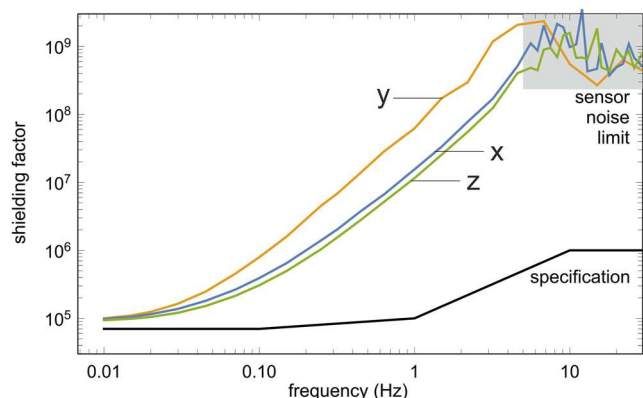


FIG. 7. Dependence of the magnetic shielding factor on frequency measured with a sinusoidal $2\ \mu\text{T}$ peak-to-peak signal for the three spatial dimensions as defined in Fig. 4. The black line shows the specified minimum required shielding factor for the depicted frequency range. The gray shaded area shows the region where the excitation signal is reduced to the level of the sensor noise due to the shield.

The measured frequency-dependent shielding factor is shown in Fig. 7. At frequencies above 5 Hz, the shielding factor is so large that the sensor reaches its noise limit. Additionally, the measurement above 5 Hz shows interference from the PSI magnetic environment, which leads to fluctuating results, with a minimum shielding factor of 10^8 . The specified performance is surpassed at all the measured frequencies.

The quasi-static shielding factor at 0.01 Hz, which is the most important for the n2EDM experiment, is $\sim 100\ 000$ in all the spatial directions: $101\ 300 \pm 500$ in the x direction, $101\ 000 \pm 1000$ in the y direction, and $94\ 900 \pm 1400$ in the z direction.

Figure 7 also shows that for frequencies between 0.03 and 5 Hz, the shielding factor in the y direction is consistently larger than in the other directions. This behavior is expected since the eddy current induced by a magnetic disturbance in the y direction is not crossing the door contacts, which are, in terms of electric conductivity, the weakest link in the eddy-current shield. A comparison of the performance in the x and y directions thus gives an estimate of the losses caused by the imperfect magnetic and electric contacts of the doors.

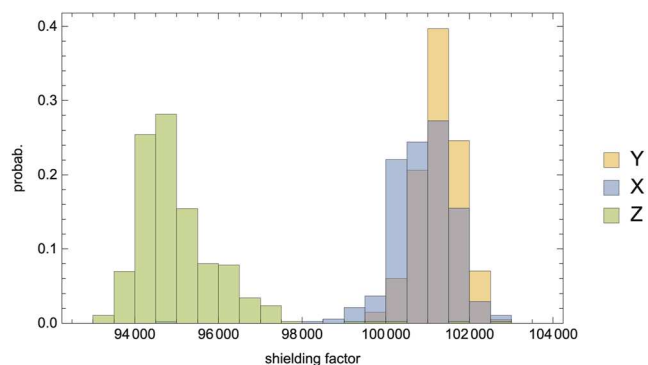


FIG. 8. Histogram of all the measurements of the quasi-static shielding factor at 0.01 Hz in the three spatial directions.

A histogram of the individual shielding factor measurements at 0.01 Hz is shown in Fig. 8. The quasi-static shielding factor in the z direction is slightly smaller than in the other directions. This is caused by the smaller distance and the offset between the inner and outer chambers in the vertical direction. The spread is likely due to a combination of the statistical uncertainty of the measurement and the changing magnetic environments over the course of the measurements, which also causes a small change in the shield response.

V. EQUILIBRATION OF MSR LAYERS

In order to minimize the remanent field in the inner chamber, all MSR walls need to be demagnetized,³¹ or more precisely “equilibrated,”³² to achieve the most energetically favorable state. This process is also sometimes colloquially referred to as “degaussing.” Therefore, four coils per spatial direction are installed with cables along the edges of every wall of layers 1–6 individually, as sketched in Fig. 9, similar to what is shown in Fig. 2 of Ref. 32, thus allowing the driving of a magnetic flux independently in the three spatial dimensions. Such an arrangement was first used in Ref. 32 for the “ZUSE” chamber at PTB, Berlin, and was also used in Ref. 33. Here, layer 6 has additional coils distributed over the width of the walls and the door to further improve the equilibration procedure for the innermost layer.³⁴

A reproducible and good equilibration result is obtained with a sequential equilibration procedure driving an oscillating magnetic

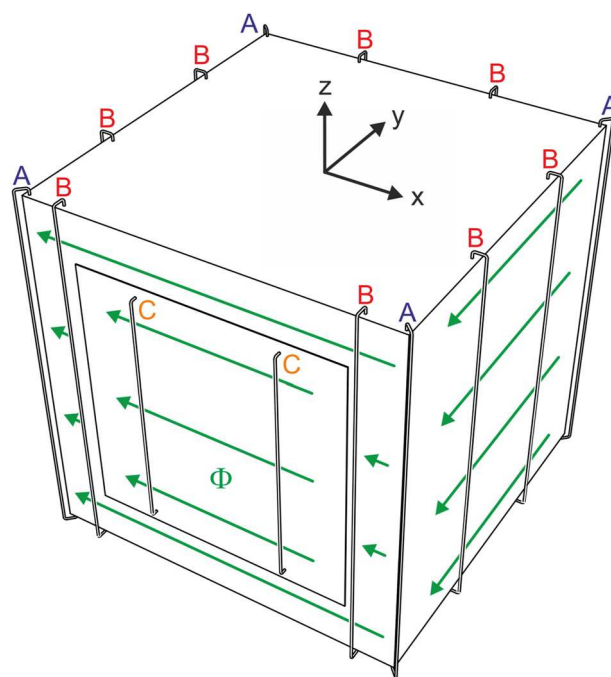


FIG. 9. Arrangement of the equilibration coils in the z direction on one MSR layer drawn as a cube box. Label A: corner coils on all layers; label B: additional coils only on layer 6; label C: additional smaller coils only on the layer 6 door. The green arrows indicate the direction of the magnetic flux Φ produced by a current through the indicated coils.

flux, with the amplitude first increasing, then being slowly ramped down to zero. All six layers are subsequently equilibrated starting at the outermost layer. In the initial characterization measurements, a 5 Hz sinusoidal signal was used to drive the current. A standard equilibration procedure took about 5 h and was repeated after every opening of the MSR doors. A more detailed description of the final optimized equilibration procedure will be part of a forthcoming publication.

VI. REMANENT MAGNETIC FIELD

A. Measurement procedure

For this investigation, the magnetic field in the inner chamber was measured with a low-noise Bartington MAG03 three-axis fluxgate³⁵ located in a plexiglass tube installed between opposite openings in the MSR walls. Position scans were recorded by sliding the fluxgate along the axes of this tube using a pushrod. The rod has pin holes every 100 mm that were used to reproducibly fix the position along the tube as well as the rotation of the fluxgate around the axis of the tube. The front view of this setup is depicted in Fig. 10. The accessible measurement positions range from -60 to $+140$ cm relative to the center of the chamber. At 140 cm, the fluxgate sensors are as close as 7 cm to the ULTRAVAC surface of the innermost shielding layer.

A typical measurement consisted of integrating the sensor signals for 3 s and then rotating the fluxgate by 90° . This procedure was repeated until all four orientations (0° , 90° , 180° , 270°) of the fluxgate were recorded before proceeding to the next position along the tube. The rotation allowed the compensation of the sensor offsets in the two transverse directions since the contribution of the local magnetic field to the sensor reading must invert when the sensors are rotated by 180° .

When scanning in the vertical direction, the tube could be installed from the outside so that the MSR doors did not have to be opened between measurements and the equilibration procedure did not have to be repeated. This means the magnetic configuration

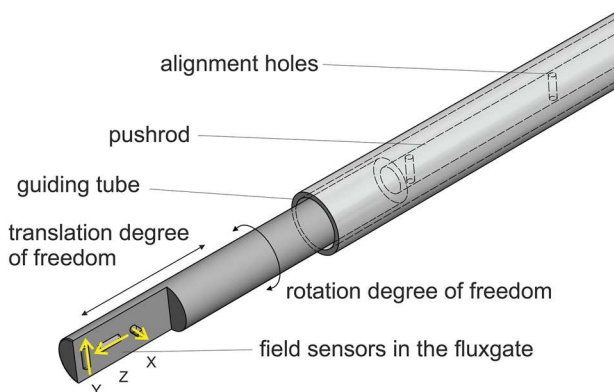


FIG. 10. Scheme of the fluxgate sensor in the guiding tube. The rotation degree of freedom is used to determine the DC-offset for absolute field measurements for the transverse sensors (x and y). A pin through the holes in the pushrod was used to fix both the rotation and translation. The directions of the x , y , and z component sensors are indicated by arrows.

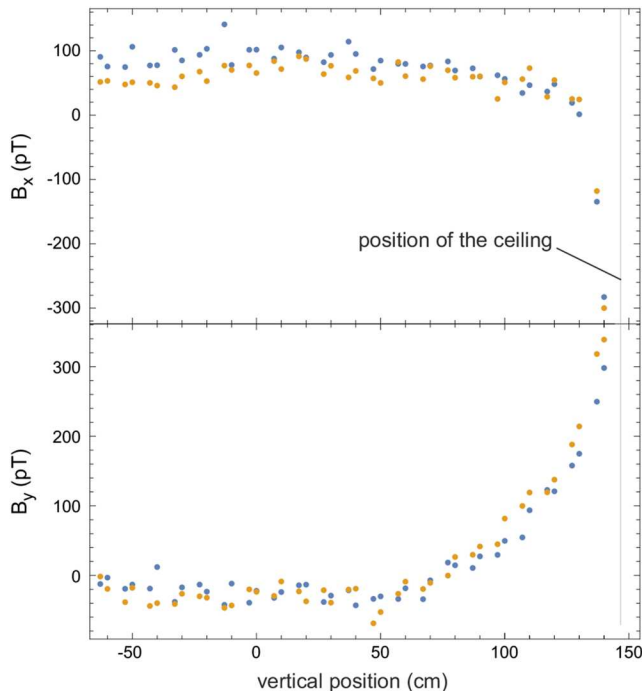


FIG. 11. Results from two vertical scans of the remanent magnetic field inside the MSR along the same axis. The recordings were taken four days apart, with the blue dots indicating the first measurement. The magnetic configuration of the MSR was not changed during this time.

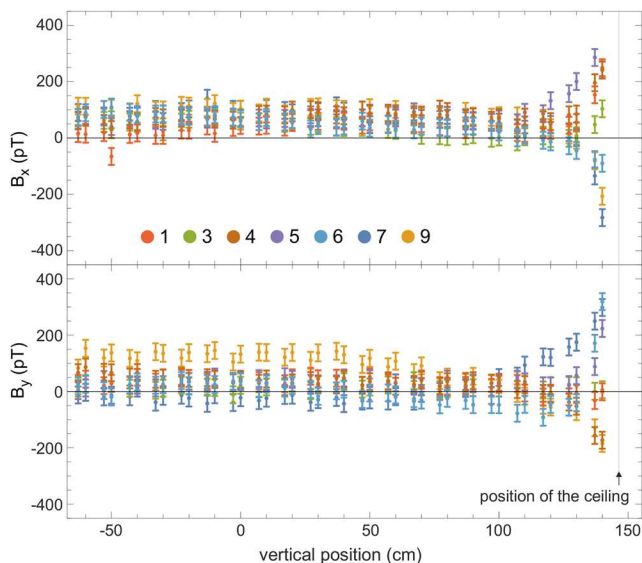


FIG. 12. All B_x and B_y field values measured in the different vertical scans. The remanent field increases to values of about 300 pT, only when approaching the ULTRAVAC wall of the inner chamber. Each color represents a vertical B_x and B_y scan through one of the openings in the roof. The numbers next to the colored filled circles reference the position of the openings as depicted in Fig. 3.

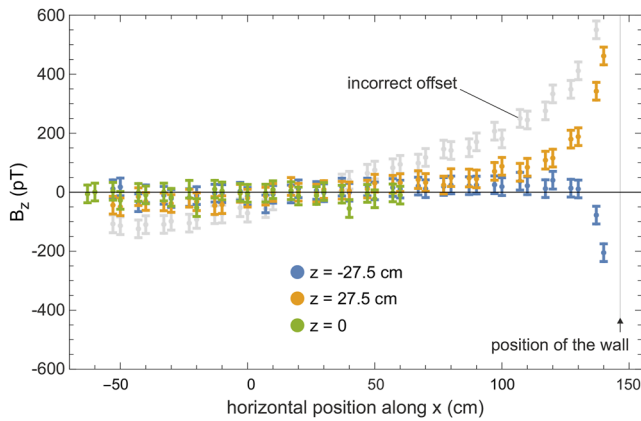


FIG. 13. B_z field values measured in a horizontal scan along x at the position of the three large openings shown in the diagram of Fig. 2, at the center of the MSR ($z = 0$) and above (27.5 cm) and below (−27.5 cm) the center. The remanent field increases to values of about 500 pT only when approaching the ULTRAVAC wall of the inner chamber. One measurement series depicted by the gray dots displays significantly larger remanent field values. This was later found to be due to an equilibration procedure with an incorrect offset. The gray color shows the measurement with incorrect offset of the equilibration procedure. The gray line indicates the position of the wall, i.e., layer 6.

of the MSR was unchanged except for possible relaxation processes in the wall material. All other measurements were performed after an equilibration of all shield layers.

B. Results

In order to assess the repeatability of the magnetic field measurements, we repeated one vertical scan after four days. Figure 11 compares the offset-corrected measurements from both these scans. The root mean square of the differences between the two measurements is 21 and 24 pT for the x and y directions, respectively. The total deviation is close to the expected statistical uncertainty but also shows a small systematic component, especially in B_x , where the

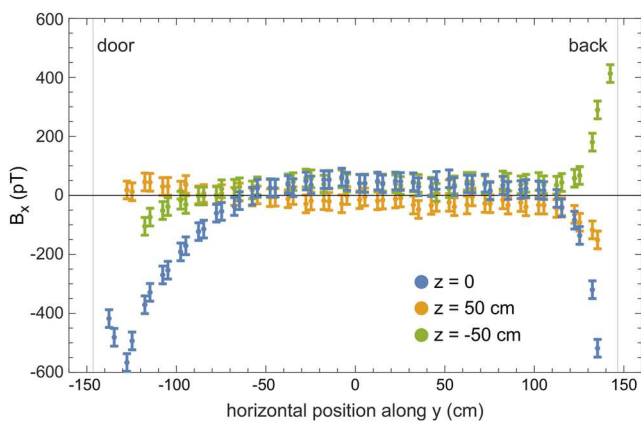


FIG. 14. B_x field values measured in a scan along the y axis at the position of three openings in the door at the center ($z = 0$) and above (50 cm) and below (−50 cm) the center. The gray lines indicate the position of the door and the back wall.

mean difference between all points of the scans amounts to 18 pT. Combining these two deviations, we conservatively estimate the total measurement error to be 30 pT, which is reflected by the error bars shown in Figs. 12–14.

All measured values for B_x and B_y taken during vertical scans in different positions are shown in Fig. 12, which shows the results obtained after a single equilibration procedure. Figure 13 shows the B_z field component, which was measured in a horizontal scan after equilibration performed on different days since the doors had to be opened in order to install the tube for the fluxgate.

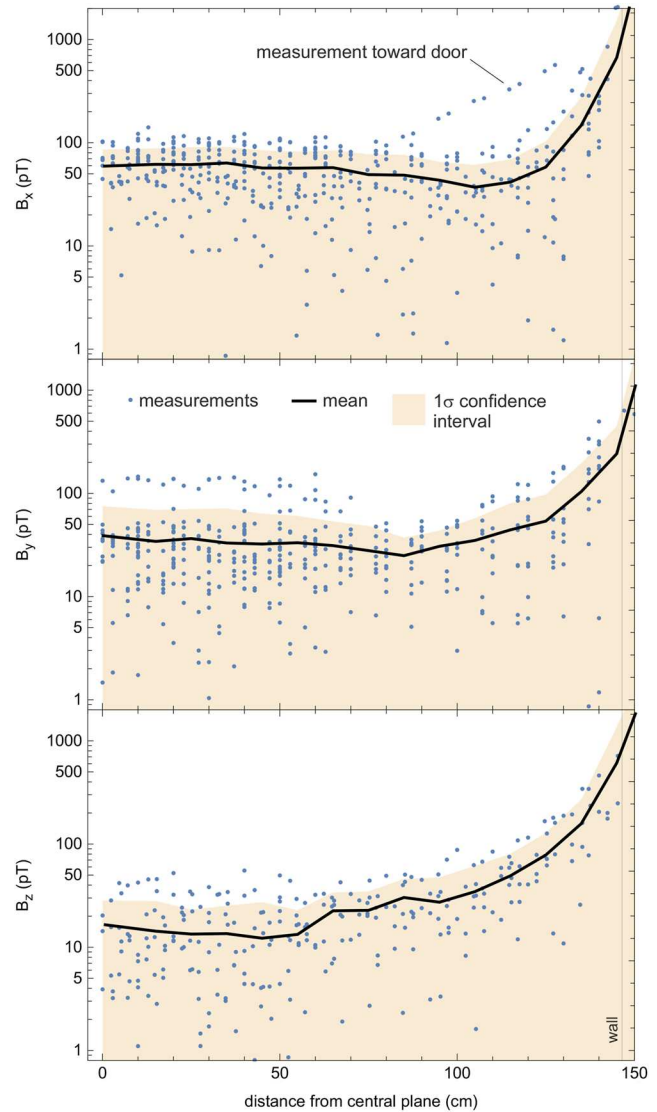


FIG. 15. Summary of all measured scans of the three field components B_x , B_y , and B_z performed after equilibration of the MSR. The magnitude of the magnetic field components is shown as a function of distance to a central plane perpendicular to the scan direction. All points in the central cubic meter thus fall into the region with distance smaller than 50 cm. The black lines give the mean values with the 1σ uncertainties displayed as the shaded area.

The largest deviation from ideal behavior was found in a horizontal scan along the y direction. The corresponding measurements of B_x are shown in Fig. 14. Here, the mechanical scan range was increased to reach from wall to wall. The measurements show the expected effect that repeating an equilibration leads to the strongest magnetic field uncertainties close to the wall and especially close to the door.

Already with a non-optimized equilibration procedure, we find a large volume, ranging from -76 to 76 cm in x and y , and -60 to 140 cm in z , in which all the measured field values for B_x , B_y , and B_z are below 150 pT, originally specified to be below 500 pT. Positions at lower x , y , and z values could not be measured with the described setup. The gradients in the central 1 m^3 were significantly smaller than originally specified (300 pT/m, see Sec. II). In this volume, the gradients are within the statistical uncertainty of the fluxgate sensors used, which is estimated to correspond to 60 pT/m at 1σ confidence level.

The remanent magnetic field measurements along the three spatial directions are summarized in Fig. 15 relative to their distance from the center of the inner chamber. This distance is computed relative to a plane through the center and perpendicular to the scan direction. Hence, all the measured points in the central 1 m^3 volume are at a distance <50 cm. The ULTRAVAC material of the layer 6 wall is at a distance of 146.5 cm. One can see that all 1σ confidence intervals in the central 8 m^3 (positions <100 cm) are below 100 pT. For the z component of the magnetic field also, which is the most important for n2EDM, the maximum deviation is below 100 pT in the central 8 m^3 . Only when approaching the wall, the remanent field values slowly increase to ~ 500 pT at a distance of about 4 cm from the ULTRAVAC.

VII. SUMMARY

We constructed a unique magnetically shielded room with excellent performance, providing 25 m^3 of usable shielded volume for the n2EDM apparatus, which will search for the neutron electric dipole moment with a baseline sensitivity of $10^{-27}e$ cm. This MSR provides the largest ultralow magnetic field environment in the world despite its numerous openings allowing for access and throughgoing connections.

Such a magnetic performance is achieved using five MUMET-ALL layers, one ULTRAVAC layer, and one aluminum layer. A quasi-static shielding factor at 0.01 Hz of $\sim 100\,000$ was measured in all three spatial directions. The shielding factor rapidly increases with frequency and already reaches 10^8 for frequencies above 3 Hz.

After applying the equilibration procedure, the MSR was found to provide an exceptionally low magnetic field environment across a large volume. As the other magnetic field components, in particular the most important field component B_z (vertical) shows remanent magnetic field values below 100 pT in the central 8 m^3 .

ACKNOWLEDGMENTS

We acknowledge the dedicated work of Lela Bauer, Markus Hein, and Michael Wüst, comprising the group for magnetically shielded rooms in the company VAC-Vacuumschmelze, Hanau; the support of Michael Meier in the planning and construction stages;

support of Thomas Stapf in the design and installation stages; and the technical support provided by Luke Noorda. We appreciate the help provided by the PSI support groups in the installation stage. Financial support by the Swiss National Science Foundation R'EQUIP under Grant No. 139140, by PSI, and by the Emil-Berthel-Fonds is acknowledged. The material scans inside BMSR-2 were supported by the Core Facility "Metrology of Ultra-Low Magnetic Fields" at Physikalisch-Technische Bundesanstalt, which received funding from the Deutsche Forschungsgemeinschaft-DFG (funding codes: Grant Nos. DFG KO 5321/3-1 and TR 408/11-1). Support by the Swiss National Science Foundation Project Nos. 200020-188700 (PSI), 200020-163413 (PSI), 200011-178951 (PSI), 172626 (PSI), 169596 (PSI), 200021-181996 (Bern), 200441 (ETH), FLARE 20FL21-186179, and 20FL20-201473 is gratefully acknowledged. The LPC Caen and the LPSC Grenoble acknowledge the support of the French Agence Nationale de la Recherche (ANR) under Reference No. ANR-14-CE33-0007 and the ERC Project No. 716651-NEDM. University of Bern acknowledges the support received via the European Research Council under the ERC Grant Agreement No. 715031-Beam-EDM. The Polish collaborators wish to acknowledge support from the National Science Center, Poland, under Grant Nos. 2018/30/M/ST2/00319 and 2020/37/B/ST2/02349. Support by the Cluster of Excellence "Precision Physics, Fundamental Interactions, and Structure of Matter" (Grant No. PRISMA+EXC 2118/1) funded by the German Research Foundation (DFG) within the German Excellence Strategy (Project No. 39083149) is acknowledged. Collaborators at the University of Sussex wish to acknowledge support from the School of Mathematical and Physical Sciences, as well as from the STFC under Grant No. ST/S000798/1. This work was partly supported by the Fund for Scientific Research Flanders (FWO), and Project No. GOA/2010/10 of the KU Leuven. Researchers from the University of Belgrade acknowledge institutional funding provided by the Institute of Physics Belgrade through a grant by the Ministry of Education, Science and Technological Development of the Republic of Serbia.

AUTHOR DECLARATIONS

Conflict of Interest

The authors have no conflicts to disclose.

Author Contributions

N. J. Ayres: Writing – review & editing (equal). **G. Ban:** Writing – review & editing (equal). **G. Bison:** Writing – review & editing (equal). **K. Bodek:** Writing – review & editing (equal). **V. Bondar:** Writing – review & editing (equal). **T. Bouillaud:** Writing – review & editing (equal). **B. Clement:** Writing – review & editing (equal). **E. Chanel:** Writing – review & editing (equal). **P.-J. Chiu:** Writing – review & editing (equal). **C. B. Crawford:** Writing – review & editing (equal). **M. Daum:** Writing – review & editing (equal). **C. B. Doorenbos:** Writing – review & editing (equal). **S. Emmenegger:** Writing – review & editing (equal). **A. Fratangelo:** Writing – review & editing (equal). **M. Fertl:** Writing – review & editing (equal). **W. C. Griffith:** Writing – review & editing (equal). **Z. D. Grujic:** Writing – review & editing (equal). **P. G. Harris:** Writing – review & editing (equal). **K. Kirch:** Writing – review & editing (equal). **J. Krempel:**

Writing – review & editing (equal). **B. Lauss**: Writing – review & editing (equal). **T. Lefort**: Writing – review & editing (equal). **O. Naviliat-Cuncic**: Writing – review & editing (equal). **D. Pais**: Writing – review & editing (equal). **F. M. Piegsa**: Writing – review & editing (equal). **G. Pignol**: Writing – review & editing (equal). **G. Rauscher**: Writing – review & editing (equal). **D. Rebreyend**: Writing – review & editing (equal). **I. Rienäcker**: Writing – review & editing (equal). **D. Ries**: Writing – review & editing (equal). **S. Roccia**: Writing – review & editing (equal). **D. Rozpedzik**: Writing – review & editing (equal). **W. Saenz-Arevalo**: Writing – review & editing (equal). **P. Schmidt-Wellenburg**: Writing – review & editing (equal). **A. Schnabel**: Writing – review & editing (equal). **N. Severijns**: Writing – review & editing (equal). **M. Staab**: Writing – review & editing (equal). **K. Svirina**: Writing – review & editing (equal). **R. Tavakoli Dinani**: Writing – review & editing (equal). **J. Thorne**: Writing – review & editing (equal). **N. Yazdandoost**: Writing – review & editing (equal). **J. Zejma**: Writing – review & editing (equal). **G. Zsigmond**: Writing – review & editing (equal).

DATA AVAILABILITY

The data that support the findings of this study are available on request from the corresponding authors. The datasets generated and/or analyzed during the current study are not publicly available.

REFERENCES

- 1 D. Dubbers, “Simple formula for multiple mu-metal shields,” *Nucl. Instrum. Methods Phys. Res., Sect. A* **243**, 511–517 (1986).
- 2 R. Boll, *Weichmagnetische Werkstoffe: Einfuehrung in den Magnetismus. VAC Werkstoffe und ihre Anwendungen*, 4th ed. (Vacuumschmelze GmbH, 1990).
- 3 R. L. Driscoll and P. T. Olsen, “Compensation of Earth’s field variations by field controlled rubidium oscillator,” *Rev. Sci. Instrum.* **42**, 1427–1431 (1971).
- 4 H. J. M. ter Brake, H. J. Wieringa, and H. Rogalla, “Improvement of the performance of a mu-metal magnetically shielded room by means of active compensation (biomagnetic applications),” *Meas. Sci. Technol.* **2**, 596–601 (1991).
- 5 S. Afach *et al.*, “Dynamic stabilization of the magnetic field surrounding the neutron electric dipole moment spectrometer at the Paul Scherrer Institute,” *J. Appl. Phys.* **116**, 084510 (2014).
- 6 M. Rawlik, A. Eggenberger, J. Krempel, C. Crawford, K. Kirch, F. M. Piegsa, and G. Quémener, “A simple method of coil design,” *Am. J. Phys.* **86**, 602–608 (2018).
- 7 D. Cohen, “Enhancement of ferromagnetic shielding against low-frequency magnetic fields,” *Appl. Phys. Lett.* **10**, 67–69 (1967).
- 8 D. Cohen, “Magnetic fields around the torso: Production by electrical activity of the human heart,” *Science* **156**, 652–654 (1967).
- 9 D. Cohen, “Magnetoencephalography: Evidence of magnetic fields produced by alpha-rhythm currents,” *Science* **161**, 784–786 (1968).
- 10 D. Cohen, E. A. Edelsack, and J. E. Zimmerman, “Magnetocardiograms taken inside a shielded room with a superconducting point-contact magnetometer,” *Appl. Phys. Lett.* **16**, 278–280 (1970).
- 11 A. Mager, “The Berlin magnetically shielded room (BMSR), section A: Design and construction,” in *Proceedings of the Third International Workshop* (De Gruyter, Berlin, 1981), pp. 51–78.
- 12 V. Kelha, J. Pukki, R. Peltonen, A. Penttinen, R. Ilmoniemi, and J. Heino, “Design, construction, and performance of a large-volume magnetic shield,” *IEEE Trans. Magn.* **18**, 260–270 (1982).
- 13 G. Kajiwara, K. Harakawa, H. Ogata, and H. Kado, “High-performance magnetically shielded room,” *IEEE Trans. Magn.* **32**, 2582–2585 (1996).
- 14 J. Bork, H. Hahlbohm, R. Klein, and A. Schnabel, “The 8-layered magnetically shielded room of the PTB,” in *Biomag 2000: Proceedings of the 12th International Conference on Biomagnetism* (2000), pp. 970–973.
- 15 T. Liu, A. Schnabel, J. Voigt, W. Kilian, Z. Sun, L. Li, and L. Trahms, “A built-in coil system attached to the inside walls of a magnetically shielded room for generating an ultra-high magnetic field homogeneity,” *Rev. Sci. Instrum.* **92**, 024709 (2021).
- 16 C. E. Loving and P. G. H. Sandars, “On the feasibility of an atomic-beam resonance experiment sensitive to the nuclear-spin-dependent weak neutral current interaction,” *J. Phys. B: At. Mol. Phys.* **10**, 2755–2766 (1977).
- 17 I. S. Altarev, Y. V. Borisov, N. V. Borovikova, A. B. Brandin, A. I. Egorov, V. F. Ezhov, S. N. Ivanov, V. M. Lobashev, V. A. Nazarenko, V. L. Ryabov, A. P. Serebrov, and R. R. Taldaev, “A new upper limit on the electric dipole moment of the neutron,” *Phys. Lett. B* **102**, 13–16 (1981).
- 18 J. M. Pendlebury, K. F. Smith, R. Golub, J. Byrne, T. J. L. McComb, T. J. Sumner, S. M. Burnett, A. R. Taylor, B. Heckel, N. F. Ramsey, K. Green, J. Morse, A. I. Kilvington, C. A. Baker, S. A. Clark, W. Mampe, P. Ageron, and P. C. Miranda, “Search for a neutron electric dipole moment,” *Phys. Lett. B* **136**, 327–330 (1984).
- 19 S. K. Lamoreaux, J. P. Jacobs, B. R. Heckel, F. J. Raab, and N. Fortson, “New constraints on time-reversal asymmetry from a search for a permanent electric dipole moment of Hg199,” *Phys. Rev. Lett.* **59**, 2275–2278 (1987).
- 20 K. F. Smith, N. Crampin, J. M. Pendlebury, D. J. Richardson, D. Shiers, K. Green, A. I. Kilvington, J. Moir, H. B. Prosper, D. Thompson, N. F. Ramsey, B. R. Heckel, S. K. Lamoreaux, P. Ageron, W. Mampe, and A. Steyerl, “A search for the electric dipole moment of the neutron,” *Phys. Lett. B* **234**, 191–196 (1990).
- 21 H. Soltner, U. Pabst, M. Butzek, M. Ohl, T. Kozielski, M. Monkenbusch, D. Sokol, L. Maltin, E. Lindgren, S. Koch, and D. Fugate, “Design, construction, and performance of a magnetically shielded room for a neutron spin echo spectrometer,” *Nucl. Instrum. Methods Phys. Res., Sect. A* **644**, 40–47 (2011).
- 22 I. Altarev, E. Babcock, D. Beck, M. Burghoff, S. Chesnevskaya, T. Chupp, S. Degenkolb, I. Fan, P. Fierlinger, A. Frei, E. Gutmiedl, S. Knappe-Grüneberg, F. Kuchler, T. Lauer, P. Link, T. Lins, M. Marino, J. McAndrew, B. Niessen, S. Paul, G. Petzoldt, U. Schlöpfer, A. Schnabel, S. Sharma, J. Singh, R. Stoepler, S. Stuiber, M. Sturm, B. Taubenheim, L. Trahms, J. Voigt, and T. Zechlau, “A magnetically shielded room with ultra low residual field and gradient,” *Rev. Sci. Instrum.* **85**, 075106 (2014); [arXiv:1403.6467](https://arxiv.org/abs/1403.6467) [physics.ins-det].
- 23 I. Altarev, M. Bales, D. H. Beck, T. Chupp, K. Fierlinger, P. Fierlinger, F. Kuchler, T. Lins, M. G. Marino, B. Niessen, G. Petzoldt, U. Schlöpfer, A. Schnabel, J. T. Singh, R. Stoepler, S. Stuiber, M. Sturm, B. Taubenheim, and J. Voigt, “A large-scale magnetic shield with 106 damping at millihertz frequencies,” *J. Appl. Phys.* **117**, 183903 (2015).
- 24 N. J. Ayres *et al.*, “The design of the n2EDM experiment,” *Eur. Phys. J. C* **81**, 512 (2021).
- 25 C. Abel, N. J. Ayres, T. Baker, G. Ban, G. Bison, K. Bodek, V. Bondar, C. B. Crawford, P.-J. Chiu, E. Chanel, Z. Chowdhuri, M. Daum, B. Dechenaux, S. Emmenegger, L. Ferraris-Bouchez, P. Flaux, P. Geltenbort, K. Green, W. C. Griffith, M. van der Grinten, P. G. Harris, R. Henneck, N. Hild, P. Iaydjiev, S. N. Ivanov, M. Kasprzak, Y. Kermaidic, K. Kirch, H.-C. Koch, S. Komposch, P. A. Koss, A. Kozela, J. Krempel, B. Lauss, T. Lefort, Y. Lemièrre, A. Leredde, P. Mohanmurthy, D. Pais, F. M. Piegsa, G. Pignol, G. Quemener, M. Rawlik, D. Rebreyend, D. Ries, S. Roccia, D. Rozpedzik, P. Schmidt-Wellenburg, A. Schnabel, N. Severijns, R. Viro, A. Weis, E. Wursten, G. Wyszynski, J. Zejma, and G. Zsigmond, “Magnetic-field uniformity in neutron electric-dipole-moment experiments,” *Phys. Rev. A* **99**, 042112 (2019).
- 26 VACUUMSCHMELZE GmbH & Co. KG, Gruener Weg 37, D-63450 Hanau, Germany.
- 27 G. Bison, B. Blau, M. Daum, L. Göttl, R. Henneck, K. Kirch, B. Lauss, D. Ries, P. Schmidt-Wellenburg, and G. Zsigmond, “Neutron optics of the PSI ultracold-neutron source: Characterization and simulation,” *Eur. Phys. J. A* **56**, 33 (2020).
- 28 B. Lauss and B. Blau, “UCN, the ultracold neutron source—Neutrons for particle physics,” *SciPost Phys. Proc.* **5**, 4 (2021).

- ²⁹M. Demper and N. Volbers, “Nickel-iron alloys (NiFe): An overview of the NiFe alloys for sensor applications,” in *UK Magnetics Society MagNews* (2015).
- ³⁰QuSpin, Inc. 331 South 104th Street, Suite 130, Louisville, CO 80027, USA.
- ³¹F. Thiel, A. Schnabel, S. Knappe-Grüneberg, D. Stollfuss, and M. Burghoff, “Demagnetization of magnetically shielded rooms,” *Rev. Sci. Instrum.* **78**, 035106 (2007).
- ³²J. Voigt, S. Knappe-Grüneberg, A. Schnabel, R. Körber, and M. Burghoff, “Measures to reduce the residual field and field gradient inside a magnetically shielded room by a factor of more than 10,” *Metrol. Meas. Syst.* **20**, 239–248 (2013).
- ³³I. Altarev, P. Fierlinger, T. Lins, M. G. Marino, B. Nießen, G. Petzoldt, M. Reisner, S. Stuiber, M. Sturm, J. Taggart Singh, B. Taubenheim, H. K. Rohrer, and U. Schlöpfer, “Minimizing magnetic fields for precision experiments,” *J. Appl. Phys.* **117**, 233903 (2015).
- ³⁴Z. Sun, P. Fierlinger, J. Han, L. Li, T. Liu, A. Schnabel, S. Stuiber, and J. Voigt, “Limits of low magnetic field environments in magnetic shields,” *IEEE Trans. Ind. Electron.* **68**, 5385–5395 (2021).
- ³⁵Bartington Instruments Ltd, Thorney Leys Park, Witney OX28 4GE, United Kingdom, Bartington.com.

Mapping of the magnetic field to correct systematic effects in a neutron electric dipole moment experiment

C. Abel,¹ N. J. Ayres,^{1,2,*} G. Ban,³ G. Bison,⁴ K. Bodek,⁵ V. Bondar,^{2,4,6} E. Chancel,⁷ P.-J. Chiu,^{2,4} B. Clément,⁸ C. B. Crawford,⁹ M. Daum,⁴ S. Emmenegger,² L. Ferraris-Bouchez,^{8,†} M. Fertl,¹⁰ P. Flaux,³ A. Fratangelo,⁷ W. C. Griffith,¹ Z. D. Grujić,^{11,12} P. G. Harris,¹ L. Hayen,^{6,‡} N. Hild,^{2,4} M. Kasprzak,^{4,6,11} K. Kirch,^{2,4} P. Knowles,¹¹ H.-C. Koch,^{4,10,11} P. A. Koss,^{6,§} A. Kozela,¹³ J. Krempel,² B. Lauss,⁴ T. Lefort,³ Y. Lemièrè,³ P. Mohanmurthy,^{2,4} O. Naviliat-Cuncic,³ D. Pais,^{2,4} F. M. Piegsa,⁷ G. Pignol,⁸ P. N. Prashanth,^{4,6} G. Quémener,³ M. Rawlik,^{2,¶} D. Ries,¹⁴ D. Rebreyend,⁸ S. Rocchia,^{8,15} D. Rozpedzik,⁵ P. Schmidt-Wellenburg,^{4,**} A. Schnabel,¹⁶ N. Severijns,⁶ J. A. Thorne,^{1,7} R. Virost,⁸ A. Weis,¹¹ E. Wursten,^{6,††} G. Wyszynski,^{2,5} J. Zejma,⁵ and G. Zsigmond⁴

¹*Department of Physics and Astronomy, University of Sussex, Falmer, Brighton BN1 9QH, UK*

²*ETH Zürich, Institute for Particle Physics and Astrophysics, CH-8093 Zürich, Switzerland*

³*LPC Caen, ENSICAEN, Université de Caen, CNRS/IN2P3, 14000 Caen, France*

⁴*Paul Scherrer Institut, CH-5232 Villigen PSI, Switzerland*

⁵*Marian Smoluchowski Institute of Physics, Jagiellonian University, 30-348 Cracow, Poland*

⁶*Instituut voor Kern- en Stralingsfysica, University of Leuven, B-3001 Leuven, Belgium*

⁷*Laboratory for High Energy Physics and Albert Einstein Center for Fundamental Physics, University of Bern, CH-3012 Bern, Switzerland*

⁸*Université Grenoble Alpes, CNRS, Grenoble INP, LPSC-IN2P3, 38026 Grenoble, France*

⁹*University of Kentucky, Lexington, KY 40506, USA*

¹⁰*Institut für Physik, Johannes-Gutenberg-Universität, D-55128 Mainz, Germany*

¹¹*Physics Department, University of Fribourg, CH-1700 Fribourg, Switzerland*

¹²*Institute of Physics Belgrade, University of Belgrade, 11080 Belgrade, Serbia*

¹³*Henryk Niewodniczanski Institute for Nuclear Physics, 31-342 Cracow, Poland*

¹⁴*Department of Chemistry - TRIGA site, Johannes Gutenberg University Mainz, D-55128 Mainz, Germany*

¹⁵*Institut Laue-Langevin, CS 20156 F-38042 Grenoble Cedex 9, France*

¹⁶*Physikalisch Technische Bundesanstalt, D-10587 Berlin, Germany*

(Dated: May 4, 2022)

Experiments dedicated to the measurement of the electric dipole moment of the neutron require outstanding control of the magnetic field uniformity. The neutron electric dipole moment (nEDM) experiment at the Paul Scherrer Institute uses a ¹⁹⁹Hg co-magnetometer to precisely monitor temporal magnetic field variations. This co-magnetometer, in the presence of field non-uniformity, is however responsible for the largest systematic effect of this measurement. To evaluate and correct that effect, offline measurements of the field non-uniformity were performed during mapping campaigns in 2013, 2014 and 2017. We present the results of these campaigns, and the improvement the correction of this effect brings to the neutron electric dipole moment measurement.

I. INTRODUCTION

Discovering a non-zero electric dipole moment (EDM) of a simple spin-1/2 particle, like the neutron, would have far-reaching implications. Indeed, the existence of such a moment implies a violation of time-reversal invariance T , and therefore a violation of CP symmetry, under the assumption that combined CPT symmetry holds [1]. The electroweak theory of the Standard Model of particle physics predicts tiny values for all subatomic particles'

EDMs, making them background free observables and ideal probes of new physics beyond the Standard Model. The experimental search for the neutron EDM has been an important research topic since the early 1950s [2]. There has been an improvement of six orders of magnitude in the measurement precision between the first experiment [3] with a beam of neutrons and the most recent measurement [4] performed at the ultracold neutron (UCN) source [5] of the Paul Scherrer Institute (PSI) by the nEDM collaboration. However, the measured neutron EDM is still compatible with zero:

$$d_n = (0.0 \pm 1.1_{\text{stat}} \pm 0.2_{\text{sys}}) \times 10^{-26} e \text{ cm}. \quad (1)$$

This result was obtained with a substantially refitted apparatus originally developed by the Sussex/RAL/ILL collaboration [6], which had given the previous most stringent limit [7] when running at the Institut Laue-Langevin (ILL). It was moved to PSI in 2009, and was then comprehensively upgraded and operated for several years, until autumn 2017. As with almost all other contemporary or future nEDM projects, the PSI nEDM ex-

* Corresponding author: ayresn@phys.ethz.ch

† Corresponding author: ferraris@lpsc.in2p3.fr

‡ Present address: Department of Physics, North Carolina State University, Raleigh, NC 27695, USA

§ Present address: Fraunhofer-Institut für Physikalische Messtechnik IPM, 79110 Freiburg i. Breisgau, Germany

¶ Present address: Paul Scherrer Institut, CH-5232 Villigen PSI, Switzerland

** Corresponding author: philipp.schmidt-wellenburg@psi.ch

†† Present address: CERN, 1211 Genève, Switzerland

periment used ultracold neutrons (UCN) stored in a bottle for hundreds of seconds. The bottle was a cylindrical chamber of height $H = 12$ cm and radius $R = 23.5$ cm. It sat coaxially in a stable and uniform vertical magnetic field with a magnitude of $B_0 \approx 1$ μ T in which the neutrons' spins precessed at the Larmor frequency of nominally $f_n \approx 30$ Hz. An electric field E of 11 kV/cm was also applied, either parallel or anti-parallel to the magnetic field.

The experimental method deployed to search for an nEDM is a precise measurement of the Larmor precession frequency, f_n , of the neutrons' spins in the chamber with the Ramsey technique of (time)-separated oscillatory fields [8]. The EDM can then be extracted from the difference of frequencies between parallel and anti-parallel fields, $d_n = \pi\hbar(f_{n,\uparrow\downarrow} - f_{n,\uparrow\uparrow})/2E$. In these experiments, the control of the magnetic field is the most important experimental challenge. Time fluctuations of B_0 must be monitored in real-time. For this reason, in the experiment [4, 6, 7], spin-polarized ^{199}Hg atoms filled the precession chamber with the neutrons and were used as a co-magnetometer. The drifts of the magnetic field were corrected using the time-averaged precession frequency of the mercury atoms' spins $f_{\text{Hg}} \approx 7.6$ Hz through the relation $f_{\text{Hg}} = \gamma_{\text{Hg}}B_0/(2\pi)$, where γ_{Hg} is the mercury gyromagnetic ratio. To maintain neutron spin coherence over the Ramsey cycle, a field uniformity better than 1 nT must be achieved inside the chamber [9].

This article is the third episode of a trilogy of papers dedicated to statistical and systematic uncertainties in nEDM searches due to the non-uniformity (gradients) of the magnetic field. The first article [9] describes the effects of magnetic-field non-uniformity for nEDM experiments. Field inhomogeneities accelerate the depolarization of the neutrons, causing a loss of statistical sensitivity. Simultaneously, they also cause systematic shifts in the neutron or mercury spin precession frequency. The second paper explains how we limit the sensitivity loss in the PSI experiment. This is achieved using an *in situ* magnetic-field homogenization strategy using an array of 16 Cs magnetometers [10]. However, the uniformity achieved thanks to this method was not enough to keep the systematic effects sufficiently low. We had then to characterize the magnetic field non-uniformity in order to correct for these effects. In this article, we present this characterization: an offline mapping of the magnetic field. First, we will summarize the systematic effects induced by the non-uniformity that need to be evaluated. Then, we will describe the experiment's magnetic field and the mapping measurements. Finally, we will detail the mapping analysis and present its results.

II. SYSTEMATIC EFFECTS RELATED TO FIELD NON-UNIFORMITY

Critical for the extraction of the nEDM from the difference of precession frequencies f_n of the stored neutrons

exposed to a positive and negative electric field is the control for coincidental or correlated changes in the magnetic field B . For this purpose B is monitored using the ^{199}Hg co-magnetometer. The largest systematic effect in this measurement, the so-called false EDM effect, arises from the combination of motional magnetic fields from the relativistic transformation of the large electric field into the rest frame of the thermal mercury atoms, which in the presence of a non-uniform magnetic field causes a shift in precession frequency linear in E , the same signature as a real electric dipole moment. Other frequency shifts not linked to E do not directly cause a systematic effect, they can indirectly interfere with the correction of the effect, and thus contribute to an overall systematic. A full overview of all relevant systematic effects can be found in Table I of Ref. [4].

The primary purpose of the offline field mapping measurement detailed in this article is to measure the magnetic field non-uniformity over the precession-chamber volume. As explained in [9], we use a harmonic polynomial expansion to describe the field. In cylindrical coordinates (ρ, ϕ, z) , this expansion can be written as follows:

$$\vec{B}(\vec{r}) = \sum_{l,m} G_{l,m} \begin{bmatrix} \Pi_{\rho,l,m}(\vec{r}) \\ \Pi_{\phi,l,m}(\vec{r}) \\ \Pi_{z,l,m}(\vec{r}) \end{bmatrix}, \quad (2)$$

where the functions $\vec{\Pi}_{l,m}$ are products of a polynomial of order l in ρ, z and a trigonometric function in $m\phi$, and $G_{l,m}$ are the expansion coefficients, which will be called gradients in the rest of this article. Expressions for the first eighty modes in cylindrical coordinates, all modes $l \leq 7$, can be found in Tables V to VII in Appendix A. Note that at each "order" l , polynomials with $-l - 1 \leq m \leq +l + 1$ exist.

Section II A discusses a frequency shift linear in E which mimics the signature of an electric dipole moment signal. Section II B describes an effect independent of E , but which must be controlled to enable our correction strategy. In Section II C we describe an effect caused by vertical magnetic-field gradients, independent of E , but which inverts with the sign of B , which we make use of to elegantly eliminate the first effect described. Finally, a significant shift in the measured frequencies caused by measuring in a rotating reference frame on Earth, not related to the magnetic field homogeneity, but reversing in sign with B and therefore relevant to our correction strategy, is described in Appendix C.

A. Mercury-induced false neutron EDM

The dominant systematic effect in the measurement of the neutron EDM at PSI was the motional false EDM. It is caused by the combination of non-uniformity of the magnetic field and a relativistic motional field experienced by the particles. It induces a linear-in-electric-field frequency shift, which is exactly the kind of signal a true

neutron EDM would produce. This shift has been extensively studied theoretically [11–20] and discussed more specifically for the nEDM experiment at PSI in [9]. It can be split in two components: a direct effect due to the neutron and an indirect one from the mercury comagnetometer, which enters the neutron EDM measurement by contaminating the correction for magnetic field drifts. Nevertheless, use of the comagnetometer to control for random drifts in the magnetic field (uncorrelated with E) is required to achieve reasonable statistical sensitivity. The direct effect is in our case two orders of magnitudes smaller than the indirect. It is implicitly accounted for in the analysis described in Sec. II C. In contrast, the effect from the mercury comagnetometer was and will be a source of a large systematic effect and is calculated as

$$d_{n\leftarrow\text{Hg}}^{\text{false}} = \left| \frac{\gamma_n}{\gamma_{\text{Hg}}} \right| d_{\text{Hg}}^{\text{false}} = \left| \frac{\gamma_n}{\gamma_{\text{Hg}}} \right| \left(-\frac{\hbar\gamma_{\text{Hg}}^2}{2c^2} \langle \rho B_\rho \rangle \right), \quad (3)$$

where the angle brackets correspond to the volume average over the precession chamber. Injecting the polynomial expansion of Eq. 2 into this expression, it becomes

$$d_{n\leftarrow\text{Hg}}^{\text{false}} = -\frac{\hbar|\gamma_n\gamma_{\text{Hg}}|}{2c^2} \sum_{l,m} G_{l,m} \langle \rho \Pi_{\rho,l,m} \rangle. \quad (4)$$

In case of a cylindrical precession chamber of radius R and height H , with the center of the cylinder being the coordinate system origin, only the modes $\Pi_{\rho,l,0}$ with l odd contribute to the false EDM, which can then be written up to order $l = 7$ as:

$$\begin{aligned} d_{n\leftarrow\text{Hg}}^{\text{false}} = & \frac{\hbar|\gamma_n\gamma_{\text{Hg}}|}{8c^2} R^2 \left[G_{1,0} - G_{3,0} \left(\frac{R^2}{2} - \frac{H^2}{4} \right) \right. \\ & + G_{5,0} \left(\frac{5R^4}{16} - \frac{5R^2H^2}{12} + \frac{H^4}{16} \right) \\ & \left. - G_{7,0} \left(\frac{7R^6}{32} - \frac{35R^4H^2}{64} + \frac{7R^2H^4}{32} - \frac{H^6}{64} \right) \right]. \end{aligned} \quad (5)$$

B. Transverse inhomogeneity

Another effect which is related to magnetic gradients is the transverse inhomogeneity. It induces a frequency shift unrelated to the electric field which moves the frequency ratio $\mathcal{R} = f_n/f_{\text{Hg}}$ by a fraction δ_T from its unperturbed value $|\gamma_n/\gamma_{\text{Hg}}|$. This effect arises from the difference in the behavior of neutrons and mercury atoms. Ultracold neutrons fall into the adiabatic regime of slow particles, $\bar{v}_n \approx 3$ m/s, where the typical rate of change of the magnetic field as the neutron crosses the precession chamber is much lower than the Larmor frequency. Mercury atoms fall into the non-adiabatic regime of fast particles, $\bar{v}_{\text{Hg}} \approx 180$ m/s, which cross the chamber many times during each precession. This difference changes the

way the particles' spins average the magnetic field, and therefore their precession frequency. While the neutrons' spins effectively average $\langle |\vec{B}| \rangle$, the mercury spins follow $\langle |\vec{B}_T| \rangle$. The latter always less than or equal to the former, increasing \mathcal{R} . The expression of the transverse shift is

$$\delta_T = \frac{\langle B_T^2 \rangle}{2B_0^2}, \quad (6)$$

where $\langle B_T^2 \rangle = \langle (B_x - \langle B_x \rangle)^2 + (B_y - \langle B_y \rangle)^2 \rangle$ is the transverse inhomogeneity, which results from field gradients. An expression for this in terms of the expansion coefficients $G_{l,m}$ is given in Appendix B.

C. Gravitational shift and correction strategy

On top of the transverse inhomogeneity, there are several other effects that can shift the ratio \mathcal{R} . For the purpose of the present discussion, we write the combination of these effects as

$$\mathcal{R} = \frac{f_n}{f_{\text{Hg}}} = \left| \frac{\gamma_n}{\gamma_{\text{Hg}}} \right| (1 + \delta_{\text{grav}} + \delta_{\text{earth}} + \delta_T + \delta_{\text{other}}). \quad (7)$$

The terms correlated to the electric field are not taken into account in this expression. We have already discussed the δ_T shift in Section II B, while the shift δ_{earth} arises from the fact that the experiment was performed in the rotating frame of the earth and is not related to the inhomogeneity of the magnetic field, see Appendix C. The last term, δ_{other} , accounts for small ($< 10^{-29} e$ cm) shifts unrelated to field uniformity that are discussed in Table I of [4] and will not be detailed here. The first term, δ_{grav} , is the dominant shift in Eq. 7 and is called the gravitational shift. It is caused by the different centers of mass of ultracold neutrons and mercury atoms,

$$\delta_{\text{grav}} = \pm \frac{G_{\text{grav}} \langle z \rangle}{|B_0|}. \quad (8)$$

The sign \pm refers to the direction of the magnetic field B_0 , G_{grav} is the so called gravitational gradient and $\langle z \rangle$ is the relative shift in the center of mass of the neutrons with respect to the mercury, which is significantly non-zero and negative: $\langle z \rangle = -0.39(3)$ cm [4]. Note, that the center of mass of mercury vapor coincides with the center of the precession chamber; its gravitational offset is negligible. The term G_{grav} depends on the difference of the magnetic field averaged by both populations and is a function of the gradients $G_{l,0}$ with l odd. Details about the calculation of that term can be found in [9]. It is based on the approximation of a neutron density linear in z in the precession chamber. With a field expansion up to order 7, the expression of G_{grav} is given by the

following combination:

$$\begin{aligned}
G_{\text{grav}} = & \left[G_{1,0} + G_{3,0} \left(\frac{3H^2}{20} - \frac{3R^2}{4} \right) \right. \\
& + G_{5,0} \left(\frac{3H^4}{112} - \frac{3R^2H^2}{8} + \frac{5R^4}{8} \right) \\
& \left. + G_{7,0} \left(\frac{H^6}{192} - \frac{9R^2H^4}{64} + \frac{21R^4H^2}{32} - \frac{35R^6}{64} \right) \right]. \quad (9)
\end{aligned}$$

The strategy to correct the motional false EDM using the gravitational shift is explained in [9] and its application is detailed in [4]. It is an extension of the method used in [7] and it will be briefly summarized hereafter. We fixed a magnetic-field configuration with a chosen gravitational gradient G_{grav} applied, varied for each sequence of measurements. A sequence was a series of consecutive measurements of the neutrons' precession frequency with a nominally fixed magnetic-field configuration. An (anti-)parallel electric field was applied in an "ABBA" pattern consisting of 28 single measurements at one electric field polarity, 8 measurements without electric field, 56 measurements at the opposite polarity, again 8 cycles at $E = 0$, and a return to the initial polarity for 28 measurements, with each repetition taking around 10 hours. This was done to compensate for any (unintentional) linear drifts in any experimental parameter. Per sequence, we extracted one value of the measured electric dipole moment and its statistical error. The cycles at $E = 0$ do not contribute directly to the EDM sensitivity, but are necessary to set operation parameters in a way not biased by the blinding or any E -dependant systematic effect. This measured EDM is then the sum of the true neutron EDM and the mercury induced false one from Eq. 5:

$$d_n^{\text{meas}} = d_n^{\text{true}} + \frac{\hbar|\gamma_n\gamma_{\text{Hg}}|}{8c^2} R^2 \left(G_{\text{grav}} + \widehat{G} \right), \quad (10)$$

where G_{grav} is separated out and the residual gradient \widehat{G} is called the phantom gradient. It is defined as the sum of odd- l order contributions once the G_{grav} contribution is subtracted:

$$\widehat{G} = \widehat{G}_3 + \widehat{G}_5 + \widehat{G}_7 + \dots, \quad (11)$$

with

$$\widehat{G}_3 = G_{3,0} \left(\frac{H^2}{10} + \frac{R^2}{4} \right), \quad (12)$$

$$\widehat{G}_5 = G_{5,0} \left(\frac{H^4}{28} - \frac{R^2H^2}{24} - \frac{5R^4}{16} \right), \quad (13)$$

$$\widehat{G}_7 = G_{7,0} \left(\frac{H^6}{96} - \frac{5R^2H^4}{64} - \frac{7R^4H^2}{64} + \frac{21R^6}{64} \right), \quad (14)$$

obtained by subtracting Equation 9 from Equation 5. For each sequence, inserting Equation 8 in Equation 7, we also extract the frequency ratio

$$\mathcal{R} = \left| \frac{\gamma_n}{\gamma_{\text{Hg}}} \right| \left(1 + \frac{G_{\text{grav}}\langle z \rangle}{B_0} + \delta_{\text{earth}} + \delta_{\text{T}} + \delta_{\text{other}} \right). \quad (15)$$

We define the corrected quantities d_n^{corr} , $\mathcal{R}^{\text{corr}}$ to be

$$d_n^{\text{corr}} = d_n^{\text{meas}} - \frac{\hbar|\gamma_n\gamma_{\text{Hg}}|}{8c^2} R^2 \widehat{G} \quad (16)$$

and

$$\mathcal{R}^{\text{corr}} = \mathcal{R} - \left| \frac{\gamma_n}{\gamma_{\text{Hg}}} \right| (\delta_{\text{T}} + \delta_{\text{earth}}). \quad (17)$$

Using the dependency of \mathcal{R} on G_{grav} , one can express a linear dependency between d_n^{corr} and $\mathcal{R}^{\text{corr}}$ as follows:

$$d_n^{\text{corr}} = d_n^{\text{true}} + B_0 \frac{\hbar\gamma_{\text{Hg}}^2}{8c^2\langle z \rangle} R^2 \left(\mathcal{R}^{\text{corr}} - \left| \frac{\gamma_n}{\gamma_{\text{Hg}}} \right| \right), \quad (18)$$

where R denotes the trap radius, and $\mathcal{R}^{\text{corr}}$ the corrected frequency ratio. With two sets of points (d_n^{corr} , $\mathcal{R}^{\text{corr}}$) for both B_0 directions, one can fit both sets with a common and opposite slope. At the crossing point (\mathcal{R}_\times , d_\times), we get $d_\times = d_n^{\text{true}}$ and $\mathcal{R}_\times = |\gamma_n/\gamma_{\text{Hg}}|$, free of the systematic effects described in this section. Therefore, to obtain the systematic-free value of the EDM, the quantities \widehat{G} and $\langle B_T^2 \rangle$ are required for every EDM measurement sequence. These quantities were extracted from magnetic field maps taken during the annual proton accelerator and UCN source shutdown. δ_{earth} is the same in magnitude for each measurement sequence, with the sign inverting depending on the direction of B . It should be noted that, due to the principle of the crossing point method, the corrections of \mathcal{R} have an impact on the nEDM measurement only if they are different for the two directions of the B_0 field.

III. THE COIL SYSTEM

A. Setup description

As mentioned in Sec. I, in order to measure the neutron EDM, a highly uniform magnetic field is required. In the PSI experiment, many components were dedicated to the production of such a field and to the reduction of its non-uniformity. The main coil used to produce the B_0 field (called the B_0 coil) was a $\cos\theta$ coil of 54 turns wound around the surface of the cylindrical vacuum tank of diameter $D = 1100$ mm and length $L = 1540$ mm (see Figure 1) to produce a vertical field. This coil produced a field with a relative uniformity $\delta B_0/B_0 \sim 10^{-3}$ in the precession chamber, a cylinder of radius 23.5 cm and

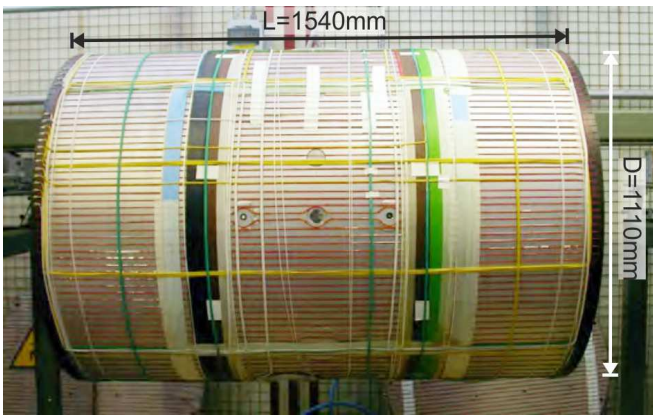


FIG. 1. Side view of the B_0 coil (red cables) and trimcoils (green, yellow and white cables) wound on the surface of the vacuum tank.

height 12 cm with its axis pointing vertically, i.e., along z in Figure 2, mounted +2 cm vertically offset from the centre of the coil. The B_0 coil was mounted within a passive magnetic shield. The four layer shield made of mu-metal, a metal alloy with high magnetic permeability, had a quasistatic shielding factor of 1500 to 14000 for small perturbations (smaller than $1 \mu\text{T}$), depending on the direction (x , y or z). This factor increases with the amplitude of the perturbation. Due to the interaction of the field produced by the B_0 coil with the innermost layer of the magnetic shield, 40% of the B_0 field came from the magnetization of the shield itself. As a result, shield imperfections were a potential source of field non-uniformity. The B_0 coil in conjunction with the passive shield generated a $\pm 1 \mu\text{T}$ field using a $\pm 17 \text{ mA}$ current.

Thirty-three correction coils were used to optimize the magnetic-field homogeneity. They were also wound on the vacuum tank, on top of the B_0 coil (see Figure 1). A homogenization algorithm, detailed in [10], allowed the calculation of the proper currents for each trimcoil for a given magnetic field configuration (nEDM sequence). Several “guiding” coils were used to maintain the polarization of the neutrons’ spins as they were transported to and from the precession chamber: the non-uniformity they potentially caused had to be taken also into account.

To keep the ambient external field as stable as possible, we used three pairs of large rectangular coils in a Helmholtz configuration surrounding the experiment. This system, called the surrounding field compensation system (SFC), added an additional “active” shielding factor of 5 to 50 at a bandwidth from 1 mHz to 500 mHz. A feedback algorithm dynamically adjusted the current through each of the six coils using the readings of ten three-axis fluxgate magnetometers positioned near the external layer of the passive shield. The setup and performance of this system are described in detail in [25].

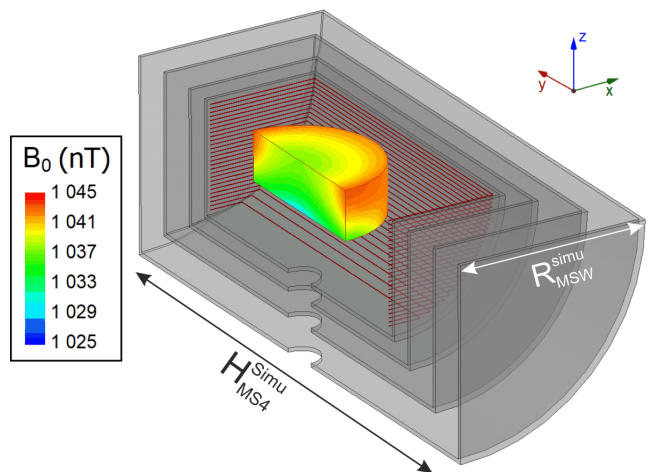


FIG. 2. Simulation of the field generated by the B_0 coil and a 4-layer mu-metal shield. The represented geometry is a quarter of the complete volume. The external dimensions of the fourth (outermost) layer of the shield were $R_{\text{MS4}}^{\text{simu}} = 0.98 \text{ m}$ and $H_{\text{MS4}}^{\text{simu}} = 2.79 \text{ m}$. The coil’s windings are represented in red. The central volume, the area of the heat map, is a cylinder of diameter 80 cm and height 50 cm, larger than the mapping volume.

B. B_0 coil simulations

To validate our understanding of and assumptions about the system, simulations of a simplified geometry of the B_0 coil and the passive shield were performed using the Ansys Maxwell software, based on the finite element method. A quarter of the simulated geometry and the simulated field is shown in Figure 2. The coil was simulated as a set of 54 independent and perfectly parallel copper loops, with 2 cm vertical spacing and a 17 mA current flowing through them. To minimize the computation time, the section of each winding was approximated as a closed rectangle. The relative magnetic permeability of the mu-metal composing the shield was set between $\mu = 10\,000$ and $\mu = 30\,000$. However, due to the small thickness (2 mm) of the shield layers compared to the scale of the whole simulation, the software had difficulties to generate an adequate meshing and a thicker version of the shield associated with a proportionally smaller value of its permeability had to be used. The shield layers were simulated with identical central holes of 20 cm diameter along the z -axis.

Simulation results and mapping data were analyzed using the same method in order to extract the field gradients (see Sec. V). Due to the symmetries of the coil, and an astucious choice of the coordinate system only a few modes of the magnetic field appear. The first one is the constant term, $G_{0,0}$, which was 1034.47 nT in the simulation at the nominal current. Then, only modes with l and m strictly positive and even appear. The simulated values and uncertainties for these modes, up to order 6, are listed in Table I. The uncertainties were estimated by

TABLE I. Ansys simulation values for the magnetic-field modes for a B_0 up configuration and their uncertainties.

	$G_{l,m}^{\text{simu}}$ (pT/cm l)	$\Delta G_{l,m}^{\text{simu}}$ (pT/cm l)
$G_{0,0}$	1034.47×10^3	5.08×10^3
$G_{2,0}$	-9.26	0.14
$G_{2,2}$	1.18	0.21
$G_{4,0}$	-3.63×10^{-3}	0.06×10^{-3}
$G_{4,2}$	1.37×10^{-3}	0.01×10^{-3}
$G_{4,4}$	-8.66×10^{-5}	0.14×10^{-5}
$G_{6,0}$	-1.16×10^{-6}	0.02×10^{-6}
$G_{6,2}$	2.77×10^{-7}	0.02×10^{-7}
$G_{6,4}$	-7.89×10^{-8}	0.04×10^{-8}
$G_{6,6}$	8.89×10^{-9}	0.16×10^{-9}

running several simulations with different parameter settings (meshing refinement, relative magnetic permeability, and proportional changes of the shield thickness). Although all uneven modes are in principle forbidden, they actually do exist because of the non-perfect geometry of the coil (for example coil connections, cable detours due to holes in the vacuum tank, and non-symmetrical holes in the different layers of the shield). It turns out, nevertheless, that they had small amplitudes compared to the even modes. A comparison between the measured B_0 field and the predicted values for these modes will be discussed later.

IV. THE MAGNETIC-FIELD MAPPING

A. Magnetic field mapper

The offline magnetic-field characterization was performed regularly during the annual accelerator shutdown period (see IV C) using an automated magnetic field measurement device, the so-called mapper. This mapper was installed inside the empty vacuum vessel, i.e., with the electrode stack removed. It allowed the movement of a precise magnetic sensor inside the vacuum vessel, as shown in Figure 3. The fully-sampled measurement volume was a cylinder of diameter 68 cm and height 32 cm.

The three stepper motors used for the sensor motion along the ρ , ϕ and z axes were located below the vacuum vessel, outside the cylindrical magnetic shield. Every part of the mapper inside the magnetic shield was made of non-magnetic materials (PEEK, POM, aluminum, ceramics, glass, etc.), with all materials screened for magnetic contamination in dedicated measurements using a sensitive SQUID (superconducting quantum interference device) magnetometer array at the Berlin magnetically shielded room 2 (BMSR-2) at the Physikalisch Technischen Bundesanstalt (PTB), Berlin. No conductive sur-

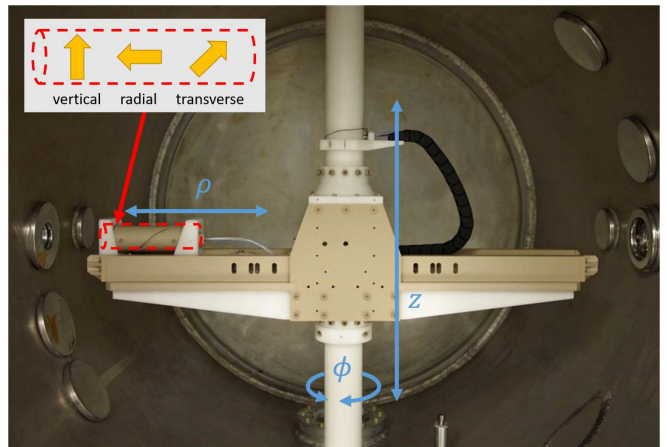


FIG. 3. Magnetic-field mapper installed in the empty vacuum vessel. The fluxgate is inside the tube on the left, in which the helical groove used for the calibration motion can be seen. The insert illustrates the relative position of the three individual fluxgate sensor axes, which are offset from each other by 20 mm in the radial direction.

faces were located close to the fluxgate sensor. This precaution avoided both eddy currents induced by the fluxgate excitation pulses and Johnson noise.

The z motion was performed using a linear column coupled with a linear transducer, shifting up or down the whole assembly from below. The ϕ motion was done by rotating the central axis of the mapper about a pair of bearings mounted on flanges at the top and bottom of the vacuum tank. Finally the ρ motion was performed using a rack and pinion connected to a vertical axle within the lower shaft (coupled to the ρ motor) and to the cart holding the sensor. The cart was guided along the main plate using twelve non-metallic radial bearing assemblies rolling against linear tracks to constrain all undesired motion.

The z -axis position was read with a linear transducer. Although the ϕ and ρ positions could be read using wire potentiometers, the best accuracy was provided by counting motor steps in an open-loop fashion. The sensor cart could hold two different sensors:

- a low-noise three-axis fluxgate magnetometer,
- a two-axis inclinometer (KELAG KAS901-51A).

As the inclinometer was slightly magnetic, it was only used to perform mechanical characterisation of the mapper and was removed during magnetic map measurements.

The fluxgate used was a FL3-2 from Sensys, see Table II, with three independent single axis detectors mounted along the ρ -axis spaced by 20 mm as shown in the insert of Figure 3. The specifications for our fluxgate are listed in Table II. The stated zero drift only accounts for temperature correlations. It turned out that for measurements with an accuracy < 1 nT, other influences, like

TABLE II. Manufacturer specification of the mapper fluxgate (Sensys FL3-2)

Characteristic	Value
Measurement range	$\pm 2 \mu\text{T}$
Accuracy	$\pm 0.5 \%$
Orthogonality	$< 0.5^\circ$
Zero drift	$< 0.1 \text{ nT/K}$
Scaling temp. coeff.	$+20 \text{ ppm/K, typ.}$
Noise	$< 20 \text{ pT}/\sqrt{\text{Hz}}$
Analog outputs	$5.0 \text{ V}/\mu\text{T}$ per sensor

$1/f$ noise, dominated the signal stability in time. We also found zero-offsets of the order 10 nT for all three independent sensors after several years of use and exposure to a variety of conditions. Sub-nT accuracy could be reached by an *in situ* zero-offset determination done with the fluxgate mounted onto the mapper, using the same electronics including cables and data acquisition system. For such a measurement, a special mechanism to rotate the fluxgate tube about the ρ -axis was used. It combined the helical groove on the fluxgate seen in Figure 3 with a pneumatically moved index finger within the upper vertical axis. The next section explains this key feature of the mapper in more detail.

B. Fluxgate zero-offset determination

A frequently used method to find the zero-offset for a magnetic field detector sensitive in only one spatial direction is the measurement of the magnetic field at one point twice, with the measuring direction reversed for the second measurement. The magnetic field value is cancelled when the time between the two measurements is short enough that a possible magnetic field change is negligible. The average value of both field readings is then the zero-offset. The accuracy of such a method depends on the accuracy of the rotation angle γ , which must be exactly 180° to reverse the measuring direction. The influence of an uncertainty $\Delta\gamma$ is proportional to the background field strength transverse to the measuring direction of the detector. Therefore, the highest accuracy for the zero-offset is reached when the background field is small and in the direction of the sensitive axis of the sensor. In our case, since the mapper did not allow adjustment of the single detectors in the fluxgate in 3D to the maximal and minimal field reading, we used the center of the magnetic shield for the zero-offset determination. We observed that the absolute value of the field was lowest close to the center when the shield was degaussed without a B_0 field applied. Indeed, when comparing the zero-offset measured in the absence and presence of a B_0 field, we observed a significant effect. Without correction, the

measured apparent zero-offsets of the horizontal field sensors (ρ , ϕ) were of order 1 nT, due to the misalignment of the fluxgate axes into the $1 \mu\text{T}$ field into the vertical (z) direction. Comparison of measurements taken in different field configurations (around $1 \mu\text{T}$ at the center of the tank in each direction x , y and z successively) allowed the determination of these angles and for this effect to be corrected.

For our fluxgate zero-offset determination, each single detector was moved one by one to the central position and readings were taken for the “normal” and the “reversed” fluxgate orientation. In the reversed position, the fluxgate was rotated by π around the radial axis, inverting the field readings of the transverse and vertical detectors. To measure the offset of the radial sensor, and increase the accuracy of the determination for the transverse and radial sensors, measurements were taken every 10° for a rotation around the vertical axis, which lead to 36 pairs of opposing field measurements for the transverse and vertical detectors and 18 (measured nominally twice) for the radial one. These measurements are combined to give the final determination of each fluxgate offset. To be able to bring each sensor to the center of the coordinate system to perform this measurement was an explicit design requirement of the system. The necessary mapper movement time to measure the positions for all three single detectors was about five minutes. Repeating the zero-offset determination immediately afterwards, in the real use scenario in a vertical $\pm 1 \mu\text{T}$ field, leads to a reproducibility of about 30 pT in the vertical sensor, 50 pT in the radial sensor and 350 pT in the transverse sensor. The poorer reproducibility for the transverse axis is due to a small amount of play that developed in the mechanism locking the fluxgate in the normal or reversed orientation during the hundreds of zero-offset measurement cycles taken during the 2017 mapping campaign, resulting in a worsening of $\Delta\gamma$ over time. This zero-offset measurement is unique to our mapper and could be performed at any time. The zero-offset determination procedure is in principle immune to any magnetic field of the parts that are rotated together with fluxgate and to the magnetic field of the fluxgate itself.

Figure 4 shows a typical behavior of the field readings over a time period of 3 to 4 hours for the three fluxgate channels with the fluxgate motionless at the center of the degaussed shield. Such measurements were performed regularly during the mapping campaigns. There is no strong correlation between the different traces and the observed drift is about 300 pT. The temperature around the shield was controlled and stable within $\pm 0.1 \text{ K}$. Therefore, the temperature could only account for $\pm 10 \text{ pT}$ (see the zero-drift coefficient in Table II). Magnetic-field drifts as the dominant source could also be excluded by reference measurements with Cs magnetometers.

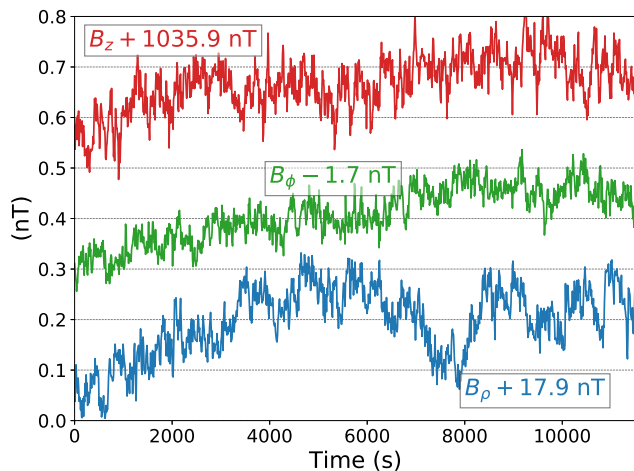


FIG. 4. Recording of the field measured by the fluxgate every ten seconds at the center of the coil to see the drifts of the three offsets.

C. Mapping campaigns

Three mapping campaigns were conducted in 2013, 2014, and 2017 during which as many as 300 full maps were recorded. A full map acquisition took between three and six hours. This time corresponds to a measurement of the vectorial magnetic field for a set of 90 rings (each with 38 points) at 5 given heights (-18, -10, -2, 6 and 14 cm in the precession chamber coordinate system, where $z = 0$ is at the center of the chamber) and 18 radii (from 0 to 34 cm, spaced by 2 cm each), as can be seen in Figure 5. The 2 cm radial spacing between each ring was chosen to match the spacing between the three single-axis sensors contained within the three-axis fluxgate, which is not necessary for the mapping analysis presented here, but useful to obtain a complete 3D representation of the field. A full map was almost always preceded and followed by one or two zero-offset determination maps to calibrate the fluxgate. Moreover, 40-minute recordings of the field were performed at the center of the chamber following each degaussing cycle. These recordings allowed us to check the drifts of the fluxgate offsets (see Sec. IV B) and gave time for the fluxgate sensor and the passive magnetic shield to stabilise.

During each mapping campaign, several kinds of maps were taken:

- B_0 maps, with only the B_0 coil powered with ± 17 mA.
- Maps of the remnant field B_{rem} , with all coil currents set to zero.
- Trimcoil maps, with only one trimcoil powered with a few mA current.
- Guiding coil maps, with only one guiding coil powered with a few mA current.

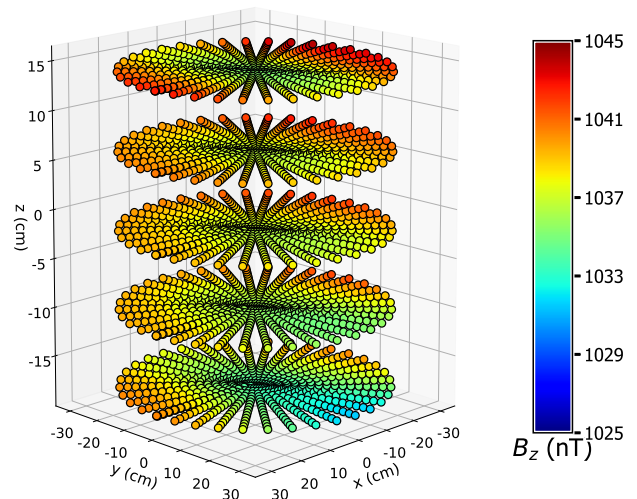


FIG. 5. B_z field for a full map of the B_0 coil. The axes are defined as in Figure 2.

- Sequence maps, replicating real nEDM measurement conditions. This included powering the trimcoils and guiding coils as they were used during data taking.

Each time the state of the B_0 coil was changed, the shield was degaussed.

V. ANALYSIS OF A SINGLE FULL MAP

In this section, we will describe the analysis method used for a single map. There were two distinct analysis groups performing differently blinded analyses of the main neutron EDM dataset. Due to the complex nature of the map analysis and the critical impact it would have on the central value of the reported neutron EDM result, both analysis groups developed independent mapping analyses. The map measurements supplied to each analysis group were not blinded, but numerical comparisons between the groups were avoided until each analysis was mature and effectively frozen. Both analyses were complete and frozen before the unblinding of the main neutron EDM result. More detailed descriptions of the mapping analyses can be found in [22, 23]. In this article we focus on the analysis procedure described in [23] and used by the Western analysis group [24]; the method described in [22] and used by the Eastern analysis group is essentially identical, with the exception that in this analysis the harmonic decomposition described in Subsection V B is done using a combined fit for all three axes simultaneously, and a compensation for the radius-dependant misalignment which will be described shortly is explicitly performed (though this was ultimately found to be not necessary when measuring typical nEDM configurations). The results of the two analysis methods ultimately showed excellent agreement. The positions

and the magnetic field will always be given in cylindrical coordinates, as illustrated in Figure 3. The correspondence with the Cartesian coordinate system used in [9] and visible on Figure 2 is the following:

$$\begin{cases} \rho = \sqrt{x^2 + y^2} \\ \phi = \arctan(y/x) \\ z = z \end{cases} \quad (19)$$

An important source of error is the possible misalignment of the {coil + mapper + sensor axes} system. Indeed, if the true vertical axis of the global coordinate system (defined by gravity, and to which the precession chamber is well aligned in normal operation) and the vertical axis of the mapper were not perfectly aligned, or if the angles between the three axes of the fluxgate were not exactly square, the three directions of the field in the chamber would be mixed with each other when measured by the mapper. A specific analysis method was developed to reduce the impact of such potential misalignment. We measured the vectorial magnetic field. Therefore, we could independently extract the gradients $G_{l,m}$ by analyzing each of the three sensor directions: radial \hat{r} , transverse $\hat{\phi}$ and vertical \hat{z} . Let's consider the simple case of a small angle α between the nominal and real axes of the fluxgate, causing a component of the large vertical field to be captured by the radial or transverse sensor. One can express the vertical and horizontal field mixing effect of such a misalignment as a function of α . Since \vec{B}_0 was mainly aligned with the mapper axis along \hat{z} (and the vertical z -axis in the global experiment coordinate system), the impact of the horizontal field components B_h in the chamber on the measured vertical z field (B_z^{meas}) could be neglected. The measured vertical and horizontal fields are

$$\begin{cases} B_z^{\text{meas}} = B_z \cos \alpha, \\ B_h^{\text{meas}} = B_h \cos \alpha + B_z \sin \alpha, \end{cases} \quad (20)$$

where ‘‘meas’’ denotes the field measured by the fluxgate sensor, and ‘‘h’’ stands for horizontal (radial \hat{r} or transverse $\hat{\phi}$) Since α is small, we can perform a Taylor expansion:

$$\begin{cases} B_z^{\text{meas}} = B_z \left(1 - \frac{\alpha^2}{2} \right) + \mathcal{O}(\alpha^3), \\ B_h^{\text{meas}} = B_h \left(1 - \frac{\alpha^2}{2} \right) + B_z \alpha + \mathcal{O}(\alpha^3). \end{cases} \quad (21)$$

It is obvious that the measured vertical field is much less impacted by a possible misalignment angle α . This is most relevant when considering field modes with order $m = 0$, due to the relatively large size of the $G_{0,0}$ term, corresponding to the target homogeneous vertical field. Therefore, to extract the $G_{l,0}$ gradients, only the vertical z sensor's analysis is used.

The analysis of one direction of the field is divided into several steps that we will describe hereafter. This method was used for all field directions individually. However, we will detail it in the next sections for the vertical z direction.

A. Ring by ring analysis

Due to the measurement pattern of a map, a full map can be seen as a set of 90 rings (ρ and z fixed) of 37 points from 0° to 360° plus an additional point at 0° (see Figure 5). The first analysis step is analogous to a Fourier decomposition ring by ring. For one ring i , since the radius ρ_i and height z_i are fixed, the magnetic field is simply a function of ϕ . We fit it with a Fourier series as follows, using a simple χ^2 fit, with the Fourier coefficients $a_{m,z,i}$ as parameters of the fit,

$$B_z(\rho_i, \phi, z_i) = \sum_{m \geq 0} [a_{m,z,i} \cos(m\phi) + a_{-m,z,i} \sin(m\phi)], \quad (22)$$

where ρ_i and z_i are respectively the radius and the height of the ring i . The 38 points of a ring are treated equally. To compute distinct weights for each point, we would need to include the error due to the fluxgate offset drift. However, we are not able to estimate that error *a priori*.

The Fourier fit step gave us a set of Fourier coefficients $a_{m,z,i}$ per ring i with their associated errors. These errors were scaled with the factor $\sqrt{\chi_i^2/NDF}$, with NDF the number of degrees of freedom of the fit, to take into account the quality of each ring i for the next analysis step. An example of this fit for a B_0 map can be seen in Figure 6(a). The fit was done up to order $|m| = 6$ (13 coefficients). This limit was chosen for several reasons:

- The improvement of the fit residuals between order 6 and order 7 was not significant.
- The contribution of the order $m = 7$ to \hat{G} was smaller than the reproducibility of the degaussing process. As we will discuss in Section VI B, this is the limiting factor in the correction of nEDM systematics.
- The contribution of the order $m = 7$ to $\langle B_T^2 \rangle$ was negligible, being much less than the degaussing reproducibility for this quantity.

We can compare the quality of a Fourier fit by looking at the square root of the mean squared residual (RMS residual). These residuals are displayed in Figure 6(b) for a B_0 map. The average value is around 20 pT, which is the same order of magnitude as the variations of the fluxgate output over a time similar to the duration of a ring measurement (80 s). One can see that the fits of the external rings tend to be of poorer quality. That may be explained by the higher order terms which grow very quickly at larger distances to the center and are not so

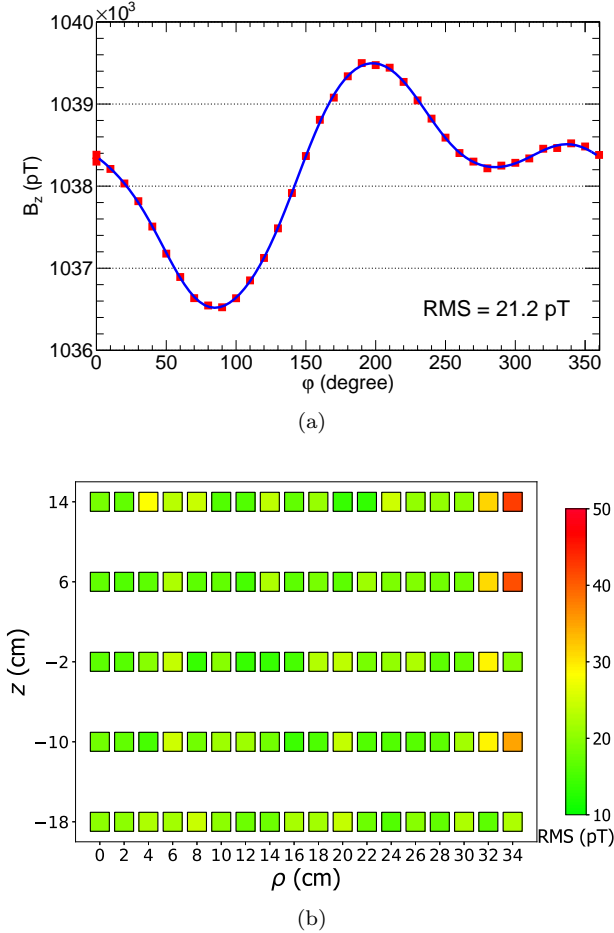


FIG. 6. Fit of the B_z field with a Fourier series up to order $m = 6$ for a B_0 up map. In (a) is the fit for the ring $\rho = 22$ cm, $z = 6$ cm. In (b) are the square root of mean squared residuals of all the rings. Each square corresponds to the RMS residual after fitting the ring at the position (ρ, z) .

well fitted. This effect is taken care of by de-weighting the external rings in the next step of the analysis.

B. Harmonic decomposition of the Fourier coefficients

After having extracted a set of Fourier coefficients for each ring i , the second step of the analysis is to fit these coefficients with the harmonic functions of the field expansion. Since we already took care of the ϕ -dependency of the field by fitting the rings, we will now fit the coefficients with the expansion functions (see Eq. 2) also freed from this dependency. As mentioned in Sec. II, these functions can be expressed as the product of a polynomial in (ρ, z) and a trigonometric function in ϕ . As an example, in the case of the z direction:

$$\Pi_{z,l,m}(\vec{r}) = \begin{cases} \tilde{\Pi}_{z,l,m}(\rho, z) \times \cos(m\phi) & \text{for } m \geq 0, \\ \tilde{\Pi}_{z,l,m}(\rho, z) \times \sin(m\phi) & \text{for } m < 0. \end{cases} \quad (23)$$

We exploit this property of the harmonic functions when expressed in cylindrical coordinates to fit the Fourier coefficients. The coefficient $a_{m,z}$ is fitted with a linear combination of the $\tilde{\Pi}_{z,l,m}$ for different values of l , with the order m being the one related to the ϕ -dependency. Similarly, $a_{-m,z}$ is fitted with a linear combination of $\tilde{\Pi}_{z,l,-m}$. Due to our choice of basis fields, there is no “mixing” between terms of different m (i.e. different ϕ -dependency). The fit of every Fourier coefficient of a given order $\pm m$ can then be written as

$$a_{m,z,i} = \sum_{l \geq 0} G_{l,m} \tilde{\Pi}_{z,l,m}(\rho_i, z_i). \quad (24)$$

This can be compared to Equations 2 and 22. For the Fourier fit, we use a χ^2 minimization. There are as many fits as the number of Fourier coefficients extracted from each ring in the first step of the analysis. On Figure 7, an example of such a fit is shown. This is the fit of the order $m = 0$, which gives us the gradients $G_{l,0}$ used to calculate \hat{G} . The harmonic fits are performed up to order $l = 6$, for the same reasons as used to justify our choice of the largest m in the ring fit stage.

After the harmonic fits, we obtain 60, 54, and 49 gradients and their associated errors, respectively for the analysis directions ρ , ϕ and z . As can be seen in Tables V to VII in the Appendix, this difference in the number of extracted coefficients is due to some gradients not producing a signal in all 3 dimensions. For fits such as the one in Figure 7, the Fourier coefficients’ error bars are underestimated, therefore the values of the χ^2 are quite large. It turns out that this underestimation of the error bars was due to the drifts of the fluxgate’s offsets. As said in Sec. IV B, the drift of these offsets was approximated as linear, but it can be seen in Figure 4 that this was not always true. During the small duration of a ring measurement (~ 80 s), the impact of the drifts was very limited and the errors coming from the Fourier fits were therefore not impacted. However, from one ring to another, with the recording of one map taking several hours, this impact became visible in the terms with $m = 0$. To

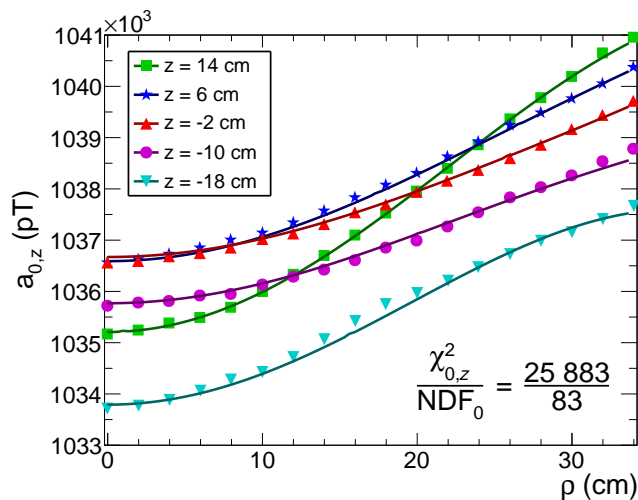


FIG. 7. Fit of gradients $G_{l,0}$ to the Fourier coefficients $a_{0,z}$ for a B_0 up map. The index $m = 0$ denotes the field components without ϕ -dependence, which are responsible for the “phantom” fields, contributing to \hat{G} . The colors represent the different values of the ring’s height z , for the same fit. Each point represents the fitted $a_{0,z}$ of a ring. Error bars are too small to be visible.

take this into account, the Fourier coefficient errors and therefore the gradients errors were scaled with the factor $\sqrt{\chi^2/NDF}$, with NDF the number of degrees of freedom of this fit. The phantom gradient \hat{G} is calculated directly at this step for the z direction, since it is a linear combination of gradients $G_{l,0}$ which come from the same fit and are therefore correlated.

The last step of the analysis is the combination of the three analysis axes, except for order $m = 0$, which is obtained from the analysis of B_z only. This combination is a simple weighted average of all axes (when available) for each gradient. After this combination, for one map, we get the 61 gradients $G_{l,m}$ that we use to calculate $\langle B_T^2 \rangle$. The uncertainties obtained from that analysis then take into account the fit error and the non-linear drifts of the fluxgate’s offsets. In the next section, we present an overview of the systematic errors of the mapping and their impact on the gradients.

C. Systematic errors

A variety of additional effects may bias the results of the mapping, arising from mechanical imperfections in the construction and installation of the mapper device. A few specific classes of errors were considered.

Firstly, the guiding rails along which the mapper cart moved radially were found to be warped. This resulted in the misalignment of several milliradians of the radial and transverse sensors into the vertical direction. As such, the large vertical magnetic field ($B_z \approx 1 \mu\text{T}$) caused large radius-dependent false fields of several nanotesla in

these sensors. This observation was validated by separate measurements using an inclinometer mounted at the same position as the fluxgate, as well as direct measurements of the rail profile using a coordinate measurement machine.

This type of misalignment does not depend on ϕ , thus the most affected field components are those with $m = 0$ due to the predominance of $G_{0,0}$ over all other terms. Such false fields do not satisfy the Maxwell equations, therefore the field decomposition basis chosen cannot describe them. Thus, in order to evaluate the misalignment in-situ, a fit of the magnetic fields described by $G_{0,0}$ to $G_{6,0}$ and two misalignment angles α and β (describing a rotation of the fluxgate about its \hat{r} and $\hat{\phi}$ axes respectively) for each radius ρ to the Fourier coefficients $a_{0,\rho,\phi,z}$ was performed. These results were compatible with the results of the inclinometer measurements and the measurement of the rail profile, and the values of $G_{l,0}$ obtained were compatible with those returned by the main analysis pathway detailed in section V. It was found that ignoring the components $a_{0,\rho}$ and $a_{0,\phi}$ in the standard analysis pathway was sufficient to result in unbiased results with comparable precision, while substantially reducing the complexity of the analysis.

Secondly, each of the three fluxgate sensors is specified to be aligned along the nominal direction with a tolerance of 0.5° . In our case, trying to measure inhomogeneities in, and small transverse components of, a large vertical field, this could have also caused undesirable false fields to appear in the radial and transverse fluxgate sensors, on the order of nanotesla. Again the predominant contribution comes from the large $G_{0,0}$ component. These false fields are then approximately constant for each magnetic-field configuration, meaning they do not cause errors in the estimation of the gradients. However, they have to be considered in the analysis of fluxgate zero-offset determination sequences performed in an offset field if absolute values independent of the applied magnetic field are required. Additionally, these angles become relevant when taking a map of a magnetic field with the largest component in the (horizontal) \hat{x} or \hat{y} direction.

Inaccuracies in the mapper positioning could also lead to measurement error. Although each small stepper motor step corresponded to a high positioning resolution of at least $50 \mu\text{m}$, the real world performance was not proven to this level. Deviation from linearity, a scaling error, or some statistical error in the ϕ position would lead to a poor fit at the stage of the ring-by-ring Fourier fit. In the case of the ρ and z positions, a poor fit would be observed at the next step when the gradients $G_{l,m}$ are fitted to the coefficients a_m . The goodness of fit in real data in the fits for terms $m \neq 0$ was sufficient to exclude such systematic effects at a relevant level, and the measurement uncertainty for the terms $m = 0$ much better explained by the aforementioned fluxgate drifts. Moreover, the zero position of each of the three axes was relatively difficult to determine and accurate to only approximately 0.5 mm . In the case of the rotational axis of

the mapper, any zero-position error of ϕ will not affect the values obtained for $\langle B_T^2 \rangle$ or \hat{G} due to the cylindrical symmetry of the precession chamber. However, a zero-position error on the radial ρ or vertical axes z could cause an anomalous reading, without substantially impacting the goodness of fit.

To estimate the magnitude of this effect, the full analysis of several real maps was repeated while adding a small offset onto each recorded position. Considering the ρ -coordinate, it was found that adding an offset of 1 mm to all points for a B_0 -up map would typically lead to a shift of around $+0.04$ pT/cm in \hat{G} and -0.02 nT² in $\langle B_T^2 \rangle$. Uncorrected, both lead to a systematic shift in the measured nEDM value of less than 2×10^{-28} e cm.

When the correction strategy described in section II C is used to correct the mercury induced false neutron EDM systematic effect described in section II A, data taken with both B_0 field directions are combined. Two lines with the same gradient but opposite sign are fitted to the corrected data of each field direction respectively following Equation 18. This yields the “crossing lines” pictured in Figure 4 of [4]. One can imagine that some systematic error like an error in the measurement of $\langle B_T^2 \rangle$ shifting \mathcal{R} in the same direction for both signs of B will not affect the crossing point d_X which gives the final corrected nEDM value d_n^{true} , only the crossing point \mathcal{R}_X will be shifted. Meanwhile, some error causing a false EDM reading, for example a systematic error in the determination of \hat{G} , will only cancel if the sign of the error is opposite for opposite polarities of B.

Considering a B_0 -down map, we find the same values and same signs for the same ρ -offset as for a B_0 -up map. Thus, any effect on $\langle B_T^2 \rangle$ is cancelled implicitly when evaluating the neutron EDM. However, the crossing point \mathcal{R}_\times would be affected. The value arising from the neutron EDM crossing lines analysis was compatible with a previous, independent determination by the collaboration [21]. There is no such cancellation in this case for the measurement of \hat{G} . Both signs of B will measure an EDM shifted in the same direction. The effect on the measured neutron EDM will then be less than 2×10^{-28} e cm per mm of offset in the ρ value, due to the effect on \hat{G} .

For shifts in the z -position, a similar effect can be observed. For both B -field directions, up and down, injecting an offset of +1 mm leads to a $+0.2$ pT/cm shift in \hat{G} , and a shift in $\langle B_T^2 \rangle$ of $+0.02$ nT². Again, although the effect on $\langle B_T^2 \rangle$ will cancel, the final measured nEDM value would be shifted by 1×10^{-27} e cm for an offset of 1 mm. We conservatively estimate 1 mm to be the upper bound on any such shift in the zero-position of the ρ and z axes, leading to an upper bound on the final nEDM systematic error due to this effect of less than 1×10^{-27} e cm.

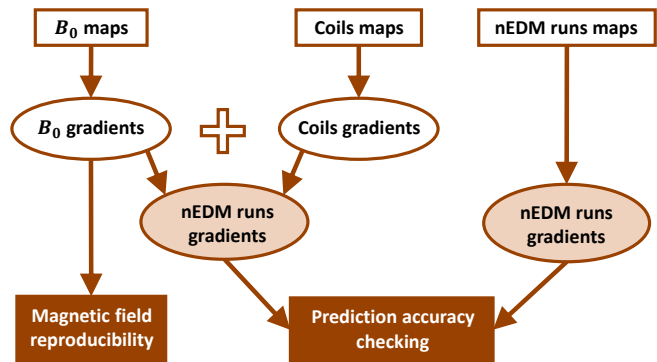


FIG. 8. Principle of the global analysis of all maps.

VI. GLOBAL ANALYSIS

Different kinds of maps were taken during the mapping campaigns. Each individual map was analyzed with the method described in the previous section to obtain the magnetic-field gradients. However, to check the quality of the maps and therefore the reliability of the extracted gradients, a global analysis of all maps was performed. A schematic diagram of the global analysis is shown in Figure 8 and its different parts will be discussed in the following sections.

The field reproducibility and the mapping repeatability were extracted from the global analysis of all the B_0 maps. These two sources of uncertainty of the mapping are defined and discussed in the following section. With these maps we also extracted the contribution of the B_0 coil to the field gradients in the precession chamber.

Using the trimcoil and guiding coil maps, we had measured the contribution to the gradients of each individual additional coil. By combining the B_0 coil gradients and those of the other coils, we obtained a prediction of the field gradients for any magnetic configuration.

A. Reproducibility and repeatability

Two important quantities to evaluate the mapping uncertainties are the field reproducibility and the mapping repeatability. The field reproducibility quantifies how reproducible the magnetic state of the system is after applying a standardized degaussing process. The mapping repeatability, on the other hand, represents our ability to measure twice the same field with the mapping and its analysis without changing any magnetic conditions (no degaussing, identical currents, etc.). A poor repeatability can be caused by measurement imperfections such as drifts in time of the sensor offset or small variances in misalignment angles. In principle, the analysis method aims to take such imperfections into account. Unlike the reproducibility, the repeatability can therefore be improved by improving either the measurement method or the analysis.

As the B_0 field was the main contribution to the magnetic field, only B_0 maps were considered to evaluate the reproducibility and the repeatability. In the following, we will only describe the extraction method for the gradient \hat{G} , the method being independent of any particular gradient. To extract the \hat{G} reproducibility, during each campaign, several groups of B_0 maps were recorded, with a degaussing of the shield in between two groups. Each group itself consisted of a series of B_0 maps taken without degaussing in between. The fluctuations of the measured \hat{G} between the different groups quantify the reproducibility. However, a naïve method would be influenced by the repeatability, which is responsible for the fluctuations of the measured \hat{G} between successive maps. The repeatability was estimated by studying the \hat{G} fluctuations within a group. Both the field reproducibility and the mapping repeatability were found to be independent of the polarity of the field. Therefore, they could be extracted by considering all B_0 maps (taking account of the different central value for different polarities).

Due to the different sizes of the groups, one to three maps per group, there was no standard statistical model to estimate the reproducibility $\sigma_{\hat{G}}$ and the repeatability $\tau_{\hat{G}}$. Therefore, we derived estimators depending on the number and size of the groups. First, we define the estimator of the average gradient of a group i containing n_i maps,

$$\bar{G}_i = \frac{1}{n_i} \sum_{j=1}^{n_i} \hat{G}_{ij}. \quad (25)$$

Then, using all groups average values with the deviation of the gradient inside each group, we estimate the repeatability as

$$\tau_{\hat{G}}^2 = \frac{1}{N-g} \sum_{i=1}^g \sum_{j=1}^{n_i} \left(\hat{G}_{ij} - \bar{G}_i \right)^2, \quad (26)$$

where N is the total number of maps and g is the number of groups. With the group averages, we also estimate the global average value of the gradient produced by the coil B_0 . This global average will be useful to predict the gradient of a magnetic configuration and is defined as

$$\bar{\bar{G}} = \frac{1}{N} \sum_{i=1}^g n_i \bar{G}_i = \frac{1}{N} \sum_{i=1}^g \sum_{j=1}^{n_i} \hat{G}_{ij}. \quad (27)$$

Finally, from the deviation between the global and individual averages, one can extract the reproducibility and subtract the repeatability contribution as follows:

$$\sigma_{\hat{G}}^2 = \frac{1}{g} \sum_{i=1}^g n_i \left(\bar{G}_i - \bar{\bar{G}} \right)^2 - \tau_{\hat{G}}^2. \quad (28)$$

The results of the mapping for the phantom gradient \hat{G} and the spread of the measurements can be seen on Figure 9. No maps from the 2013 campaign and only a

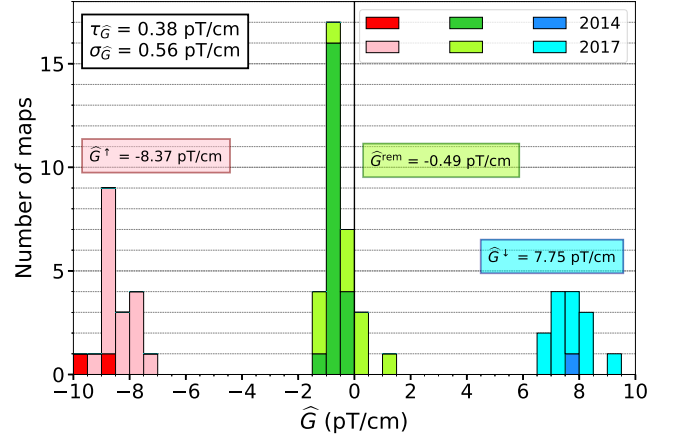


FIG. 9. Histogram of the values of \hat{G} and its global averages for all the B_0 up (red) and down (blue) maps and the remnant field (green) maps. The reproducibility and repeatability were only calculated with the B_0 maps.

part of the 2014 campaign maps were used to correct the nEDM data or for this meta-analysis. This was due to the presence of magnetic elements within the shield which were removed during the 2014 campaign. The decision to not use the maps recorded before the removal of those elements was taken to avoid any bias in the gradient estimations. However, it should be said that these maps were studied, too, and confirm an excellent reproducibility of the phantom gradient over the duration of the different campaigns. The field reproducibility and mapping repeatability were found to be $\sigma_{\hat{G}} = 0.56$ pT/cm and $\tau_{\hat{G}} = 0.38$ pT/cm, respectively. Note that the phantom gradient produced by the B_0 coil was very symmetric about zero in up and down configurations as shown in Figure 9. For the remnant field, this gradient was close to zero, which was not the case for all the field coefficients. For the other quantity of interest, the transverse inhomogeneity $\langle B_T^2 \rangle$, the reproducibility and the repeatability were $\sigma_{\langle B_T^2 \rangle} = 0.28$ nT² and $\tau_{\langle B_T^2 \rangle} = 0.02$ nT².

The most important conclusion here is that the repeatability of the mapping is better than the field reproducibility. It means that the mapping uncertainty is not dominated by the performance of the mapping measurement and analysis methods. Indeed, although the degaussing procedure and the opening and closing of the shield is already very reproducible, it still dominates the field map precision.

Another relevant point to highlight is the comparison between the repeatability and the propagated error calculated with the analysis method. The values of these quantities are listed in Table III for \hat{G} and $\langle B_T^2 \rangle$. On one hand, the repeatability quantifies all the uncertainties due to measurement differences from one map recording to another, for example position errors or varying misalignments, or in particular drifts of the fluxgate offset. On the other hand, the fit error Δx_{fit} also takes sev-

TABLE III. Reproducibility, repeatability and fit error of \widehat{G} and $\langle B_T^2 \rangle$ calculated from a global analysis of the B_0 maps. Reproducibility and repeatability are calculated with formulae 28 and 26 respectively.

x	Unit	σ_x	τ_x	Δx_{fit}
\widehat{G}	pT/cm	0.56	0.38	0.19
$\langle B_T^2 \rangle$	nT ²	0.28	0.02	0.02

eral other error sources into account, the obvious one being a potential model incompleteness, since we only consider field modes $G_{l,m}$ with $l \leq 7$. As an example, some complex fields caused by a local contamination or a deformation on the magnetic shield could be impossible to describe with the limited set of coefficients we restrict ourselves to. One might think that the fit error (propagated from the uncertainties on each Fourier coefficient $a_{m,\{\rho,\phi,z\},i}$) should be bigger than or at least equal to the repeatability. Nevertheless, it is not the case for \widehat{G} , $\langle B_T^2 \rangle$ and for most of the generalized gradients, as correlations occur as the fluxgate drifts are slow. While each ring individually fits well suggesting a lower uncertainty, considering the map as a whole the drift grows large. We rescaled this fit error with the square root of the reduced fit χ^2 to allow us to take the error due to the fluxgate drifts into account. We therefore use the repeatability (rather than the error propagated from the fit) as our key metric of the measurement uncertainty for parameters extracted from a single map.

The global analysis of all B_0 maps was also used to compare the measurements with the simulations which is discussed in Sec. VII. In the following section, we discuss the method to extract the value of the phantom gradient \widehat{G} and the transverse inhomogeneity $\langle B_T^2 \rangle$ for each nEDM sequence.

B. Gradient reconstruction method

We identified two possible methods to obtain the gradients from the mapping for each magnetic configuration corresponding to an nEDM datataking sequence. The first option is to map all the different configurations used for EDM measurements and extract the gradients from the analysis of each individual map. The second method is to use the linear dependence of the field on the applied coil currents and combine the analysis results of B_0 maps, trimcoil maps and guiding coil maps to reconstruct the magnetic field. Once we obtain the gradients with one of these methods, the calculation of the transverse inhomogeneity $\langle B_T^2 \rangle$ is simply an application of the formulae given in Appendix B. In this section, we will briefly describe the global analysis of the coil maps, verify the linearity to validate the second method and then compare the accuracy of both methods.

Unlike for the B_0 coil, the currents used in the trimcoils during the EDM sequences changed from one magnetic

configuration to another. Therefore, to obtain the contribution to the gradients of each coil, the relation between the current flowing through the coil and the field produced had to be used. This relation is linear in the case where no ferromagnetic material is present. In our case, the B_0 coil was within a large mu-metal shield which was responsible for 40% of the B_0 field. However, as the shield was far from the saturated regime, the field produced should have been linear in the coil currents. As we will show below our analysis proves that the linearity assumption was valid.

For every coil (trimcoils and guiding coils), one to five maps were taken with the coil powered with a current of 10 or 20 mA. Each time a coil map was taken, a map of the remnant field B_{rem} was recorded, too. Both maps were analyzed and the gradients were extracted with the method described in Sec. V. The remnant field gradients were subtracted from the coil ones so that we consider only the field created by the coil. The gradients thus obtained were then scaled with the value of the current flowing through the coil in order to obtain the gradients produced by 1 μ A. Finally, when there were several maps of one coil, we combined them after analyzing them all by calculating the weighted mean.

With these coefficients and the results of the B_0 maps analysis, we are able to calculate the gradients of any magnetic-field configuration by using the linearity of the gradients,

$$\widehat{G} = \widehat{G}_{B_0}^{\text{or}\downarrow} + \sum_c^{N_{\text{coils}}} i_c \widehat{g}_c, \quad (29)$$

where $\widehat{G}_{B_0}^{\text{or}\downarrow}$ is the average value of \widehat{G} measured in up or down B_0 maps, estimated with Eq. 27, N_{coils} is the number of additional coils, i_c is the current and \widehat{g}_c is the gradient produced by 1 μ A in coil c .

In order to check the validity of this prediction method, we compared the gradients extracted from the maps of the EDM sequence configurations to their predicted values using the linear superposition method. The results of this comparison for the gradient \widehat{G} and for the transverse inhomogeneity $\langle B_T^2 \rangle$ are shown on Figs. 10(a) and 10(b). For both \widehat{G} and $\langle B_T^2 \rangle$, one can see that the prediction and the measurement are in good agreement. We can therefore validate the accuracy of the prediction method, since it reliably reconstructs the measured gradients. The mean square differences of the comparison are:

$$\left\langle \left(\widehat{G}^{\text{meas}} - \widehat{G}^{\text{pred}} \right)^2 \right\rangle = (0.80 \text{ pT/cm})^2 \quad (30)$$

$$\left\langle \left(\langle B_T^2 \rangle^{\text{meas}} - \langle B_T^2 \rangle^{\text{pred}} \right)^2 \right\rangle = (0.20 \text{ nT}^2)^2. \quad (31)$$

There are several contributions to these differences. The main contribution for both \widehat{G} and $\langle B_T^2 \rangle$ is the B_0 reproducibility (0.56 pT/cm for \widehat{G} and 0.28 nT² for $\langle B_T^2 \rangle$). On the one hand, for the transverse inhomogeneity $\langle B_T^2 \rangle$, the

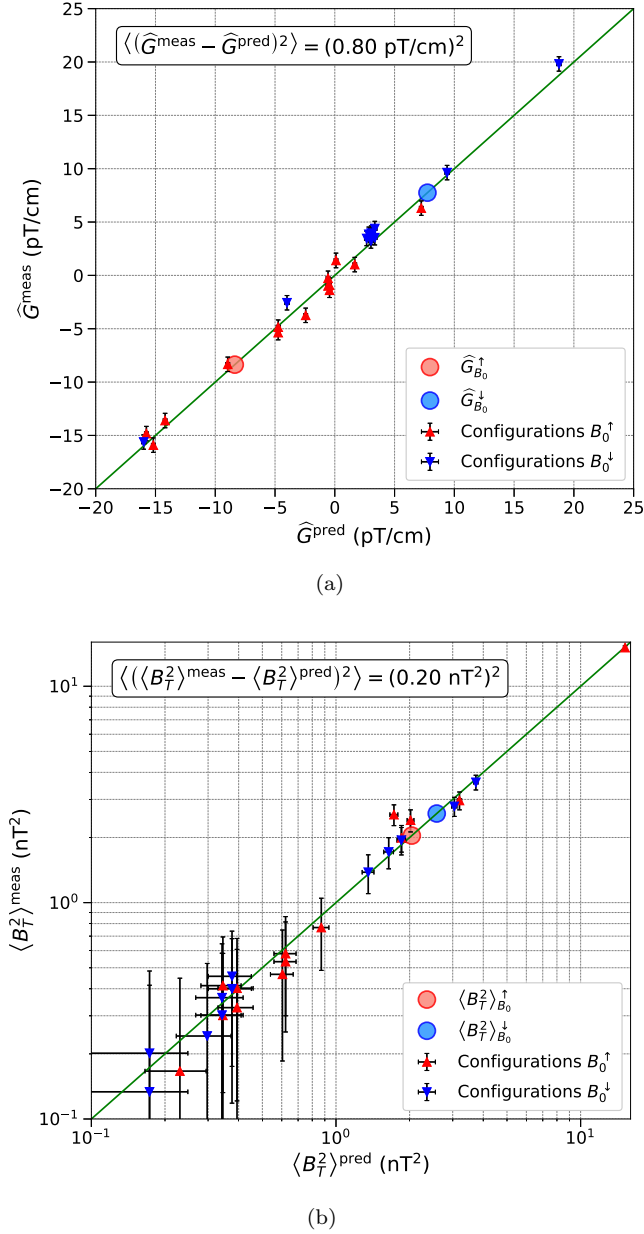


FIG. 10. Comparison of the measured and predicted values for the maps of the nEDM sequence configurations. The green line is the first bisector $y = x$. The RMS written in the top left corner of each plot is the mean square difference square root. (a) Comparison for the gradient \hat{G} . The large dots are the average values of the gradient extracted from the analysis of the B_0 maps, see Figure 9. (b) Comparison for the transverse inhomogeneity $\langle B_T^2 \rangle$. The $\langle B_T^2 \rangle \sim 15 \text{ nT}^2$ point in the upper right corner corresponds to the magnetic configuration of one of the first nEDM data sequences, when the uniformity optimisation method [10] was not used yet.

mean square difference is a little smaller than the reproducibility. On the other hand, we can see for the phantom gradient \hat{G} that other sources of error seem to contribute. One of them is the error arising from the incorporation of

the trimcoil and guiding coil contributions to the prediction. To estimate the size of this error, we did another specific comparison to eliminate the B_0 reproducibility contribution. We compared the gradients of the sequence maps subtracted from the gradients of B_0 maps taken in the same group of measurements (no shield degaussing) with the prediction coming from the additional coils. For \hat{G} , the mean square difference of this second comparison was $(0.70 \text{ pT/cm})^2$. The quadratic contributions to this difference are:

- The mapping method uncertainty, for which we take the repeatability $\tau_{\hat{G}}$. It must be taken into account twice, once for the sequence map and once for the B_0 map: $2 \cdot (0.38 \text{ pT/cm})^2$.
- The coils prediction error, which can be deduced from the other contribution: $(0.45 \text{ pT/cm})^2$.

One can see that the coils prediction error is the same order of magnitude as the repeatability. However, it is still subdominant compared to the field reproducibility, which remains the limiting uncertainty. We now have a full explanation of all contributions to the uncertainties and can compare the accuracy of both methods to obtain the gradients for one magnetic configuration.

As said in the beginning of this section, the two methods to obtain the gradients for one nEDM sequence magnetic configuration are:

1. Extracting them by offline measurement of the same magnetic-field configuration.
2. Calculating them by combining individual offline measurements of all the coils, B_0 and all trim coils, contributing to the generation of the field.

Since the largest systematic effect on the EDM result is due to the gradient \hat{G} , we will compare the uncertainties for this gradient to determine which method is more accurate. However, for each individual gradient $G_{l,m}$, the uncertainty sources are the same, so the uncertainty expressions are identical in form. The expressions of the uncertainty are, for the first method,

$$\left(\Delta \hat{G}^{\text{meas}(1)}\right)^2 = \sigma_{\hat{G}}^2 + \sigma_{\hat{G}}^2 + \tau_{\hat{G}}^2, \quad (32)$$

and for the second method,

$$\left(\Delta \hat{G}^{\text{pred}(2)}\right)^2 = \sigma_{\hat{G}}^2 + \frac{\sigma_{\hat{G}}^2 + \tau_{\hat{G}}^2}{N^{\uparrow\text{or}\downarrow}} + \sum_c \left(i_c \Delta \hat{G}_c\right)^2. \quad (33)$$

As the shield is opened and degaussing between neutron datataking and mapping measurements, the field reproducibility is the largest contribution to the prediction error, and is unavoidable. This is the first term, and the same in each expression.

For the first method, the second contribution to Eq. 32 is again the B_0 field reproducibility. Since this method uses the analysis of one map, the reproducibility error

has to be taken into account again. The last term is then simply the uncertainty coming from the mapping analysis of one map: the mapping repeatability $\tau_{\hat{G}}$. With the second method, the other contributions to the uncertainty in Eq. 33 are the errors on the prediction accuracy. The two last terms are the respective uncertainties of the terms of Eq. 29.

The B_0 field reproducibility is the main contribution among all these terms. Therefore, one can see from the expressions in Eq. 32 and 33 that if all other contributions are negligible, the uncertainty coming from the first method $\Delta\hat{G}^{\text{meas}(1)}$ is bigger than the one from the second method, $\Delta\hat{G}^{\text{pred}(2)}$, by a factor $\sqrt{2}$. It turns out that the other terms are in fact not negligible but $\Delta\hat{G}^{\text{meas}(1)}$ is still bigger than $\Delta\hat{G}^{\text{pred}(2)}$. We therefore chose the second method to predict the gradients of all the nEDM sequence magnetic configurations. This has the additional benefit that any anomalous maps would be easily identified and removed from the analysis. Indeed, with the second method, all B_0 and coil maps were measured multiple times. Contrastingly, most of the 22 nEDM data sequence base configurations (as defined in [4], optimised field configurations used for datataking that were modified only by adding small well characterised vertical gradients up to around $|\Delta G_{1,0}| \leq 30$ pT/cm) were mapped only once.

VII. COMPARISON WITH SIMULATIONS

As said in Sec. VI A, the global analysis method of the B_0 maps can be applied to compare the results of the measurements with the simulations. The values of the gradients for the allowed modes, their measurement uncertainties and a relative difference with the simulation are listed in Table IV. These measured gradients can be compared with the ones simulated, in Table I. One can see that the uniform mode $G_{0,0}$ is very well predicted (0.03%) by the simulations. The other allowed modes are predicted within 20% of agreement with the measurement, except for the $G_{2,2}$ and $G_{6,6}$ modes. For this last mode, it can be explained by the precision of the analysis method. Indeed, since the analysis is performed up to order $l = 6$ and $m = 6$, the order $G_{6,6}$ is less constrained in the harmonic fit step of the analysis and is also influenced by higher order components that are not fitted separately. Concerning the other modes, for both the simulation and the measurement, the uncertainties cannot explain the differences. By changing the parameters of the simulation, its numerical precision can be estimated, and this also does not provide an explanation. We therefore assume that the difference is due to the simplification of the system geometry (perfectly symmetric coil and shield, small shield holes ignored, etc.). However, what is to remember is that we are able to predict very accurately the uniform term for a field produced by a coil in a multiple-layer shield and obtain the magnitude

TABLE IV. Ansys simulation predicted value for the magnetic-field modes allowed by the symmetries of the B_0 coil and comparison with the measured values. The value $\Delta G_{l,m}^{B_0 \text{ pred}}$ here corresponds to the error on the prediction of the gradient produced by B_0 when in up configuration and is $\Delta G_{l,m}^{B_0 \text{ pred}} = ((\sigma_{G_{l,m}}^2 + \tau_{G_{l,m}}^2)/N^\dagger)^{1/2}$.

Mode	$G_{l,m}^{\text{meas}}$	$\Delta G_{l,m}^{B_0 \text{ pred}}$	$\frac{ G_{l,m}^{\text{simu}} - G_{l,m}^{\text{meas}} }{G_{l,m}^{\text{meas}}}$
Unit	(pT/cm ^l)	(pT/cm ^l)	-
$G_{0,0}$	1034.15×10^3	0.23×10^3	0.03%
$G_{2,0}$	-7.62	0.06	21.46%
$G_{2,2}$	2.24	0.02	47.55%
$G_{4,0}$	-4.03×10^{-3}	0.09×10^{-3}	9.97%
$G_{4,2}$	1.59×10^{-3}	0.01×10^{-3}	13.67%
$G_{4,4}$	-1.10×10^{-4}	0.03×10^{-4}	21.13%
$G_{6,0}$	-1.35×10^{-6}	0.05×10^{-6}	13.48%
$G_{6,2}$	2.57×10^{-7}	0.04×10^{-7}	8.07%
$G_{6,4}$	-1.03×10^{-7}	0.02×10^{-7}	23.09%
$G_{6,6}$	-1.49×10^{-8}	0.12×10^{-8}	166.22%

of the higher order allowed modes of the field.

VIII. DISCUSSION

A. EDM corrections

In this section we discuss how the magnetic corrections affect the analysis and result of the nEDM measurement. In total 99 nEDM measurement sequences were used in the analysis. For each of these sequences, we correct the measured ratio \mathcal{R} with $\langle B_T^2 \rangle$ and the measured EDM d_n with the phantom \widehat{G} , using Equations 6 and 10, respectively. Then, all these sequences are analysed together, and the apparent nEDM d_n^{corr} and $\mathcal{R}^{\text{corr}}$ found in each sequence are fit to Equation 18 to account for the gravitational shift δ_{grav} and the fraction of the mercury induced false EDM proportional to G_{grav} . Since for a fixed G_{grav} the sign of δ_{grav} inverts while the sign of $d_{n\leftarrow\text{Hg}}^{\text{false}}$ does not, this fit can be visualized as fitting a pair of lines of opposite, fixed, slope (see Fig. 4 in [10]). Where the two lines cross, it can be inferred that $G_{\text{grav}} = 0$, and so these two effects are eliminated. As such, this step is sometimes referred to as the “crossing lines” or “crossing point” analysis.

As detailed in Sec. II C, the corrections affect the ratio \mathcal{R} . Therefore, the corrections coming from the transverse inhomogeneity $\langle B_T^2 \rangle$ shift the crossing point nEDM value if they are different for each polarity of the B_0 field. If these shifts are the same for both signs of B_0 , then the crossing point \mathcal{R} will be affected, but the crossing point d_n will not be affected. In each of the sequences, a correction between 2×10^{-7} and 175×10^{-7} was subtracted from the measured ratio \mathcal{R} . After this procedure, the crossing point was shifted by $(0 \pm 5) \times 10^{-28}$ e cm, where the uncertainty given reflects the overall systematic uncertainty from the correction of the shift due to $\langle B_T^2 \rangle$. The correction of $\langle B_T^2 \rangle$ thus did not impact the value of the measured nEDM. However, it marginally improved the quality of the crossing point fit, corresponding to a reduction in χ^2 of 4%.

The values of the magnetic-field related corrections of d_n coming from the predicted gradient \widehat{G} for the 99 sequences can be seen in Figure 11. One can see that the values of \widehat{G} for the sequences are different from the ones produced by the B_0 coil alone. Since we used the trimcoils to compensate small inhomogeneities in the B_0 field (using the optimisation technique described in [10] after each degaussing) and also to produce a particular value of the gradient G_{grav} for each measurement sequence, a unique value of \widehat{G} was calculated for each sequence. The values of the \widehat{G} corrections on some sequences can reach up to seven times the global statistical uncertainty of the EDM. Once we took all \widehat{G} corrections into account, the shift of the crossing point value was $(69 \pm 10) \times 10^{-28}$ e cm. This shift of the nEDM measurement is about 60% of the nEDM statistical error and is the largest systematic effect. The uncertainty from that effect is the biggest source of systematic error in [4].

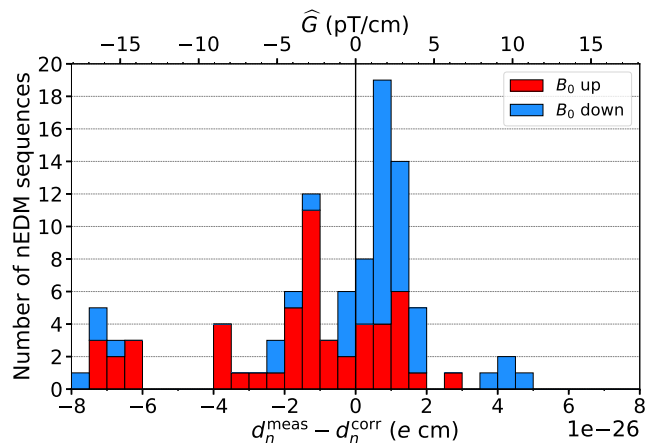


FIG. 11. Predicted values of \widehat{G} and the corresponding corrections of d_n for the 99 nEDM measurement sequences.

B. Conclusion

We discussed the offline measurement of the magnetic-field non-uniformity for the most sensitive neutron EDM measurement [4] and compared two methods for a calculation of mandatory systematic corrections (see Eq.29 and 33). As explained in Sec. II, the predicted values of the gradient \widehat{G} and the transverse inhomogeneity $\langle B_T^2 \rangle$ are needed to correct the values of d_n and \mathcal{R} for the crossing point method. The explanation of this method and its result can be found in [4].

This paper concludes the trilogy of articles [9, 10] describing the effects, control and correction of magnetic-field non-uniformity in a neutron EDM measurement experiment. The experience gained, the knowledge acquired, and the techniques developed during experiments using the single chamber nEDM will be extremely valuable for future experiments, such as the n2EDM experiment at PSI [26].

ACKNOWLEDGMENTS

The experimental data were taken at PSI Villigen. We acknowledge the excellent support provided by the PSI technical groups and by various services of the collaborating universities and research laboratories. The authors would like to thank their collaborators from the LPC Caen CAD group and workshop for their deep involvement in the design, manufacture and assembly of the mapper. We gratefully acknowledge financial support from the Swiss National Science Foundation through projects 137664 (PSI), 117696 (PSI), 144473 (PSI), 126562 (PSI), 181996 (Bern), 200441 (ETH), 172639 (ETH) and 140421 (Fribourg); and from STFC, via grants ST/M003426/1, ST/N504452/1 and ST/N000307/1. The LPC Caen and the LPSC Grenoble acknowledge the support of the French Agence Na-

tionale de la Recherche (ANR) under reference ANR-09-BLAN-0046 and the ERC project 716651-NEDM. The Polish collaborators wish to acknowledge support from the National Science Center, Poland, under grants 2016/23/D/ST2/00715, 2018/30/M/ST2/00319 and 2020/37/B/ST2/02349. P. Mohanmurthy acknowledges grant SERI-FCS 2015.0594. This work was also partly supported by the Fund for Scientific Research Flanders (FWO), and Project GOA/2010/10 of the KU Leuven. In addition we are grateful for access granted to the computing grid infrastructure PL-Grid.

Appendix A: Harmonic polynomials in cylindrical coordinates

It is useful to derive the expressions of the harmonic modes in cylindrical coordinates (ρ, ϕ, z) since this coordinate system is the most relevant for the mapping analysis. The polynomials can be obtained by deriving the formula of the magnetic potential cited in [9]:

$$\Sigma_{l,m} = C_{l,m}(\phi)r^l P_l^{|m|}(\cos \theta), \quad (\text{A1})$$

where P_l^m are the associated Legendre polynomials and

$$C_{l,m}(\phi) = \frac{(l-1)!(-2)^{|m|}}{(l+|m|)!} \cos(m\phi) \quad \text{for } m \geq 0 \quad (\text{A2})$$

$$C_{l,m}(\phi) = \frac{(l-1)!(-2)^{|m|}}{(l+|m|)!} \sin(|m|\phi) \quad \text{for } m < 0.$$

The radial, azimuthal and vertical components respectively of the mode l, m are then given by

$$\Pi_{\rho,l,m} = \partial_{\rho}\Sigma_{l+1,m} \quad (\text{A3})$$

$$\Pi_{\phi,l,m} = \frac{1}{\rho}\partial_{\phi}\Sigma_{l+1,m} \quad (\text{A4})$$

$$\Pi_{z,l,m} = \partial_z\Sigma_{l+1,m}, \quad (\text{A5})$$

and are listed up to order 7 in Tables V, VI and VII.

TABLE V. The basis of harmonic polynomials sorted by order in cylindrical coordinates, to order $l = 0$ to $l = 4$.

l	m	Π_ρ	Π_ϕ	Π_z
0	-1	$\sin \phi$	$\cos \phi$	0
0	0	0	0	1
0	1	$\cos \phi$	$-\sin \phi$	0
1	-2	$\rho \sin 2\phi$	$\rho \cos 2\phi$	0
1	-1	$z \sin \phi$	$z \cos \phi$	$\rho \sin \phi$
1	0	$-\frac{1}{2}\rho$	0	z
1	1	$z \cos \phi$	$-z \sin \phi$	$\rho \cos \phi$
1	2	$\rho \cos 2\phi$	$-\rho \sin 2\phi$	0
2	-3	$\rho^2 \sin 3\phi$	$\rho^2 \cos 3\phi$	0
2	-2	$2\rho z \sin 2\phi$	$2\rho z \cos 2\phi$	$\rho^2 \sin 2\phi$
2	-1	$\frac{1}{4}(4z^2 - 3\rho^2) \sin \phi$	$\frac{1}{4}(4z^2 - \rho^2) \cos \phi$	$2\rho z \sin \phi$
2	0	$-\rho z$	0	$-\frac{1}{2}\rho^2 + z^2$
2	1	$\frac{1}{4}(4z^2 - 3\rho^2) \cos \phi$	$\frac{1}{4}(\rho^2 - 4z^2) \sin \phi$	$2\rho z \cos \phi$
2	2	$2\rho z \cos 2\phi$	$-2\rho z \sin 2\phi$	$\rho^2 \cos 2\phi$
2	3	$\rho^2 \cos 3\phi$	$-\rho^2 \sin 3\phi$	0
3	-4	$\rho^3 \sin 4\phi$	$\rho^3 \cos 4\phi$	0
3	-3	$3\rho^2 z \sin 3\phi$	$3\rho^2 z \cos 3\phi$	$\rho^3 \sin 3\phi$
3	-2	$\rho(3z^2 - \rho^2) \sin 2\phi$	$\frac{1}{2}\rho(6z^2 - \rho^2) \cos 2\phi$	$3\rho^2 z \sin 2\phi$
3	-1	$\frac{1}{4}z(4z^2 - 9\rho^2) \sin \phi$	$\frac{1}{4}z(4z^2 - 3\rho^2) \cos \phi$	$\rho(3z^2 - \frac{3}{4}\rho^2) \sin \phi$
3	0	$\frac{3}{8}\rho(\rho^2 - 4z^2)$	0	$\frac{1}{2}z(2z^2 - 3\rho^2)$
3	1	$\frac{1}{4}z(4z^2 - 9\rho^2) \cos \phi$	$\frac{1}{4}z(3\rho^2 - 4z^2) \sin \phi$	$\rho(3z^2 - \frac{3}{4}\rho^2) \cos \phi$
3	2	$\rho(3z^2 - \rho^2) \cos 2\phi$	$\frac{1}{2}\rho(\rho^2 - 6z^2) \sin 2\phi$	$3\rho^2 z \cos 2\phi$
3	3	$3\rho^2 z \cos 3\phi$	$-3\rho^2 z \sin 3\phi$	$\rho^3 \cos 3\phi$
3	4	$\rho^3 \cos 4\phi$	$-\rho^3 \sin 4\phi$	0
4	-5	$\rho^4 \sin 5\phi$	$\rho^4 \cos 5\phi$	0
4	-4	$4\rho^3 z \sin 4\phi$	$4\rho^3 z \cos 4\phi$	$\rho^4 \sin 4\phi$
4	-3	$\frac{1}{4}(24\rho^2 z^2 - 5\rho^4) \sin 3\phi$	$\frac{3}{4}(8\rho^2 z^2 - \rho^4) \cos 3\phi$	$4\rho^3 z \sin 3\phi$
4	-2	$4(\rho z^3 - \rho^3 z) \sin 2\phi$	$2(2\rho z^3 - \rho^3 z) \cos 2\phi$	$(6\rho^2 z^2 - \rho^4) \sin 2\phi$
4	-1	$\frac{1}{8}(8z^4 - 36\rho^2 z^2 + 5\rho^4) \sin \phi$	$\frac{1}{8}(8z^4 - 12\rho^2 z^2 + \rho^4) \cos \phi$	$(4\rho z^3 - 3\rho^3 z) \sin \phi$
4	0	$\frac{1}{2}(3\rho^3 z - 4\rho z^3)$	0	$\frac{1}{8}(8z^4 - 24\rho^2 z^2 + 3\rho^4)$
4	1	$\frac{1}{8}(8z^4 - 36\rho^2 z^2 + 5\rho^4) \cos \phi$	$-\frac{1}{8}(8z^4 - 12\rho^2 z^2 + \rho^4) \sin \phi$	$(4\rho z^3 - 3\rho^3 z) \cos \phi$
4	2	$4(\rho z^3 - \rho^3 z) \cos 2\phi$	$-2(2\rho z^3 - \rho^3 z) \sin 2\phi$	$(6\rho^2 z^2 - \rho^4) \cos 2\phi$
4	3	$\frac{1}{4}(24\rho^2 z^2 - 5\rho^4) \cos 3\phi$	$-\frac{3}{4}(8\rho^2 z^2 - \rho^4) \sin 3\phi$	$4\rho^3 z \cos 3\phi$
4	4	$4\rho^3 z \cos 4\phi$	$-4\rho^3 z \sin 4\phi$	$\rho^4 \cos 4\phi$
4	5	$\rho^4 \cos 5\phi$	$-\rho^4 \sin 5\phi$	0

TABLE VI. The basis of harmonic polynomials sorted by order in cylindrical coordinates, from order $l = 5$ to $l = 6$.

l	m	Π_ρ	Π_ϕ	Π_z
5	-6	$\rho^5 \sin 6\phi$	$\rho^5 \cos 6\phi$	0
5	-5	$5\rho^4 z \sin 5\phi$	$5\rho^4 z \cos 5\phi$	$\rho^5 \sin 5\phi$
5	-4	$\frac{1}{2}(20\rho^3 z^2 - 3\rho^5) \sin 4\phi$	$\rho^3(10z^2 - \rho^2) \cos 4\phi$	$5\rho^4 z \sin 4\phi$
5	-3	$\frac{5}{4}(8\rho^2 z^3 - 5\rho^4 z) \sin 3\phi$	$\frac{5}{4}(8\rho^2 z^3 - 3\rho^4 z) \cos 3\phi$	$\frac{5}{4}(8\rho^3 z^2 - \rho^5) \sin 3\phi$
5	-2	$\frac{5}{16}(16\rho z^4 - 32\rho^3 z^2 + 3\rho^5) \sin 2\phi$	$\frac{5}{16}(16\rho z^4 - 16\rho^3 z^2 + \rho^5) \cos 2\phi$	$5(2\rho^2 z^3 - \rho^4 z) \sin 2\phi$
5	-1	$\frac{1}{8}(8z^5 - 60\rho^2 z^3 + 25\rho^4 z) \sin \phi$	$\frac{1}{8}(8z^5 - 20\rho^2 z^3 + 5\rho^4 z) \cos \phi$	$\frac{5}{8}(8\rho z^4 - 12\rho^3 z^2 + \rho^5) \sin \phi$
5	0	$\frac{5}{16}(-8\rho z^4 + 12\rho^3 z^2 - \rho^5)$	0	$\frac{1}{8}(8z^5 - 40\rho^2 z^3 + 15\rho^4 z)$
5	1	$\frac{1}{8}(8z^5 - 60\rho^2 z^3 + 25\rho^4 z) \cos \phi$	$-\frac{1}{8}(8z^5 - 20\rho^2 z^3 + 5\rho^4 z) \sin \phi$	$\frac{5}{8}(8\rho z^4 - 12\rho^3 z^2 + \rho^5) \cos \phi$
5	2	$\frac{5}{16}(16\rho z^4 - 32\rho^3 z^2 + 3\rho^5) \cos 2\phi$	$-\frac{5}{16}(16\rho z^4 - 16\rho^3 z^2 + \rho^5) \sin 2\phi$	$5(2\rho^2 z^3 - \rho^4 z) \cos 2\phi$
5	3	$\frac{5}{4}(8\rho^2 z^3 - 5\rho^4 z) \cos 3\phi$	$-\frac{5}{4}(8\rho^2 z^3 - 3\rho^4 z) \sin 3\phi$	$\frac{5}{4}(8\rho^3 z^2 - \rho^5) \cos 3\phi$
5	4	$\frac{1}{2}(20\rho^3 z^2 - 3\rho^5) \cos 4\phi$	$-\rho^3(10z^2 - \rho^2) \sin 4\phi$	$5\rho^4 \cos 4\phi z$
5	5	$5\rho^4 z \cos 5\phi$	$-5\rho^4 z \sin 5\phi$	$\rho^5 \cos 5\phi$
5	6	$\rho^5 \cos 6\phi$	$-\rho^5 \sin 6\phi$	0
6	-7	$\rho^6 \sin 7\phi$	$\rho^6 \cos 7\phi$	0
6	-6	$6\rho^5 z \sin 6\phi$	$6\rho^5 z \cos 6\phi$	$\rho^6 \sin 6\phi$
6	-5	$\frac{1}{4}\rho^4(60z^2 - 7\rho^2) \sin 5\phi$	$\frac{5}{4}\rho^4(12z^2 - \rho^2) \cos 5\phi$	$6\rho^5 z \sin 5\phi$
6	-4	$\rho^3 z(20z^2 - 9\rho^2) \cos 4\phi$	$2\rho^3 z(10z^2 - 3\rho^2) \cos 4\phi$	$\frac{3}{2}\rho^4(10z^2 - \rho^2) \sin 4\phi$
6	-3	$\frac{3}{16}\rho^2(80z^4 - 100\rho^2 z^2 + 7\rho^4) \cos 3\phi$	$\frac{3}{16}\rho^2(80z^4 - 60\rho^2 z^2 + 3\rho^4) \cos 3\phi$	$\frac{5}{2}\rho^3 z(8z^2 - 3\rho^2) \sin 3\phi$
6	-2	$\frac{1}{8}\rho z(48z^4 - 160\rho^2 z^2 + 45\rho^4) \cos 2\phi$	$\frac{1}{8}\rho z(48z^4 - 80\rho^2 z^2 + 15\rho^4) \cos 2\phi$	$\frac{15}{16}\rho^2(16z^4 - 16\rho^2 z^2 + \rho^4) \sin 2\phi$
6	-1	$\frac{1}{64}(64z^6 - 720\rho^2 z^4 + 600\rho^4 z^2 - 35\rho^6) \cos \phi$	$\frac{1}{64}(64z^6 - 240\rho^2 z^4 + 120\rho^4 z^2 - 5\rho^6) \cos \phi$	$\frac{3}{4}\rho z(8z^4 - 20\rho^2 z^2 + 5\rho^4) \sin \phi$
6	0	$\frac{3}{8}\rho(-8z^5 + 20\rho^2 z^3 - 5\rho^4 z)$	0	$\frac{1}{16}(16z^6 - 120\rho^2 z^4 + 90\rho^4 z^2 - 5\rho^6)$
6	1	$\frac{1}{64}(64z^6 - 720\rho^2 z^4 + 600\rho^4 z^2 - 35\rho^6) \sin \phi$	$-\frac{1}{64}(64z^6 - 240\rho^2 z^4 + 120\rho^4 z^2 - 5\rho^6) \sin \phi$	$\frac{3}{4}\rho z(8z^4 - 20\rho^2 z^2 + 5\rho^4) \cos \phi$
6	2	$\frac{1}{8}\rho z(48z^4 - 160\rho^2 z^2 + 45\rho^4) \sin 2\phi$	$-\frac{1}{8}\rho z(48z^4 - 80\rho^2 z^2 + 15\rho^4) \sin 2\phi$	$\frac{15}{16}\rho^2(16z^4 - 16\rho^2 z^2 + \rho^4) \cos 2\phi$
6	3	$\frac{3}{16}\rho^2(80z^4 - 100\rho^2 z^2 + 7\rho^4) \sin 3\phi$	$-\frac{3}{16}\rho^2(80z^4 - 60\rho^2 z^2 + 3\rho^4) \sin 3\phi$	$\frac{5}{2}\rho^3 z(8z^2 - 3\rho^2) \cos 3\phi$
6	4	$\rho^3 z(20z^2 - 9\rho^2) \sin 4\phi$	$-2\rho^3 z(10z^2 - 3\rho^2) \sin 4\phi$	$\frac{3}{2}\rho^4(10z^2 - \rho^2) \cos 4\phi$
6	5	$\frac{1}{4}\rho^4(60z^2 - 7\rho^2) \cos 5\phi$	$-\frac{5}{4}\rho^4(12z^2 - \rho^2) \sin 5\phi$	$6\rho^5 z \cos 5\phi$
6	6	$6\rho^5 z \cos 6\phi$	$-6\rho^5 z \sin 6\phi$	$\rho^6 \cos 6\phi$
6	7	$\rho^6 \cos 7\phi$	$-\rho^6 \sin 7\phi$	0

TABLE VII. The basis of harmonic polynomials sorted by order in cylindrical coordinates of order $l = 7$.

l	m	Π_ρ	Π_ϕ	Π_z
7	-8	$\rho^7 \sin 8\phi$	$\rho^7 \cos 8\phi$	0
7	-7	$7\rho^6 z \sin 7\phi$	$7\rho^6 z \cos 7\phi$	$\rho^7 \sin 7\phi$
7	-6	$\rho^5(21z^2 - 2\rho^2) \sin 6\phi$	$\frac{3}{2}\rho^5(14z^2 - \rho^2) \cos 6\phi$	$7\rho^6 z \sin 6\phi$
7	-5	$\frac{7}{4}\rho^4 z(20z^2 - 7\rho^2) \sin 5\phi$	$\frac{35}{4}\rho^4 z(4z^2 - \rho^2) \cos 5\phi$	$\frac{7}{4}\rho^5(12z^2 - \rho^2) \sin 5\phi$
7	-4	$\frac{7}{4}\rho^3(20z^4 - 18\rho^2 z^2 + \rho^4) \sin 4\phi$	$\frac{7}{8}\rho^3(40z^4 - 24\rho^2 z^2 + 3\rho^4) \cos 4\phi$	$\frac{7}{2}\rho^4 z(10z^2 - 3\rho^2) \sin 4\phi$
7	-3	$\frac{7}{16}\rho^2 z(48z^4 - 100\rho^2 z^2 + 21\rho^4) \sin 3\phi$	$\frac{21}{16}\rho^2 z(16z^4 - 20\rho^2 z^2 + 3\rho^4) \cos 3\phi$	$\frac{7}{16}\rho^3(80z^4 - 60\rho^2 z^2 + 3\rho^4) \sin 3\phi$
7	-2	$\frac{7}{16}\rho(16z^6 - 80\rho^2 z^4 + 45\rho^4 z^2 - 2\rho^6) \sin 2\phi$	$\frac{7}{32}\rho(32z^6 - 80\rho^2 z^4 + 30\rho^4 z^2 - \rho^6) \cos 2\phi$	$\frac{7}{16}\rho^2 z(48z^4 - 80\rho^2 z^2 + 15\rho^4) \sin 2\phi$
7	-1	$\frac{1}{64}z(64z^6 - 1008\rho^2 z^4 + 1400\rho^4 z^2 - 245\rho^6) \sin \phi$	$\frac{1}{64}z(64z^6 - 336\rho^2 z^4 + 280\rho^4 z^2 - 35\rho^6) \cos \phi$	$\frac{7}{64}\rho(64z^6 - 240\rho^2 z^4 + 120\rho^4 z^2 - 5\rho^6) \sin \phi$
7	0	$\frac{7}{128}\rho(-64z^6 + 240\rho^2 z^4 - 120\rho^4 z^2 + 5\rho^6)$	0	$\frac{1}{16}z(16z^6 - 168\rho^2 z^4 + 210\rho^4 z^2 - 35\rho^6)$
7	1	$\frac{1}{64}z(64z^6 - 1008\rho^2 z^4 + 1400\rho^4 z^2 - 245\rho^6) \cos \phi$	$-\frac{1}{64}z(64z^6 - 336\rho^2 z^4 + 280\rho^4 z^2 - 35\rho^6) \sin \phi$	$\frac{7}{64}\rho(64z^6 - 240\rho^2 z^4 + 120\rho^4 z^2 - 5\rho^6) \cos \phi$
7	2	$\frac{7}{16}\rho(16z^6 - 80\rho^2 z^4 + 45\rho^4 z^2 - 2\rho^6) \cos 2\phi$	$-\frac{7}{32}\rho(32z^6 - 80\rho^2 z^4 + 30\rho^4 z^2 - \rho^6) \sin 2\phi$	$\frac{7}{16}\rho^2 z(48z^4 - 80\rho^2 z^2 + 15\rho^4) \cos 2\phi$
7	3	$\frac{7}{16}\rho^2 z(48z^4 - 100\rho^2 z^2 + 21\rho^4) \cos 3\phi$	$-\frac{21}{16}\rho^2 z(16z^4 - 20\rho^2 z^2 + 3\rho^4) \sin 3\phi$	$\frac{7}{16}\rho^3(80z^4 - 60\rho^2 z^2 + 3\rho^4) \cos 3\phi$
7	4	$\frac{7}{4}\rho^3(20z^4 - 18\rho^2 z^2 + \rho^4) \cos 4\phi$	$-\frac{7}{8}\rho^3(40z^4 - 24\rho^2 z^2 + 3\rho^4) \sin 4\phi$	$\frac{7}{2}\rho^4 z(10z^2 - 3\rho^2) \cos 4\phi$
7	5	$\frac{7}{4}\rho^4 z(20z^2 - 7\rho^2) \cos 5\phi$	$-\frac{35}{4}\rho^4 z(4z^2 - \rho^2) \sin 5\phi$	$\frac{7}{4}\rho^5(12z^2 - \rho^2) \cos 5\phi$
7	6	$\rho^5(21z^2 - 2\rho^2) \cos 6\phi$	$-\frac{3}{2}\rho^5(14z^2 - \rho^2) \sin 6\phi$	$7\rho^6 z \cos 6\phi$
7	7	$7\rho^6 z \cos 7\phi$	$-7\rho^6 z \sin 7\phi$	$\rho^7 \cos 7\phi$
7	8	$\rho^7 \cos 8\phi$	$-\rho^7 \sin 8\phi$	0

Appendix B: Transverse inhomogeneity

In this appendix we give the expression for the averaged squared transverse field inhomogeneity,

$$\langle B_T^2 \rangle = \langle (B_x - \langle B_x \rangle)^2 + (B_y - \langle B_y \rangle)^2 \rangle, \quad (\text{B1})$$

in terms of the generalized gradients $G_{l,m}$ up to order $l = 4$ for a cylindrical precession chamber of radius R and height H . Note that in the analysis, all contributions up to order $l = 6$ were considered, having been derived using a computer algebra program, though they are too large to reasonably include here and contribute little to the discussion. It can be expressed as a sum of several contributions, one being the contributions of l order modes and the other being the contributions of interferences between modes with different order l and same ϕ -dependence m :

$$\langle B_T^2 \rangle = \langle B_T^2 \rangle_{10} + \langle B_T^2 \rangle_{20} + \langle B_T^2 \rangle_{30} + \langle B_T^2 \rangle_{40} + \langle B_T^2 \rangle_{311} + \langle B_T^2 \rangle_{412}. \quad (\text{B2})$$

The linear-order contribution is:

$$\langle B_T^2 \rangle_{10} = \frac{R^2}{2} \left(G_{1,-2}^2 + G_{1,2}^2 + \frac{1}{4} G_{1,0}^2 \right) + \frac{H^2}{12} \left(G_{1,-1}^2 + G_{1,1}^2 \right). \quad (\text{B3})$$

The quadratic-order contribution is:

$$\langle B_T^2 \rangle_{20} = \frac{R^4}{3} \left(G_{2,-3}^2 + G_{2,3}^2 \right) + \frac{R^2 H^2}{12} \left(2G_{2,-2}^2 + 2G_{2,2}^2 + \frac{1}{2} G_{2,0}^2 \right) + \left(\frac{R^4}{24} + \frac{H^4}{180} \right) \left(G_{2,-1}^2 + G_{2,1}^2 \right). \quad (\text{B4})$$

The cubic-order contribution is:

$$\langle B_T^2 \rangle_{30} = \frac{R^6}{4} \left(G_{3,-4}^2 + G_{3,4}^2 \right) + \frac{R^4 H^2}{4} \left(G_{3,-3}^2 + G_{3,3}^2 \right) + \left(\frac{5R^6}{32} - \frac{R^4 H^2}{8} + \frac{9R^2 H^4}{160} \right) \left(G_{3,-2}^2 + G_{3,2}^2 \right) + \left(\frac{5R^4 H^2}{64} - \frac{3R^2 H^4}{160} + \frac{H^6}{448} \right) \left(G_{3,-1}^2 + G_{3,1}^2 \right) + \left(\frac{9R^6}{256} - \frac{R^4 H^2}{32} + \frac{9R^2 H^4}{640} \right) G_{3,0}^2. \quad (\text{B5})$$

The fourth order contribution is:

$$\begin{aligned} \langle B_T^2 \rangle_{40} &= \frac{R^8}{5} (G_{4,-5}^2 + G_{4,5}^2) \\ &+ \frac{R^6 H^2}{3} (G_{4,-4}^2 + G_{4,4}^2) \\ &+ \frac{1}{4} \left(\frac{17R^8}{20} - R^6 H^2 + \frac{3R^4 H^4}{5} \right) (G_{4,-3}^2 + G_{4,3}^2) \\ &+ \frac{1}{2} \left(\frac{5R^6 H^2}{12} - \frac{R^4 H^4}{5} + \frac{R^2 H^6}{28} \right) (G_{4,-2}^2 + G_{4,2}^2) \\ &+ \frac{1}{8} \left(\frac{R^8}{5} - \frac{R^6 H^2}{4} + \frac{R^4 H^4}{4} - \frac{R^2 H^6}{35} + \frac{H^8}{450} \right) (G_{4,-1}^2 + G_{4,1}^2) \\ &+ \frac{1}{8} \left(\frac{3R^6 H^2}{8} - \frac{R^4 H^4}{5} + \frac{R^2 H^6}{28} \right) G_{4,0}^2. \end{aligned} \quad (\text{B6})$$

Finally, there are the interference terms, one between the linear and cubic modes and another between quadratic and fourth orders. Note that the odd l modes do not interfere with the even ones.

$$\begin{aligned} \langle B_T^2 \rangle_{311} &= \left(-\frac{R^4}{2} + \frac{R^2 H^2}{4} \right) (G_{1,-2} G_{3,-2} + G_{1,2} G_{3,2}) \\ &+ \left(-\frac{R^2 H^2}{8} + \frac{H^4}{40} \right) (G_{1,-1} G_{3,-1} + G_{1,1} G_{3,1}) \\ &+ \frac{1}{4} \left(-\frac{R^4}{2} + \frac{R^2 H^2}{4} \right) (G_{1,0} G_{3,0}). \end{aligned} \quad (\text{B7})$$

$$\begin{aligned} \langle B_T^2 \rangle_{412} &= \left(-\frac{R^6}{2} + \frac{R^4 H^2}{3} \right) (G_{2,-3} G_{4,-3} + G_{2,3} G_{4,3}) \\ &+ \left(-\frac{R^4 H^2}{3} + \frac{R^2 H^4}{10} \right) (G_{2,-2} G_{4,-2} + G_{2,2} G_{4,2}) \\ &+ \frac{1}{4} \left(-\frac{R^6}{4} + \frac{R^4 H^2}{6} - \frac{R^2 H^4}{15} + \frac{H^6}{105} \right) (G_{2,-1} G_{4,-1} + G_{2,1} G_{4,1}) \\ &+ \frac{1}{4} \left(-\frac{R^4 H^2}{3} + \frac{R^2 H^4}{10} \right) G_{2,0} G_{4,0}. \end{aligned} \quad (\text{B8})$$

Appendix C: Earth's rotation

Though not strictly related to the inhomogeneity of the magnetic field, one effect relevant to the correction strategy arises from the Earth's rotation [27]. The neutron EDM measurement took place at the Paul Scherrer Institute in Switzerland. The main B_0 magnetic field pointed approximately up or down, as defined by gravity. As such, there was an angle between the Earth's rotational axis and the quantization axis of the system of $\theta = 42.4833^\circ$. Thus, the neutron EDM measurement was

effectively taken in a rotating reference frame, effectively shifting the measured neutron and mercury frequencies, and thus \mathcal{R} . The correction can be computed as

$$\delta_{\text{earth}} = \mp \left(\frac{f_{\text{earth}}}{f_n} + \frac{f_{\text{earth}}}{f_{\text{Hg}}} \right) \cos \theta. \quad (\text{C1})$$

The shift is opposite for each direction of B_0 . While this does not directly cause a false-EDM like systematic effect as the frequency shift does not depend on the electric field direction, if not considered it can bias the correction strategy described in Subsection II C to produce an error of the order $-2.6 \times 10^{-26} e \text{ cm}$.

-
- [1] G. Lüders, Dan. Mat. Fys. Medd. **28**, 1, (1954).
 [2] E. M. Purcell and N. F. Ramsey, Phys. Rev. **78**, 807 (1950).
 [3] J. H. Smith, E. M. Purcell, and N. F. Ramsey, Phys. Rev. **108**, 120 (1957).
 [4] C. Abel *et al.*, Phys. Rev. Lett. **124**, 081803 (2020).
 [5] G. Bison *et al.*, Eur. Phys. J. A **56**, 33 (2020).
 [6] C. A. Baker *et al.*, Nucl. Instrum. Meth. A **736**, 184 (2014).
 [7] J. M. Pendlebury *et al.*, Phys. Rev. D **92**, 092003 (2015).
 [8] N. F. Ramsey, Phys. Rev. **78**, 695 (1950).
 [9] C. Abel *et al.*, Phys. Rev. A **99**, 042112 (2019).
 [10] C. Abel *et al.*, Phys. Rev. A **101**, 053419 (2020).
 [11] G. Pignol, M. Guigue, A. Petukhov, and R. Golub, Phys. Rev. A **92**, 053407 (2015).
 [12] J. M. Pendlebury *et al.*, Phys. Rev. A **70**, 032102 (2004).
 [13] S. K. Lamoreaux and R. Golub, Phys. Rev. A **71**, 032104 (2005).
 [14] A. L. Barabanov, R. Golub, and S. K. Lamoreaux, Phys. Rev. A **74**, 052115 (2006).
 [15] S. M. Clayton, J. Magn. Reson. **211**, 89 (2011).
 [16] G. Pignol and S. Rocchia, Phys. Rev. A **85** 042105 (2012).
 [17] C. M. Swank, A. K. Petukhov, and R. Golub, Phys. Lett. A **376**, 2319 (2012).
 [18] A. Steyerl *et al.*, Phys. Rev. A **89**, 052129 (2014).
 [19] R. Golub, C. Kaufman, G. Müller, and A. Steyerl, Phys. Rev. A **92**, 062123 (2015).
 [20] C. M. Swank, A. K. Petukhov, and R. Golub, Phys. Rev. A **93**, 062703 (2016).
 [21] S. Afach *et al.*, Phys. Lett. B **739**, 128 (2014).
 [22] N. J. Ayres, *Data and Systematic Error Analysis for the Neutron Electric Dipole Moment Experiment at the Paul Scherrer Institute and Search for Axionlike Dark Matter*, PhD Thesis, University of Sussex (2018). <http://sro.sussex.ac.uk/id/eprint/83852/>
 [23] L. Ferraris-Bouchez, *Measurement of the neutron electric dipole moment: correction of the phantom field systematic effect*, PhD Thesis, Université Grenoble Alpes (2020). <https://tel.archives-ouvertes.fr/tel-03130525>
 [24] N. J. Ayres *et al.*, Eur. Phys. J. A **57**, 152 (2021); and Erratum Eur. Phys. J. A **57**, 244 (2021)
 [25] S. Afach *et al.*, J. Appl. Phys. **116**, 084510 (2014).
 [26] N. J. Ayres *et al.*, Eur. Phys. J. C **81**, 512 (2021)
 [27] S. K. Lamoreaux and R. Golub Phys. Rev. Lett. **98**, 149101 (2007)



A large ‘Active Magnetic Shield’ for a high-precision experiment

nEDM collaboration

C. Abel¹, N. J. Ayres², G. Ban³, G. Bison⁴, K. Bodek⁵, V. Bondar^{2,a}, T. Bouillaud⁶, E. Chanel^{7,14}, J. Chen³, W. Chen^{2,4}, P. -J. Chiu^{2,4,15}, C. B. Crawford⁸, M. Daum⁴, C. B. Doorenbos^{2,4}, S. Emmenegger^{2,16}, L. Ferraris-Bouchez⁶, M. Ferti⁹, A. Fratangelo⁷, W. C. Griffith¹, Z. D. Grujic¹⁰, P. Harris¹, K. Kirch^{2,4,b}, V. Kletzl^{2,4}, P. A. Koss^{12,17}, J. Krempel^{2,c}, B. Lauss⁴, T. Lefort³, P. Mullan², O. Naviliat-Cuncic³, D. Pais^{2,4}, F. M. Piegsa⁷, G. Pignol⁶, M. Rawlik^{2,18}, I. Rienäcker⁴, D. Ries⁴, S. Rocca⁶, D. Rozpedzik⁵, W. Saenz-Arevalo³, P. Schmidt-Wellenburg⁴, A. Schnabel¹¹, E. P. Segarra⁴, N. Severijns¹², T. Shelton⁸, K. Svirina⁶, R. Tavakoli Dinani¹², J. Thorne⁷, R. Viro⁶, N. Yazdandoost¹³, J. Zejma⁵, N. Ziehl², G. Zsigmond⁴

¹ Department of Physics and Astronomy, University of Sussex, Falmer, Brighton BN1 9QH, UK

² ETH Zürich, Institute for Particle Physics and Astrophysics, 8093 Zurich, Switzerland

³ Normandie Univ, ENSICAEN, UNICAEN, CNRS/IN2P3, LPC Caen, 14000 Caen, France

⁴ Paul Scherrer Institut (PSI), 5232 Villigen, Switzerland

⁵ Marian Smoluchowski Institute of Physics, Jagiellonian University, 30-348 Cracow, Poland

⁶ LPSC, Université Grenoble Alpes, CNRS/IN2P3, Grenoble, France

⁷ University of Bern, Albert Einstein Center for Fundamental Physics, 3012 Bern, Switzerland

⁸ University of Kentucky, Lexington, USA

⁹ Institute of Physics, Johannes Gutenberg University, 55128 Mainz, Germany

¹⁰ Institute of Physics Belgrade, University of Belgrade, 11080 Belgrade, Serbia

¹¹ Physikalisch Technische Bundesanstalt, Berlin, Germany

¹² Institute for Nuclear and Radiation Physics, KU Leuven, 3001 Leuven, Belgium

¹³ Department of Chemistry-TRIGA site, Johannes Gutenberg University, 55128 Mainz, Germany

¹⁴ Present address: Institut Laue Langevin, 71 avenue des Martyrs CS 20156, 38042 Grenoble Cedex 9, France

¹⁵ Present address: University of Zurich, 8057 Zurich, Switzerland

¹⁶ Present address: Hochschule Luzern, 6002 Luzern, Switzerland

¹⁷ Present address: Fraunhofer Institute for Physical Measurement Techniques, 79110 Freiburg, Germany

¹⁸ Present address: Paul Scherrer Institut (PSI), 5232 Villigen, Switzerland

Received: 15 July 2023 / Accepted: 6 November 2023 / Published online: 20 November 2023

© The Author(s) 2023

Abstract We present a novel Active Magnetic Shield (AMS), designed and implemented for the n2EDM experiment at the Paul Scherrer Institute. The experiment will perform a high-sensitivity search for the electric dipole moment of the neutron. Magnetic-field stability and control is of key importance for n2EDM. A large, cubic, 5 m side length, magnetically shielded room (MSR) provides a passive, quasi-static shielding-factor of about 10^5 for its inner sensitive volume. The AMS consists of a system of eight complex, feedback-controlled compensation coils constructed on an irregular grid spanned on a volume of less than 1000 m^3 around the MSR. The AMS is designed to provide a stable and uniform magnetic-field environment around the MSR, while

being reasonably compact. The system can compensate static and variable magnetic fields up to $\pm 50\ \mu\text{T}$ (homogeneous components) and $\pm 5\ \mu\text{T/m}$ (first-order gradients), suppressing them to a few μT in the sub-Hertz frequency range. The presented design concept and implementation of the AMS fulfills the requirements of the n2EDM experiment and can be useful for other applications, where magnetically silent environments are important and spatial constraints inhibit simpler geometrical solutions.

1 Introduction

High-precision measurements in fundamental physics, using particles, nuclei, atomic, or molecular systems, require exquisite temporal stability and spatial uniformity of many environmental parameters to control systematic effects and

^a e-mail: klaus.kirch@psi.ch (corresponding author)

^b e-mail: bondarv@phys.ethz.ch (corresponding author)

^c e-mail: jochen.krempel@phys.ethz.ch (corresponding author)

fully exploit their statistical sensitivity. The control of the magnetic field is of particular importance in those experiments sensitive to the coupling of the magnetic field to the spin of the system through its magnetic moment. For example, experiments searching for permanent or variable electric dipole moments (EDMs), signals of dark matter fields, neutron-antineutron and mirror-neutron oscillations, Lorentz invariance violation, or new forces [1–5]. Most of them deploy dedicated coil systems generating uniform magnetic fields inside magnetically shielded volumes. Shielding of these volumes can be achieved by means of passive or active magnetic shielding (AMS), separately, or, in combination. Passive shields are built from high-permeability materials and rely on their magnetic properties. Active magnetic shields are based on feedback-controlled coils, where magnetic sensors detect changes of the magnetic field, and an algorithm calculates the proper response to adjust the coil currents and counteract the perturbation.

Since the 1980s, numerous active shields have been built for different applications [6–12], covering a wide range of research areas such as ion beams, electron microscopes, and bio-medical applications, as well as high-precision measurements of EDMs [1, 2, 13, 14]. In particular, an active magnetic shield was successfully used for the first time by our collaboration in the nEDM experiment, which provides the current best measurement of the neutron EDM [15]. The system consisted of six actively-controlled rectangular coils with size of approximately $8\text{ m} \times 6\text{ m}$, located in a Helmholtz-like positioning. The coils were built around a control volume of $2.5\text{ m} \times 2.5\text{ m} \times 3\text{ m}$. The system was crucial to fully exploit the statistical sensitivity of the experiment [6].

In this paper, we report on the design-path, implementation, and initial performance characterization of a dedicated AMS for the n2EDM experiment [16–18], currently undergoing commissioning at the ultracold neutron (UCN) source [19–21] at the Paul Scherrer Institute (PSI). A ten-fold improvement in statistical sensitivity of n2EDM over nEDM will be realized by many innovations, primarily by improved adaption to the UCN source and two enlarged vertically-stacked UCN storage-chambers. The target systematic error budget yields stringent requirements for the magnetic-field stability and uniformity, and, thus, advanced shielding from magnetic-field disturbances. The n2EDM experiment uses a combination of passive and active shieldings around the sensitive volume. The passive shielding is provided by a Magnetically Shielded Room (MSR) [22] with a base size of $5.2\text{ m} \times 5.2\text{ m}$ and a height of 4.8 m . It is composed of five mu-metal layers, one ULTRAVAC layer, and one intermittent RF-shielding layer with a shielding factor of 10^5 at 0.01 Hz and rising with frequency to 10^8 at 1 Hz , as shown in Fig. 1.

The specifications for the n2EDM internal magnetic field are discussed in detail in Ref. [16]. Although the variations of the magnetic field will be continuously monitored by quan-

tum magnetometers, the field instabilities within a measurement cycle of 300 s need to be limited. This is crucial because the principle of the nEDM measurement relies on Ramsey's method performed with neutrons, which achieves its optimal sensitivity at a so called "working point" and any shifts in magnetic field lead to departure from this point. To provide a sense of scale – variations of 30 pT within one cycle would result in 50% loss of sensitivity. To stay on the safe side, we chose to require the magnetic field to be stable on a level of 10 pT , which corresponds to 2% sensitivity loss.

For the same reason it is crucial that the average magnitudes of the magnetic fields in the two UCN storage chambers (with centers vertically separated by 18 cm) do not differ by more than this 10 pT , corresponding to a vertical magnetic-field gradient smaller than 0.6 pT/cm .

Variations of the magnetic field will also be detected by the quantum magnetometers, and a field change larger than 25 fT over 180 s will be seen in the precession signals of the mercury co-magnetometer. While it would be desirable to reach this extreme stability level of 25 fT , this is not a sine-qua-non condition for the experiment, compare Tab. 4 of Ref. [16].

Due to the quasi-static shielding factor of the MSR of 10^5 , slow external field changes of order $1\text{ }\mu\text{T}$ will lead to internal field changes of order 10 pT . As the shell structure of the MSR and its high-quality, innermost layer tend to homogenize magnetic field changes, internal magnetic-field gradients resulting from external gradients are further suppressed [23]. Thus, an external, inhomogeneous variation of a few μT around the MSR can be tolerated. However, larger field variations on the outside of the MSR could cause larger-than-allowed internal gradients. In addition, larger external field changes can change the magnetization of the outermost mu-metal layer of the MSR, which will, in turn, slowly propagate through the MSR layers, and result in undesirable drifts of the inner magnetic field.

The task for the AMS in n2EDM is thus to provide a magnetic field around the MSR that is stable to within a few μT , even with sub-Hertz external variations, in order to meet the 10 pT conditions on the inside. For large, slow magnetic field variations, of order ten or several tens of μT , this also corresponds to an improved overall shielding performance in the low-frequency regime, see Fig. 1.

This paper describes the design and implementation of the AMS system for the n2EDM experiment (see [17, 18]) and is organized as follows:

- (i) The magnetic fields over the complete volume occupied by the entire experimental apparatus were mapped before setting up the n2EDM experiment and are described in Sect. 2. The disturbance of the field resulting from neighbouring magnetic instruments was eval-

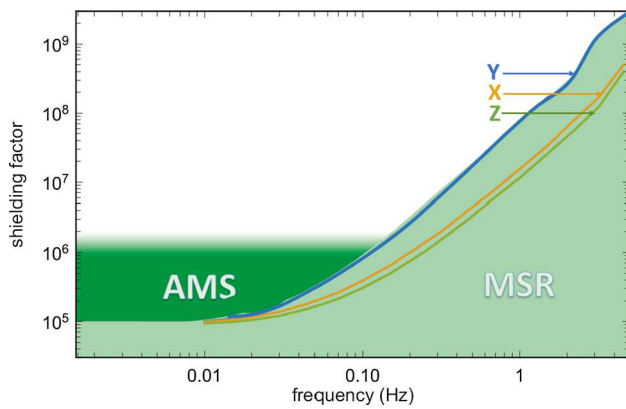


Fig. 1 Frequency-dependent shielding-factors of the MSR. The light green region and the colored curves for each spatial direction were obtained using external reference excitation coils to produce $2\ \mu\text{T}$ peak-to-peak sinusoidal fields at the central position of the MSR final location prior to the MSR assembly. The dark green region is the expected improved shielding-factor provided by the AMS system for large disturbances of order several $10\ \mu\text{T}$ in the low-frequency range. Adapted from Ref. [22]



Fig. 2 Picture taken during a magnetic-field mapping in UCN area South at PSI [18]. The area was emptied before the n2EDM experiment was set up. Two people are moving the ‘mapping tower’ around. About half height of the tower in the displayed position marks the center of n2EDM. The UCN source is behind the concrete shielding to the left, and a superconducting magnet (blue) to fully polarize UCN directed to n2EDM, is visible on the platform. See main text for further details

uated. All relevant fields could be reproducibly measured and described to μT precision by superpositions of homogeneous (three directions) and first-order gradient (five independent components) magnetic-field contributions. This established the need for eight independent and ideally ‘orthogonal’ coils for the field compensation system.

- (ii) A method was developed to design optimal coils for specific magnetic fields when constraining the current-carrying wires to a predetermined, irregular grid on a surface around the volume of interest [17,24], described in Sect. 3.
- (iii) A scaled-down prototype was developed and served as a proof-of-concept system, see Sect. 4. It allowed tests of various design options, including an irregular geometry, the powering of the coils, and the implementation of feedback sensors and appropriate algorithms, with and without mu-metal.
- (iv) A scheme to systematically simplify the individual, optimal, full-scale coils was developed to ease practical construction of the AMS without sacrificing the specified performances [18] (Sect. 5.1). This included reducing windings in the eight coils and their efficient powering with eight current sources, each feeding three circuits.
- (v) The system was constructed with careful quality control during assembly of the system with more than 55 km of cabling, as described in Sect. 5.2.
- (vi) Current sources were developed and implemented (Sect. 5.3). An array of three-axis fluxgate sensors was implemented to monitor the magnetic field and inform the feedback algorithm (Sect. 5.4).

- (vii) The commissioning of the full AMS system was successfully completed with various performance studies, as described in Sect. 6.

2 Mapping of the experimental area

The n2EDM experiment is located at PSI in UCN area South. Before setting up n2EDM, its predecessor nEDM was disassembled and the area cleared. Figure 2 shows a view of the empty experimental area. The concrete blocks are part of the biological shield of the UCN source (to the left) and of the medical cyclotron COMET (forward direction and to the right). These blocks cannot be moved, and thus ultimately limit the space available for the n2EDM experiment. The MSR was decoupled from the rest of the hall on its own foundation, which is seen in the picture as brown floor, indicating approximately the size of the MSR base. Given the size of the MSR and the spatial constraints of the biological shields, the coils of the AMS system have to be as close as around 1 m to the MSR, and still providing the desired homogeneous field in the volume of interest. This immediately excludes AMS field generation with simple Helmholtz-like coil systems.

Before designing the AMS system, the magnetic field of the experimental area was extensively mapped [17,18] to determine the components of the magnetic field that have to be compensated. The measured field was then decomposed, by a least-squares fit, into zeroth order, homogeneous fields, first-order gradients, and higher-order contributions, obtaining field maps and interpolated continuous fields.

Figure 2 shows the mobile ‘mapping tower’ in action. The tower was constructed using up to five identical, 2 m-long aluminum triangle-truss segments from commercially available event stage equipment. Each segment carried three 3-axis fluxgate sensors. The segments were vertically stacked and mounted on a heavy aluminum base plate on wheels. The position and orientation of this cart in the area was measured by three string potentiometers attached to a rigid coordinate system referenced to the area. The full area could thus be magnetically mapped within minutes, with spatial resolution limited by the reproducibility of the order of 0.1 m.

Several strong superconducting magnets at 10–50 m distances contribute with fields in the tens of μT range and field gradients of a few $\mu\text{T}/\text{m}$. Their influence is particularly severe as their fields can change during n2EDM measurements without prior notice. Typical time scale of such uncontrolled changes can vary from minutes to tens of minutes, possibly several times a day. So that the AMS can compensate those changes, for each of the known strong nearby magnets, the mapping was performed with it on and off. Thereby, the change of the magnetic field in the space of the n2EDM experiment was measured.

The superconducting magnet shown in Fig. 2 is less problematic, as it is self-shielded with a known steep field gradient and controlled by the n2EDM experiment operation. During n2EDM operation it is always ramped up and running very stably in a persistent mode.

The reproducibility of maps taken under similar conditions was of the order of a few μT , where the limitation might be due to drifts of the fields themselves or uncertainties of the measurement and the analysis procedures. Importantly, it was found that the measured fields could be sufficiently described, with 1 μT -accuracy, with only homogeneous and first-order gradient fields.

We concluded that the AMS needed only coils to compensate homogeneous fields in the three independent spatial directions, and five independent first-order gradients. Therefore, a system could be designed using only eight independent coils.

Concerning field strengths, it was found that a range of $\pm 50 \mu\text{T}$ for the three homogeneous components of the field, and up to $\pm 5 \mu\text{T}/\text{m}$ for the five first-order gradients would be sufficient to meet our requirements. These values already include a safety margin of 20%.

3 The concept of the AMS design

3.1 Working principle

In a volume with no magnetised parts, any magnetic field can be generated by the correct current distribution on the surface of this volume. The currents on the surface can thus be

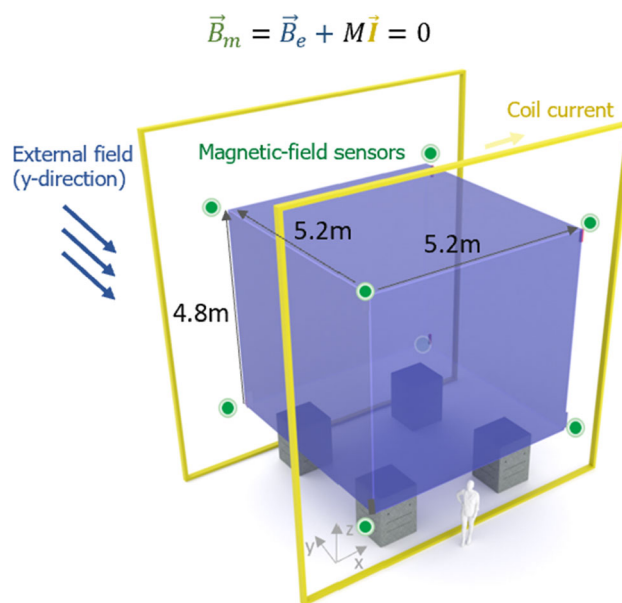


Fig. 3 The volume of interest for the target fields of the n2EDM AMS system are given by the outside wall of the MSR (depicted in violet). An external magnetic field B_e is detected by magnetic-field sensors (green). As an example, the yellow coils could aim to compensate the external field. In practice, the AMS coils are more complicated due to spatial limitations and their close proximity to the MSR

chosen to exactly counteract the effect of any external field, stabilising the field inside. In a practical realisation, there is a finite number of coils on the surface, and the field is measured only in a finite number of points. Figure 3 depicts a simple realisation with a single coil (shown in yellow) and eight 3-axis sensors (shown in green). Here, an external magnetic field B_e influences the target volume, in which the field is to be stabilised (depicted in blue, occupied by the MSR of n2EDM). We aim, however, for optimal (in the least-squares sense) stabilization at the eight green points where three-axis sensors are placed. Their readings B_m are used to calculate currents I feeding a coil system to counteract external field changes. Obviously, in the real application, the coils are much more complicated than shown. In principle one can aim at any target field at the surface of the sensitive volume. In our application aiming at zero field is most reasonable.

In the absence of the MSR and other magnetization, one obtains a linear dependence between B_m and the coil currents. In fact, we initially assume, and later prove experimentally in Sect. 6.2, that a linear dependence also holds for a demagnetized MSR exposed only to small magnetic fields. One can write:

$$B_m = B_e + M I. \quad (1)$$

The matrix M contains the proportionality factors, which relate the current in the AMS coils to the magnetic fields measured at the sensor positions. For a built system, the entries of

M can be measured using the installed coils and sensors (see Sect. 4.2). During design of the coil itself, they can be calculated, without the MSR using Biot–Savart’s law, and with the MSR, using a sufficiently realistic finite-element simulation of the full system. Equation 1 can be written components-wise in the following way:

$$\begin{pmatrix} B_{m,1x} \\ B_{m,1y} \\ B_{m,1z} \\ \vdots \\ B_{m,nz} \end{pmatrix} = \begin{pmatrix} B_{e,1x} \\ B_{e,1y} \\ B_{e,1z} \\ \vdots \\ B_{e,nz} \end{pmatrix} + \begin{pmatrix} M_{11x} & M_{21x} & \dots & M_{k1x} \\ M_{11y} & M_{21y} & \dots & M_{k1y} \\ M_{11z} & M_{21z} & \dots & M_{k1z} \\ \vdots & \vdots & \ddots & \vdots \\ M_{1nz} & M_{2nz} & \dots & M_{knz} \end{pmatrix} \begin{pmatrix} I_1 \\ I_2 \\ \vdots \\ I_k \end{pmatrix}. \tag{2}$$

Matrix M has dimensions $3n \times k$, where k is the number of coils (for the AMS system $k = 8$, see Sect. 3.3), and n is the number of magnetic-field sensors.

Next, one implements an iterative process using the measured changes in B_m (see Sect. 5.5) to calculate appropriate changes for I to zero B_m again. In the applied feedback algorithm the pseudo-inverse of M is used. In order to calculate the pseudo-inverse we start with a Singular Value Decomposition:

$$M = USV^T, \tag{3}$$

where U and V are unitary matrices and S is diagonal. The latter is called the spectrum and describes the effect of combinations of coils on the magnetic sensors. The pseudo-inverse M^{-1} can be calculated as:

$$M^{-1} = VS^{-1}U^T. \tag{4}$$

The ratio of extreme values of the spectrum, s_{min} and s_{max} , defines a *condition number* C of the matrix M :

$$C = \frac{s_{max}}{s_{min}}. \tag{5}$$

The condition number is an important characteristic of the system design of the feedback-matrix quality. It represents the sensitivity of the sensors to current changes. A low condition number means that there are particular combinations of currents I that have small influence on the readings of the sensors measuring B_m . When inverted, this leads to small changes in the sensors to cause large changes in the currents, rendering the system to be unstable. The condition number is later used in the optimization of the sensor positions in the AMS system (Sect. 4).

3.2 Design challenges

In a volume with no magnetized parts, any magnetic field can be generated by the correct current distribution on the surface of this volume. In particular, the currents on the surface can be chosen to exactly counteract the effect of any external field, making the inner magnetic field zero. The MSR can be demagnetized and reside in the zero field inside the volume with exactly the same currents as needed for the empty volume without the MSR.

In the real experiment, currents cannot be arbitrarily distributed on a surface. They must follow predefined, discrete paths and the fields can only be adjusted by varying current values. The spatial discretization is a grid to which the current carrying wires are fixed. The discretized current distribution can approximate the target field well, if the discretization is small compared to the distance between the target volume and the surface.

Several constraints for the AMS system were already mentioned. The coil system must be large compared to the size of the MSR, however, the walls of the experimental area ultimately limit the size of the surface to which the AMS could be mounted. In addition, the experimental area must be accessible. It should be possible for persons with reasonably sized equipment to enter the experiment without breaking the currents in the AMS. It should also be possible to open the AMS from the top to insert large equipment with the crane. Various other installations penetrate surfaces around the MSR such that the grid for the AMS must be adapted to the needs of other subsystems.

The shielding blocks seen in Fig. 2 as well as the regular floor of the experimental hall are made of steel-reinforced concrete with some magnetic response. The latter was investigated and fortunately found to be rather weak and finally negligible if a minimal distance to the walls is maintained. Namely, these effects are smaller than the AMS field homogeneity.

3.3 Method of simple coil design and its application for the AMS system

The aforementioned requirements and constraints of the system called for the development of a flexible method to design coils that could be practically built.

The employed method of coil design [17,24] is based on three key inputs: (i) target fields, which have to be compensated by the coils; (ii) a fixed grid where coil wires can be placed; and (iii) points of interest (POIs) of target fields, covering the fiducial volume of interest densely enough (Fig. 4, left). The grid can be subdivided into many small coils called tiles. A tile is the smallest building block of the grid. The smaller this elementary building block is, the more homogeneous the field can be. For practical reasons, we have

chosen to make most tiles rectangular; however, the method could deal with any shape. It is also worth reiterating that the method does not require the grid to be regular. In fact, the AMS system of the n2EDM experiment (Sect. 5) is implemented on an irregular grid.

Once target fields, grid, and POIs are defined, the magnetic field at the POIs, \mathbf{B}_{POI} , created by the currents \mathbf{I} in the tiles, can be described similarly to Eq. (1) by

$$\mathbf{B}_{\text{POI}} = \mathbf{M}_{\text{D}} \mathbf{I}. \quad (6)$$

In this design phase, each element of proportionality matrix \mathbf{M}_{D} can now be calculated numerically using Biot–Savart’s law. Using a least-squares method we find the current needed in each tile to approximate the target field. For the AMS system, there were 308 tiles in total (see Sect. 5.1). The calculation is simplified by cancelling counteracting currents on the grid structure. The algorithm described in [17] decomposes this grid of currents into simple loops, which are closed current paths that can be wound on the grid. The result of this step is a set of such loops, that each need to be powered with a specific design current to generate the target field. Examples of such simple loops are depicted in different colors in the right panel of Fig. 4.

In order to change the magnitude of the field generated by a system of loops, all loop currents in the system need to change proportionally to the design current. Thus, the set of loops for a specific target field can be connected in series, creating one *coil*. The number of windings for each loop can be adjusted, such that the coil could be powered by one current source. However, for the AMS system it was decided to split each coil into three electrical circuits: with large, medium and small elementary currents (which will still be changed with the same proportionality and are integer multiples of the smallest current). For example, choosing elementary currents as [15A, 5A, 1A], a loop with a current of 73A would be wound as follows:

$$73\text{A} = 4 \times 15\text{A} + 2 \times 5\text{A} + 3 \times 1\text{A}. \quad (7)$$

The choice of the smallest elementary current leads to some imperfection, here on the order of $0.5/73 \approx 0.7\%$ or $0.4 \mu\text{T}$ for $50 \mu\text{T}$, within the requirements of the system. This approach allowed minimization of winding efforts and self-inductance, while keeping the number of current source channels reasonable. In our case, we constructed eight independent coils, each with three circuits for the elementary currents. They are operated by eight current sources, each with three channels for the different currents.

The described method of coil design for an AMS offers advantages over approaches using simple geometric coils, namely in two areas. (1) The size of the coil system can be decreased relative to the size of the sensitive volume. A loss

of performance, e.g., in the homogeneity of a given volume, can always be counteracted by choosing a denser grid. (2) The method allows construction of a coil for any field and the grid geometry that can be chosen almost arbitrarily. In particular, we have chosen to construct coils that produce orthogonal fields. The magnetic field is described as a superposition of orthogonal, cartesian harmonic polynomials:

$$\mathbf{B}(\mathbf{r}) = \sum_{n=1}^{n_{\text{max}}} H_n \mathbf{P}_n(\mathbf{r}). \quad (8)$$

Here H_n are expansion coefficients and $\mathbf{P}_n(\mathbf{r}) = (P_{nx}, P_{ny}, P_{nz})$ are polynomials as defined in Table 1 for the three homogeneous and five first-order gradient fields. Terms of higher n correspond to higher-order gradients. The advantages of this decomposition are that the polynomials are orthogonal and each basis state satisfies Maxwell’s equations. This method was initially considered by Wyszynski [25]. We used this approach to define eight AMS coils: three coils to compensate homogeneous fields, and five to compensate linear magnetic field gradients.

4 The AMS prototype

Before applying the simple-coil method to design and construct the AMS system for n2EDM, we studied a smaller-scale prototype [17, 18] at ETH Zurich (Fig. 5).

4.1 The prototype design and construction

The prototype consisted of the eight types of coils as intended for the AMS system. Similar in specifications, the system was designed to compensate target fields of $\pm 50 \mu\text{T}$ for homogeneous fields, and $\pm 20 \mu\text{T/m}$ for the first-order gradients. It also aimed at a homogeneity of a few μT in the volume of interest.

The prototype was built on an aluminum-profile frame of $1.3 \text{ m} \times 2.3 \text{ m} \times 1.3 \text{ m}$ in x -, y -, and z -directions, respectively, providing a grid of squares as shown in Fig. 5. The sensitive, fiducial volume for the target fields was chosen to be a cube of $98 \text{ cm} \times 98 \text{ cm} \times 98 \text{ cm}$, placed asymmetrically in y -direction and centered in x and z , as shown in Fig. 6 (grey contour), in which a cubic mu-metal shield could be placed. We kept the $x - z$ side of the frame at $y = 0$ completely open, opposite to the front-side seen in Fig. 5. This enabled easy access to the inside, e.g., to install a magnetic-field mapping device and the mu-metal, and in addition demonstrated the feasibility of designing and building coils with a more complex, irregular geometry.

The mu-metal cube in the prototype served as the emulation of the MSR of n2EDM concerning the fields on its out-

Fig. 4 Illustrations of the method of simple coil design [24]. Left: Initial definition of the grid (bold tiles) around points of interest (blue dots). Right: a set of simple loops (different colors) obtained in the course of simple coil design, representing the current paths needed to create the desired field (here: homogeneous in the indicated direction). Numbers and arrows indicate values of the currents and their directions in the corresponding loops. More details can be found in [17]

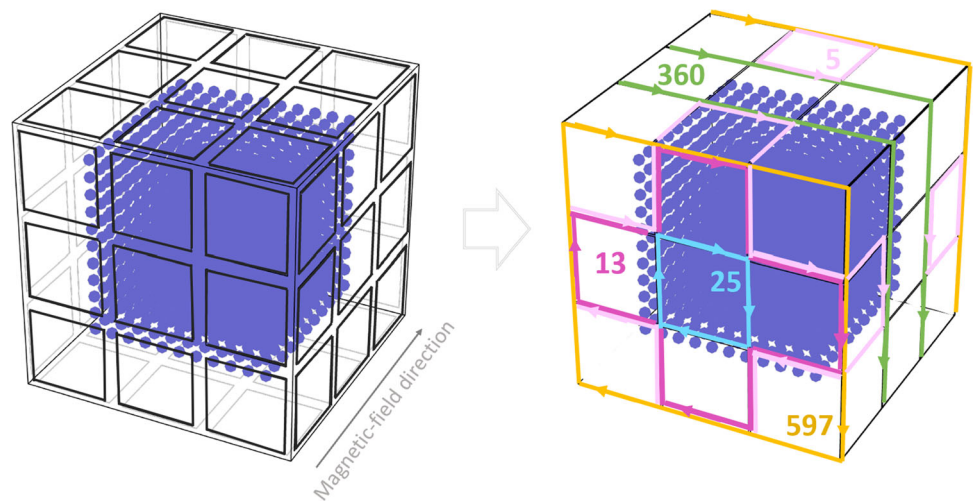


Table 1 List of the Cartesian harmonic polynomials and associated names of the individual coils

Coil	n	P_{nx}	P_{ny}	P_{nz}
x	1	1	0	0
y	2	0	1	0
z	3	0	0	1
G ₁	4	x	0	-z
G ₂	5	y	x	0
G ₃	6	0	y	-z
G ₄	7	z	0	x
G ₅	8	0	z	y

side. Its purpose was not to be an efficient magnetic shield but rather to provide a mu-metal surface to affect the fields between the mu-metal and the coil cage. It can be demagnetized using a set of demagnetization coils wound through the cube.

The design method restricted the wires of the coil system to take paths on the grid, similar to the ones shown in the right panel of Fig. 4. As described in Sect. 3.1, each of the coils used three circuits with different values of maximal currents (here: 5, 1, and 0.2 A). In total, eight current sources, each feeding three circuits, were used to provide all eight coils with their currents.

As an example, Fig. 6 shows a simulation of the y-component of the magnetic field produced by the homogeneous y-field coil of the prototype in the x - y midplane. The map depicts deviations of the magnetic field from the target value of 50 μT. The designed and predicted homogeneity of the field did not exceed a few μT in the sensitive volume. Similar results were obtained for all the coils.

4.2 Performance of the prototype

Validation of the AMS fields We built a mapper robot carrying a movable three-axis fluxgate sensor to automatically mea-



Fig. 5 Photo of the AMS prototype [17,18] mounted in the ETH laboratory. The smaller side of the frame, facing the window as seen on the photo, was kept open without windings – to allow easy access to the inside of the system

sure the magnetic field in a large part of the volume inside the coil cage. In a first characterization, the static performance of the prototype was assessed by comparing the predicted and the measured fields for each coil. As an example, Fig. 7 shows measurement results for the magnetic field produced by the first-gradient coil G₁ (as defined in Table 1) at the central x - z plane, at y = 115 cm. As expected, the coil produces mainly B_x and B_z components of the field. The deviation of the measured fields from the target values do not exceed a few μT, which was the design goal and have been confirmed for all coils.

Dynamic field stabilisation As a next step, we implemented a dynamic field stabilisation to actively suppress variable

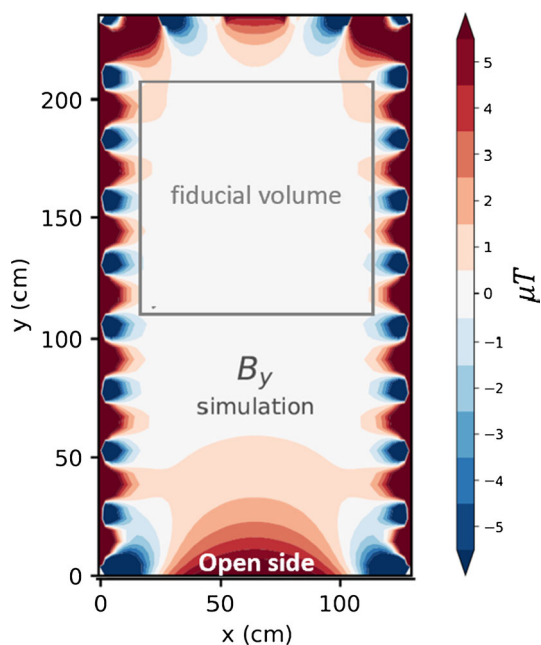


Fig. 6 Simulation of the y-component of the magnetic field produced by the y-coil of the AMS prototype in the x–y midplane. Shown are deviations of the magnetic field from the target value of $50 \mu\text{T}$. The grey contour depicts the volume of a removable cubic mu-metal shield, which was not considered in the simulation. Figure is adapted from [17]

magnetic-field perturbations. This mode is based on continuous monitoring of the magnetic-field changes by fluxgate sensors with $\pm 200 \mu\text{T}$ range, 1 kHz bandwidth, and $\pm 0.5 \mu\text{T}$ accuracy. The sensors were mounted around the volume of interest and a dedicated DAQ system, based on Beckhoff EtherCAT modules [26], was used to read their outputs, and to control the coil currents [17].

The dynamic mode of operation relies on the quality of the feedback matrix \mathbf{M} (Eq. 1), which itself strongly depends on the number and positioning of the fluxgates, requiring opti-

mization. The optimization without mu-metal is straightforward. It is somewhat more challenging with mu-metal due to its strong position-dependent impact on the magnetic field in its vicinity. The magnetic fields of the setup with the mu-metal cube were simulated with COMSOL [27] and validated by measurements. With these simulations, the condition number (see Sect. 3.1) of the feedback matrix \mathbf{M} could be minimized by selecting proper positions for the feedback sensors.

It was found that sufficiently stable performance can be reached with eight sensors placed close to the corners of the mu-metal. This fits well the intuitive understanding of the effects of mu-metal. Close to the surface of the mu-metal, field components parallel to the surface will be small while the orthogonal component remains. As the fluxgate magnetometers used for feedback are three-axis devices, this would mean that a fluxgate aligned near a large flat surface can measure the orthogonal field well with one axis, while two axes provide relatively little useful information. Thus, positioning fluxgates closer to mu-metal edges and corners turns out to be more informative.

With the fluxgates mounted at their optimal positions, the feedback matrix was determined by measuring the magnetic-field components while scanning each coil current separately over the whole available range. For fields up to $\pm 50 \mu\text{T}$, relevant here, the response was found to be linear. The slopes, obtained by linear regressions for each spatial field component versus current, correspond to the elements of the matrix \mathbf{M} . They are displayed in Fig. 8 for the eight 3-axis sensors and eight coils.

Shielding performance of the AMS prototype The obtained feedback matrix was used to operate the AMS in dynamic-stabilization mode. To test this regime, magnetic-field perturbations can be generated using a coil placed at some location around the setup. For this measurement, the square excitation coil with sides around 1 m was used. The coil was oriented

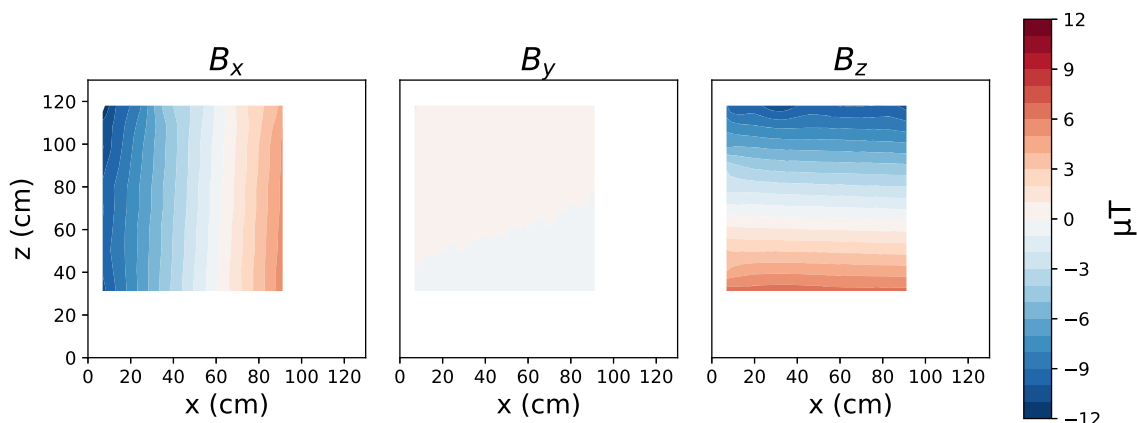


Fig. 7 The map of the magnetic field produced by the first-gradient coil of the AMS prototype (G_1 , as defined in Table 1), measured at the central x–z plane at $y = 115 \text{ cm}$. Adapted from [17]

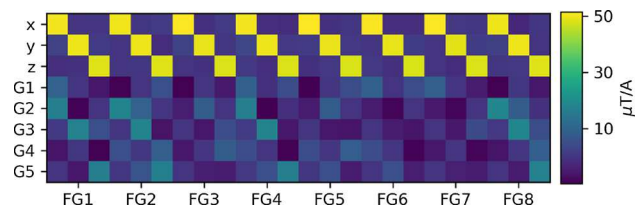


Fig. 8 Visualization of the feedback matrix M (see Eq. 1 and [17]). The rows designate the coils of the AMS prototype and the columns correspond to the absolute readings in x , y and z directions of the eight fluxgates (FG)

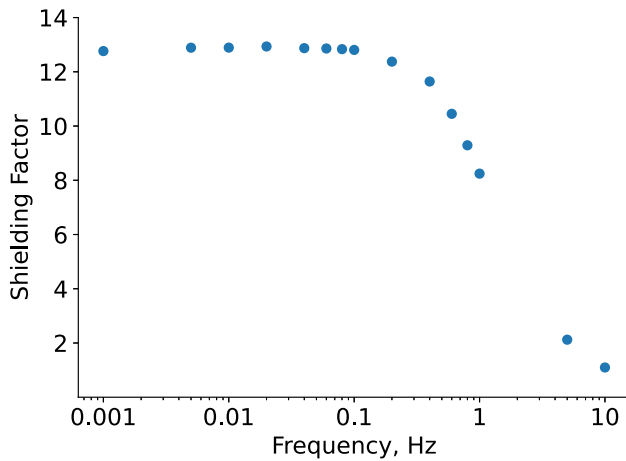


Fig. 9 Frequency-dependent shielding factor of the AMS prototype along its x direction measured with the perturbation from a square-shaped coil with 1 m side at a distance of about 3 m, producing external sinusoidal fields of different frequencies. Adapted from [18]. See text for details

perpendicular to the x axis and placed at about $x = 3$ m with its center on the y, z coordinate of the center of the sensitive volume. The current source for the coil was modulated with a waveform generator to produce sinusoidal fields, with an uncompensated, maximal amplitude of about $8 \mu\text{T}$ at the central sensor position. The readout bandwidth was 200 Hz and the update rate of the feedback system was around 30 Hz.

The AMS shielding performance was characterized by a shielding factor S , defined as the ratio:

$$S = \frac{B_{\text{center}}^{\text{on}}}{B_{\text{center}}^{\text{off}}}, \tag{9}$$

where $B_{\text{center}}^{\text{on/off}}$ denotes the magnetic-field value at the center of the sensitive volume (corresponding also to the center of the mu-metal cube) with the active compensation on or off, respectively. The mu-metal cube was not used for the particular measurement explained here. In addition to the feedback sensors, one additional sensor to measure B_{center} was mounted.

Figure 9 shows the obtained result for S and its frequency dependence up to 1 Hz. The measured shielding factor stays stable around 12 in the low-frequency range. The decrease of the shielding factor above 100 mHz is from the limited response of the system caused by the inductance of the coils on the aluminum frame of the cage. The frequency dependence of the shielding factor stays the same for similar measurements with the coil positioned at other locations. However, the magnitude of S strongly depends on the distance and orientation of the excitation coil. This can be understood qualitatively, as the magnitude of the higher order gradients of the fields within the sensitive volume depends on distance and orientation of the coil, and cannot in principle be compensated by a first-order AMS. Also, this was quantitatively confirmed using a COMSOL simulation of the system.

In summary, we successfully demonstrated an implementation of the method of simple coil design with the prototype AMS system, achieving the expected static and dynamic performance. The prototype design with an open-side demonstrated that this approach is capable of handling irregular grids, which is important to account for doors and other openings at the n2EDM experiment. Based on this feasibility demonstration, confidence was gained for the design and construction of the much larger AMS for n2EDM.

5 The AMS system for n2EDM

Given the experience with the prototype and the requirements resulting from the mapping of the experimental area, the AMS system for n2EDM was designed. Compared to the prototype, the definition of the grid structure was more constrained by the needs of n2EDM and the available space, much more ampere-turns were necessary for similar field strengths, mechanical stability was more important, and much improved quality control was needed for the construction process.

5.1 AMS coil design

The design of the AMS coil system involved several steps, with iterations: (i) the choice of a surface and a grid on which the coil system could be constructed around the MSR, taking into account all constraints from experimental needs, equipment and area; (ii) finding the currents on the grid structure to create the target homogeneous and first-order gradient fields; (iii) organization of the currents in loops and coils as well as simplification of the optimal solution by the exclusion of (simple loop) currents contributing negligibly within the specified uncertainties.

Grid design Placing the grid structure as far away as possible from the surface of the MSR ensures better field homogene-

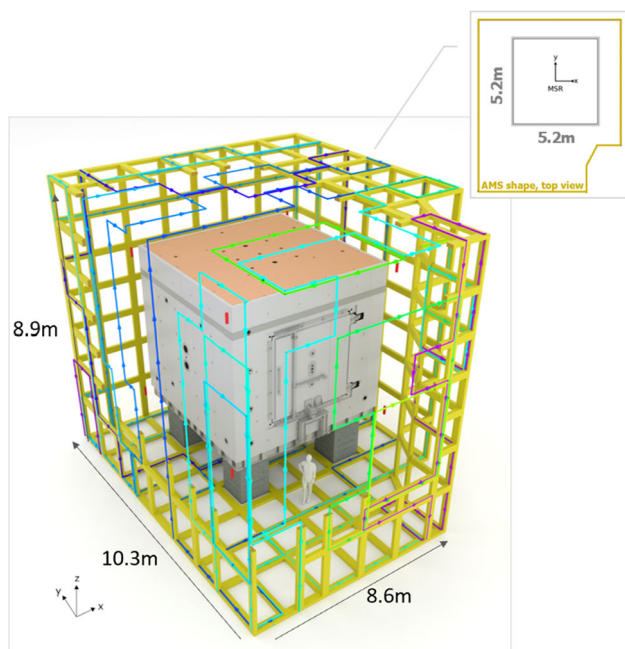


Fig. 10 The AMS grid (in yellow) around the MSR. Part of the grid is not shown in the picture to allow the view onto the MSR. The colored lines represent as an example the main simple loops of the Y-coil

ity. The main limitation was the size of the experimental area. Similarly, the whole experiment, and the MSR in particular, benefits from a clean, temperature-stabilized environment. The n2EDM experiment therefore must be separated from the main experimental hall and requires a thermal enclosure. The solution was the construction of a wooden house (‘thermohouse’), similar in principle to the one of the nEDM experiment [6]. The AMS was planned to be installed on the inside of the walls of the thermohouse, which could then almost fill the experimental area. This way, optimal access to the experimental equipment and the coil system was guaranteed. The power dissipation from the coils was studied and taken into account in the lay-out of the air-conditioning system of the enclosure. It was assumed and later verified that the total the dissipated heat was quite stable for all observed external field conditions, even with dynamically controlled currents of the AMS.

The possibility to fix the AMS to the walls and the roof of the thermohouse simplified its construction, given the mechanical stability of the structure, which was designed to carry the additional, substantial weight of the coils.

Figure 10 shows the final grid of the AMS coil system with dimensions of $10.3\text{ m} \times 8.6\text{ m} \times 8.9\text{ m}$ around the MSR. It has rectangular tiles of around 1.5 m average side-length, with a total of 308 tiles, 473 vertices, and 778 edges.

The process of designing the grid was mainly heuristic and required several iterations. The density of the grid mesh was optimized [18] to achieve the best possible field-homogeneity

around the MSR, while trying to keep the wiring effort reasonable. To make easy access for doors and other openings for the infrastructure of the experiment, we increased the size of tiles when possible or introduced special pieces, called ‘connected doors’ (see Fig. 12). A connected door is a separate grid structure placed on a detachable part, which is electrically part of a coil but, for the optimization of the circuit, topologically separated from the rest of the grid. The design method easily allows such separations. For maintenance, it is then possible to completely detach the connected door making a larger opening to access the experiment.

Given the irregular layout of the experimental area and the thermohouse, the AMS tiles located at the kink in the wall (see Fig. 10, lower right corner of the layout; and Fig. 12 for the top view) would carry high currents while having little effect on the field quality. Such high currents are not ideal for the AMS system: they increase cable thickness and heating effects, requiring bulky cabling and possibly dedicated cooling. To solve this, a regularization procedure was used in the optimization, turning the proportionality equation Eq. (1) into a system of equations:

$$\begin{pmatrix} \mathbf{B} \\ 0 \end{pmatrix} = \begin{pmatrix} \mathbf{M} \\ \lambda \cdot \mathbb{1} \end{pmatrix} \cdot \mathbf{I} \quad (10)$$

where \mathbf{M} is the proportionality matrix, \mathbf{B} is the target magnetic field and \mathbf{I} represents the currents in the tiles. The second equation penalizes large currents. It includes the regularization parameters λ , which must be numerically determined for each coil, so a set of eight λ -values is necessary for the full system. Optimal λ -values should then produce solutions with low total currents and still achieve the performance goal of μT -fields.

An example of the λ optimization for the X-coil is shown in Fig. 11. Increasing λ reduces the mean edge-currents and thus the total current, as expected, while λ -values above 10^{-8} T/A cause the residual from the target field to diverge. The total current is minimal and constant for $\lambda \leq 6 \cdot 10^{-9}\text{ T/A}$. Appropriate values for λ were determined for all eight coils. *Choice of optimization volume* A shell of 20 cm thickness around the outer layer of the MSR was chosen as the volume of interest for the optimization (shown in blue on Fig. 12). In the real system, magnetic-field sensors are installed inside of this shell. The sensors need to be placed at a distance from the mu-metal to work reliably and the target fields need only to be reached close to the MSR surface. Making the volume for the target fields larger would require larger currents and smaller grid spacing for the AMS. Within the shell, the AMS field was numerically evaluated on random POIs, drawn from a uniform distribution. A set of 9600 POIs was used in the performance evaluation. It was checked that the sampling of the MSR surface by these points was sufficiently dense.

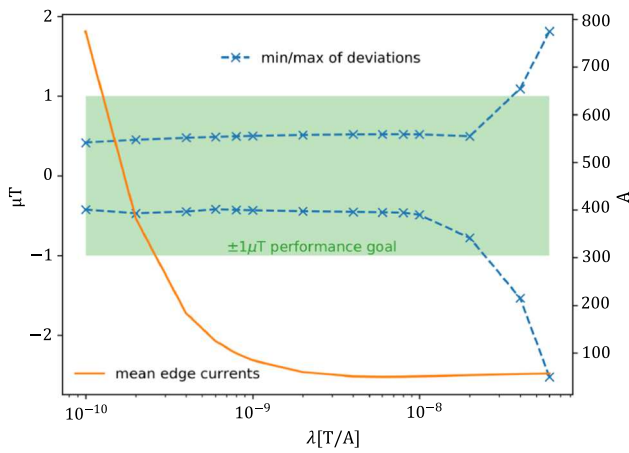


Fig. 11 The largest deviations (‘min’ for negative and ‘max’ for positive) from the target field at the MSR are plotted against the λ -parameter for the procedure of optimizing currents of the X-coil. More details in [18]. A $\pm 1 \mu\text{T}$ performance goal is indicated by the green box. The axis on the right gives the average currents in the edges of the grid and the orange curve shows its decrease with increasing λ

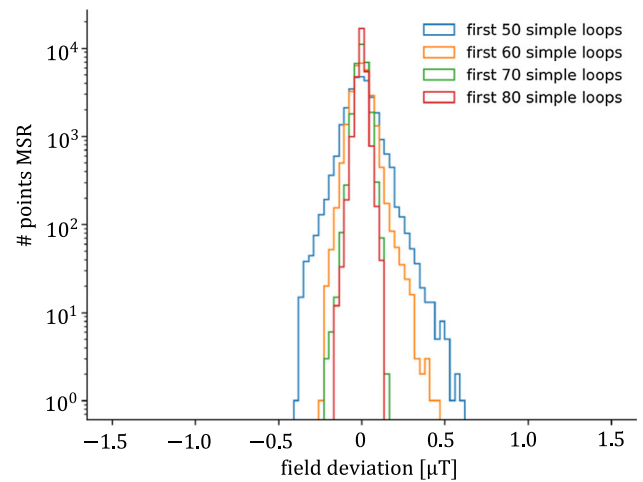


Fig. 13 Histogram of the residual fields around the MSR for different numbers of most important simple loops used in the 4th gradient coil of the system. Adapted from [18]

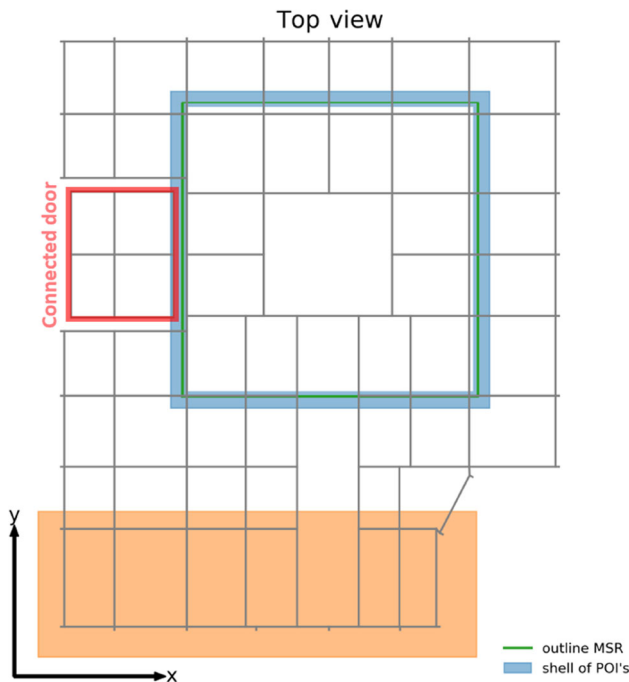


Fig. 12 Schematic top view of the AMS grid. A connected door is shown in red. The volume of the POI is indicated in blue around the MSR (green). The orange area depicts part of the AMS, which has only a minor impact on the field homogeneity around the MSR. Adapted from [18]

Final adjustments The application of our method of coil design (Sect. 3.3) yields a large number of simple loops on the predefined grid. These loops are not all equally important for the performance of the AMS. For the practical implementation, the number of loops can be reduced as long as the

target fields can be achieved. The initial set of simple coils was ordered by importance with respect to the field intensity they produced in the volume of interest. The performance of the system was then recalculated for configurations where subsequently the least important simple loops were left out.

As an example, Fig. 13 shows a comparison of the residual fields at the POI close to the MSR for different numbers of the most important loops of the 4th gradient coil. The target field for the gradients is $5 \mu\text{T}/\text{m}$ and residuals refer to the ‘full field’ configuration producing this gradient. The best solution for this coil had 123 simple loops. However, the performance stays close to optimal down to a reduced number of the 70 most important loops. This procedure was used for all eight AMS coils, yielding a reduction of 40% in the total number of simple loops while still reaching the target fields.

Complete system The final design of the AMS system comprises eight coils matched to the optimized grid. Each of the coils consists of 50–70 simple loops to achieve the target fields. An example of a subset of the main simple loops of the Y-coil is shown in Fig. 10. As in the prototype, each coil consists of three electrical circuits with large, medium, and small elementary currents. This minimized wiring effort, total weight, and power dissipation, while keeping the number of current sources at a manageable level. Table 2 summarizes the chosen elementary currents and the numbers of simple loops for all coils.

The calculated residual fields from the target field of the finalized coils are shown in Fig. 14 for the so-called ‘full-field’ configuration, in which all coils are powered to simultaneously produce the homogeneous fields of $50 \mu\text{T}$ in each spatial direction as well as the five $5 \mu\text{T}/\text{m}$ gradients, see Tab. 1. Each coil was designed individually to compensate one of these eight basis fields. Due to the discretization and

Table 2 Values of the three elementary currents I and numbers of simple loops N for the eight coils of the final AMS design

Coil	Currents I	N loops
X	15A/5A/1A	59
Y	15A/5A/1A	68
Z	15A/5A/1A	60
1G	10A/3A/1A	50
2G	12A/5A/1A	69
3G	15A/4A/1A	60
4G	8A/3A/1A	70
5G	12A/5A/1A	69

the simplification inherent to the design method, the fields generated by the coils slightly deviate from their target fields, within the allowed ranges. Such deviations will add up (vectorially) when operating the coils together. Large deviations do not usually occur at the same place and in the same directions, they appear rather more randomly, leading even to some ‘cross compensation’, with the result displayed in Fig. 14. The residual of each coil’s field from its target value can itself be represented as an expansion in the same basis fields produced by the other coils (plus neglected higher-order fields). Therefore, when measuring the response matrix for the built system, these effects are taken into account automatically.

Other, potentially important aspects of the real-world AMS system are the unavoidable imperfections of the current paths. One of these issues arises from the bending of cable bundles at each vertex. Obviously, these are not 90° corners but require bending radius up to 10 cm. Another imperfection is the position of the wires in the bundles with respect to the ideal grid. On some edges of the system, the area

crossed by all cables was up to 80 cm^2 ; necessarily some wires are displaced by several cm from their ideal position. All these effects were simulated and in all cases we concluded that they were tolerable or even negligible. Again, aforementioned cross-compensation helps considerably: while a coil might slightly deviate from its ideal performance, it will still be completely linearly independent of the other seven coils and the system can function almost equally well.

5.2 The AMS technical implementation

The AMS coil system was mounted in the thermohouse of n2EDM over the course of approximately one year. An overview of the construction process is presented here, while more details are found in Ref. [18]. Figure 15 shows a picture of the finalized system.

The AMS grid structure was formed by cable trays out of stainless steel, mounted directly onto the inner walls of the wooden thermohouse around the MSR. The cable trays were grounded in a way to inhibit closed loops and eddy currents through the trays. In order to mount the coils of Table 2 efficiently onto the grid (Fig. 10) along their calculated paths, one could not simply wind long cables. Instead, cables of a simple loop were bundled and installed on the cable trays along the roughly 500 different paths. The ends of the wires of the bundles were carefully crimped to form the loops. All the simple loops for each elementary current were connected in series such that a ‘coil’ consisted of three independent circuits. The installation of a bundle carefully followed a detailed plan, connecting it at some start position in the thermohouse and following a prescribed path along numbered vertices. The start and the end position of the circuits were later connected to terminals on DIN rails, which themselves were connected appropriately with interconnection wires. At each vertex of

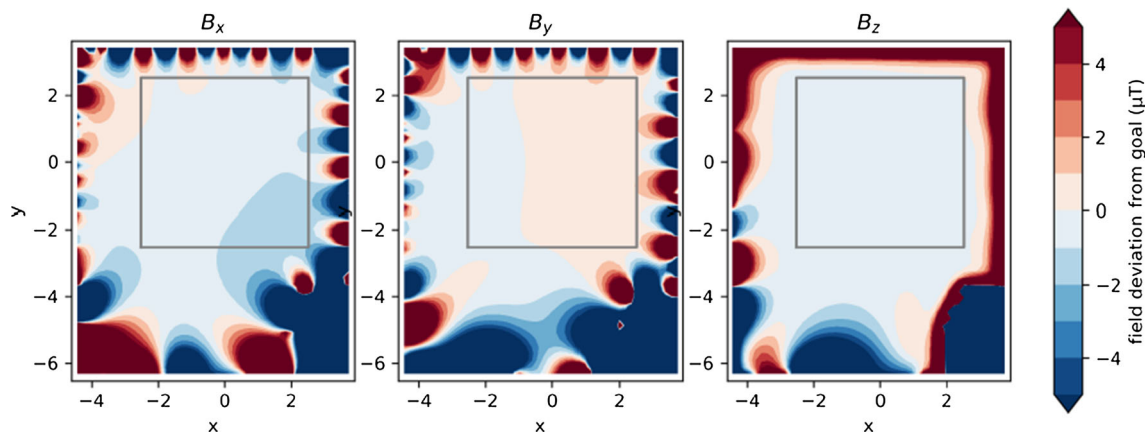


Fig. 14 Two-dimensional maps of the calculated magnetic-field residuals at $z = 0$, which is the vertical center of the MSR. The x and y coordinates are given in meters. The outline of the MSR is depicted

as a gray square. The residuals are plotted for the full field in all coils including cross compensation, see text. Adapted from [18]



Fig. 15 Photograph of the AMS coil system constructed on the walls of the thermohouse around the MSR. On the right-hand side, in the middle tiles, and on the back-side to the left of the MSR, a few DIN rails are visible which are wired to connect circuits, as explained in the main text. Of course, the AMS extends fully around the MSR, also on the entire floor. The platform visible in front of the MSR is about 2.5 m above floor level

the grid the correct direction had to be checked, going straight or around a corner. A system of bar-codes on the wires and QR-codes near the vertices on the walls, both completed with human-readable names, along with a dedicated smartphone scanning-app, were developed for a continuous verification and quality control during the installation. Completed circuits were electrically checked and DC resistances were measured to guarantee quality of crimp connections. This way, a total of 55 km of wire was installed, without any indications of error.

5.3 AMS current sources

To power the AMS coils, we have designed and built bipolar high-power current sources in-house at PSI, based on APEX-PA93 linear operational amplifiers [28].

Each current source consists of three channels, delivering the elementary currents to the corresponding three circuits of a coil (Fig. 16). The currents of all three channels change proportionally to their control voltages, which can be set in the range from -10 to 10 V. This allows for an efficient realization of the three-fold powering approach described in Sect. 3.3. For coils with different design currents (see Table 2) the software will command them with properly reduced values. Depending on the channel, up to six APEX amplifiers were connected in parallel and complemented by a system of matched resistors to deliver the required output current and distribute the power dissipation. An internal stabilization network combined with external damping resistors enables the current source to drive inductive loads up to 1 H. This is important because although the self-inductance of the coils

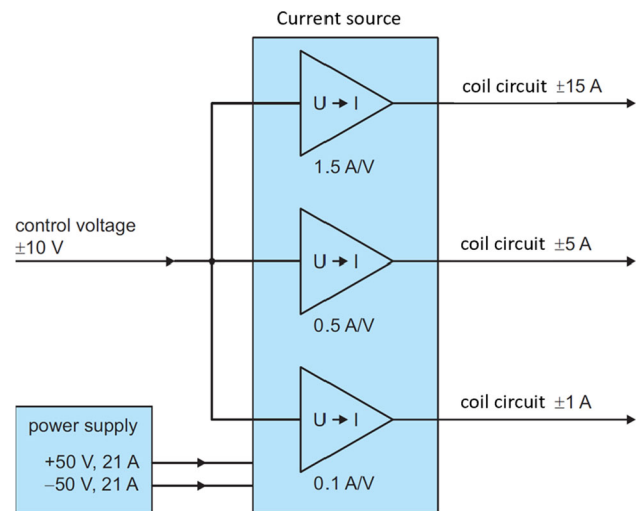


Fig. 16 Simplified scheme of the bipolar current source, developed to power AMS coil. Each current source consists of three channels (here: 15, 5 and 1 A), with their output currents proportionally to their individual control voltage

ranges only from 3 to 75 mH, their mutual inductance is up to 500 mH.

Each of the current sources is supplied with ± 50 V from an external switching power supply with a large filter capacitor to ensure a low-noise level of operation. The total heat dissipation in each of the current sources can reach up to 500 W, which is removed by an efficient built-in cooling system.

As part of the performance verification of the current sources, they were connected to the coils and their responses measured to a square-shaped input signal with the maximum amplitude of 10 V. The output signals reached their maxima with typical time constants of approximately 80 ms, fast enough for dynamic AMS operation in the sub-Hertz frequency range, as required.

5.4 Fluxgates sensors

Eight 3-axis SENSYS fluxgate sensors [29] were installed around the MSR to measure the magnetic field and provide feedback information for the dynamic mode of the AMS. The initial optimization of their positions was carried out similarly to the one of the prototype (Sect. 4.2) and positions close to the corners of the MSR were found.

In Sect. 6.2, results of the dynamic shielding performance are reported, based on these positions of the fluxgates and the control system, described in the next section.

5.5 Control system

The control system is based on Beckhoff modules ELM3148 (24 bit ADCs) and EL4134 (16 bit DACs) operating at 1 kHz. The readings from all fluxgate channels are stored in

the array \mathbf{B}_m that has up to 51 entries. There is a minimal delay of two cycles for any reaction. Thus, the currents I of the next cycle $[i + 1]$ are calculated as:

$$I[n + 1] = I[n] + k \times (M^{-1} \times (B_t - B_m[n - 1])), \quad (11)$$

where B_t is the target field, normally chosen as 0. The feedback matrix M^{-1} is the pseudo-inverse (calculated offline as explained in Eq. (4)) of the response matrix M . The latter is obtained by scanning all coil currents individually and analysing their response by linear regression (as described in Sect. 4.2). A multiplication constant k slows down the feedback to avoid oscillations. We use the same value of 0.013, found empirically, for all eight coils. This results in a characteristic time constant of about 50 ms. A faster operation is prevented by the current sources, but was never intended.

While the performance is satisfactory already, potential improvements will be studied once commissioning of other n2EDM subsystems, which it would interfere with, is completed. A more detailed simulation model with improved utility for various numerical studies is being deployed, additional fluxgate sensors are being installed, and further optimization of sensor positions and feedback algorithms pursued.

6 The AMS performance measurements

After the installation and the commissioning of all AMS coils and power supplies, we validated the static magnetic-field generation and measured the shielding performance of the AMS, as described below.

6.1 Magnetic fields generated by the AMS coils

As the MSR was installed in the experimental area before the AMS system, the actual magnetic fields generated by the AMS coils are not the simple homogeneous and first-order gradient fields as designed, but are modified by the MSR.

Thus, after the quality control described in Sect. 5.2, which guaranteed the proper pathways for the currents, actual magnetic-field measurements were compared to results of a FEM simulation model implemented in COMSOL [27]. We used the design fields as imported background fields and the outermost mu-metal surface of the MSR as a 10 cm thick layer of high magnetic permeability. It was verified that above a certain permeability and thickness, the results of the simulation became independent of these details.

As the experimental area around the AMS was already partially occupied by other equipment after its completion, magnetic-field measurements around the MSR had to be done in a sampling mode rather than in form of full field maps (as described for the empty area in Sect. 2).

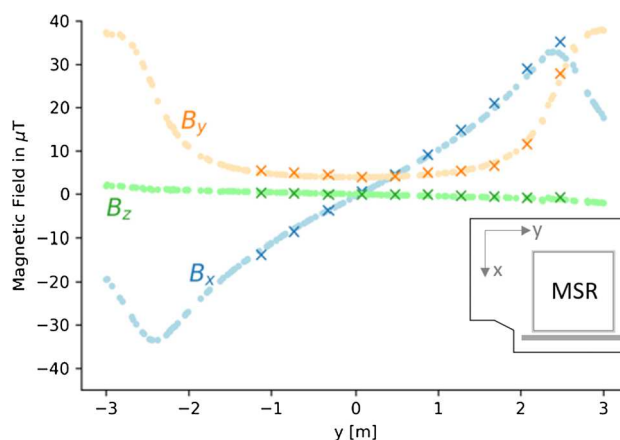


Fig. 17 Example of an AMS validation measurement: comparison between the measured (crosses) and the simulated (dotted line) magnetic field values for B_x , B_y , and B_z components produced by the Y-coil. The measurements were taken along the grey line in the inset (y -direction) at $z = -1$ m. Adapted from [18]

The magnetic fields created by individual coils were measured in some selected, easily accessible areas, usually along a straight aluminum profile with one fluxgate, and compared to the simulation. Figure 17 shows an example of such a comparison. The measured and the simulated magnetic-field values for the B_x , B_y and B_z components produced by the Y-coil are shown. The current of the Y-coil was pulsed on and off for the measurement to enable proper background-field subtraction. The coil current was chosen to be half of the maximum current. The measurements were taken along the grey line shown in the inset, at a height of $z = -1$ m (below the center of the MSR) in the y -direction at a distance of about 20 cm from the MSR surface.

The result of the measurement agrees with the simulations, and the behaviour of the magnetic-field components is as expected for this example. The design field at the sampled positions without MSR would only have a B_y component, with $B_x = B_z = 0$. One can see this feature emerging for large positive and negative values of y . While the non-existent B_z component is unaffected by the mu-metal shield, the B_y component gets absorbed into the mu-metal by drawing it into the B_x component with maximal amplitude at the edge of the MSR around $y \approx -2.8$ m. A similar qualitative and quantitative agreement was observed for the other coils, which confirms a good understanding of the AMS coil system as built.

6.2 AMS shielding measurements

Commissioning measurements of the dynamic AMS shielding were performed outside and inside the MSR during ramps of the superconducting high magnetic-field facility ‘SULTAN’ [30]. Magnets of this facility were already of concern to

the predecessor nEDM experiment [6]. The facility is about 30 m away from the n2EDM experiment. Its magnets can ramp up to 11.5 T, producing fields up to 40 μT at the MSR front and back walls mainly in horizontal direction with the AMS system off.

The magnetic fields outside the MSR were measured by the eight 3-axis SENSYS fluxgates [29] involved in the feedback, as previously described, and by several additional monitor fluxgates. The magnetic field inside the MSR was measured by a much more sensitive optically-pumped QuSpin magnetometer (Gen3, zero-field configuration) [31]. It was placed roughly at the center of the MSR with one of its two sensitive directions along the z -axis, the most relevant for nEDM measurements, and the other one was oriented along the direction of the largest SULTAN perturbation. A second QuSpin sensor, installed close to the first one, was used to ensure that field changes could be identified as such and readings of one sensor were not simply due to sensor drift.

Figure 18 shows magnetic-field values measured during the SULTAN ramps with the AMS in static mode and dynamic mode, respectively. In static mode, Fig. 18a, the background field was compensated only approximately some time before the ramp, keeping AMS currents constant. Thus, the initial spread of the fluxgate readings was not illustrating an optimal zero-field setting. During the SULTAN ramp, the measured magnetic field changed from several μT up to roughly 100 μT , depending on the positions of the fluxgates. The fluxgates positioned near the corners of the MSR, fields get amplified and are at some points much larger than in the empty-area mapping (Sect. 2). When the AMS system is operated in dynamic mode, Fig. 18b, the corresponding magnetic-field changes in the feedback fluxgates are reduced to a level of a few μT .

The measurements with the QuSpin sensor, shown in Fig. 18c, additionally show the passive shielding of the MSR. As determined with the earlier mapping campaign, the field variation from the SULTAN ramp at the location of the QuSpin sensor would be about 40 μT without the MSR. A rough analysis of the magnetic field as measured by the QuSpin inside the MSR, during the ramps, found field changes of about 60–80 pT. This would correspond to a quasi-static shielding factor of the MSR of roughly $(5 - 7) \times 10^5$. It is well known that the magnetic-shielding performance of such magnetic shields improves for larger field variations due to the increase of permeability μ_r for larger magnetic-field strength H until saturation effects set in. It is therefore very important to describe the excitation field when quoting a shielding factor. For this particular example, the MSR of n2EDM has a quasi-static shielding factor of 1×10^5 for an excitation field corresponding to $\pm 2 \mu\text{T}$ at the unshielded sensor location [22]. This is the relevant shielding factor for n2EDM, as μT -size perturbations will still be possible, even with a perfectly functioning AMS.

When the AMS system is in dynamic mode, the QuSpin sensor measures a more attenuated signal, see Fig. 18d. The amplitude of this remaining field change is about 8 pT, a factor of 7–10 smaller, compared to the SULTAN ramp when the AMS is in static mode. It is, however, not straightforward to take this as the shielding factor of the AMS system alone, as we just saw that the passive, quasi-static shielding performance of the MSR depends on the size of field perturbations on the shield, which in turn depends on AMS performance.

Nevertheless, we can deduce the approximate shielding factor for the combined system of the AMS and the MSR for large and slowly changing perturbations (here a one-hour ramp to 40 μT) as 5×10^6 . More importantly, the result demonstrates that the goal of suppressing field changes down to below 10 pT inside the MSR was achieved, which was set up as a requirement for the n2EDM experiment.

Another interesting observation from the comparison between Fig. 18c, d is that at least in this set of measurements it appears that the larger field variation on the outside of the MSR in the static case caused the field inside of the MSR to drift more, about 30–40 pT, compared to the dynamic case with a drift of less than 10 pT. One can see, that the drift following the ramp-up in (c) is opposite to the induced change, while the drift following the ramp-down is in opposite direction. This is expected from the reaction of the mu-metal layers of the MSR to the perturbation. Such drifts are part of unwanted behaviour of a passive magnetic shield, which, when exposed to large external field variations, slowly absorbs the remanent field until it reaches the state of lowest energy. The AMS system largely reduces the impact of such effects.

7 Summary

The AMS system was designed and built to compensate homogeneous and first-order gradient external magnetic-field changes around the MSR of the n2EDM experiment. It was developed using a novel method of coil design. After successful prototyping at ETH Zurich, the AMS system was constructed and commissioned at the n2EDM experiment at PSI. First performance measurements demonstrated its ability to suppress magnetic-field changes of about $\pm 50 \mu\text{T}$ (homogeneous) and $\pm 5 \mu\text{T/m}$ (first-order gradients), to the level of a few μT . The optimization of the AMS system using measurements and improved simulations, e.g., concerning fluxgate positioning and feedback algorithm, is ongoing and might further improve its performance. In any case, with the performance demonstrated in this paper, the combined system of AMS and MSR meets the specifications of the n2EDM experiment, providing a magnetic-field stability within the neutron volume at the 10 pT level.

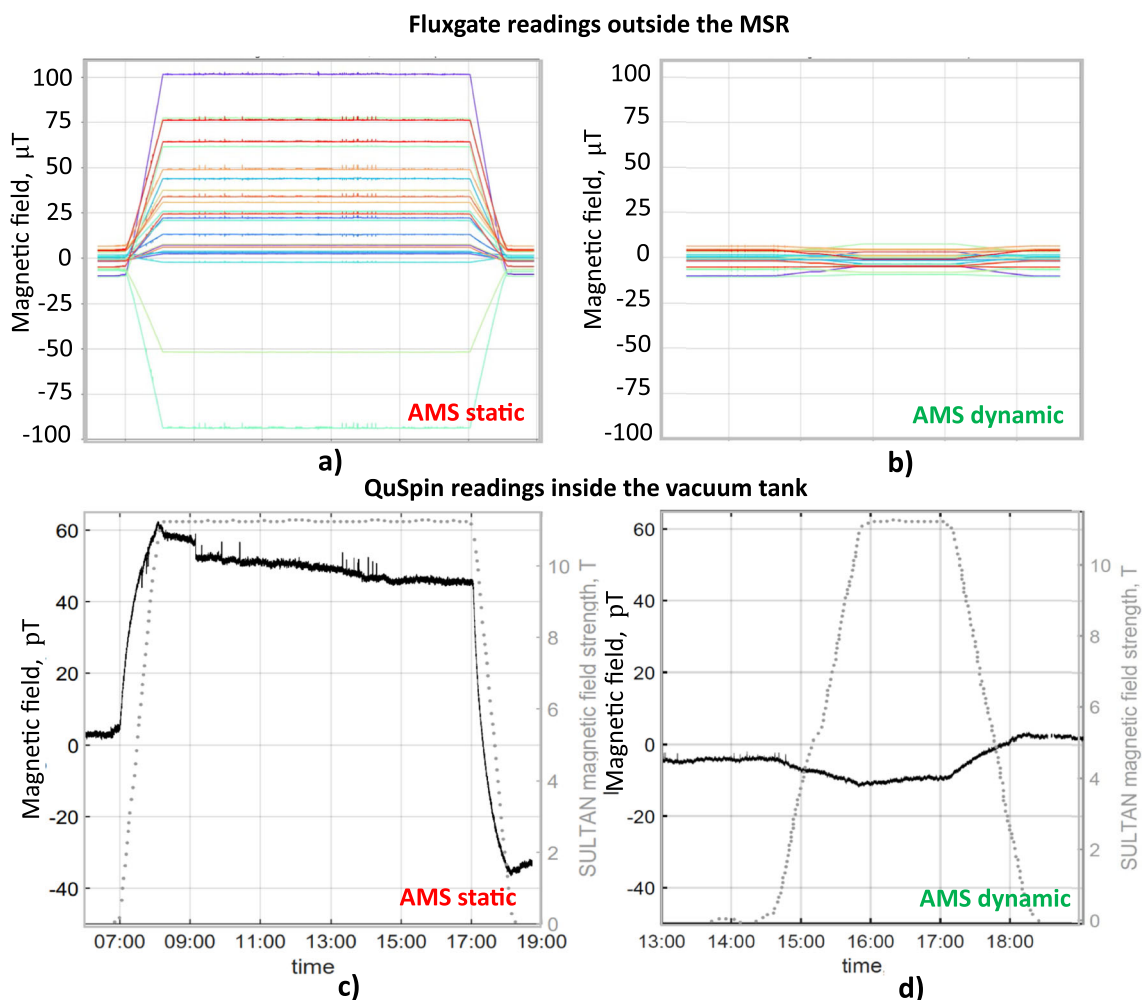


Fig. 18 The AMS suppression of magnetic fields from SULTAN: **a, b** magnetic fields measured by the feedback fluxgates outside the MSR during two different SULTAN ramps with the AMS system in static (**a**) and dynamic (**b**) modes; **c, d** the magnetic fields of the SULTAN magnet

for the two ramps (dotted grey line, right scale) along with the corresponding magnetic field measured by an optically-pumped (QuSpin) magnetometer [31] inside the MSR (black line, left scale)

Acknowledgements We gratefully acknowledge the support provided by ETH and PSI technicians, electrical engineers and electricians. In particular, we appreciate the efforts of M. Meier, L. Noorda, A. Angerer, R. Wagner, S. Hug, R. Schwarz, M. Etenreich, L. Künzi, D. Di Calafiori, P. Bryan, E. Hüsler, R. Käch, H. Scheppus. We acknowledge financial support from the Swiss National Science Foundation through projects No. 117696 (PSI), No. 137664 (PSI), No. 144473 (PSI), No. 157079 (PSI), No. 172626 (PSI), No. 126562 (PSI), No. 169596 (PSI), No. 178951 (PSI), No. 181996 (Bern), No. 162574 (ETH), No. 172639 (ETH), No. 200441 (ETH). The group from Jagiellonian University Cracow acknowledges the support of the National Science Center, Poland, Grants no. UMO-2015/18/M/ST2/00056, No. UMO-2020/37/B/ST2/02349, and No. 2018/30/M/ST2/00319, as well as by the Excellence Initiative - Research University Program at the Jagiellonian University. This work was supported by the Research Foundation-Flanders (BE) under Grant no. G.0D04.21N. Collaborators at the University of Sussex acknowledge support from the School of Mathematical and Physical Sciences, as well as from the STFC under Grant ST/S000798/1. We acknowledge the support from the DFG (DE) on PTB core facility center of ultra-low magnetic field KO 5321/3-1

and TR 408/11-1. We acknowledge funding provided by the Institute of Physics Belgrade through a grant by the Ministry of Education, Science and Technological Development of the Republic of Serbia. This work is also supported by Sigma Xi grants # G2017100190747806 and # G2019100190747806, and by the award of the Swiss Government Excellence Scholarships (SERI-FCS) # 2015.0594.

Data Availability Statement This manuscript has no associated data or the data will not be deposited. [Authors' comment: Data is available upon request from the Authors.]

Open Access This article is licensed under a Creative Commons Attribution 4.0 International License, which permits use, sharing, adaptation, distribution and reproduction in any medium or format, as long as you give appropriate credit to the original author(s) and the source, provide a link to the Creative Commons licence, and indicate if changes were made. The images or other third party material in this article are included in the article's Creative Commons licence, unless indicated otherwise in a credit line to the material. If material is not included in the article's Creative Commons licence and your intended

use is not permitted by statutory regulation or exceeds the permitted use, you will need to obtain permission directly from the copyright holder. To view a copy of this licence, visit <http://creativecommons.org/licenses/by/4.0/>.

Funded by SCOAP³. SCOAP³ supports the goals of the International Year of Basic Sciences for Sustainable Development.

References

- G. Pignol, arXiv (2019). <https://doi.org/10.48550/arXiv.1912.07876>
- R. Alarcon et al., arXiv (2022). <https://doi.org/10.48550/arXiv.2203.08103>
- T. Bitter et al., Nucl. Instrum. Methods. Phys. Res. A **309**(3), 521 (1991). [https://doi.org/10.1016/0168-9002\(91\)90257-Q](https://doi.org/10.1016/0168-9002(91)90257-Q)
- M.S. Safronova et al., Rev. Mod. Phys. **90**(2), 025008 (2018). <https://doi.org/10.1103/RevModPhys.90.025008>
- C. Abel et al., Phys. Lett. B **812**, 135993 (2021). <https://doi.org/10.1016/j.physletb.2020.135993>
- S. Afach et al., J. Appl. Phys. **116**(8), 084510 (2014). <https://doi.org/10.1063/1.4894158>
- H.J.M. ter Brake, H.J. Wieringa, H. Rogalla, Meas. Sci. Technol. **2**(7), 596 (1991). <https://doi.org/10.1088/0957-0233/2/7/004>
- V. Kelha et al., IEEE Trans. Magn. **18**(1), 260 (1982). <https://doi.org/10.1109/TMAG.1982.1061780>
- J. Voigt et al., Metrol. Meas. Syst. (2), 239 (2013). <https://doi.org/10.2478/mms-2013-0021>
- D. Spemann et al., Nucl. Instrum. Methods. Phys. Res. B **210**, 79 (2003). [https://doi.org/10.1016/S0168-583X\(03\)01027-9](https://doi.org/10.1016/S0168-583X(03)01027-9)
- T. Bryś et al., Nucl. Instrum. Methods. Phys. Res. A **554**(1), 527 (2005). <https://doi.org/10.1016/j.nima.2005.08.040>
- K. Kobayashi et al., IEEE Trans. Magn. **48**(11), 4554 (2012). <https://doi.org/10.1109/TMAG.2012.2197854>
- K. Jungmann, Ann. Phys. **525**(8–9), 550 (2013). <https://doi.org/10.1002/andp.201300071>
- T. Chupp, M. Ramsey-Musolf, Phys. Rev. C **91**(3), 035502 (2015). <https://doi.org/10.1103/PhysRevC.91.035502>
- C. Abel et al., Phys. Rev. Lett. **124**(8), 081803 (2020). <https://doi.org/10.1103/PhysRevLett.124.081803>
- N.J. Ayres et al., Eur. Phys. J. C **81**(6), 512 (2021). <https://doi.org/10.1140/epjc/s10052-021-09298-z>
- M. Rawlik, Active Magnetic Shielding and axion-dark-matter search. Doctoral Thesis, ETH Zurich (2018). <https://doi.org/10.3929/ethz-b-000273039>
- S. Emmenegger, Next generation Active Magnetic Shielding for n2EDM and axion-like particle search. Doctoral Thesis, ETH Zurich (2021). <https://doi.org/10.3929/ethz-b-000515206>
- B. Lauss, B. Blau, SciPost Phys. Proc. **5**, 004 (2021). <https://doi.org/10.21468/SciPostPhysProc.5.004>
- G. Bison et al., Eur. Phys. J. A **58**(6), 103 (2022). <https://doi.org/10.1140/epja/s10050-022-00747-1>
- B. Lauss, on behalf of the PSI UCN Project Team, Hyperfine interact. **211**(1), 21 (2012). <https://doi.org/10.1007/s10751-012-0578-7>
- N.J. Ayres et al., Rev. Sci. Instrum. **93**(9), 095105 (2022). <https://doi.org/10.1063/5.0101391>
- C.P. Bidinosti, J.W. Martin, AIP Adv. **4**(4), 047135 (2014). <https://doi.org/10.1063/1.4873714>
- M. Rawlik et al., Am. J. Phys. **86**(8), 602 (2018). <https://doi.org/10.1119/1.5042244>
- G. Wyszynski et al., AIP Adv. **7**(3), 035216 (2017). <https://doi.org/10.1063/1.4978394>
- Beckhoff | New Automation Technology. <https://www.beckhoff.com/>
- COMSOL AB. COMSOL Multiphysics®. <https://www.comsol.com/>
- Apex Microtechnology. <https://www.apexanalog.com/>
- SENSYS GmbH. <https://sensysmagnetometer.com/>
- J. Elen et al., IEEE Trans. Magn. **17**(1), 490 (1981). <https://doi.org/10.1109/TMAG.1981.1060978>
- QuSpin: An Atomic Devices Company. <https://quspin.com/>

What can a GNOME do?

Search targets for the Global Network of Optical Magnetometers for Exotic physics searches

S. Afach,^{1,2} D. Aybas Tunturk,³ H. Bekker,^{1,2} B. C. Buchler,⁴ D. Budker,^{2,1,3} K. Cervantes,⁵ A. Derevianko,⁶ J. Eby,⁷ N. L. Figueroa,^{2,1} R. Folman,⁸ D. Gavilán Martín,^{2,1} M. Givon,⁸ Z. D. Grujić,^{9,10} H. Guo,¹¹ P. Hamilton,¹² M. P. Hedges,⁴ D. F. Jackson Kimball,^{5,*} S. Khamis,¹² D. Kim,^{13,14,†} E. Klinger,^{1,2,‡} A. Kryemadhi,¹⁵ X. Liu,¹¹ G. Łukasiewicz,¹⁶ H. Masia-Roig,^{2,1} M. Padniuk,¹⁶ C. A. Palm,⁵ S. Y. Park,^{17,§} H. R. Pearson,¹⁷ X. Peng,¹¹ M. Pospelov,^{18,19} S. Pustelny,¹⁶ Y. Rosenzweig,⁸ O. M. Ruimi,²⁰ T. Scholtes,^{9,21} P. C. Segura,^{17,¶} Y. K. Semertzidis,^{14,13} Y. C. Shin,¹⁴ J. A. Smiga,^{2,1,**} Y. V. Stadnik,²² J. E. Stalnaker,¹⁷ I. A. Sulai,²³ D. Tandon,¹⁷ K. Vu,⁵ A. Weis,⁹ A. Wickenbrock,^{2,1} T. Z. Wilson,^{5,††} T. Wu,¹¹ W. Xiao,¹¹ Y. Yang,^{11,24} D. Yu,¹¹ F. Yu,²⁵ J. Zhang,¹¹ and Y. Zhao¹¹

¹*Helmholtz-Institut, GSI Helmholtzzentrum für Schwerionenforschung, Mainz 55128, Germany*

²*Johannes Gutenberg University, Mainz 55128, Germany*

³*Department of Physics, University of California at Berkeley, Berkeley, California 94720-7300, USA*

⁴*Research School of Physics, Australian National University, Canberra ACT 2601, Australia*

⁵*Department of Physics, California State University – East Bay, Hayward, California 94542-3084, USA*

⁶*Department of Physics, University of Nevada, Reno, Nevada 89557, USA*

⁷*Kavli Institute for the Physics and Mathematics of the Universe (WPI),*

The University of Tokyo Institutes for Advanced Study,

The University of Tokyo, Kashiwa, Chiba 277-8583, Japan

⁸*Department of Physics, Ben-Gurion University of the Negev, Be'er Sheva 84105, Israel*

⁹*Physics Department, University of Fribourg, CH-1700 Fribourg, Switzerland*

¹⁰*Institute of Physics Belgrade, Pregrecica 118, Belgrade 11080, Serbia*

¹¹*State Key Laboratory of Advanced Optical Communication Systems and Networks, Department of Electronics, and Center for Quantum Information Technology, Peking University, Beijing 100871, China*

¹²*Department of Physics & Astronomy, University of California at Los Angeles, Los Angeles, California, 90095-1547, USA*

¹³*Department of Physics, KAIST, Daejeon 34141, South Korea*

¹⁴*Center for Azion and Precision Physics Research, IBS, Daejeon, 34051, South Korea*

¹⁵*Dept. Computing, Math & Physics, Messiah University, Mechanicsburg PA 17055, USA*

¹⁶*Marian Smoluchowski Institute of Physics, Jagiellonian University, Łojasiewicza 11, 30-348, Kraków, Poland*

¹⁷*Department of Physics & Astronomy, Oberlin College, Oberlin, Ohio 44074, USA*

¹⁸*School of Physics and Astronomy, University of Minnesota, Minneapolis, MN 55455, USA*

¹⁹*William I. Fine Theoretical Physics Institute, School of Physics and Astronomy, University of Minnesota, Minneapolis, MN 55455, USA*

²⁰*Racah Institute of Physics, Hebrew University of Jerusalem, Jerusalem 9190401, Israel*

²¹*Leibniz Institute of Photonic Technology, Albert-Einstein-Strasse 9, D-07745 Jena, Germany*

²²*School of Physics, University of Sydney, Sydney, NSW 2006, Australia*

²³*Department of Physics & Astronomy, Bucknell University, Lewisburg, Pennsylvania 17837, USA*

²⁴*Beijing Institute of Applied Meteorology, Beijing 100029, China*

²⁵*PRISMA+ Cluster of Excellence & Mainz Institute for Theoretical Physics, Johannes Gutenberg University, Mainz 55128, Germany*

(Dated: May 8, 2023)

Numerous observations suggest that there exist undiscovered beyond-the-Standard-Model particles and fields. Because of their unknown nature, these exotic particles and fields could interact with Standard Model particles in many different ways and assume a variety of possible configurations. Here we present an overview of the Global Network of Optical Magnetometers for Exotic physics searches (GNOME), our ongoing experimental program designed to test a wide range of exotic physics scenarios. The GNOME experiment utilizes a worldwide network of shielded atomic magnetometers (and, more recently, comagnetometers) to search for spatially and temporally correlated signals due to torques on atomic spins from exotic fields of astrophysical origin. We survey the temporal characteristics of a variety of possible signals currently under investigation such as those from topological defect dark matter (axion-like particle domain walls), axion-like particle stars, solitons of complex-valued scalar fields (Q-balls), stochastic fluctuations of bosonic dark matter fields, a solar axion-like particle halo, and bursts of ultralight bosonic fields produced by cataclysmic astrophysical events such as binary black hole mergers.

* derek.jacksonkimball@csueastbay.edu

† present address: Mechatronics Research, Samsung Electronics,

I. INTRODUCTION

There are widespread hints from nature suggesting there exist exotic, heretofore undiscovered particles. Perhaps the most prominent hint is the accumulated evidence for dark matter. A leading hypothesis to explain dark matter is that it consists of ultralight bosons such as axions or axion-like particles (ALPs) with masses $m_a \ll 1 \text{ eV}$ [1, 2]. Such ultralight bosonic dark matter (UBDM) can couple to Standard Model particles through a variety of “portals” [3, 4], one of which is the direct interaction of the UBDM field with atomic spins [5, 6]. If such an interaction exists, a UBDM field would generate a spin-dependent energy shift similar to that caused by the Zeeman effect due to an external magnetic field. This opens the possibility of using atomic-spin-based magnetometers [7, 8] to search for UBDM.

Several experiments use atomic magnetometers and nuclear magnetic resonance (NMR) techniques to search for the interaction of UBDM fields with spins [9–20]. The results of these experiments are interpreted using models that assume that the UBDM is a virialized ensemble of non-interacting bosons described by the standard halo model (SHM) [21–23]. These isotropic SHM UBDM models typically ignore any small-scale structure in the dark matter halo, beyond the stochastic fluctuations of the UBDM due to its finite coherence time [24–27]. Thus the sensors in these experiments are assumed to be quasi-continuously bathed in the UBDM field.

The **Global Network of Optical Magnetometers for Exotic physics searches** (GNOME) [28–30] tests a different hypothesis. Perhaps the energy density of the UBDM field is concentrated in large composite structures. In this case, most of the time the Earth would be in a region of space where there is little or no dark matter [31]. In this case, the Earth would only occasionally and briefly pass through dark matter, leading to rare and short-lived signals in dark matter detectors. In principle, a single sensor could detect such transient events. However, it would be exceedingly difficult to confidently distinguish a signal generated by an encounter with a composite UBDM structure from “false positives”. Such false positives can be induced by occasional abrupt changes of sensor operational conditions (such as those due to electronic noise

spikes, laser mode hops, or vibrations). The GNOME is a time-synchronized array of atomic magnetometers, widely distributed geographically (Fig. 1). The design of GNOME enables vetoing of false positive events, suppression of uncorrelated noise, and confident identification of transient signals attributable to exotic, beyond-the-Standard-Model physics.

In this paper, we review a variety of theoretical models describing sources of transient signals potentially detectable with GNOME. We focus in particular on phenomenological descriptions of the temporal characteristics of the signals that would manifest in the GNOME sensors, which informs our data-analysis strategies.

II. INTERACTIONS BETWEEN ATOMIC SPINS AND ULTRALIGHT BOSONIC FIELDS

The optical atomic magnetometers (OAMs) [7, 8] comprising GNOME are sensitive to interactions of atomic spins \mathbf{F} with hypothetical exotic fields $\mathbf{\Upsilon}$, as well as magnetic fields \mathbf{B} , where \mathbf{F} is the total atomic angular momentum. For the exotic spin-dependent interactions considered here, the Hamiltonian has the form:

$$\mathcal{H}_{\Upsilon} = - \sum_{i=e,p,n} g_{\Upsilon i} \frac{\mathbf{S}_i}{|\mathbf{S}_i|} \cdot \mathbf{\Upsilon} = - \sum_i g_{\Upsilon i} \sigma_i \frac{\mathbf{F}}{|\mathbf{F}|} \cdot \mathbf{\Upsilon}, \quad (1)$$

where $g_{\Upsilon i}$ is the coupling constant characterizing the interaction of $\mathbf{\Upsilon}$ with the fermion spin [where the fermions considered include electrons ($i = e$), protons ($i = p$), and neutrons ($i = n$)], σ_i is the fractional fermion spin polarization for a given atom (see the Supplemental Material in Ref. [30]), \mathbf{F} is the total atomic angular momentum of the atomic state probed, and $|\mathbf{S}_i| = 1/2$ and $|\mathbf{F}|$ are the maximum spin projections. The exotic-field Hamiltonian \mathcal{H}_{Υ} can be compared to the Zeeman Hamiltonian describing the interaction of atomic spins with a magnetic field:

$$\mathcal{H}_B = g_F \mu_B \mathbf{F} \cdot \mathbf{B}, \quad (2)$$

where g_F is the Landé g-factor, μ_B is the Bohr magneton, and \mathbf{B} is the external magnetic field experienced by the atom. Comparing Eqs. (1) and (2), it is evident that the physical manifestations of the ordinary magnetic field coupling and the coupling of exotic fields to spins are analogous. Furthermore, by measuring OAM response to \mathbf{B} , the response to an exotic field $\mathbf{\Upsilon}$ can be inferred [32]. Therefore, we can consider $\mathbf{\Upsilon}$ to be a “pseudomagnetic” field: a field that shifts Zeeman energy levels and generates torques on atomic spins, but does not couple proportionally to spins of different species according to their gyromagnetic ratios (i.e., comparing across different atomic species, $\sum_i g_{\Upsilon i} \sigma_i / |\mathbf{F}|$ is not proportional to $g_F \mu_B$). Furthermore, unlike a magnetic field, it may be the case that $\mathbf{\Upsilon}$ has nonzero divergence (see, for example, Ref. [33]).

Hwaseong, 18448, South Korea

‡ present address: Université de Franche-Comté, SupMicroTech-ENSM, UMR 6174 CNRS, institut FEMTO-ST, 25000 Besançon, France

§ present address: Department of Physics, University of Colorado, Boulder Colorado 80309, USA

¶ present address: Department of Physics, Harvard University, Cambridge, Massachusetts, 02138, USA

** present address: Department of Physics and Astronomy, University of Rochester, Rochester, New York 14627, USA

†† present address: Department of Physics, University of Illinois at Urbana-Champaign, Urbana, Illinois 61801, USA

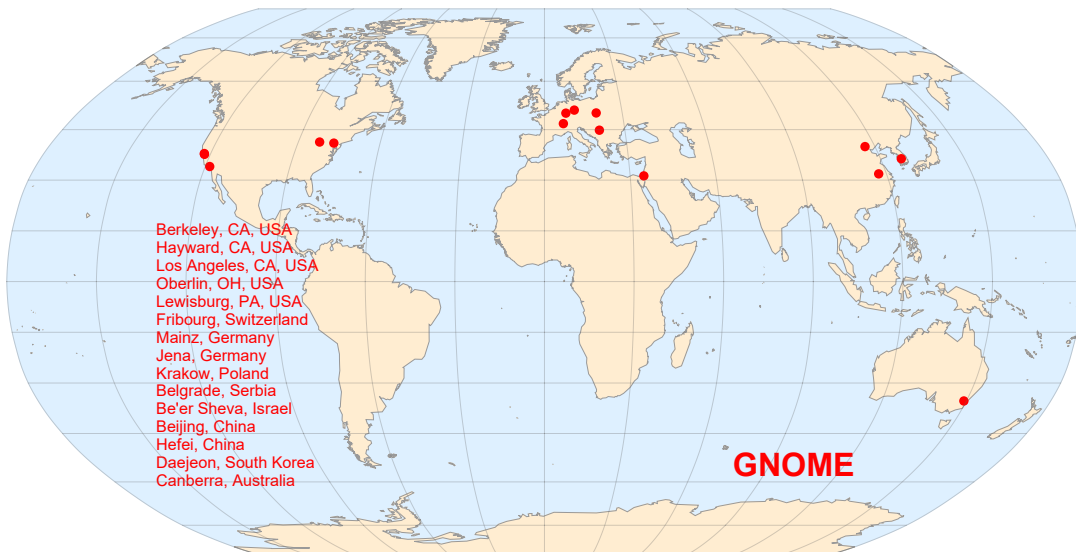


FIG. 1. Map and list of locations of GNOME stations. Note that the Fribourg station was moved to Jena in 2018.

In order to reduce environmental noise from ambient magnetic fields, the atomic vapor cells that contain the gases at the heart of GNOME’s OAMs are placed inside multilayer magnetic shields composed of soft ferromagnetic or ferromagnetic materials (such as mu-metal) [34]. As noted in Ref. [35], if the exotic field Υ interacts primarily with electron spins, there is an approximate cancellation of the effect of the field Υ on electron spins within the magnetic shield. This is due to the fact that it is the electron spins within shielding materials such as mu-metal that respond to the external magnetic field, so they similarly respond to an electron-coupled field Υ . This response generates a corresponding magnetic field approximately cancelling the electron-spin-dependent energy shift within the shield [35].¹ Consequently, GNOME OAMs are primarily sensitive to exotic field couplings to nuclear spins. At present, GNOME OAMs use alkali atoms such as rubidium (Rb) and cesium (Cs) whose nuclei have valence protons, and thus GNOME predominantly measures interactions of exotic fields with the proton spin S_p [36, 37].

The principal hypothesis GNOME has sought to test is that dark matter is composed of ultralight spin-0 bosons known as axions or axion-like particles (ALPs). Such exotic spin-0 bosons are ubiquitous features of the theoretical landscape beyond the Standard Model. The axion originally emerged from a proposed solu-

tion to the strong-CP problem [38–41], the mystery of why nucleon EDMs and CP-violating nuclear electromagnetic moments are many orders of magnitude smaller than nominally predicted by quantum chromodynamics (QCD). Since then, a variety of other beyond-the-Standard-Model theories have emerged predicting similar spin-0 bosons known as ALPs [1, 42–45]. Axions and ALPs are commonly thought to be ultralight (masses $m_a \ll 1$ eV). They can be copiously produced in the early universe [46–52] and have all the requisite characteristics to be the dark matter [2, 52–54].

The most commonly considered manifestation of a coupling between an ALP field φ and atomic spins is given by the Lagrangian [55]

$$\mathcal{L}_l = \frac{(\hbar c)^{3/2}}{f_l} J^\mu \partial_\mu \varphi, \quad (3)$$

where f_l is the characteristic energy scale associated with the spin “portal” between ALPs and fermions (the subscript l denoting that the interaction is linear in the ALP field φ) and J^μ is the axial-vector current for fermions ψ ,

$$J^\mu = \bar{\psi} \gamma^\mu \gamma_5 \psi, \quad (4)$$

where γ^μ and γ_5 are Dirac matrices. The corresponding Hamiltonian \mathcal{H}_l can be derived from the Euler-Lagrange equations (see, for example, Refs. [1, 56]):

$$\mathcal{H}_l \psi = -\frac{(\hbar c)^{3/2}}{f_l} \gamma_0 \gamma^\mu \gamma_5 (\partial_\mu \varphi) \psi. \quad (5)$$

In the nonrelativistic limit, where the spacelike component of the derivative of φ is much larger than the time-like component,

$$\mathcal{H}_{li} = -\frac{(\hbar c)^{3/2}}{f_{li}} \frac{\mathbf{S}_i}{|S_i|} \cdot \nabla \varphi, \quad (6)$$

¹ Note that cancellation of the effects of an electron-spin-coupled Υ is not exact within the ferromagnetic shielding due to imperfect shielding and nonzero nuclear magnetic moments. If the techniques of noble-gas-alkali-metal comagnetometry are employed (see Sec. III E), electron-spin-coupled fields Υ are measurable inside the shields because the nuclear spins of the noble gas respond to the Υ -induced magnetic field from the shielding material.

where the subscript i specifies the interaction with fermion $i = e, p, n$. Comparing Eq. (6) to Eq. (1), we see that the coupling constant for ALPs in the above parameterization is given by $g_{\Upsilon i} = (\hbar c)^{3/2}/f_{ii}$ and the exotic pseudo-magnetic field is described by $\Upsilon_i = \nabla\varphi$. Note that not only does \mathcal{H}_i generate an interaction between spins and the spatial gradient of φ , but \mathcal{H}_i also generates an interaction between spins that move with respect to the ALPs, since the momentum is related to the gradient operator via $\mathbf{p} = -i\hbar\nabla$. The latter interaction is often referred to as the ‘‘axion wind’’ [5, 55, 57, 58].

We also consider an alternative ‘‘quadratic’’ coupling between spins and the gradient of the intensity of the ALP field, $\nabla\varphi^2$ [31]. Whereas the QCD axion associated with the Peccei-Quinn solution to the strong-CP problem [38, 39] generally possesses the linear gradient interaction described by Eqs. (3) and (6) [55], the quadratic gradient interaction can arise in effective field theories predicting ALPs not associated with the QCD sector [59]. It is possible that under certain circumstances (see, for example, Refs. [60–62]), linear-in- φ interactions may be suppressed, and the interaction of photons, electrons and nuclei with scalar fields starts at the quadratic order, φ^2 . A very important consequence of such a modification is the relaxation of the most stringent astrophysics bounds compared to the linear case [59], opening up a parameter space for the direct searches of φ^2 coupling to spins. Also note that quadratic-in- φ interactions are required for complex-valued φ , as is the case for the Q-ball scenario discussed in Sec. IV C. Furthermore, there are novel experimental signatures and modalities that can be employed to search for the quadratic-in- φ interactions [63].

The Lagrangian describing the quadratic gradient coupling between an ALP field and atomic spins is given by [31]

$$\mathcal{L}_q = \frac{\hbar^2 c^2}{f_q^2} J^\mu \partial_\mu \varphi^2. \quad (7)$$

The corresponding Hamiltonian is described by

$$\mathcal{H}_q \psi = -\frac{\hbar^2 c^2}{f_q^2} \gamma_0 \gamma^\mu \gamma_5 (\partial_\mu \varphi^2) \psi, \quad (8)$$

and in the nonrelativistic limit the Hamiltonian describing the interaction of φ with the spin of fermion i is approximately

$$\mathcal{H}_{qi} = -\frac{\hbar^2 c^2}{f_{qi}^2} \frac{\mathbf{S}_i}{|S_i|} \cdot \nabla \varphi^2. \quad (9)$$

Comparing Eq. (9) to Eq. (1), we see that the coupling constant for ALPs in the above parameterization is given by $g_{\Upsilon i} = (\hbar c)^2/f_{qi}^2$ and the exotic pseudo-magnetic field is described by $\Upsilon_q = \nabla\varphi^2$.²

² Note that, as defined here, the units of $\Upsilon_q = \nabla\varphi^2$ differ from

It is of interest to note the discrete symmetry properties of the interactions described by Eqs. (6) and (9). Consider as a reference the discrete symmetry properties of the standard Zeeman interaction of Eq. (2). The atomic angular momentum \mathbf{F} is even under parity (P-even), since it is an axial- or pseudo-vector, and odd under time-reversal (T-odd), since angular momentum reverses its sign when time runs backward. The magnetic field \mathbf{B} , generated by current flow, is also P-even and T-odd, and thus \mathcal{H}_B is P- and T-even. For the linear gradient interaction of Eq. (6), the pseudoscalar ALP field φ is P-odd and T-odd and the gradient ∇ is P-odd and T-even, and thus $\nabla\varphi$ is a P-even, T-odd quantity, matching the discrete symmetry properties of the magnetic field. Consequently, $\mathcal{H}_l \propto \mathbf{S} \cdot \nabla\varphi$ is P- and T-even. On the other hand, for the quadratic gradient interaction of Eq. (9), $\nabla\varphi^2$ is P-odd and T-even because of the extra factor of the ALP field φ , which means that the quantity $\mathbf{S} \cdot \nabla\varphi^2$ is P- and T-odd. Based on CPT invariance (where C is the charge conjugation symmetry), it follows that \mathcal{H}_q describes a CP-violating interaction, and as a result could play a role in baryogenesis [64].

III. GNOME OVERVIEW

The idea of the GNOME experiment is to carry out synchronous measurements of spin-dependent interactions using OAMs operating within magnetically-shielded environments in distant locations. In this section we review the basic feature of the GNOME network, give an overview of the data collected so far, and describe ongoing improvements to the GNOME sensors that will significantly enhance the network sensitivity.

A. GNOME magnetometers

As mentioned above, OAMs utilize the interaction of atomic spins with external magnetic fields [7]. Typically, alkali metal vapors, contained in glass cells, are used for the measurements. To prevent spin-depolarizing collisions with cell walls, which can limit the OAM sensitivity, either the walls are coated with special (e.g., paraffin) layer or the cells are filled with an additional inert gas (e.g., noble gas) to slow down diffusion. In OAMs, the atoms are optically polarized, resulting in optical anisotropy of the medium. As the spins of the polarized atoms precess due to a nonzero magnetic field (or, perhaps, due to an exotic field coupled to atomic spins), detection of the corresponding change in optical properties of the medium provides quantitative information

those of $\Upsilon_l = \nabla\varphi$. The correct units for the associated Hamiltonian, described by Eq. (1), are obtained through the respective coupling constants g_Υ also having different units for the quadratic and linear ALP gradient interactions.

about the field. The signals of the GNOME magnetometers are recorded using a custom data acquisition (DAQ) system [65], providing accurate timing from the Global Positioning System (GPS).

In the first incarnation of the GNOME, various OAMs employed different elements (Rb and Cs) and were based on different techniques; spin-exchange-relaxation-free (SERF) [66], M_x [67], and nonlinear-magneto-optical-rotation (NMOR) [68] magnetometers were used for the measurements. On the one hand, this diversity offers flexibility, opens a greater range of theoretical parameter space for exploration, and improves the robustness of the network. On the other hand, it results in sensors having different sensitivities and bandwidths, which complicates data analysis. In general, however, magnetometers used in the GNOME have an operational sensitivity better than $1 \text{ pT}/\sqrt{\text{Hz}}$, corresponding to a sensitivity to Zeeman energy shifts below $10^{-17} \text{ eV}/\sqrt{\text{Hz}}$, and bandwidths up to 100 Hz [29].

Although OAMs enable searches for non-magnetic spin couplings, the devices are highly sensitive to magnetic fields. Therefore, despite shielding from the external environment, uncontrollable magnetic disturbances are a significant source of noise. In order to reduce magnetic noise, the next generation of the GNOME experiment (Advanced GNOME) is using comagnetometers [69, 70]: sensors with limited sensitivity to magnetic fields that still maintain sensitivity to non-magnetic spin couplings. Comagnetometers are briefly described in Sec. III E.

B. Monitoring of glitches

While by its nature the GNOME can suppress uncorrelated noise and false positive events, additional measures are implemented in the network to further increase the data quality and trustworthiness of each station. In order to veto signatures in the data which might have been produced by technical issues or changing experimental conditions (e.g., mechanical shocks, magnetic or electric pulses from neighboring technical devices), each GNOME station features a tailored automated system to continuously check for environmental perturbations. The system is based on the Arduino microcontroller board MEGA 2560 additionally equipped with the Arduino 9 Axes motion shield (magnetometer, accelerometer and gyroscope, three axes each) in a separate “sensor box”. The sensor box is mounted on the optical table of the GNOME station near the magnetic shielding. In this way, it can check for mechanical shocks or vibration of the optical setup. In addition, the system features additional analog voltage inputs, which are used to monitor the operational status of the station (e.g., magnetometer signal amplitude, error signal of the magnetometer feedback and/or the laser lock, readings of temperature sensors, and signals of a photo diode monitoring laser or ambient light power). For each GNOME station, depending on the specific setup, the system is set to monitor its critical

parameters.

A dedicated Python-based software allows the system to display, save, and define “sane” ranges for all monitored parameters. If one of the parameters falls out of the “sane” range, the system will output a signal to the DAQ system indicating the data recorded meanwhile should be rejected in data analysis. The software writes a log file allowing one to trace back the event to the individual monitored parameter. It is also possible to set alarms to notify station operators about irregularities over email and/or the Telegram app.

C. Calibration pulses

A possible concern with the continuous operation of the magnetometers over the course of several months is variation in the calibration and bandwidth of the detectors. Such variations could result from drifts in laser power, laser frequency, or temperature of the vapor cells. To monitor this, a series of oscillating magnetic fields are periodically applied to each magnetometer station via coils inside the magnetic shields. The frequency of the applied magnetic field is stepped from 1 to 180 Hz over the course of 9 s using a programmable function generator.³ During the most recent experimental campaign (Science Run 5), the pulse sequence was applied hourly. The response of the magnetometers at the different frequencies provides a convenient check on the operation of the magnetometers as well as a method for measuring the frequency response and bandwidth of the detectors. The pulses also provide a test of the timing of the stations. The pulses are triggered by the GPS pulse-per-second (pps) signal of the GNOME DAQ system or a time synchronized computer clock. These tests indicate that the stations are synchronized at a level of better than the sample period, $T_{\text{samp}} = 1/512 \text{ s}$.⁴

D. The GNOME experiment so far

To date, the GNOME collaboration has completed five “Science Runs” as well as a number of test and calibration runs. According to Eqs. (6) and (9) and the surrounding discussion in Sec. II, GNOME sensors seek to measure characteristic global patterns of pseudo-magnetic fields Υ . Typically, GNOME magnetometers are sensitive to the projection of Υ along a particular sensitive axis. Thus the amplitudes of signals from exotic fields Υ scale proportionally to $\hat{m} \cdot \Upsilon$, where \hat{m} is

³ The pulse sequence used in a recent Science Run 5 was 1 Hz for 4 s, 10 Hz for 2 s, 35 Hz for 1 s, 55 Hz for 0.6 s, 70 Hz for 0.4 s, 80 Hz for 0.2 s, 90 Hz for 0.2 s, 110 Hz for 0.2 s, 130 Hz for 0.2 s, 160 Hz for 0.1 s, and 180 Hz for 0.1 s.

⁴ The GPS DAQ system provides timing with a precision better than 100 ns.



FIG. 2. One-day rolling average of the GNOME noise level according to Eq. (10) over the course of the first five Science Runs. The standard deviation at each magnetometer is calculated using the data for one second. Then this information is averaged for one hour. The color of the line indicates the number of active stations as indicated on the color map legend at the upper right.

a unit vector pointing along the sensitive axis of a magnetometer. Since the direction of the field Υ is essentially unknown, in order to assess the sensitivity of the GNOME, this directional sensitivity must be taken into account. Additionally, the various parameters of individual sensors must be considered along with the relationship between the sensor response and the underlying physical theory (which must account for atomic and nuclear structure [36, 37]). These issues are discussed in more detail in Refs. [30, 71, 72].

A summary of the network performance for the five GNOME Science Runs is shown in Fig. 2. Since the GNOME data can be utilized in different ways to test different exotic physics hypotheses, discussed in Sec. IV, for simplicity we adopt for the summary a relatively simple, model-independent evaluation. The plot in Fig. 2 shows the one-hour-average noise level as defined by

$$\sigma_{\text{network}} \equiv \sqrt{\frac{1}{\sum_j \sigma_j^{-2}}}, \quad (10)$$

where σ_j is the variance of magnetometer j , calculated using the standard deviation for each second of data. As can be seen from Fig. 2, the GNOME experiment has accumulated over a year of data sensitive to pseudo-magnetic fields with equivalent magnitudes \lesssim pT that can be searched for a variety of exotic physics signals.

E. Advanced GNOME: noble gas comagnetometers

The further development of the GNOME experiment focuses on the diversification and upgrade of the sensors implemented in the network. There are three main

directions for the improvement of sensors: enhancing their sensitivity, increasing their bandwidth, and expanding the types of couplings probed. Although a number of various experimental techniques could be used for GNOME sensors (e.g., spin-based amplifiers [73], noble gas masers [74, 75], dual-species nuclear-spin comagnetometers [76, 77], alkali comagnetometers [78–80], liquid-state NMR comagnetometers operating in the zero-to-ultralow field (ZULF) regime [81, 82], etc.), efforts are presently focused on developing self-compensating noble-gas-alkali-metal comagnetometers [69, 70] for implementation in the “Advanced GNOME” experiment [32, 83].

In addition to the coupling of exotic fields to proton spins, which was the only coupling probed at a competitive level by the first-generation GNOME [30], self-compensating noble-gas-alkali-metal comagnetometers can also probe both neutron and electron spin couplings. The ability to measure neutron spin couplings to Υ comes from the fact that the noble gases (such as ^3He) employed in these sensors have nuclei with valence neutrons [36].⁵ However, the reason for the ability of these sensors to measure electron spin couplings is somewhat more subtle. If we assume that Υ couples primarily to electron spins, then the ferromagnetic (or ferrimagnetic) shielding responds to Υ by creating an induced magnetic field that cancels the effect of Υ on electrons within the shield where the vapor is located [35]. However, if we assume no coupling of Υ to neutron spins,

⁵ Note that ^3He -alkali-metal comagnetometers retain sensitivity to proton couplings via a reasonably well-measured and understood proton-spin polarization in the ^3He nucleus and the proton-spin polarization of the alkali metal nucleus [36].

then neutrons will respond to the induced magnetic field from the shields and thus a detectable effect is generated. This further highlights the advantages of comagnetometry for exotic physics searches with the GNOME. At sub-Hz frequencies, the sensitivity of the comagnetometer is also significantly improved by the suppression of the magnetic field response due to the self-compensation regime in which the comagnetometer is operated.

Initial tests of Advanced GNOME sensors demonstrate a sensitivity at the level of 10^{-21} eV/ $\sqrt{\text{Hz}}$ (at 1 Hz) for exotic fields coupling to neutron spins, and about 10^{-19} eV/ $\sqrt{\text{Hz}}$ (at 1 Hz) for the proton spin coupling (surpassing that of GNOME magnetometers by a factor of 100), see Fig. 3. For the electron spin couplings, the expected sensitivity is comparable to the sensitivity of the first-generation GNOME magnetometers to the proton exotic spin couplings. The noble-gas-alkali-metal comagnetometers have an optimal sensitivity to the nuclear spin couplings for frequencies below a few hertz. However, enhanced sensitivity to exotic fields (as compared to the first-generation of GNOME magnetometers) is expected over the whole bandwidth of the ordinary magnetometers, even at frequencies for which the comagnetometer performance is sub-optimal.

The Advanced GNOME sensors also bring another significant qualitative advantage for exotic physics searches. The difference in the response to the magnetic and non-magnetic spin couplings can be used to discriminate events of magnetic origin from those driven by non-magnetic spin couplings, just from a single sensor readout [32]. Although ultimate verification of a global exotic physics event will rely on the correlation between signals observed in multiple GNOME stations, more effective discrimination between magnetic and non-magnetic signals will enable efficient suppression of the “false positive” rate and therefore improve the overall sensitivity of the network.

IV. SEARCH TARGETS AND THEIR SIGNALS

By analyzing correlations between signals from the geographically separated magnetometers and comagnetometers comprising GNOME, it is possible to probe a wide variety of exotic beyond-the-Standard-Model hypotheses. In this section we survey some exotic physics scenarios that can be searched for using GNOME data and highlight examples of their particular temporal signatures.

A. Axion domain walls

The first proposed search targets for GNOME were axion or ALP domain walls [28, 31]. Domain walls are topological defects that form between regions of space in which the ALP field possesses different, but energy-degenerate, vacuum states [84, 85]. Such a scenario arises

due to the non-trivial vacuum topology that ALP fields typically possess: there can be multiple local field energy minima (and corresponding vacuum states) that, in the abstract space describing the field, are not “simply connected” in a topological sense [86]. When spontaneous symmetry breaking occurs in the early universe, different regions of space (domains) acquire different vacuum states. The domain walls are the field configurations at the boundaries between these domains. In order for the ALP field to transition from one energy minimum to another across these boundaries, the ALP field necessarily acquires values above those corresponding to the minimum energy. These non-vacuum states are associated with considerable potential energy, and the change of the field over space means that the ALP field has a nonzero gradient.

1. Theoretical description

ALP domain walls are macroscopic field configurations that could be stable and long lived, and continue to exist today [85]. They can be of astrophysical extent, potentially much larger than the size of Earth. If the ALP field primarily manifests in the form of domain walls, the associated energy density would be concentrated into compact spatial regions. While in most theoretical models such domain walls are unstable [84, 87], in some other models [31, 85, 88] domain walls can compose a significant fraction of dark matter. These objects can be considered virialized in the galaxy according to the standard halo model (SHM). Based on this assumption, the rate and duration of the ALP domain wall encounters can be estimated. A region of theoretically plausible parameter space is expected to have an average encounter rate with Earth of a year or less [31, 88]. This opens the possibility to directly search for such encounters. Atomic magnetometers and comagnetometers are sensitive to domain walls, since the ALP-field gradient can interact with the spin of electrons, neutrons and protons [see Eqs. (6) and (9)].

2. Signal model

Consider an ALP domain wall in the yz -plane ($x = 0$) separating two degenerate ALP vacuum states as pictured in the upper diagram in Fig. 4. The solution of the field equations for φ yields [30, 31, 89]

$$\varphi(x) = \varphi_0 \arcsin [\tanh (x/\lambda_c)], \quad (11)$$

where φ_0 is a constant proportional to the spontaneous symmetry-breaking scale associated with the ALP and $\lambda_c = \hbar/(m_a c)$ is the Compton wavelength of the ALP of mass m_a . Atomic spins can interact with the ALP field through the linear and quadratic gradient interactions of

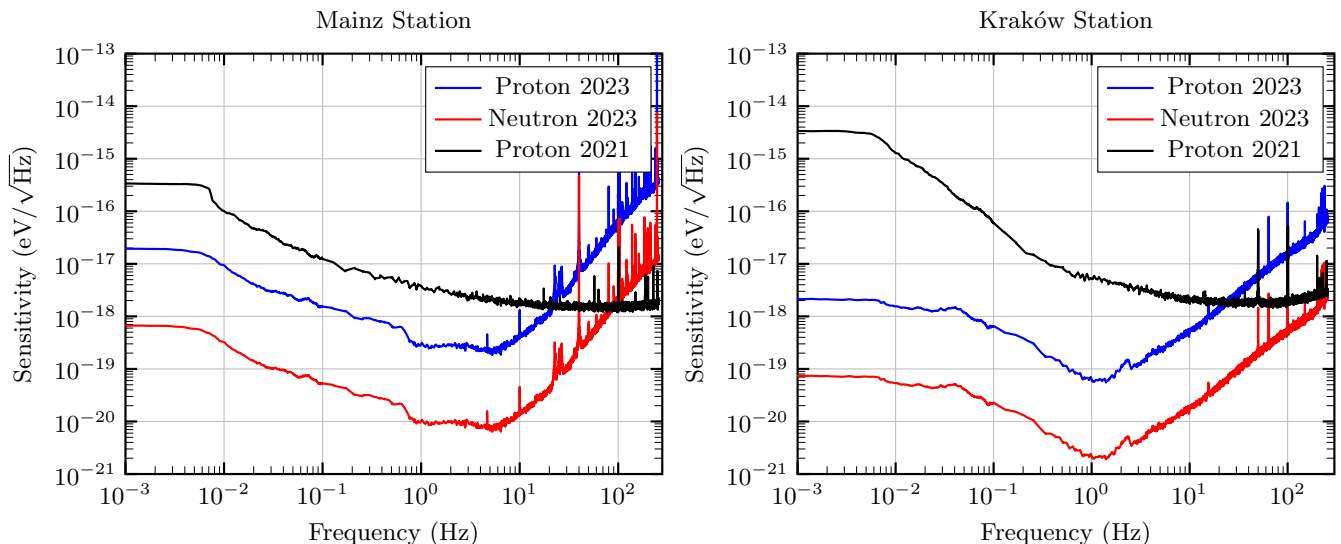


FIG. 3. Sensitivities of Advanced GNOME stations in Mainz (left) and Kraków (right) obtained during a Test Run in January 2023, compared with the typical sensitivity of the first-generation GNOME stations during Science Run 5 (see Fig. 2). **Red curves**: sensitivities of the comagnetometers to the neutron exotic spin couplings; **blue curves**: sensitivity of the comagnetometers to the proton spin couplings; **black curves**: magnetometer sensitivities to exotic proton couplings. The sensitivities are presented in terms of Zeeman-like energy splitting generated by the considered perturbation. The presented data sets were undersampled for illustration purposes.

Eqs. (6) and (9), which can be described by the pseudo-magnetic fields

$$\Upsilon_l = \nabla\varphi(x) = \frac{\varphi_0}{\lambda_c} \operatorname{sech}(x/\lambda_c) \hat{x} \quad (12)$$

and

$$\Upsilon_q = \nabla\varphi^2(x) = \frac{2\varphi_0^2}{\lambda_c} \arcsin[\tanh(x/\lambda_c)] \operatorname{sech}(x/\lambda_c) \hat{x}, \quad (13)$$

respectively. The signal measured by a GNOME sensor is $\propto \hat{\mathbf{m}} \cdot \Upsilon$, where $\hat{\mathbf{m}}$ is directed along the sensitive axis of the magnetometer. The expected time-dependent line-shapes for the linear and quadratic couplings are shown in the lower plots of Fig. 4. While all the GNOME sensors experience a common transient pseudo-magnetic field Υ , because of the varying directions of their sensitive axes $\hat{\mathbf{m}}$ (as well as differences in the magnetometers employed), the signals in different sensors would have varying amplitudes and signs. For a given relative velocity between the ALP domain wall and Earth, there is a characteristic signal timing and amplitude pattern that can be used to distinguish true domain-wall-crossing events from spurious noise [30, 71, 90]. Once an event is detected, one can relate the signal properties (width and the amplitude of the signal, as well as the inferred expected distribution of domain walls) to ALP parameters, including the mass of the ALP and the interaction and symmetry-breaking scales [30].

The GNOME collaboration has developed data analysis algorithms to search for ALP domain walls [71, 90],

and has completed a full analysis of the data from Science Run 2 carried out in 2017 [30]. Our searches did not find any statistically significant signals above background that could point to the existence of ALP domain walls. Consequently, our results can be interpreted as constraints on the properties of ALP domain walls. The excluded (model-dependent) ALP parameter space covers masses in the range $\sim 10^{-15} - 10^{-7}$ eV [30]. A new analysis procedure is currently being developed to improve on the sensitivity to narrower domain wall widths with respect to our previous work [30]. The new analysis is based on a preselection of candidate signals groups occurring within a given time window. Then each group is tested for consistency with the domain wall crossing model. This allows an efficient scrutiny of the data compared to the previous method. In Ref. [30] all possible domain wall configurations were scanned and their agreement with the data were evaluated. The new procedure results in a comparatively less computer-intensive routine.

B. Axion stars

Instead of the ALP dark matter being primarily in the form of topological defects such as domain walls as discussed above in Sec. IV A, it may be the case that inhomogeneities in the dark matter distribution provide seeds that enable ALP self-interactions or gravity to attract together a large local density of ALPs, thereby forming a spherical bound-state (see Refs. [91–94] and references therein). Such spherical bound states are referred to as

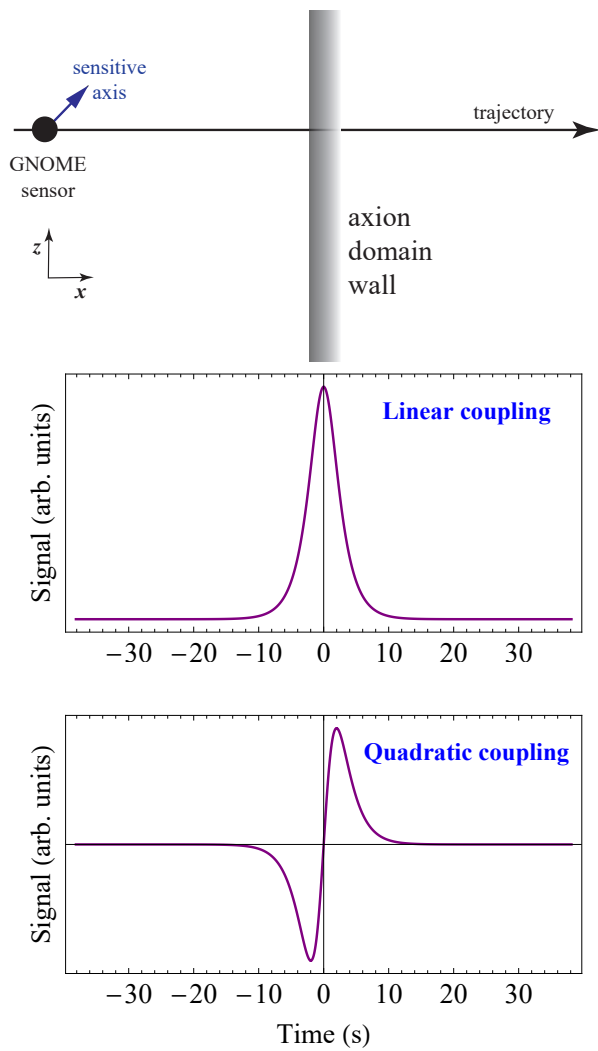


FIG. 4. Upper diagram: schematic depiction of a GNOME sensor passing through an ALP domain wall (thickness $\approx R_E/10$), indicating with the long black arrow the trajectory of the sensor along \mathbf{v} (parallel to \mathbf{k} , along $\hat{\mathbf{x}}$, $v \approx 10^{-3}c$) and the sensitive axis of a GNOME sensor (blue arrow, tilted at 45° to $\hat{\mathbf{x}}$). The plots below show example signals due to the linear spin coupling (middle plot) and quadratic spin coupling (lower plot) from an ALP-domain-wall encounter corresponding to the schematic at top.

axion or ALP stars, and they may constitute a significant fraction of the dark matter density [91]. Under certain conditions, ALP stars are stable under perturbations and radiative decay [95–98], and can be efficiently formed in the early Universe [99–102]. The extensive theoretical studies of ALP stars to determine their evolution, stability, and characteristic radii and masses for different models of the ALP self-interaction establish that ALP stars are, indeed, a plausible dark matter scenario [91, 103, 104]. As described in Ref. [105], ALP stars are a compelling search target for the GNOME, since there is a range of masses and radii for ALP stars (not ruled out by existing empirical observations) for which the terrestrial

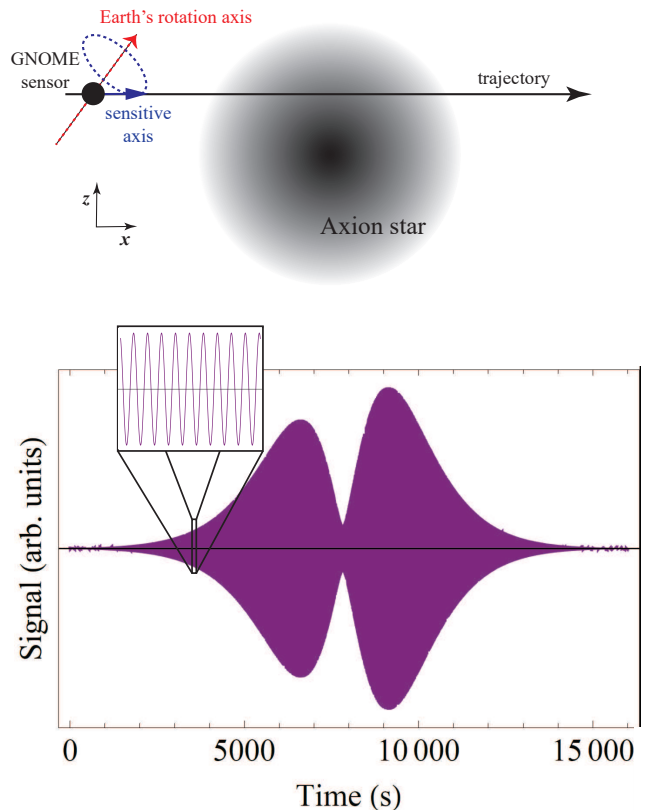


FIG. 5. Upper diagram: schematic depiction of a GNOME sensor passing through an ALP star, indicating with the long black arrow the trajectory of the sensor along \mathbf{v} (parallel to \mathbf{k} , along $\hat{\mathbf{x}}$), the initial direction of the sensitive axis of the GNOME sensor (blue arrow, along $\hat{\mathbf{x}}$), and the axis of Earth's rotation (dashed red arrow, 45° to the x -axis). Lower plot: example signal due to the linear spin coupling [Eq. (19)] from an ALP star passage corresponding to the above schematic. For this example, the ALP star radius $R \approx 200R_E$, $v = 10^{-3}c$, and at $t = 0$ the sensor is located at $(x_0, y_0, z_0) = (2R, 0, R/2)$, where the origin is defined to be the center of the ALP star. The ALP field oscillation frequency is chosen to be $\omega = 2\pi \times 10$ Hz, and we assume $\omega \approx \omega_c$, neglecting the binding energy. The ALP-star signal in the plot is based on the exponential model, Eq. (16). The inset plot shows an ≈ 1 s long segment of the simulated signal.

encounter rate can be sufficiently high (at least once per year) that a detection would be feasible. ALP stars can interact with atomic spins via the linear or quadratic gradient interactions [Eqs. (6) and (9)]. Thus if an ALP star passed through Earth, it would cause oscillatory pseudo-magnetic field pulses in GNOME sensors that, in principle, could be within the sensitivity range of GNOME [105].

1. Theoretical description

Axion or ALP stars held together via self-interactions are called *oscillons* [106] or *axitons* [107]. There have been a number of theoretical studies of such composite systems, and a few general features are observed. Models of oscillons and axitons demonstrate that they can persist in a stable or quasi-stable regime [108–110], however if the ALP density is too large, they tend to radiate ALP waves and lose mass [91]. Sufficiently dilute ALP stars can be stable over long time scales [108, 109, 111]. The ALP fields bound in the form of oscillons have a characteristic field oscillation frequency ω which is somewhat smaller than the ALP Compton frequency ω_c . This stems from the fact that, while free ALPs oscillate at the Compton frequency ω_c , because the energy of the ALPs in the star is reduced by a binding energy ϵ_b , the oscillation frequency of ALPs in the oscillon is given by

$$\omega = \omega_c - \epsilon_b/\hbar. \quad (14)$$

This is a key difference between the ALP domain walls considered in Sec. IV A and the ALP stars considered here: the ALP field of the domain wall does not oscillate, being a topological defect related to the ALP field potential energy, whereas the ALP field of the star does oscillate, since most of the field energy is in the form of kinetic energy. The mass M of an oscillon is $M \approx N(m_a - \epsilon_b/c^2)$, where N is the number of ALPs in the star.

Alternatively, axion stars could be held together by gravity [95–98, 112–115]. However, in this case it may be expected that gravitational tidal forces due to the Sun, Earth, and other bodies in the solar system could cause distortions and disruptions of the axion star [116], complicating the details of the shape profile in ways that are difficult to predict. Thus, for simplicity, here we focus on the oscillon or axiton models where self-interactions stronger than gravity dominate.

2. Signal model

A number of different approximate analytic wavefunctions for ALP stars have been studied in the literature (see Ref. [94] for a review). Two of the more widely used

radial wavefunctions $\Psi(r)$, where r is the radial distance from the center of the ALP star, are the Gaussian approximation,

$$\Psi(r) = \sqrt{\frac{N\kappa^3}{\pi^{3/2}R^3}} e^{-\kappa^2 r^2/(2R^2)}, \quad (15)$$

and the exponential approximation,

$$\Psi(r) = \sqrt{\frac{N\kappa^3}{\pi R^3}} e^{-\kappa r/R}, \quad (16)$$

where R is the characteristic radius of the ALP star enclosing 99% of its mass and κ is a numerical parameter ($\kappa = 2.8$ for the Gaussian wavefunction and $\kappa = 4.2$ for the exponential wavefunction [94]). In Ref. [94] it is argued that, in fact, a more accurate description of an ALP star in many relevant scenarios is given by a “linear-plus-exponential” wave function:

$$\Psi(r) = \sqrt{\frac{N\kappa^3}{7\pi R^3}} \left(1 + \frac{\kappa r}{R}\right) e^{-\kappa r/R}. \quad (17)$$

In any case, the ALP field as observed from the reference frame of a GNOME sensor is given by

$$\varphi(\mathbf{r}, t) = \Psi(r) \cos(\mathbf{k} \cdot \mathbf{r} - \omega t + \theta), \quad (18)$$

where \mathbf{k} is the ALP wave vector, \mathbf{r} is the distance from the center of the ALP star to the sensor, and θ is a random phase. Since the ALP field in the star is essentially a Bose condensate with long coherence time [91], we can treat the phase θ as constant throughout the duration of the passage of the GNOME sensor through the ALP star, and for simplicity in the following discussion we set $\theta = 0$.

The expected signal in a GNOME sensor can be calculated based on the exotic pseudo-magnetic fields $\Upsilon_l = \nabla\varphi$ and $\Upsilon_q = \nabla\varphi^2$ obtained from the expression (18), where (as above) the subscripts denote the linear or quadratic fields:

$$\begin{aligned} \Upsilon_l &= (\nabla\Psi) \cos(\mathbf{k} \cdot \mathbf{r} - \omega t) - \mathbf{k}\Psi(r) \sin(\mathbf{k} \cdot \mathbf{r} - \omega t), \\ &= \frac{\partial\Psi}{\partial r} \cos(\mathbf{k} \cdot \mathbf{r} - \omega t) \hat{\mathbf{r}} - \frac{m_a v}{\hbar} \Psi(r) \sin(\mathbf{k} \cdot \mathbf{r} - \omega t) \hat{\mathbf{k}}, \end{aligned} \quad (19)$$

and

$$\begin{aligned} \Upsilon_q &= (\nabla\Psi^2) \cos^2(\mathbf{k} \cdot \mathbf{r} - \omega t) - 2\mathbf{k}\Psi(r) \cos(\mathbf{k} \cdot \mathbf{r} - \omega t) \sin(\mathbf{k} \cdot \mathbf{r} - \omega t), \\ &= 2\Psi(r) \frac{\partial\Psi}{\partial r} \cos^2(\mathbf{k} \cdot \mathbf{r} - \omega t) \hat{\mathbf{r}} - \frac{2m_a v}{\hbar} \Psi(r) \cos(\mathbf{k} \cdot \mathbf{r} - \omega t) \sin(\mathbf{k} \cdot \mathbf{r} - \omega t) \hat{\mathbf{k}}. \end{aligned} \quad (20)$$

There are two generally non-orthogonal components of

the signal along $\hat{\mathbf{k}}$ and $\hat{\mathbf{r}}$, which change in magnitude as

the GNOME sensor passes through the ALP star. Note that the sensitive axis $\hat{\mathbf{m}}$ changes in time as Earth rotates, so this can introduce additional time dependence of the signal which is $\propto \hat{\mathbf{m}} \cdot \boldsymbol{\Upsilon}$. Figure 5 shows an example of a simulated signal in a GNOME sensor passing through an ALP star for a particular set of parameters. Both the direction and magnitude of $\boldsymbol{\Upsilon}$ change as the GNOME sensor passes through the ALP star, as well as the direction of $\hat{\mathbf{m}}$, leading to the somewhat complicated time-dependence.

The GNOME collaboration is currently developing an analysis method to search for ALP stars exhibiting this type of signal using the excess power statistic [117].

C. Q-balls

Another class of compact composite dark matter objects are *Q-balls* or *Q-stars* [118–121]. Q-balls are non-topological solitons: bound states of a complex scalar field φ . If complex scalar field φ obeys global $U(1)$ symmetry, and has a non-zero net charge density Q , the self-interaction of the scalar field makes it energetically favorable for the field to fragment into clumps, called Q-balls [122, 123]. In some models, Q-balls could comprise the entirety of dark matter [124, 125]. There are also various theoretical extensions of the Q-ball concept, involving, for example, multiple scalar fields [126] or local $U(1)$ symmetries instead of global [127]. The distinction between Q-balls and ALP stars is somewhat subtle. Q-balls, because of the global $U(1)$ symmetry, are true solitons since they are stable due to the conserved charge associated with φ . On the other hand, oscillons, our model for ALP stars, represent “quasi-solitons” because, while under particular conditions they can be very long-lived, they are technically unstable. The Q-ball is composed of a complex field, whereas the oscillon is composed of a real field. For both Q-balls and oscillons, an attractive potential is required for formation. As we see in the following, the differences between the underlying theoretical models describing oscillons and Q-balls lead to distinct experimental signatures in GNOME.

1. Theoretical description

The complex scalar field of a Q-ball takes the form [118]

$$\varphi(\mathbf{r}, t) = \Psi(r)e^{i\omega t}, \quad (21)$$

where $\omega \lesssim \omega_c$ is the angular oscillation frequency. The stability of the Q-ball is a consequence of its conserved charge Q

$$Q = \frac{\omega}{\hbar^2 c^3} \int |\varphi(\mathbf{r}, t)|^2 d^3\mathbf{r}. \quad (22)$$

The necessary conditions for Q-ball formation are that $Q \neq 0$ averaged over the whole space and the existence of

a self-interaction potential $U(\Psi)$ possessing at least two distinct minima at $\Psi = 0$ and at $\Psi = \Psi_0$ [118–121]. In this case, there are regions of space with different vacuum energy values, and the regions where $\Psi = \Psi_0$ can deform but not disappear because of the conserved charge Q . A characteristic feature of the Q-ball is that the potential energy of the field, $U(\Psi)$, is nonzero in the Q-ball’s transitional surface region where the field goes from $\Psi = 0$ to $\Psi = \Psi_0$. Therefore the Q-ball’s energy is minimized when its surface area is minimized, leading to a spherical bound-state. Furthermore, it is energetically favorable for the constituent particles corresponding to the field φ (ALPs in our considered case) to remain within the Q-ball in the case where $\omega \lesssim \omega_c$, since ALPs inside the Q-ball have energy $\hbar\omega$ while those outside the Q-star have energy $\hbar\omega_c$. The values of ω^2 and ω_c^2 are proportional to $\partial^2 U / \partial \Psi^2$ at the respective potential minima inside ($\Psi = \Psi_0$) and outside ($\Psi = 0$) the Q-ball, and can thus be different [118, 121]. The condition $\omega \lesssim \omega_c$ ensures stability of the Q-star with respect to radiative decay via ALP emission.

2. Signal model

The precise form of $\Psi(r)$ depends on details of the potential function, and, although there are special forms of $U(\Psi)$ admitting analytic solutions [128–130], in general numerical computation is required. However, there have been a number of analyses, for example Refs. [131–133], that have derived useful approximate radial profile functions that closely correspond to numerical solutions. For simplicity of mathematical description, here we adopt the form given by Ref. [131],

$$\Psi(r) = \frac{C_0}{\sqrt{1 + C_1 \cosh(\alpha r)}}, \quad (23)$$

where C_0 , C_1 , and α are constants determined by fitting to numerical solutions for various potentials and values of Q and ω . In contrast to the cases of ALP domain walls and ALP stars as described in Secs. IV A and IV B, for the complex-valued field $\varphi(r)$ forming Q-balls [Eq. (21)], any couplings of spins to $\varphi(r)$ *must* be quadratic in $\varphi(r)$ [134]. This is required in order to respect the global $U(1)$ symmetry that endows the Q-ball with its charge: from a mathematical point-of-view, interactions must involve products of $\varphi(r)$ and $\varphi(r)^*$ to give a real-valued energy. Therefore we consider the pseudo-magnetic field $\boldsymbol{\Upsilon}_q$ arising from the quadratic interaction,

$$\begin{aligned} \boldsymbol{\Upsilon}_q &= \nabla |\varphi(r, t)|^2 = \nabla \Psi^2(r), \\ &= \alpha C_0^2 C_1 \frac{\sinh(\alpha r)}{[1 + C_1 \cosh(\alpha r)]^2} \hat{\mathbf{r}}. \end{aligned} \quad (24)$$

Figure 6 shows a schematic example of the signal that would be measured by a GNOME sensor passing through a Q-ball. In contrast to the ALP star considered in

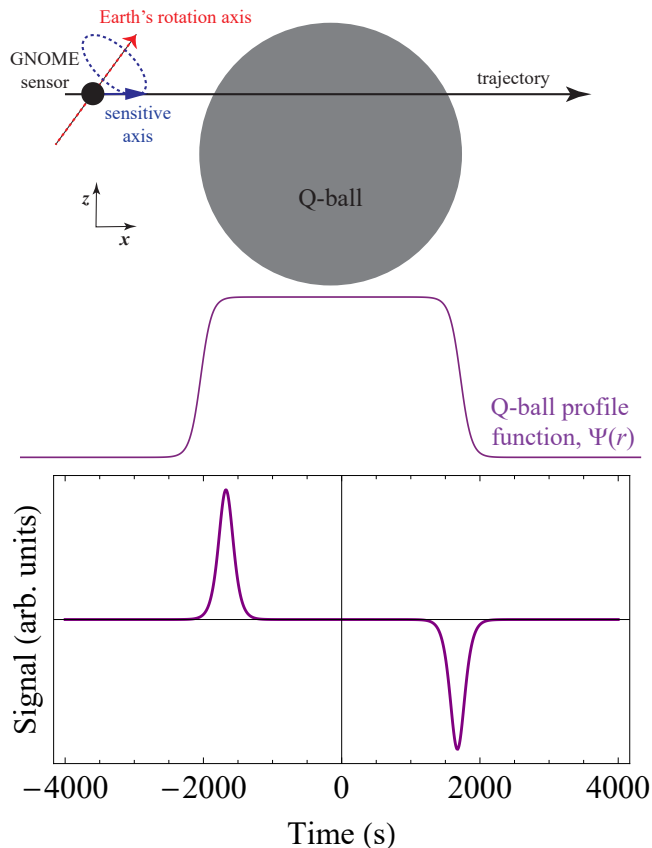


FIG. 6. Upper diagram: schematic depiction of a GNOME sensor passing through an astronomically large Q-ball (radius $\approx 100R_E$), indicating with the long black arrow the trajectory of the sensor along \mathbf{v} (parallel to \mathbf{k} , along $\hat{\mathbf{x}}$, $v \approx 10^{-3}c$), the initial direction of the GNOME-sensor sensitive axis (blue arrow, along $\hat{\mathbf{x}}$), and the axis of Earth’s rotation (dashed red arrow, 45° to the x -axis). The purple curve below shows the profile function of the Q-ball. Lower plot: example signal due to the quadratic spin coupling from a Q-ball passage corresponding to the above schematic.

Sec. IV B, the signal of the Q-ball does not exhibit oscillatory behavior, and is in fact more similar to the signature of an ALP domain wall considered in Sec. IV A. However, there is the notable difference that for a Q-ball there should be two correlated time-separated signals corresponding to entry and exit from the $\Psi = \Psi_0$ region, offering a unique signature pattern that can be exploited for noise rejection.

Note that the signal pattern in GNOME corresponding to a Q-ball encounter (Fig. 6) closely resembles that from two consecutive domain-wall encounters (Fig. 4), or a domain-wall encounter with a quadratic coupling in the case of a domain wall that is “thick” compared to the size of Earth. This suggests that our data analysis strategies applied to domain-wall searches [30, 71, 90] can be adapted to the case of Q-balls. Development of an analysis algorithm based on this concept is under way.

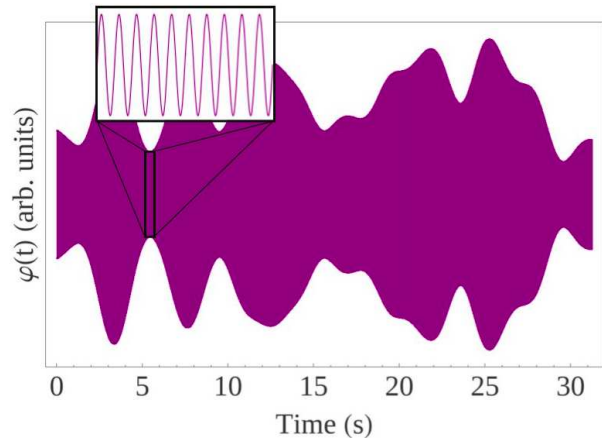


FIG. 7. Visualisation of the dark matter field oscillating at its Compton frequency with fluctuations of the envelope function.

D. Dark-matter field fluctuations

Unlike the compact dark matter objects described so far, in this section we consider the more commonly assumed model for UBDM, namely that the UBDM field is spread more evenly throughout the galactic halo volume and not concentrated in large, compact objects. Due to their ultralight nature and (if they constitute a sizable fraction of the dark matter) their enormous number density, ALPs can be treated as classical plane waves. In the standard halo model (SHM), ALPs are virialized in the gravitational potential of the Milky Way, and their energy is given by $\hbar\omega \approx m_a c^2 + m_a v^2/2$ where ω is the observed ALP field oscillation frequency and $v \sim 10^{-3}c$ is the ALP velocity. Due to the ALPs’ randomized velocities, different ALP field modes interfere with one another resulting in a net field that stochastically fluctuates on a characteristic time scale given by the ALP field coherence time $\tau_{\text{coh}} \sim \hbar/(m_a v^2)$ [24]. Given that the virial velocity of dark matter in the Milky Way galaxy at the location of our solar system is $\approx 10^{-3}c$ [135, 136], $\tau_{\text{coh}} \sim 10^6 \times (2\pi/\omega_c)$. This means that the ALP field fluctuations occur on a time scale that is a factor of a million slower than the ALP field oscillations. The stochastically varying properties of the virialized ALP field are well-described by the Rayleigh distribution [25, 137], which, notably, also describes thermal (chaotic) light. If the coherence length of the virialized ALP field, λ_{coh} , is large compared to the diameter of Earth, GNOME magnetometers could detect common mode fluctuations of the ALP dark matter field.

There are several experiments aiming to detect the ultralight dark-matter field through an observation of a resonant spin coupling to ALPs at their Compton frequency [9–20]. Such measurements can also be performed with GNOME and Advanced GNOME sensors. Given the close analogy between the behavior of virial-

ized ALP fields and thermal light, we can take full advantage of the fact that GNOME is a network of spatially distributed sensors by implementing a detection scheme similar to Hanbury-Brown-and-Twiss intensity interferometry [138] as recently proposed in Ref. [63]. The quadratic ALP interaction with spins [Eq. (9)] leads to a signal in GNOME magnetometers related to the intensity of the ALP field, $\varphi^2(\mathbf{r}, t)$. A measurement of the stochastic intensity-like fluctuations of the dark matter field amplitude can be performed using GNOME by correlating time series from distant sensors in order to detect the common-mode signal. Instead of detecting fast oscillations at $\approx \omega_c$, the slowly varying (at characteristic frequency $\sim 10^{-6}\omega_c$) ALP field envelope function would be measured. In this way, the probed ALP mass range could be extended to masses several orders of magnitude larger in comparison to resonant measurements performed with the same bandwidth-limited sensors: GNOME's ~ 100 -Hz-bandwidth sensors could search for ALPs with Compton frequencies up to ~ 100 MHz [63].

1. Theoretical description

At each point in space, the dark matter field can be described as a superposition of plane waves representing individual modes of the ALP field (i.e., summing over all the individual ALPs composing the field),

$$\varphi(\mathbf{r}, t) = \sum_{n=1}^N \frac{A}{\sqrt{N}} \cos(\omega_n t - \mathbf{k}_n \cdot \mathbf{r} + \theta_n). \quad (26)$$

The amplitude is defined to be $A = \hbar\sqrt{2\rho_{\text{dm}}}/(m_a c)$ so that the average ALP field energy density corresponds to the average dark matter density ρ_{dm} . The n -th ALP has a random velocity \mathbf{v}_n corresponding to the wave vector $\mathbf{k}_n = m_\varphi \mathbf{v}_n / \hbar$. Based on the SHM, the probability distribution function of the velocities, \mathbf{v}_n , follows a displaced Maxwell-Boltzmann distribution:

$$f_{\text{lab}}(\mathbf{v}) \approx \frac{1}{\pi^{3/2} v_0^3} \exp\left[-\frac{(\mathbf{v} - \mathbf{v}_{\text{lab}})^2}{v_0^2}\right], \quad (27)$$

where $|\mathbf{v}_{\text{lab}}| \approx 233$ km/s is the Sun's velocity with respect to the Galactic rest frame and $v_0 \approx 220$ km/s is the velocity dispersion of the ALPs.

The n -th oscillation frequency is mostly determined by the Compton frequency $\omega_c = m_\varphi c^2 / \hbar$, but shifted due to the relativistic Doppler effect for particle waves. For $v_n/c \ll 1$ the effect can be approximated by [27]

$$\omega_n = \omega_c \left(1 + \frac{v_n^2}{2c^2}\right). \quad (28)$$

The fluctuations of the dark matter field in time arise from the random directions, phases, and spread in frequencies of constituent waves. See Fig. 7 for a visualisation of the ALP dark matter field amplitude as a function of time.

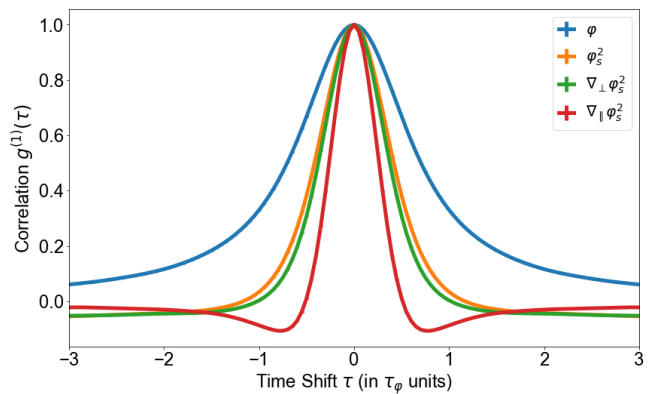


FIG. 8. Auto-correlation of a simulated ALP dark matter field φ , the low-frequency component of its square φ_s^2 associated with stochastic fluctuations, and two gradient components perpendicular and parallel to \mathbf{v}_{lab} : namely $\nabla_\perp \varphi_s^2$ and $\nabla_\parallel \varphi_s^2$, where the subscript s denotes the low-frequency component associated with stochastic fluctuations.

2. Signal model

Assuming the quadratic coupling Hamiltonian [Eq. (9)], the pseudo-magnetic field is given by $\Upsilon_q = \nabla \varphi^2$ and the signal observed in a GNOME sensor is $\propto \hat{\mathbf{m}} \cdot \Upsilon_q$. As the detectors have limited bandwidth $\Delta\omega$, for the case where $\Delta\omega \ll \omega_c$ the fast oscillations at $2\omega_c$ are not observable in the measurement. The measured pseudo-magnetic field can be approximated by the near-dc component

$$\Upsilon_q = \nabla \varphi^2 \approx \frac{A^2}{2N} \sum_{n,m=1}^N \mathbf{k}_{nm} \sin(\omega_{nm} t - \mathbf{k}_{nm} \cdot \mathbf{r} + \theta_{nm}), \quad (29)$$

where $\omega_{nm} = \omega_n - \omega_m$, $\mathbf{k}_{nm} = \mathbf{k}_n - \mathbf{k}_m$, and $\theta_{nm} = \theta_n - \theta_m$. Such a signal can be well characterized by two parameters: coherence time and amplitude.

For a solitary magnetometer or comagnetometer, a UBDM signature would be difficult to distinguish from comparably large background noise. Our strategy for analysis of GNOME data, presently underway, is to measure the cross-correlation between data measured at different stations. For stations with aligned sensitive axes and separations $\lesssim \lambda_{\text{coh}}$ and time delays $\lesssim \tau_{\text{coh}}$, UBDM quadratically coupled to atomic spins could generate a common-mode signal that might be distinguishable from uncorrelated background noise for sufficiently strong interactions. Figure 8 shows the auto-correlation function of simulated ALP signals, which is equivalent to the cross-correlation between stations with aligned sensitive axes within a coherence patch (ignoring any contribution from uncorrelated noise). The width of the correlation feature is $\approx \tau_{\text{coh}}$ in relative time shift units. This technique of intensity interferometry will enable a search for the quadratic coupling to ALPs over a mass range $\sim 10^{-14}$ eV – 10^{-9} eV using GNOME [63].

E. Solar axion halo

Another theoretical possibility, closely related to the axion star model described in Sec. IV B, is that tidal shearing forces may enable astrophysical bodies such as Earth and the Sun to capture UBDM in their gravitational fields and form a local halo [139–143], see Fig. 9. In these models, the Earth or Sun effectively acts as a seed in the formation process of the axion star. If such a process occurs, there would be a substantial overdensity of the ALP field near these bodies as compared to the average dark matter density as discussed in Refs. [139, 141]. Possible mechanisms for capture of dark matter by dense astrophysical bodies have been studied, for example, in Refs. [144–149], and continue to be actively investigated.

1. Theoretical description

Here we assume the model of a gravitationally bound solar ALP halo described in Refs. [139, 141], and also assume that the halo is non-rotating (i.e., at rest with respect to the Sun). For a solar halo, the ALP field amplitude at the position of Earth exponentially decays

over a characteristic length scale given by

$$R_\star \approx \frac{\hbar^2}{G_N M_\odot m_a^2}, \quad (30)$$

where G_N is Newton’s gravitational constant and M_\odot is the Sun’s mass. For the solar ALP halo to extend to the position of Earth, we require $R_\star \gtrsim 1$ AU. This imposes the requirement that $m_a c^2 \lesssim 10^{-14}$ eV. The ALP field oscillates at $\approx \omega_c$ with a coherence time $\tau_{\text{coh}} \gtrsim m_a R_\star^2 / \hbar$. For $m_a c^2 \lesssim 10^{-14}$ eV, the coherence time is longer than $\sim 10^7$ s; therefore, we can treat oscillations of the ALP field as effectively single frequency (i.e., monochromatic). Thus the ALP field can be described as [139, 141]:

$$\varphi(\mathbf{r}, t) \approx \varphi_0 \cos(\omega_c t - \mathbf{k} \cdot \mathbf{r} + \theta) e^{-r/R_\star}, \quad (31)$$

where φ_0 is a constant determined by the overall energy density in the solar ALP halo and θ is a random phase, constant over the coherence time and coherence length. For simplicity, in this example we set $\theta = 0$.

2. Signal model

The exotic pseudo-magnetic field due to a solar ALP halo for the linear spin interaction is given by

$$\Upsilon_l = \nabla \varphi(\mathbf{r}, t) = \varphi_0 e^{-r/R_\star} \left[\mathbf{k} \sin(\omega_c t - \mathbf{k} \cdot \mathbf{r}) - \frac{\hat{\mathbf{r}}}{R_\star} \cos(\omega_c t - \mathbf{k} \cdot \mathbf{r}) \right], \quad (32)$$

and for the quadratic spin interaction is given by

$$\Upsilon_q = \nabla \varphi^2(\mathbf{r}, t) = \varphi_0^2 e^{-2r/R_\star} \left[\mathbf{k} \sin(2\omega_c t - 2\mathbf{k} \cdot \mathbf{r}) - \frac{2\hat{\mathbf{r}}}{R_\star} \cos^2(\omega_c t - \mathbf{k} \cdot \mathbf{r}) \right]. \quad (33)$$

We note that in both cases there are two components of Υ in the lab frame [141]: (1) a radial component from the spatial ALP gradient directed toward the Sun’s position and (2) a transverse component along \mathbf{k} due to the ALP wind interaction [5, 6]. Because the relative velocity of Earth with respect to the Sun is dominated by its orbital motion (~ 100 times faster than the velocity component due to Earth’s rotation about its axis), it turns out that all GNOME sensors have approximately the same \mathbf{k} and thus see the same field. The amplitudes of the radial and transverse components of Υ are relatively constant in time, so the signal observed in a particular GNOME sensor has a predictable daily modulation due to the time dependence of $\hat{\mathbf{r}} \cdot \hat{\mathbf{m}}$ and $\hat{\mathbf{k}} \cdot \hat{\mathbf{m}}$ caused by the rotation of Earth. An example of the time dependence of such a signal is shown in the lower plot of Fig. 9.

Analysis of GNOME data to search for a solar ALP halo is in progress. The strategy is to search for a per-

sistent single-frequency signal in cross-correlation data between stations, and then use the predicted daily modulation to distinguish between a signal from a solar ALP halo and systematic backgrounds.

F. Exotic Low-mass Fields (ELFs) emitted from black hole mergers

In Ref. [56], a subset of the present authors considered a possibility that bursts of ultrarelativistic scalar fields can be produced in the course of some high energy astrophysical event such as a supernova explosion, a binary black hole merger, or in conjunction with a fast radio

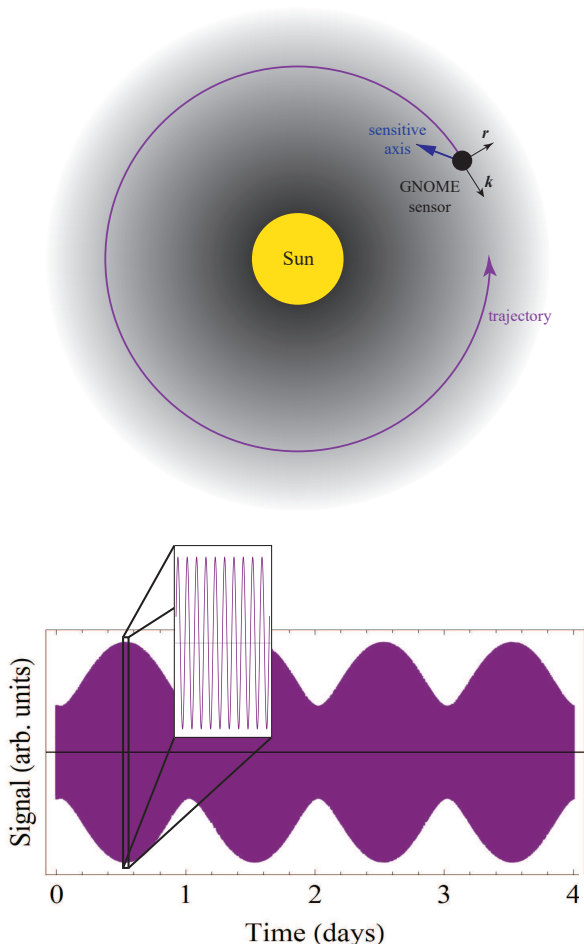


FIG. 9. Upper diagram: Schematic diagram of Earth moving through a solar ALP halo. The pseudo-magnetic field associated with a solar ALP halo coupling to atomic spins has both a radial component in the $-\hat{r}$ direction due to the spatial gradient and a transverse component due to the “ALP wind” directed along the ALP halo’s relative velocity with respect to the lab frame, \hat{k} . Lower plot: example signal due to the linear spin coupling. Signal is shown over four days, exhibiting an envelope function due to the daily modulation of the signal due to the rotation of the GNOME sensor’s sensitive axis with respect to the pseudo-magnetic field \mathbf{Y} . Inset shows the fast oscillation at the Compton frequency.

burst via some as yet unknown coherent process⁶ (see, for example, Ref. [151]). These “exotic low-mass fields”

⁶ Note that due to the energy-time uncertainty relation, if the high-energy astrophysical event generating the ELF has duration τ_0 , the corresponding spread in energies of the emitted ELF wave packet is $\gtrsim \hbar/\tau_0$. Thus the spread in frequencies at the source is $\Delta\omega_0 \gtrsim 2\pi/\tau_0$. Our discussion here assumes coherent production, which requires $\Delta\omega_0 \ll \omega$. To interpret results in terms of the model presented here and in Ref. [56], we must restrict considerations to the regime where the relativistic energy $\varepsilon = \hbar\omega$ of the ELF satisfies $\varepsilon \gg \hbar/\tau_0$, as noted in Ref. [150].

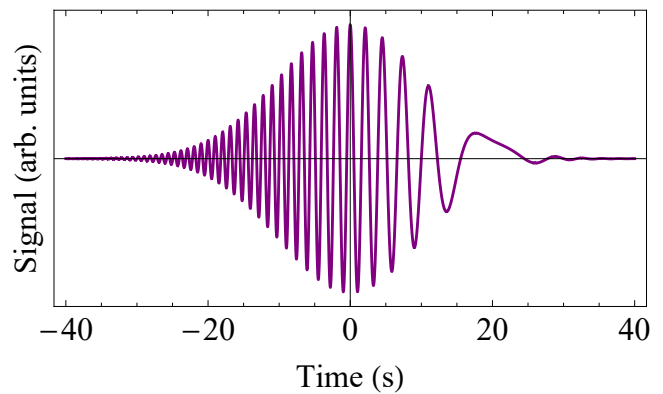


FIG. 10. Example signal of an ELF measured by a GNOME sensor based on Eq. (34), with $\omega_0 = 2\pi \times (0.5 \text{ Hz})$, $\tau = 10 \text{ s}$, and $\delta t = 10 \text{ s}$.

(ELFs) would thus have large mode occupation numbers, enabling their treatment as classical waves with oscillation frequency given by $\hbar\omega = \sqrt{m^2c^4 + p^2c^2} \approx pc$. Such ELFs can be searched for with GNOME.

1. Theoretical description

Consider a scenario where some energy ΔE is radiated isotropically in the form of a Gaussian ELF burst with duration τ_0 at the source. The Klein-Gordon equation for $\varphi(r)$ can be solved to obtain

$$\varphi(t) \approx \frac{A_0}{R} \sqrt{\frac{\tau_0}{\tau}} \exp\left(-\frac{(t-t_s)^2}{2\tau^2}\right) \times \cos\left(\omega_0(t-t_s) - \frac{\omega_0}{4\delta t}(t-t_s)^2\right), \quad (34)$$

where ω_0 is the central frequency of the wave packet, τ the duration of the pulse as measured by sensors on Earth, $t_s = R/v_g$ represents the transit time of the ELF pulse from a source at distance R from Earth, and v_g the group velocity. The delay time between an electromagnetic or gravitational wave trigger and an ELF pulse is $\delta t = R/v_g - R/c$. In terms of the total energy released, the amplitude A_0 is given by

$$A_0 \approx \frac{1}{\pi^{1/4}} \left(\frac{1}{\omega_0} \sqrt{\frac{c\Delta E}{2\pi\tau_0}} \right). \quad (35)$$

Equations (34) and (35) describe a Gaussian wavepacket which disperses with a chirp rate

$$\frac{d\omega(t)}{dt} = -\frac{1}{\tau_0\tau} = -\frac{\omega_0}{2\delta t}. \quad (36)$$

Notably, the chirp rate is constrained by the central frequency and the delay from the electromagnetic or gravitational wave trigger.

2. Signal model

As a consequence of the couplings described in Eqs. (3) to (9), the existence of scalar fields with a form such as that described by Eq. (34) would lead to pseudo-magnetic fields in GNOME due to interaction terms proportional to $\mathbf{S} \cdot \nabla\varphi(\mathbf{r}, t)$ and $\mathbf{S} \cdot \nabla[\varphi(\mathbf{r}, t)]^2$. A signal due to an ELF event (Fig. 10) would therefore: (1) originate from the same source as the electromagnetic or gravitational wave trigger; (2) have a spatial pattern in the GNOME network given by the projection of the ELF velocity vector on the axes of the sensors in the network; and (3) have a characteristic chirp pattern given by Eq. (36). Using these characteristics, we have designed an analysis algorithm to search for ELF signals in GNOME data. Measurements from the GNOME sensors are projected into the time-frequency plane with a resolution chosen to match the expected signal dispersion. We then construct a network-wide test statistic and search for signals consistent with ELFs in the GNOME data in intervals of time shortly after reported binary black hole merger and fast radio burst events.

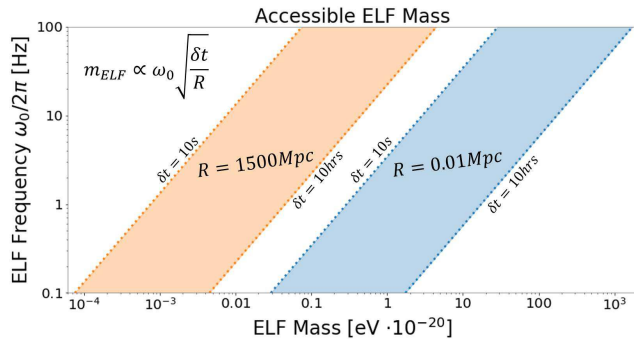


FIG. 11. Accessible masses for ELFs from sources located at distances $R = 1500$ Mpc and $R = 0.01$ Mpc. The left and right edges of the bands are set by the delay times $10\text{ s} < \delta t < 10\text{ hr}$.

We show in Fig. 11 the range of masses that are accessible by GNOME given the bandwidth of the magnetometers, assuming an observation time of 10 hours after the trigger. Thus GNOME can act as a “telescope” to detect ELF signals from sources that generate ALP bursts of sufficient intensity.

G. Other potential candidates

There are many other exotic physics scenarios that can potentially be searched for using data from the GNOME experiment, demonstrating the versatility of the general approach. For example, as already noted, it may be that there are relatively strong interactions between particles in the dark sector. Such interactions could cause dark matter particles to coalesce into large composite “blobs” [33]. In contrast to the axion star, Q-ball, and solar axion-halo scenarios already considered above, which

are composite states of ultralight particles, there could be dark matter blobs formed from heavy fermions or bosons that exert long-range forces mediated by other fundamental constituents of the dark sector [33, 152]. Other possible search targets for the GNOME experiment are ALP waves emanating from black hole superradiance [153] or from the collapse of axion stars [151]. In related work, unshielded magnetometer networks have been used to search for signals from dark (or hidden) photons [154, 155] and axions [156].

Yet another possible search target for GNOME are UBDM streams, in particular those gravitationally focused by other bodies in the solar system. Cosmological simulations indicate that up to 10^{12} small-velocity-dispersion (compared to that in the SHM) streams of DM may be present in the vicinity of the solar system [157]. The deflection experienced by these particles depends on the mass distribution of the source of gravitational focusing, is independent of the DM particle mass, and is inversely proportional to the square of its velocity. For UBDM, its wave nature has to be considered for a full description of the spectral signatures due to gravitational focusing [158]. Generally, for deflection of particles by the gravitational potential of the Earth, efficient focusing on Earth’s surface (where GNOME operates) occurs for particles with velocities of approximately 10 to 20 km/s [159, 160]. In this case, flux enhancements of up to 10^9 are predicted. Gravitational deflection by other objects in the solar system, such as Jupiter, can also generate flux enhancements on Earth. This requires larger stream velocities of approximately $10^{-3}c$ and results in smaller enhancements of only 10^6 [161]. Again, the networked approach of GNOME offers several advantages when searching for such gravitationally focused streams. Namely, the small size of such stream foci, on the order of a few km for deflection in Earth’s gravitational potential and much less for that of Jupiter, leads to transient signals lasting only about 10 s. This can be difficult to distinguish from noise when only a single detector is employed. For long streams, there is a chance of the detecting the enhanced DM flux daily with one or more detectors over the course of several weeks. Obviously, the likelihood of encountering the high flux regions increases with the number of sensors in a network. A network also allows for precisely determining the spatial direction of the stream, which can help to better understand the origins of such streams when detected, although this can be a complex endeavor as upstream sources of gravitational deflection also have to be considered. Furthermore, sensors at approximately the same latitudes could produce correlated signals from the same focused-DM source (Fig. 12). The geographical locations of GNOME sensors make it viable for such correlations.

While GNOME is primarily a tool for detection of transient “new-physics” signals, its sister experiment, the Cosmic Axion Spin-Precession Experiment (CASPER) [9, 11, 16], is searching for oscillating (but not necessarily transient) effects of galactic dark matter and dark

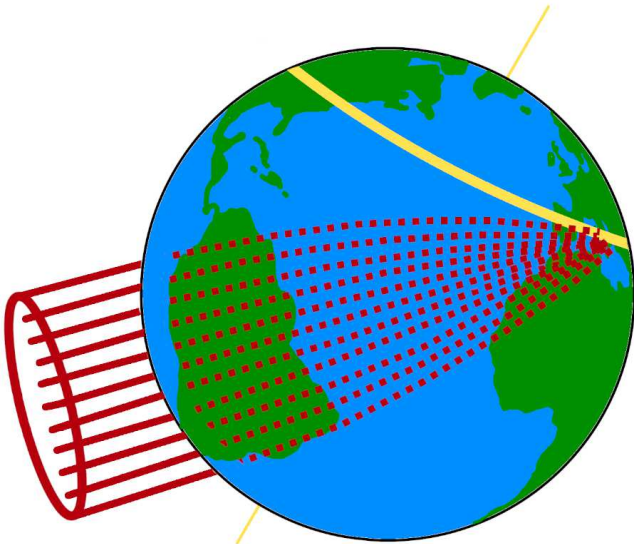


FIG. 12. Example of a low velocity UBDM stream (red) gravitationally focused into a small region on Earth’s surface, the trajectories are approximately following predictions made in Ref. [159]. As Earth rotates around its axis, the focus follows a path (yellow) along a fixed latitude.

matter concentrated in the Sun- and Earth-bound halos. CASPER operates simultaneously in two locations, Boston University (USA) and the Helmholtz Institute, Johannes Gutenberg University, Mainz (Germany). The central idea of CASPER is that it is a nuclear magnetic resonance (NMR) experiment, where the role of the transverse oscillating magnetic field “ B_1 ” is relegated to the ambient Axion/ALP field either through its coupling to gluons (CASPER-electric) or via its gradient interactions [see Eqs. (6) and (9); CASPER-gradient]. While CASPER will reach up to Compton frequencies ≈ 600 MHz, it has already ventured into the much lower-frequency range [12, 13], from near DC to several hertz. The low-frequency range has also been explored by various other experiments [10, 17, 18, 20, 26].

The Advanced-GNOME comagnetometers [32, 83] are ideally suited to contribute to “CASPER-like” searches in the Compton frequency range from near-DC to several hundred hertz, with the sensitivity that is estimated to be competitive to the best previous searches. The results of the first experiments in this direction may be expected already at the early stages of Advanced GNOME, as a search in this mode does not require the full network capabilities. However, as with GNOME, we expect that the network will be immediately useful in vetoing spurious signals from various laboratory inferences, which will likely be different in different laboratories. Moreover, the network offers interesting possibilities of correlating the stochastic behavior of the signal in different stations that may offer an additional tool for discriminating the new-physics signals.

V. CONCLUSION AND OUTLOOK

The idea of GNOME is to carry out synchronous measurements using optical atomic magnetometers and comagnetometers operating within magnetically shielded environments in distant locations. The GNOME experiment searches for a class of signals different from that probed by most other experiments, namely transient and stochastic effects that could arise from ALP fields of astrophysical origin passing through Earth during a finite time. By analyzing the correlation between the signals from multiple, geographically separated sensors, it is possible to probe a wide variety of exotic physics scenarios.

When the idea of GNOME was conceived, ALP domain walls were the sole targets of the search [28, 31]. As the collaboration expanded and matured, we gradually realized that there are many more interesting physics scenarios that can be investigated with this tool, as, we hope, we have been able to convince the reader of this “GNOME science-case” article. Extrapolating from the first 10 years of the GNOME collaboration’s work, we may only expect the science case to continue its expansion, hopefully leading to a discovery of “new” physics.

The advent of GNOME was soon followed by the establishment of networks of atomic clocks [88] introduced to search for scalar UBDM whose effect is to produce apparent oscillation of fundamental constants, rather than causing spin precession. At the same time, it was realized that certain UBDM candidates like the relaxion [162, 163] may have mixed intrinsic parity and displaying both the scalar and pseudoscalar properties. This provides a motivation for building hybrid-sensor networks (for example, (co)magnetometer-clock networks) to cross-correlate the signals and enhance the background-suppression capabilities. We expect this cross-network approach to become commonplace in future work. Moreover, GNOME is planning future science runs to be synchronized with gravitational-wave detector networks such as LIGO/VIRGO in order to carry out “exotic” multimessenger astronomy [56].

It appears that the science case for search networks such as GNOME is mostly limited by our current scientific horizons and there are, in fact, many other interesting and unexpected signals we could be looking for, had we better imagination. But could we perhaps look for such signals before we realize what they are? It appears that modern machine-learning approaches indeed offer us such an exciting opportunity. It might work along the following lines: a machine-learning system is trained on the data from GNOME (and/or an expanded hybrid-sensor network) and establishes the “normal” dynamic state of the network. It is then further trained on a variety of new-physics scenarios. As a result of the training that can continue for the lifetime of the experiment, the artificial intelligence (AI) system would be able to recognize unusual events or patterns on the network. While this may look like a remote prospect, one should recognize that the task at hand is not too different from that of

detection of unidentified threats, which is routinely done at present by automated security systems.

In conclusion of our overview of the “GNOME science”, we mention that, apart from fundamental physics, magnetometer networks may also be useful in more “down-to-Earth” applications such as, for example, the study of magnetic signal patterns in urban environments and what they reveal about cities [164, 165].

ACKNOWLEDGEMENTS

The authors are grateful to Konstantin Zioutas for bringing the gravitational focusing effects to the attention of the GNOME collaboration. The GNOME collaboration thanks the Mainz Institute for Theoretical Physics (MITP) of the Cluster of Excellence “Precision Physics, Fundamental Interactions, and Structure of Matter” (PRISMA+ EXC 2118/1) for its hospitality and its partial support during the completion of this work. This work was additionally supported by the

U.S. National Science Foundation under grants PHY-1307507, PHY-1707875, PHY-1707803, PHY-2110370, PHY-2110388, and PHY-2207546; by the German Research Foundation (DFG) under grant no. 439720477 and within the German Excellence Strategy (Project ID 39083149); by COST (European Cooperation in Science and Technology); ZDG acknowledges institutional funding provided by the Institute of Physics Belgrade through a grant by the Ministry of Science, Technological Development and Innovations of the Republic of Serbia. The work of SP and GL is supported by the National Science Centre of Poland within the Opus program (grant 2019/34/E/ST2/00440) and in part by the Excellence Initiative – Research University of the Jagiellonian University in Kraków. The work of YVS was supported by the Australian Research Council under the Discovery Early Career Researcher Award DE210101593. The work of AD was supported in part by the Heising-Simons Foundation. The work of JE was supported by the World Premier International Research Center Initiative (WPI), MEXT, Japan and by the JSPS KAKENHI Grant Numbers 21H05451 and 21K20366. RF and DFJK acknowledge support by the NSF-BSF grant No. 2016635.

-
- [1] D. F. Jackson Kimball and K. van Bibber, *The Search for Ultralight Bosonic Dark Matter* (Springer, 2022).
- [2] P. W. Graham, I. G. Irastorza, S. K. Lamoreaux, A. Lindner, and K. A. van Bibber, Experimental searches for the axion and axion-like particles, *Annu. Rev. Nucl. Part. Sci.* **65**, 485 (2015).
- [3] P. W. Graham, D. E. Kaplan, J. Mardon, S. Rajendran, and W. A. Terrano, Dark matter direct detection with accelerometers, *Phys. Rev. D* **93**, 075029 (2016).
- [4] M. Safronova, D. Budker, D. DeMille, D. F. Jackson Kimball, A. Derevianko, and C. W. Clark, Search for new physics with atoms and molecules, *Rev. Mod. Phys.* **90**, 025008 (2018).
- [5] Y. Stadnik and V. Flambaum, Axion-induced effects in atoms, molecules, and nuclei: Parity nonconservation, anapole moments, electric dipole moments, and spin-gravity and spin-axion momentum couplings, *Phys. Rev. D* **89**, 043522 (2014).
- [6] P. W. Graham, D. E. Kaplan, J. Mardon, S. Rajendran, W. A. Terrano, L. Trahms, and T. Wilkason, Spin precession experiments for light axionic dark matter, *Phys. Rev. D* **97**, 055006 (2018).
- [7] D. Budker and D. F. Jackson Kimball, *Optical Magnetometry* (Cambridge University Press, 2013).
- [8] D. Budker and M. Romalis, Optical magnetometry, *Nature Phys.* **3**, 227 (2007).
- [9] D. Budker, P. W. Graham, M. Ledbetter, S. Rajendran, and A. O. Sushkov, Proposal for a cosmic axion spin precession experiment (casper), *Phys. Rev. X* **4**, 021030 (2014).
- [10] C. Abel, N. J. Ayres, G. Ban, G. Bison, K. Bodek, V. Bondar, M. Daum, M. Fairbairn, V. V. Flambaum, P. Geltenbort, *et al.*, Search for axionlike dark matter through nuclear spin precession in electric and magnetic fields, *Phys. Rev. X* **7**, 041034 (2017).
- [11] A. Garcon, D. Aybas, J. W. Blanchard, G. Centers, N. L. Figueroa, P. W. Graham, D. F. Jackson Kimball, S. Rajendran, M. G. Sendra, A. O. Sushkov, L. Trahms, T. Wang, A. Wickenbrock, T. Wu, and D. Budker, The Cosmic Axion Spin Precession Experiment (CASPER): a dark-matter search with nuclear magnetic resonance, *Quantum Sci. Technol.* **3**, 014008 (2017).
- [12] T. Wu, J. W. Blanchard, G. P. Centers, N. L. Figueroa, A. Garcon, P. W. Graham, D. F. Jackson Kimball, S. Rajendran, Y. V. Stadnik, A. O. Sushkov, *et al.*, Search for axionlike dark matter with a liquid-state nuclear spin comagnetometer, *Phys. Rev. Lett.* **122**, 191302 (2019).
- [13] A. Garcon, J. W. Blanchard, G. P. Centers, N. L. Figueroa, P. W. Graham, D. F. Jackson Kimball, S. Rajendran, A. O. Sushkov, Y. V. Stadnik, A. Wickenbrock, *et al.*, Constraints on bosonic dark matter from ultralow-field nuclear magnetic resonance, *Science Advances* **5**, eaax4539 (2019).
- [14] D. Aybas, H. Bekker, J. Blanchard, D. Budker, G. Centers, N. Figueroa, A. Gramolin, D. F. Jackson Kimball, A. Wickenbrock, and A. Sushkov, Quantum sensitivity limits of nuclear magnetic resonance experiments searching for new fundamental physics, *Quantum Sci. Technol.* **6**, 034007 (2021).
- [15] T. S. Roussy, D. A. Palken, W. B. Cairncross, B. M. Brubaker, D. N. Gresh, M. Grau, K. C. Cossel, K. B. Ng, Y. Shagam, Y. Zhou, *et al.*, Experimental constraint on axionlike particles over seven orders of magnitude in mass, *Phys. Rev. Lett.* **126**, 171301 (2021).
- [16] D. Aybas, J. Adam, E. Blumenthal, A. V. Gramolin, D. Johnson, A. Kleyheeg, S. Afach, J. W. Blanchard, G. P. Centers, A. Garcon, M. Engler, N. L. Figueroa,

- M. G. Sendra, A. Wickenbrock, M. Lawson, T. Wang, T. Wu, H. Luo, H. Mani, P. Mausekopf, P. W. Graham, S. Rajendran, D. F. Jackson Kimball, D. Budker, and A. O. Sushkov, Search for axionlike dark matter using solid-state nuclear magnetic resonance, *Phys. Rev. Lett.* **126**, 141802 (2021).
- [17] M. Jiang, H. Su, A. Garcon, X. Peng, and D. Budker, Search for axion-like dark matter with spin-based amplifiers, *Nature Phys.* **17**, 1402 (2021).
- [18] I. M. Bloch, G. Ronen, R. Shaham, O. Katz, T. Volansky, and O. Katz, New constraints on axion-like dark matter using a Floquet quantum detector, *Sci. Adv.* **8**, eabl8919 (2022).
- [19] J. Lee, M. Lisanti, W. A. Terrano, and M. Romalis, Laboratory Constraints on the Neutron-Spin Coupling of feV-scale Axions, arXiv:2209.03289 10.48550/arXiv.2209.03289 (2022).
- [20] C. Abel, N. Ayres, G. Ban, G. Bison, K. Bodek, V. Bondar, E. Chanel, C. Crawford, M. Daum, B. Dechenaux, *et al.*, Search for ultralight axion dark matter in a side-band analysis of a Hg-199 free-spin precession signal, arXiv:2212.02403 10.48550/arXiv.2212.02403 (2022).
- [21] K. Freese, M. Lisanti, and C. Savage, Colloquium: Annual modulation of dark matter, *Rev. Mod. Phys.* **85**, 1561 (2013).
- [22] A. Pillepich, M. Kuhlen, J. Guedes, and P. Madau, The distribution of dark matter in the Milky Way's disk, *Astrophys. J.* **784**, 161 (2014).
- [23] N. W. Evans, C. A. O'Hare, and C. McCabe, Refinement of the standard halo model for dark matter searches in light of the gaia sausage, *Phys. Rev. D* **99**, 023012 (2019).
- [24] J. W. Foster, N. L. Rodd, and B. R. Safdi, Revealing the dark matter halo with axion direct detection, *Phys. Rev. D* **97**, 123006 (2018).
- [25] G. P. Centers, J. W. Blanchard, J. Conrad, N. L. Figueroa, A. Garcon, A. V. Gramolin, D. F. Jackson Kimball, M. Lawson, B. Pelssers, J. A. Smiga, *et al.*, Stochastic fluctuations of bosonic dark matter, *Nature Comm.* **12**, 7321 (2021).
- [26] M. Lisanti, M. Moschella, and W. Terrano, Stochastic properties of ultralight scalar field gradients, *Phys. Rev. D* **104**, 055037 (2021).
- [27] A. V. Gramolin, A. Wickenbrock, D. Aybas, H. Bekker, D. Budker, G. P. Centers, N. L. Figueroa, D. F. Jackson Kimball, and A. O. Sushkov, Spectral signatures of axionlike dark matter, *Phys. Rev. D* **105**, 035029 (2022).
- [28] S. Pustelny, D. F. Jackson Kimball, C. Pankow, M. P. Ledbetter, P. Włodarczyk, P. Wcislo, M. Pospelov, J. R. Smith, J. Read, W. Gawlik, *et al.*, The global network of optical magnetometers for exotic physics (gnome): A novel scheme to search for physics beyond the standard model, *Annalen der Physik* **525**, 659 (2013).
- [29] S. Afach, D. Budker, G. DeCamp, V. Dumont, Z. D. Grujić, H. Guo, D. Jackson Kimball, T. Kornack, V. Lebedev, W. Li, *et al.*, Characterization of the global network of optical magnetometers to search for exotic physics (gnome), *Phys. Dark Universe* **22**, 162 (2018).
- [30] S. Afach, B. C. Buchler, D. Budker, C. Dailey, A. Derevianko, V. Dumont, N. L. Figueroa, I. Gerhardt, Z. D. Grujić, H. Guo, *et al.*, Search for topological defect dark matter with a global network of optical magnetometers, *Nature Phys.* **17**, 1396 (2021).
- [31] M. Pospelov, S. Pustelny, M. P. Ledbetter, D. F. Jackson Kimball, W. Gawlik, and D. Budker, Detecting domain walls of axionlike models using terrestrial experiments, *Phys. Rev. Lett.* **110**, 021803 (2013).
- [32] M. Padniuk, M. Kopciuch, R. Cipolletti, A. Wickenbrock, D. Budker, and S. Pustelny, Response of atomic spin-based sensors to magnetic and nonmagnetic perturbations, *Scientific Reports* **12**, 324 (2022).
- [33] D. M. Grabowska, T. Melia, and S. Rajendran, Detecting dark blobs, *Phys. Rev. D* **98**, 115020 (2018).
- [34] V. Yashchuk, S. Lee, and E. Paperno, Magnetic shielding, in *Optical Magnetometry* (Cambridge University Press, 2011) pp. 225–248.
- [35] D. Jackson Kimball, J. Dudley, Y. Li, S. Thulasi, S. Pustelny, D. Budker, and M. Zolotarev, Magnetic shielding and exotic spin-dependent interactions, *Phys. Rev. D* **94**, 082005 (2016).
- [36] D. F. Jackson Kimball, Nuclear spin content and constraints on exotic spin-dependent couplings, *New J. Phys.* **17**, 073008 (2015).
- [37] Y. Stadnik and V. Flambaum, Nuclear spin-dependent interactions: searches for wimp, axion and topological defect dark matter, and tests of fundamental symmetries, *Eur. Phys. J. C* **75**, 1 (2015).
- [38] R. Peccei and H. Quinn, CP conservation in the presence of pseudoparticles, *Phys. Rev. Lett.* **38**, 1440 (1977).
- [39] R. Peccei and H. Quinn, Constraints imposed by CP conservation in the presence of pseudoparticles, *Phys. Rev. D* **16**, 1791 (1977).
- [40] S. Weinberg, A new light boson?, *Phys. Rev. Lett.* **40**, 223 (1978).
- [41] F. Wilczek, Problem of strong p and t invariance in the presence of instantons, *Phys. Rev. Lett.* **40**, 279 (1978).
- [42] P. W. Graham, D. E. Kaplan, and S. Rajendran, Cosmological Relaxation of the Electroweak Scale, *Phys. Rev. Lett.* **115**, 221801 (2015).
- [43] R. T. Co, L. J. Hall, and K. Harigaya, Predictions for axion couplings from ALP cogenesis, *J. High Energy Phys.* **2021**, 172.
- [44] P. Svrček and E. Witten, Axions in string theory, *J. High Energy Phys.* **06**, 051.
- [45] A. Arvanitaki, S. Dimopoulos, S. Dubovsky, N. Kaloper, and J. March-Russell, String axiverse, *Phys. Rev. D* **81**, 123530 (2010).
- [46] L. F. Abbott and P. Sikivie, A cosmological bound on the invisible axion, *Physics Letters B* **120**, 133 (1983).
- [47] J. Preskill, M. B. Wise, and F. Wilczek, Cosmology of the invisible axion, *Physics Letters B* **120**, 127 (1983).
- [48] M. Dine and W. Fischler, The not-so-harmless axion, *Physics Letters B* **120**, 137 (1983).
- [49] B. Freivogel, Anthropic explanation of the dark matter abundance, *Journal of Cosmology and Astroparticle Physics* **2010**, 021.
- [50] S. Chang, C. Hagmann, and P. Sikivie, Studies of the motion and decay of axion walls bounded by strings, *Phys. Rev. D* **59**, 023505 (1998).
- [51] N. Arkani-Hamed, D. P. Finkbeiner, T. R. Slatyer, and N. Weiner, A theory of dark matter, *Phys. Rev. D* **79**, 015014 (2009).
- [52] P. Arias, D. Cadamuro, M. Goodsell, J. Jaeckel, J. Redondo, and A. Ringwald, WISPy cold dark matter, *J. Cosm. Astropart. Phys.* **2012**, 013 (2012).
- [53] P. W. Graham and A. Scherlis, Stochastic axion scenario, *Phys. Rev. D* **98**, 035017 (2018).

- [54] L. D. Duffy and K. Van Bibber, Axions as dark matter particles, *New J. Phys.* **11**, 105008 (2009).
- [55] P. W. Graham and S. Rajendran, New observables for direct detection of axion dark matter, *Phys. Rev. D* **88**, 035023 (2013).
- [56] C. Dailey, C. Bradley, D. F. Jackson Kimball, I. A. Sulai, S. Pustelny, A. Wickenbrock, and A. Derevianko, Quantum sensor networks as exotic field telescopes for multi-messenger astronomy, *Nature Astron.* **5**, 150 (2021).
- [57] V. V. Flambaum, Axioelectric effect and other manifestations of dark matter and dark energy in laboratory experiments, Proceedings of the 9th Patras Workshop on Axions, WIMPs and WISPs, Mainz, Germany, 2013, https://axion-wimp2013.desy.de/e201031/index_eng.html.
- [58] D. F. Jackson Kimball, S. Afach, D. Aybas, J. Blanchard, D. Budker, G. Centers, M. Engler, N. Figueroa, A. Garcon, P. Graham, *et al.*, Overview of the cosmic axion spin precession experiment (CASPER), in *Microwave Cavities and Detectors for Axion Research*, edited by G. Carosi, G. Rybka, and K. van Bibber (Springer, 2020) pp. 105–121.
- [59] K. A. Olive and M. Pospelov, Environmental dependence of masses and coupling constants, *Phys. Rev. D* **77**, 043524 (2008).
- [60] T. Damour and K. Nordtvedt, General relativity as a cosmological attractor of tensor-scalar theories, *Phys. Rev. Lett.* **70**, 2217 (1993).
- [61] T. Damour and K. Nordtvedt, Tensor-scalar cosmological models and their relaxation toward general relativity, *Phys. Rev. D* **48**, 3436 (1993).
- [62] T. Damour and A. M. Polyakov, The string dilation and a least coupling principle, *Nucl. Phys. B* **423**, 532 (1994).
- [63] H. Masia-Roig, N. L. Figueroa, A. Bordon, J. A. Smiga, D. Budker, G. P. Centers, A. V. Gramolin, P. S. Hamilton, S. Khamis, C. A. Palm, *et al.*, Intensity interferometry for ultralight bosonic dark matter detection, arXiv:2202.02645 [10.48550/arXiv.2202.02645](https://arxiv.org/abs/10.48550/arXiv.2202.02645) (2022).
- [64] W. Bernreuther, Cp violation and baryogenesis, in *CP Violation in Particle, Nuclear and Astrophysics*, edited by M. Beyer (Springer Berlin Heidelberg, Berlin, Heidelberg, 2002) pp. 237–293.
- [65] P. Włodarczyk, S. Pustelny, D. Budker, and M. Lipiński, Multi-channel data acquisition system with absolute time synchronization, *Nucl. Instrum. Methods. Phys. Res. A* **763**, 150 (2014).
- [66] I. Kominis, T. Kornack, J. Allred, and M. Romalis, A subfemtotesla multichannel atomic magnetometer, *Nature* **422**, 596–599 (2003).
- [67] S. Groeger, G. Bison, J. L. Schenker, R. Wynands, and A. Weis, A high-sensitivity laser-pumped Mx magnetometer, *Eur. Phys. J. D* **38**, 239–247 (2006).
- [68] S. Pustelny, A. Wojciechowski, M. Gring, J. Kotyrba, M. amd Zachorowski, and G. W., Magnetometry based on nonlinear magneto-optical rotation with amplitude-modulated light, *J. Appl. Phys.* **103**, 063108 (2008).
- [69] T. W. Kornack and M. V. Romalis, Dynamics of two overlapping spin ensembles interacting by spin exchange, *Phys. Rev. Lett.* **89**, 253002 (2002).
- [70] W. A. Terrano and M. V. Romalis, Comagnetometer probes of dark matter and new physics, *Quantum Science and Technology* **7**, 014001 (2021).
- [71] H. Masia-Roig, J. A. Smiga, D. Budker, V. Dumont, Z. Grujic, D. Kim, D. F. Jackson Kimball, V. Lebedev, M. Monroy, S. Pustelny, *et al.*, Analysis method for detecting topological defect dark matter with a global magnetometer network, *Phys. Dark Universe* **28**, 100494 (2020).
- [72] J. A. Smiga, Assessing the quality of a network of vector-field sensors, *Eur. Phys. J. D* **76**, 4 (2022).
- [73] M. Jiang, Y. Qin, X. Wang, Y. Wang, H. Su, X. Peng, and D. Budker, Floquet spin amplification, *Phys. Rev. Lett.* **128**, 233201 (2022).
- [74] A. G. Glenday, C. E. Cramer, D. F. Phillips, and R. L. Walsworth, Limits on anomalous spin-spin couplings between neutrons, *Phys. Rev. Lett.* **101**, 261801 (2008).
- [75] M. Jiang, H. Su, Z. Wu, X. Peng, and D. Budker, Floquet maser, *Sci. Adv.* **7**, eabe0719 (2021).
- [76] B. J. Venema, P. K. Majumder, S. K. Lamoreaux, B. R. Heckel, and E. N. Fortson, Search for a Coupling of Earth’s Gravitational Field to Nuclear Spins in Atomic Mercury, *Phys. Rev. Lett.* **68**, 135 (1992).
- [77] Y. Feng, D. Ning, S. Zhang, Z. Lu, and D. Sheng, Search for monopole-dipole interactions at the sub-millimeter range with a ^{129}Xe - ^{131}Xe -Rb comagnetometer, *Phys. Rev. Lett.* **128**, 231803 (2022).
- [78] D. F. Jackson Kimball, I. Lacey, J. Valdez, J. Swiatkowski, C. Rios, R. Peregrina-Ramirez, C. Montcrieffe, J. Kremer, J. Dudley, and C. Sanchez, A dual-isotope rubidium comagnetometer to search for anomalous long-range spin-mass (spin-gravity) couplings of the proton, *Annalen der Physik* **525**, 514 (2013).
- [79] D. F. Jackson Kimball, J. Dudley, Y. Li, D. Patel, and J. Valdez, Constraints on long-range spin-gravity and monopole-dipole couplings of the proton, *Phys. Rev. D* **96**, 075004 (2017); Erratum: Constraints on long-range spin-gravity and monopole-dipole couplings of the proton [Phys. Rev. D 96, 075004 (2017)], *Phys. Rev. D* **107**, 019903(E) (2023).
- [80] Z. Wang, X. Peng, R. Zhang, H. Luo, J. Li, Z. Xiong, S. Wang, and H. Guo, Single-species atomic comagnetometer based on rb 87 atoms, *Phys. Rev. Lett.* **124**, 193002 (2020).
- [81] M. Ledbetter, S. Pustelny, D. Budker, M. V. Romalis, J. Blanchard, and A. Pines, Liquid-state nuclear spin comagnetometers, *Phys. Rev. Lett.* **108**, 243001 (2012).
- [82] T. Wu, J. W. Blanchard, D. F. Jackson Kimball, M. Jiang, and D. Budker, Nuclear-spin comagnetometer based on a liquid of identical molecules, *Phys. Rev. Lett.* **121**, 023202 (2018).
- [83] E. Klinger, T. Liu, M. Padniuk, M. Engler, T. Kornack, S. Pustelny, D. F. Jackson Kimball, D. Budker, and A. Wickenbrock, Polarization dynamics in a nuclear spin gyroscope, arXiv:2210.07687 [10.48550/arXiv.2210.07687](https://arxiv.org/abs/10.48550/arXiv.2210.07687) (2022).
- [84] P. Sikivie, Axions, domain walls, and the early universe, *Phys. Rev. Lett.* **48**, 1156 (1982).
- [85] M. Kawasaki, K. Saikawa, and T. Sekiguchi, Axion dark matter from topological defects, *Phys. Rev. D* **91**, 065014 (2015).
- [86] A. Vilenkin and A. E. Everett, Cosmic strings and domain walls in models with goldstone and pseudo-goldstone bosons, *Phys. Rev. Lett.* **48**, 1867 (1982).
- [87] M. Nagasawa and M. Kawasaki, Collapse of axionic domain wall and axion emission, *Phys. Rev. D* **50**, 4821 (1994).

- [88] A. Derevianko and M. Pospelov, Hunting for topological dark matter with atomic clocks, *Nature Physics* **10**, 933 (2014).
- [89] Y. B. Zeldovich, I. Y. Kobzarev, and L. B. Okun, Cosmological Consequences of the Spontaneous Breakdown of Discrete Symmetry, *Zh. Eksp. Teor. Fiz.* **67**, 3 (1974).
- [90] D. Kim, D. F. Jackson Kimball, H. Masia-Roig, J. A. Smiga, A. Wickenbrock, D. Budker, Y. Kim, Y. C. Shin, and Y. K. Semertzidis, A machine learning algorithm for direct detection of axion-like particle domain walls, *Phys. Dark Universe* **37**, 101118 (2022).
- [91] E. Braaten and H. Zhang, Colloquium: The physics of axion stars, *Rev. Mod. Phys.* **91**, 041002 (2019).
- [92] J. Eby, M. Leembruggen, L. Street, P. Suranyi, and L. Wijewardhana, Global view of QCD axion stars, *Phys. Rev. D* **100**, 063002 (2019).
- [93] J. Eby, L. Street, P. Suranyi, and L. Wijewardhana, Global view of axion stars with nearly Planck-scale decay constants, *Phys. Rev. D* **103**, 063043 (2021).
- [94] J. Eby, M. Leembruggen, L. Street, P. Suranyi, and L. Wijewardhana, Approximation methods in the study of boson stars, *Phys. Rev. D* **98**, 123013 (2018).
- [95] P.-H. Chavanis, Mass-radius relation of Newtonian self-gravitating Bose-Einstein condensates with short-range interactions. I. Analytical results, *Phys. Rev. D* **84**, 043531 (2011).
- [96] P.-H. Chavanis and L. Delfini, Mass-radius relation of newtonian self-gravitating bose-einstein condensates with short-range interactions. ii. numerical results, *Phys. Rev. D* **84**, 043532 (2011).
- [97] J. Eby, P. Suranyi, and L. Wijewardhana, The lifetime of axion stars, *Mod. Phys. Lett. A* **31**, 1650090 (2016).
- [98] J. Eby, M. Ma, P. Suranyi, and L. Wijewardhana, Decay of ultralight axion condensates, *J. High Energy Phys.* **2018** (1), 066.
- [99] H.-Y. Schive, M.-H. Liao, T.-P. Woo, S.-K. Wong, T. Chiueh, T. Broadhurst, and W. P. Hwang, Understanding the core-halo relation of quantum wave dark matter from 3D simulations, *Phys. Rev. Lett.* **113**, 261302 (2014).
- [100] D. Levkov, A. Panin, and I. Tkachev, Gravitational Bose-Einstein condensation in the kinetic regime, *Phys. Rev. Lett.* **121**, 151301 (2018).
- [101] B. Eggemeier and J. C. Niemeyer, Formation and mass growth of axion stars in axion miniclusters, *Phys. Rev. D* **100**, 063528 (2019).
- [102] K. Kirkpatrick, A. E. Mirasola, and C. Prescod-Weinstein, Relaxation times for bose-einstein condensation in axion miniclusters, *Phys. Rev. D* **102**, 103012 (2020).
- [103] L. Visinelli, S. Baum, J. Redondo, K. Freese, and F. Wilczek, Dilute and dense axion stars, *Phys. Lett. B* **777**, 64 (2018).
- [104] H. Zhang, Axion stars, *Symmetry* **12**, 25 (2019).
- [105] D. F. Jackson Kimball, D. Budker, J. Eby, M. Pospelov, S. Pustelny, T. Scholtes, Y. V. Stadnik, A. Weis, and A. Wickenbrock, Searching for axion stars and Q-balls with a terrestrial magnetometer network, *Phys. Rev. D* **97**, 043002 (2018).
- [106] M. Gleiser, Pseudostable bubbles, *Phys. Rev. D* **49**, 2978 (1994).
- [107] E. W. Kolb and I. I. Tkachev, Axion miniclusters and Bose stars, *Phys. Rev. Lett.* **71**, 3051 (1993).
- [108] E. P. Honda and M. W. Choptuik, Fine structure of oscillons in the spherically symmetric φ^4 Klein-Gordon model, *Phys. Rev. D* **65**, 084037 (2002).
- [109] M. Gleiser, d-dimensional oscillating scalar field lumps and the dimensionality of space, *Phys. Lett. B* **600**, 126 (2004).
- [110] K. Mukaida, M. Takimoto, and M. Yamada, On longevity of i-ball/oscillon, *JHEP* **03**, 122, [arXiv:1612.07750](https://arxiv.org/abs/1612.07750) [hep-ph].
- [111] K. Mukaida, M. Takimoto, and M. Yamada, On longevity of I-ball/oscillon, *J. High Energy Phys.* **2017** (3), 122.
- [112] D. J. Kaup, Klein-gordon geon, *Phys. Rev.* **172**, 1331 (1968).
- [113] R. Ruffini and S. Bonazzola, Systems of self-gravitating particles in general relativity and the concept of an equation of state, *Phys. Rev.* **187**, 1767 (1969).
- [114] F. E. Schunck and E. W. Mielke, General relativistic boson stars, *Class. Quantum Grav.* **20**, R301 (2003).
- [115] J. Barranco and A. Bernal, Self-gravitating system made of axions, *Phys. Rev. D* **83**, 043525 (2011).
- [116] P. Tinyakov, I. Tkachev, and K. Zioutas, Tidal streams from axion miniclusters and direct axion searches, *J. Cosmol. Astropart. Phys.* **2016** (01), 035.
- [117] W. Anderson, P. Brady, J. Creighton, and E. Flanagan, Excess power statistic for detection of burst sources of gravitational radiation, *Phys. Rev. D* **63**, 042003 (2001).
- [118] S. Coleman, Q-balls, *Nucl. Phys. B* **262**, 263 (1985).
- [119] T. D. Lee, Soliton stars and the critical masses of black holes, *Phys. Rev. D* **35**, 3637 (1987).
- [120] T.-D. Lee and Y. Pang, Nontopological solitons, *Phys. Rep.* **221**, 251 (1992).
- [121] A. Kusenko and P. J. Steinhardt, Q-ball candidates for self-interacting dark matter, *Phys. Rev. Lett.* **87**, 141301 (2001).
- [122] M. Colpi, S. L. Shapiro, and I. Wasserman, Boson stars: Gravitational equilibria of self-interacting scalar fields, *Phys. Rev. Lett.* **57**, 2485 (1986).
- [123] E. Y. Nugaev and A. Shkerin, Review of nontopological solitons in theories with $U(1)$ -symmetry, *J. Exp. Theor. Phys.* **130**, 301 (2020).
- [124] A. Kusenko and M. Shaposhnikov, Supersymmetric Q-balls as dark matter, *Phys. Lett. B* **418**, 46 (1998).
- [125] A. Kusenko, V. Kuzmin, M. Shaposhnikov, and P. G. Tinyakov, Experimental signatures of supersymmetric dark-matter q-balls, *Phys. Rev. Lett.* **80**, 3185 (1998).
- [126] R. Friedberg, T. Lee, and A. Sirlin, Class of scalar-field soliton solutions in three space dimensions, *Phys. Rev. D* **13**, 2739 (1976).
- [127] K. Lee, J. A. Stein-Schabes, R. Watkins, and L. M. Widrow, Gauged Q balls, *Phys. Rev. D* **39**, 1665 (1989).
- [128] G. Rosen, Dilatation covariance and exact solutions in local relativistic field theories, *Phys. Rev.* **183**, 1186 (1969).
- [129] S. Theodorakis, Analytic Q-ball solutions in a parabolic-type potential, *Phys. Rev. D* **61**, 047701 (2000).
- [130] I. Gulamov, E. Y. Nugaev, and M. Smolyakov, Analytic Q-ball solutions and their stability in a piecewise parabolic potential, *Phys. Rev. D* **87**, 085043 (2013).
- [131] T. Ioannidou and N. Vlachos, On the Q-ball profile function, *J. Math. Phys.* **44**, 3562 (2003).
- [132] T. Ioannidou, A. Kourioukidis, and N. Vlachos, Universality in a class of Q-ball solutions: An analytic approach, *J. Math. Phys.* **46**, 042306 (2005).

- [133] J. Heeck, A. Rajaraman, R. Riley, and C. B. Verhaaren, Understanding Q-balls beyond the thin-wall limit, *Phys. Rev. D* **103**, 045008 (2021).
- [134] D. Jackson Kimball, D. Budker, J. Eby, M. Pospelov, S. Pustelny, T. Scholtes, Y. Stadnik, A. Weis, and A. Wickenbrock, Searching for axion stars and q-balls with a terrestrial magnetometer network, *Phys. Rev. D* **97**, 043002 (2018).
- [135] A. Helmi, S. D. White, and V. Springel, The phase-space structure of a dark-matter halo: Implications for dark-matter direct detection experiments, *Phys. Rev. D* **66**, 063502 (2002).
- [136] M. Kamionkowski and S. M. Koushiappas, Galactic substructure and direct detection of dark matter, *Phys. Rev. D* **77**, 103509 (2008).
- [137] A. Derevianko, Detecting dark-matter waves with a network of precision-measurement tools, *Phys. Rev. A* **97**, 042506 (2018).
- [138] R. Hanbury Brown and R. Q. Twiss, Correlation between photons in two coherent beams of light, *Nature* **177**, 27 (1956).
- [139] A. Banerjee, D. Budker, J. Eby, H. Kim, and G. Perez, Relaxion stars and their detection via atomic physics, *Commun. Phys.* **3**, 1 (2020).
- [140] H. Grote and Y. Stadnik, Novel signatures of dark matter in laser-interferometric gravitational-wave detectors, *Phys. Rev. Research* **1**, 033187 (2019).
- [141] A. Banerjee, D. Budker, J. Eby, V. V. Flambaum, H. Kim, O. Matsedonskyi, and G. Perez, Searching for earth/solar axion halos, *J. High Energy Phys.* **2020** (9), 4.
- [142] S. M. Vermeulen, P. Relton, H. Grote, V. Raymond, C. Affeldt, F. Bergamin, A. Bisht, M. Brinkmann, K. Danzmann, S. Doravari, *et al.*, Direct limits for scalar field dark matter from a gravitational-wave detector, *Nature* **600**, 424 (2021).
- [143] O. Tretiak, X. Zhang, N. L. Figueroa, D. Antypas, A. Brogna, A. Banerjee, G. Perez, and D. Budker, Improved bounds on ultralight scalar dark matter in the radio-frequency range, *Phys. Rev. Lett.* **129**, 031301 (2022).
- [144] X. Xu and E. Siegel, Dark matter in the solar system, arXiv:0806.3767 [10.48550/arXiv.0806.3767](https://arxiv.org/abs/10.48550/arXiv.0806.3767) (2008).
- [145] I. Khriplovich and D. Shepelyansky, Capture of dark matter by the solar system, *Int. J. Mod. Phys. D* **18**, 1903 (2009).
- [146] I. Khriplovich, Capture of dark matter by the solar system: simple estimates, *Int. J. Mod. Phys. D* **20**, 17 (2011).
- [147] I. Khriplovich, Capture of dark matter by the solar system. analytical estimates, in *Gribov-80 Memorial Volume: Quantum Chromodynamics and Beyond* (World Scientific, 2011) pp. 471–478.
- [148] R. Brito, V. Cardoso, and H. Okawa, Accretion of dark matter by stars, *Phys. Rev. Lett.* **115**, 111301 (2015).
- [149] R. Brito, V. Cardoso, C. F. Macedo, H. Okawa, and C. Palenzuela, Interaction between bosonic dark matter and stars, *Phys. Rev. D* **93**, 044045 (2016).
- [150] Y. V. Stadnik, Comment on “Quantum sensor networks as exotic field telescopes for multi-messenger astronomy”, arXiv:2111.14351 (2021).
- [151] J. Eby, S. Shirai, Y. V. Stadnik, and V. Takhistov, Probing relativistic axions from transient astrophysical sources, *Phys. Lett. B* **825**, 136858 (2022), arXiv:2106.14893 [hep-ph].
- [152] S. Baum, M. A. Fedderke, and P. W. Graham, Searching for dark clumps with gravitational-wave detectors, *Phys. Rev. D* **106**, 063015 (2022).
- [153] M. Baryakhtar, M. Galanis, R. Lasenby, and O. Simon, Black hole superradiance of self-interacting scalar fields, *Phys. Rev. D* **103**, 095019 (2021).
- [154] M. A. Fedderke, P. W. Graham, D. F. Jackson Kimball, and S. Kalia, Earth as a transducer for dark-photon dark-matter detection, *Phys. Rev. D* **104**, 075023 (2021).
- [155] M. A. Fedderke, P. W. Graham, D. F. Jackson Kimball, and S. Kalia, Search for dark-photon dark matter in the supermag geomagnetic field dataset, *Phys. Rev. D* **104**, 095032 (2021).
- [156] A. Arza, M. A. Fedderke, P. W. Graham, D. F. J. Kimball, and S. Kalia, Earth as a transducer for axion dark-matter detection, *Phys. Rev. D* **105**, 095007 (2022).
- [157] M. Vogelsberger and S. D. M. White, Streams and caustics: the fine-grained structure of Λ CDM haloes, *Mon. Not. Roy. Astron. Soc.* **413**, 1419 (2011), arXiv:1002.3162 [astro-ph.CO].
- [158] H. Kim and A. Lenoci, Gravitational focusing of wave dark matter, *Phys. Rev. D* **105**, 063032 (2022), arXiv:2112.05718 [hep-ph].
- [159] Y. Sofue, Gravitational focusing of low-velocity dark matter on the earth’s surface, *Galaxies* **8**, 10.3390/galaxies8020042 (2020).
- [160] A. Kryemadhi, M. Maroudas, A. Mastronikolis, and K. Zioutas, Gravitational focusing effects on streaming dark matter as a new detection concept [10.48550/arXiv.2210.07367](https://arxiv.org/abs/10.48550/arXiv.2210.07367) (2022), [2210.07367](https://arxiv.org/abs/2210.07367).
- [161] B. R. Patla, R. J. Nemiroff, D. H. H. Hoffmann, and K. Zioutas, Flux enhancement of slow-moving particles by sun or jupiter: Can they be detected on earth?, *Astrophys. J.* **780**, 158 (2013).
- [162] P. W. Graham, D. E. Kaplan, and S. Rajendran, Cosmological relaxation of the electroweak scale, *Phys. Rev. Lett.* **115**, 221801 (2015).
- [163] A. Banerjee, H. Kim, and G. Perez, Coherent relaxion dark matter, *Phys. Rev. D* **100**, 115026 (2019).
- [164] T. A. Bowen, E. Zhivun, A. Wickenbrock, V. Dumont, S. D. Bale, C. Pankow, G. Dobler, J. S. Wurtele, and D. Budker, A network of magnetometers for multi-scale urban science and informatics, *Geosci. Instrum. Methods Data Syst.* **8**, 129 (2019).
- [165] V. Dumont, T. A. Bowen, R. Roglans, G. Dobler, M. S. Sharma, A. Karpf, S. D. Bale, A. Wickenbrock, E. Zhivun, T. Kornack, J. S. Wurtele, and D. Budker, Do cities have a unique magnetic pulse?, *J. of Appl. Phys.* **131**, 204902 (2022).



Achieving ultra-low and -uniform residual magnetic fields in a very large magnetically shielded room for fundamental physics experiments

N. J. Ayres¹, G. Ban², G. Bison^{3,a}, K. Bodek⁴, V. Bondar¹, T. Bouillaud⁵, D. Bowles⁶, E. Chanel⁷, W. Chen^{1,3}, P.-J. Chiu⁸, C. B. Crawford⁶, O. Naviliat-Cuncic², C. B. Doorenbos^{1,3}, S. Emmenegger¹, M. Fertl⁹, A. Fratangelo⁷, W. C. Griffith¹⁰, Z. D. Grujic¹¹, P. G. Harris¹⁰, K. Kirch^{1,3}, V. Kletzl^{1,3}, J. Krempel¹, B. Lauss³, T. Lefort², A. Lejuez², R. Li¹², P. Mullan¹, S. Pacura⁴, D. Pais^{1,3}, F. M. Piegsa⁷, I. Rienäcker³, D. Ries³, G. Pignol⁵, D. Rebreyend⁵, S. Rocchia⁵, D. Rozpedzik⁴, W. Saenz-Arevalo², P. Schmidt-Wellenburg³, A. Schnabel¹³, E. P. Segarra^{3,b}, N. Severijns¹², K. Svirina⁵, R. Tavakoli Dinani¹², J. Thorne⁷, J. Vankeirsbilck¹², J. Voigt¹³, N. Yazdandoost¹⁴, J. Zejma⁴, N. Ziehl¹, G. Zsigmond³, The nEDM collaboration at PSI

- ¹ Institute for Particle Physics and Astrophysics, ETH Zürich, 8093 Zurich, Switzerland
² Normandie Université, ENSICAEN, UNICAEN, CNRS/IN2P3, LPC Caen, 14000 Caen, France
³ Paul Scherrer Institut, 5232 Villigen PSI, Switzerland
⁴ Marian Smoluchowski Institute of Physics, Jagiellonian University, 30-348 Kraków, Poland
⁵ Université Grenoble Alpes, CNRS, Grenoble INP, LPSC-IN2P3, 38026 Grenoble, France
⁶ Department of Physics and Astronomy, University of Kentucky, Lexington, KY 40506, USA
⁷ Laboratory for High Energy Physics and Albert Einstein Center for Fundamental Physics, University of Bern, 3012 Bern, Switzerland
⁸ University of Zürich, 8057 Zurich, Switzerland
⁹ Institute of Physics, Johannes Gutenberg University, 55128 Mainz, Germany
¹⁰ Department of Physics and Astronomy, University of Sussex, Falmer, Brighton BN1 9QH, UK
¹¹ Institute of Physics, Photonics Center, University of Belgrade, Belgrade 11080, Serbia
¹² Instituut voor Kern-en Stralingsfysica, University of Leuven, 3001 Leuven, Belgium
¹³ Physikalisch-Technische Bundesanstalt, Abbestr. 2-12, 10587 Berlin, Germany
¹⁴ Department of Chemistry-TRIGA Site, Johannes Gutenberg University Mainz, 55128 Mainz, Germany

Received: 10 October 2023 / Accepted: 8 December 2023 / Published online: 8 January 2024
© The Author(s) 2024

Abstract High-precision searches for an electric dipole moment of the neutron (nEDM) require stable and uniform magnetic field environments. We present the recent achievements of degaussing and equilibrating the magnetically shielded room (MSR) for the n2EDM experiment at the Paul Scherrer Institute. We present the final degaussing configuration that will be used for n2EDM after numerous studies. The optimized procedure results in a residual magnetic field that has been reduced by a factor of two. The ultra-low field is achieved with the full magnetic-field-coil system, and a large vacuum vessel installed, both in the MSR. In the inner volume of $\sim 1.4 \text{ m}^3$, the field is now more uniform and below 300 pT. In addition, the procedure is faster and dissipates less heat into the magnetic environment, which in turn, reduces its thermal relaxation time from 12 h down to 1.5 h.

1 Introduction

n2EDM is the current state of the art experiment, carrying out a high-precision search for an electric dipole moment of the neutron [1] at the ultra-cold neutron source [2] of the Paul Scherrer Institute. The experiment will deliver an order of magnitude better sensitivity than previous efforts [3], down to $1 \times 10^{-27} e \text{ cm}$. The experiment precisely extracts the spin precession frequency of ultra-cold neutrons in a weak magnetic field, B_0 and a strong electric field, E , via Ramsey's method of separated oscillating fields [4]. In order to reach this sensitivity, a stable and uniform magnetic field environment is critical. Thus, shielding the precession chamber from external magnetic flux is crucial.

The n2EDM precession chamber is held in a magnetically shielded room (MSR), utilizing both active and passive magnetic shielding components [1, 5–7]. The active magnetic shielding compensates external magnetic-field drifts, maintaining a constant field environment on the outside of the

^a e-mail: georg.bison@psi.ch (corresponding author)

^b e-mail: efrain.segarra@psi.ch (corresponding author)

MSR of $\sim 1 \mu\text{T}$ [7]. In the MSR, passive shielding materials are used to reduce the magnetic flux to the innermost volume [6]. Passive material often used for shielding have a high magnetic permeability, such as MUMETALL[®], a soft ferromagnetic alloy of nickel and iron used in the construction of this MSR.

The MSR inner volume is almost perfectly cubic, with a side length of 2.93 m and internal volume of 25 m^3 for the experimental apparatus. The outside dimensions of the MSR is $5.2 \text{ m} \times 5.2 \text{ m}$ horizontally and 4.8 m vertically. To achieve a quasi-static shielding factor of $\sim 10^5$ at 0.01 Hz, the MSR is composed of seven shielding layers: one aluminium layer (serving as an eddy current shield) and six soft magnetic layers (five layers of MUMETALL[®] and one layer, “layer 6”, of the alloy ULTRAVAC 816[®]) [6].

The magnetic environment during data-taking for the n2EDM experiment consists of a constant, vertical magnetic field, B_0 , of about $1 \mu\text{T}$ in the direction of the $\pm z$ -axis, produced by a cuboid coil [1].

To obtain a pristine magnetic environment that is equilibrated to the weak magnetic field $B_0 \sim 1 \mu\text{T}$, contributions of the residual magnetic field must be near-zero. Near-zero residual magnetic field is achieved via “degaussing” the passive shielding, or “equilibrating” it to stable field conditions, with respect to the additional $1 \mu\text{T}$ of the experiment.

Degaussing reduces, ideally “erases”, the residual magnetization of a material. It is typically done by applying a strong, alternating polarity, sinusoidal magnetic field. The magnetic flux must be initially strong enough to completely saturate the material everywhere, thereby erasing the previous magnetization state. The amplitude of the oscillating field then slowly decays to zero, producing randomized magnetic domains in the material. If the field does not decay to exactly zero, i.e., if any DC current offset exists, a residual magnetization will remain. See Refs. [8–11] for recent reviews and efforts of degaussing MSRs. Additionally, degaussing will heat the material. During the thermal relaxation after degaussing, magnetic field drifts occur. A reduction of dissipated heat would reduce the thermal relaxation time towards stable field conditions, and is therefore ideal.

To produce the alternating magnetic flux for degaussing, currents are applied to coils wound around the shielding layers. As also developed in Ref. [11], n2EDM features a novel distributed coil design for a more complete degaussing of the innermost shielding layer. A successful degaussing of the MSR, with low field values of below 600 pT for the entire inner volume of the MSR ($\sim 25 \text{ m}^3$), has already been demonstrated in Ref. [6]. While the residual field found there is sufficient enough to allow for a sensitive n2EDM measurement, improvements were sought due to the long duration of the degaussing procedure (3.5 h) and the long thermal relaxation time after a degaussing (12 h).

In this article, we present further improvements to the degaussing procedure, including further reducing the residual magnetic field and improving its uniformity, all while taking less time and dissipating less heat. This paper presents the experimental constraints, discusses the degaussing design and procedure, and outlines improvements made.

2 Experimental requirements

In order to reach the sensitivity goal of the n2EDM experiment [1], the influence of the residual field on the overall strength and non-uniformity of the $1 \mu\text{T}$ B_0 magnetic field should be minimal. The specific design requirements is that the residual field must be below 500 pT in the central 1 m^3 with a field gradient less than 300 pT/m, see Ref. [1]. The length of time to degauss, and the heat dissipation due to degaussing, should be minimized to maximize available measurement time under stable magnetic-field conditions.

3 Design of the degaussing system

In order to degauss each layer of the MSR individually, coils are installed in order to produce a magnetic flux around each spatial direction, x , y , and z axes. This corresponds to x , y , and z degaussing. In the initial setup of the n2EDM degaussing system, we followed the procedures laid out in Refs. [8, 9].

The construction and installation of the coils were done by the company VAC,¹ which produced the MSR. Prior to mounting, all parts of the coils of the inner MSR were checked for magnetic contamination with a 3D superconducting quantum interference device (SQUID) array installed in the BMSR-2 of Physikalisch Technische Bundesanstalt (PTB), Berlin [13].

3.1 Layers 1-5

The outer five MUMETALL[®] layers of the MSR (layers 1–5) follow the same coil design, with wires running along the edges, labeled A in Fig. 1 for the z -degaussing. x -, y -, and z -degaussing each has four coils along the edge of each spatial direction, making twelve coils per layer in total. Each coil has seven turns fabricated out of 6 mm^2 copper cables. The coils for each spatial direction are connected in series by a 6 mm^2 coaxial cable, where the shielding is used as a current return in order to avoid stray magnetic fields by the loop. Between the RF shield of the MSR and the electrical cabinet hosting the electrical circuits, the coaxial cables are additionally shielded by nested copper tubes. They protect

¹ VACUUMSCHMELZE GmbH & Co. KG, Gruener Weg 37, D-63450 Hanau, Germany.

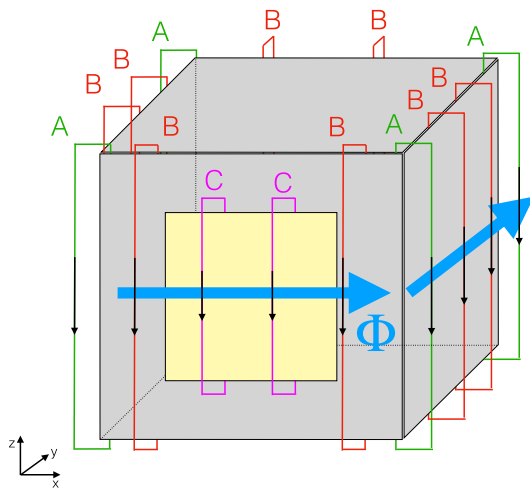


Fig. 1 Arrangement of the degaussing coils, which produce flux around the z-axis on MSR layer 6 drawn as a cube box. The yellow square represents the access door. Label A (green): corner coils similar on all layers; Label B (red): additional coils only on layer 6; Label C (purple): additional smaller coils only on the layer 6 door. The blue arrows indicate the direction of the magnetic flux Φ produced inside the shielding material by a current through the indicated coils

against interference capacitively coupling to the degaussing coils, but do not connect the ground potential of the MSR and the special EMI-shielded electrical cabinet.

Inside the cabinet, relays can connect the cables from the coils to the power amplifier. Figure 2 shows the electrical scheme for connecting the power amplifier that is controlled by Digital-Analog-Converters (DACs) to the coils for layer 1. It allows for switching on and off the coils for the three spatial directions in a defined sequence. This is identical for layers 2–5.

3.2 Layer 6

The innermost ULTRAVAC® layer (layer 6) utilizes a distributed coil design in each spatial direction, using more coils over the width of the walls between each corner. The additional coils along the surfaces are labeled B and C in Fig. 1, where coils C specifically cover the MSR door.

This distributed design allows a more uniform magnetic flux to be obtained, and as a consequence, less residual magnetization along the edges and in the corners. See Ref. [11] for a detailed discussion on distributed coils.

Each spatial direction, thus, has at least twelve coils – four on each corner plus two distributed approximately equidistant along the wall. In generating the magnetic flux around the x- and z-axis, two additional coils are used around the innermost MSR access door. Therefore, layer 6 has 40 coils in total.

In order to drive the coils in any combination of up to three spatial directions, each with independent polarities, at

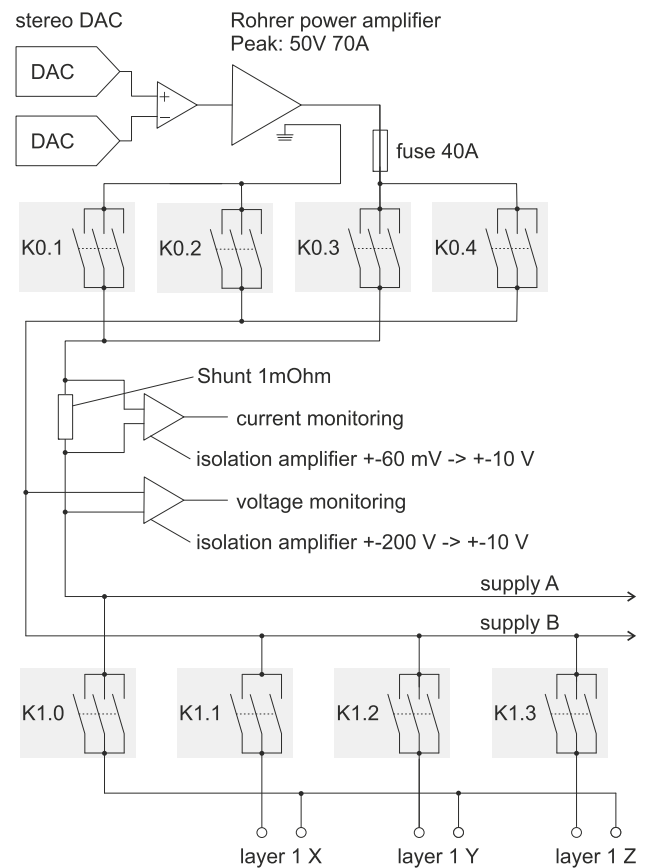


Fig. 2 Scheme of the electrical connections from the DACs to the degaussing coils of layer 1. The relays K0.1 to K0.4 are the main switches, which can connect the supply rails “supply A” and “supply B” in either polarity to the power amplifier. The relays K1.1 to K1.3 are used to connect the degaussing coils of layer 1 to the supply rails, selecting which of the x-, y-, and z-degaussing coil is supplied with current. In order to activate the return path for layer 1, K1.0 is closed. In the idle state when the layer one coil is not powered, all K1 relays are open. Identical schemes are used for layers 2 to 5

the same time, layer 6 also has a unique electrical scheme, see Fig. 3. For example, a flux generated simultaneously along x, y, and z would correspond to a flux around one of the four corner-axes of the MSR, see Fig. 4.

3.3 Generating the degaussing magnetic flux

In order to degauss a ferromagnetic material with an AC magnetic field, the material must first be magnetically saturated to remove the magnetic history. After saturation, any strong AC function with alternating sign and decreasing amplitude can lead to a non-magnetic material state (excluding any DC offset of the AC field), if enough cycles are used, and if done in a zero-field environment. For the n2EDM experiment, the outer 5 layers of the MSR provide a nearly zero-field environment for layer 6 degaussing.

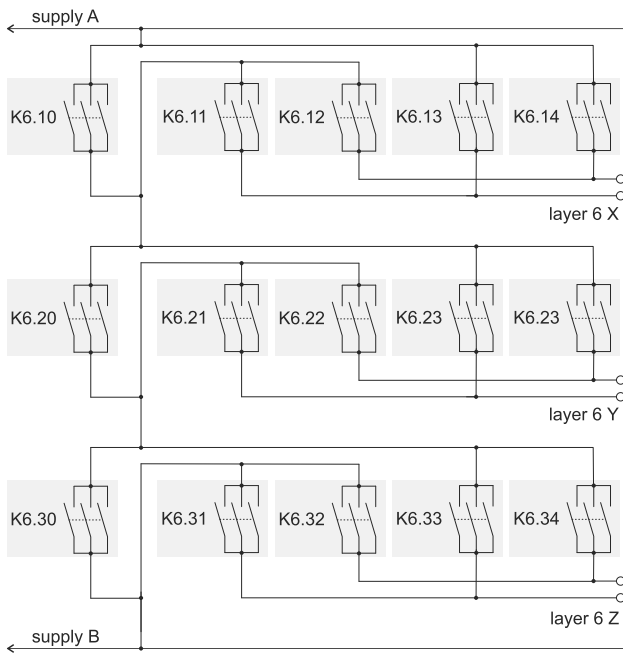


Fig. 3 The scheme of the relay connections for layer 6 is more elaborate than for the other layers. It enables connection to any of the three coils in series with arbitrary relative polarity. The signal always goes from the rails supply A to supply B (see Fig. 2). The relays K6.10, K6.20, and K6.30 select which coils are not powered by providing a current path that bypasses the coil. The hardware (using relay logic) does not permit all three of those relays to close simultaneously, avoiding a short circuit. When K6.10 is open, two of the relays K6.11 to K6.14 are closed in order to select in which polarity the current runs through the x degaussing coil of layer 6. The same scheme is used to power independently the y and z coils. In the idle state when the layer 6 coil is not powered all K6 relays are open

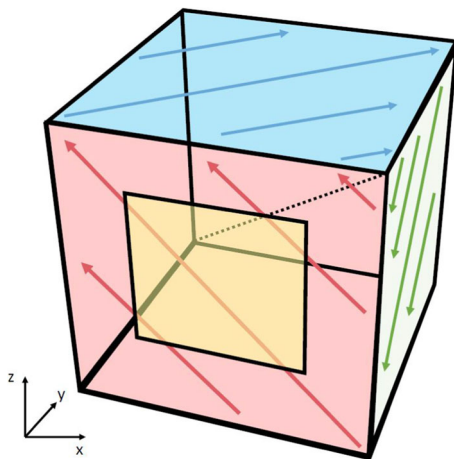


Fig. 4 Visualization of magnetic flux across the surface of layer 6 during a simultaneous excitation of x, y, and z coils, when the coils are connected with the sign combination x_+, y_-, z_+ . The arrows indicate the flux direction inside the walls for a positive half-wave of the degaussing function. The dotted line indicates the corner axis around which the flux is generated. Here, the axis definition matches Fig. 1, where the red surface has the access door (again yellow)

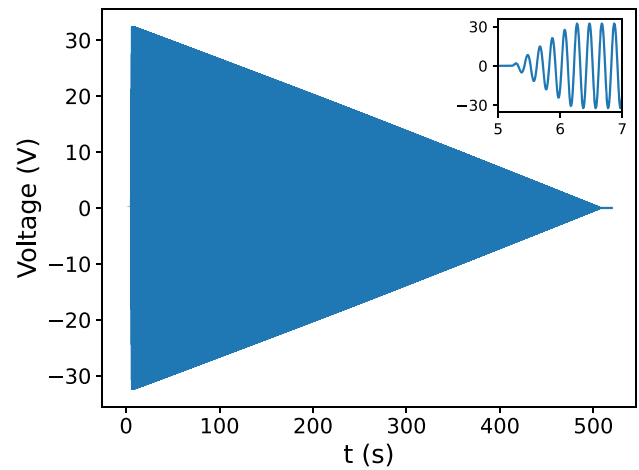


Fig. 5 Voltage monitoring of the Rohrer amplifier output as a function of time with a linear increase/decrease of amplitude. The zoomed inset shows the oscillating behavior. An up-time of 1 s, hold-time of 1 s, down-time of 500 s, and frequency of 5 Hz is used

We control the voltage over time supplied to the degaussing coil to produce a degaussing waveform. The supplied waveform is divided into three segments: “up-time” (time-to-peak), “hold-time” (time-at-peak), and “down-time” (time-to-zero). Additional parameters that can be varied are the maximal peak amplitude and the frequency. The final degaussing waveform to degauss with a finite number of cycles (i.e., finite time) is shown in Fig. 5. Although only linear ramps have been used, one could easily introduce non-linear ramps.

The frequency of the degaussing oscillation was reduced from 10 Hz used in the former setup, to 5 Hz here, in order to reduce the maximal current needed to reach saturation throughout the shielding material. The disadvantage of this is a prolonged degaussing time for the same number of down cycles. And practically, a transformer cannot be used to eliminate a DC offset on the degaussing signal after the power amplifier, as the lowest frequency for commercial transformers that fit the space constraints is 7 Hz. Instead, the DC offset of the power amplifier is measured regularly with a multimeter and is adjusted to be 0 within ± 0.005 mV. Together with the chosen 500 s down time (2500 down cycles), this was sufficient to prove that a polarity change does not lead to a significant residual field change. The DC offset was originally optimized with a magnetometer installed close to the MSR-center, searching for which offset led to the lowest residual field at this position. It was confirmed that a zero-voltage offset at the degaussing coil leads to the lowest residual field.

The degaussing waveform is generated by two DC-coupled 32 bit audio DACs with opposite polarity and converted to a single-ended signal by a low-noise differential

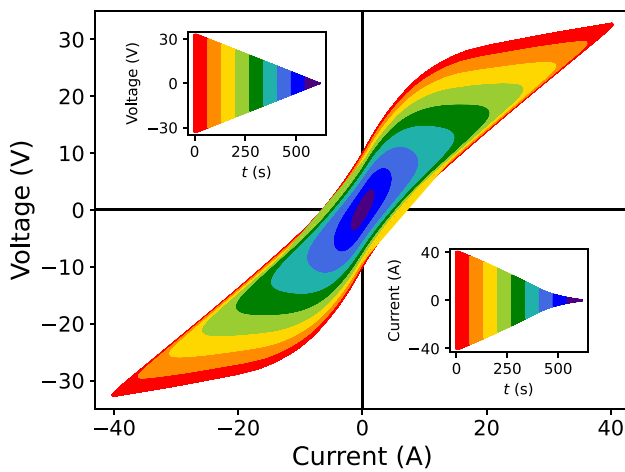


Fig. 6 Voltage output of Rohrer amplifier as a function of current. The upper-left inset figure shows the voltage monitoring as a function of time, similar to Fig. 5, and is linear as the Rohrer is operated in voltage-mode. The different colors highlight which part of the degaussing waveform populates the current–voltage space. The lower-right inset is the same but for current as a function of time. See text for details

amplifier. A Rohrer PA2088A 3.5 kW power amplifier² is operated in voltage mode and generates a high power signal of up to ± 50 V proportional to the input waveform. Current and voltage monitoring is implemented using isolation amplifiers. Figure 6 shows the voltage vs current monitoring while degaussing along one axis in one layer. Reaching saturation is indicated by the nearly linear relation at the tips of the voltage–current curve of Fig. 6, showing the loss of the inductive part with the remaining ohmic part of the degaussing coil resistance. In practice, there will always be a small inductive part. Firstly, there are places where shielding material overlaps, and at the MSR access door, where shielding material is thicker, requiring very large currents to reach complete saturation. Additionally, for larger currents, the field lines will cross gaps between layers, and thus, use the next shielding layer as a return path. For sequential degaussing of layers 1–5, the field lines can also take the path over the two surfaces of the shielding layer that are not in the main path of the magnetic flux Φ as indicated in Fig. 1.

3.4 Measuring residual magnetic fields

In order to quantify the residual magnetic field in the MSR after degaussing, a magnetic-field mapper was used. The magnetic-field mapper can move a low-noise Bartington MAG13 three-axis fluxgate³ along the cylindrical coordinates ρ , ϕ , z . The fluxgate can move between $\phi \in [-30, 380]^\circ$, $\rho \in [-5, 76]$ cm, and $z \in [-39.6, 50]$ cm,

² Rohrer GmbH, D-81457 Munich, Germany, rohrer-muenchen.de.

³ Bartington Instruments Ltd, Thorney Leys Park, Witney OX28 4GE, United Kingdom, Bartington.com.

which samples a volume larger than the one relevant for n2EDM measurements. Due to the sampling time of the mapper in the large volume, magnetic field maps can be taken before and after degaussing for these studies, but not during. This mapper follows a similar design as the one utilized in the nEDM experiment [16] but with substantial upgrades. A more detailed description of the internal coil system of n2EDM, including the magnetic field mapper used here, will be part of a forthcoming publication [17].

We emphasize that the magnetic field mapping done in this work was accomplished with this automated mapper installed inside the MSR. This was not used in the work of Ref. [6]. Furthermore, here, the full magnetic coil system and vacuum vessel were both installed, neither of which were in place during the work of Ref. [6].

4 Degaussing procedure

During initial studies of the MSR, degaussing in layers 1–6 were performed identically. Working from outer layers to inner layers, each layer first had flux generated around x , then y , then z , independently. This is referred to as “serial” degaussing. Layers 1–5 only have the option to be degaussed serially due to the implemented switch setup, as shown in Fig. 2. Layer 6 has the additional flexibility to degauss simultaneous x , y and z , as shown in Fig. 3. However, initially, it was degaussed serially as well. The degaussing waveform was also identical for each layer and each spatial axis: up-time of 200 s, hold-time of 10 s, down-time of 500 s, and frequency of 5 Hz. This waveform was initially chosen relying on previous works and experience. This degaussing procedure already allowed us to achieve extremely low residual field values over the inner volume of the MSR, as published in Ref. [6].

Yet, with the aforementioned degaussing waveform and serially degaussing of each layer, a full degaussing of the MSR takes roughly 3.5 h. This procedure (which in the rest of this paper is referred to as the ‘previous sequence’) also introduces significant heat into the MSR. After a full degaussing, the residual magnetic field took many hours to thermally equilibrate (see discussion later).

With this in mind, a series of studies were performed to optimize the degaussing procedure with two goals: (1) reduce the time spent and heat dissipated of degaussing, and (2), minimize, and make more uniform, the residual magnetic field. In order to test the effectiveness of different degaussing procedures independently, layer 6 is magnetized before each degaussing. This is achieved by turning on the B_0 field to 10 μT , magnetizing mainly in the z -direction (mapper coordinates). This is a factor of 10 higher than the nominal B_0 field setting for n2EDM operation [1]. To magnetize in ϕ and ρ , it was observed that this can be achieved by a large

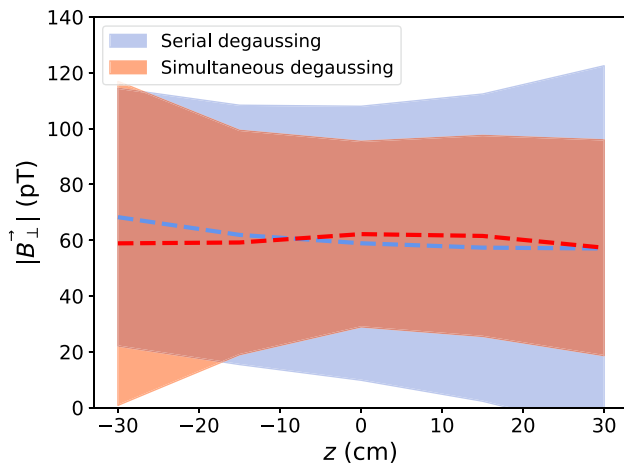


Fig. 7 ϕ -averaged transverse residual magnetic field, B_{\perp} , at $\rho = 50$ cm, as a function of z , for the serial degaussing sequence (blue) and the simultaneous degaussing sequence with polarity $x_+y_-z_+$ (red). The dashed line shows the average field sampled in ϕ at $\rho = 50$ cm with fixed z points, and the envelope is 2σ spread around the average at each z

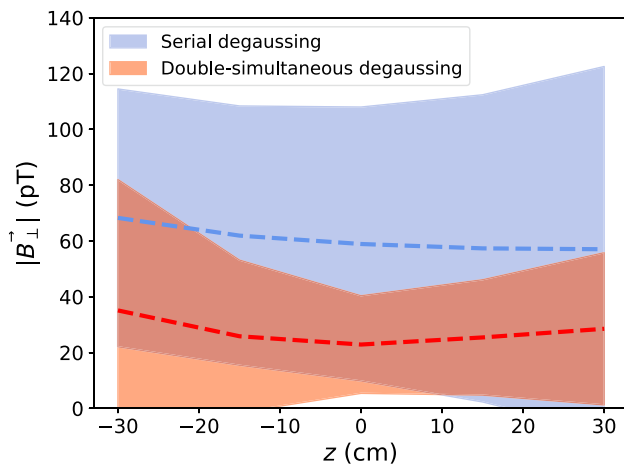


Fig. 8 Same as Fig. 7 but for the serial degaussing sequence (blue) and the double-simultaneous degaussing sequence with polarity $x_+y_-z_-$ then $x_+y_-z_+$ (red)

DC current through the layer 6 y -axis degaussing coils. This yields a larger magnetization than expected during nominal operation. In comparison to the inside field, this magnetization is of similar magnitude when the MSR door is opened for maintenance and closed afterwards. After each degaussing test, the MSR was able to thermally equilibrate over a few hours, depending on the test, see below.

4.1 Optimizing degaussing waveform

Since layers 1–5 only have the option to be degaussed serially, the obvious candidate for improvement of time-spent and heat-output is varying the degaussing waveform. The time and heat can be reduced with a shorter or smaller-amplitude

degaussing waveform. Numerous studies were done varying the amplitude, up-time, down-time, and hold-time. For each test, layers 1–6 were always degaussed in the same manner.

It was found that an up-time of 1 s, a hold-time of 1 s, and a down-time of 500 s (see Fig. 5) produced similar residual magnetic field strengths as the previous sequence. This suggests that magnetic saturation can be reached quickly (in 1 s) and reliably with the setup of our system. This reduces the overall degaussing time from roughly 3.5 to 2.5 h. In addition, these changes significantly reduce the heat output, as the coils have the maximum current for only a tenth of the time as previous. Decreasing the amplitude worsened the residual magnetic field, and thus, was not changed.

4.2 Optimizing degaussing order

Layer 6 is the innermost layer, and therefore, has the largest effect on the residual field. Initially, the order of the degaussing axes was varied to investigate the impact on the strength of the residual magnetic field. Instead of degaussing layer 6 in order of x, y, z , a degaussing order of y, x, z was studied. This allows for a double-degaussing around the MSR access door in the last two steps, where it is assumed to have worse field uniformity due to the discontinuities in the MUMETALL[®]. However, no significant improvement of the residual magnetic field with a y, x, z degaussing was found, while not ending the sequence along z always led to a worse residual field.

Layer 6 is also equipped with the possibility to degauss two or three axes simultaneously. This is the most appealing candidate for further reducing the residual magnetic field. Simultaneously degaussing around x, y , and z (i.e., producing magnetic flux around a corner-axis of the MSR) has a large potential to reduce the necessary time and heat impact. As layer 6 also has the flexibility to independently vary the polarity of the degaussing in each axis, there are 8 different flux variations: (1) $x_+y_+z_+$, (2) $x_+y_+z_-$, (3) $x_+y_-z_+$, (4) $x_+y_-z_-$, (5) $x_-y_+z_+$, (6) $x_-y_+z_-$, (7) $x_-y_-z_+$, (8) $x_-y_-z_-$. For example, Fig. 4 shows the flux direction (3), $x_+y_-z_+$. The last four combinations are just an inversion of the current direction of the first four. For an AC degaussing, the overall sign should not have an impact if the down-time is long enough, and if the DC offset is close enough to zero.

Using the degaussing waveform with the smaller up- and hold-time as mentioned in Sect. 4.1, each of the 8 possible degaussing combinations were tested. In between each test, layer 6 was re-magnetized and the MSR was able to thermally equilibrate over 1.5 h. The shorter time necessary to equilibrate already reflects the reduced heat output of simultaneous degaussing.

It was found that degaussing x, y , and z simultaneously produced a similar residual magnetic field as the serial procedure, but with better uniformity. This is shown in Fig. 7 by

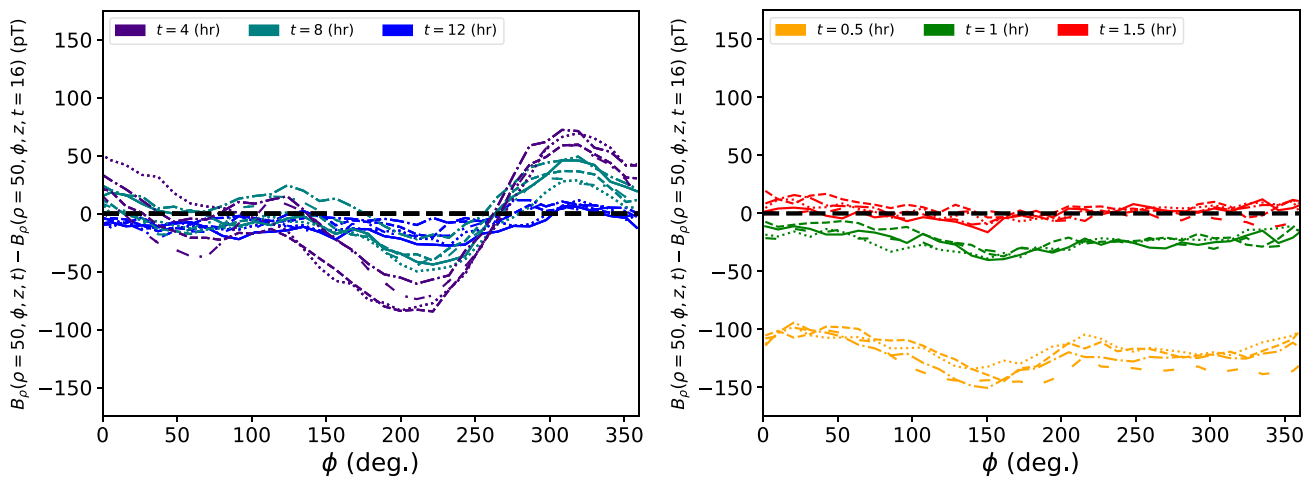


Fig. 9 Thermal relaxation effect on the residual magnetic field B_ρ , after a full degaussing. (Left): using the previous sequence, the difference of the magnetic field at various wait times [4 (purple), 8 (teal), and 12 (blue) hours] and the field after 16h, at $\rho = 50$ cm as a function of ϕ for different z positions [(solid): $z = -30$ cm, (dotted): $z = -15$ cm, (dashed): $z = 0$ cm, (dotted-dashed): $z = 15$ cm, (loosely-dashed): $z = 30$ cm]. The different line styles indicate the various z positions

sampled. (Right): The same but for the optimized degaussing sequence for wait times [0.5 (yellow), 1.0 (green), and 1.5 (red) hours]. Already after 1.5 h, the field has reached equilibrium with the state after 2 h, and, even initially, the field is much more uniform in ϕ . Uncertainty has been omitted for clarity, but the spread in the different lines of the same color give a sense of the field non-uniformity in the precession volume

the reduced envelope of $|\mathbf{B}_\perp| = \sqrt{B_x^2 + B_y^2}$, but similar central value. We compare the residual field at $\rho = 50$ cm, as this spans the inner-volume relevant for n2EDM. $|\mathbf{B}_{\text{tot}}|$ is not plotted as the fluxgate DC-offset for B_z was not determined here (see Fig. 11 for a high-resolution map that included the offset correction). It also takes significantly less time and dissipates less heat. However, this improved result was only achieved for the polarity configuration $x_+y_-z_+$. The other polarity configurations yielded larger residual magnetic fields, but all had a significantly lower heat output than the previous sequence.

In order to try to reduce the residual magnetic field even more, two subsequent simultaneous degaussings were studied – i.e., first $x_+y_+z_+$ then $x_+y_-z_+$. A total of 12 tests were performed, using all combinations of two subsequent simultaneous degaussings.

Iterations that ended with the configuration $x_+y_-z_+$ resulted in the smallest residual magnetic field. It was found that the sequence $x_+y_-z_-$ then $x_+y_-z_+$ performed the best, as shown in Fig. 8. This is likely due to generating magnetic flux in perpendicular directions through sides of the MUMETALL[®] and ULTRAVAC[®] that have more imperfections, most significantly at the sides of the MSR access door.

Double-degaussing using the same sequence (i.e., the same polarity configuration) did not yield improvements. It was also observed that additional simultaneous degaussings (i.e., more than a sequence of 2) did not reduce the residual magnetic field further. Thus, we found no need to do further degaussings of layer 6 beyond the two.

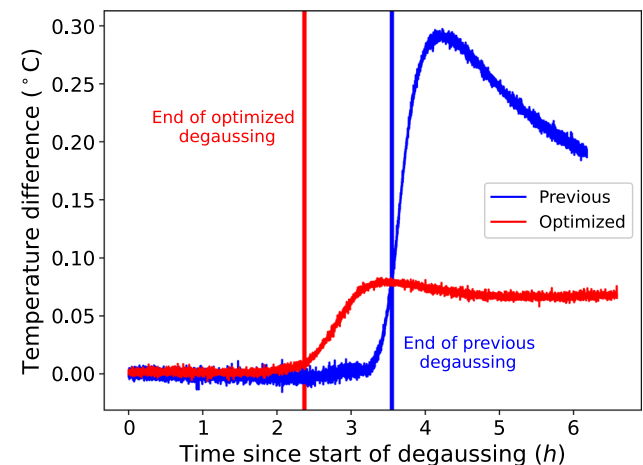


Fig. 10 Temperature drift after starting a degaussing with the optimized sequence (red) and previous sequence (blue), measured by a thermocouple mounted on the inside of the MSR on layer 6. The solid lines indicate when the degaussing sequence is finished (red at ~ 2.5 h and blue at ~ 3.5 h). With the previous sequence, there is a significantly longer decay time until thermal stability (~ 12 h), whereas the new sequence reaches stability in about 1.5 h after the degaussing finishes, as supported by Fig. 9

With the double simultaneous degaussing ($x_+y_-z_-$ then $x_+y_-z_+$) and the shorter degaussing waveform, the time spent to degauss only layer 6 was reduced from 35.5 to 16.7 min, with a smaller residual magnetic field, and generated less heat as compared to the previous degaussing waveform. This marks a simultaneous improvement of all optimization criteria in the degaussing procedure.

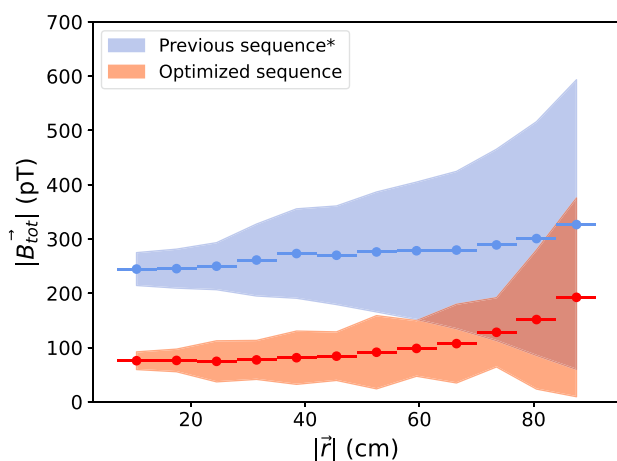


Fig. 11 Average total residual magnetic field $|\mathbf{B}_{\text{tot}}(\mathbf{r})| = \sqrt{B_x^2 + B_y^2 + B_z^2}$, as a function of distance from center of the vacuum tank, for the serial degaussing sequence (blue) and the optimized sequence (red). The envelope is 2σ of the average field sampled in $|\mathbf{r}| = 7$ cm bins, where the bins are indicated by the horizontal bars. The optimized sequence includes a fluxgate correction for B_z (~ 90 pT), where the correction was extracted by rotating the fluxgate 180° . The previous sequence (*) did not measure this offset, due to a mechanical issue during the measurement, however the same correction that was extracted in the optimized sequence was applied here as well. This leaves an undetermined offset, added in quadrature, still possible to the blue curve

4.3 New degaussing procedure

The optimized degaussing procedure for the full MSR is now: degauss layers 1–5 serially (in x , y , then z) and degauss layer 6 with a double simultaneous sequence of $x_+y_-z_-$ then $x_+y_-z_+$. All layers utilize the shorter degaussing waveform with an up-time of 1 s, a hold-time of 1 s, a down-time of 500 s, and a frequency of 5 Hz. The total time to fully degauss all layers of the MSR with the new procedure is roughly 2.4 h, down from roughly 3.5 h, excluding time for thermal relaxation.

In Fig. 9, the relaxation time of the residual magnetic field with the optimized procedure is compared to the previous degaussing procedure. With the less time taken to degauss and the less heat output, the optimized procedure yields a magnetic configuration that is already thermally stable after 1.5 h. This is an order of magnitude faster than the time to achieve thermal relaxation for the previous degaussing procedure (previously ~ 12 h). Similarly, Fig. 10 shows the temperature difference of a sensor in the MSR after a degaussing has started. With the new sequence, there is a factor of ~ 4 less rise in temperature, and a quicker time to thermal stability.

As compared to the previous serial degaussing of layers 1–6 with the longer degaussing waveform, the new procedure produces a substantially smaller residual field that is significantly more uniform in the innermost volume. For $|\mathbf{r}|$ up to

50 cm, the new procedure has at least a factor of 2 smaller residual field, and is a factor of 2 more uniform (less spread). Figure 11 illustrates the improvement of the average residual magnetic field for an inner volume of ~ 1.4 m³ for the simultaneous degaussing achieved as a result of this work, compared to the serial degaussing of layer 6 used previously.

5 Conclusions

We developed an optimized degaussing procedure of the magnetically shielded room for n2EDM, the next-generation experimental search of the neutron electric dipole moment at the Paul Scherrer Institute [1].

This procedure utilizes distributed coils, whose novel electrical design allows for producing a magnetic flux simultaneously across x , y , and z axes in the innermost, passive-shielding layer.

This resulted in a residual magnetic field was reduced down to below 300 pT in the inner spin precession volume (~ 1.4 m³) of the n2EDM experiment, despite the presence of the large experimental components inside the MSR. Even more, the residual field has been made more uniform, and all while taking less time to degauss and inputting less heat into the magnetic environment, allowing for faster thermal relaxation.

While a successful degaussing of the MSR was already demonstrated in Ref. [6], with low residual field values (below 100 pT in the inner 1 m³), the field values found there and here are not directly comparable. For one, the magnetic mapper described here was not used in Ref. [6]. Additionally, the inner MSR now houses many components for the experiment, most significantly, a large vacuum tank, which contributes to the overall residual magnetic field. What is comparable are the results of Fig. 11, which showcase the performance of the previous and optimized degaussing sequence, with the same experimental components installed and same measurement procedure.

Looking to the future, further studies are planned to investigate the limits on how-small and how-uniform a residual magnetic field can be in such a large volume. These studies will include testing variable current amplitude or frequency during degaussing, such as Ref. [18] performed. We will also study how the residual field is impacted if we skip a degaussing of outer layers when the B_0 field polarity is changed.

Acknowledgements Excellent technical support by Michael Meier and Luke Noorda is acknowledged. We also especially acknowledge the excellent construction work of the group for magnetically shielded rooms of the company VAC - Vacuumschmelze, Hanau; namely of Lela Bauer, Markus Hein, Maximilian Staab, and Michael Wüst. Various PSI LOG groups supported the electrical components construction. The magnetic field mapper has been designed and installed by the LPSC mechanical department; namely Johann Menu. Support by the Swiss

National Science Foundation Projects 200020-188700 (PSI), 200020-163413 (PSI), 200011-178951 (PSI), 200021-204118 (PSI), 200021-172626 (PSI), 206021-213222 (PSI), 169596 (PSI), 200021-181996 (Bern), 200441 (ETH), and FLARE 20FL21-186179, and 20FL20-201473 is gratefully acknowledged. This project has received funding from the European Union's Horizon 2020 research and innovation programme under the Marie Skłodowska-Curie grant agreement No 884104. This work is supported by the DFG (DE) by the funding of the PTB core facility center of ultra-low magnetic field KO 5321/3-1 and TR 408/11-1. The LPC Caen and the LPSC Grenoble acknowledge the support of the French Agence Nationale de la Recherche (ANR) under reference ANR-14-CE33-0007 and the ERC project 716651-NEDM. University of Bern acknowledges the support via the European Research Council under the ERC Grant Agreement No. 715031-Beam-EDM. The Polish collaborators wish to acknowledge support from the National Science Center, Poland, under grant No. 2018/30/M/ST2/00319, and No. 2020/37/B/ST2/02349, as well as by the Minister of Education and Science under the agreement No. 2022/WK/07. Support by the Cluster of Excellence 'Precision Physics, Fundamental Interactions, and Structure of Matter' (PRISMA+ EXC 2118/1) funded by the German Research Foundation (DFG) within the German Excellence Strategy (Project ID 39083149) is acknowledged. Collaborators at the University of Sussex wish to acknowledge support from the School of Mathematical and Physical Sciences, as well as from the STFC under grant ST/S000798/1. This work was partly supported by the Fund for Scientific Research Flanders (FWO), and Project GOA/2010/10 of the KU Leuven. Researchers from the University of Belgrade acknowledge institutional funding provided by the Institute of Physics Belgrade through a grant by the Ministry of Education, Science and Technological Development of the Republic of Serbia.

Data Availability Statement This manuscript has no associated data or the data will not be deposited. [Authors' comment: The data underlying this article will be shared on reasonable request to the corresponding author.].

Open Access This article is licensed under a Creative Commons Attribution 4.0 International License, which permits use, sharing, adaptation, distribution and reproduction in any medium or format, as long as you give appropriate credit to the original author(s) and the source, provide a link to the Creative Commons licence, and indicate if changes were made. The images or other third party material in this article are included in the article's Creative Commons licence, unless indicated otherwise in a credit line to the material. If material is not included in the article's Creative Commons licence and your intended use is not permitted by statutory regulation or exceeds the permitted use, you will need to obtain permission directly from the copyright holder. To view a copy of this licence, visit <http://creativecommons.org/licenses/by/4.0/>.

Funded by SCOAP³.

References

1. N.J. Ayres et al., Eur. Phys. J. C **81**, 512 (2021)
2. B. Lauss, B. Blau, SciPost Phys. Proc. 004 (2021)
3. C. Abel et al., Phys. Rev. Lett. **124**, 081803 (2020)
4. N.F. Ramsey, Phys. Rev. **78**, 695 (1950)
5. S. Afach et al., J. Appl. Phys. **116**, 084510 (2014)
6. N.J. Ayres et al., Rev. Sci. Instrum. **93**, 095105 (2022)
7. nEDM collaboration, A large 'Active Magnetic Shield' for a high-precision experiment, forthcoming publication (2023). [arXiv:2307.07588](https://arxiv.org/abs/2307.07588)
8. F. Thiel, A. Schnabel, S. Knappe-Grüneberg, D. Stollfuß, M. Burghoff, Rev. Sci. Instrum. **78**, 035106 (2007). <https://doi.org/10.1063/1.2713433>
9. J. Voigt, S. Knappe-Grüneberg, A. Schnabel, R. Körber, M. Burghoff, Metrol. Meas. Syst. **239** (2013)
10. I. Altarev et al., J. Appl. Phys. **117**, 233903 (2015). <https://doi.org/10.1063/1.4922671>
11. Z. Sun, P. Fierlinger, J. Han, L. Li, T. Liu, A. Schnabel, S. Stuiber, J. Voigt, IEEE Trans. Ind. Electron. **68**, 5385 (2021)
12. VACUUMSCHMELZE GmbH & Co. KG, Gruener Weg 37, D-63450 Hanau, Germany
13. J. Bork, H. Hahlbohm, R. Klein, A. Schnabel, *Proceedings of the 12th International Conference on Biomagnetism*, 970 (2000)
14. Rohrer GmbH, D-81457 Munich, Germany, rohrer-muenchen.de
15. Bartington Instruments Ltd, Thorney Leys Park, Witney OX28 4GE, United Kingdom, Bartington.com
16. C. Abel et al., Phys. Rev. A **106**, 032808 (2022)
17. nEDM collaboration, The ultra-uniform magnetic field for the n2EDM experiment, forthcoming publication (2023)
18. F. Allmendinger, et al., Degaussing procedure and performance enhancement by low-frequency shaking of a 3-layer magnetically shielded room (2023). [arXiv:2307.07225](https://arxiv.org/abs/2307.07225)

An upgrade of the primary length standard of Republic of Serbia where digital stabilization is performed by Arduino Due board

An upgrade of the primary length standard of Republic of Serbia where digital stabilization is performed by Arduino Due board

Zoran D. Grujić,^{1, a)} Marko G. Nikolić,¹ Slobodan Zelenika,² and Mihailo D. Rabasović¹

¹⁾*Institute of Physics Belgrade, University of Belgrade, Serbia*

²⁾*Directorate of Measures and Precious Metals, Mike Alasa 14, 11158 Belgrade, Serbia*

(*Electronic mail: rabasovic@ipb.ac.rs)

(Dated: 30 January 2024)

An upgrade of the electronic system for frequency stabilization of the HeNe laser, primary length standard of Republic of Serbia, based on digital electronics, is described. Arduino microcontrollers have been used for stabilization, and laptop computer has been used only to communicate with user. Also, an analog electronics have been developed in order to boost performance of the setup. Setup is simple and inexpensive, made of off-the-shelf electronics components. Despite this, good performances have been achieved.

I. INTRODUCTION

The HeNe laser stabilized by saturation absorption at iodine vapor was the most common standard of optical frequency (wavelength)^{1,2}. Although the new types of lasers have appeared in the field of the frequency/wavelength metrology^{3,4}, the HeNe lasers are still common standards of optical frequency. They are relatively simple and robust devices, and their performances are still acceptable for most applications, e.g. Allan variance better than 10^{-11} can be routinely achieved.

We describe upgrade of the primary length standards of the Republic of Serbia. The standard is actually a HeNe laser stabilized at iodine vapor (I_2). The stabilization is performed according to Bureau International des Poids et Mesures (BIPM) recommendations⁵. Briefly, the red HeNe laser at 633 nm, running at single longitudinal mode, has been stabilized at f component of the I_2 vapor (f component - $^{127}I_2$ a₁₆ R(127) 11-5). Method of intracavity saturation spectroscopy of the I_2 vapor has been applied. The so called $3f$ lock-in technique (detection of the third harmonic of modulation/dithering frequency in the laser power) was adopted.

Aforementioned technique is widely used. The technique's practical implementation can vary, e.g. the first HeNe primary length standard of the Republic of Serbia, was developed using fully analog electronics, including lock-in amplifier and PID (Proportional Integral Differential) controllers for laser wavelength stabilization and temperature control. Then, the standard got upgrade by Pantelic et.al.⁶, where advances in digital electronics have been implemented for stabilization of laser wavelength. Personal computer (PC) was acquiring signals via AD (Analog-to-Digital) conversion card. Software was developed to perform lock-in detection and PID stabilization. Feedback to laser was achieved via DA (Digital-to-Analog) conversion. The whole driving electronics was built-in the computer case.

However, it turned out that the maintenance of the previous digital version of the length standard was an issue. Namely, the driving electronics was in the computer case, and it was based on AD/DA card with a slot connector specific to that era of PC industry. Repairing the system was virtually impossible when the old PC broke down. Spare parts for very old

PCs are usually with no warranty and hard to find. Also, old AD/DA electronics were not compatible with motherboards of new PCs. Thus, it was decided to build new control electronics.

In the paper, we have shown how to achieve performances that was previously only possible with sophisticated and expensive electronics, using very cheap and affordable setup. The same approach can be used with devices other than length standard(s).

II. EXPERIMENTAL SETUP

Existing laser head⁶ was refurbished, we kept mechanical construction but had to rebuild iodine cell temperature stabilization. Based on experiences with two previous generations of the standard, method of digital stabilization was selected. Long-term exploitation of personal computers has proven to be a serious problem. Thus, we switched to concept where the computer is used as graphical user interface (GUI) only: to display and record data, and to transmit user commands. The control electronics is integrated into head of the HeNe laser, connected to the computer via USB. This concept allows easy replacement of the computer in case of malfunction or obsolescence. Namely, we assume that USB communication will be supported for a long time to come, and also that the GUI software, written in Python, will be portable to a different operating system in future.

Recently, affordable and powerful microcontrollers/mini-computers appeared on the market. Examples are Arduino⁷ and Raspberry Pi⁸. As it is impossible to have exact timing on a device with operating system (there is variant of Linux on Raspberry Pi), we selected Arduino Due board (ADB) to be the "brain" of our updated HeNe standard. Besides 32 bit processor at 84 MHz, it has AD/DA inputs/outputs with moderate 12 bit resolution.

Block diagram of Serbian HeNe standard after update is shown in Fig. 1. Windows laptop computer receives commands from a user, displays and saves the results, but it doesn't perform any direct control on the standard itself.

The block scheme of analog electronic connected to the ADB is presented in Fig. 2. The ADB performs sweeps of HeNe spectrum, and locks the laser's wavelength on the transition indicated by a user using GUI on the computer. Both, output coupler (OC) and high reflectivity mirror (HR) perform

^{a)}Institute of Physics Belgrade, University of Belgrade, Serbia

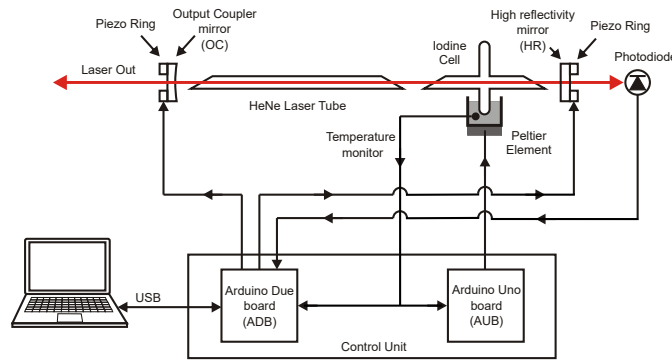


FIG. 1: Block diagram of the primary length standard of Republic of Serbia. HeNe tube and I_2 cell have windows at Brewster angle. The control unit, based on the two Arduino boards, is standalone device integrated into laser head. The control unit drives both cavity mirrors. Stabilization of the laser's wavelength is based on the signal detected by photodiode beyond high reflectivity mirror. Temperature of the iodine cell is maintained using Peltier element. Connection between laptop and Arduino Due is established by USB. Arduino Uno can be connected to the PC directly via USB, as well. However, in everyday use, this is not required. Unplugging Arduino Uno prevents accidental settings changes by the user or reset of the board.

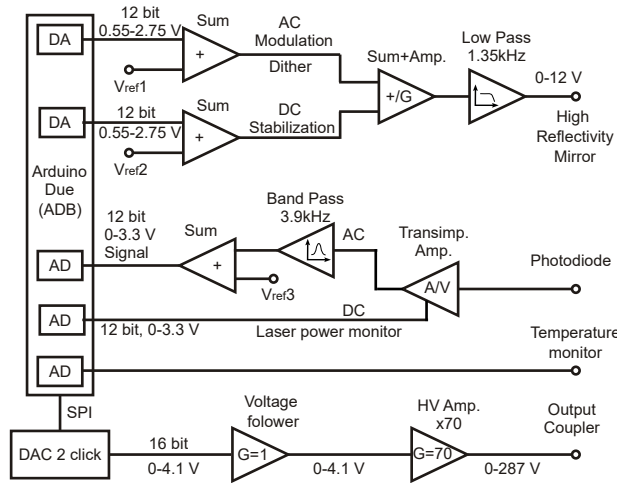


FIG. 2: The schematic of connections to the Arduino Due board. The signal from DAC 2 click controls PZT of output coupler (OC) via voltage follower and high voltage amplifier. The PZT of high reflectivity mirror (HR) is driven by ADB's DA converter via series of the summing amplifiers and filters. The signal from photodiode is divided into AC and DC component with special transimpedance amplifier. AC component is filtered and up shifted in order to match ADB's analog input range (0 – 3.3 V).

longitudinal motion (along lasers optical axes) driven by their corresponding ring shaped PZT (Piezoelectric) disc. Motion of the OC is used to scan over the whole laser spectral range (HeNe gain curve) spanning hundreds of MHz. This allows us to detect seven components of iodine transition R(127) 11-5 (d, e, f, g, h, i, j) within HeNe laser gain profile. To increase resolution of OC scan we employed external 16 bit

DA converter "DAC 2 Click" from MikroElektronika⁹ instead of 12 bit ADB's DA converter. To extend scan's range a high voltage amplifier (F06, EMCO High Voltage Corporation, Sutter Creek, USA) is used. The HR mirror performs sinusoidal motion (dither for lock-in detection) with amplitude adjusted to shift laser's cavity mode back and forth by 6 MHz⁵ (CIPM recommended value). Additionally to dither, a DC component (from a different DA output of the ADB, see Fig. 2) is superimposed for stabilization of the laser's wavelength. Thus movement resolution of HR mirror is higher (12 bit DA, limited range) than in case of OC (16 bit DA, huge range extended by HV amplifier). The ADB use signal from photodiode positioned beyond the HR mirror for recording of the HeNe spectrum and stabilization. The board based on the Arduino Uno (AUB) performs temperature stabilization (by means of digitally implemented PID controller) of the container in which the iodine cell (cold-finger) is immersed. The temperature is maintained by a Peltier element, in the range (15 ± 0.2)°C⁵, supplied by current from an IGBT (Insulated-Gate Bipolar Transistor) transistor that is controlled with filtered PWM (Pulse Width Modulation) output of the AUB. Detailed circuit schematics are given in supplementary material, see Appendix A.

A. Digitization of photodiode signal

First, the photodiode signal is amplified by transimpedance amplifier (TIA). Inspiration for design of the TIA comes from LIGO collaboration¹⁰. This kind of amplifier enables separation of AC and DC signal's components already at first amplification stage and separate gain control. The TIA's circuit diagram is given in the Appendix A.

DC component is connected to AD input of ADB and used for monitoring of laser power. Calibration is occasionally performed by comparison with a commercial power meter.

The AC component is filtered and amplified by the fourth order Butterworth band pass filter. Filter was designed to have central frequency at 3900 Hz and gain equal to 100. The goal of filtering is to remove noise and specially harmonics of dither signal other than third where $3f$ detection is intended. Gain was set so that in combination with up-shift by +1.65 V signal matches to full input range of ADB's AD converter to minimize digitization noise. The circuit diagram is given in Appendix A. This signal is used for digital lock-in detection and laser stabilization.

III. SOFTWARE

There are Python GUI for user interaction on laptop computer, firmware for ADB the real "brain" of the setup and AUB firmware for temperature stabilization.

A. Arduino Due firmware

This is the brain of entire setup. The ADB receives commands from GUI on laptop and then manages operation of the standard in all the aspects except for temperature stabilization

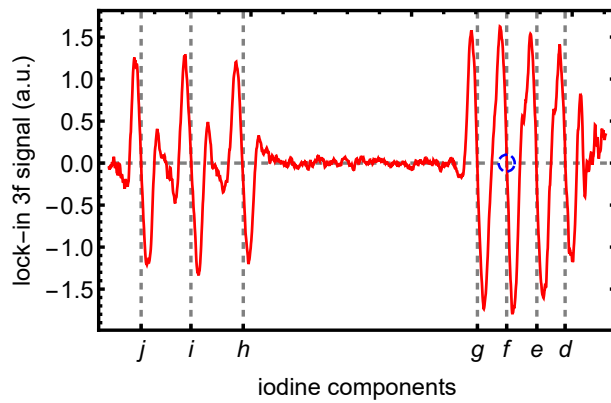


FIG. 3: Identified components of the I_2 spectrum obtained while scanning by output coupler. The lock-in signal from photodiode at $3f$ was detected. Blue circle denotes lock point of the HeNe standard at f component. Check Sec. IV B for explanation on distortion of the spectrum.

performed by AUB. There are two operation modes: scan and lock.

1. ADB scan mode

When in its default "scan" mode ADB accepts from GUI individual positions where to move OC and returns result of lock-in detection. GUI sends OC positions in small increments (x -axes) and forms spectrum by collecting response from ADB.

2. ADB lock mode

At some point, while in scan mode, ADB will receive lock command from GUI. This command contains position of iodine f component selected by user while observing spectrum. This position then becomes initial lock point for stabilization procedure. The OC will then move to the indicated position and ADB will find nearest zero crossing of the $3f$ signal using PI (Proportional Integral) driven feedback that moves HR mirror. Thermal (or any other drift) expansion of the laser cavity will be compensated by HR movement while maintaining system at the zero crossing of the selected component. After some time, due large drift compensation, the HR position could achieve one of two extreme positions (min or max). If this happens ADB will move OC by one step (in right direction), and HR by equivalent number of steps (in laser frequency) towards center of its range. By this simultaneous move of both mirrors, laser's frequency is unchanged, while standard's effective lock range is substantially extended.

Proper point selection is essential for lock, it must be on a slope of a I_2 component as indicated by blue dashed circle on Fig. 3. The lock will work on any of 7 visible components, but only f is of metrological interest.

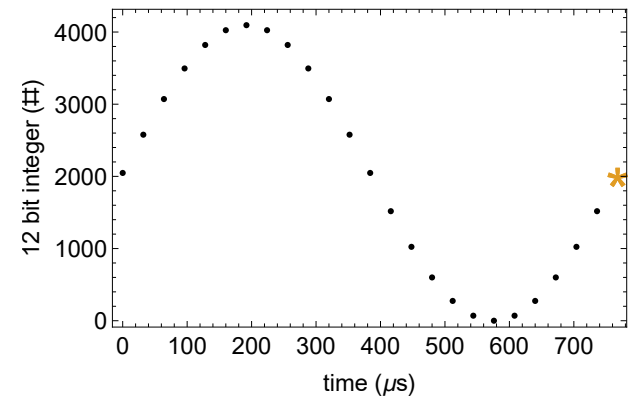


FIG. 4: Calculated 24 samples of dither sinusoidal waveform for 12 bit DA converter of ADB. The last, 25th point (labeled by a star), belongs to the next period of the waveform.

3. Generation of dither signal

Important decision on software design, taking into account computing power of the ADB, was at which sample rate to perform dither generation and sampling for lock-in detection. It appeared that $32 \mu\text{s}$ is sufficient to perform AD and DA conversions, plus required computation in real time. Then the sinewave of the dither signal was digitized in 24 samples at $1/32 \mu\text{s}$ sample rate, leading to actual frequency of $1/(24 \text{ pts} * 32 \mu\text{s}) = 1302.08 \text{ Hz}$. To minimize noise of DA conversion we use full span of 12 bit DA converter, see Fig. 4. Downside of this approach is loss of digital control on signal's amplitude.

4. Lock-in detection

This is the most critical part of ADB firmware. Here the useful signal is extracted from noisy spectroscopic signal. After AD conversion the mean DC offset (obtained by exponential filtering) is subtracted. In next step the signal is multiplied (mixed) by in-phase (giving m_i^X) and in-quadrature (yielding m_i^Y) third harmonic of numerically generated dither (in other words, the signal is mixed with references shifted by $\pi/2$). Both references are shifted by a phase ϕ commanded by GUI to obtain X as dispersive (like first derivative of Lorentzian) and Y as flat feature-less shapes. Then, a digital lowpass filter should be applied to extract both X (in-phase) and Y (in-quadrature) components. In "lock mode" the Y component, as it is not needed for stabilization, is not calculated. In our case, due to limited computational power, filtering process is a bit complex.

a. Synchronous filtering is the first step with goal to suppress any remaining $1f$ component at 1.3 kHz. We keep in memory last 24 samples of the signal and of the mixed signals. The value that is used in following operations is obtained by averaging with previous one (Eq. 1) that is exactly in opposite phase ($-\pi/2$ or $\Delta t = -12 \cdot 32 \mu\text{s}$) from the current:

$$ms_i^{X,Y} = \frac{m_i^{X,Y} + m_{i-12}^{X,Y}}{2}. \quad (1)$$

b. *Exponential filter* (a type of lowpass filter) is very simple for realization:

$$me_i^{X,Y} = \alpha ms_i^{X,Y} + (1 - \alpha)me_{i-1}^{X,Y}, \quad (2)$$

where $\alpha \in [0, 1]$ is filter coefficient and $me_i^{X,Y}$ result of filtering. We selected $\alpha = 0.002$. This gives cut-off frequency of

$$f_c = \frac{f_{sr}}{2\pi} \arccos\left(\frac{\alpha^2 + 2\alpha - 2}{2\alpha - 2}\right) \approx 10 \text{ Hz}, \quad (3)$$

with sample rate $f_{sr} = 1/32 \mu\text{s} = 31250 \text{ Hz}$ (see Sec. III A 3). While value of f_c is very low we discovered that overall noise suppression is insufficient.

c. *Decimation* is then performed (we do not need new X and Y values every $32 \mu\text{s}$). The second order Infinite Impulse Response (IIR) filter consumes substantial computing resources and it was decided to perform this calculation on every 35th iteration, i.e. with repetition rate of $1/(35 \cdot 32 \mu\text{s}) \approx 893 \text{ Hz}$.

d. *Second order lowpass IIR filter* of Butterworth¹¹ type was calculated using SciPy¹² package of Python programming language.

```
import numpy as np
from scipy import signal
import matplotlib.pyplot as plt

f_c = 0.03 # relative cut-off frequency
b,a=signal.butter(2, f_c, 'low', analog=False)
```

Parameters a and b are employed in a following way:

$$X_i = \frac{b_0 me_i^X + b_1 me_{i-1}^X + b_2 me_{i-2}^X - a_1 X_{i-1} - a_2 X_{i-2}}{a_0}. \quad (4)$$

Please note that index i has different meaning than in Eqs. 1 and 2 due decimation by factor 35. Result is filter with 27 Hz cut-off frequency and slope of -12 dB/octave .

e. *Communication* with GUI is performed over ADB's native USB port (there is also programming USB port available). The built-in "SerialUSB" class of Arduino Due environment was used. This ensures improved stability and increased data rate. Values of ADB's timestamp, OC position, HV position, X and Y are sent to GUI every 10 ms.

B. Graphical User Interface (GUI)

Function of the GUI is control of ADB's operation. It could be built in any programming language, but we selected Python 3+ due its portability to other operating systems and wide range of scientific libraries that will enable future development of the application. PyQt¹³, a Python binding of the cross-platform GUI toolkit Qt, is adopted as tool to build windowed interface with form fields, buttons and plotted elements. Python library Matplotlib is great for generation of scientific figures, but slow and not very suitable for GUI interactions. Instead, PyQtGraph¹⁴ is employed to plot spectrum, and to interact with user. Connection with ADB is established over serial interface. Use of dark GUI theme (light letters on dark colored background) improves user experience in intentionally dark laboratory environment. The GUI is split in two tabs, Scan and Lock.

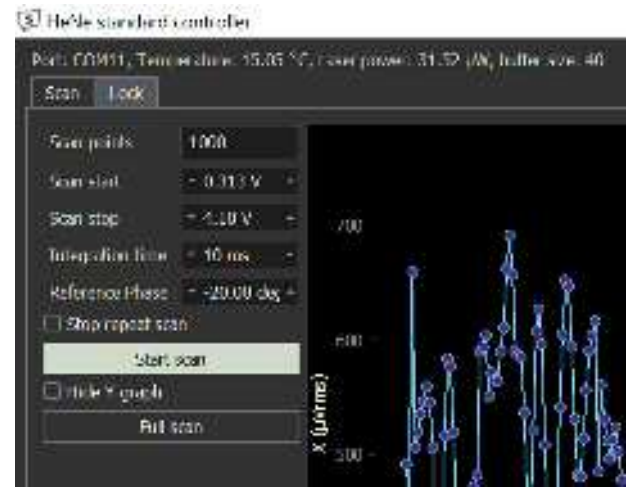


FIG. 5: Partial printscreen of the Scan tab.

1. Scan tab

After ADB - GUI communication is established first thing user wish to do is scan over I_2 spectrum. The Scan tab, Fig. 5, gives options to control how scan is performed and displays plot of recorded X and Y spectrum. There are input fields for number of scan points, start & stop scan voltage, averaging time per point, and reference phase ϕ . Those settings are applied when scan actually (re)starts on press of "Start scan" button. If the "Full scan" button is pressed a set of default settings is used to obtain maximally wide scan. If checkbox "Stop scan when completed" is not checked the scan procedure repeats indefinitely. If shape of X plot is not dispersive one can adjust the reference phase ϕ accordingly. One can hide Y plot with "Hide Y plot" checkbox to enlarge X plot. Spectrum can be saved using PyQtGraph popup interface accessible by right click on the plot.

Typical operation of the Scan tab would be:

- Click on "Full scan" button and wait for spectrum to be recorded.
- Recognize and click the f component on X plot (see Fig. 3) to zoom in and scan its vicinity.
- Repeat previous step(s) if necessary.
- Double click on the f component's zero crossing (blue dashed circle on Fig. 3). This triggers switching to Lock tab and ADB transition to the "lock mode". Laser's frequency should be stabilized at selected component.

2. Lock tab

Purpose of the Lock tab, Fig. 6, is to display performance of the stabilization procedure and control of PI parameters. User can change proportional (P) and integral (I) gains if necessary. Also there is input for OC vs HR movement ratio (see Sec. III A 2) and fine adjustment of the lock point. Settings are applied by clicking "Submit" button.

User can observe three plots: value of X (should be zero centered noise), and voltage applied to OC and HR PZTs. If

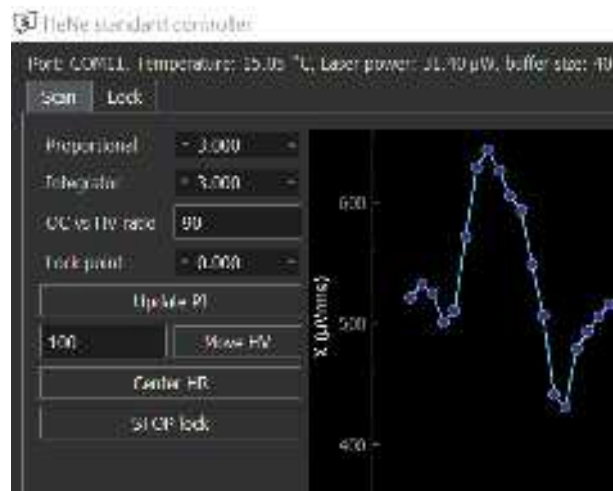


FIG. 6: Partial printscreen of the Lock tab.

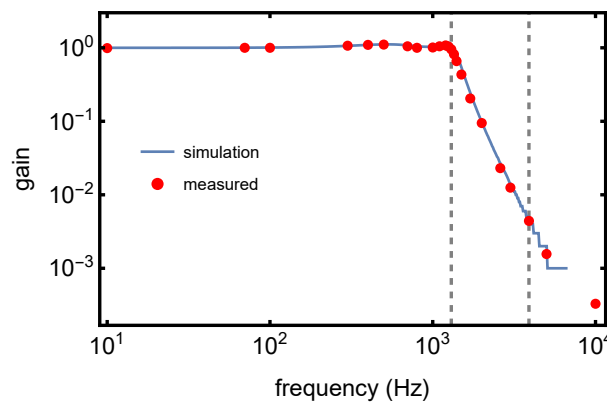


FIG. 7: Transmission curve of the low-pass filter used to clean up signal that drives motion of the high reflectivity mirror. Dashed vertical lines denote 1.3 kHz and 3.9 kHz, first and third harmonics of the dither signal.

any of values is out of range "Stop lock" button will bring the ADB back to scan mode and GUI to Scan tab. Scanning will be centered on the last values applied to OC PZT, then user can check if lock position was as intended.

IV. RESULTS AND DISCUSSION

We have tested all the components before assembly. After whole system has been assembled individual electronic components have been fine tuned.

A. Analog filters

1. Lowpass filter

The lowpass filter is located after summing amplifier of ADB's DA outputs and its output drives PZT of HR mirror, see Figs. 2 and 12. The DA outputs and following amplifiers might have some non-linearity, leading to rise of higher harmonics of which the third is specially harmful for $3f$ lock-in detection. The purpose of the lowpass filter is to pass the

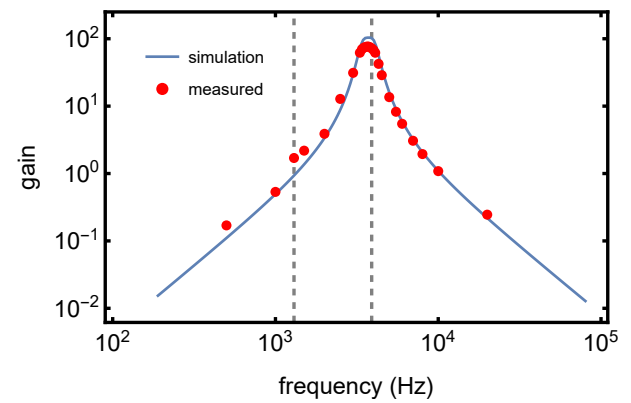


FIG. 8: Transmission curve of the band-pass filter in photodiode circuit. Dashed vertical lines denote 1.3 kHz and 3.9 kHz, first and third harmonics of the dither signal.

DC component and fundamental harmonic of dither signal at 1300 Hz, while suppressing dither's higher harmonics, most importantly the third one at 3900 Hz. This should provide pure sinus and variable offset (range below 100 Hz) in order to scan the HR mirror and tune laser frequency precisely. Measurement of its transmission showed excellent agreement with simulation, Fig. 7. Briefly, transmission of the DC component is 99%, at 1300 Hz is 95%, and at 3900 Hz is 0.44%. Analog Devices Filter Wizard tool¹⁵ was used for design.

2. Bandpass filter

Due to limited computational power of ADB, i.e. inability to strongly suppress unwanted frequency components by digital filtering in lock-in algorithm we placed analog band-pass filter before AD converter, see Figs. 2 and 11. The filter is designed to pass $3f$ signal at 3900 Hz while strongly suppressing broadband noise, DC fluctuations, first, second, and other harmonics than third one. We used Analog Devices Filter Wizard tool¹⁵ for its design and simulation of performance. Comparison of measured and simulated gain curves is shown in Fig. 8. To help matching input range of ADB's AD input there is builtin gain of 100 times. There is a slight discrepancy between the simulated and measured curves due to the tolerances of used components. Thus, transmission peak is shifted to the 3700 Hz, and the gain is 77 (instead of 100). Still, the resulting curve is completely satisfactory.

B. Intracavity spectroscopy of I_2 vapor

After assembly of the standard and extensive fine tuning of electronics and software, a typical spectrum was recorded, Fig. 3. The HR mirror was dithered by sinus at 1302 Hz while OC was used to perform scanning, and lock-in signal at the third harmonic was detected. Seven iodine components are clearly visible in the spectrum (j, i, h, g, f, e, d). In the Figure 3 we see third derivative of the actual spectrum. Their dispersive shapes are used by software PI to stabilize laser's frequency at desired point. Blue circle at the f transition is the lock point recommended by BIPM⁵ for length standard.

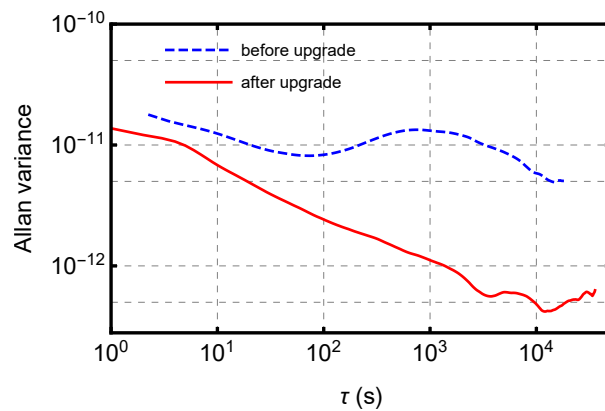


FIG. 9: Allan variance of the stabilized laser, before and after upgrade. “Old”⁶, and “New”¹⁹ results obtained during metrological comparisons.

TABLE I: “Measurement result” of participant obtained at intercomparison.¹⁹

Expected frequency f_e	473 612 353 594.1(12.0) kHz
Measurement of host laboratory	
Measured frequency f_m	473 612 353 592.654(0.070) kHz
Comparison Result	
Frequency diff. $\Delta f = f_e - f_m$	+1.4(12.0) kHz
Fractional frequency diff. $\Delta f / f_e$	+3.1(25.3) $\times 10^{-12}$
Degree of equivalence as E_n value	+0.06

Please note that this spectrum is quick scan used to identify the lock point and monitor resonator’s stability. The cutoff frequency of the lock-in is ≈ 10 Hz, the scan rolls over a single resonance in one second, thus shown line-shapes are widened and distorted. In general the spectrum is influenced by the intracavity laser power¹⁷, and contamination^{16,18} of I_2 in the cell. The one-way intracavity beam power was 6-10 mW.

C. Intercomparison of length standards

Performance of the upgraded primary length standard of Republic of Serbia was evaluated in Vienna, Austria, August 2021 as part of “CCL Key Comparison for 2021”¹⁹. The results of the Allan variance before²⁰ and after upgrade¹⁹ are given in Fig. 9. The results from latest intercomparison¹⁹ are summarized in the Table I. It is clear that the upgrade improved performances of the setup.

V. CONCLUSION

We have shown that the HeNe length standard can achieve high stability driven with home made low-cost analog and digital electronics assembled from of-the-shelf components. Analog electronics was carefully built (and tested) to clean spectrum of input and output signals thus removing noise and undesired frequency components. Schematics are provided in Appendix A. Lock-in detection and wavelength stabilization are performed by software running on Arduino Due microcontroller board. Very simple, but highly effective user interface

was built using Python programming language. We provide all source files in supplementary material.

We proved quality and performance of the upgrade by Allan variance recorded during metrological comparisons. Stability of $5 \cdot 10^{-13}$ at 10^4 s is demonstrated.

SUPPLEMENTARY MATERIAL

For benefit of the reader, we have supplemented software source code of GUI and of ADB firmware.

ACKNOWLEDGMENT

We acknowledge funding provided by the Institute of Physics Belgrade through a grant by the Ministry of Education, Science and Technological Development of the Republic of Serbia.

AUTHOR DECLARATIONS

Conflict of Interest

The authors declare no conflict of interest.

Author Contributions

Zoran D. Grujić: Conceptualization (equal); Investigation (equal); Methodology (equal); Data curation (equal); Software (lead); Validation (equal); Writing – review & editing (equal). **Marko G. Nikolić:** Conceptualization (equal); Investigation (equal); Software (supporting); **Slobodan Ze-lenika:** Conceptualization (equal); Data curation (equal); Validation (equal); **Mihailo Rabasović:** Conceptualization (equal); Investigation (equal); Methodology (equal); Data curation (equal); Writing – original draft (lead); Writing – review & editing (equal)

DATA AVAILABILITY

The data that support the findings of this study are available from the corresponding author upon reasonable request.

REFERENCES

- ¹M. Matus and S. Haas, *Annalen der Physik* **531**, 1800287 (2019), <https://onlinelibrary.wiley.com/doi/pdf/10.1002/andp.201800287>.
- ²J.-M. Chartier and A. Chartier, in *Laser Frequency Stabilization, Standards, Measurement, and Applications*, Vol. 4269, edited by J. L. Hall and J. Ye, International Society for Optics and Photonics (SPIE, 2001) pp. 123 – 133.
- ³T. Fortier and E. Baumann, *Communications Physics* **2**, 153 (2019).
- ⁴D. K. Aswal, S. Yadav, T. Takatsuji, P. Rachakonda, and H. Kumar, *Handbook of Metrology and Applications* (Springer Singapore, 1982).
- ⁵BIPM, “Mep 2003,” Recommended values of standard frequencies (Bureau International des Poids et Mesures, 2003) Standard frequency: 474 THz (≈ 633 nm) – I_2 .

This is the author's peer reviewed, accepted manuscript. However, the online version of record will be different from this version once it has been copyedited and typeset.
PLEASE CITE THIS ARTICLE AS DOI: 10.1063/5.0182704

- ⁶D. V. Pantelić, B. M. Panić, and A. G. Kovacčević, Review of Scientific Instruments **74**, 3155 (2003), https://pubs.aip.org/aip/rsi/article-pdf/74/6/3155/11349529/3155_1_online.pdf.
- ⁷Arduino, "Arduino," <https://www.arduino.cc/> (2005), [Online; accessed 19-September-2023].
- ⁸Raspberry Pi Foundation, "Raspberry Pi," <https://www.raspberrypi.org/> (2009), [Online; accessed 19-September-2023].
- ⁹MikroElektronika, "DAC 2 Click," <https://www.mikroe.com/dac-2-click> (2005), [Online; accessed 19-September-2023].
- ¹⁰N. A. Lockerbie and K. V. Tokmakov, Review of Scientific Instruments **85**, 114705 (2014), https://pubs.aip.org/aip/rsi/article-pdf/doi/10.1063/1.4900955/13416918/114705_1_online.pdf.
- ¹¹S. Butterworth *et al.*, Wireless Engineer **7**, 536 (1930).
- ¹²P. Virtanen, R. Gommers, T. E. Oliphant, M. Haberland, T. Reddy, D. Cournapeau, E. Burovski, P. Peterson, W. Weckesser, J. Bright, S. J. van der Walt, M. Brett, J. Wilson, K. J. Millman, N. Mayorov, A. R. J. Nelson, E. Jones, R. Kern, E. Larson, C. J. Carey, Í. Polat, Y. Feng, E. W. Moore, J. VanderPlas, D. Laxalde, J. Perktold, R. Cimrman, I. Henriksen, E. A. Quintero, C. R. Harris, A. M. Archibald, A. H. Ribeiro, F. Pedregosa, P. van Mulbregt, and SciPy 1.0 Contributors, Nature Methods **17**, 261 (2020).
- ¹³Riverbank Computing, "PyQt," <https://www.riverbankcomputing.com/software/pyqt/>, [Online; accessed 19-September-2023].
- ¹⁴"PyQtGraph," <https://www.pyqtgraph.org/>, [Online; accessed 19-September-2023].
- ¹⁵Analog Devices, "Analog Filter Wizard," <https://tools.analog.com/en/filterwizard/>, [Online; accessed 19-September-2023].
- ¹⁶P. Balling and J. Blabla, IEEE Transactions on Instrumentation and Measurement **47**, 1481 (1998).
- ¹⁷H. P. Layer, IEEE Transactions on Instrumentation and Measurement **29**, 358 (1980).
- ¹⁸J. Hrabina, M. Zucco, C. Philippe, T. M. Pham, M. Holá, O. Acef, J. Lazar, and O. Číp, Sensors **17** (2017), 10.3390/s17010102.
- ¹⁹M. Matus, S. Zelenika, N. Stanković, A. Küng, P. Balling, P. Křen, and G. Zechner, Metrologia **59**, 04004 (2022).
- ²⁰M. Matus, M. del Mar Pérez, S. Zelenika, A. Daultbayev, C. Kuanbayev, H. Hussein, and L. Robertsson, Metrologia **49**, 04009 (2012).
- ²¹Texas Instruments, "Filter Design Tool," <https://webench.ti.com/filter-design-tool/>, [Online; accessed 19-September-2023].

Appendix A: Schematics of analog electronics

This is the author's peer reviewed, accepted manuscript. However, the online version of record will be different from this version once it has been copyedited and typeset. PLEASE CITE THIS ARTICLE AS DOI: 10.1063/5.0182704

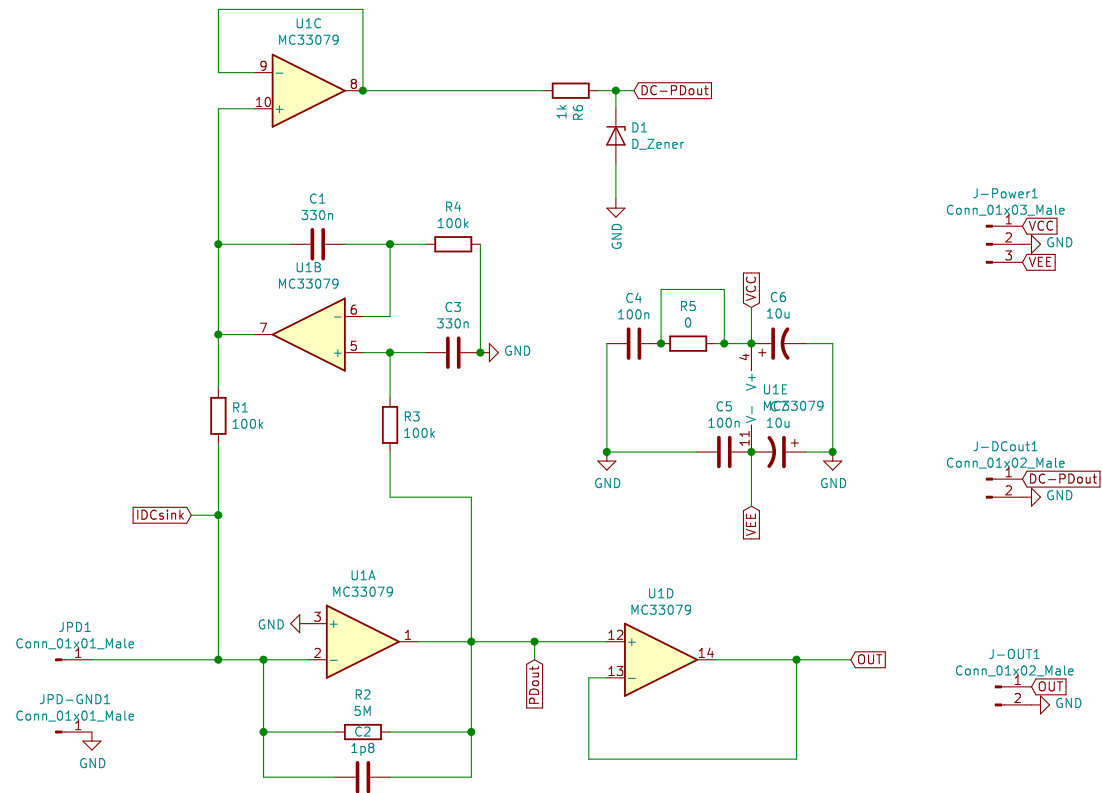


FIG. 10: Trans-impedance amplifier. It has separate DC and AC outputs. The DC output is used for power measurement. The AC output was used for lock-in detection. Photodiode is connected on the left side, pad "OUT" is AC output, and pad "DC-PDout" is DC output of the amplifier.

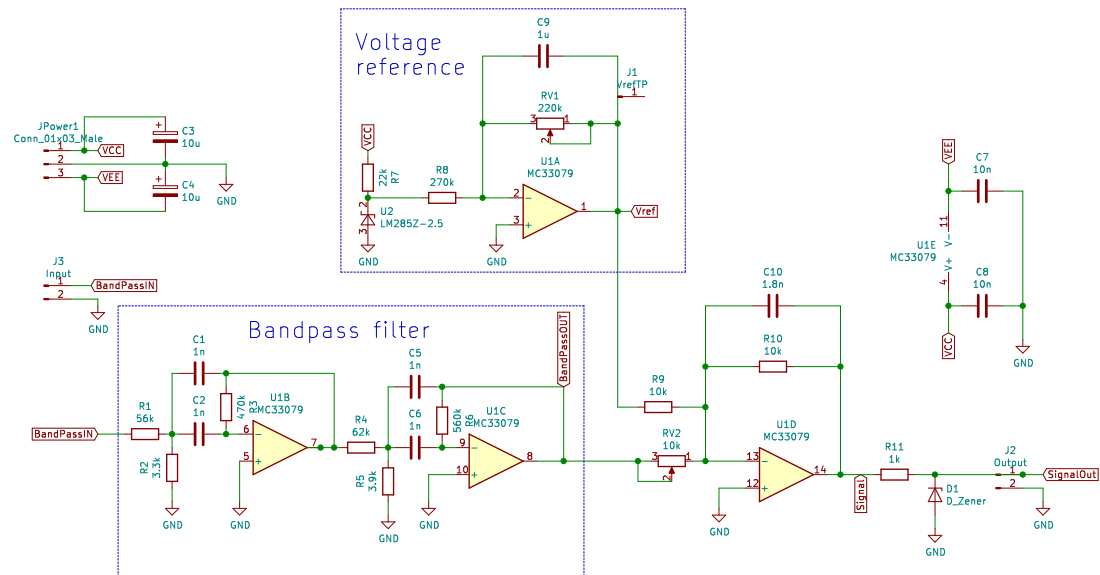


FIG. 11: Circuit for filtering, amplification and offset of the AC signal from photodiode. The filter was designed using Analog Devices Filter Wizard tool¹⁵.

This is the author's peer reviewed, accepted manuscript. However, the online version of record will be different from this version once it has been copyedited and typeset. PLEASE CITE THIS ARTICLE AS DOI: 10.1063/5.0182704

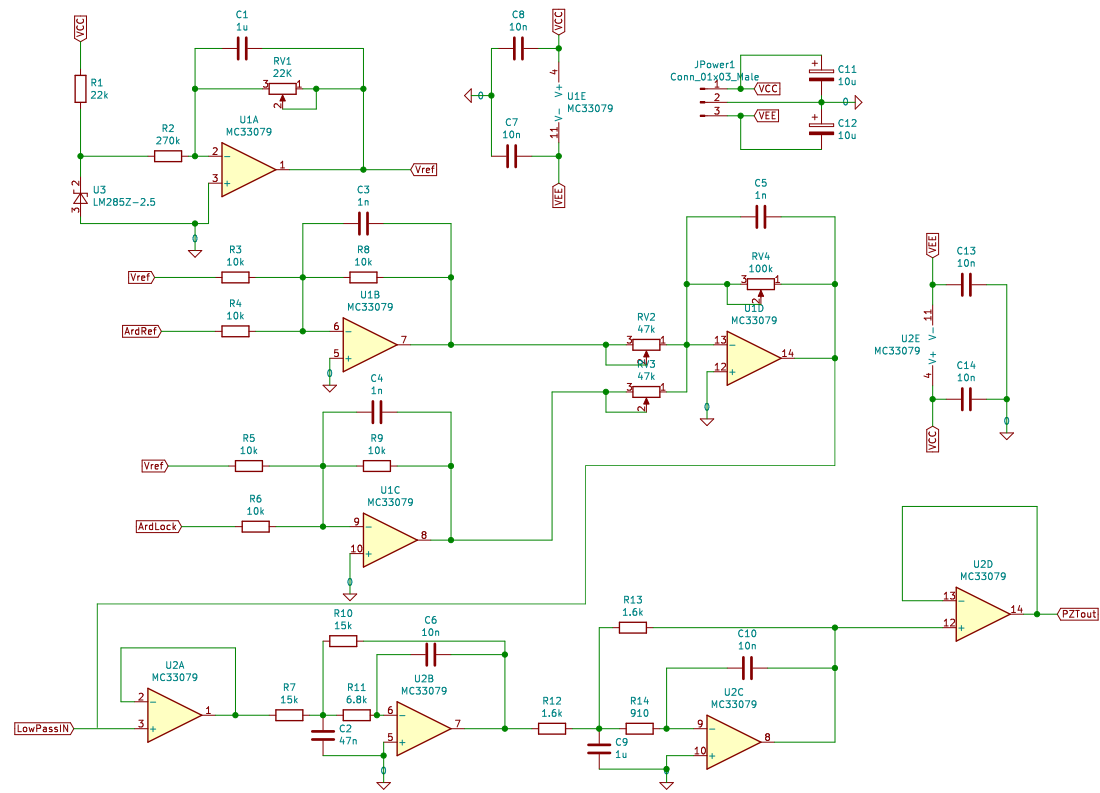


FIG. 12: Analog electronic circuit for driving of the HR mirror. Two Arduino DA outputs are used, one for DC component, and second one for AC component. Lowpass filter was designed using Texas Instruments Filter Design Tool²¹.

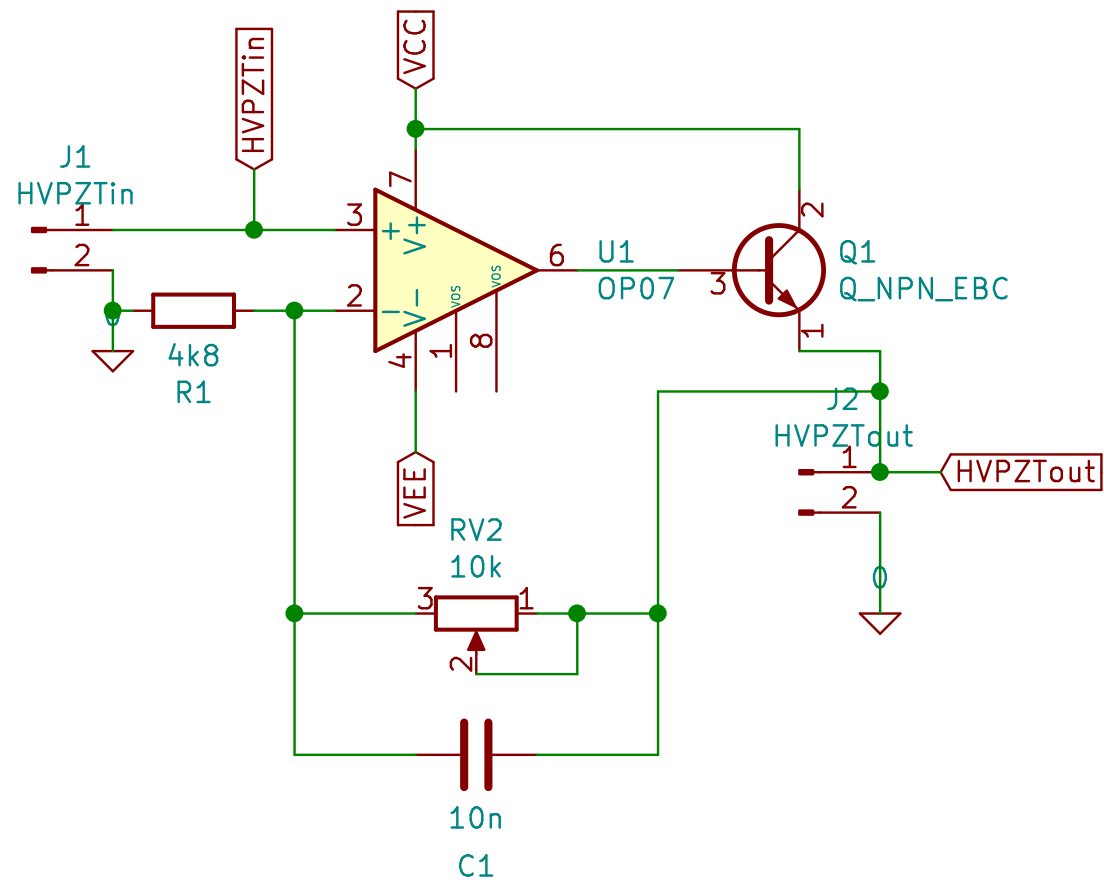


FIG. 13: Voltage follower for impedance matching of ADB's AD output and high voltage amplifier input.

The new limit of the neutron Electrical Dipole Moment

Zoran D. Grujić on behalf of nEDM collaboration

Institute of Physics Belgrade, *Pregrevica 118, 11080 Belgrade, Serbia*

Contact: Z. D. Grujić (zoran.grujic@ipb.ac.rs)

Abstract. The values of electrical dipole moments, as they brake parity and time-reversal symmetries, set very narrow constraints on theories beyond standard model (SM) of particle physics. They must include low level of CP (charge, parity) violation in K (decays of the neutral K mesons) and B (beauty mesons) systems and to explain the large baryon asymmetry of the Universe in the same time. The current limit of the neutron Electrical Dipole Moment (nEDM) has already set requirements for considerable fine-tuning of MSSM parameters - the so-called “SUSY CP problem”.

The world most sensitive nEDM experiment was operated by the nEDM international collaboration at the Paul Scherrer Institute (PSI) in Switzerland. Historically, precursor to PSI experiment has been built by C. A. Baker et al. at Institute Laue-Langevin, Grenoble where upper limit was determined 2006 to be $d_n < i 2.9 \times 10^{-26}$ e cm (90% CL) [1]. Latter the experimental setup was dismantled, transferred to PSI, upgraded and 2015 yielded measurement of $d_n = i -0.21 \pm 1.82 \times 10^{-26}$ e cm [2]. After another upgrade and three years of data collection the experiment measured new best nEDM limit to be $d_n = i (0.0 \pm 1.1 \text{ stat} \pm 0.2 \text{ sys}) \times 10^{-26}$ e cm that will be published shortly [3].

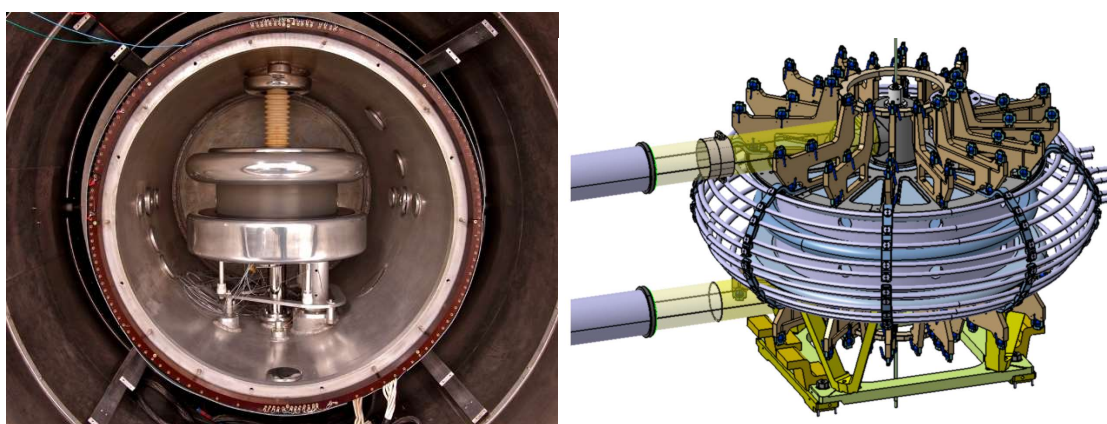


Figure 1. The old nEDM (left), and new, currently under construction, n2EDM (right) apparatus.

In my talk I will present the old nEDM experiment at PSI and its new greatly improved version (n2EDM) that is being constructed using the same PSI infrastructure. From December 2018 the Institute of Physics Belgrade is full member of the nEDM collaboration with Dr. Zoran D. Grujić as its representative.

REFERENCES

- [1] C. A. Baker et al., *Phys. Rev. Lett.* **97** (2006), 131801
- [2] J. M. Pendlebury, S. Afach, N. J. Ayres, et al., *Phys. Rev. D* **92** (2015), 092003.
- [3] C. Abel et al., *Phys. Rev. Lett.* (Accepted 3 February 2020)

Tunable single frequency blue VECSELs for spectroscopy of Rydberg states in K and Rb atoms

M. M. Ćurčić¹, M. Großmann², R. Bek², R. Löw³, M. Jetter², Z. Grujić¹, B. Jelenkvić¹

(1) *Photonics Center, Institute of Physics, 11000 Belgrade, Serbia*

(2) *Institut für Halbleiteroptik und Funktionelle Grenzflächen, Center for Integrated Quantum Science and Technology (IQST) and SCoPE, University of Stuttgart, Allmandring 3, 70569 Stuttgart, Germany*

(3) *5. Physikalisches Institut and Center for Integrated Quantum Science and Technology IQST, Universität Stuttgart, Germany*

Contact: M. M. Ćurčić (marijac@ipb.ac.rs)

Abstract. We present our recent progress on a development of intracavity-frequency-doubled vertical-external-cavity-surface-emitting laser (VECSEL) [1] emitting in blue spectral range. The development of this laser is motivated by a need to obtain stable, single frequency emission near 460 nm and 475 nm for the excitation of Rydberg states [2] in alkali metals, such as potassium and rubidium. Since this type of laser possesses a unique combination of features such as high output power, low noise properties, wide spectral coverage, high functionality offered by the external cavity designs and compact form, it can be an excellent candidate for the application in the studies of quantum effects employing Rydberg states. So far, we have devoted significant attention to design and fabrication of adequate semiconductor gain chips, and performed their characterization in simple linear laser cavity. Gain mediums consist of packets of InGaAs QWs embedded in AlGaAs and GaAsP barrier layers. Fundamental emission is obtained at the wavelengths of 915 nm and 957 nm. Emitting in the blue is produced with the intracavity frequency doubling in BBO crystal. Our final set up employs Z-shaped cavity. This type of resonator geometry allows us to use intracavity elements, such as birefringent filters and etalons, for obtaining laser emission in single mode regime and possibility to tune the wavelength to desired one. We present our experimental results utilizing new cavity shape and give an outlook for the further improvements of laser characteristics.

REFERENCES

- [1] M. Kuznetsov, F. Hakimi, R. Sprague, and A. Mooradian, *IEEE Photon. Technol. Lett.*, vol. 9, pp. 1063–1065 (1997).
- [2] R. Low, H. Weimer, J. Nipper, J. B. Balewski, B. Butscher, H. P. Buchler, and T. Pfau, *J. Phys. B: At. Mol. Opt. Phys.* 45, 113001 (2012).

Applications of optically pumped magnetometers

Zoran. D. Grujić¹, Saša Topić^{1,2}

¹*Institute of Physics Belgrade, 11070 Belgrade, Serbia*

²*Faculty of Physics, Studentski Trg 12, University of Belgrade. 11001 Belgrade, Serbia*

Contact: Z. D. Grujić (zoran.grujic@ipb.ac.rs)

Abstract. From discovery of lodestone (naturally magnetized magnetite) we became aware of and started to use magnets and magnetic fields. First application was navigation, a lodestone, suspended so it could turn, would orient itself in direction of Earth's magnetic field – first compass! Advances in science and technology led to development of wide variety of sensors detecting magnetic field [1]. What kind of sensor will be used for specific application is determined by sensitivity, size, accuracy, price, operational costs, operational temperature range, intensity, gradient and bandwidth of measured magnetic field... Optically pumped magnetometers (OPMs) hold their ground in between of highly sensitive, but expensive and cumbersome SQUIDS (Superconducting Quantum Interference Device) from one side and fluxgates, giant-magneto-resistive magnetometers (GMR), hall sensors, and many other being less expensive, but also less sensitive and less accurate. In other hand OPMs might be categorized by medium on which they operate where most notable are alkali vapor, noble gases, and nitrogen vacancy (NV) based magnetometers.

OPMs have broad range of applications in biomedical research, for example magnetoencephalography [2] and magnetocardiography [3]. They are used for mapping of geomagnetic fields in ore exploration, and archaeology [5]. In other hand OPMs are exploited in fundamental research for exotic interactions detection [6] and for measurement of neutron electrical dipole moment [7]. Nitrogen vacancies (NV) in diamond present miniature version of OPM that could be placed very close to a source of magnetic field thus overcoming its, presently, not very high sensitivity.

In the presentation several applications of OPMs will be discussed.

REFERENCES

- [1] A. Grosz, M.J. Haji-Sheikh, S.C. Mukhopadhyay, editors, *High sensitivity magnetometers*, Springer, Switzerland (2017)
- [2] N.V. Nardelli, A.R. Perry, SP Krzyzewski, and SA Knappe, *EPJ Quantum Technology* **7** (2020),11.
- [3] G. Bison, R. Wynands, A. Weis, *App. Phys. B* **76** (2003), 325-8.
- [4] J.M. Taylor, P. Cappellaro, L. Childress, L. Jiang, D. Budker, P.R. Hemmer, A. Yacoby, R. Walsworth, M.D. Lukin, *Nature Physics* **4** (2008), 810-6
- [5] G. Oelsner, V. Schultze, R. IJsselsteijn, F Wittkämper, R. Stolz, *Phys. Rev. A* **99** (2019), 013420.
- [6] S. Afach, D. Budker, G. DeCamp, V. Dumont, Z.D. Grujić, H. Guo, D.J. Kimball, T.W. Kornack, V. Lebedev, W. Li, H. Masia-Roig, *Physics of the Dark Universe* **22** (2018), 162-80.
- [7] C. Abel, et. al., *Phys. Rev. A* **101** (2020), 053419

All-optical Cs magnetometer based on free alignment precession

Marija M. Ćurčić¹, Andrej Bunjac¹, Saša Topić¹, Jonas Hinkel², Theo Scholtes²,
Zoran. D. Grujić¹

(1) *Institute of Physics, Pregrevica 118, 11080 Belgrade, Serbia*

(2) *Leibniz Institute of Photonic Technology, Albert-Einstein-Strasse 9, 07745 Jena, Germany*

Contact: M. M. Ćurčić (marijac@ipb.ac.rs)

Abstract. Since their first demonstration, in 1960s [1], optically pumped atomic-based magnetometers (OPM) [2] have been in the focus of many scientific studies. Recently, they have been of special interest due to their wide range of application, including measurements of magnetic fields in bio-medical science, environmental and geo-science.

Our focus is on the development of a compact, portable magnetometer for geophysical field measurements. We present the design and operating principle of a novel kind of OPMs, optically-pumped Cs magnetometer based on a free alignment precession (FAP). This type of magnetometer is free of some limitations of conventional OPMs, such as frequency shifts and systematic displacements. We use a paraffin-coated Cs vapor cell. Magnetometer operates at room temperature. The atomic medium is pumped with linearly polarized amplitude-modulated light at a double Larmor frequency, $2\omega_L$. This process generates spin alignment. After the optical pumping, the decay of the spin polarization can be detected in the weaker probe beam passing through the cell. The information on the magnetic field and Larmor frequency can be gathered via further signal processing.

We will discuss the influence of various parameters on the performance of our magnetometer – state of polarization of the probe and pump beam, angle between the probe and the external magnetic field, probe and pump powers and lengths. We will present our set-up and first test measurements. Finally, we will give an outlook for the further work.

REFERENCES

- [1] A. L. Bloom, *Principles of operation of the rubidium vapor magnetometer*, Appl. Opt. **1**, 61 (1962).
- [2] A. Weis, G. Bison, Z. D. Grujić, *High Sensitivity Magnetometers - Magnetic Resonance Based Atomic Magnetometers*, pp 361-424 (2016).

New bounds on ultralight bosonic ALP matter mass and SM fermion coupling strengths from Science run 5 of GNOME OPM network

Saša Topić, and Zoran D. Grujić on behalf of the GNOME collaboration

Institute of Physics, Pregrevica 118, 11080 Belgrade, Serbia

Contact: Saša Topić (stopic@ipb.ac.rs)

Abstract. In this progress report we present newest results from the science Run 5 of Global Network of Optical Magnetometers for Exotic physics (GNOME). Long uninterrupted time series and novel pre-processing methods provide more stringent bounds that are used to estimate exclusion domain of mass and interaction strength of hypothetical axionic or axion like dark matter in form of topological defects. Hypothetical axions or Axion Like Particles (ALP's) are form of ultralight bosonic matter that are postulated in order to solve strong CP problem and matter-antimatter imbalance in the Universe [1] [2]. This type of Dark Matter (DM) has a number of detectable signatures, one being in form of axionic field coupling to fermions that results in formation of pseudo-magnetic fields during passage through topological defect. The GNOME experiment described in [3] and [4] is designed as GPS referenced worldwide distributed network of quantum cross-correlated sensors that increases its sensitivity reach and excludes false positives. Science Run 5 lasted from 24. August to 26. October of 2022 and included, at the highest extent, 11 stations and is characterized by lowest amount of noise, optimal station placement and highest quality of data compare to previous Science Runs [5]. Novel scheme for measuring bandwidth of each station and its frequency response was devised along with pulse sequences that made possible re-scaling in order of site-specific coupling of Optically pumped magnetometers (OPM) to magnetic perturbation as presented (Fig. 1). We present various sensors in the GNOME network and will quantify some of them in terms of bandwidth, test pulse regularity and Allen plots. Special accent will be given to still unofficial exclusion domain that is extrapolated from GNOME Science Run 2 [6] processing with the Run 5 data and pre-processing methods.

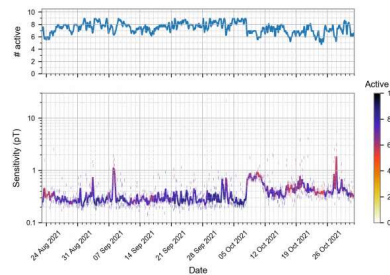


Figure 1: Representation of number of active sensore over time (upper frame); representation of rescaled magnetic field sensitivity of entire network (lower frame).

REFERENCES

- [1] D. Budker and M.V. Romalis, *Nat. Phys.*, **23** (2007), 229
- [2] M. Pospelov, et al., *Phys. Rev. Lett.* **110** (2013), 021803
- [3] Pustelny et al., *Ann. Phys.* **525** (2013), 659-670
- [4] M.P. Ledbetter, M.V. Romalis and D.F. Jackson Kimball, *Phys. Rev. Lett.* **110** (2013), 040402
- [5] S. Afach et. *Nature Physics.* **17** (2021), 1396-1401
- [6] S. Afach et al. *Physics of The Dark Universe.* **22**, (2018), 162

Why do we need accurate magnetometers and how to realize them

Zoran D. Grujić¹, Andrej Bunjac¹, Saša Topić¹, Marija M. Ćurčić¹,
Jonas Hinkel², Theo Scholtes²

(1) *Institute of Physics, Pregrevica 118, 11080 Belgrade, Serbia*

(2) *Leibniz Institute of Photonic Technology, Albert-Einstein-Straße 9, 07745 Jena, Germany*

Contact: Z. Grujić (zoran.grujic@ipb.ac.rs)

Abstract. In most cases magnetometers have been developed with accent on sensitivity in order to detect very small changes of magnetic fields like brain waves, magnetic field of beating heart or variations of geomagnetic field. For such applications exist wide range of devices like fluxgates, GMR, SQUID, OPM (Optically Pumped Magnetometer), etc. [1]. Our goal is to improve accuracy or precision of OPMs based on vapors of alkali metals while retaining most of their sensitivity. Alkali metals are very well studied, their properties are measured and theoretically calculated to high precision. It is to expect that a sensor, based on, for example cesium, should be easy to deploy and understand in various schemes. It turned out this is not the case and future research is required in order to overcome heading errors of cesium based OPMs.

Accurate OPMs would have broad range of applications like precision experiments in fundamental research (like measurement of nEDM – neutron Electrical Dipole Moment), metrology, space explorations and for mapping of geomagnetic fields. The latter would benefit in archaeology, mining operations and from improved quality in tracking changes in global distribution and intensity of the Earth's magnetic field.

In my talk I will present the old nEDM experiment at PSI [2] and its improvements towards its next generation – n2EDM [3]. The last part of the talk will be dedicated to accurate magnetometry with Free Spin Precession (FSP) [4] and Free Alignment Precession (FAP) magnetometers. If time permits, prospects of a ⁴He magnetometer will be discussed.

REFERENCES

- [1] A. Grosz, M. J. Haji-Sheikh and S. C. Mukhopadhyay (eds), *High Sensitivity Magnetometers*, Springer International Publishing, Cham (2017)
- [2] C Abel, ... Z.D. Grujić, ... et. al., *Phys. Rev. Lett.* **124** (2020), 081803
- [3] NJ Ayres, ... Z.D. Grujić, ... et. al., *The European Physical Journal C* **81** (2021), 1-32
- [4] Z.D. Grujić, P.A. Koss, G. Bison, A. Weis, *The European Physical Journal D* **69** (2015), 135

Heading error of Free Alignment Precession optically pumped magnetometer

Zoran D. Grujić¹, Marija Ćurčić¹, Aleksandra Milenković¹, Jonas Hinkel², Theo Scholtes²

(1) *Institute of Physics Belgrade, Pregrevica 118, 11080, Serbia*

(2) *Leibniz Institute of Photonics Technology, Albert-Einstein-Strasse 9, 07745 Jena, Germany*

Contact: Zoran D. Grujić (zoran.grujic@ipb.ac.rs)

Abstract. While optically pumped magnetometers (OPMs) have demonstrated competitive sensitivities and low cost with respect to competition, their performance for high accuracy applications is not well studied. Our first attempt [1] to optimize an all optical free spin precession (FSP) magnetometer was success. In unpublished investigations that followed that work it was discovered that FSP magnetometer suffers from a heading error two orders of magnitude larger than its sensitivity. In order to improve the performance a method that uses linearly polarized light Free Alignment Precession (FAP) was proposed.

In this study we measure the Larmor frequency, in a spherical cesium cell with antirelaxation coating, simultaneously with two linearly polarized beams. The experimental setup allows arbitrary mutual orientations of magnetic field $B_0 \approx 1.58 \mu\text{T}$ and directions of polarizations of light beams.

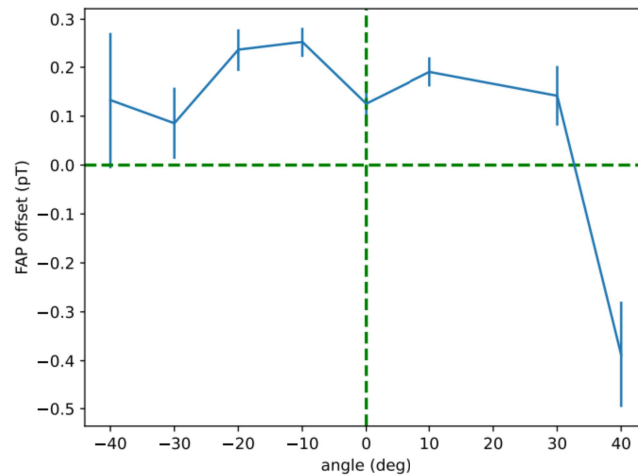


Figure 1. Preliminary measurement of the heading error of a FAP magnetometer. Direction of the B_0 and polarization direction of one of probe beams was fixed while we varied the polarization direction of the second probe beam.

From Fig. 1. we learn that, in this particular case, the heading error is below 1 pT, thus at least six orders of magnitude below B_0 . Further investigation is under way.

REFERENCES

- [1] ZD Grujić, PA Koss, G Bison, A Weis, *Eur. Phys. J. D* **69** (2015), 135

Optically pumped magnetometer aiming for highest accuracy

Jonas Hinkel, Theo Scholtes, Zoran D. Grujić and Ronny Stolz

(1) Leibniz Institute of Photonic Technology, *Albert-Einstein-Straße 9, 07745 Jena (Germany)*

(2) *Institute of Physics Belgrad, Pregrevica 118, Belgrad (Serbia)*

Contact: J. Hinkel (Jonas.Hinkel@leibniz-ipht.de)

Abstract. Today, the demand for magnetometers with highest resolution is driven by applications relying on the detection of tiny magnetic field changes, typically in the pT down to the fT range, as encountered in biomagnetism [1], geophysics [2], or in fundamental physics experiments [3]. In addition to sensor resolution and noise level, properties like accuracy and rotational invariance of the measurement are vital in scenarios where the sensor has to be applied from mobile platforms such as in geophysical exploration methods [2]. While optically pumped magnetometers (OPMs) [4] are based on a principle which enables them to yield scalar and absolute measurements of the magnetic field, they do suffer from systematic effects which may exceed their intrinsic sensitivity limit, thus severely compromising their performance especially in mobile applications.

I am going to present the concept and first experimental results of a novel OPM measurement technique called free alignment precession. Sensors based on this technique will offer highest sensitivity combined with unprecedented accuracy by strongly reducing systematic effects inherent to other state-of-the-art OPMs [5].

REFERENCES

- [1] Wyllie, R. et al. *Optics Letters* 37, 2247-2249 (2012).
- [2] Stolz, R., Becken, M., et al. *Miner. Econ.* (2022).
- [3] Ayres, N.J., Ban, G., Bienstman, L. et al. *Eur. Phys. J. C* 81, 512 (2021).
- [4] Budker, D., Romalis, M., *Nature Phys* 3, 4 (2007).
- [5] Oelsner, G., et al. *Phys. Phys. Rev. A* 99 (2019).

Acknowledgements

We gratefully acknowledge financial support from the Federal Ministry of Education and Research (BMBF) of Germany under Grant No. 01DS21006 (FRAPOPM) handled and supervised by DLR Projektträger (DLR-PT) and under Grant No. 13N15436 (OPTeM) handled and supervised by Verein deutscher Ingenieure (VDI).

Response of a scalar M_x magnetometer to modulation the of transverse magnetic field

Marija M. Ćurčić¹, Aleksandra Milenković¹, Jonas Hinkel², Theo Scholtes², Zoran D. Grujić¹

(1) Institute of Physics Belgrade, Pregrevica 118, 11080, Serbia

(2) Leibniz Institute of Photonics Technology, Albert-Einstein-Strasse 9, 07745 Jena, Germany

Contact: M. M. Curcic (marijac@ipb.ac.rs)

Abstract. We present our work on behavior of a M_x variant of OPM (Optically Pumped Magnetometer) [1] under modulation of the transverse magnetic field. Set-up is based on a single beam double-resonance scalar magnetometer with spherical Cs paraffin coated cell, operating in free running mode at room temperature. The medium is pumped at D_1 line at $F_g=4 \rightarrow F_e=3$ transition with circularly polarized light, where direction of light is parallel to the oscillating magnetic field that is driving the magnetic resonance at Larmor frequency, Fig. 1. We have studied the response of our magnetometer to the changes in applied magnetic field, perpendicular to the main offset field. Set of Helmholtz coils is used for the generation of additional modulating field. Using lock-in detection we obtained in-phase and quadrature components of the transmitted laser power oscillations. Specially, with the main offset field in z-direction, and applied modulation in yz plane, phase of the signal experience unexpected behavior for a scalar magnetometer.

We will present our measurements results and discuss which conditions, with respect to amplitude and frequency of modulating field, so as its orientation, give rise to the before mentioned signal abnormalities.

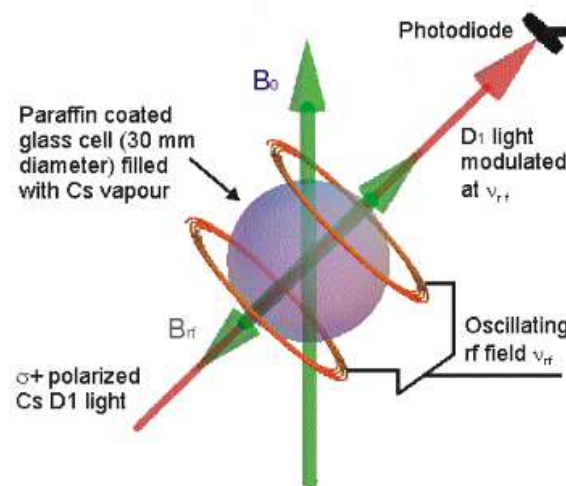


Figure 1. Schematic of the scalar M_x optically pumped magnetometer.

REFERENCES

- [1] A. Weis, G. Bison, Z.D. Grujić, *High Sensitivity Magnetometers – Magnetic Resonance Based Atomic Magnetometers*, Springer, pp 361-424 (2016).

Affordable VCSEL diode laser for high resolution spectroscopy of cesium D₁ line

Aleksandra Milenković¹, Marija Ćurčić¹, Jonas Hinkel², Theo Scholtes², Zoran D. Grujić¹

(1) *Institute of Physics Belgrade, Pregrevica 118, 11080, Serbia*

(2) *Leibniz Institute of Photonics Technology, Albert-Einstein-Strasse 9, 07745 Jena, Germany*

Contact: Aleksandra Milenković (aleksandra.milenkovic@ipb.ac.rs)

Abstract. This study tests the applicability of the commercially available VCSEL Laser diodes from Throlabs (part number L895VH1) for laser spectroscopy of cesium D₁ line. This 895 nm, 0.2 mW AlGaAs VCSEL diode is a compact light source suited for a variety of applications. It comes in a TO-46 package with an H pin configuration. It outputs a circular Gaussian beam, which is linearly polarized. Its spectral profile is single mode and it is suitable for single frequency applications [1]. On of first use cases of VCSEL's in magnetometry has been presented by P. Swindt et. al. [2].

The laser diode in experiments is mounted inside a high thermal-conductivity aluminum block with an NTC temperature sensor in close proximity to the laser diode and a Peltier element below the aluminum mount connecting it with a larger aluminum bottom plate serving as heatsink. A home-made laser driver consists of laser current source and PID controller for temperature stabilization. The current source can be controlled via a potentiometer allowing currents from 0 mA up to 2 mA and via modulation input. The temperature of the diode is measured by a NTC connected to a PID which controls a Peltier element. The laser threshold was estimated to approximately be 0.6 mA, and we obtained output power of 250 μW at 2 μA of current. We compared performance of the Thorlabs diode with Toptica ECDL laser system. Interestingly, the signal of the Toptica ECDL had more noise above 500 Hz than the VCSEL diode. Measurements also show that it is possible to use the diode for FSP (Free Spin Precession) experiment.

Compactness and affordability and performance of the L895VH1 laser diode at wavelength of cesium D₁ line shows great prospects in development of laser spectroscopy based devices like portable magnetometers and student exercises for education.

REFERENCES

- [1] Thorlabs, *Product Specification Sheet*, <https://www.thorlabs.com/thorproduct.cfm?partnumber=L895VH1>, (accessed: 10.02.2023.).
- [2] P. Swindt, S. Knappe, V. Shah, L. Hollberg, J. Kitching, L-A. Liew, and J. Moreland . "Chip-scale atomic magnetometer." *Applied Physics Letters* 85.26 (2004): 6409-6411.

Frequency Estimating Device for Optically Pumped Magnetometer

Miloš Subotić^{1,2}, Zoran D. Grujić²

(1) Faculty of Technical Sciences, Trg Dositeja Obradovića 6, 21102 Novi Sad, Serbia

(2) Institute of Physics Belgrade, Pregrevica 118, 11080 Belgrade, Serbia

Contact: M. Subotić (milos.subotic@uns.ac.rs)

Abstract. For high precision measurement of magnetic field at high rate with Optically Pumped Magnetometer (OPM) device for frequency estimating is used. This device beside acquisition of sinusoidal exponentially decaying signal also need to process samples with algorithm, such as least-squares curve fitting [1], to estimate Larmor frequency ω_L (or $2\omega_L$) which is proportional to magnetic field. Architecture of frequency estimating device is shown Fig. 1. For acquisition of OPM output electrical signal with duration up to 100 ms is done with 3 MSPS 18-bit Analog-Digital Converter (ADC) with digitized samples being sent to Field Programmable Gate Array (FPGA) from Zynq family [2]. Samples are stored to DDR memory and later are processed by ARM CPU and Coprocessor in FPGA fabric. FPGA boots its software with frequency estimation algorithm from SD Card and results are sent to Personal Computer (PC).

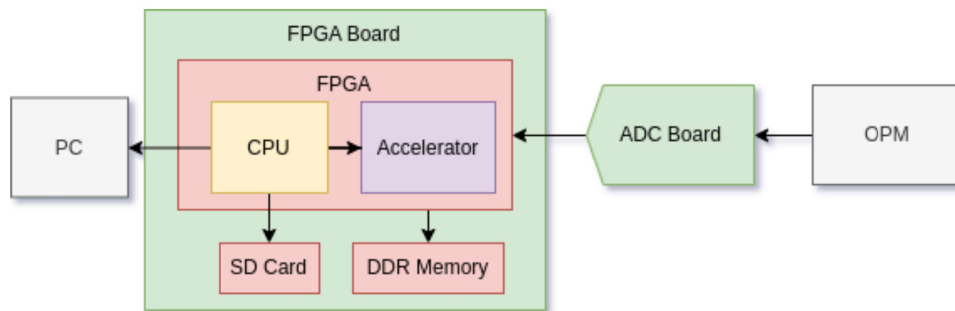


Figure 1. Architecture of measurement device.

Algorithm is first implemented using off-the-shelf least-squares curve fitting library in Julia language and run on PC with synthetic and measured signals. Duration of single estimation is 4 s. To make this estimation running below needed 100 ms, appropriate acceleration is needed by parallelisation. Code is further profiled to expose most demanding parts which will be accelerated. That code is then simplified and transcribed in C++ language, which could be compiled on PC and for ARM on FPGA. Accelerator is implement in FPGA fabric as double precision floating point SIMD processor with simplified instruction set. While the most algorithm is run on ARM CPU, the most demanding parts of algorithm are implemented in assembly language and run on accelerator processor. Such partitioning approach gives flexibility to easily change existing algorithm or faster implementing new algorithm. Prototype of device is implemented on ZedBoard FPGA board with accelerator working at 190 MHz with single estimation around 400 ms, which is limited by size and speed of FPGA. Further step is obtaining Zynq Ultrascale family FPGA board from Trezz, which will enable needed 100 ms estimation time.

REFERENCES

- [1] Visschers, Jim C., et al. "Rapid parameter determination of discrete damped sinusoidal oscillations". *Optics Express* 29.5 (2021): 6863-6878.
- [2] Crockett, Louise H., et al. "The Zynq book: embedded processing with the ARM Cortex-A9 on the Xilinx Zynq-7000 all programmable SoC". *Strathclyde Academic Media* (2014).

Analysis of the dynamic RF projection phase in True Scalar Cs Magnetometers

Andrej B. Bunjac¹, Zoran D. Grujić¹, M. M. Ćurčić¹, Theo Scholtes², Jonas Hinkel²

(1) *Institute of Physics Belgrade, Pregrevica 118a, 11000 Belgrade, Serbia*

(2) *Leibniz Institute of Photonic Technology, Albert-Einstein-Straße 9, 07745 Jena, Germany*

Contact: Andrej B. Bunjac (bunjac@ipb.ac.srs)

Abstract. A true scalar magnetometer (TSM) is one where the phase is independent of the magnetic field orientation and instead depends on the modulus only. We analyzed a magnetometer consisting of a paraffin-coated glass cell filled with CS vapor where the RF field is parallel to the light propagation direction while oscillating at Larmor frequency [1]

The magnetometer was applied in the measurement of small magnetic field components orthogonal to the main field direction. Experimental measurements of the RF projection phase show significantly different behavior in cases where the transversal field component is perpendicular to the RF field and when it is in the plane formed by the main magnetic and the RF fields. For the “in-plane” case the RF projection phase doesn’t show any perturbation on changing the intensity or field direction, while the “perpendicular” case shows significant peaks and slow relaxations under the same circumstances.

This phenomenon was initially explored through numerical simulations with a model that shows good agreement with experimental results and later backed with analytical calculations of the Bloch equation for this case in Cartesian spin components. The equations were solved analytically by moving into a rotating frame of reference and applying the Rotating Wave Approximation (RWA) and the disambiguation of the remaining solution terms by the significance of their contribution. The results show a simplified picture of the described problem but capture the qualitative behavior well. The measurements, numerical solution and the analytical approach will all be presented in a wholesome description and analysis of the described phenomenon.

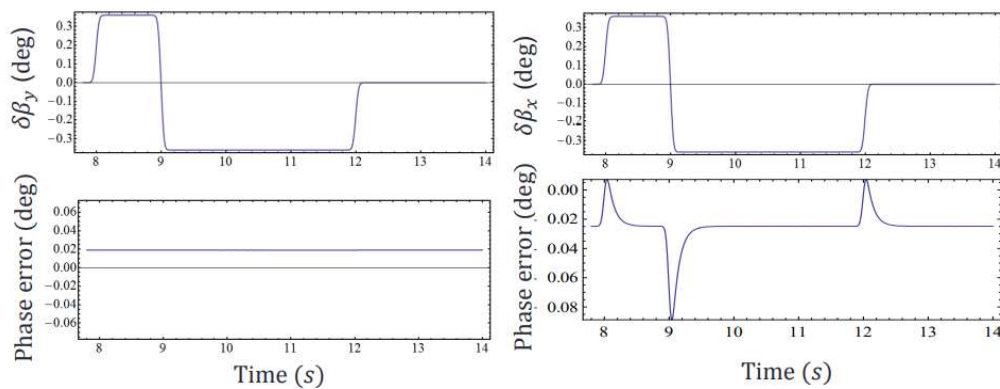


Figure 1. Two different field geometries considered for the DC transverse magnetic field scans. Left: The “in-plane” case with constant phase error, Right: The “perpendicular” case with phase error perturbations.

REFERENCES

- [1] Weis A., Bison G., Grujić Z.D. (2017) Magnetic Resonance Based Atomic Magnetometers. In: Grosz A., Haji-Sheikh M., Mukhopadhyay S. (eds) High Sensitivity Magnetometers. Smart Sensors, Measurement and Instrumentation, vol 19. Springer, Cham.

On prospects of the free alignment precession based optically pumped magnetometer

Zoran D. Grujić¹, Marija Ćurčić¹, Aleksandra Kocić¹, Theo Scholtes²

(1) *Institute of Physics Belgrade, Pregrevica 118, 11080 Belgrade, Serbia*

(2) *Leibniz Institute of Photonic Technology, Albert-Einstein-Strasse 9, D-07745 Jena, Germany*

Contact: Zoran D. Grujić (zoran.grujic@ipb.ac.rs)

Abstract. The optically pumped magnetometers (OPMs) with respectable sensitivity, moderate dimensions and low maintenance costs have their niche as the preferred tools for a number of applications. We pay special attention to a sub niche of applications where high accuracy is the priority. For such applications we use Free Alignment Precession (FAP) in Cs cells with antirelaxation coating. The first step involves optical pumping with linearly polarized light, followed by the observation of a FAP signal in the intensity of a weak probe beam in the second step. The applied method is similar to the previously demonstrated free spin precession magnetometer [1].

We will present our current progress in study of the accuracy of a FAP magnetometer related to the light shift. We will also share our recent results on the proposal for an improved method of optical pumping by frequency modulated light that leads to the increased signal quality and, hopefully, improved accuracy too.

REFERENCES

- [1] Z.D. Grujić, P.A. Koss, G. Bison, A. Weis, *Eur. Phys. J. D* **69**, 135, (2015)

Lock-in Frequency Estimation Algorithm for Optically Pumped Magnetometer

Miloš Subotić^{1,2}, Zoran D. Grujić²

(1) Faculty of Technical Sciences, Trg Dositeja Obradovića 6, 21102 Novi Sad, Serbia

(2) Institute of Physics Belgrade, Pregrevica 118, 11080 Belgrade, Serbia

Contact: M. Subotić (milos.subotic@uns.ac.rs)

Abstract. In previous work [1], device for estimation of Larmor frequency f_L (which is proportional to magnetic field) was proposed. That device was based on least-squares curve fitting algorithm [2]. In this work, lock-in method based on unwrapped phase φ fitting for frequency estimation is implemented. Algorithm diagram of frequency estimating is shown in Fig. 1. First step to calculate phase difference φ between f_{est} and input signal. If frequencies of the signals are not equal, the phase difference φ is linear function with deviations only due to noise. The φ is further fitted to linear model and f_{est} is incremented by line slope φ' . Process is iterated until φ' drops below threshold i.e. phase difference become close to zero, i.e. f_{est} and f_L are almost equal.

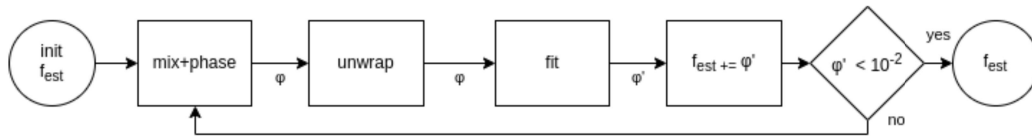


Figure 1. Lock-in frequency estimation algorithm.

Fig. 2. shows in detail calculation of phase difference φ by mixing sine and cosine of estimated frequency f_{est} with input signal, band-pass FIR filtering and argument extraction [3]. Due to use of band-pass filter, exponential decay and offset are also filtered.

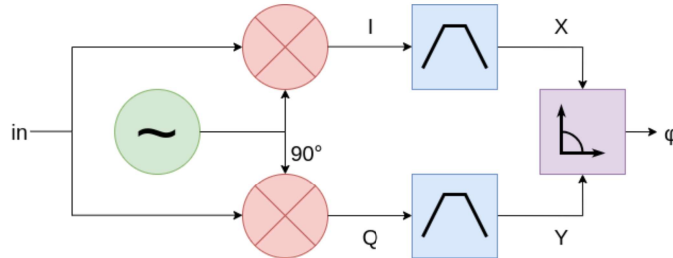


Figure 2. Mixing and phase calculation.

This algorithm is currently implemented as PC program and has similar accuracy and precision below Cramer-Rao Lower Bound as previous work [1]. Implementation of computationally most intensive part of this algorithm (which is mixing, especially FIR filtering) in a FPGA accelerator is a work in progress.

REFERENCES

- [1] Subotic, Milos, et al. "Frequency Estimating Device for Optically Pumped Magnetometer". *16th Photonics Workshop* (2023).
- [2] Visschers, Jim C., et al. "Rapid parameter determination of discrete damped sinusoidal oscillations". *Optics Express* 29.5 (2021): 6863-6878.
- [3] Macias-Bobadilla, Gonzalo, et al. "Dual-phase lock-in amplifier based on FPGA for low-frequencies experiments." *Sensors* 16.3 (2016): 379.

Experimental and theoretical study of the dynamic phase projection error of M_x magnetometer – Progress report

Marija Ćurčić¹, Aleksandra Kocić¹, Zoran D. Grujić¹, Theo Scholtes²

(1) *Institute of Physics Belgrade, Pregrevica 118, 11080 Belgrade, Serbia*

(2) *Leibniz Institute of Photonic Technology, Albert-Einstein-Strasse 9, D-07745 Jena, Germany*

Contact: Marija Ćurčić (marijac@ipb.ac.rs)

Abstract. We will present our recent results of the study of a true scalar optically pumped magnetometer M_x [1]. We will show the design of our experimental set-up, based on the sensing of the magnetic field by the means of the optically pumped Cs vapor, at room temperature. Specially, we have been interested in the response of our magnetometer to the fast modulating transversal magnetic field. The active medium is pumped with a circularly polarized light. The same laser beam is being used for both, optical pumping, and reading out the spin state of the Cs atom ensemble. The precessing spin, driven by oscillating magnetic rf field, imprints a variation in the light intensity of the transmitted light at the Larmor frequency. The phase of the signal is analyzed by the lock-in amplifier.

Alongside the experimental work, we have also performed a theoretical study of the effect of interest. The model is based on the Bloch equation. We have solved it both analytically and numerically. We will present the obtained results and compare them to the ones experimentally measured. The results of the analytical model will be presented in the case of the resonant magnetic field, while the numerical model has been applied in the case of the frequency detuned magnetic field. We will demonstrate a good agreement between the experimental and theoretical results in both cases. Finally, with the obtained observations and conclusions, we are able to point out to the limitations of this type of optically pumped magnetometer when it comes to particular applications.

REFERENCES

- [1] A. Weis, G. Bison, Z.D. Grujić, *High Sensitivity Magnetometers – Magnetic Resonance Based Atomic Magnetometers*, Springer, pp 361-424 (2016).

Experimental and theoretical study of the phase response of M_x magnetometer to modulating transversal magnetic field

M.M. Ćurčić¹, A. Milenković¹, A. Bunjac¹, T. Scholtes² and Z. Grujić¹

¹*Institute of Physics Belgrade, University of Belgrade, Serbia*

²*Leibniz Institute of Photonic Technology, Jena, Germany*

e-mail: zoran.grujic@ipb.ac.rs

We will present our results on the study of a scalar optically pumped magnetometer (OPM) [1]. More precisely, we investigate the phase response of a true scalar M_x magnetometer to the sudden changes of transversal magnetic field. As a sensing element we employ paraffin coated cell filled with Cs. A single light source is used for both pumping (polarizing) the medium and probing i.e. reading out a variation in the intensity of the resonant light due to the applied magnetic field. Pump light is circularly polarized. The wave vector and RF magnetic field that drives the spin precession are at 45° with the respect to the main static magnetic field B_0 as presented on Fig. 1. Magnetometer operates at room temperature. Set of Helmholtz coils is used for the generation of additional modulating field. The sensor head is placed inside a three layer mu-metal shielding. Changes of the magnetometer response are detected with a lock-in amplifier, which enables us to obtain in-phase and quadrature components of the transmitted probe signal.

In addition to experimental study, we did both numerical and analytical modeling of a described system. Theoretical study is based on the transient Bloch equation. Analytically, the equation is solved in rotating frame after applying a rotating wave approximation (RWA). In this manner, we were able to obtain set of simple equations describing detected signal, decomposed into in-phase and quadrature components, for comparison with experimental results and tracking of the phase evolution.

The model results show good agreement with the experiment. Being a scalar magnetometer, our sensor should not experience any changes in the measured phase depending on the orientation of the applied modulating field. However, both experimental measurements and model predictions have demonstrated this is not the case. With the main offset field in z-direction, and applied modulation in yz plane, phase of the signal shows an unexpected behavior for a scalar magnetometer. We will present obtained results, and discuss which conditions lead to the before mentioned signal abnormalities.

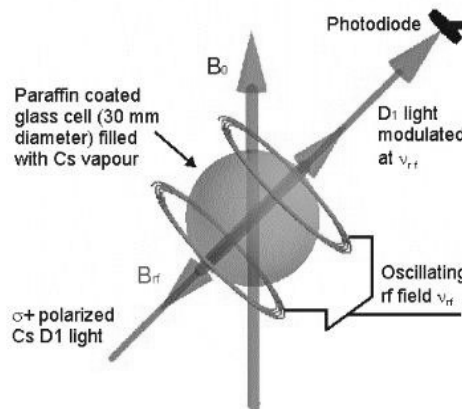


Figure 1. Schematic of the scalar M_x optically pumped magnetometer.

REFERENCES

- [1] A. Weis *et al.*, High Sensitivity Magnetometers – Magnetic Resonance Based Atomic Magnetometers, Springer, pp 361-424 (2016).

An upgrade of the primary length standard of Republic of Serbia

Z.D. Grujić¹, M.G. Nikolić¹, S. Zelenika² and M.D. Rabasović¹

¹*Institute of Physics Belgrade, University of Belgrade, Photonica Center, Pregrevica 118, 11080 Belgrade – Zemun, Serbia*

²*Directorate of Measures and Precious Metals, Mike Alasa 14, 11158 Belgrade, Serbia*

e-mail: rabasovic@ipb.ac.rs

We have performed upgrade of the electronics for frequency stabilization of the primary length standard of Republic of Serbia. The standard is red HeNe laser at 633 nm. The stabilization is done by standalone electronics based on Arduino microcontroller. We have used off-the-shelf electronics components, thus, setup is simple and inexpensive. The stabilization electronics is connected to the computer via USB port. The purpose of the computer is only to communicate with the user, not to perform stabilization, thus, the computer can be easily replaced in case of failure. Namely, the previous version of the standard, based on the computer, broke down because the computer broke down, and the repair was not cost effective.

The stabilization procedure is very well known [1]. Namely, the saturation spectroscopy of the I₂ vapor has been used. Back mirror is scanned at frequency f , and the signal of the laser power at $3f$ is detected. Digital lock-in detection is used to improve signal-to-noise ratio. Also, we have developed analog electronics to improve performances of the setup.

We achieved very good results despite using cheap and simple components. E.g. we have reached fractional frequency difference equal to $3.1 (25.3) \times 10^{-12}$.

REFERENCES

[1] https://www.bipm.org/documents/20126/41549560/M-e-P_I2_633.pdf/c4c25f25-ae65-e05d-402a-9bfc84c715c3.

Measurement of the heading error of a free alignment precession magnetometer

Z.D. Grujić¹, M. Ćurčić¹, A. Milenković¹, J. Hinkel² and T. Scholtes²

¹*Institute of Physics Belgrade, Serbia*

²*Leibniz Institute of Photonic Technology, Jena, Germany*

e-mail: zoran.grujic@ipb.ac.rs

Optically pumped magnetometers (OPMs) have proved competitive sensitivities, robustness, and low cost with respect to competition, but their performance for high accuracy applications is not well studied. Optimization of an all optical free spin precession (FSP) magnetometer [1] has shown possible high accuracy of a such device. But, in unpublished investigations that followed that work it emerged that FSP magnetometer suffers from a heading error two orders of magnitude larger than its sensitivity. Then an investigation on applicability of Free Alignment Precession (FAP) produced by linearly polarized light was started.

We studied Larmor frequency measured simultaneously by two linearly polarized beams, in a spherical cesium cell with antirelaxation coating. If frequencies measured by those beams are different and function of the angle between their polarizations a heading error is detected. The experimental setup allows arbitrary mutual orientations of magnetic field $B_0 \approx 1.58 \mu\text{T}$ and directions of polarizations of light beams.

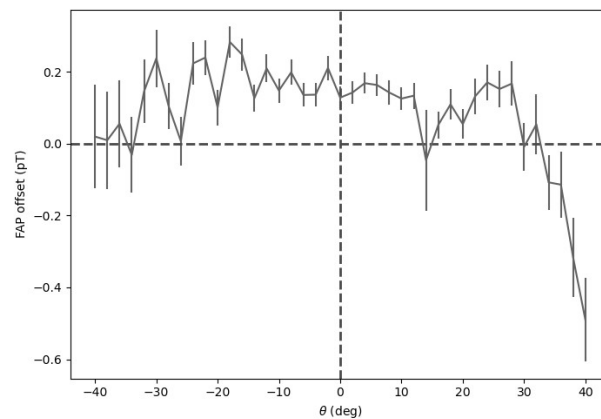


Figure 1. Measurement of the heading error of a FAP magnetometer. Direction of the B_0 and polarization direction of one of probe beams was fixed while we varied the polarization direction of the second probe beam.

In this particular case (see Fig. 1), the heading error is below 1 pT, thus at least six orders of magnitude below B_0 . Further investigation is under way.

REFERENCES

[1] Z.D. Grujić *et al.*, Eur. Phys. J. D 69, 135 (2015).

Search for topological defects of bosonic ultralight field with optically pumped magnetometer: design, calibration, and sensitivity of the Belgrade GNOME station

S. Topić^{1,2}, and Z. D. Grujić¹

¹*Institute of Physics, Belgrade, Serbia*

²*Faculty of Physics, University of Belgrade, Serbia*

e-mail: sasa.topic.sale@gmail.com

We present the design and calibration of optically pumped magnetometer (OPM), based on a paraffin coated cesium cell, and estimate its ultimate reach in terms of mass and interaction strength of hypothetical axionic or axion-like dark matter fields in form of a topological defects. Hypothetical axions or Axion Like Particles (ALP's) are form of ultralight bosonic matter that are postulated in order to solve strong CP problem, matter-antimatter imbalance in the Universe and maybe even solve current Λ CDM observational discrepancies and H_0 tensions. Dark matter problem, exuberated by negative results of search for WIMP's, core-cusp problem, missing satellites problem and others may be solved by a type of ultralight matter model which can reconcile GR and MOND paradigms.

This model has several detectable signatures, one being in the form of axionic field couplings to Standard Model fermions via the pseudomagnetic fields that are generated during passage through topological defects. The GNOME experiment is designed as a GPS referenced worldwide distributed network of quantum cross-correlated sensors that increases its sensitivity, discovery reach and excludes false positives by methodology similar to LIGO network. Belgrade GNOME station is built around a double resonant optical cesium magnetometer in Mx configuration and is functioning as a scalar magnetometer with a sensitivity less than $100 \text{ fT}/\sqrt{\text{Hz}}$. We will present different modes of operations, give an overview of atomic magnetometry and quantify various noise contributions. Special attention will be given to PSD, sensitivities, and stability over short and long baselines of the setup. Guidelines for future work and a foreseen improvements shall also be mentioned.

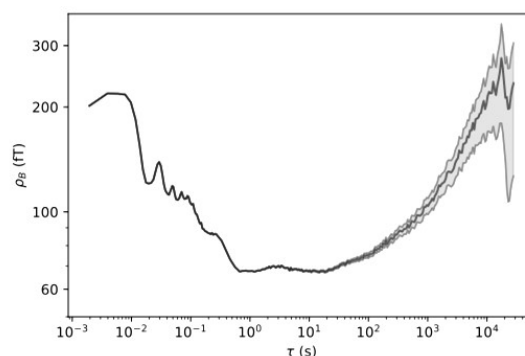


Figure 1. Allan standard deviation of magnetic field recorded by OPM in phase-locked loop.

REFERENCES

- [1] D. Budker and M.V. Romalis, *Nat. Phys.*, 23 (2007), 229
- [2] M. Pospelov, et al., *Phys. Rev. Lett.*, 110 (2013), 021803
- [3] J. Preskill, M. B. Wise and F. Wilczek, *Phys. Lett.*, B120 (1983), 127
- [4] S. M. Carroll, *Phys. Rev. Lett.*, 81 (1998), 3067
- [5] Pustelny et al., *Ann. Phys.*, 525 (2013), 659-670
- [6] M.P. Ledbetter, M.V. Romalis and D.F. Jackson Kimball, *Phys. Rev. Lett.*, 110 (2013), 040402

Phase projection errors in rf-driven optically pumped magnetometers

Zoran D. Grujić¹, Marija Ćurčić¹, Aleksandra Kocić¹, Theo Scholtes²

¹ Institute of Physics Belgrade, University of Belgrade, Serbia

² Leibniz Institute of Photonic Technology, Albert-Einstein-Strasse 9, D-07745 Jena, Germany

Very prominent implementations of optically pumped magnetometers (OPM) detect the magnetic resonance in an alkali atomic vapor within a static magnetic field by the help of a small radio-frequency (rf) magnetic field [1]. Here, in the so-called M_x magnetometer, the amplitude and phase of modulation of light transmitted through a vapor cell is monitored in dependence on the rf field frequency. Magnetic resonance is observed when the rf frequency coincides with the Larmor frequency of the atoms, which is given by the external magnetic field of interest. In this case the modulation amplitude is maximized, and the phase displays a dispersive and monotonic dependence on rf field frequency. This is made use of to form an active feedback circuit, in which the rf field frequency is tuned to follow changes of the (quasi-)static magnetic field by means of a phase-locked-loop (PLL).

We discuss the dependence of the phase on important experimental quantities, especially the angles between light propagation direction, rf and static magnetic field vectors. While the static dependence is considered to be well understood [2], we find a hitherto unknown dynamic phase response in the M_x magnetometer when subject to rotations of the static magnetic field. By solving Bloch equations we obtain analytical expressions which can explain our experimental observations using a paraffin-coated spherical Cs vapor cell [3]. We show the resulting fundamental limitations of rf-driven OPMs and highlight the importance of the findings in terms of real-world sensing applications.

[1] A. Weis, G. Bison, and Z. D. Grujić, Magnetic resonance based atomic magnetometers, in *High Sensitivity Magnetometers*, edited by A. Grosz, M. J. Haji-Sheikh, and S. C. Mukhopadhyay (Springer International Publishing, Cham 2017) pp 361-424.

[2] S. Colombo, V. Dolgovskiy, T. Scholtes, Z. D. Grujić, V. Lebedev, and A. Weis, *Applied Physics B* **123**, 1432 (2017).

[3] N. Castagna, G. Bison, G. Di Domenico, A. Hofer, P. Knowles, C. Macchione, H. Saudan, and A. Weis, *Applied Physics B* **96**, 763 (2009).

Search for ultralight bosonic ALP dark matter in form of topological defects: design, calibration, sensitivities of Belgrade GNOME station

Saša Topic^{1,2,3}, and Zoran D. Grujić³

¹*Faculty of Physics, Studentski Trg 12, University of Belgrade. 11001 Belgrade, Serbia*

²*Faculty of Mathematics, Studentski Trg 16, University of Belgrade., 11158 Belgrade, Serbia*

³*Institute of Physics, Center for Photonics, Pregrevica 118, 11080 Belgrade, Serbia*

Contact: Saša Topic (sasa.topic.sale@gmail.com)

Abstract. In this work we present design, calibration of double resonant magnetometer and estimate on mass and interaction strength of hypothetical axionic or axion like dark matter namely their topological defects in form of domain walls or spatially distributed agglomerations (Q balls, axion stars, condensates etc.). Hypothetical axions or Axion Like Particles (ALP's) are form of ultralight bosonic matter that are postulated in order to solve strong CP problem and matter-antimatter imbalance in the Universe. Dark matter problem, exuberated by negative results of search for WIMP's, supersymmetric particles, core-cusp problem, missing satellites problem and others may be solved by type of ultralight matter into which axions fit. Also, by this type of matter GR and MOND can be reconciled and it has a many detectable signatures, one being in form of axionic field coupling to fermions that results in formation of pseudomagnetic fields during passage through topological defect. The GNOME experiment is designed as GPS referenced worldwide distributed network of quantum cross-correlated sensors that increases its sensitivity reach and excludes false positives by methodology similar to LIGO network. Belgrade GNOME station is built around double resonant RF optical cesium magnetometer in Mx configuration and is capable to function as scalar magnetometer with a sensitivity less than $100\text{fT}/\sqrt{\text{Hz}}$. We will quantify various noise contributions, PSD, sensitivities, and stability over short and long baselines of the setup. Special accent will be given to experiment design and comparison between laser and lamp pumped magnetometer. Guidelines for future work and improvements shall also be mentioned.

REFERENCES

- [1] D. Budker and M.V. Romalis, *Nat. Phys.*, **23** (2007), 229
- [2] M. Pospelov, et al., *Phys. Rev. Lett.* **110** (2013), 021803
- [3] J. Preskill, M. B. Wise and F. Wilczek, *Phys. Lett*, **B120** (1983), 127
- [4] S. M. Carroll, *Phys. Rev. Lett.* **81** (1998), 3067
- [5] Pustelny et al., *Ann. Phys.* **525** (2013), 659-670
- [6] M.P. Ledbetter, M.V. Romalis and D.F. Jackson Kimball, *Phys. Rev. Lett.* **110** (2013), 040402

DC Transverse Magnetic Field Scan in True Scalar Cs Magnetometers

Andrej B. Bunjac¹, Zoran D. Grujić¹, M. M. Ćurčić¹, S. Topić¹, Theo Scholtes², Jonas Hinkel²

(1) *Institute of Physics Belgrade, Pregrevica 118a, 11000 Belgrade, Serbia*

(2) *Leibniz Institute of Photonic Technology, Albert-Einstein-Straße 9, 07745 Jena, Germany*

Contact: Andrej B. Bunjac (bunjac@ipb.ac.srs)

Abstract. We present a true scalar magnetometer (TSM) consisting of a paraffin-coated glass cell filled with Cs vapor with the $\vec{B}_{rf} \parallel \vec{k}$ geometry where \vec{k} is the light propagation direction for the optical pumping and \vec{B}_{rf} is a magnetic field oscillating at Larmor frequency [1]. Spin dynamics of this system are described by the Bloch equations in Cartesian spin components:

$$\frac{d\vec{S}}{dt} = \vec{S} \times \vec{\omega} - \gamma\vec{S} + \gamma_p\vec{k}.$$

The measurement of a DC magnetic field transverse to the main magnetic field in the system produced unexpected signal shapes in different transverse directions. Specifically, with the RF field in the YZ plane, the DC field in the x-direction produces unfavorable signal when modulated at sufficiently high frequencies. This difference in the dynamic RF projection phase is investigated by solving the above equation both analytically and numerically with different transverse field geometries. The theoretical calculations produce results that are in good agreement with the observed systematic effects during measurement.

We will present the measurements in both described geometries and discuss the differences between the obtained signals. We will also present the details of both calculation processes and discuss how the results compare to the measurements.

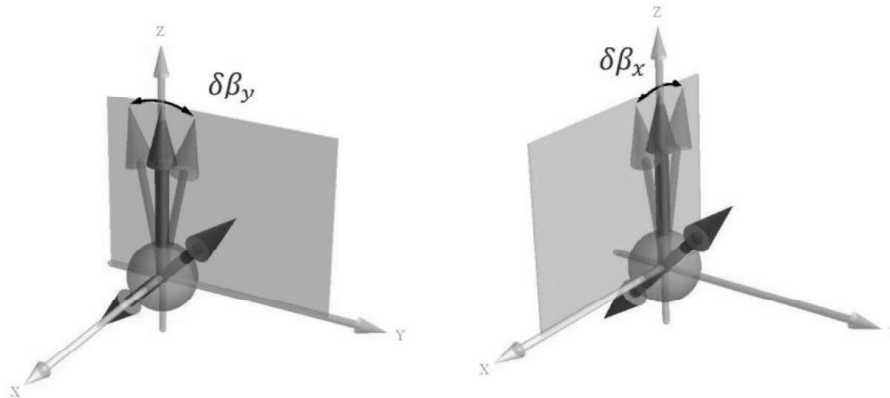


Figure 1. Two different field geometries considered for the DC transverse magnetic field scans. The additional magnetic DC field manifests as a small “rotation” of the main field in the appropriate direction.

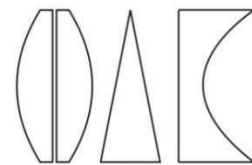
REFERENCES

- [1] Weis A., Bison G., Grujić Z.D. (2017) Magnetic Resonance Based Atomic Magnetometers. In: Grosz A., Haji-Sheikh M., Mukhopadhyay S. (eds) High Sensitivity Magnetometers. Smart Sensors, Measurement and Instrumentation, vol 19. Springer, Cham.

University of Belgrade
Institute of Physics Belgrade
Kopaonik, March 14-17, 2021



Book of Abstracts
14th Photonics Workshop
(Conference)



14th Photonics Workshop (2021)

Book of abstracts

Kopaonik, Serbia, March 14-17, 2021

Publisher, 2021:

Institute of Physics Belgrade

Pregrevica 118

11080 Belgrade, Serbia

Editors:

Dragan Lukić, Marina Lekić, Zoran Grujić

ISBN 978-86-82441-52-6

Printed by:

NEW IMAGE d.o.o.

Tošin Bunar 185, Belgrade

Number of copies: 30

CIP - Каталогизација у публикацији - Народна библиотека Србије, Београд

535(048)

681.7(048)

66.017/.018(048)

PHOTONICS Workshop (14 ; 2021 ; Kopaonik)

Book of Abstracts / 14th Photonics Workshop, (Conference), Kopaonik,
March 14-17, 2021 ; [editors Dragan Lukić, Marina Lekić, Zoran Grujić]. -
Belgrade : Institute of Physics, 2021 (Belgrade : New image). - 46 str. :
ilustr. ; 25 cm

Tiraž 30. - Registar.

ISBN 978-86-82441-52-6

а) Оптика - Апстракти б) Оптоелектроника - Апстракти с) Технички
материјали - Апстракти

COBISS.SR-ID 33997321

University of Belgrade
Institute of Physics Belgrade
Kopaonik, March 13-16, 2022



Book of Abstracts
15th Photonics Workshop
(Conference)



15th Photonics Workshop (2022)

Book of abstracts

Kopaonik, Serbia, March 13-16, 2022

Publisher, 2022:

Institute of Physics Belgrade

Pregrevica 118

11080 Belgrade, Serbia

Editors:

Dragan Lukić, Marina Lekić, Zoran Grujić

ISBN 978-86-82441-55-7

Printed by:

NEW IMAGE d.o.o.

Tošin Bunar 185, Belgrade

Number of copies: 55

CIP - Каталогизација у публикацији - Народна библиотека Србије, Београд

535(048)

681.7(048)

66.017/.018(048)

PHOTONICS Workshop (15; 2022; Kopaonik)

Book of Abstracts / 15th Photonics Workshop, (Conference), Kopaonik,
March 13-16, 2022; [editors Dragan Lukić, Marina Lekić, Zoran Grujić]. -
Belgrade: Institute of Physics, 2022 (Belgrade: New image). - 72 str.:

ilustr.; 25 cm

Tiraž 55. - Registar.

ISBN 978-86-82441-55-7

а) Оптика - Апстракти б) Оптиелектроника - Апстракти с) Технички
материјали - Апстракти

COBISS.SR-ID 60055049

University of Belgrade
Institute of Physics Belgrade
Kopaonik, March 12-15, 2023



Book of Abstracts
16th Photonics Workshop
(Conference)



16th Photonics Workshop (2023)

Book of abstracts

Kopaonik, Serbia, March 12-15, 2023

Publisher, 2023:

Institute of Physics Belgrade

Pregrevica 118

11080 Belgrade, Serbia

Editors:

Dragan Lukić, Marina Lekić, Zoran Grujić

ISBN 978-86-82441-59-5

Printed by:

NEW IMAGE d.o.o.

Tošin Bunar 185, Belgrade

Number of copies: 55

CIP - Каталогизација у публикацији - Народна библиотека Србије, Београд

535(048)
681.7(048)
66.017/.018(048)

PHOTONICS Workshop (16; 2023; Kopaonik)

Book of Abstracts / 16th Photonics Workshop, (Conference), Kopaonik, March 12-15, 2023;
[organized by Institute of Physics Belgrade, Photonics center [and] Optical Society of Serbia];
[editors Dragan Lukić, Marina Lekić, Zoran Grujić]. - Belgrade: Institute of Physics, 2023
(Belgrade: New image). - 68 str.: ilustr; 25 cm

Tiraž 55. - Registar.

ISBN 978-86-82441-59-5

а) Оптика -- Апстракти б) Оптоелектроника -- Апстракти в) Технички материјали -- Апстракти

COBISS.SR-ID 109912585

University of Belgrade
Institute of Physics Belgrade
Kopaonik, March 10-14, 2024



Book of Abstracts
17th Photonics Workshop
(Conference)



17th Photonics Workshop (2024)

Book of abstracts

Kopaonik, Serbia, March 10-14, 2024

Publisher, 2024:

Institute of Physics Belgrade

Pregrevica 118

11080 Belgrade, Serbia

Editors:

Dragan Lukić, Marina Lekić, Zoran Grujić

ISBN 978-86-82441-62-5

Printed by:

NEW IMAGE d.o.o.

Tošin Bunar 185, Belgrade

Number of copies: 60

CIP - Каталогизacija y publikaciji
Народна библиотека Србије, Београд

535(048)

681.7(048)

66.017/.018(048)

PHOTONICS Workshop (17 ; 2024 ; Kopaonik)

Book of Abstracts / 17th Photonics Workshop, (Conference), Kopaonik, March 10-14, 2024 ;
[organized by Institute of Physics Belgrade, Photonics center [and] Optical Society of Serbia] ;
[editors Dragan Lukić, Marina Lekić, Zoran Grujić]. - Belgrade : Institute of Physics, 2024
(Belgrade : New image). - 75 str. : ilustr. ; 25 cm

Tiraž 60. - Registar.

ISBN 978-86-82441-62-5